ASME
SETTING THE STANDARD

Journal of Engineering for Gas Turbines and Power

Published Monthly by ASME

VOLUME 132 • NUMBER 1 • JANUARY 2010

Transactions of the ASME, Journal of Engineering for Gas Turbines and Power (ISSN 0742-4795) is published monthly by The American Society of Mechanical Engineers, Three Park Avenue, New York, NY 10016. Periodicals postage paid at New York, NY and additional mailing offices. POSTMASTER: Send address changes to Transactions of the ASME, Journal of Engineering for Gas Turbines and Power, c/o THE AMERICAN SOCIETY OF MECHANICAL ENGINEERS, 22 Law Drive, Box 2300, Fairfield, NJ 07007-2300. **CHANGES OF ADDRESS** must be received at Society headquarters seven weeks before they are to be effective. Please send old label and new address. **STATEMENT from By-Laws.** The Society shall not be responsible for statements or opinions advanced in papers or ... printed in its publications (B7.1, par. 3).

(Contents continued on inside back cover)

This journal is printed on acid-free paper, which exceeds the ANSI Z39.48-1992 specification for permanence of paper and library materials. ♾™
♻ 85% recycled content, including 10% post-consumer fibers.

Journal of Engineering for Gas Turbines and Power JANUARY 2010

Volume 132, Number 1

The ASME Journal of Engineering for Gas Turbines and Power is abstracted and indexed in the following:

AESIS (Australia's Geoscience, Minerals, & Petroleum Database), Applied Science & Technology Index, Aquatic Sciences and Fisheries Abstracts, Civil Engineering Abstracts, Compendex (The electronic equivalent of Engineering Index), Computer & Information Systems Abstracts, Corrosion Abstracts, Current Contents, Engineered Materials Abstracts, Engineering Index, Enviroline (The electronic equivalent of Environment Abstracts), Environment Abstracts, Environmental Science and Pollution Management, Fluidex, INSPEC, Mechanical & Transportation Engineering Abstracts, Mechanical Engineering Abstracts, METADEX (The electronic equivalent of Metals Abstracts and Alloys Index), Pollution Abstracts, Referativnyi Zhurnal, Science Citation Index, SciSearch (The electronic equivalent of Science Citation Index), Shock and Vibration Digest

Journal of Engineering for Gas Turbines and Power

Editorial

A Monthly Publication Schedule for *Journal of Engineering for Gas Turbines and Power* (JEGTP)

A happy new year to all of you! I am pleased to announce that effective 1 January 2010, JEGTP will be published monthly. This is made possible because JEGTP continues to receive a large number of outstanding papers from all over the world in the field of gas turbines, nuclear power, internal combustion engines, and fossil energy. Strong synergies exist among these seemingly diverse fields. For example, nuclear reactor power generation cycles are beginning to employ gas turbines operating with novel working fluids such as helium. Also, advances in gas turbine radial blade designs, secondary flow controls, aerodynamic flutter, rotor dynamics, bearing technology, and thermal barrier coatings are readily finding applications in tomorrow's steam turbine and turbo generator designs. JEGTP has successfully integrated these papers into an "energy and power" journal for which *the whole is greater than the sum of its parts*. To celebrate this success, JEGTP has a new front cover, more journal resources, and ASME has doubled the number of published issues. All these improvements represent a "win-win" situation for authors, readers, subscribers, and other journal stakeholders.

The year 2008 ended with a global economic downturn, and during 2009 many uncertainties remain as to the future. Professional societies and technical journals face challenges on various fronts such as research funding, conference attendance, industry participation, and journal paper numbers. However, confronting these challenges creates new opportunities, strengths, and eventual success; JEGTP falls into this mold. JEGTP is positioned extremely well in the most important global priority today—Gas Turbines, Energy, and Power. Further, ASME seeks to galvanize a "Grand Energy Challenge," focused on achieving a sustainable and diverse national and global energy system/environment. JEGTP papers provide the best technological solutions to define the technology, policy, and market issues to achieve a more sustainable energy system. Finally, improvements put into effect during the last three years have increased JEGTP's five-year impact factor (paper citation index) almost threefold and a record number of reprints are being ordered. So, your papers are being read, cited, and purchased. The JEGTP editorial team comprises associate editors, editorial assistant, reviewers, and ASME journal production staff. I am very grateful to all the team members for their superlative efforts.

To secure rapid publication of your papers, below are a few tips for the authors:

- JEGTP publishes papers on a first-come, first-publish basis. Therefore, authors must remain engaged during the publication process and check the status of their papers regularly on the journaltool as it progresses through various stages of review, copyright form submission, production files uploading, and *electronic* editing of page proofs. Please contact an associate editor with your journal paper number if your paper continues to remain inactive.
- This year, ASME has simplified the 1903 (copyright release) form significantly. Please sign and file this form electronically and *not* by fax. This is more efficient and, should this form get lost or misplaced, you will have an e-mail record. Also, ASME is in the process of integrating the conference and journal copyright forms. Therefore, beginning in 2010, authors will not have to file a duplicate conference form if their conference paper is accepted for journal publication.
- Prepare the production files of your paper by following the exact procedure (do not be creative here!) taking care to eliminate all errors (visit "Authors Center" and read the instructions). Also, graphics must have a resolution of at least 600 dpi. Poor-quality graphics are unacceptable and color figures must be checked on your B&W laser printer for adequate contrast before digitizing them. Graphics files must be labeled with Fig. or Figure (.tif or .eps).

In summary, JEGTP's editorial team and resources are available to meet your publication needs and the global energy challenges for the emerging decade. During 2009, JEGTP has grown to cover a wide range of topics in gas turbines, nuclear engineering, internal combustion engines, and fossil power generation. Now, JEGTP truly represents a centerpiece of ASME's "Grand Energy Challenge" strategy. JEGTP remains the number ONE ranked journal in the world in the area of gas turbine engineering, nuclear power, internal combustion engines, and fossil energy. Your outstanding and continuing research contributions will keep it there!

Dilip R. Ballal
Editor

Ceramic Gas Turbine Development: Need for a 10 Year Plan

Mark van Roode
Solar Turbines Incorporated,
San Diego, CA 92186

Ceramic gas turbine development that started in the 1950s has slowed considerably since most of the large-scale ceramic gas turbine development programs of the 1970s–1990s ended. While component durability still does not meet expectations, the prospect of significant energy savings and emission reductions, potentially achievable with ceramic gas turbines, continues to justify development efforts. Four gas turbine applications have been identified that could be commercially attractive: a small recuperated gas turbine (microturbine) with ~35% electrical efficiency, a recuperated gas turbine for transportation applications with ~40% electrical efficiency with potential applications for efficient small engine cogeneration, a ~40% efficient midsize industrial gas turbine, and a ~63% (combined cycle) efficient utility turbine. Key technologies have been identified to ensure performance and component durability targets can be met over the expected life cycle for these applications. These technologies include a Si_3N_4 or SiC with high fracture toughness, durable EBCs for Si_3N_4 and SiC, an effective EBC/TBC for SiC/SiC, a durable oxide/oxide ceramic matrix composite (CMC) with thermally insulating coating, and the next generation CMCs with high strength that can be used as structural materials for turbine components for small engines and for rotating components in engines of various sizes. The programs will require integrated partnerships between government, national laboratories, universities, and industry. The overall cost of the proposed development programs is estimated at U.S. $100M over 10 years, i.e., an annual average of U.S. $10M. [DOI: 10.1115/1.3124669]

Introduction

Ceramic gas turbine development activity has been ongoing since the 1950s, heavily supported by governments in the United States, Japan, the countries of the European Union, and those of the former Soviet Union. Primary drivers for the programs were promises of improved high temperature durability, compared to superalloys, improved engine performance, light weight, and independence from strategic elements (Co, Cr, Ni, etc.). The technical literature on this topic is extensive as can be seen from several recent reviews [1–4].

Rig and engine testing during the early development work, typically for up to several hundreds of hours, showed good potential for performance improvements with ceramics. However, long-term engine tests that started in the 1990s, conducted for many thousands of hours at field demonstration sites, revealed shortcomings that severely dampened the enthusiasm of the gas turbine designers for ceramics. The major problems were poor impact resistance of the leading monolithic ceramics (Si_3N_4 and SiC), and accelerated degradation of ceramic components fabricated from silicon-based monolithics and ceramic matrix composites (CMCs) because of water vapor attack in the gas turbine hot section. The poor impact resistance of the monolithics is related to their fracture toughness (K_{1C}5–9 MPa $m^{0.5}$), which is much lower than for gas turbine alloys (K_{1C}35–65 MPa $m^{0.5}$) [5]. SiC/SiC ceramic matrix composites (CMCs), introduced for gas turbine development in the 1990s, have improved toughness (K_{1C}~20 MPa $m^{0.5}$), compared to monolithics, but do not have the strength required for long-life rotating components (200–300 MPa). The allowable stress for SiC/SiC CMCs is limited by the proportional limit stress (PLS). For current SiC/SiC CMCs, the PLS is ~180 MPa in the direction of loading. The ultimate tensile strength (UTS), which determines the design limit for oxide/oxide CMCs, is ~195 MPa [6]. CMCs therefore have been mostly used for stationary gas turbine parts (combustor liners, transition pieces, nozzles, and shrouds).

There have been substantial efforts to extend the life of ceramic hot section components against water vapor attack by applying protective coatings. Environmental barrier coatings (EBCs) have successfully extended the life of silicon-based CMCs while thermal insulation barriers have made oxide-based CMCs feasible design materials as well. The application of EBCs to reduce environmental degradation of silicon-based monolithics has been less successful thus far. The environmental limitations of the ceramics and life extension through protective coatings have been extensively documented in the aforementioned review publications [1–4]. The allowable range of operating temperatures and pressure ratios range for gas turbines of different sizes with ceramic components was the topic of a recent ASME paper [5].

Several roadmap studies have resulted in recommendations for development work to overcome the deficiencies of ceramic materials [7,8]. While these studies were commendable, they implicitly assumed that the resources for the recommended programs would be available. Historically, funding for ceramic gas turbine development work has come primarily from government. And since this source of funding has been greatly reduced worldwide over the past 5 years, it should not come as a surprise that, several years after the publication of the roadmap studies, the pace of ceramic gas turbine technology development has slowed considerably. While good progress is still being made with the evaluation of CMCs for stationary components for midsize and larger gas turbines, primarily because of the ongoing work at several United States gas turbine manufacturers with some government support, the advancements for monolithics for commercial gas turbine applications over the past decade have been minimal. The author has

Contributed by the International Gas Turbine Institute for publication in the JOURNAL OF ENGINEERING FOR GAS TURBINES AND POWER. Manuscript received March 28, 2008; final manuscript received April 4, 2008; published online September 29, 2009. Review conducted by Dilip R. Ballal. Paper presented at the ASME Turbo Expo 2008: Land, Sea and Air (GT2008), Berlin, Germany, June 9–13, 2008.

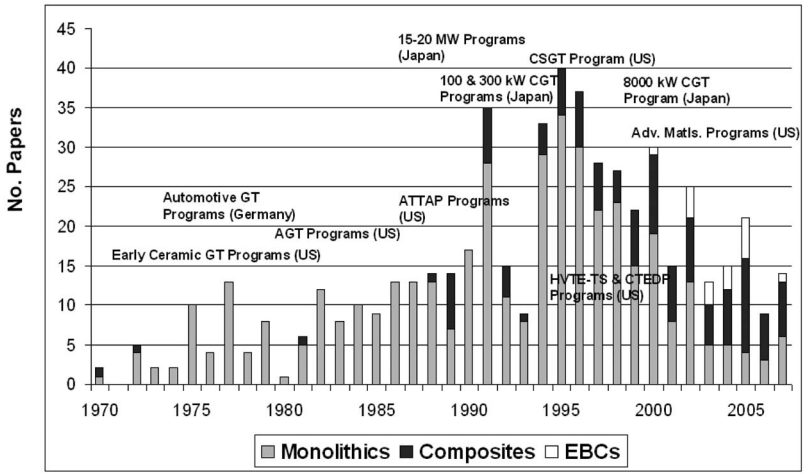

Fig. 1 Number of ceramic papers at the Annual Gas Turbine Conference of ASME/IGTI since the 1970s

tallied the number of papers published at the annual conference of the International Gas Turbine Institute (IGTI) of ASME from 1970 through 2007 (see Fig. 1). Notice that the high level of activity during the 1970s through the 1990s started to drop off substantially since 2000 when most of the large-scale ceramic gas turbine development programs ended. Also, note that in the 1990s CMCs started to emerge while the interest in monolithics dropped precipitously. An even more recent development is represented by EBCs, required for long life of Si-based ceramics.

The purpose of this paper is to review key deficiencies in materials properties required for durable ceramic gas turbines, to briefly outline the technological gaps on the road to commercial viability, and outline areas where support will be needed to overcome the technical hurdles.

Ceramic Gas Turbine Field Test Experience

Figure 2 summarizes the approximate performance ranges of three classes of gas turbines and selected milestones in ceramic gas turbine engine experience, primarily from endurance field testing (see also Ref. [5]). It can be seen that the only commercial applications are in low-firing small engines. Honeywell International is using APU pump rings, TFE 731 seal rings, and air turbine starter cutting rings. There have been a number of long-term engine field tests by Solar Turbines Incorporated (Solar), Rolls-Royce USA, and General Electric Co., but thus far these have not resulted in commercial applications. There is good potential for SiC/SiC and oxide/oxide CMCs, provided protective coatings are applied. Solar has accumulated over 88,000 h of engine field test experience with CMCs with a long term test of ~15,000 h on a set of SiC/SiC combustor liners with Si/Mullite+BSAS/BSAS EBC and ~25,000 h on a single hybrid oxide CMC (aluminosilicate/alumina CMC+aluminosilicate friable graded insulation (FGI)) liner [5,9–11]. General Electric Co. has tested a limited number of SiC/SiC shrouds with EBC for ~5,000 h in a 7FA engine [12]. Additional long term testing of stationary hot section CMC parts is ongoing at General Electric Co. and Siemens Power Generation, and it is expected that these tests will eventually lead to commercial application of CMCs, perhaps in the 2010–2015 time frame.

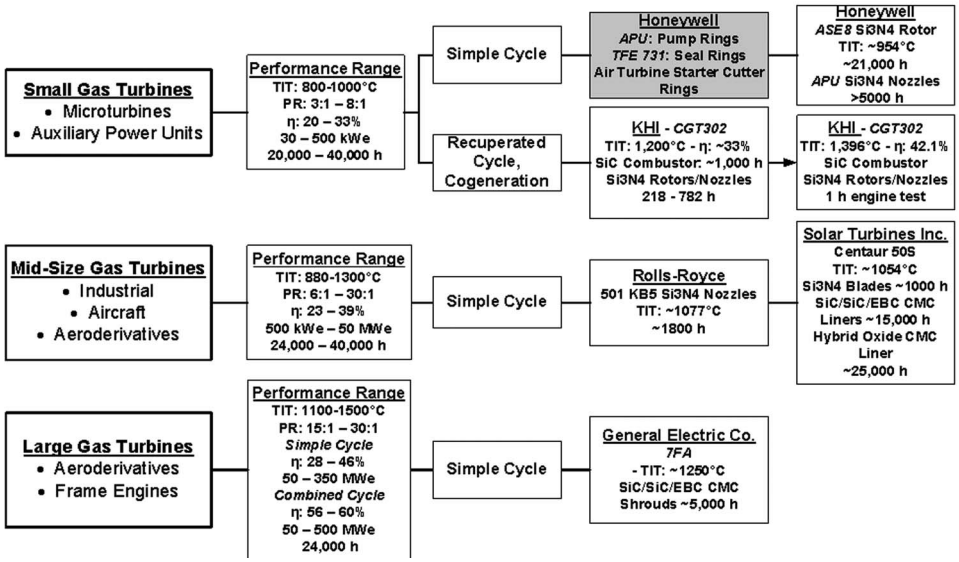

Fig. 2 Classes of gas turbines and ceramic engine field test experience—commercial applications (shaded text)

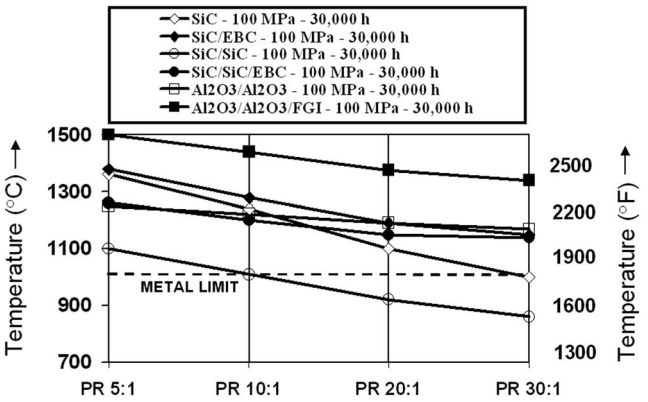

Fig. 3 Upper use temperatures for various ceramic materials for combustor liners (modified from Ref. [5])

Closing Technology Gaps

van Roode and Ferber [5] analyzed the temperature/stress limitations for the application of monolithic silicon-based ceramics and CMCs, considering two long-term failure modes, creep and water vapor attack in the ceramic hot section. The model used was based on extrapolations of existing data for these materials for the conditions in the hot section of gas turbines, operating over a range of pressure ratios (PR 5:1 to 30:1), component temperatures (up to 1500°C), and typical gas turbine life (up to 30,000 h). The model assumes that the allowable design stress and temperatures in a ceramic component are reduced from the creep rupture limits because the component cross section decreases as a result of surface recession from environmental attack in the gas turbine hot section. The model for oxide/oxide CMCs with a thick FGI has recently been updated by assuming a gradual increase in the temperature of the substrate with recession of the FGI. This assumption results in an increase in upper use temperature (UUT) for the hybrid oxide system over the data reported previously [5]. Figure 3 shows the modified approximate UUT for various ceramic combustor liners over a range of pressure ratios. Figure 4 shows UUT for ceramic nozzles and rotating parts. Material systems include monolithic Si_3N_4 and SiC, and SiC/SiC and Al_2O_3/Al_2O_3 CMCs. Coatings considered were Si/mullite/BSAS type EBCs and alumina-based FGIs.

In this paper, it is assumed that the major technical impediments for the application of monolithic ceramics (Si_3N_4 and SiC) in commercial gas turbine products are insufficient resistance against impact from debris, creep, and water vapor attack in the hot section. The latter two limitations also apply to CMCs. Other technical factors such as fatigue and erosion/corrosion resistance have not been considered.

Additionally, there are economic factors such as component cost and markets, and funding for development. Next, we will discuss ceramic technology development needs by focusing on selected ceramic gas turbine applications that are representative of small gas turbines (microturbines), midsize industrial gas turbines, and utility gas turbines. The four advanced gas turbine applications listed in Table 1 have performance objectives that represent a performance improvement (1–3% efficiency) over current all-metal engines.

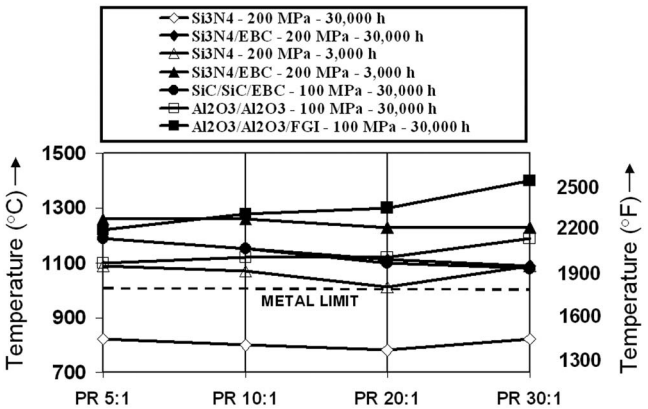

Fig. 4 Upper use temperatures for various ceramic materials for nozzles/rotating parts (modified from Ref. [5])

(1) A 35% efficient microturbine (recuperated) operating at 1200°C TIT (turbine inlet temperature). McDonald and Rogers reported 35% as the projected efficiency limit for an all-metal small engine but noted that the majority of first metallic microturbines fall short of 30% [13]. The highest efficiency reported for an all-metal microturbine is ~33.5% for the 200 kW Capstone C200 [14]. A microturbine with a ceramic turbine stage and recuperator with a high-Ni alloy core such as Alloy 625 or equivalent material, operating at a TIT of 1200°C, could achieve efficiency in the 35–37% range based on calculations reported by McDonald and Rogers [13]. A 35% efficiency objective would be a realistic intermediary step on the road to a 40% efficient small ceramic gas turbine.

(2) A 40% efficient recuperated small gas turbine, similar to the prototype engines of the automotive ceramic gas turbine programs in the United States, Japan, and Europe during the 1980s and 1990s. To achieve this level of efficiency a TIT of ~1370°C would be required, necessitating a ceramic turbine and most likely a ceramic recuperator [13]. On the other hand, Kawasaki Heavy Industries (KHI), under the Japanese 300 kW CGT program, reported having achieved an efficiency of 42.1% at 1396°C TIT with 322 kW of output power in a ceramic engine with metallic recuperator operating at a pressure ratio of 8:1 [15]. An efficiency of 40% will make these small gas turbines competitive with reciprocating engines. An application with a long service life (30,000 h) would be extremely challenging. A shorter life application would be more readily achievable. A 3000 h life goal as represented by a passenger car would be ideal. Unfortunately, the automotive application has receded from view as a development target because of the wide acceptance of hybrid vehicles and the expected emergence of all-electrical vehicles. Still, there may be other transportation applications such as buses, trucks, etc., that could benefit from a highly efficient small ceramic engine with excellent emissions signature. Gaining experience with such an application may facilitate a future small 40% efficient ceramic gas turbine for long-term (30,000 h) service life.

(3) An efficient industrial gas turbine operating with efficiencies 1–2% greater than existing all-metal gas turbines, currently operating in simple, recuperated, and/or intercooled cycles. Examples of already efficient all-metal gas turbines are the 4.6 MW recuperated Solar *Mercury*™ 50 that has a rated electrical efficiency of 38.5% and emits low-single digit NO_x and the industrialized aeroderivative 25 MW Pratt & Whitney FT8 engine with ~38% electrical efficiency [16]. The incorporation of ceramics combined with TIT increase could improve the efficiency to 40%. Note that very efficient aeroderivatives that already have efficiencies >40% would achieve further efficiency enhancement.

(4) An advanced utility gas turbine with 2–3% improvement in thermal efficiency. With H-technology utility gas turbines achieve 60% efficiency in combined cycle operation. The

Table 1 Ceramic gas turbines and requirements for development (TBO: time between overhauls—shaded: not applicable)

			Critical technologies		
Engine class	Performance objectives	Ceramic components	Ox/Ox CMC	SiC/SiC CMC	Si_3N_4, SiC
Small gas turbine (microturbine)	Recuperated cycle TIT=1200°C PR=3:1–8:1 η=35% 100–300 kWe NO_x<10 ppmv TBO: 30,000 h	Combustor liner	+FGI	+EBC	Uncoated or +EBC
		Nozzles	+FGI Small radii	+EBC Small radii	+EBC K_{1C}=15–20 MPa $m^{0.5}$
		Integral rotors	Small radii NGCMC σ>200 MPa	+EBC NGCMC Small radii σ>200 MPa	+EBC K_{1C}=15–20 MPa $m^{0.5}$
Small gas turbine	Recuperated cycle TIT=1370°C PR=5:1 η=40% 100–300 kWe NO_x<10 ppmv TBO: 3000 h	Combustor liners, scroll	+FGI	+EBC	+EBC
		Nozzles		N/A	+EBC K_{1C}=15–20 MPa $m^{0.5}$
		Integral rotors	Small radii σ>200 MPa T: 1400°C	EBC-NGCMC small radii σ>200 MPa T: 1400°C	+EBC K_{1C}=15–20 MPa $m^{0.5}$
Industrial gas turbine	Simple/recuperated/intercooled cycle TIT=1200–1400°C PR=10:1–25:1 η=40% 5–30 MW NO_x<10 ppmv TBO: 30,000 h	Combustor liners, transition pieces	+FGI	+EBC	N/A
		Nozzles, shrouds	+FGI	+EBC/TBC	+EBC K_{1C}=15–20 MPa $m^{0.5}$
		Integral rotors	+FGI NGCMC σ>200 MPa	+EBC NGCMC σ>200 MPa	N/A
		Inserted blades			+EBC K_{1C}=15–20 MPa $m^{0.5}$
Large frame engine	Combined cycle TIT=1400–1600°C PR=20:1–30:1 η=63% 200 MW NO_x<10 ppmv TBO: 24,000 h	Combustor liners, transition pieces	+FGI	+EBC/TBC	N/A
		Nozzles, shrouds	+FGI-NGCMC T: 1600°C	+EBC/TBC NGCMC T: 1600°C	N/A
		Inserted blades	+FGI NGCMCs σ>200 MPa T: 1500°C	+EBC/TBC NGCMC σ>200 MPa T: 1500°C	N/A

potential benefits of incorporating ceramics in the hot section of utility gas turbines were pointed out by Grondahl and Tsuchiya, who predicted a combined cycle efficiency improvement of 2–3% for the MS9001FA engine with maximum operating temperatures for the ceramic components of 1204°C and 1315°C, respectively [17]. Future utility gas turbines my have very high TITs up to 1700°C [18]. Ceramics in such applications likely will need to be cooled, or conversely, the savings in cooling requirements may translate into achieving equivalent performance at somewhat lower TIT. A project goal of 63% efficiency at 1500°C TIT would be a worthwhile target.

Also listed in Table 1 are critical ceramic materials technologies and properties required to enable realization of these performance objectives:

- Si_3N_4 and SiC for impact resistant turbine airfoils. This requires improved fracture toughness—K_{1C}: 15–20 MPa $m^{0.5}$, significantly better than the current limit of K_{1C} ~9 MPa $m^{0.5}$ for Si_3N_4, while retaining excellent high temperature strength.
- Protective EBCs for Si_3N_4 and SiC that limit component surface recession in service. It is assumed that recession of the ceramic substrate in excess of 50% of the original thickness for combustor components and 10% for nozzle and rotating component airfoils is the upper limit.
- Protective EBC/TBCs (thermal barrier coatings) for SiC/SiC CMCs and improved FGIs for oxide/oxide CMCs. At high firing temperatures (TIT>1350°C) current EBCs and FGIs will likely be inadequate for substrate protection and a new generation of protective coatings needs to be developed for turbine components of midsize industrial, aeroderivative and utility gas turbines.
- Next generation CMCs (NGCMC) with (1) improved strength that will enable the design of rotating components and (2) that will enable the design of small turbine airfoil components with sharp radii of curvature. Typical stresses in rotating components are on the order of 200 MPa or more. The CMCs should have a minimum creep rupture strength in excess of 200 MPa over the operating temperature range. In fact, 300 MPa would be a desirable creep rupture strength target.
- Improved component lifing methodologies for monolithics and CMCs that will enable design for the broad range of

Technology	Key requirements/status	Task	Year									
			1	2	3	4	5	6	7	8	9	10
All technologies	Funding Availability	Program Funding Development										
High-K_{1C} Si_3N_4	RT K_{1C} 15-20 MPa.$m^{0.5}$	Laboratory Development										
	30,000-h/1200°C Creep Life	Supplier Process Development										
	3,000-h/1370°C Creep Life	Component Design at GT OEMs										
	TRL 0 – Nozzles	Prototype Component Fabrication										
	TRL 0 – Rotating Components	Development Rig/Engine Testing										
		Supplier Scale up to Production										
EBC for Si_3N_4	30,000-h life - 1300°C	Laboratory Development										
	3,000-h life - 1370°C	Supplier Process Development										
	Si_3N_4 Surface Recession <10%	Component Design at GT OEMs										
	TRL 6 – Nozzles - 1300°C	Prototype Component Fabrication										
	TRL 0 – Rotating Components	Development Rig/Engine Testing										
		Supplier Scale up to Production										
EBC/TBC for SiC/SiC CMC FGI for Ox/Ox CMC	30,000-h life - 1300-1600°C	Laboratory Development										
	TRL 6 – Combustor Liners	Supplier Process Development										
	TRL 4 – Nozzles, Shrouds	Component Design at GT OEMs										
		Prototype Component Fabrication										
		Development Rig/Engine Testing										
		Supplier Scale up to Production										
NGCMC SiC/SiC CMC Ox/Ox CMC	Forming Capability Small Parts	Laboratory Fiber Development										
	σ up to 300 MPa	Supplier CMC Process Development										
	TRL 0 – Stationary Parts	Component Design at GT OEMs										
	TRL 0 – Rotating Parts	Prototype Component Fabrication										
		Development Rig/Engine Testing										
		Supplier Scale up to Production										
Life Prediction	Addresses All Key Failure Modes	Life Prediction Development										
NDE	Process, In-Line NDE	NDE Methods Development										

Fig. 5 Time scale for development of key technologies for the ceramic gas turbine

conditions experienced in the gas turbine, including creep, fatigue, and environmental degradation.

- Component health monitoring technologies, based on nondestructive evaluation (NDE) for detection of critical defects at various stages of processing and during operation in service.

It will require a very significant effort to develop these technologies. Work will involve multiple teams working on fundamental materials process development and properties measurements in a laboratory setting, ceramic component development at suppliers, in tandem with ceramic component design at original equipment manufacturers (OEMs) of gas turbines, leading up to in-house and engine field testing. If successful and attractive for commercialization, ceramic suppliers will need development to transition to fabrication of commercial volumes of components with as end goal a cost-effective manufacturing process with solid quality control. Figure 5 gives examples of development schedules for critical technologies for the four engine scenarios summarized in Table 1, and supportive technologies.

Technology readiness levels (TRLs) of various ceramic technologies have been indicated in Fig. 5. The TRL concept is a scoring system, pioneered by NASA [19,20]. It assigns a subjective maturity score to a technology, based on feedback from technical experts, and helps in establishing the level of effort required to further mature technology development towards a product application. The score is a good indication of technological and associated programmatic risk. A score of 0 represents the highest risk and lowest readiness, a score of 9 the lowest risk and highest level of readiness. The NASA TRL scoring system, shown in Table 2, has been adapted to score the technologies in Table 1. For nonflight applications it has been assumed that TRL 8 indicates a ceramic technology that was incorporated in a gas turbine and successfully passed an engine acceptance test prior to customer shipment and TRL 9 is associated with a ceramic technology that has operated trouble-free for 1–3 years in a field application. TRLs 5–7 require having tested a ceramic component in an in-house engine or rig under conditions simulating actual engine operation. Lower TRLs represent concept development, design or laboratory testing.

The schedules in Fig. 5 are within a 10 year time frame, believed to be necessary to accomplish the technology development and demonstration objectives. The technologies are high risk and it is believed that no single industry and/or company has the financial and technical resources to conduct the proposed program without development partners. To accomplish the program will require collaborative ventures between government agencies, national laboratories, academia, and private industry, supported with adequate funding. Private industry encompasses innovative research companies, suppliers of ceramic components, and gas turbine OEMs.

The substantial technological advancements in ceramics for gas turbines made under the large-scale gas turbine programs between 1970 and 2000 in various areas of the world was supported by an infrastructure, which has now largely disappeared. Funding for advanced ceramic gas turbine development has greatly diminished, suppliers have largely abandoned ceramic gas turbine process and component development (many of the leading suppliers have ceased to exist), laboratories have refocused their efforts to more near-term and better-funded endeavors and the development expertise at the gas turbine OEMs has dwindled to small research groups. Fortunately, much of the development work has been extensively documented and lessons learned have been captured

Table 2 NASA technology readiness levels (TRL)

TRL	Description
0	No concept formulation—only basic ideas
1	Basic principles observed and recorded
2	Technology concept formulated
3	Analytical and/or experimental proof of concept
4	Component validation in a laboratory environment
5	Component validation in a relative environment
6	Model or prototype demonstrated in a relevant environment
7	System prototype demonstrated in flight
8	Actual system tested and flight qualified
9	Actual system proven on operational flight

[1–4]. Therefore, resuming the work will not have to start from scratch. There still exists a solid body of ceramic process development expertise and turbine and component design know-how. However, waiting too long with initiating new programs will inevitably lengthen the time required for development.

Re-energizing the ceramic gas turbine enterprise will need a comprehensive effort to reestablish the infrastructure necessary for conducting development programs aimed at progress toward technology objectives. Restoring the funding mechanisms that were facilitating the substantial ceramic development in the past will likely require several years of policy development and advocacy in the technology branches of government in the industrialized world. Proposed program initiatives will require approval in the legislative branches of government. Proposals will need to be solicited from consortia of technology partners. It is estimated that the preparatory work will require at least 2 years before development will gain momentum. Initial work for critical technologies will largely need to be conducted in centers of materials excellence, represented by national laboratories, universities, and small agile research companies. It is recommended that seed funding be made available to initiate preliminary studies in the areas summarized in Fig. 5.

Technology Challenges

Strategies to address the technology challenges for monolithics have been summarized previously by Carruthers et al. [21]. Approaches to improve fracture toughness while preserving strength include next-generation self-reinforced Si_3N_4, characterized by highly aligned elongated reinforcing grains, and control of sintering additives, which combine high strength (1.4 GPa) with high fracture toughness (K_{1C} up to 11 MPa $m^{0.5}$). High fracture toughness has also been achieved using strategies involving high-strength nanocomposite Si_3N_4, tape casting of alternate dense and porous layers, and a combination of high porosity with aligned fibrous grains [21]. This line of research could be extended to include development of SiC with improved toughness and strength.

EBC development for monolithics and CMCs has been summarized by van Roode and Ferber [5]. Development for monolithics can benefit from the findings of past and ongoing R&D, primarily in the United States and Japan. A key issue is matching the coefficients of thermal expansion (CTEs) between EBC and substrate (critical during thermal cycling). EBC configurations that proved successful on SiC/SiC CMCs, e.g., compositions of the Si/mullite/BSAS type are less suited for Si_3N_4 substrates because this monolithic has a significantly lower CTE than SiC and causes through-thickness cracking in the coating and an unacceptable reduction in room temperature strength. Bhatia et al. [22], at United Technologies Research Center (UTRC), recently reported the development of a bond coat system consisting of a low-modulus ceramic interlayer and a CVD (chemical vapor deposition) Si layer, which helped retain the baseline strength of monolithic Si_3N_4 substrates. Kyocera [23] evaluated thick and thin $Yb_2Si_2O_7$ and ZrO_2 slurry-deposited EBCs for application to Si_3N_4 stationary gas turbine components. Testing for up to 1000 h showed almost no degradation, except for minor volatilization of Si_3N_4 grains, incorporated into the thin $Yb_2Si_2O_7$ EBC [24]. Another approach would be to develop high-strength SiC as an alternative to Si_3N_4 for airfoil components. The advantage of SiC would be that, because of the CTE match, EBC compositions developed for SiC/SiC CMCs could be utilized as a starting point for development. A drawback is the lower strength and fracture toughness of current SiC materials compared to Si_3N_4.

Regardless of whether EBCs are developed for Si_3N_4 or SiC, to be truly useful in a gas turbine application the coating development should be done in parallel with efforts to improve the fracture toughness to the K_{1C} 15–20 MPa $m^{0.5}$ level while retaining excellent strength, a prerequisite for improved impact-resistant monolithics. Thus, monolithics that meet the needs of the gas turbine designer need to posses excellent fracture toughness and strength, and be environmentally resistant.

For small gas turbines, improving fracture toughness of monolithic Si_3N_4 or SiC and developing EBCs for Si-based monolithics with surface recession comparable to state-of-the-art compositions developed for SiC/SiC CMCs will probably only be useful for turbine airfoil components with temperatures not exceeding ~1200°C. This limits the development of small gas turbines to TITs not exceeding about 1200°C, since effective cooling cannot easily be incorporated in small components. Also, first stage nozzles are typically subjected to temperatures in excess of the nominal TIT because of hot spots resulting from the combustor pattern factor. These conditions are compatible with a small gas turbine (e.g., a microturbine) with an electrical efficiency of about 35% (first example in Table 1).

For small engines to reach the full performance potential (electrical efficiencies: 40% or greater—second example in Table 1) as was envisioned in the automotive, small engine cogeneration, and microturbine programs in the United States and Japan, will require EBCs with greatly reduced surface recession compared to state-of-the-art EBCs for SiC/SiC CMCs (Si/mullite/BSAS compositions). This is easier for automotive applications with expected service life of several thousands of hours than for commercial stationary applications with expected service life on the order of 30,000 h.

The constraints for monolithic components are less severe for midsize (industrial and aircraft/aeroderivative) gas turbines with high efficiency (40% or better—third example in Table 1). The larger size of the components will enable the incorporation of simple but effective component cooling schemes in combination with EBC/TBC hybrid coatings. For SiC turbine components, EBC/TBC compositions similar to those pioneered for SiC/SiC CMCs, in which a TBC layer is incorporated on top of standard Si/mullite/BSAS (see below [25,26]) would be of interest. Potentially, surface temperatures approaching ~1500°C would be feasible since certain SiC and Si_3N_4 compositions have excellent creep resistance if environmental attack is mitigated. For Si_3N_4, a TBC topcoat would need to be applied on top of a CTE-compatible EBC. If such EBC development work were successful, monolithic Si_3N_4 or SiC turbine components could potentially be used in gas turbines with high TIT (1300–1450°C). It should be reiterated that the fracture toughness of these materials also needs to be improved, and that this improvement should not come at the expense of material strength.

The challenges for robust monolithic turbine materials are very significant and can be expected to require 7–10 years of focused development work (Fig. 5), assuming conditions are favorable, i.e., adequate funding for development, dedicated efforts at national laboratories, universities and suppliers, and visionary gas turbine OEMs that perceive opportunities to further improve the performance of their advanced power generation equipment. Even if technology development is successful in the laboratory, at the suppliers, and in in-house testing at the gas turbine OEMs, the high risks associated with introducing novel technologies into the product typically requires operation at a field site of an end user for a TBO cycle, i.e., 3–4 years. The need for iterative development may extend the introduction of the commercialization of the technology even further. Given that the technology readiness for most of this technology is at a very low level (TRL 0), a prolonged development phase is envisioned.

Promising progress has been made in recent years with the development of SiC/SiC and oxide/oxide CMCs for stationary gas turbine components. The CMCs have superior impact resistance (K_{1C} ~ 20 MPa $m^{0.5}$) compared to monolithic Si-based ceramics. Effective EBCs have been developed for SiC/SiC CMCs and promising thermally protective coating systems for oxide/oxide CMCs. Field testing for many thousands of hours of SiC/SiC CMC combustor liners in Solar's *Centaur*® 50S indus-

trial gas turbine [5,9], evaluation of SiC/SiC CMC shrouds in the 7FA engine of General Electric Co. [12], ongoing development work of hybrid oxide CMCs at Siemens Power Generation and Solar [10,11], and promising EBC development at UTRC [25], supported by development efforts from CMC suppliers, suggest a high likelihood of future commercial application of stationary CMC gas turbine technology, perhaps as early as 2012–2013. This time frame takes into account the 3–4 years of testing under real engine operating conditions of technologies that are already at TRL 4–6 (see Fig. 5).

Current CMCs are particularly suitable for stationary parts, including combustor liners, turbine nozzles, and shrouds. In frame engines, components can be substantial in size and effective cooling schemes can be incorporated. This enables operation at high TIT. Work at UTRC and at NASA Glenn Research Center has focused on cooled SiC/SiC CMC nozzles with tailored EBC/TBC hybrid coatings [25,26].

One shortcoming of the current CMCs is their relatively low strength capability compared to monolithics. The design allowable stress of SiC/SiC CMC components is determined by the PLS, which for various SiC/SiC CMCs is ~180 MPa. For oxide/oxide CMCs, the maximum stress is capped by the UTS, which is typically ~195 MPa [6]. These limitations generally preclude the use of CMCs for rotating components in gas turbines that need to operate for thousands of hours, since the combined stress contributions of the centrifugal, thermal, and aerodynamic loads are typically in excess of 200 MPa. To enable the use of CMCs for rotating parts will require the development of stronger fibers, and fiber architectures that accommodate high stresses in the principal loading directions.

CMCs are currently not considered design materials for small components due to fiber bending limitations and the unavailability of sharp radii of curvature [6]. These shortcomings need to be addressed as well in order to make CMC structural design materials for small gas turbines. These challenging requirements portend a long development schedule, on the order of 8 years or perhaps longer (see Fig. 5). If successful, SiC/SiC CMCs with current EBCs could be used as structural material for hot section components up to about 1200°C in small gas turbines with low-pressure ratio ($\sim$PR5:1). Again, because effective cooling is not an option, $\sim$1200°C would be the practical TIT limit for SiC/SiC CMC with current EBCs (see Fig. 4). More effective EBCs would be needed to enable higher TIT with SiC/SiC CMCs. A FGI is not really an option for small uncooled oxide/oxide CMC components, and consequently the limited for the current alumina-based CMCs is only $\sim$1100°C (see Fig. 4) because very little surface recession is allowed for small airfoil components.

Higher TITs, in the 1350–1450°C range will be required for small gas turbines with electrical efficiencies of $\sim$40%. For both SiC/SiC and oxide/oxide CMCs significant improvements in strength and durability would be required to increase the TIT capability. Again, for SiC/SiC CMCs, this may necessitate further EBC development. Needless to say, this would add to the development effort and cost.

Development of a more effective FGI is not an option for small oxide/oxide CMC components because cooling will not be available. Therefore, the focus for oxide/oxide CMCs needs to be on improving the strength and durability of the composite and its constituents through improvement in the fiber, matrix, and fiber-matrix interface (for a dense CMC). Since the current alumina constituent limits fiber strength, attention should be directed toward alternate materials. The work in Japan by Waku et al. [27] on melt growth composites (MCGs) may be of interest in this respect. The MGC compositions have a microstructure consisting of continuous networks of single crystal Al_2O_3 phases interspersed with other single crystal oxide compounds ($Y_3Al_5O_{12}$: YAG, $GdAlO_3$: GAP, $Er_3Al_5O_{12}$: EAG, $Al_2O_3/YAG/ZrO_2$). These materials reportedly retain high strength and show neither weight gain nor grain growth upon heating in air at 1700°C for 1000 h [27]. These materials or some of their constituents could be of interest for further development. YAG, GAP, EAG, and ZrO_2 could be starting compositions for fiber and matrix development for the next generation oxide/oxide CMCs. The ultimate objective is to develop an oxide-based CMC that can be used for components of varying sizes (including small turbine components), without the need for a thermally or environmentally protective coating and that has sufficient strength to be used as structural material for rotating components. YAG may be a good first choice for development since it has shown to have significantly less weight change than Al_2O_3 in corrosion testing in a simulated gas turbine environment [28]. General Atomics reported that YAG fibers prepared by sol-gel process had very good high temperature creep properties [29].

An important consideration for commercialization is component cost. Key factors are process complexity and volumes of parts produced. Fabrication of ceramic components, from monolithics or CMCs, requires multistep processing, with furnace operations, quality control (in-process NDE, etc.), and finish machining being significant cost adders. Development of net shape processing provides opportunities for cost reduction. For medium-size and large-size gas turbines with a few hundred engines a year per model, annual component volumes will be aerospace quantities, i.e., on the order of thousands to a few tens of thousands. It is doubtful whether a high-volume application with millions of parts per year such as represented by the automotive sector would emerge in the near future. Automotive development over the past 10 years has turned toward electrical and hybrid applications, and the once bright prospects for automotive ceramic gas turbines have dimmed considerably. There is a potential application for gas turbines for buses and trucks, but component volumes will not be millions per year for these applications. Controlling cost is a strong driver for small engines. Therefore, to be commercially viable, monolithic ceramic components should not be more expensive than the metal parts they intend to replace. For larger gas turbines that will be using primarily CMCs, a cost range of $1-2x$ the cost of metal parts may be acceptable, provided significant improvements in performance can be achieved compared to the all-metal baseline.

Finally, design and diagnostic tools need to be available to support the development work. A well developed set of life prediction tools that incorporate the critical mechanical, thermal, and environmental failure modes and diagnostic nondestructive methodologies to conduct component in-process fabrication and in-service health monitoring are vital tools for the designer of ceramic hot section components.

Development Scope and Cost

An effective development effort addressing the areas summarized in Fig. 5 will require a comprehensive program, stretching out over up to 10 years. To lower the risk of not achieving the program objectives, multiple teams working toward common project targets at all stages of development will be desirable. These projects should be planned as part of an overall program that progresses from initial laboratory process development and materials characterization through fabrication scale up in conjunction with introduction of gas turbines with robust ceramic components in the market place.

Reconstituting a viable supplier base will be a key element in a successful strategy. To rekindle the interest of ceramic suppliers, an economic analysis needs to show that the new ceramic technologies result in viable products at attractive pricing. There have to be incentives to both suppliers and gas turbine OEMs that will be commercializing the end products.

Much of the design work required by the gas turbine OEMs can build on the advancements in ceramic design technology made under the large funded programs during the 1970s through the 1990s. Many of the design solutions conceived were sound but could not be realized because of inadequate materials properties

for long-term service. The proposed development work will require major efforts in the initial and final phases, i.e., to demonstrate that the technological targets have been achieved and that the technologies pass the scrutiny of long-term operation in service and are cost-effective.

Each of the lines of development should not be pursued independently, but integrated in an overall materials development strategy. Successfully developed technologies need to become elements in development/demonstration programs led by gas turbine OEMs.

With this strategy in mind, it is estimated that to support each of the four key areas identified for development (high-K_{1C} Si_3N_4 and SiC, EBC for Si_3N_4 and SiC, EBC/TBC for SiC/SiC, oxide/oxide CMC+FGI, next generation CMCs), and to support life prediction and NDE development efforts throughout the program, it would require an overall funding commitment from the program partners of about $100M over a 10 year period, or an annual average of $10M.

Summary

Ceramic gas turbine development programs that have been ongoing since the 1950s have thus far failed to realize significant benefits in meeting component durability and equipment performance goals. As a result, development efforts have slowed considerably after most of the large-scale ceramic gas turbine development programs of the 1970s–1990s ended.

Still, the prospect of significant energy savings and emission reductions potentially achievable with ceramic gas turbine hot section components have continued to encourage development work at gas turbine equipment manufacturers, government agencies, universities, and national laboratories. Roadmaps have been devised that show technological improvements necessary for meeting design and market requirements. However, the financial basis and programmatic infrastructure to realize the milestones and broad objectives of the roadmaps are currently inadequate.

Four potentially commercially attractive ceramic gas turbine applications have been identified: a small recuperative gas turbine (microturbine) with 35% electrical efficiency, a recuperative gas turbine with 40% electrical efficiency with potential applications for efficient transportation and small engine cogeneration, a 40% efficient midsize industrial gas turbine, and a 63% efficient utility turbine.

To realize these applications, key technologies have been identified to ensure the performance targets can be met with durable ceramic components over the expected life cycle of the applications. These technologies include Si_3N_4, SiC with high fracture toughness and superior strength, durable EBCs for Si_3N_4 and SiC, effective EBC/TBC for SiC/SiC CMCs, and FGI for oxide/oxide CMCs, and next generation CMCs, and supportive life prediction and NDE methods. The programs will require integrated partnerships between government, national laboratories, universities, and industry. The overall cost of the proposed development programs is estimated at U.S. $100M over a 10 year period, averaging of $10M annually.

References

[1] 2002, "Ceramic Gas Turbine Design and Test Experience," *Progress in Ceramic Gas Turbine Development*, Vol. I, M. van Roode, M. K. Ferber, D. W. Richerson, eds., ASME, New York.

[2] 2003, "Ceramic Gas Turbine Component Development and Characterization," *Progress in Ceramic Gas Turbine Development*, Vol. II, M. van Roode, M. K. Ferber, D. W. Richerson, eds., ASME, New York.

[3] Richerson, D. W., 2004, "Ceramic Components in Gas Turbine Engines: Why Has It Taken so Long?," Ceram. Eng. Sci. Proc., **25**(3), 3–32.

[4] Richerson, D. W., 2006, "Historical Review of Addressing the Challenges of Use of Ceramic Components in Gas Turbine Engines," ASME Paper No. GT2006-90330.

[5] van Roode, M., and Ferber, M. K., 2007, "Long-Term Degradation of Ceramics for Gas Turbine Applications," ASME Paper No. GT2007-27956.

[6] DiCarlo, J. A., and van Roode, M., 2006, "Ceramic Composite Development for Gas Turbine Engine Hot Section Components," ASME Paper No. GT2006-90151.

[7] Energetics, Incorporated, and Richerson and Associates, 2000, "Advanced Ceramics Technology Roadmap—Charting Our Course—Sponsored by the United States Advanced Ceramics Association and the U.S. Department of Energy."

[8] Veitch, L. C., and Hong, W. S., 2001, "Will Pigs Fly Before Ceramics Do?," Ceram. Eng. Sci. Proc., **22**(3), 31–37.

[9] van Roode, M., Price, J. R., Kimmel, J., Miriyala, N., Leroux, D., Fahme, A., and Smith, K., 2005, "Ceramic Matrix Composite Combustor Liners: A Summary of Field Evaluations," Trans. ASME: J. Eng. Gas Turbines Power, **129**(1), 21–30.

[10] Lane, J. E., Morrison, J. A., Marini, B., and Campbell, C. X., 2007, "Hybrid Oxide CMC Mitigates the Design Hurdles Typically Seen for Oxide CMC," ASME Paper No. GT2007-27532.

[11] van Roode, M., Price, J., Otsuka, J., Szweda, A., More, K., and Sun, J., 2008, "25,000 Hour Hybrid Oxide CMC Field Test Summary," ASME Paper No. GT2008-51379.

[12] Corman, G., Luthra, K., Mitchell, D., Meschter, R., Nimmer, R., Bruce, K., and Landini, D., 2004, "Melt Infiltrated CMC Gas Turbine Shroud Development and Testing," presented at the 28th Annual Conference on Composites, Materials and Structures, Cocoa Beach, FL.

[13] McDonald, C. F., and Rogers, C., 2005, "Ceramic Recuperator and Turbine: The Key to Achieving a 40% Efficient Microturbine," ASME Paper No. GT2005-68644.

[14] Haught, D., 2005, "Microturbines and Small Gas Turbines Technology: Progress and Challenges," panel presentation at the 2005 ASME TURBO EXPO, Reno, NV, Jun. 6–9.

[15] Tatsumi, T., 2002, "Development of the 300 kW Ceramic Gas Turbine CGT302," *Progress in Ceramic Gas Turbine Development*, ASME, New York, Chap. 15, pp. 331–360.

[16] "2006 GTW Handbook," Vol. 25, Section 3, Specifications.

[17] Grondahl, C. M., and Tsuchiya, T., 1998, "The Performance Benefit Assessment of Ceramic Components in an MS9001FA Gas Turbine," Trans. ASME: J. Eng. Gas Turbines Power, **123**(3), 508–512.

[18] Kizuka, N., Sagae, K., Anzai, S., Ikeguchi, T., and Kawaike, K., 1999, "Test Results of Closed-Circuit Cooled Blades for 1700°C Hydrogen-Fueled Combustion Gas Turbines," *Proceedings of the International Gas Turbine Congress*, T. Tamaru, ed., Kobe, Japan, Nov. 14–19, Vol. 1, pp. 343–350.

[19] Mankins, J. C., 1995, "Technology Readiness Levels," White Paper.

[20] Bryce Roth, M. G., Graham, M., and Mavris, D., 2002, "Adaptive Selection of Aircraft Engine Technologies in the Presence of Risk," ASME Paper No. GT-2002-30623.

[21] Carruthers, W. D., van Roode, M., Becher, P. F., Ferber, M. K., and Pollinger, J., 2002, "Advances in the Development of Silicon Nitride and Other Ceramics," ASME Paper No. GT-2002-30504.

[22] Bhatia, T., Srinivasan, G. V., Tulyani, S. V., Barth, R. A., Vedula, V. R., and Tredway, W. K., 2007, "Environmental Barrier Coatings for Monolithic Silicon Nitride-Bond Coat Development," ASME Paper No. GT2007-27685.

[23] Fukudome, T., Tsuruzono, S., Tatsumi, T., Ichikawa, Y., Hisamatsu, T., and Yuri, I., 2005, "Development and Evaluation of Ceramic Components and EBCs for Gas Turbine," Ceram. Eng. Sci. Proc., **26**(3), 147–157.

[24] Fukudome, T., Tsuruzono, S., Tatsumi, T., Ichikawa, Y., Hisamatsu, T., and Yuri, I., 2005, "Development of Silicon Nitride Components for Gas Turbine," Key Eng. Mater., **287**, 10–15.

[25] Vedula, V., Shi, J., Jarmon, D., Ochs, S., Oni, L., Lawton, T., Green, K., Prill, L., Schaff, J., Linsey, G., and Zadrozny, G., 2005, "Ceramic Matrix Composite Turbine Vanes for Gas Turbine Engines," ASME Paper No. GT2005-68229.

[26] Verrilli, M., Calamino, A., Robinson, R. C., and Thomas, D. J., 2006, "Ceramic Matrix Composite Vane Subelement Testing in Gas Turbine Environment," ASME Paper No. GT2004-53970.

[27] Nakagawa, N., Ohtsubo, H., Shibata, K., Mitani, A., Shimizu, K., and Waku, Y., 2005, "High Temperature Stability of MGC's Gas Turbine Components in Combustion Gas Flow Environments," ASME Paper No. GT2005-68568.

[28] Klemm, H., Fritsch, M., and Schenk, B., 2004, "Corrosion of Materials in Hot Gas Environment," Ceram. Eng. Sci. Proc., **25**(4), 463–468.

[29] Morscher, G. N., Chen, K. C., and Mazdiyasni, K. S., 1995, "Creep-Resistance of Developmental Polycrystalline Yttrium-Aluminum Garnet Fibers," Ceram. Eng. Sci. Proc., **15**(4), 181–188.

Biodiesel as an Alternative Fuel in Siemens Dry Low Emissions Combustors: Atmospheric and High Pressure Rig Testing

Kexin Liu[1]
e-mail: kexin.liu@siemens.com

John P. Wood[2]
e-mail: jpwood@qinetiq.com

Eoghan R. Buchanan

Pete Martin

Victoria E. Sanderson

Siemens Industrial Turbomachinery Ltd.,
P.O. Box 1,
Waterside South,
Lincoln LN5 7FD, UK

Atmospheric and high pressure rig tests were conducted to investigate the feasibility of using biodiesel as an alternative fuel to power industrial gas turbines in one of the world's leading dry low emissions (DLE) combustion systems, the SGT-100. At the same conditions, tests were also carried out for mineral diesel to provide reference information to evaluate biodiesel as an alternative fuel. In atmospheric pressure rig tests, the likelihood of the machine lighting was identified based on the measured probability of the ignition of a single combustor. Lean ignition and extinction limits at various air temperatures were also investigated with different air assist pressures. The ignition test results reveal that reliable ignition can be achieved with biodiesel across a range of air mass flow rates and air fuel ratios (AFRs). In high pressure rig tests, emissions and combustion dynamics were measured for various combustor air inlet pressures, temperatures, combustor wall pressure drops, and flame temperatures. These high pressure rig results show that biodiesel produced less NO_x than mineral diesel. The test results indicate that the Siemens DLE combustion system can be adapted to use biodiesel as an alternative fuel without major modification. [DOI: 10.1115/1.3204617]

1 Introduction

Renewable fuels are of increasing interest for many applications including gas turbines [1,2] due to environmental issues, fossil fuel conservation, and energy price increases. Biofuels including biogas, bioethanol and biodiesel are renewable and environment friendly in many ways such as being carbon neutral and in theory producing zero carbon dioxide (CO2), but the production of biofuels should avoid competition with food production. The current work focuses on the technical issue of biofuels in terms of operability and emissions.

Biodiesel is produced by the process of transesterification of vegetable oil, animal oil/fats, tallow and waste cooking oil to form fatty acid methyl esters (FAME). The advantage of treating the vegetable oil in this way is that the resulting oil has properties that are significantly closer to those of mineral diesel than in the case for the original feedstock. The precise properties of the fuel produced in this way are dependent on the original feedstock [3,4]. Oils derived straight from crops such as rapeseed, palm and soybean have the greatest potential; however, there are issues with land availability and cost. Waste vegetable oils from restaurants and animal oil/fat from the food industry represent the economic way to produce biodiesel.

Biodiesel fuels have been widely used in internal combustion engines, either pure biodiesel BD100 or blended with diesel as BD5 (biodiesel 5%, diesel 95%), BD10 (biodiesel 10%, diesel 90%). Lapuerta et al. [5] used pure biodiesel fuels in a diesel engine and found that pure biodiesel, compared with the reference mineral diesel, resulted in a slight increase in fuel consumption, very slight differences in NO_x emissions, and sharp reductions in total hydrocarbon emissions, smoke opacity and particle emissions. Biodiesel is indeed an environmentally friendly fuel when applied to internal combustion engines.

To the authors' best knowledge, biodiesel was not widely used in industrial gas turbines, but some test experience was built up on heavy duty gas turbines [1,2], small gas turbines [6], microturbines [7,8] and simulated gas turbine burner tests [9,10]. Comparable NO_x emissions were found in the work on heavy duty gas turbines [1,2] and on small gas turbines [6]. Chiang et al. [8] reported carbon deposits on the fuel nozzle burning biodiesel, and Bolszo et al. [7] found that engine cold start becomes a significant challenge under more extreme conditions. The major concerns using biodiesel to power industrial gas turbine are operability, NO_x emission, materials, component life, fuel storage [11], cold start [7], and carbon deposits [8].

Siemens Industrial Turbomachinery Ltd. was involved in the recently finished European project, Alternative Fuels for Industrial Gas Turbines (AFTUR), to investigate the feasibility of using biodiesel as an alternative fuel to power industrial gas turbines. Siemens conducted both atmospheric and high pressure rig tests in the SGT-100 using one of the world's leading DLE combustion systems. Reference data were obtained by carrying out the same tests with mineral diesel.

In an atmospheric pressure rig, extensive ignition tests were conducted, to investigate engine start reliability, lean ignition, and extinction limits to establish the biodiesel's operability in gas turbines. In high pressure rig testing, emissions and combustion dynamics were investigated. The biodiesel selected for this study was supplied by C Zero Energy Ltd. (Coventry, UK), produced from recycled cooking oil, and was consequently derived from a mixture of feedstocks. All tests were with the standard DLE SGT-100 burner, combustor, and transition duct, and 100% biodiesel (BD100) was used. The reference mineral diesel was BS 2869 Class A2/D.

2 Siemens DLE Combustion System

Siemens Industrial Turbomachinery Ltd. is the manufacturer of small industrial gas turbines from the SGT-100 at approximately 5 MW to the SGT-400 at 13.4 MW, which have now accumulated more than 3 million hours of experience. The SGT-300 and SGT-400 are offered commercially for less than 10 ppmv NO_x

[1]Corresponding author.
[2]Now in QineitiQ, Cody Technology Park, Farnborough GU14 0LX, UK.

Manuscript received March 24, 2009; final manuscript received March 30, 2009; published online September 14, 2009. Review conducted by Dilip R. Ballal.

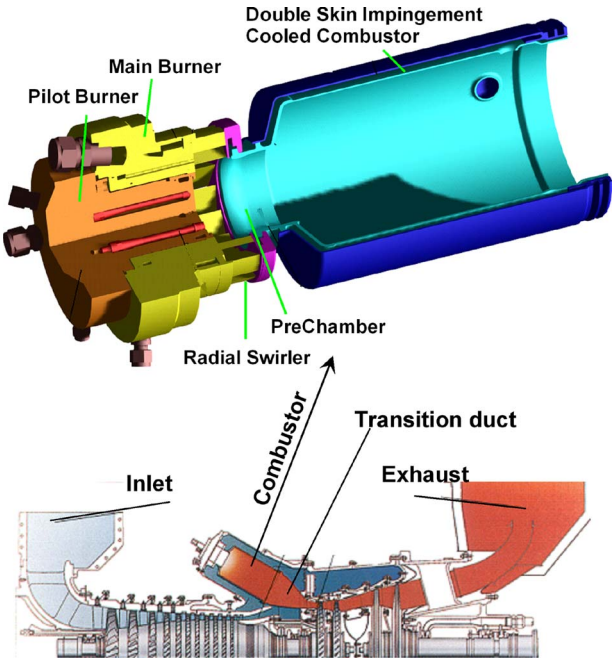

Fig. 1 Siemens DLE combustor construction

(at $15\%O_2$) emissions for certain markets, for example, the SGT-300, operating at the University of New Hampshire, USA.

The dual fuel DLE combustion system is designed as a reverse-flow tuboannular type, as shown in Fig. 1. The combustor consists of three main sections: (1) the pilot burner, which houses the pilot fuel galleries and injectors for both gaseous and liquid fuels; (2) the main burner, which houses the main air swirler and main gas and liquid fuel injection systems; and (3) the combustor, which includes the prechamber, and is of a double skin construction, cooled through impingement cooling. At the downstream of the combustor, a transition duct is used to condition the flow from the circular combustor exit to a sector of the turbine entry annulus.

In order to cover all the power range, rather than having a single combustor design and applying different numbers of combustors to each engine type, the combustors have been scaled. Figure 2 shows the DLE combustor family. The SGT-100, 300, and 400 have 6 combustors per engine, and the SGT-200 has 8.

A schematic of the combustion concept is shown in Fig. 3. The main combustion air enters through a single radial swirler at the head of the combustor. The flow then turns through a right angle into the prechamber, followed by a sudden expansion into the combustion chamber.

The swirl number is sufficiently high to induce a vortex breakdown reverse flow zone along the axis. This is termed as the internal reverse flow zone. In the concept, this reverse flow zone

Fig. 2 Siemens DLE combustor family

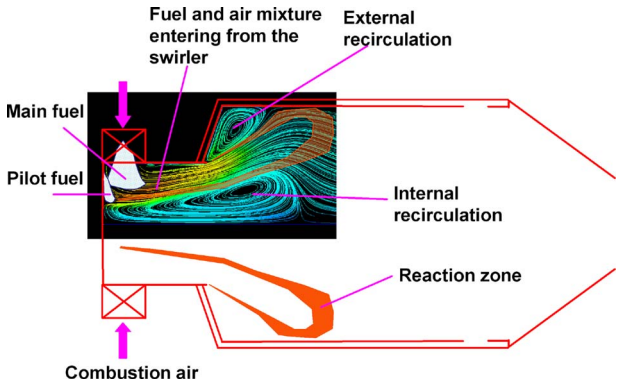

Fig. 3 Siemens DLE combustion concept

remains attached to the surface of the pilot burner, thereby establishing a firm aerodynamic base for flame stabilization. In the wake of the sudden expansion, an external reverse flow zone is established. The flame is stabilized in the shear layers around the internal and external reverse flow zones.

The fuel, either gas or liquid, is introduced in two stages, as shown in Fig. 4: the main, which results in a high degree of premixedness, and hence, low NO_x emissions, and the pilot, which steadily increases as the load demand decreases in order to ensure flame stability. The pilot is arranged, such that, as the pilot fuel split increases, the fuel is biased towards the axis of the combustor.

3 Capability of the DLE System for Fuel Flexibility

Siemens has a continuous policy of expanding its fuel capability. As well as the above mentioned DLE combustion system, Siemens also has conventional combustion systems, which can burn various fuels in the Wobbe index range from 4 MJ/m^3 to 70 MJ/m^3. In this section, the fuel flexibility for the DLE system is described.

The Siemens standard DLE combustion system is capable of burning conventional fuels with a Wobbe index from 37 MJ/m^3 to 49 MJ/m^3 with guaranteed NO_x, CO, and UHC emissions. With modification when necessary, the DLE system is also capable of burning fuels with a lower Wobbe index. For example, the standard SGT-300 operates in Libya with a gas having a Wobbe index of about 32 MJ/m^3, modified SGT-400 engines operate at Yadana in the Andaman Sea with a Wobbe index of 28 MJ/m^3, and at Kandhkot, Pakistan with 32 MJ/m^3.

Siemens is interested in expanding their fuel flexibility with alternative fuels such as syngas, biogas, bioethanol, and biodiesel. High pressure rig tests have been completed with biogases, simulated by diluting natural gas with inert gases and syngases, mixtures of natural gas with hydrogen, carbon monoxide, and inerts.

The current liquid fuel capability for the Siemens DLE system includes mineral diesels and kerosenes. As part of its policy to increase liquid fuel flexibility, Siemens was involved in the Euro-

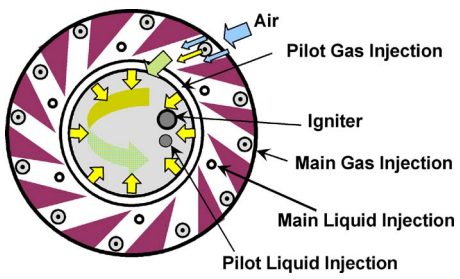

Fig. 4 Conceptual details of fuel injectors and air paths

pean project AFTUR to investigate the feasibility of using biodiesel as an alternative fuel to power industrial gas turbines. Siemens conducted both atmospheric and high pressure rig tests in the SGT-100 DLE combustion system to investigate ignition, emission, and combustion dynamics using biodiesel as an alternative fuel. Reference data were obtained by carrying out the same tests with mineral diesel. Valuable experience has been gained on biodiesel, and the test results are the basis for this paper.

4 Rig Tests Using Biodiesel to Fuel a Standard SGT-100 Combustor

4.1 Ignition Tests in an Atmospheric Rig. In the atmospheric rig testing, extensive ignition testing of biodiesel has been conducted to investigate the feasibility of using it as a fuel to power industrial gas turbines. For all the tests performed in the atmospheric rig, 100% of the fuel was supplied from the pilot fuel nozzle. Two series of tests were performed to identify the key properties of the proposed fuel. In the first set of tests, an attempt was made to identify the likelihood of the engine lighting, based on the measured probability of the ignition of a single combustor. The second series of tests investigated the lean ignition and extinction limits at various air temperatures and at different air assist pressures.

In order to assess the engine start reliability operating with biodiesel, it is necessary to determine the ignition reliability of a single combustor, and then convert this into an overall probability for the engine lighting. The probability of a single combustor lighting is easily determined by counting the number of sparks required to initiate combustion during the atmospheric rig testing. The probability of ignition is then just the reciprocal of the number of sparks that was taken to ignite the combustor. In practice, the experiment was repeated three times, and an average number of sparks was taken to ensure the consistency, and compensate for noise factors, for example, in the spark.

An algorithm was developed to convert the single combustor ignition probability into a probability for lighting the engine. The method consists of calculating the probability of various permutations of combustors lighting on the first round, based on a given fixed probability of an individual combustor lighting P_i. Any probability of any combination from this first round $P(\text{of } k \text{ from } n) = P_i^k (1-P_i)^{n-k} n!/[(n-k)!k!]$ is then multiplied by the probabilities for lighting various combinations of the remaining unlit combustors. The same process is repeated in the third round. All probabilities for sequences, which lead to all combustors lit, are added together, apart from those, which are excluded by the time-out rules built into the control algorithm. This gives the final probability of a successful system light for a given fixed individual combustor light probability. A number of calculations are then run with different fixed probabilities for the individual combustor, and a polynomial fit is applied to model the system response over the interesting high light reliability end of the curve.

The lean ignition limit was found by activating the igniter, and then gradually increasing the fuel flow rate until ignition took place. Ignition was deemed to have occurred when the flame persisted without the presence of a spark. The effect of air assist pressure and air temperature on lean ignition limit was investigated. The lean extinction limit was determined by taking the stable flame at each of the air flow rates studied, and reducing the amount of fuel until extinction occurred. At this point, the air and fuel flow rates were recorded. Each test was repeated three times to ensure the consistency, and compensate for the noise factors such as fluctuations in the air or fuel flow rates.

4.2 Emissions and Dynamics Tests in a High Pressure Rig. High pressure rig tests were performed in one of the high pressure facilities at Firth Road, Lincoln, of Siemens Industrial Turbomachinery Ltd. The maximum pressure, temperature, and air mass flow rate are 20 bar, 873 K, and 5 kg/s, respectively.

The high pressure rig tests investigated the behavior of the fuel injection system, which directly affects the degree of premixedness of the air and fuel mixture, as the operating condition was altered under a biodiesel fuel operation. This was achieved by making measurements of the bulk emissions at the exit of the combustor, and then inferring the impact on the spray from the observed change.

The key parameters influencing the quality of the atomization are believed to be inlet air pressure, temperature, mass flow rate, and flame temperature. A different air mass flow rate results in a different combustor wall pressure drop, which is a key parameter to control air fuel mixing and flame stability. As a consequence, the variation in these parameters formed the basis of the present testing for biodiesel. At the same operating conditions, reference tests were also performed for a mineral diesel operation. During the tests, combustion dynamics were also recorded. For all the tests, 100% of the fuel was supplied from main fuel nozzles with no fuel supplied from the pilot fuel nozzle. The pilot fuel nozzle is an air assist injector, and the main nozzle is a pressure swirl injector.

Table 1 The comparison of fuel properties of biodiesel with those of diesel

Property	Diesel	Biodiesel
Low heating value (MJ/kg)	42.397	37.414
Density at 15°C (kg/m^3)	867.8	832.2
Carbon (% mass)	87.1	76.8
Hydrogen (% mass)	12.7	12.1
Oxygen (% mass)	0.0	10.6
Nitrogen (mg/kg)	335.0	25.0
Kinematic viscosity at 40°C (mm^2/s)	3.45	4.91
Kinematic viscosity at 50°C (mm^2/s)	–	2.67

4.3 Biodiesel Supply and Its Properties. The biodiesel selected for this study was composed of recycled cooking oil. The fuel samples of biodiesel and diesel were collected before and after the test, and were sent to a laboratory for analysis. The comparison of the important properties of the two fuels is listed in Table 1. One can see that biodiesel has a lower heating value, contains oxygen, and in particular, the kinematic viscosity is about 42.3% higher than that of diesel at a temperature of 40°C. When the fuel temperature is increased to 50°C, the biodiesel's kinematic viscosity is reduced to 54.4% of its value at 40°C.

Tate et al. [3,4] studied the fuel properties of three biodiesel fuels from different sources, methyl esters (ME) from canola and soy, and ethyl esters (EE) from fish oil. All three of these biodiesel fuels have much higher kinematic viscosity than diesel, and the viscosity of biodiesel exponentially decays as temperature increases, with significant change with the temperature at the range of 20–100°C. The boiling points of the three biodiesel fuels are also higher than diesel.

Wilson et al. [11] showed that their four kinds of biodiesel fuels have higher viscosity than diesel, and the carbon content varies from 76.8% to 77.52%. The hydrogen content varies from 12.59% to 12.77%, oxygen content varies from 9.37% to 9.94%, and the nitrogen content varies from 0.34% to 0.38%. One can see that the biodiesel selected for the current work has less nitrogen content than that of Wilson et al. [11].

Panchasara et al. [9] also reported that the viscosity of biodesel is 45–55% higher, compared with that of mineral diesel. The higher fuel viscosity of biodiesel could result in poor atomization, which will be quantified later on by droplet size predictions. Surface tension is required in order to evaluate the droplet size of the fuels. It was calculated for both fuels at different fuel pressures by

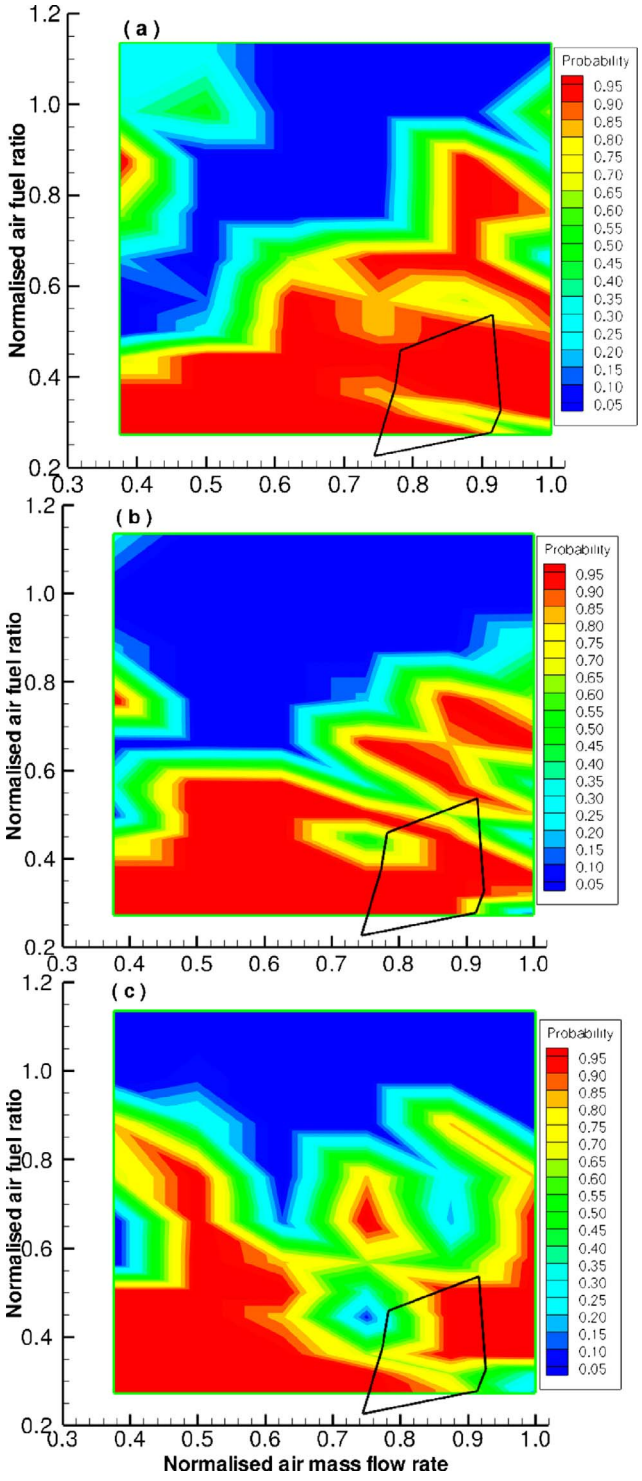

Fig. 5 Probability of engine lighting, fueled with biodiesel and calculated from single combustor tests for three different air assist pressures: (*a*) 2.31 bar, (*b*) 2.72 bar, and (*c*) 3.21 bar

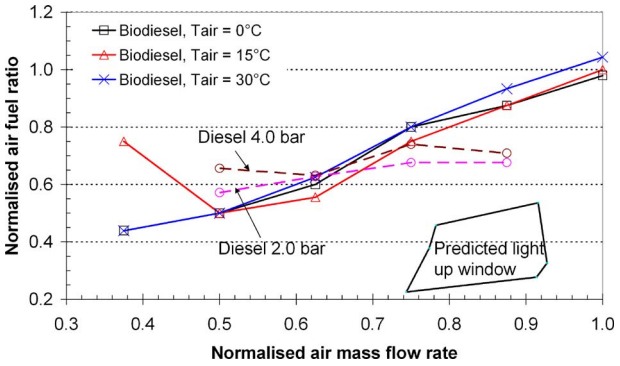

Fig. 6 Lean ignition limit for SGT-100 burning biodiesel at different ambient air temperatures at an air assist pressure of 2.72 bar, and the comparison with diesel

the method of Odgers and Krestschmer [12]. The calculation showed that both fuels have comparable surface tension, which is also confirmed by Panchasara et al. [9].

5 Test Results and Discussion

5.1 Ignition. Figure 5 shows the predicted probabilities of the engine lighting with biodiesel, based on the measured probability for the ignition of a single combustor. Also, three levels of air assist pressure are shown in the figure. The black quadrilateral overlaying these plots shows the predicted extreme limits of the SGT-100 light up window, which incorporates the combustor to combustor variation as the engine lights for biodiesel. The prediction for the light up window of diesel is very close to that of biodiesel.

At low air mass flow and low air fuel ratio, it seems that air assist pressure has little impact on the probability of engine lighting. At higher air mass flow rates, the air assist pressure has a greater impact on the probability of engine lighting. Increasing the air assist pressure reduces the probability of lighting. It is surprising that increasing the air assist pressure has a negative impact on ignition as it would be expected to increase the atomization, and thus make combustion more likely. It has, however, been suggested by Wilbraham [13] that the flame is stabilized by the wake formed by the spray, and that if the atomization is promoted excessively, this wake can be disrupted, preventing the flame from stabilizing. It is, consequently, a compromise between promoting atomization to aid ignition and providing sufficiently dense spray efflux to produce sufficient wake to stabilize the flame.

From Fig. 5, it can be seen that over the majority of the SGT-100 ignition window, a 95% start reliability could be achieved with biodiesel at air assist pressures lower that 3 bar. Even for an air assist pressure of 3.21 bar, a very high start reliability could be achieved.

Figure 6 shows the lean ignition limit for biodiesel fuel at air assist pressure of 2.72 bar and the comparison with those of mineral diesel by Martin [14]. The results suggest that at high air flow rates, the biodiesel is easier to ignite than diesel with the ignition being possible at significantly higher AFRs. At lower flow rates, the opposite is true with diesel igniting at higher values of the AFRs. The results also suggest that the lean ignition limit of biodiesel is not sensitive to air temperature, although the scatter at the lowest air flow rate is bigger. Also shown in the figure is the extreme of predicted light up window for the SGT-100 engine for biodiesel. It further suggests that reliable ignition can be achieved for SGT-100 operating with biodiesel.

The air assist pressure has a minimal impact on the lean ignition limit of diesel, although higher air pressure slightly broadens the limit. This also seems to be the case for biodiesel, as shown in Fig. 7, except at low air mass flow rates, where significantly different AFR is required for ignition at different air assist pressures.

The lean extinction limit was also recorded for the biodiesel at air temperatures of 0°C and 30°C, and is illustrated in Fig. 8. This showed that the lean extinction occurred for both cases at the same conditions, and furthermore, that these conditions were similar to those seen for the lean ignition.

The close similarity in the position of the ignition and extinction could indicate that the igniter is placed in a region where combustion is most likely to be sustained. If there had been a

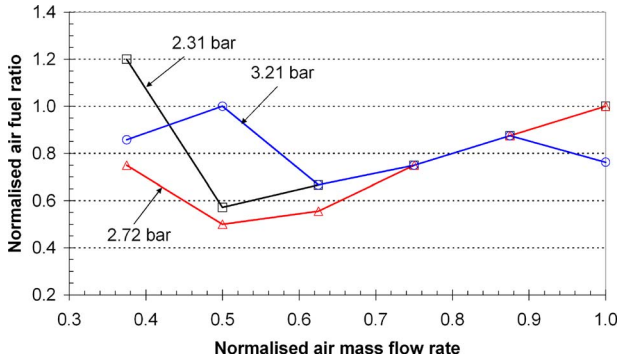

Fig. 7 Effect of air assist pressure on SGT-100 lean ignition limit burning biodiesel at ambient air temperature of 15°C

significant difference between the extinction and ignition curves, it would indicate that the spark was poor or that it was being introduced in an inappropriate place. As the two curves are coincident, within the measurement accuracy available, it indicates that the ignition occurs at the optimal AFR. This in turn would suggest that the design for the igniter position and spark quality for diesel is also optimal for biodiesel.

It is interesting to mention that Wilson et al. [11] showed that their four kinds of biodiesel fuels were harder to ignite than diesel, and that the location of the igniter had a significant impact on the performance. There are several possible reasons for different results from the two different groups. It was found that at the same air mass flow rate, Wilson et al. [11] operated at a much richer fuel condition than Siemens for both fuels. Also, the two groups used different injectors; Siemens used air assist injectors, and Wilson et al. [11] used nonair assist injectors. Different mechanisms for flame stabilization can also contribute to the difference.

5.2 Emissions and Combustion Dynamics. The impact of flame temperature and combustor pressure drop on NO_x emissions are shown in Fig. 9 for two different air inlet pressures of 9 bar and 14 bar at a typical engine combustor full load inlet temperature. Flame temperatures presented in this paper were normalized to the full load flame temperature, and as a result, a normalized value of 1.0 represents the full load condition. At both inlet pressures, diesel had a higher NO_x emission than biodiesel, and, as expected, higher flame temperature resulted in a higher NO_x emission for both fuels. At lower inlet pressure, the combustor pressure drop had an insignificant effect on NO_x formation for both fuels. However, at higher inlet pressure, there was a strong dependence on combustor pressure drop for biodiesel, with the NO_x reduced with the increasing combustor pressure drop. This dependence was not seen for diesel.

It is expected that the NO_x formation would be reduced as the

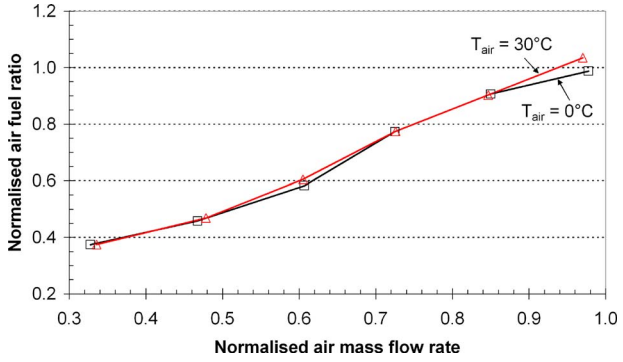

Fig. 8 Effect of ambient air temperature on SGT-100 lean extinction limit burning biodiesel at air assist pressure of 2.72 bar

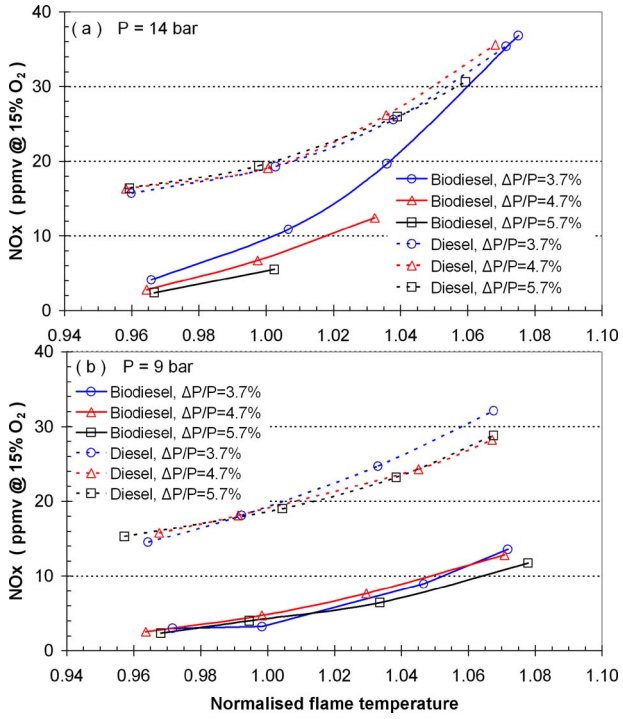

Fig. 9 The effect of the flame temperature and combustor pressure drop on NO_x emission for biodiesel at two different air inlet pressures, and its comparison with diesel

combustor pressure drop is increased for three reasons: (1) the burnt gas residence time in the burner is reduced as the mixture velocity is increased, and as a consequence, the NO_x level is reduced due to the diminished influence of the slow Zeldovich mechanism; (2) particularly for the liquid fuel, as the velocity of the mixture inside the combustor increases, the evaporation and droplet size of the fuel are improved [15], and the mixing with air is enhanced, as a result, NO_x level is reduced; and (3) the mixing of air and fuel is further enhanced by the possible downstream displacement of the flame. However, once perfect mixing is achieved, then the impact of combustor pressure drop on the NO_x emission would be limited to reducing the burnt gas residence time. Syed and Buchanan [16] showed that the NO_x formation is independent of combustor pressure drop, once optimal levels of mixing are achieved in their modified swirler under a gas operation.

Based on the above arguments, for diesel fuel, the optimal level of mixing was achieved in the SGT-100 combustor, regardless of the inlet pressure. However, for biodiesel, at the lower inlet pressure of 9 bar, the optimal level of mixing was achieved, so the combustor pressure drop had a little influence on the NO_x formation, but at the higher inlet pressure of 14 bar, the optimal level of mixing was not achieved, the combustor pressure drop had a great impact on NO_x formation, and mixing was improved by increasing the combustor pressure drop.

As shown in Fig. 9, for biodiesel fuel, comparable levels of NO_x are produced at low flame temperature at the two different inlet pressures, regardless of the combustor pressure drop. As the flame temperature is increased, NO_x formation at higher pressure begins to diverge from those of low pressure, and result in higher NO_x emissions. For diesel fuel, the inlet pressure effect is not significant, although higher pressure produces slightly higher NO_x.

The insignificant dependence of inlet pressure and combustor pressure drop on the NO_x emission for diesel for all the investigated flame temperatures, and for biodiesel at low flame temperature, suggests that well premixed mixtures were achieved, and

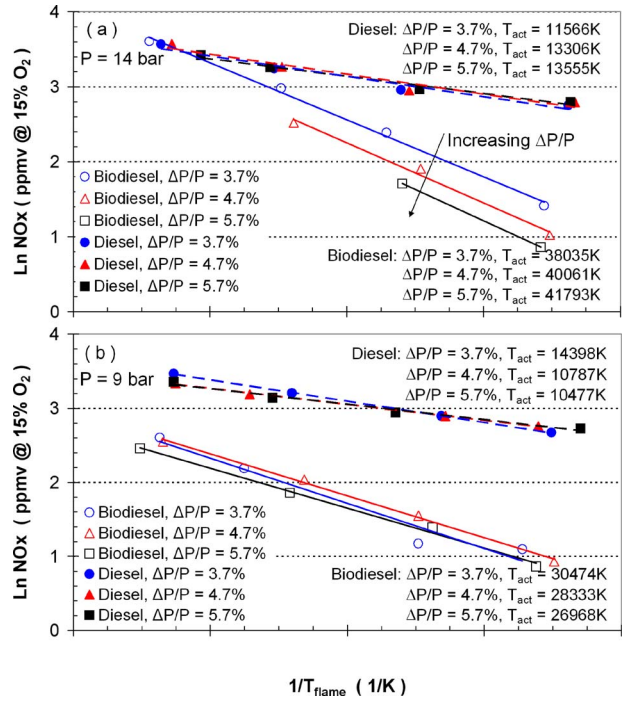

Fig. 10 Activation temperatures for biodiesel and diesel fuel at different air inlet pressures and combustor pressure drops

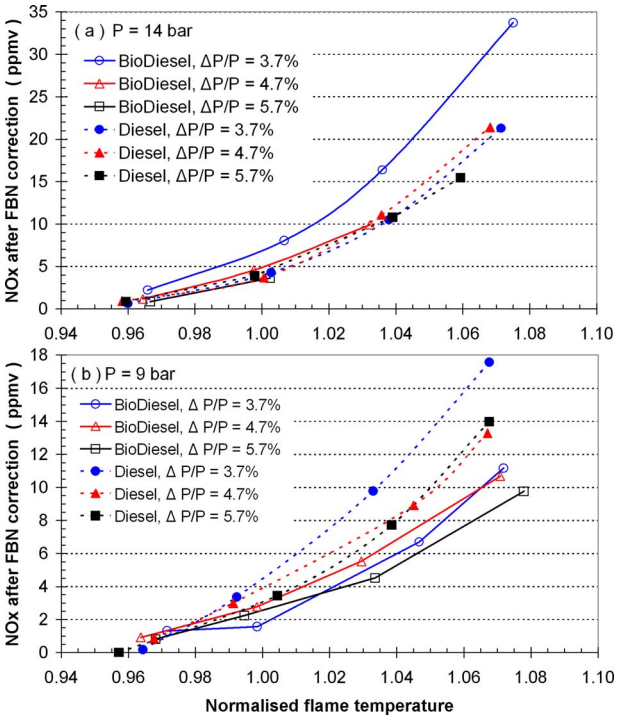

Fig. 11 Comparison of NO_x emissions from biodiesel and diesel after FBN correction

mixing was completed prior to the reaction zone under these conditions. However, for biodiesel, at higher pressure and high flame temperature, as the amount of fuel is increased, there is a clear move away from the minimum level for low pressure. This would suggest that once the amount of fuel supplied exceeds a certain level, mixing is incomplete at the reaction zone.

Figure 9 was replotted as an Arrhenius-type plot in Fig. 10 to get the approximate activation temperature for NO_x formation, based on a simple Arrhenius expression.

Syed and Buchanan [16] demonstrated that the apparent activation temperature is increased as the degree of premixing is increased for gas fuel, and once the optimal mixing level is achieved, the activation temperature is not sensitive to combustor pressure drop. It would be expected that similar behavior would be seen with liquid fuel. This would be complicated by the presence of a fuel bound nitrogen and the NO_x it generates.

As shown in Fig. 10, only for biodiesel at the higher inlet pressure of 14 bar is there a clear trend of activation temperature increasing with the increasing combustor pressure drop. From the link established between activation temperature and mixedness, Fig. 10 further indicates that the degree of premixedness is quite high for diesel at both pressures and for biodiesel at low pressure, but for biodiesel premixedness at higher inlet pressure increases with higher combustor pressure drop. Biodiesel has a higher activation temperature than diesel at the same inlet pressure, and has lower NO_x emissions, which suggests that activation temperature would be an important indicator for NO_x formation.

Campbell et al. [1] and Lapuerta et al. [5] demonstrated that biodiesel fuels have a comparable NO_x emission in industrial gas turbines and internal combustion diesel engines, respectively. This could be because their biodiesel and diesel fuels had comparable nitrogen content. As mentioned before, the biodiesel used in the current study has ten times less nitrogen content than Wilson et al. [11]. Also, the fuel sample analysis showed that the biodiesel used in this study had a significantly less nitrogen content than diesel as listed in Table 1. The experimental study by Eberius et al. [17] and the chemical kinetics study by Warnatz et al. [18] on a propane air flame with 2400 ppm CH_3-NH_2 (methylamine) can be used as a model system for the fuel nitrogen conversion into pollutants. Both studies show that about two-thirds of the fuel nitrogen are oxidized to form NO under fuel lean conditions, and the rest is converted into N_2. Nicol et al. [19] demonstrated that at low equivalence ratios of about 0.5 and 0.6, most of the NO_x is formed by the nitrous oxide mechanism. In the detailed internal measurements on the SGT-100 [20] fueled by mineral diesel, the concentrations of NO and NO_2 were measured. It was found that NO was dominant and was about 80% of the total NO_x. Based on these arguments, an attempt has been made to correct for the fuel bound nitrogen (FBN) effect, assuming that all the nitrogen in the fuel is converted to NO. This correction isolates the influence of FBN, and the effect of mixing and combustion can be identified.

The NO_x emissions corrected for FBN are shown in Fig. 11. A huge reduction in the NO_x level can be seen for diesel, and little reduction is observed for biodiesel. At an inlet pressure of 14 bar, comparable NO_x levels for both fuels can be seen for all flame temperatures and combustor pressure drops, except for biodiesel at the combustor pressure drop of 3.7%, which has the highest NO_x level for all flame temperatures. For an inlet pressure of 9 bar at a lower flame temperature, the NO_x levels are comparable, but diesel shows slightly higher NO_x levels when the flame temperature is increased.

The comparisons of CO emission for both fuels at 15% O_2 are shown in Fig. 12. At an inlet pressure of 14 bar at all flame temperatures investigated, biodiesel has a higher CO emission. This difference is larger at the lowest flame temperature. At the lowest flame temperature, both diesel and biodiesel show strong combustor pressure drop influence on CO emission; CO level is reduced when combustor pressure drop is reduced. When the normalized flame temperature is higher than 0.99, the effect of the combustor pressure drop on the CO level is diminished. At an inlet pressure of 9 bar, the influence of the combustor pressure drop on CO is reduced. Biodiesel has much higher CO emission levels than diesel at the lowest flame temperature, and the difference becomes smaller when the flame temperature is increased until the CO levels for the two fuels are comparable.

For diesel, the effect of the air inlet pressure on CO emission is

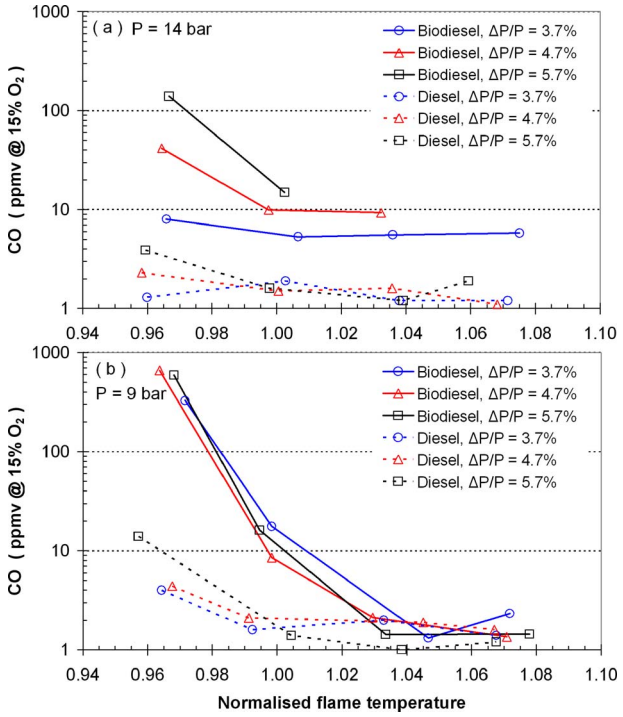

Fig. 12 The effect of flame temperature, combustor pressure drop on CO emission of biodiesel at two inlet pressures, and its comparison with diesel

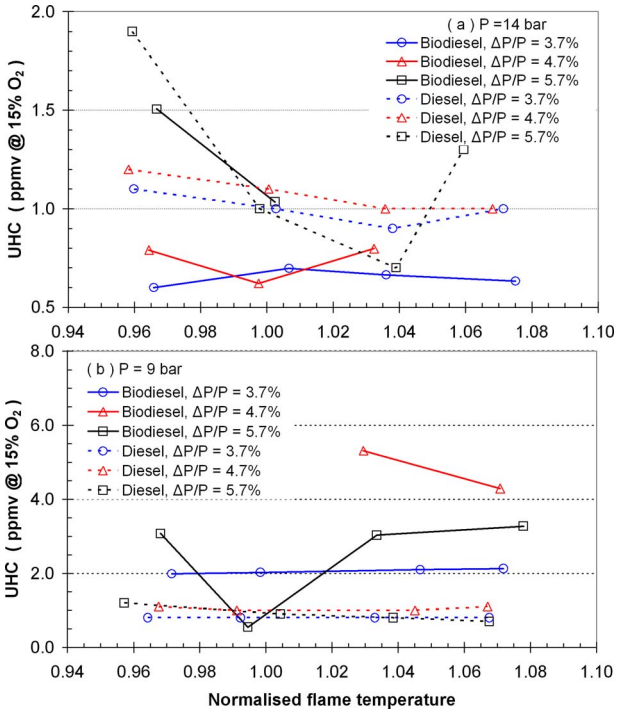

Fig. 13 Comparison of UHC emissions from biodiesel and diesel at two inlet pressures

small when the normalized flame temperature is higher than 0.99. There is some pressure effect at the lower flame temperature, where CO emission is higher when the air inlet pressure is lower. It is interesting to note that for biodiesel at normalized flame temperature of 0.99, there is little pressure effect on CO emission. However, a clear pressure effect is observed at other flame temperatures, with the CO level increased as flame temperature is reduced, and decreased as flame temperature is increased.

The comparisons of unburned hydrocarbon (UHC) emissions are shown in Fig. 13. At a higher air inlet pressure of 14 bar, biodiesel has lower UHC emissions. However, the differences are within 0.5 ppm, and the authors would consider that the two fuels have comparable UHC emissions considering the measurement accuracy. At the lower air inlet pressure of 9 bar, biodiesel has slightly higher UHC emissions, but the differences are within 3 ppm, except at a combustor pressure drop of 4.7%, which has the highest difference of about 4 ppm.

For high pressure rig testing, combustion dynamics were also measured by a pressure transducer mounted at the pilot burner face. The comparisons of combustion dynamic pressure from the two fuels at inlet pressure of 14 bar are shown in Fig. 14 in terms of frequency and root mean square (rms) amplitude. The frequencies and rms pressures were normalized using typical values for the SGT-100 engine at full load conditions. The dynamics frequencies increase as the flame temperature increases for both fuels, but both fuels have comparable dynamics frequencies. Biodiesel has lower rms dynamics pressures at lower flame temperatures, and has higher dynamics when the flame temperatures exceed full load value.

The Sauter mean diameter (SMD) droplet sizes have been estimated to investigate the evaporation process in mixing and combustion. According to Lefebvre [15], the droplet size is a function of dynamic viscosity having $\mathrm{SMD} \propto \mu_L^a$ and a between 0.06 and 0.215. It is also a function of surface tension having $\mathrm{SMD} \propto \sigma^b$ and b about 0.25. The surface tension for biodiesel and diesel were calculated, and the results showed that the surface tension is comparable.

According to Lefebvre [15], SMD can be calculated by Eq. (1) as

$$\mathrm{SMD} = 2.25\sigma^{0.25}\mu_L^{0.25}\dot{m}_L^{0.25}\Delta P_L^{-0.5}\rho_A^{-0.25} \tag{1}$$

where σ is the surface tension (kg/s^2), μ_L is the dynamic viscosity (kg/m s), $\dot{m}_L$ is the liquid mass flow rate (kg/s), ΔP_L is the pres-

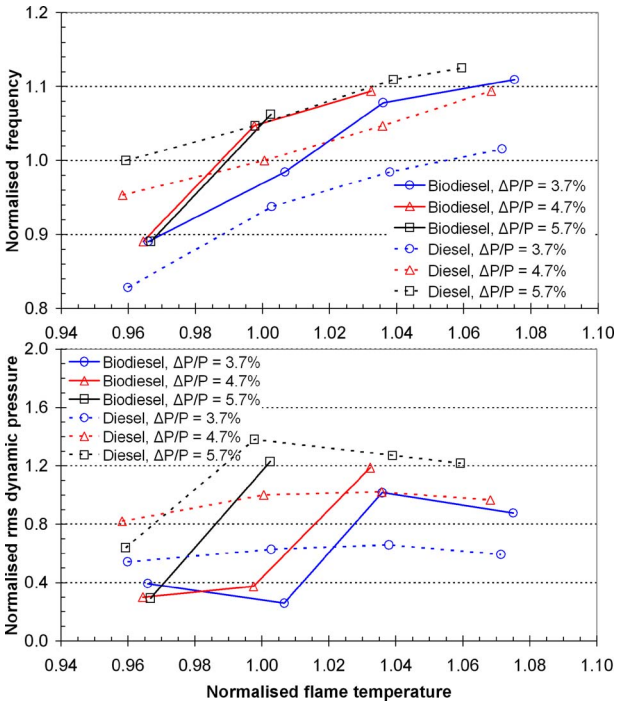

Fig. 14 Comparison of combustion dynamics fueled with biodiesel and diesel at an air inlet pressure of 14 bar

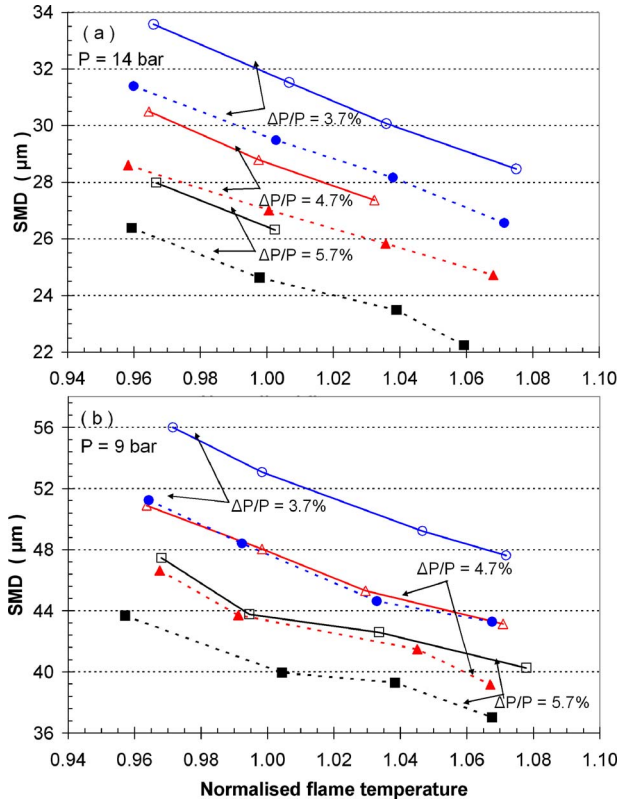

Fig. 15 SMD droplet diameter for biodiesel (solid line) and diesel (dashed line) at different air inlet pressures and combustor pressure drops

sure difference across nozzle (Pa), and ρ_A is the air density (kg/m^3).

The droplet diameters, thus calculated, are shown in Fig. 15. It can be seen that biodiesel has a larger droplet size than diesel at the same condition, and the droplet size is bigger when pressure is reduced for both fuels. According to Eq. (1), the dominant contribution to the different droplet size of both fuels comes from the Dynamic viscosity; as at 313 K, the dynamic viscosities are 4.18×10^{-3} kg/m s and 3.06×10^{-3} kg/m s for biodiesel and diesel, respectively. Biodiesel has a higher dynamic viscosity than diesel, hence, it has a bigger droplet size. It is also significant that evaporation for diesel is better than biodiesel.

Panchasara et al. [9] measured the droplet size of two different biodiesel fuels, and found that the droplet size of biodiesel is bigger than that of diesel. They also demonstrated that the atomization and fuel-air mixing processes have a major impact on NO_x and CO formation. Sequera et al. [10] found that even though the fuel properties are important, the flow effects can dominate the emissions of NO_x and CO, for example, the fraction of the total air used for atomization had a significant effect on both NO_x and CO emission, and emissions decreased with the increase in the atomizing air. They suggest that for a given fuel, the emissions can be minimized by properly tailoring the injector design and the associated combustion processes.

6 Conclusions

Extensive ignition, emissions, and combustion dynamics testing of biodiesel on standard DLE SGT-100 combustion hardware has been conducted to investigate the feasibility of using biodiesel as a fuel to power industrial gas turbines.

In ignition testing, two series of tests were performed to identify the key properties of the proposed fuel. The first set of tests identified the likelihood of the engine lighting, based on the measured probability of the ignition of a single combustor. This demonstrated that a high likelihood of ignition would be possible, depending on the choice of air assist pressure. The second series of tests investigated the lean ignition and extinction limits at various air temperatures. This showed that the ignition limit was different to that measured for mineral diesel, with the biodiesel being easier to ignite at high air mass flow rates, and harder at lower flow rates. It was also demonstrated that air temperature did not have a significant impact on the lean ignition limit. It was further shown that the ignition window for the SGT-100 lays well within the predicted curves for the lean ignition limit, and therefore, good ignition should be possible. The lean extinction limits were found to be very similar to the ignition limits.

Emissions and combustion dynamics were measured in a high pressure test rig. The performance of the burner on the biodiesel was mapped by variation in operating conditions such as the air inlet pressure, temperature, combustor pressure drop, and flame temperature. The results were compared with those of diesel at the same conditions. For all the operating conditions tested, biodiesel had a lower NO_x emission than diesel. For biodiesel at an air inlet pressure of 14 bar, there was a strong link between NO_x and the combustor pressure drop, where the NO_x level was reduced as the combustor pressure drop was increased. It was not the case for the biodiesel at 9 bar, and for the mineral diesel at all the pressures investigated. However, after the FBN correction, comparable NO_x emissions were obtained, although diesel showed a slightly higher NO_x emission than biodiesel at 9 bar inlet pressure.

The analysis of the high pressure rig testing results showed that for biodiesel at low flame temperature and low air inlet pressure, a high degree of premixing was achieved, so NO_x level was independent of the inlet pressure and combustor pressure drop. At high pressure and high flame temperature, the optimal level of mixing could not be achieved due to the amount of fuel supplied. Where mixing is not optimal, the thermal NO_x formation is higher and dependent on the inlet pressure and combustor pressure drop. However, for mineral diesel, good premixing was achieved at all the pressures investigated, and little dependence on the inlet pressure and combustor pressure drop was observed.

At lower flame temperature, biodiesel had significantly higher level of CO than diesel, particularly at a lower inlet pressure of 9 bar. For both fuels, the combustor pressure drop had apparent influence on CO at lower flame temperature with CO level decreasing with the combustor pressure drop decrease, and this influence diminished as the flame temperature was increased.

Both fuels had a comparable level of UHC emission at higher inlet pressure, and biodiesel had slightly higher UHC emissions at lower inlet pressure.

For combustion dynamics, both fuels had comparable frequencies, but biodiesel had lower rms dynamic pressures at lower flame temperatures, and higher when flame temperatures exceed the full load value.

Fuel droplet sizes were calculated, and biodiesel had a bigger droplet size, particularly at lower pressure, lower flame temperature, and lower combustor pressure drop. The dominant contribution of big droplet size for biodiesel came from its much higher viscosity.

Acknowledgment

The tests reported here were partly funded by the European commission as part of the Alternative Fuels for Industrial Gas Turbines (AFTUR) project under Grant No. ENK5-CT-2002-00662.

References

[1] Campbell, A., Goldmeer, J., Healy, T., Washam, R., Molière, M., and Citeno, J., 2008, "Heavy Duty Gas Turbines Fuel Flexibility," ASME Paper No. GT2008-51368.

[2] Molière, M., Panarotto, E., Aboujaib, M., Bisseaud, J. M., Campbell, A., Citeno, J., Mire, P. A., and Ducrest, L., 2007, "Gas Turbines in Alternative Fuel

Applications: Biodiesel Field Test," ASME Paper No. GT2007-27212.
[3] Tate, R. E., Watts, K. C., Allen, C. A. W., and Wilkie, K. I., 2006, "The Densities of Three Biodiesel Fuels at Temperature up to 300°C," Fuel, **85**, pp. 1004–1009.
[4] Tate, R. E., Watts, K. C., Allen, C. A. W., and Wilkie, K. I., 2006, "The Viscosities of Three Biodiesel Fuels at Temperature up to 300°C," Fuel, **85**, pp. 1010–1015.
[5] Lapuerta, M., Herreros, J. M., Lyons, L. L., García-Contreras, R., and Yolanda Briceño, Y., 2008, "Effect of the Alcohol Type Used in the Production of Waste Cooking Oil Biodiesel on Diesel Performance and Emissions," Fuel, **87**, pp. 3161–3169.
[6] Lupandin, V., Thamburaj, R., and Nikolayev, A., 2005, "Test Results of the OGT2500 Gas Turbine Engine Running on Alternative Fuels: Biooil, Ethanol, Biodiesel and Crude Oil," ASME Paper No. GT2005-68488.
[7] Bolszo, C., McDonell, V., and Samuelsen, S., 2007, "Impact of Biodiesel on Fuel Preparation and Emissions for a Liquid Fired Gas Turbine Engine," ASME Paper No. GT2007-27652.
[8] Chiang, H. W. D., Chiang, I. C., and Li, H. L., 2007, "Performance Testing of Mircoturbine Generator System Fueled by Biodiesel," ASME Paper No. GT2007-28075.
[9] Panchasara, H, Simmons, B. M., Agrawal, A. K., Spear, S. K., and Daly, D. T., 2008, "Combustion Performance of Biodiesel and Diesel-Vegetable Oil Blends in a Simulated Gas Turbine Burner," ASME Paper No. GT2008-51496.
[10] Sequera, D., Agrawal, A. K., Spear, S. K., and Daly, D. T., 2007, "Combustion Performance of Liquid Bio-Fuels in a Swirl-Stabilized Burner," ASME Paper No. GT2007-28326.
[11] Wilson, C., Blakey, S., Darbyshire, O., Woolley, R., Cornwell, S., Sidaway, T., and Weiss, S., 2007, *Preparing the Way for Gas Turbines to Run on Alternative Fuel, Developments in Industrial Burner Technology to Meet the Challenges of the Efficient Combustion of New and Difficult Fuels*, British Flame, Birmingham, UK.
[12] Odgers, J., and Krestschmer, D., 1986, *Gas Turbine Fuels and Their Influence on Combustion, Energy and Engineering Science Series*, A. K. Gupta and D. G. Lilley, eds., Abacus, Kent, England.
[13] Wilbraham, N., 2005, "G30 DLE Pilot Liquid Fuel System-Fleet-Wide Development Status," Siemens Industrial Turbomachinery Ltd. Internal Report No. TDR 05/223.
[14] Martin, D. A., 1999, "Production and Development DLE RM Liquid Primary Air Assist Lance Tests on the LP Rig," Siemens Industrial Turbomachinery Ltd. Internal Report No. TDR 99/012.
[15] Lefebvre, A. H., 1999, *Gas Turbine Combustion*, 2nd ed., New York.
[16] Syed, J. K., and Buchanan, E., 2005, "The Nature of NO_x Formation Within an Industrial Gas Turbine Dry Low Emission Combustor," ASME Paper No. GT2005-68070.
[17] Eberius, H., Just, T., Kelm, S., Warnatz, J., and Nowak, U., 1987, "Konversion von brennstoffgebundenem Stickstoff am Beispiel von dotierten Propan-Luft-Flammen," VDI-Ber., **645**, pp. 626–645.
[18] Warnatz, J., Maas, U., and Dibble, R. W., 2006, *Combustion: Physical and Chemical Fundamentals, Modeling and Simulation, Experiments, Pollutant Formation*, 4th ed., Springer, New York.
[19] Nicol, D., Malte, P. C., Lai, J., Marinov, N. N., and Pratt, D. T., 1992, "NO_x Sensitivities for Gas Turbine Engines Operated on Lean-Premixed Combustion and Convertional Diffusion Flames," ASME Paper No. 92-GT-115.
[20] Wedlock, M., Wood, J. P., Miller, M. N., Sims, G. J., Liu, K., Syed, K., Bowen, P., Crayford, A., and Sevcenco, Y., 2008, "Detailed Internal Measurements of a Siemens Combustor Operating at Gas Turbine Relevant Conditions," ASME Paper No. GT2008-50790.

Laboratory Investigations of Low-Swirl Injectors Operating With Syngases

David Littlejohn

Robert K. Cheng

Environmental Energy Technology Division,
Lawrence Berkeley National Laboratory,
Berkeley, CA 94720

D. R. Noble

Tim Lieuwen

School of Aerospace Engineering,
Georgia Institute of Technology,
Atlanta, GA 30332

The low-swirl injector (LSI) is a lean premixed combustion technology that has the potential for adaptation to fuel-flexible gas turbines operating on a variety of fuels. The objective of this study is to gain a fundamental understanding of the effect of syngas on the LSI flame behavior, the emissions, and the flowfield characteristics for adaptation to the combustion turbines in integrated gasification combined cycle clean coal power plants. The experiments were conducted in two facilities. Open atmospheric laboratory flames generated by a full size (6.35 cm) LSI were used to investigate the lean blow-off limits, emissions, and the flowfield characteristics. Verification of syngas operation at elevated temperatures and pressures were performed with a reduced scale (2.54 cm) LSI in a small pressurized combustion channel. The results show that the basic LSI design is amenable to burning syngases with up to 60% H_2. Syngases with high H_2 concentration have lower lean blow-off limits. From particle image velocimetry measurements, the flowfield similarity behavior and the turbulent flame speeds of syngases flames are consistent with those observed in hydrocarbon and pure or diluted hydrogen flames. The NO_x emissions from syngas flames show log-linear dependency on the adiabatic flame temperature and are comparable to those reported for the gaseous fuels reported previously. Successful firing of the reduced-scale LSI at 450 $K<T<505$ K and 8 atm verified the operability of this concept at gas turbine conditions. [DOI: 10.1115/1.3124662]

1 Introduction

The objective of our research is to adapt the low-swirl combustion concept to the gas turbines in integrated gasification combined cycle (IGCC) power plant that burn syngases derived from gasification of coal. Low-swirl combustion is a novel lean premixed combustion method that has been commercialized for industrial heaters. Low-swirl injectors (LSIs) for gas turbines have also been developed for natural gas engines of 5–7 MW in partnership with Solar Turbines of California and for microturbines of 100 kW in partnership with Elliott Energy Systems of Florida [1,2].

To verify the feasibility of the LSI for IGCC combustion turbines, our previous study reported laboratory experiments at atmospheric condition that demonstrated LSI operation with H_2 and diluted H_2 [3]. The velocity data obtained from particle image velocimetry (PIV) showed that the overall flowfield features of the H_2 flames are not significantly different than those of the hydrocarbon flames. The turbulent flame speeds of the H_2 flames correlate linearly with turbulence intensity u'. The value of the turbulent flame speed correlation constant is about 50% higher than the constant determined for the hydrocarbon flames. Comparison of the mean and rms velocity profiles showed that the nearfields of the H_2 flames exhibit self-similarity features that are consistent with those found in hydrocarbon flames. Therefore, the LSI mechanism is not sensitive to the differences in the hydrocarbons and H_2 flame properties and the LSI concept is amenable to burning of H_2.

This paper reports a study of LSI operation with syngases. The syngases derived from gasification of coal generally consist of a blend of H_2 and CO, CO_2, CH_4, and other diluents such as N_2 and steam. The concentration of each constituent varies depending on the type of coal that is being gasified and the heat content of the syngases is generally lower than natural gas. Our previous studies showed that the LSI can deliver <5 ppm NO_x (at 15% O_2) performance while burning fuels of a wide range of heating contents [2–5]. This can be explained by invoking an analytical model that describes the coupling of the self-similar features of the LSI nearfield to the turbulent flame speed S_T. Additionally, these studies showed that lean blow-off limits are insensitive to bulk flow velocity U_0 and the NO_x emissions from atmospheric LSI flames have log-linear dependency on the adiabatic flame temperature T_{ad}. The feasibility of operating the LSI with syngases has already been demonstrated in a study by Sequera and Agrawal [6]. The goal of this paper is to conduct laboratory experiments at atmospheric pressure to determine the lean blow-off limits and obtain more NO_x emissions from syngases to verify the log-linear dependency. Velocity statistics obtained by PIV were used to determine if the analytical model also applies to syngas operation. These were followed by verification of LSI operation at high temperatures and pressures using a reduced scale prototype.

2 Background

The LSI is based on an aerodynamic flame stabilization method that utilizes a divergent flow to sustain a detached propagating premixed turbulent flame [7]. The divergent flow is formed only when the swirl intensities are well below the critical vortex breakdown threshold. Linear decay of the axial velocity within the divergent flow allows the flame to settle where the local velocity is equal and opposite of the turbulent flame speed. Matching the flowfield velocities to the turbulent flame speed is therefore the critical design criterion.

The key component of the LSI is a swirler that supplies the reactants through two passages: an outer annular region with swirl vanes and an open center-channel that allows a portion of the reactants to remain unswirled [8] (Fig. 1). The supply of unswirled reactants through its center is the unique feature of the LSI and its presence retards the formation of a central recirculation zone and promotes the formation of flow divergence. The

Contributed by the International Gas Turbine Institute of ASME for publication in the JOURNAL OF ENGINEERING FOR GAS TURBINES AND POWER. Manuscript received April 4, 2008; final manuscript received May 12, 2008; published online September 30, 2009. Review conducted by Dilip R. Ballal. Paper presented at the ASME Turbo Expo 2008: Land, Sea, and Air (GT2008), Berlin, Germany, June 9–13, 2008.

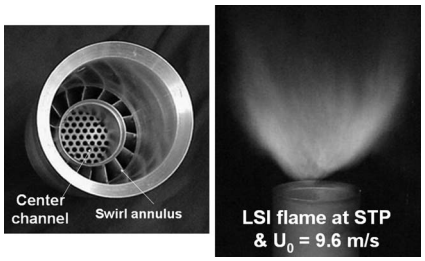

Fig. 1 LSI prototype for Taurus 70 engine

lift-off position of the detached flame is controlled by the divergence rate that can be adjusted by changing the flow split between the swirled and the unswirled flows. The most convenient means to change the flow split is by varying the blockage ratio of the perforated screen covering the center-channel.

The LSI of Fig. 1 utilizes an annular vane swirler for Solar Turbine's T70 SoLoNOx injector [1]. To convert the swirler from high-swirl to low-swirl operation, its center bluff body is removed and replaced by a perforated plate whose blockage ratio is selected to give a swirl number S of 0.4–0.55. The swirl number is defined as [8]

$$S = \frac{2}{3}\tan\alpha\frac{1-R^3}{1-R^2+[m^2(1/R^2-1)^2]R^2} \quad (1)$$

where α is the vane angle and $R=R_c/R_i$. The parameter $m=m_c/m_s$ is the ratio between the mass fluxes of the unswirled m_c and the swirled m_s flows. It is inversely proportional to the blockage ratio of the perforated plate. The SoLoNOx swirler has an internal radius of 3.175 cm and consists of 16 curved vanes with a discharge angle $\alpha=40$ deg. The center-channel to injector radius ratio R is 0.63. As reported in Ref. [2] a fully functional LSI has been developed. Test results showed that the LSI meets all the operational and performance requirements of the T70 engine.

The scientific foundation obtained for the LSI has provided useful insights for its adaptation to gas turbines [9–14]. Analyses of the velocity measurements show that the LSI nearfield exhibits self-similarity behavior. Two parameters deduced from the centerline velocity profiles are invoked to characterize self-similarity [4,5]. They are the virtual origin of the divergent flow x_0, and the nondimensional axial aerodynamic stretch rate a_x. To characterize the flame, the local turbulent flame speeds S_T and the position of the leading edge of the flame brush x_f both determined at the centerline are used. Analysis of S_T shows a linear dependency on turbulence intensity u'. An analytical equation (Eq. (2)) for the velocity balance at x_f shows that a coupling of the self-similar flowfield and a linear turbulent flame speed correlation with u' is the reason why the LSI flame remains stationary through a wide range of velocities and fuel air equivalence ratios ϕ.

$$1-\frac{dU}{dx}\frac{(x_f-x_o)}{U_0}=\frac{S_T}{U_0}=\frac{S_L}{U_0}+\frac{Ku'}{U_0} \quad (2)$$

The two terms on the far RHS simply state that S_T for hydrocarbon flames increases linearly with u' above the baseline value of the laminar flame speed S_L at a slope of K. This slope is an empirical correlation constant derived from the experimental measurements.[1] The first term on the RHS tends to a small value at large bulk flow velocity U_0 because the laminar flame speeds of typical hydrocarbon and hydrogen flames at the ultra-lean operating conditions of gas turbines are on the order of 0.2–0.3 m/s. The second term on the RHS is a constant because turbulence in the center core of the LSI is controlled by the perforated plate and

[1]Linear dependency of S_T on u' is not universal as S_T in other burners tends to be nonlinear and shows "bending" [15].

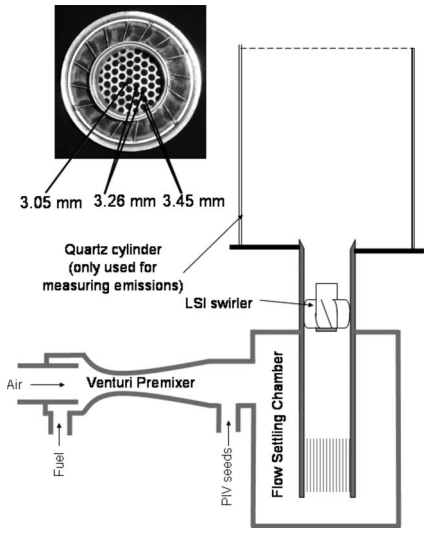

Fig. 2 Schematics of the LSI setup for atmospheric studies

scales with U_0. On the left hand side, self-similar means that $a_x=dU/dx/U_0$ in the second term is constant. The main consequence is that for a given value of K the flame position x_f-x_0 has an asymptotic value at large U_0. Therefore, when S_L is held constant at a certain ϕ, significant flame shift, i.e., changes in x_f, occurs only at low velocities where U_0 is in the same order as S_L. When $U_0 \gg S_L$, changing stoichiometry and/or U_0 do not generate significant flame shift.

Equation (2) is a simple linear analytical expression that describes the relationship between the LSI flowfield and the turbulent flame properties. Because the aerodynamic stretch rate is proportional to the swirl number [8], this expression is a convenient top order model to show how the LSI can be adjusted to accept different fuels.

3 Experimental Apparatus and Diagnostics

The LSI referred to as LSI-LH1 in our previous study [3] was chosen for our atmospheric studies on syngas operation because it can accept fuels with high H_2 concentrations. It is 6.35 cm in diameter with a center-channel of 4 cm in diameter. The swirler from Solar Turbines described earlier is recessed 9.5 cm from the exit. The center-channel plate has variable hole sizes, as shown in the insert of Fig. 2. By measuring the effective areas of the center-channel covered by the plate and the swirl annulus, the ratio of the flows through the unswirled and the swirled passages m is 0.39 to give a swirl number of $S=0.51$. The LSI was mounted vertically on top of a cylindrical settling chamber (Fig. 2). Air supplied by a fan blower entered at the side of a 25.4 cm diameter chamber and flowed into the LSI via a centrally placed 30 cm long straight feed-tube. To produce a uniform flow into the LSI, a perforated screen was placed 5 cm upstream. The air flow rate was adjusted by a computer controlled valve and monitored by a turbine meter. Fuel was injected into a commercial venturi premixer to ensure a supply of homogeneous mixture to the injector. Both the fuel and the PIV seeder flows were controlled by electronic mass flow controllers and set according to a predetermined value of mixture compositions and ϕ. The fuel and air supply system had a maximum capacity of 65 g/s to deliver maximum bulk flow velocity $U_0=22$ m/s.

Flowfield information on the open flames was obtained using PIV. The PIV system consists of a New Wave Solo PIV laser with double 120 mJ pulses at 532 nm and a Kodak/Red Lake ES 4.0 digital camera with 2048×2048 pixel resolution. The optics captured a field of view of approximately 13×13 cm^2 covering the nearfield and the farfield of the flames with 0.065 mm/pixel reso-

Table 1 Syngas compositions and conditions for the PIV experiments

Name	Composition	ϕ	T_{ad} (K)	S_L (m/s)
SG1	0.2 H_2–0.4 CO–0.4 CH_4	0.52	1591	0.14
		0.58	1708	0.18
SG2	0.3 H_2–0.3 CO=0.4 CO_2	0.55	1575	0.14
		0.64	1698	0.22
SG3	0.6 H_2–0.4 CO	0.45	1586	0.22
		0.5	1696	0.29

lution. A cyclone type particle seeder seeds the air flow with 0.6–0.8 μm Al_2O_3 particles, which should track velocity fluctuations up to 10 kHz [16].

Data acquisition and analysis were performed using a software developed by Wernet [17]. Because of the complex and 3D nature of the swirling flowfield, care had to be taken to optimize interframe timing, camera aperture setting, light sheet thickness, and seed density to ensure high data fidelity. Using a portion of the light sheet with approximately 1.1 mm thickness (away from the 0.3 mm waist produced by the 450 mm spherical lens) and a short interframe time (25 μs) helped to freeze the out-of-plane motion of seed particles. Sets of 224 image pairs were recorded for each experiment corresponding to minimum criterion required to produce stable mean and rms velocities. The PIV data were processed using 64×64 pixel cross-correlation interrogation regions with 25% overlap. This rendered a spatial resolution of approximately 2 mm. The velocity statistics were checked to ensure that significant spatial bias or "peak-locking" was not taking place.

The NO_x and CO emissions from the syngas flames were measured by enclosing the flame in a 30 cm long quartz cylinder, 20 cm in diameter (Fig. 2) to prevent the entrainment of ambient air into the combustion products. A water cooled sampling probe was placed at the center of the quartz tube at the exit. The samples were dried by a desiccant before being analyzed by a Horiba PG-250 analyzer that was calibrated using 7.9 ppm NO in nitrogen and 31.8 ppm CO in nitrogen (Scott Specialty Gases, Plumsteadville, PA). The instrument has an accuracy of ±0.5 ppm for NO_x measurements.

Tests of the LSI syngas operations at gas turbine conditions were performed in an optically accessible pressurized combustor. The facility uses a 7.6 cm diameter quartz tube to simulate the combustor casing. Therefore, it can only accommodate a reduced scale LSI. The LSI chosen for these pressurized tests is based on the design of Hwang et. al. [18]. It has a diameter of 2.54 cm with a swirler with a $R=0.55$ center-channel and eight straight blades at $\alpha=45$ deg. Hwang et. al. [18] operated this reduced scale LSI at 1–5 atm but at a relatively low bulk flow velocity of 3 m/s. To configure the LSI for velocities >25 m/s, laboratory atmospheric pressure tests were performed to select the perforated plate that will give optimum flame positions and lean blow-off. The LSI configured with this process has a swirl number of 0.425.

4 Results

4.1 Atmospheric Pressure Experiments. The compositions of the three simulated syngases chosen for the atmospheric pressure laboratory studies are listed in Table 1. They represent the syngases generated by various gasification processes. The laminar flame speeds are determined from the "premix" module of CHEMKIN using GRI 3.0.

To start, lean blow-off limits for the three syngases were determined at bulk flow velocities of 7 m/s$<U_0<$20 m/s. The results are shown in Fig. 3 together with the blow-off limits obtained previously for CH_4, diluted CH_4, and H_2. From Fig. 3, it is

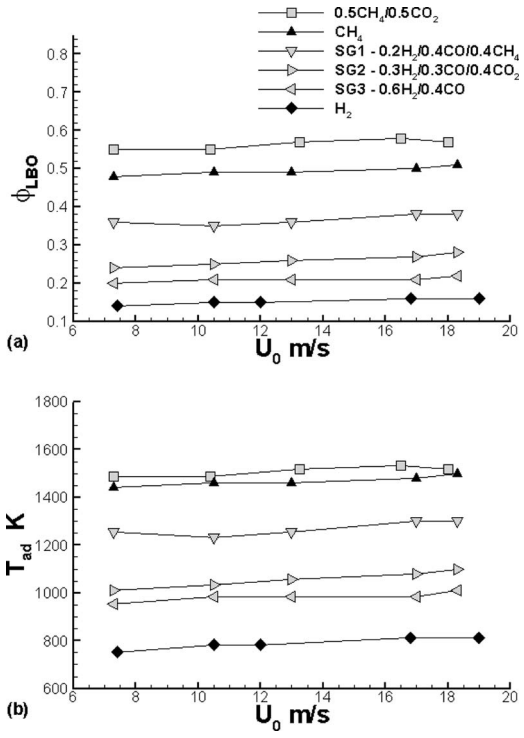

Fig. 3 Lean blow-off limits determined for simulated dry syngases CH_4 and H_2

clear that the lean blow-off limits of the syngases have the same trend as all the other fuels in that they are relatively insensitive to the bulk flow velocity U_0. The equivalence ratio ϕ and the adiabatic flame temperature T_{ad} at which blow-off occur decrease with increasing H_2 concentration and provide more evidence to show that the addition of H_2 promotes flammability. A comparison of the lean blow-offs for SG1 and SG2 illustrates the effectiveness of H_2 addition. SG1 has a higher heat content and 10% less H_2 than SG2. But SG2 blows off at T_{ad} of about 100 K lower than SG1.

The NO_x and CO emissions from the syngas flames are shown in Fig. 4. These measurements were made with the air supplied to the LSI at 27 g/s ($U_0\approx10$ m/s). In Fig. 4(*a*), the NO_x emissions from syngas flames are shown to be consistent with those from the hydrocarbon flames at STP and at gas turbine conditions [1,4,5]. This is the same conclusion from an earlier study by Sequera and Agrawal [6]. Due to the high flammability of the syngases, the flames burn at low T_{ad}, where NO_x can be <1 ppm (at 15% O_2). Though the uncertainties of the emissions data at these conditions are relatively high (±0.5 ppm) the NO_x data from syngases provide more evidence to support the log-linear dependency of LSI NO_x on T_{ad}.

The CO emissions shown in Fig. 4(*b*) are mostly below 20 ppm. The exceptions are for SG1 and a fuel with 0.5 H_2/0.5 CO at 1500 K$<T_{ad}<$1900 K. These modest increases in CO concentrations do not seem to correspond to the CO concentrations in the fuels but their trends (i.e., CO decreasing with decreasing T_{ad} and ϕ) are consistent with insufficient residence time for CO burnout to occur. In their study of LSI firing with syngases, Sequera and Agrawal [6] reported NO_x and CO concentrations at different locations downstream of the flame. They found that the CO concentrations just downstream of syngas flames with the same T_{ad} can differ by almost an order of magnitude. But with sufficient residence time for burnout to occur, their CO concentrations are compatible at the enclosure exit. Therefore, the differences shown in Fig. 4(*b*) may be attributed to the short residence

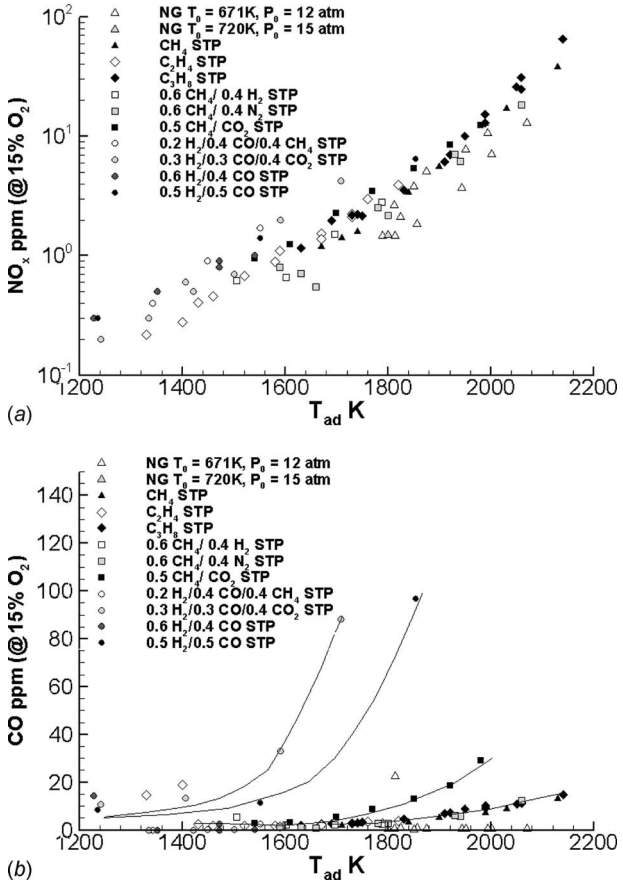

Fig. 4 NO_x and CO emissions of LSI fueled with syngases compared with results from other LSI tests with hydrocarbons and hydrogen at laboratory and gas turbine conditions

time of our experiments (about 10 ms) compared to the Sequera and Agrawal experiments (about 30 ms).

Table 1 also lists the mixtures used for the PIV experiments. The reactant compositions were set at the conditions corresponding to $T_{ad} \approx 1600$ K and 1700 K. For each mixture, PIV measurements were made at three bulk flow velocities $U_0 = 10$, 14, and 18 m/s.

Shown in Fig. 5 are the normalized mean velocity vectors for the flames at $U_0 = 14$ m/s and $T_{ad} \approx 1600$ K. It can be seen that the overall features of the flowfields are not significantly different. In the nearfield ($x/D < 0.5$), the divergent nature of the flow is shown by the outward pointing vectors. The flow discharge angles (outlined by the blue and red contours of high shear stress region of the outer mixing layers) of the three cases are also quite similar. The main differences are shown in the farfield where the SG1 and SG2 flames generated small central recirculation zones while the SG3 flame did not generate recirculation. The reason for the difference may be explained by the differences in their flame dynamics. In premixed turbulent flames, heat release through the thin reaction zone is accompanied by a sharp increase in the flow velocity [19]. This velocity jump Δu can be estimated by $\Delta u = S_L(\tau - 1)$ where τ is the expansion ratio T_{ad}/T_0. For the three flames in Fig. 5, their τ values are the same but their S_L are not. From Table 1, it can be seen that Δu in the SG3 flame is about 50% higher. The consequence of the larger velocity jumps across the flame fronts is evident by comparing the lengths of the velocity vectors at $x/D > 0.5$. Due to the higher axial momentum generated in the product region of SG3, the central recirculation is not formed as all the velocity vectors leaving the upper boundary of the PIV domain are positive. These results demonstrate that the farfield features of the LSI are coupled to the flame/turbulence interactions at the flame fronts. The presence and the absence of the central recirculation zone are artifacts of the dynamic processes associated with the interactions.

The centerline profiles of the syngas flames with $T_{ad} \approx 1600$ K are shown in Fig. 6. Because these flame brushes are close to the LSI exit, only a very small portion of their nearfield linear velocity decay regions is shown (Fig. 6(*a*)). As a consequence, the parameters to characterize the nearfield region, i.e., the virtual origin x_0 of the divergent flow and normalized axial divergence rate $a_x = \delta U/\delta x/U_0$ [4], cannot be determined from these data with a high degree of confidence. Therefore, these axial profiles can only be used to compare the velocity distribution downstream of the flame brush where the flow accelerations associated with the higher Δu from the SG3 flames can be seen. Profiles of the normalized 2D turbulent kinetic energy $q' = ((u'^2 + v'^2)^{1/2})/2$ of Fig. 6(*b*) show that turbulence along the centerline remains relatively constant. This is the same behavior observed in most of the other hydrocarbon flames.

Radial profiles for the syngas flames with $T_{ad} \approx 1600$ K are shown in Fig. 7. These profiles were extracted at $x = 10$ mm just below the flame brushes. Unlike the axial profiles, the radial pro-

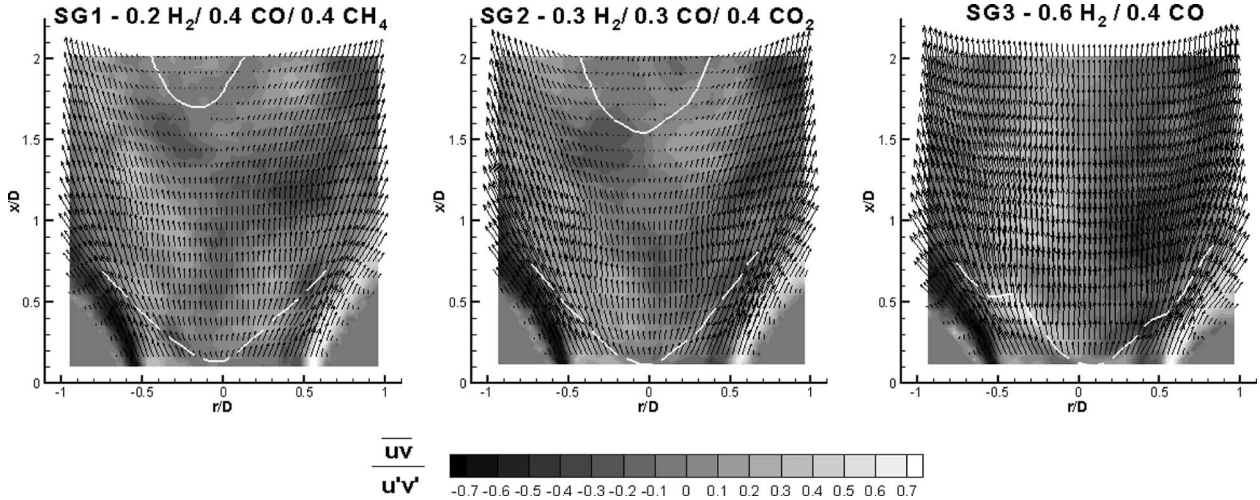

Fig. 5 Normalized velocity vectors for syngas flames at $U_0 = 14$ m/s and $T_{ad} \approx 1700$ K. The top continuous lines mark the boundaries of the recirculation bubble, and lower dashed lines mark the leading edges of the flame brushes.

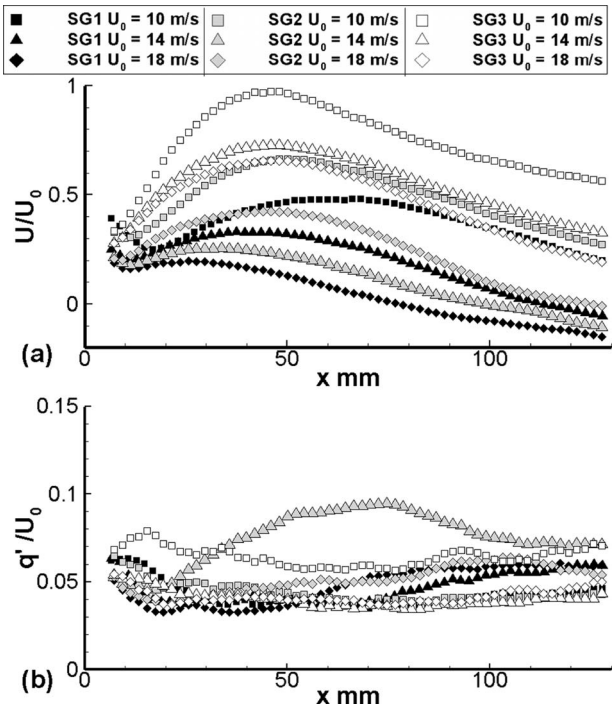

Fig. 6 Centerline profiles of the syngas flames with T_{ad} ≈1600 K: (*a*) mean axial velocity and (*b*) turbulent kinetic energy

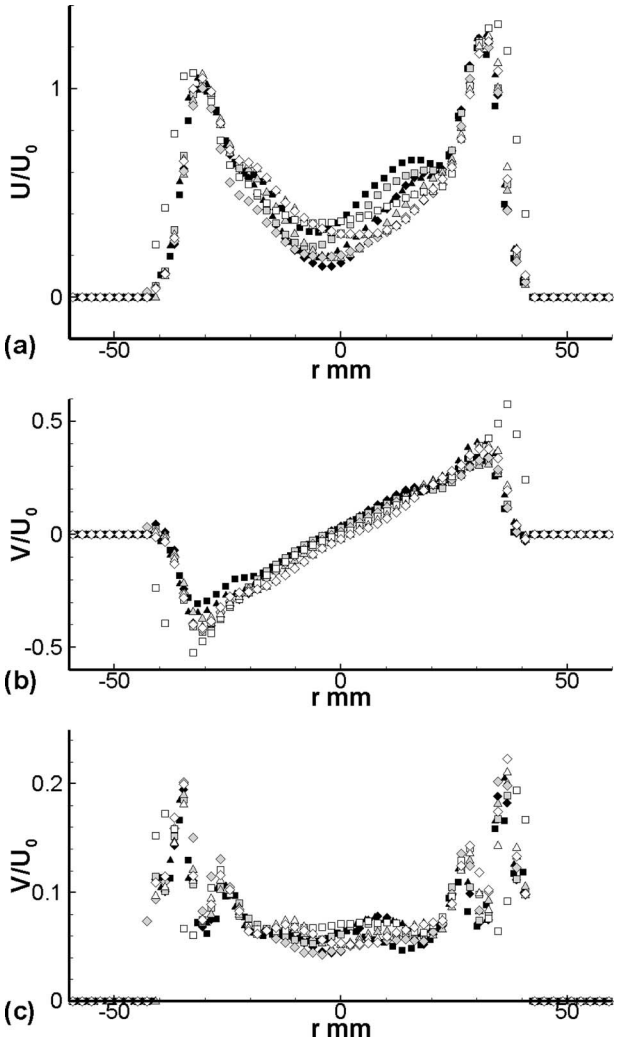

Fig. 7 Radial profiles (at x=10 mm) of the syngas flames with T_{ad}≈1600 K: (*a*) mean axial velocity, (*b*) mean radial velocity, and (*c*) turbulent kinetic energy. Legend same as for Fig. 6.

files collapse onto consistent trends to show self-similar behavior. In Fig. 7(*a*), the U/U_0 profiles have a central low velocity region that has a deficit corresponding to the nonswirling flow supplied through the center-channel. The central nonuniform distribution is a feature of this LSI that uses a perforated plate with varying hole size [3]. Variation in U/U_0 within the core regions corresponds to the scatter in U/U_0, as shown in Fig. 6(*a*), at x=10 mm. The two velocity peaks flanking the central region correspond to the swirling flow. In Fig. 7(*b*), the linear regions of the V/U_0 profiles within the center region (-15 mm$<r<$15 mm) show that the normalized radial divergence rates $a_r = \delta V/\delta r/U_0$ are nearly the same for all cases and averaged about 0.012 mm^{-1}. In the absence of the normalized axial divergence rate data, the a_r data provide the evidence to show that the nearfields of the syngas flames are self-similar. However, the values of a_r are higher than those found in the hydrocarbon flames and seem to be a consequence of the close proximity of the flame brush to the LSI exit. The q'/U_0 profiles (Fig. 7(*c*)) have relatively flat distributions in the center regions surrounded by intense turbulence peaks. These features are the same as those found in all other LSI flames.

The local turbulent flame speed S_T at the LSI centerline is the basic turbulent flame property that explains the LSI stabilization mechanism because the freely propagating flame settles at the point within the center divergent flow region where the mean flow velocity is equal and opposite to S_T. From previous studies using low-swirl burners fitted with air jets [9,13], it has been shown that S_T/S_L correlates linearly with u'/S_L. More recent data from the CH_4/air LSI flames at 7 m/s$<U_0<$22 m/s [4] and from two 5.08 cm ID LSBs of R=0.8 and 0.6 [8] give further support to this correlation.

The S_T for the syngas flames were also deduced from the current data set but because of the close proximity of the SG3 flames to the LSI exit, only three out of the six flames were deemed suitable for extracting reliable S_T information. Figure 8 compares the S_T obtained for the 15 syngas flames together with all previous S_T measurements from the LSI. This plot differs from previous S_T plots in two significant respects. First of all, it contains S_T data obtained only in the LSI whereas previous plots include data from all other low-swirl burners. Second, recent S_L values for unstretched laminar flames were used for the normalization [20]. The most significant change is the new S_L values at the ultralean conditions being much higher than the old. Due to this difference, the maximum values of S_T/S_L and u'/S_L for our data set are reduced. However, the adjustment does not change the linear increasing trend of S_T/S_L with u'/S_L or the correlation constant K. The value of K for the methane/air flames generated by the LSI is 1.73. This is slightly lower than the value of 2.14 obtained by including the S_T data from all the other low-swirl burners. The correlation constant K of 3.15 for the H_2 flames is the same because only the LSI has been used for H_2 flame studies.

Figure 8 shows that the S_T of syngas flames are between those for methane and hydrogen and the results for each syngas exhibit linear dependencies on u' but with slight differences in their turbulent flame speed correlation constants. These trends show that the syngas turbulent flame speed behaves in ways that are consistent with previous conclusion. That is, the primary effect of H_2 addition is to increase the S_T correlation constant K. Based on the analytical model Eq. (2), an increase in K implies a slight decrease in the flame brush position if the swirl number and the bulk flow velocity of the LSI are held constant. This is verified qualitatively

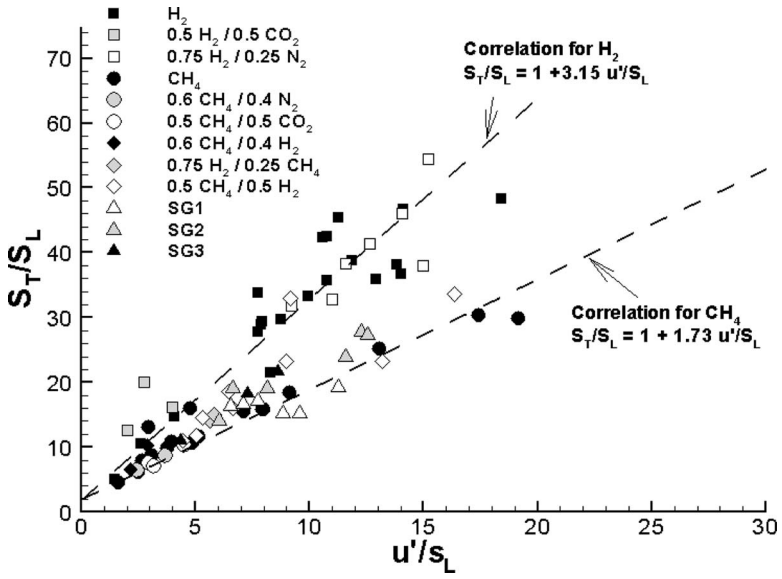

Fig. 8 Turbulent flame speed correlation for LSI flames with fuel blends consisting of H_2, CH_4, CO, N_2, and CO_2

by the lowered flame brush positions of the high H_2 content SG3 flames as mentioned above.

4.2 High Pressure Experiments. A series of tests was performed with CH_4 and H_2/CH_4 blends to verify the compatibility of the reduced-scale LSI with the pressurized combustor and to obtain baseline lean blow-off limits. The experimental conditions covered a nozzle exit velocity range of 20–40 m/s, temperatures at 450 K $< T <$ 505 K, and pressures at 1.5 atm $< P <$ 14 atm. The flame was monitored by a standard JVC camcorder at 30 fps and thermocouples mounted at various positions on the combustor and in the LSI. Although the lean blow-off limits of the reduced-scale LSI are consistent with those observed in other systems, the experience indicated that this LSI with straight swirler blades is not highly compatible with the pressurized combustor because the optimum operating range is restricted to $U_0 < 20$ m/s. Therefore, the high pressure syngas experiments were mostly conducted at the low velocity range.

The compositions of the fuels tested at 450 K $< T <$ 505 K and $P = 8$ atm are shown as circular dots in Fig. 9 where the corners of the triangle represent 100% concentration. The ranges of the concentrations for each component are $20\% < H_2 < 56\%$, $25\% < CO < 60\%$, and $19\% < CH_4 < 51\%$. The equivalence ratios tested, shown in Fig. 10, varied from 0.3 to 0.55 corresponding to adiabatic flame temperatures of 1350 K $< T_{ad} <$ 1800 K. These experiments were performed by starting with a CH_4 flame and adding H_2 and CO into the fuel stream while the flame was lit.

Four representative images are shown in Fig. 11 to illustrate the flame shape as determined from a single video frame. Figure 11(*a*) shows a flame with low H_2 fuel concentration and it assumes a bowl shape similar to the open flame of Fig. 1. The flame is lifted from the LSI though it is not obvious from the camcorder image because the LSI exit is obscured by the lip of the mounting flange of the quartz liner. Figure 11(*b*) shows one of the few syngas flames studied at higher velocity of 31 m/s. The shape and location of this lean $\phi = 0.28$ flame are not very different than the flame of Fig. 11(*a*). The flame in Fig. 11(*c*) is not very discernable due to the apparent increase in background luminosity by the camcorder's built-in auto-exposure feature that compensated for the reduction in luminosity of this flame burning a syngas with a higher 15% H_2 concentration. However, the region of high luminosity associated with the flame impingement on the quartz liner suggests that the position of the flame is relatively unaffected by the change in fuel composition. Figure 11(*d*) shows the image of a syngas flame with 51% H_2 that has very low luminosity. The useful information provided by this image is that significant flame shift does not seem to occur with the higher H_2 fuel concentration.

These syngas flame images show that the flame position and to a lesser extent the flame shape are not significantly changed at high temperatures and pressures. Although the test conditions were limited, the range of the fuel compositions explored and the

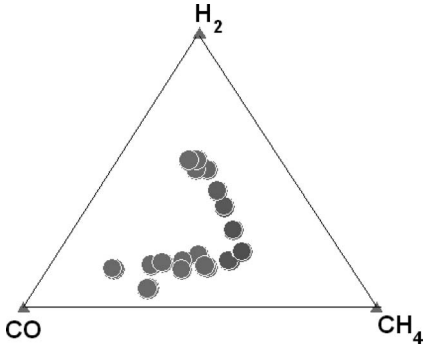

Fig. 9 Syngas compositions evaluated at a 75 cm ID pressurized combustor

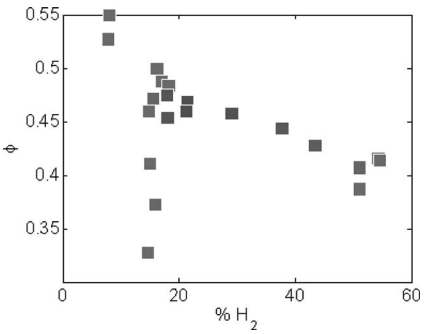

Fig. 10 Equivalence ratios of the high pressured syngas experiments

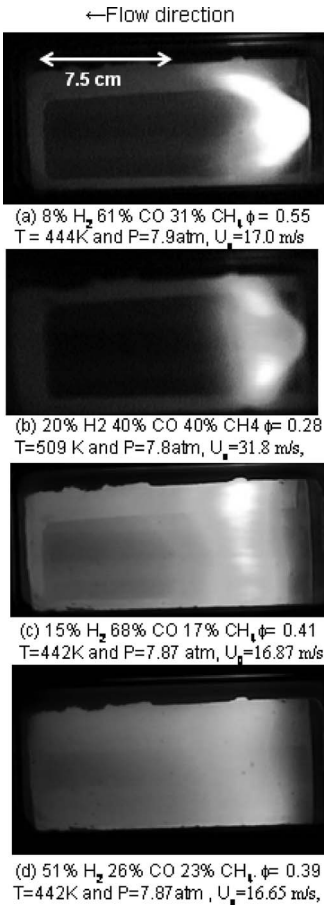

Fig. 11 Luminosity images of syngas flames generated by a reduced scale LSI captured by a camcorder

fact that the LSI can easily transition from one fuel composition to the next demonstrated the viability of this concept for syngases.

5 Conclusion

Open laboratory flames generated by a full size LSI (6.35 cm) were used to investigate the lean blow-off limits, emissions, and the flowfield characteristics. The results show that the basic LSI design is amenable to burning syngases with H_2 up to 60%. Syngases with high H_2 concentration have lower lean blow-off limits to show the effectiveness of H_2 addition to enhance flammability. The PIV measurements show that the overall features of the flowfields of the syngas flames are the same as those found in the hydrocarbon and the hydrogen flames. The nearfields show similarity behavior and the turbulent flame speeds correlate linearly with turbulence intensity u'. These results show that the analytical model developed for the LSI is also valid for syngases. The main implication is that the syngas flame positions change with the H_2 concentration due to the increase in the turbulent flame speed correlation constant K. The NO_x emissions from syngas flames show log-linear dependency on the adiabatic flame temperature and are comparable to those reported for the gaseous fuels reported previously. Verification of syngas operation at elevated temperatures and pressures were performed with a reduced scale (2.54 cm) LSI in a small pressurized combustion channel. Successful firing of the reduced-scale LSI at 450 K $<$ T $<$ 505 K and 8 atm verified the operability of this concept at gas turbine conditions.

Acknowledgment

This work was supported by the U.S. Department of Energy, Office of Fossil Energy under Contract No. DE-AC02-05CH11231.

Nomenclature

$a_x = dU/dx/U_0$ = normalized axial flow divergence (1/mm)
$a_r = dV/dr/U_0$ = normalized radial flow divergence (1/mm)
L_i = swirler recess distance
$m = m_c/m_s$ = mass flux ratio
m_c = mass flux through center channel
m_s = mass flux through swirl annulus
q' = 2D turbulent kinetic energy $= \frac{1}{2}(u'^2 + v'^2)^{1/2}$
Re = Reynolds number $2R_iU_0/\nu$
$R = R_c/R_i$ = ratio of the center channel radius R_c to injector radius R_i
R = radial distance
S = swirl number
S_L = laminar flame speed
S_T = turbulent flame speed
T_{ad} = adiabatic flame temperature
U_0 = bulk flow velocity
U = axial velocity
u' = axial rms velocity
v' = radial rms velocity
uv = shear stress
x = axial distance from injector exit
x_f = leading edge position of the flame brush
x_o = virtual origin of divergent flow

References

[1] Johnson, M. R., Littlejohn, D., Nazeer, W. A., Smith, K. O., and Cheng, R. K., 2005, "A Comparison of the Flowfields and Emissions of High-Swirl Injectors and Low-Swirl Injectors for Lean Premixed Gas Turbines," Proc. Combust. Inst., **30**, pp. 2867–2874.
[2] Nazeer, W. A., Smith, K. O., Sheppard, P., Cheng, R. K., and Littlejohn, D., 2006, "Full Scale Testing of a Low Swirl Fuel Injector Concept for Ultra-Low NO_x Gas Turbine Combustion Systems," ASME Paper No. GT2006-90150.
[3] Cheng, R. K., and Littlejohn, D., 2008, "Laboratory Study of Premixed H2-Air & H_2-N_2-Air Flames in a Low-Swirl Injector for Ultra-Low Emissions Gas Turbines," ASME J. Eng. Gas Turbines Power, **130**(5), pp. 31503-1–31503-9.
[4] Cheng, R. K., Littlejohn, D., Nazeer, W. A., and Smith, K. O., 2008, "Laboratory Studies of the Flow Field Characteristics of Low-Swirl Injectors for Application to Fuel-Flexible Turbines," ASME J. Eng. Gas Turbines Power, **130**(2), p. 021501.
[5] Littlejohn, D., and Cheng, R. K., 2007, "Fuel Effects on a Low-Swirl Injector for Lean Premixed Gas Turbines," Proc. Combust. Inst., **31**(2), pp. 3155–3162.
[6] Sequera, D., and Agrawal, A. K., 2007, "Effects of Fuel Composition on Emissions From a Low-Swirl Burner," ASME Paper No. GT2007-28044.
[7] Chan, C. K., Lau, K. S., Chin, W. K., and Cheng, R. K., 1992, "Freely Propagating Open Premixed Turbulent Flames Stabilized by Swirl," Sym. (Int.) Combust., [Proc.], **24**, pp. 511–518.
[8] Cheng, R. K., Yegian, D. T., Miyasato, M. M., Samuelsen, G. S., Pellizzari, R., Loftus, P., and Benson, C., 2000, "Scaling and Development of Low-Swirl Burners for Low-Emission Furnaces and Boilers," Proc. Combust. Inst., **28**, pp. 1305–1313.
[9] Bedat, B., and Cheng, R. K., 1995, "Experimental Study of Premixed Flames in Intense Isotropic Turbulence," Combust. Flame, **100**(3), pp. 485–494.
[10] Cheng, R. K., 1995, "Velocity and Scalar Characteristics of Premixed Turbulent Flames Stabilized by Weak Swirl," Combust. Flame, **101**(1–2), pp. 1–14.
[11] Plessing, T., Kortschik, C., Mansour, M. S., Peters, N., and Cheng, R. K., 2000, "Measurement of the Turbulent Burning Velocity and the Structure of Premixed Flames on a Low Swirl Burner," Proc. Combust. Inst., **28**, pp. 359–366.
[12] Shepherd, I. G., and Cheng, R. K., 2001, "The Burning Rate of Premixed Flames in Moderate and Intense Turbulence," Combust. Flame, **127**(3), pp. 2066–2075.
[13] Cheng, R. K., Shepherd, I. G., Bedat, B., and Talbot, L., 2002, "Premixed Turbulent Flame Structures in Moderate and Intense Isotropic Turbulence," Combust. Sci. Technol., **174**(1), pp. 29–59.
[14] Bell, J. B., Day, M. S., Shepherd, I. G., Johnson, M. R., Cheng, R. K., Grcar,

J. F., Beckner, V. E., and Lijewski, M. J., 2005, "Numerical Simulation of a Laboratory-Scale Turbulent V-Flame," Proc. Natl. Acad. Sci. U.S.A., **102**(29), pp. 10006–10011.
[15] Lipatnikov, A. N., and Chomiak, J., 2002, "Turbulent Flame Speed and Thickness: Phenomenology, Evaluation, and Application in Multi-Dimensional Simulations," Prog. Energy Combust. Sci., **28**(1), pp. 1–74.
[16] Melling, A., 1997, "Tracer Particles and Seeding for Particle Image Velocimetry," Meas. Sci. Technol., **8**, pp. 1406–1416.
[17] Wernet, M. P., 1999, "Fuzzy Logic Enhanced Digital PIV Processing Software," 18th International Congress on Instrumentation for Aerospace Simulation Facilities, Toulouse, France.
[18] Hwang, Y., Ratner, A., and Bethel, B., 2007, "Chamber Pressure Perturbation Coupling With a Swirl-Stabilized Lean Premixed Flame at Elevated Pressures," Fifth U.S. Combustion Meeting, Western States Section of the Combustion Institute, San Diego.
[19] Cheng, R. K., 1984, "Conditional Sampling of Turbulence Intensities and Reynolds Stress in Premixed Flames," Combust. Sci. Technol., **41**, pp. 109–142.
[20] Jomaas, G., Zheng, X. L., Zhu, D. L., and Law, C. K., 2005, "Experimental Determination of Counterflow Ignition Temperatures and Laminar Flame Speeds of C_2–C_3 Hydrocarbons at Atmospheric and Elevated Pressures," Proc. Combust. Inst., **30**(1), pp. 193–200.

Second Law Efficiency of the Rankine Bottoming Cycle of a Combined Cycle Power Plant

S. Can Gülen
Principal Engineer
Plant System Analysis,
GE Energy,
1 River Road,
Schenectady, NY 12345
e-mail: can.gulen@ge.com

Raub W. Smith
Chief Consulting Engineer
Combined Cycle,
GE Energy,
1 River Road,
Schenectady, NY 12345
e-mail: raub.smith@ge.com

A significant portion of the new electrical generating capacity installed in the past decade has employed heavy-duty gas turbines operating in a combined cycle configuration with a steam turbine bottoming cycle. In these power plants approximately one-third of the power is generated by the bottoming cycle. To ensure that the highest possible combined cycle efficiency is realized it is important to develop the combined cycle power plant as a system. Doing so requires a solid understanding of the efficiency entitlement of both, topping and bottoming, cycles separately and as a whole. This paper describes a simple but accurate method to estimate the Rankine bottoming cycle power output directly from the gas turbine exhaust exergy, utilizing the second law of thermodynamics. The classical first law approach, i.e., the heat and mass balance method, requires lengthy calculations and complex computer-based modeling tools to evaluate Rankine bottoming cycle performance. In this paper, a rigorous application of the fundamental thermodynamic principles embodied by the second law to the major cycle components clearly demonstrates that the Rankine cycle performance can be accurately represented by several key parameters. The power of the second law approach lies in its ability to highlight the theoretical entitlement and state-of-the-art design performances simultaneously via simple fundamental relationships. By considering economically and technologically feasible upper limits for the key parameters, the maximum achievable bottoming cycle power output is readily calculable for any given gas turbine from its exhaust exergy.
[DOI: 10.1115/1.3124787]

1 Introduction

The modern combined cycle (CC) power plant, which embodies the seamless integration of gas and steam turbine (ST) generators, is a challenging subject for fundamental engineering analysis. The individual gas and steam turbine systems are commonly referred to as the topping and bottoming cycles, respectively, as a result of their respective positions in a T-s diagram. Herein, they will be referred to as the Brayton topping cycle (BTC) and the Rankine bottoming cycle (RBC), respectively, in reference to the eponymous thermodynamic cycles governing their major processes. The BTC governing the gas turbine (GT) performance is readily amenable to rigorous thermodynamic analysis via compact analytic formulas. As such it has been widely studied over the past 75 years with excellent published references available to the practitioner (e.g., Refs. [1,2]). It is the paucity of compact analytic formulations for the RBC that makes the analysis dependent on complex heat balance models, which denies the engineer the opportunity to analyze the overall system parametrically to gain insight into further optimization and development while being aware of the limits imposed by the physics.

This paper develops a compact, analytic formulation of the RBC performance. The formulation draws on the second law of thermodynamics in the form of an exergy balance for the control volume (CV) encompassing the RBC. Earlier studies that employed the second law focused on the CC with an emphasis on the BTC losses accounting for the RBC contribution via an "effectiveness" term [3]. Chin and El-Masri [4] applied the exergy analysis to a two-pressure reheat (2PRH) steam BC and identified the individual losses. A similar analysis was done by Horlock et al. [5], which also put the emphasis on GT losses. In an earlier paper, Hofer and Gülen [6] developed a simple expression for the second law entitlement efficiency for an ideal BC where the temperature of the working fluid (i.e., water/steam) exactly matches that of the GT exhaust. Hofer and Gülen show that this maximum work (per unit exhaust gas mass flow rate) is identical to the exhaust gas exergy, which is a thermodynamic property and, using a suitable equation of state, readily calculable from known values of gas composition and temperature. The analysis in Ref. [6] suggested that the RBC performance is readily amenable to a simplified parametric formulation via a BC efficiency that uses the exhaust gas exergy as the yardstick. In the present work, the emphasis is on the development of a compact parametric model in lieu of curve-fit formulas derived from a large number of complex model runs. The fundamental exergy loss and destruction mechanisms are derived from the fundamental principles and cast into simple expressions dependent on a few cardinal parameters. The model is readily amenable to parametric analysis by the practitioner and sheds light on the maximum possible efficiency that can be expected from the modern three-pressure reheat (3PRH) CC plant.

2 Conceptual Model

2.1 Exergy Balance for the Rankine BC. Consider the simplified CC bottoming cycle diagram in Fig. 1. The bottoming cycle consists of a multipressure heat-recovery steam generator (HRSG), a multipressure ST, a water-cooled condenser, and the balance of plant (BOP) equipment.

For the CV encompassing the RBC shown in Fig. 1, the steady-state, exergy rate balance can be written as follows [7]:

$$0 = \dot{m}_{\text{exh}} \cdot (e_{\text{exh}} - e_{\text{stck}}) \pm \sum_j \left(1 - \frac{T_o}{\bar{T}_j}\right) \cdot \dot{Q}_j - \dot{W}_{\text{BC}} - \dot{I} \qquad (1)$$

Contributed by the International Gas Turbine Institute of ASME for publication in the JOURNAL OF ENGINEERING FOR GAS TURBINES AND POWER. Manuscript received July 9, 2008, July 9, 2008; final manuscript received July 15, 2008; published online September 30, 2009. Review conducted by Dilip R. Ballal. Paper presented at the ASME Turbo Expo 2008: Land, Sea and Air (GT2008), Berlin, Germany, June 9–13, 2008.

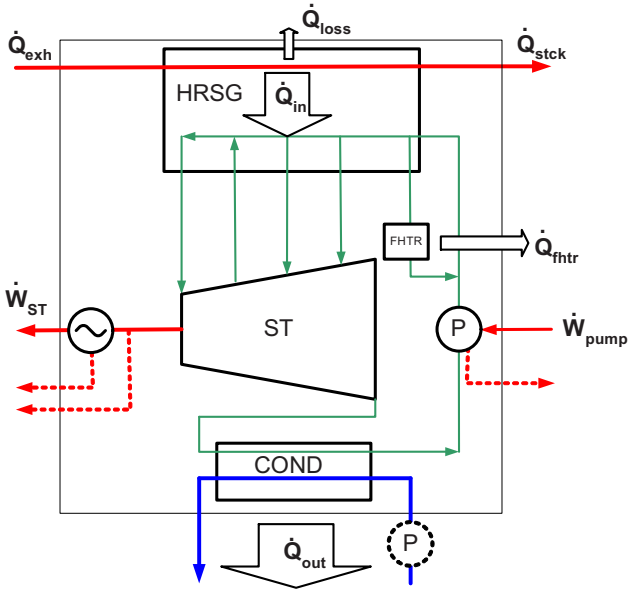

Fig. 1 Simplified CC Rankine bottoming cycle diagram

In Eq. (1), the term $\dot{Q}_j$ is the time rate of heat transfer at a given location on the CV boundary where the instantaneous temperature is $\bar{T}_j$.[1] The most significant heat transfer rate for the RBC is the heat rejection, $\dot{Q}_{out}$, from the condensing steam to the surroundings via the cooling water in the ST condenser. The other two heat transfer rates that are readily identifiable albeit much smaller than $\dot{Q}_{out}$ in magnitude are the HRSG heat loss and the heat transfer from the HRSG feed water to the GT fuel gas in the performance heater. These three heat transfer rates are going to be handled separately. The remaining heat transfer rates are associated with miscellaneous pipe, valve, and equipment heat losses that are too small and numerous to merit individual treatment. They are going to be lumped into a single irreversibility term to represent miscellaneous CV losses.

The net electric power generated by the RBC, $\dot{W}_{BC}$, is the difference between the ST power output at the generator terminals and the total feed water pump motor power. All mechanical (i.e., shaft bearing friction), and electrical (generator and motor) losses are accounted for in the irreversibility balance below. The power consumed by the cooling water circulation pump and other BOP equipment that are outside the RBC are not considered herein. However, they impact the net CC performance via their contribution to the plant's auxiliary power consumption.

The total irreversibility (i.e., rate of exergy destruction) of the RBC is the sum of individual component irreversibilities

$$\dot{I} = \dot{I}_{HRSG} + \dot{I}_{ST} + \dot{I}_{COND} + \dot{I}_{MISC} + \dot{I}_{MECL} + \dot{I}_{ELEC} \tag{2}$$

The first three terms in Eq. (2) are going to be developed from the first principles in Secs. 2.2–2.8. The fourth term is a lumped representation of many small thermodynamic loss mechanisms, which amount to approximately 1.5% of the GT exhaust exergy. The fifth term is the mechanical losses due to friction between turbine and pump shafts and their bearings and—if any—gear losses. The last term is the electrical loss in the ST generator and pump motors. In modern CC plants with state-of-the-art (SOA) generators, motors (~99% efficiency), and shaft rotor-dynamic designs; these last two items add up to approximately 1.5% of $\dot{W}_{BC}$.

The second term (with the minus sign) and the fourth term on the RHS of Eq. (1). represent the "lost" opportunity of generating useful shaft/generator work due to (i) exergy transfer out of the RBC and (ii) exergy destruction. They can be lumped into a single term that will be referred to as "lost work," which is commonly used in the academic literature. Doing that and rearranging the terms slightly, Eq. (1) can be rewritten as follows:

$$\dot{m}_{exh} \cdot (e_{exh} - e_{stck}) + \sum_j \left(1 - \frac{T_o}{\bar{T}_j}\right) \cdot \dot{Q}_j = \dot{W}_{BC} + \dot{W}_{lost} \tag{3}$$

This equation provides a concise description of the RBC from a second law point of view. The total useful work generation potential represented on the LHS of Eq. (3) is due to the net exergy transfer from the GT exhaust gas and other heat transfer (if any) into the RBC. The distribution represented on the RHS shows that a portion of that potential is irretrievably lost. Thus, identifying the mechanisms contributing to the lost work is another way to calculate the net RBC work, which will provide additional insight about what can and cannot be done to improve it practically and/or feasibly.

2.2 Exergy Transfer Via Heat Transfer. The most significant rate of exergy transfer (i.e., loss) out of the RBC is associated with the heat rejection from the ST condenser

$$\dot{E}_{COND} = \left(1 - \frac{T_o}{\bar{T}_{CW}}\right) \cdot \dot{Q}_{cond} \tag{4}$$

The average condenser cooling water temperature in Eq. (4), as well as other important RBC average temperatures, which will be encountered later in the paper, is defined in the Appendix. Note that $\dot{Q}_{cond}$ in Eq. (4) is the same as $\dot{Q}_{out}$ in Fig. 1.

The other readily identifiable rate of exergy transfer out of the RBC is associated with the heat loss from the HRSG. The heat loss from the HRSG is typically quantified by the heat loss factor, κ. A typical value for κ of a modern HRSG is 0.005, i.e., 0.5% of the heat transferred from the GT exhaust gas is lost to the surroundings. The associated exergy transfer is

$$\dot{E}_{HRSG} = \left(1 - \frac{T_o}{\bar{T}_{exh}}\right) \cdot \kappa \cdot \dot{Q}_{in} \tag{5}$$

Performance fuel heating is a standard feature of modern CC plants, where the gaseous fuel from the pipeline is heated in a shell-and-tube heat exchanger to high temperatures (typically 185°C/365°F or higher) utilizing the hot water extracted from the HRSG. Higher fuel temperatures (higher than that needed for the minimum superheat to preclude condensation) reduce the fuel consumption of the GT and improve the GT and CC efficiency with a slight penalty in output due to reduced flow in the GT expander and the reduced IP steam production. While an improvement for the overall cycle, the heat transfer from the HRSG feed water (typically, IP economizer water is used for the fuel heating) is a source of exergy loss for the BC. The rate of exergy transfer out of the RBC via GT fuel gas heating is

$$\dot{E}_{FHTR} = \left(1 - \frac{T_o}{\bar{T}_{fw}}\right) \cdot (\dot{m} \cdot c_p \cdot \Delta T)_f \tag{6}$$

There are two significant exergy addition terms that should be considered for the advanced CC plants with steam-cooled GTs and/or GTs with cooling-air cooling (CAC). These special cases can easily be handled similarly if the relevant design conditions are known. Since these two technologies are highly proprietary no generalized assumptions or information are going to be provided herein.

2.3 HRSG Irreversibility. In order to develop a compact representation of the exergy destruction in the HRSG, consider the

[1]The sign is + for heat transfer into the CV and − for heat transfer out of the CV.

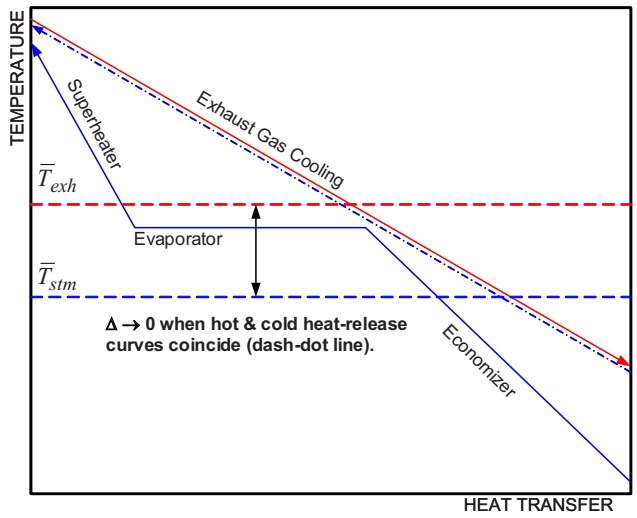

Fig. 2 Heat release diagram for a single-pressure HRSG

heat release diagram for a single-pressure HRSG in Fig. 2.

Using the definition of exergy and average temperature, the energy and exergy balances for the HRSG can be combined and rearranged into the following form:

$$\dot{I}_{\mathrm{HRSG}} = (1-\kappa)\cdot \dot{Q}_{\mathrm{in}} \cdot \frac{T_o}{\bar{T}_{\mathrm{stm}}} \cdot \left(1 - \frac{\bar{T}_{\mathrm{stm}}}{\bar{T}_{\mathrm{exh}}}\right) \tag{7}$$

2.4 Condenser Irreversibility. The first and second laws of thermodynamics for the condenser can be combined in a manner similar to those for the HRSG. Using the definitions of exergy and average temperature, these will result in the following expression for the condenser irreversibility:

$$\dot{I}_{\mathrm{COND}} = \dot{Q}_{\mathrm{cond}} \cdot \frac{T_o}{\bar{T}_{\mathrm{CW}}} \cdot \left(1 - \frac{\bar{T}_{\mathrm{CW}}}{\bar{T}_{\mathrm{cond}}}\right) \tag{8}$$

A method to estimate the condenser heat duty, which is the heat rejection from the BC, and the condensate flow is given in the Appendix. Equations (7) and (8) quantify the major exergy loss mechanism at work in the HRSG and the condenser, respectively; the exergy destruction due to irreversible heat transfer across a finite temperature difference.

2.5 Steam Turbine Irreversibility. A simple expression for the irreversibility of a ST section is developed in the Appendix. In modern CC power plants, the ST consists of multiple sections, the current standard being $N_{\mathrm{ST}}=3$ for modern three-pressure reheat CC systems. For the entire ST, Eq. (A10) can be expanded to

$$\dot{I}_{\mathrm{ST}} = \sum_{i=1}^{N_{\mathrm{ST}}} \left\{ c \cdot \dot{m}_{s,i} \cdot T_o \cdot (1-\eta_i) \cdot \frac{(PR_i - 1)}{k_i \cdot (PR_i + 1)} \right\} \tag{9}$$

The proportionality factor c in Eq. (8) is $\frac{1}{8}$ for a consistent set of English units, e.g., kW, lb/s and R. Conversion to a system in SI units, kW, kg/s, and K, is straightforward.

2.6 Net BC Output From Exergy Balance. The net BC output per unit mass flow rate of the GT exhaust mass flow rate is found by substituting the equations derived above into Eq. (3) and dividing both sides of the equation by $\dot{m}_{\mathrm{exh}}$. Note that the total cooling system lost work from the sum of Eqs. (4) and (8) is simply

$$\dot{W}_{\mathrm{lost}} = \dot{Q}_{\mathrm{cond}} \cdot \left(1 - \frac{T_o}{\bar{T}_{\mathrm{cond}}}\right) \tag{10}$$

Similarly, the total exhaust gas heat-recovery system lost work from the sum of Eqs. (5) and (7) can be combined into

$$\dot{W}_{\mathrm{lost}} = \dot{Q}_{\mathrm{in}} \cdot \left\{ \kappa + \frac{T_o}{\bar{T}_{\mathrm{stm}}} \cdot \left(1 - \kappa - \frac{\bar{T}_{\mathrm{stm}}}{\bar{T}_{\mathrm{exh}}}\right) \right\} \tag{11}$$

Substitution of all lost work terms into Eq. (3) and dividing both sides of the equation by GT exhaust flow, the result is

$$\dot{w}_{\mathrm{BC}} = \left\{ e_{\mathrm{exh}} \cdot (1-\varepsilon_{\mathrm{misc}}) - e_{\mathrm{stck}} - \left\{ \kappa + \frac{T_o}{\bar{T}_{\mathrm{stm}}} \cdot \left(1 - \kappa - \frac{\bar{T}_{\mathrm{stm}}}{\bar{T}_{\mathrm{exh}}}\right) \right\} \cdot \dot{q}_{\mathrm{in}} - \left(1 - \frac{T_o}{\bar{T}_{\mathrm{cond}}}\right) \cdot \dot{q}_{\mathrm{out}} - \left(1 - \frac{T_o}{\bar{T}_{\mathrm{fw}}}\right) \cdot \frac{(c_p \cdot \Delta T)_f}{1 + 1/f} \right.$$
$$\left. - \sum_{i=1}^{N_{\mathrm{ST}}} \left\{ c \cdot \mu_{s,i} \cdot T_o \cdot (1-\eta_i) \cdot \frac{(PR_i - 1)}{k_i \cdot (PR_i + 1)} \right\} \right\} \cdot \frac{1}{1+\varepsilon_{\mathrm{FP}}} \tag{12}$$

In Eq. (12), $\varepsilon_{\mathrm{misc}}$ and $\varepsilon_{\mathrm{FP}}$ are contributions of miscellaneous cycle losses and feed pumps, typically 1.5% each for typical CC applications. The key gas and water/steam parameters that specify the RBC are given in Table 1. The key hardware design parameters that specify the RBC are given in Table 2. The net specific RBC output can easily be calculated from Eq. (12).

The following calculation sequence (or algorithm) is straightforward.

1. GT calculations determine T_{exh}, $\dot{m}_{\mathrm{exh}}$, and f.
2. Total steam flow per unit GT exhaust mass flow rate, μ, is calculated from Eq. (A7).
3. T_{stck} is calculated from Eq. (A8).
4. $\bar{T}_{\mathrm{exh}}$, $\bar{T}_{\mathrm{stm}}$, $\bar{T}_{\mathrm{CW}}$ and $\bar{T}_{\mathrm{fw}}$ are calculated from Eqs. (A2), (A3*a*), (A3*b*), (A4), and (A5) in the Appendix.
5. Remaining terms are evaluated from the equations and tables given above and substituted into Eq. (12).

2.7 Accounting for Other Energy Inputs. For a "pure" CC system, the only energy source to the steam BC is the exhaust energy of the gas topping cycle. Advanced systems such as G-class turbines and H-System™ incorporate more complex integration of the Brayton and Rankine cycles via closed-loop steam cooling (CL-SC) of turbine parts [14]. Another feature of the advanced turbines, especially those with high compressor PRs, is the cooling of the turbine cooling air (CAC) in a heat exchanger that utilizes the IP and/or HP feed water and produces steam. For the CC systems with advanced integration features, the exergy input into the BC via the heat picked up by the cooling steam and/or feed water should be added in Eq. (12). For each separate exergy input to the RBC, a term similar to Eq. (4) or Eq. (8) should be

Table 1 Key Rankine BC thermodynamic design parameters, Refs. [8–10]

Parameter	Description	SOA	Range
T_{exh}	GT exhaust temperature	1100°F (593°C)	1100–1200°F (593–649°C)
T_f	GT fuel temperature	365°F (185°C)	365–400°F (185–204°C)
T_{stm}	Steam temperature	1050°F (565°C)	1000–1100°F (538–593°C)
P_{stm}	HP steam pressure	1800 psi g (124 bar g)	1600–2400 psi g (110–165 bar g)
P_{cond}	Condenser pressure	1.5 in. Hg (51 mbar)	1.2–1.8 in. Hg (41–61 mbar)[a]
T_{stck}	HRSG stack temperature	175°F (79°C)	See footnote b
$T_{CW,in}$	Cooling water inlet temperature	63°F (17°C)	61–68°F (16–20°C) [c]

[a]A function of available hardware, ambient conditions, and economic considerations
[b]Typically not an independent design parameter; can be limited by environmental regulations.
[c]Not an independent parameter. Specified by the choice of cooling system and economic considerations at a given ambient.

Table 2 Key Rankine BC hardware design parameters, Refs. [11–13]

Parameter	Description	SOA	Range
ΔT_{pinch}	Evaporator pinch	15°F (8°C)	10–20°F (6–11°C)
ΔT_{subc}	Economizer subcool	10°F (8°C)	0–20°F (6–11°C)
κ	HRSG heat loss parameter	0.5%	0–1.0%
TTD	Condenser TTD	7°F (4°C)	>5°F (3°C)
ΔT_{CW}	Condenser cooling water temperature increase	18°F (10°C)	>15°F (8°C) [a]
ΔT_{app}	Cooling tower (CT) approach	15°F (8°C)	>5°F (3°C) [a]
η_i	ST section efficiencies	90+%	See Fig. 4
l_x	Specific exhaust loss	7 Btu/lb (16 kJ/kg)	6–10 Btu/lb (14–23 kJ/kg)
PR_i	ST section pressure ratios	5–70	See footnote b
ΔP_{rht}	Reheater pressure loss	10%	See footnote b

[a]Only two of the three can be independent: CT approach to wet bulb, condenser TTD, and cooling water temperature increase. All three determine the cooling water inlet and exit temperatures.
[b]Subject to ST aerodynamic and mechanical design limitations and thermal cycle optimization.

added to Eq. (12). The particular average heat addition temperature can be determined from requisite cycle conditions via Eq. (A1). Such features are highly proprietary and system specific. In general, the exergy addition to the RBC via CAC or CL-SC can be expected to be equivalent to 5–8% of the exhaust exergy.

Steam-cooled GT-based RBCs (with or without CAC) are highly integrated cycles, which are really in a different class by themselves. Another well-known example of the highly integrated heat-recovery cycles is the humidified air turbine (HAT). Cascaded HAT or CHAT [15] and evaporative GT (EvGT) [16] are among many proposed variants of this particular power plant cycle. Jonsson and Yan [17] investigated the latter utilizing a second law approach similar to the one used here. They focused on the exergetic efficiencies of cycle components rather than exergy destruction and transfer associated with those components. Highly integrated cycles such as EvGT are not amenable to a meaningful separation such as topping and bottoming cycles. They can only be analyzed as a whole, in which case, not surprisingly, the GT combustor loss is going to dominate all other contributors. In Ref. [17], combustor exergy destruction is ~25% of the fuel exergy. The largest non-GT exergy loss contributor is the flue gas condenser, ~7% of the fuel exergy, followed by the other heat exchangers and the humidification tower. One-to-one comparison with the exergetic efficiency herein, which is based on the GT exhaust gas exergy, is not possible due to the fact that the modification of the cycle via humidification significantly impacts the exhaust gas composition and temperature.

2.8 Combined Cycle Output and Efficiency. Combined cycle net output is the sum of the GT and ST generator outputs after subtracting the plant auxiliary power consumption. For a CC with N gas turbines and a steam turbine

$$\dot{W}_{CC} = \{N \cdot \dot{W}_{GT} + \dot{W}_{BC}\} - \dot{W}_{aux} \tag{13}$$

The exergetic efficiency of the RBC is defined as the fraction of the GT exhaust exergy that is converted into net RBC work. For a CC with N gas turbines and a steam turbine, this results in

$$\varepsilon_{BC} = \frac{\dot{W}_{BC}}{N \cdot \dot{m}_{exh} \cdot e_{exh}} = \frac{\dot{w}_{BC}}{e_{exh}} \tag{14}$$

The exergetic efficiency in Eq. (14) is identical to the second law BC effectiveness of Ref. [4] or the "rational" efficiency of Ref. [5], with the implicit assumption that the exergy of the exhaust gas at $T_{stck}=T_{amb}=T_o$ is zero.[2] This ignores the fact that at $T_{stck}=T_{amb}=15°C$ (59°F) some of the H_2O vapor in the exhaust gas would condense with the release of latent heat. The potential for work utilizing that heat is ignored. For the exhaust gas with 10%(v) H_2O the condensation would start at ~116°F/47°C (h_{fg}=1,028 Btu/lb or 239.1 kJ/kg.) For 454 kg/s (1000 lb/s) exhaust gas flow about 25.4 kg/s (56 lb/s) water would condense releasing ~60 MW heat with a potential of 6 MW useful work. This is about 4–5% of the exhaust exergy at 454 kg/s-621°C (1000 lb/s-1150°F) Nevertheless, extracting work out of water vapor condensing at 47°C (116°F) would be extremely expensive and difficult and ignoring this does not impact the current analysis. Using the definition in Eq. (13), the CC net efficiency is simply its ratio to total GT heat consumption (HC)

$$\eta_{CC} = \frac{N \cdot \{\dot{W}_{GT} + \varepsilon_{BC} \cdot \dot{m}_{exh} \cdot e_{exh}\} - \dot{W}_{aux}}{N \cdot HC} \tag{15}$$

Note that the auxiliary power in Eq. (15) is about 3% of $\dot{W}_{BC}$

[2]The properties herein are calculated using JANAF package [29] with the zero enthalpy reference set to T_o. As such the enthalpy and entropy of the exhaust gas at $T_o(=T_{amb})$ are exactly zero.

Table 3 Key GT and CC data from GTW 2006 Handbook [18]

	F	G	Reheat
Exhaust flow (lb/s (kg/s))	447–1521 (203–690)	1284–1625 (582–737)	972–1410 (441–640)
Exhaust temp. (°F (°C))	1068–1164 (576–629)	1089–1135 (587–613)	1125–1139 (607–615)
GT output (MW)	75.9–286.6	267.5–334	188.8–289
GT efficiency	35–39.5%	39.1–39.5%	38.1–39.2%
ST output (MW)	44.4–303.7	134.5–348	N/A
CC output (MW)	118–836	397–999	277–856
CC efficiency	54.4–59.2%	58.4–59.5%	56.4–59.0%

with reasonable design assumptions adopted herein and a limited standard BOP scope. Since the RBC contribution is about one-third of the total CC output, not accounting for this will overstate the CC net efficiency by about 0.6 points at the current 58–60% level. Any CC net performance that is cited without stating the basis for the plant auxiliary load (or implies an unrealistically low auxiliary load assumption) is essentially meaningless.

From Eq. (15), the relationship between CC efficiency and BC exergetic efficiency is easily obtainable

$$\frac{\partial \eta_{CC}}{\partial \varepsilon_{BC}} = \frac{\dot{m}_{exh} \cdot e_{exh}}{HC} \cdot (1 - \alpha) = \frac{\dot{E}_{exh}}{HC} \cdot (1 - \alpha) \tag{16}$$

where α is the plant auxiliary power consumption as a fraction of the net RBC power output.

For modern GTs with 1100+ °F (593+ °C) exhaust temperatures, the exhaust exergy is about 50% of the exhaust energy, which in turn is about 60% of the GT heat consumption. Thus, to a very good approximation each 1% in BC exergetic efficiency, on a relative basis, is worth about $\frac{1}{3}$% in CC net efficiency. On an absolute basis, this translates into approximately $\frac{1}{4}$ CC points for each additional percentage point in BC exergetic efficiency.

3 Rankine BC Performance

3.1 Today's State of the Art. In order to establish a performance benchmark for modern heavy-duty, industrial GTs and CC plants, original equipment manufacturer (OEM) data extracted from a widely used industry source [18] is analyzed with the model developed above. This also provided a good test for the predictive powers of Eq. (12). The data comprises 50 Hz and 60 Hz F-Class, G-Class, and reheat (RHT) turbines ranging from 75 MW to 330 MW (ISO rating.) Only 3PRH systems, both in 2 $\times$1 and 1 $\times$ 1 configuration, have been analyzed. Table 3 shows a summary of the data.

OEM-reported GT data is used "as is" with no adjustments. No attempt has been made to test the data for heat balance consistency similar to that undertaken in Ref. [19].[3] The focus herein is on the BC, which only needs the exhaust flow and temperature. The BC parameters from Tables 1 and 2 have been used in the calculation. A baseline of 89%/90%/91% is assumed for HP/IP/LP efficiencies. Minimum 25 deg (°C) superheater approach is used for T_{stm} with a maximum of 565 °C (1050 °F). Condenser pressure is set to 41 mbar (1.2 in. Hg) unless specified otherwise in the data set, which is the typical condition assumed for published reference data. In all cases 185 °C (365 °F) fuel heating is assumed, which may or may not be the case for some machines. For the G-class turbines, exergy input to the BC via cooling steam is assumed. For the purposes of the current work, it is assumed that the reported ST number is the generator output and compared with the value calculated from Eq. (12), which is multiplied by a factor of 1.015 to account for the feedpump work.

Figure 3 shows that the simple parametric model of Eq. (12) is in excellent agreement with the OEM-reported ST generator data. The absolute average deviation between the data and the model is 1.5% in a ST output range of 45–290 MW. This is a testament to the predictive power and the accuracy of the second law-based model when one considers that the model is used as is with SOA design data in Tables 1 and 2 without knowing anything about the actual ST designs.

Rankine BC exergetic efficiencies implied by the OEM data in Ref. [18] are summarized in Fig. 4. The data points covers F-class air-cooled, G-class steam-cooled, and reheat machines. The impact of CL-SC and CAC are excluded.

As the next step, baseline HP/IP/LP efficiencies have been scaled in lockstep to match the reported ST output. The resulting average section efficiencies are tabulated in Table 4. In general, the "implied" ST section efficiencies are in good agreement with published data for modern large CC steam turbines [20], also in-

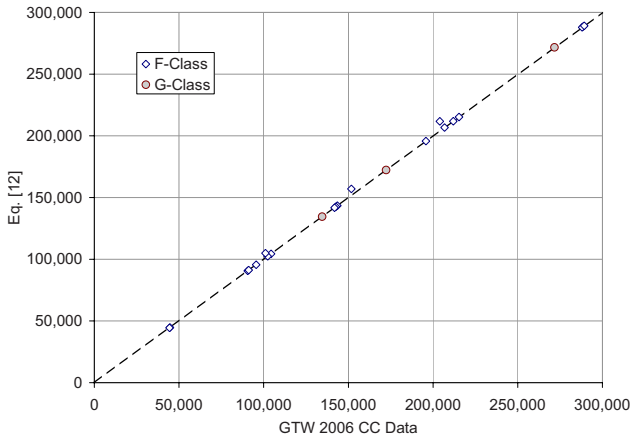

Fig. 3 Comparison of OEM-reported CC ST outputs with the predictions from Eq. (12) using the GT exhaust data

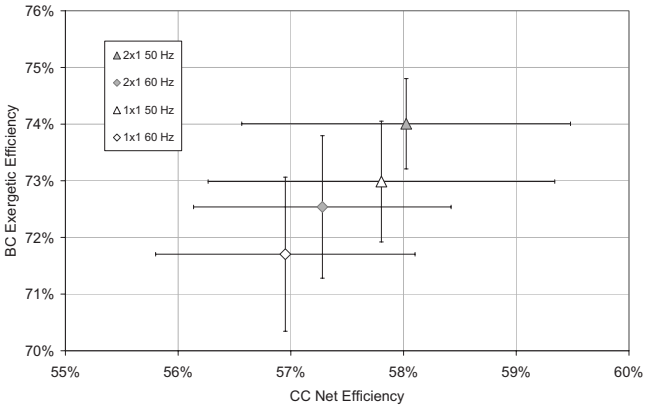

Fig. 4 RBC exergetic efficiencies from the OEM data in Ref. [18]

[3]This is essentially a futile task due to the paucity of information regarding cycle details, auxiliary loads, and the impossibility of weeding out the margins.

Table 4 ST section efficiencies

	HP (%)	IP (%)	LP (%)
Base	89.0	90.0	91.0
Ref. [20]-unfired	89.5	92.2	94.2
Ref. [20]-fired	89.4	92.3	92.7
2×1 50 Hz F (±1.5%)	90.1	91.1	91.4
Min–max	86.9–91.9	87.8–92.9	88.1–93.2
2×1 60 Hz F (±2.5%)	87.8	88.8	89.1
Min–max	84.0–92.0	85.0–93.1	85.2–93.4
1×1 50 Hz F (±1.6%)	88.7	89.7	90.0
Min–max	85.9–90.7	86.8–91.8	87.1–92.1
1×1 60 Hz F (±2.6%)	86.5	87.5	87.7
Min–max	82.6–90.3	83.6–91.3	83.8–91.6

cluded in the table.

Note that the efficiencies reported in Ref. [20] are "cylinder" or steam-path efficiencies, measured from bowl to exhaust. The efficiencies used herein are "section" efficiencies, which include the losses associated with stop and control valves and other piping. For the LP the efficiency definition used herein is the base value from bowl to used energy end point (UEEP) with zero exhaust losses (see Ref. [21] for details.) Depending on the valve design HP/IP section efficiencies are typically lower than the corresponding cylinder efficiencies by about 1 point.

The results of the data analysis can be summarized as follows.

1. Today's SOA in Rankine BC design indicates, on average, an exergy conversion rate of 72% to 74%. The individual data cover a wider range, 70–75%, and reflect the differences in OEM equipment, quoting and margining practices, as well as size effects.
2. The impact of larger size, i.e., volumetric flow, on ST efficiencies is, on average, about +2.3 points for larger 50 Hz machines and about +1.4 points for larger 2×1 plants. Note however that, at the higher end of the spectrum, the efficiency delta between 60 Hz and 50 Hz machines is only +0.5 points.
3. This size effect adds, on average, about one percentage point to the exergetic efficiency; for GT size (60 Hz versus 50 Hz), as well as plant size (1×1 versus 2×1), in favor of larger machines and plants.

Note that steam cooling or CAC (reheat turbines) add exergy to the BC. For the H-class machines where both stationary and rotating parts are steam-cooled published estimates from Refs. [19,22] indicate exergy addition equivalent to 5.5–7.5% of e_{exh}. One estimate for the GT-CAC heat load for the reheat turbine (GT26B in Ref. [22]) suggests that the exergy added to the BC is ~6% of the e_{exh}. This corresponds to a ST output of nearly 11 MW and is also confirmed by the published number by the OEM [23]. The addition of exergy equivalent of about 5–8% of GT e_{exh} to the BC is one of the key advantages of CL-SC and CAC and can boost the "effective" exergetic efficiency to 80–81%.

Finally, it must be recognized that the data reflects an unbiased look at the published OEM data within a consistent conceptual framework. The numbers should be interpreted as characterization parameters that quantify the ability of the Rankine BC to convert exhaust gas exergy into useful work.

3.2 Rankine BC Losses. The distribution of the e_{exh} among different loss mechanisms in the BC is shown in Fig. 5. The breakdown is based on an average F-class GT-based CC plant's bottoming cycle performance from Eq. (12). based on the SOA assumptions in Tables 1 and 2. While the shown performance, 70.5% RBC exergetic efficiency, is closer to the lower end of the spectrum displayed in Fig. 4, considering that OEMs typically publish their most optimistic performance levels with the most optimistic assumptions and margins, it should be quite representative of a modern CC plant performance.

Figure 5 illustrates the impact of the physical design limitations and the constant temperature evaporation and condensation of water on the two cardinal assumptions of ideality implied by $\varepsilon_{BC} = 100\%$ as follows.

1. Coincident temperature profiles of exhaust gas and working fluid in the HRSG so that the exhaust gas is cooled to the same temperature as the working fluid at its coldest while the latter is heated to the same temperature as the exhaust gas at its hottest. The HRSG temperature mismatch is by far

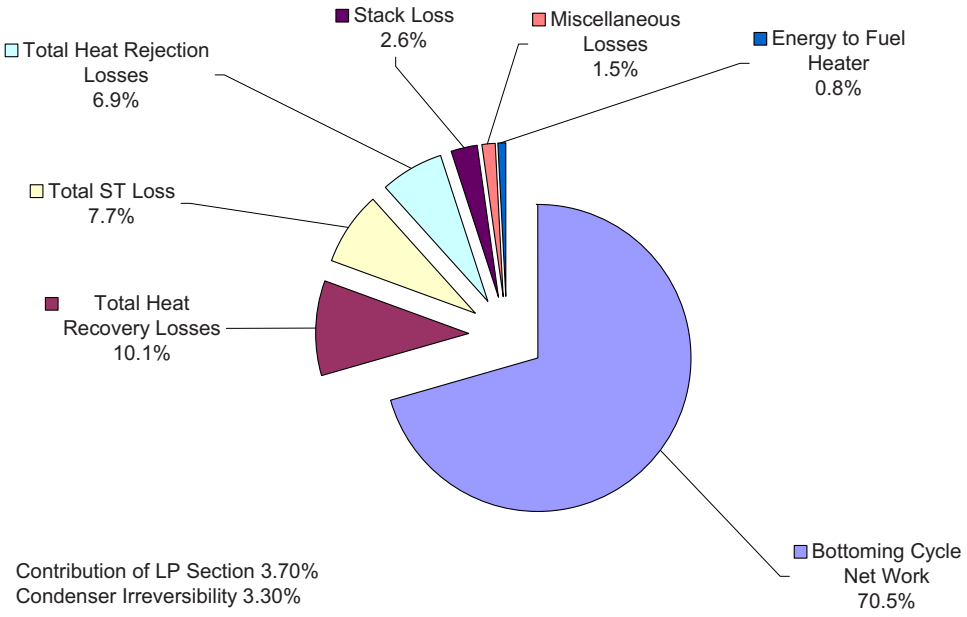

Fig. 5 Distribution of GT exhaust gas exergy in CC Rankine bottoming cycle

the largest exergy loss mechanism (approximately one-third of the total.)
2. Heat rejection from the working fluid at a constant temperature that is equal to the ambient temperature so that exhaust gas is cooled to the same temperature as the ambient. This loss mechanism constitutes approximately one-fourth of the total. The loss mechanisms, about in equal measures, are the exergy transfer out of the RBC-CV via cooling water and temperature mismatch in the condenser.

These two nonidealities prevent approximately 20% of the exhaust gas exergy from being converted to power at the generator terminals. Additional RBC nonidealities that add to this are the following.

1. Nonisentropic expansion in the ST and turbine bearing and generator losses, which add up to about 7.5% of the exhaust gas exergy. Particularly significant is the LP turbine irreversibility including nonisentropic expansion and exhaust losses.
2. Miscellaneous losses in the BOP equipment (mainly heat loss and pressure drops, about 1.5%).
3. Energy utilized to heat the GT fuel (about 1%).

A practically achievable advanced RBC exergetic efficiency, with no regard to the actual cost of building one, can be calculated considering the following:

1. upgrading base SOA assumptions of condenser pressure and ST efficiencies to GTW 2006 levels, estimated in Sec. 3.1
2. SOA plus 1% ST efficiencies: 92%, 93%, and 94%, respectively, for HP, IP, and LP sections and 165 bar g (2400 psi g) steam cycle
3. larger HRSG heat transfer surface area quantified by 6 deg (°C) evaporator pinch and 0 degree economizer subcool.

All these add another 6.4 points so that the RBC exergetic efficiency reaches ~77%. This can be considered as an upper limit for 593°C (1100°F) T_{exh} class GT with an advanced RBC. Per Eq. (16), a 6.4 point improvement in ε_{BC} to achieve the RBC performance entitlement is worth 1.6 points in η_{CC}. Further reduction in exergy losses and RBC improvement will require higher GT exhaust temperatures, leading to better heat recovery and higher steam temperatures, as well as system optimization and innovative designs.

The loss breakdown in Fig. 5 clearly illustrates that opportunities for RBC performance improvement lie in three major cycle components: HRSG, ST, and condenser. The technology is at such a level of maturity that truly innovative solutions are few and far in between. Examples of such recent ideas are the *Kalina* cycle [24] and fuel moisturization [25], of which only the latter proved feasible to be a feature of an actual CC plant. Brute force solutions via "bigger and more" approach have always been around, e.g., very low condenser pressures and very high p-T (even supercritical) steam cycles [26], which can only be feasible under specific conditions, i.e., very cold climates and very high GT exhaust temperatures of 649°C (1200°F) or higher, respectively. The true and tested method of RBC performance improvement, apart from advances in GT technology with higher exhaust temperatures, has always been via advances in ST design [27]. Future improvement will always involve a careful balance of cost versus performance. Some irreversibility reductions are either unavoidable within the normal course of technology development or even available today, e.g.,

1. Advances in GT exhaust temperatures as they happen via higher firing temperatures will improve the HRSG performance and reduce the irreversibility by pushing the stack temperature down and increasing the steam temperatures commensurately as far as available materials and implied costs permit. Note that stack temperatures lower than 57°C (135°F) are unlikely to be targeted due to environmental considerations.
2. In geographic locations, where availability of cooling water as low as 12°C (53°F) is possible, a once-through open-loop cooling system with a surface condenser can easily achieve pressures as low as 27 mbar (0.8 in. Hg). Combined with STs with large enough exhaust annulus to operate at such low pressures, drastic performance improvement is possible even today. It is only a matter of economic feasibility.

Thus, in lock step with any future GT development and exploiting favorable site conditions another 7.5 points of reduction in RBC exergy losses is conceivable. A practical entitlement of 76.8%+7.5%=84.3% is within grasp provided that an advanced GT with firing temperatures higher than today's SOA, and an exhaust temperature of 704°C (1300°F) is available to the designer. Note that it remains to be seen whether such an advanced BC design is going to be cost-effective or not. Considering unspecified improvements to reduce miscellaneous RBC losses for rounding up to a final clean number, $\varepsilon_{BC}=85\%$ is a thermodynamically achievable, practical entitlement for a RBC with air-cooled GTs. It is important to understand that there is no fundamental, thermodynamic reasoning that prohibits 90% or 95%. The limits are imposed by the economic and site criteria, including local regulations, which dictate the equipment selection, size and materials, and the availability of such materials. Consider that in a certain locality, where water scarcity prohibits the deployment of water-cooled steam condensers, even the SOA levels shown above are not feasible. This is simply due to the fact that dry condensing systems cannot achieve pressures lower than 3 in. of Hg economically.

Note that, it is shown above that steam cooling in G and H-class turbines and/or CAC can add 5–10% for $\varepsilon_{BC}\sim 90\%$. Nevertheless, in terms of the true measure of the effectiveness in converting the exhaust gas exergy to net electric power the correct yardstick is the formulation that excludes these two (or other possible) external exergy inputs to the BC.

3.3 Technology Curves. Equation (12) can be easily programmed in an Excel spreadsheet for rapid estimation of Rankine BC contribution for a given GT and technology choice. Evidently, the key parameter is the GT exhaust temperature, which sets the theoretically possible maximum (i.e., the entitlement) and the percentage of that entitlement value that can be converted to net electric power via technically and economically feasible design choices. Thus, based on the premise that there is a well-designed (or optimal) Rankine BC design for a given GT exhaust, different technology curves in the form of $f(T_{exh})$ can be generated. In principle, many technology levels can be selected based on specific assumptions. However, herein only the base (SOA) and the advanced 3PRH levels are chosen. Two series of cases, one for each level, are calculated for a range of GT exhaust temperatures. The results are plotted in Fig. 6.

The chart in Fig. 6 gives a reasonably accurate predictive tool for estimating the bottoming cycle performance for a given GT exhaust temperature. Note that there is a spectrum of RBC configurations that covers the range of possible GT exhaust temperatures. Temperatures below ~538°C (1000°F) are not enough to support a feasible reheat design because there is not enough energy to heat the steam twice to the same temperature. At the high end, for sufficiently high temperatures, there is a transition from three-pressure to two-pressure because the exhaust gas energy dedicated to HP steam production, superheating and economizing, "squeezes" the IP section out. At still higher temperatures, typically ~871°C (1600°F) or higher, the temperature pinch transitions from the LP evaporator to the HRSG economizer inlet. This can be visualized by imagining the exhaust gas cooling line in Fig. 2 as a cantilever beam rotating around the evaporator pinch point

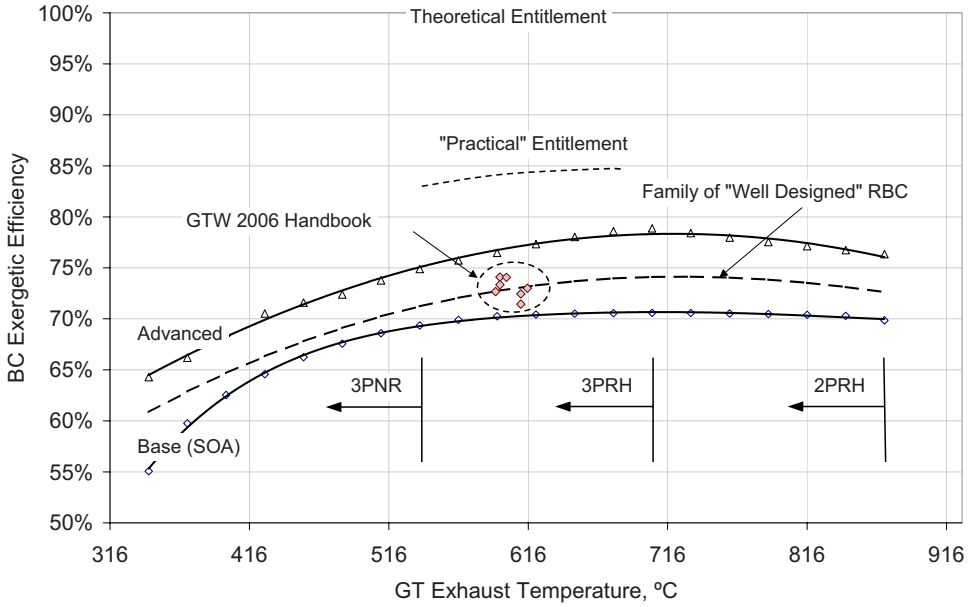

Fig. 6 Rankine bottoming cycle technology curves. (Note that 593°C=1100°F, each 100°C increment is 212°F.)

as the exhaust gas temperature increases. At a certain T_{exh}, the blue and red lines for the economizer section will become parallel so that further increase will "pinch" them together at the HRSG inlet. At that point the LP evaporator is also "squeezed out" and the system reverts to a single-pressure system.

A curve that represents the family of "well-designed" RBCs and implicitly contains the preceding design spectrum considerations is also given in Fig. 6. This optimal curve goes through the data points representing the RBC exergetic efficiencies extracted from the GTW 2006 Handbook data and is adequately described by the following quadratic formula with T_{exh} in degrees °F

$$\varepsilon_{BC} = 0.2441 + 0.0746 \cdot \left(\frac{T_{exh}}{100}\right) - 0.00279 \cdot \left(\frac{T_{exh}}{100}\right)^2 \quad (17)$$

Equation (17) is very well suited to CC analysis of air-cooled GTs with the implicit assumption of a well-designed Rankine bottoming cycle based on today's most optimistic SOA technology.

3.4 Why Second Law? As far as the final results are concerned, there is nothing that cannot be accomplished by using only the first law of thermodynamics. The technology curves in Fig. 6 can be reconstructed from a first law perspective to result in RBC efficiency. The power of second law comes from the following two perspectives.

1. It reveals the true potential of individual components. The best example is the condenser, which accounts for a huge energy loss from the RBC (>30% of the GT heat consumption in modern 3PRH plants), whereas from a work potential point it is rather puny, i.e., less than 1% of the GT heat consumption. On the other hand it also reveals that, although a very small player from a total CC system point of view, from a RBC system perspective, the condenser is essentially the most important lost work component.
2. It provides a readily available yardstick toward the "entitlement," i.e., the theoretically possible maximum performance. From a first law perspective, one can certainly find that for a given GT by setting all losses to zero and all efficiencies to 100%. However, this would require a detailed heat balance calculation and the final answer is totally uninteresting, e.g., 40%, 45%, etc. On the other hand, the second law provides the answer unambiguously and unassailably by just a single thermodynamic property calculation. This sets the 100% effectiveness, an intuitive upper limit or entitlement value. And just by evaluating the ST power output, the designer can immediately assess the current status from an entitlement perspective (both theoretical and practical) and can also judge how difficult or easy the improvement steps toward that goal are.

4 Conclusions

Starting from the fundamental principles of thermodynamics, specifically the second law and the exergy concept, a simple but rigorous CC-RBC performance model is developed. The model enables the engineer to accurately estimate the performance that can be expected from a RBC for a given GT exhaust gas temperature and a few fundamental assumptions about the bottoming cycle design.

The theoretical entitlement of 100% exergetic efficiency is set by the GT exhaust gas exergy. Using the model it is shown that with the current F-class GT technology and SOA RBC, the exergetic efficiency of the RBC is 71%. Future advances in GT materials and designs leading to higher firing temperatures and reduced cooling requirements are likely to result in higher GT exhaust temperatures. A practical entitlement level that is achievable with GT exhaust temperature of 704°C (1300°F) is shown to be ~85% with a commensurate steam cycle. A purely theoretical upper limit with zero losses, T_{stck} of 57°C (135°F), and heat rejection at a condenser pressure of 41 mbar (1.2 in. Hg) is ~94–95% at T_{exh} of 593–704°C (1100–1300°F), respectively.

Advanced cycles with complex integration of the topping and bottoming cycles such as CL-SC or CAC, could provide exergy input equivalent to 5–10% of the GT exhaust exergy, leading to *effective* exergetic efficiency of 90%.

Nomenclature

c_p = constant pressure specific heat, kJ/kg K (Btu/lb R)
e = specific exergy or availability, kJ/kg (Btu/lb)
f = GT fuel to air ratio
h = specific enthalpy, kJ/kg (Btu/lb)

i = irreversibility per unit GT exhaust gas flow, kJ/kg (Btu/lb)
$\dot{I}$ = total exergy destruction or *irreversibility*, kW
l_x = steam turbine last-stage exhaust loss, kJ/kg (Btu/lb)
$\dot{m}$ = mass flow rate, kg/s (lb/s)
N_{ST} = number of steam turbine sections
p = pressure, bar (psi)
$p_{HP,IP,LP}$ = steam pressure at the inlet of HP, IP, and LP turbines, respectively, bar (psi)
$\dot{Q}$ = total heat transfer, kW or kJ/h (Btu/h)
$\dot{q}$ = heat transfer per unit GT exhaust gas flow, kJ/kg (Btu/lb)
s = specific entropy, kJ/kg K (Btu/lb R)
T = temperature, °C or K (°F or R)
$\bar{T}_{cond}$ = saturated steam temperature in the condenser, °C or K (°F or R)
T_{LP} = temperature of LP steam that is equal to the saturation temperature corresponding to the LP drum pressure
y = steam moisture fraction, % or fraction
ΔP_{rht} = pressure drop between HP turbine exit (cold reheat) and IP turbine inlet (as a fraction)
ΔT_{pinch} = temperature difference between steam generated in the evaporator and the exhaust gas leaving the evaporator
ΔT_{subc} = temperature difference between steam generated in the evaporator and the feedwater leaving the economizer
$\dot{w}$ = power output per unit GT exhaust gas flow, kJ/kg (Btu/lb)
$\dot{W}$ = total power output, kW or kJ/h (Btu/h)

Greek Symbols

κ = HRSG heat loss factor, % or fraction
χ = ratio of GT exhaust gas and water specific heats
η = thermal efficiency
μ = ratio of steam/condensate and exhaust gas flows
τ = temperature ratio

Subscripts

o = reference state for the exergy
amb = ambient
cond = condensate from the condenser to the HRSG inlet (approximately equal to total steam flow)
CW = condenser cooling water
f = fuel
w and fw = boiler feedwater
exh = GT exhaust or HRSG inlet
s = isentropic process
stck = HRSG exit (stack)
stm = steam or water between HRSG inlet and ST inlet

Appendix

1 Average Temperatures. All fundamental definitions and concepts pertaining to second law and exergy can be found in textbooks, e.g., Ref. [7]. Consider a steady-state steady-flow (SSSF) heat transfer process in which the temperature of a fluid changes from T_1 to T_2 at a constant or negligible change in pressure.[4] The average temperature of the fluid during this process is given by

$$\bar{T} = \frac{(h_2 - h_1)}{(s_2 - s_1)} \tag{A1}$$

Equation (A1) defines temperature for a hypothetical, reversible, and isothermal process that takes place between the same initial and final states as the actual case. From Eq. (A1), ignoring the change in c_p, the average temperature of the hot GT exhaust gas is

$$\bar{T}_{exh} = T_{exh} \cdot \frac{\tau_x - 1}{\ln \tau_x}, \quad \tau_x = \frac{T_{stck}}{T_{exh}} \tag{A2}$$

For the typical GT exhaust and HRSG stack temperatures, e.g., 593F ± 56°C (1100 ± 100°F) and 88 ± 4°C (190 ± 40°F), respectively, the difference in $\bar{T}_{exh}$ from Eqs. (A1) and (A2) using JANAF tables is 6–12 deg (°C).

For a reliable estimation of the average HRSG steam/water temperature, $\bar{T}_{stm}$, without detailed model calculations, a simple model in the form of $\Delta h/\Delta s$ is adequate. The model parameters have been defined by a curve-fit to actual heat balance model data for 2×1 and 1×1 CC plants. The result is as follows.

For $T_{stm} = 565°C(1050°F)$,

$$\bar{T}_{stm}[°F] = 0.8 \cdot \frac{c_{p,exh} \cdot (1-\kappa) \cdot (T_{exh} - T_{stck})}{\mu \cdot (1.19 \cdot s(p'_{stm}, T_{stm}) - s_{cond})} - 260 \tag{A3a}$$

$$p'_{stm}[psia] = 1650 + \frac{(p_{stm} - 1650)}{3}$$

For $T_{stm} > 565°C(1,050°F)$,

$$\bar{T}_{stm}[°F] = \bar{T}_{stm} + 3.5 \cdot \frac{T_{stm} - 1050}{50} \tag{A3b}$$

Average condenser cooling water temperature in Eq. (2) can easily be evaluated per Eq. (A1) as

$$\bar{T}_{CW} = \frac{\Delta T_{CW}}{\ln\left(1 + \frac{\Delta T_{CW}}{T_{CW,in}}\right)} \tag{A4}$$

Starting from the energy balance for the fuel heater and using Eq. (A1) it can be shown that the average temperature of the HRSG feed water that is used to heat the fuel is

$$\bar{T}_{fw} \approx \frac{-\Delta T_f}{\ln\left(1 - \frac{\Delta T_f}{T_f} \cdot \left(1 - \frac{\Delta}{T_f}\right)\right)} \tag{A5}$$

where Δ stands for the heat exchanger inlet and outlet approach temperatures.[5]

2 Condenser Heat Duty and Total Condensate Flow. The rate of heat transfer out of the bottoming cycle CV in Eq. (2) can be more conveniently written as

$$\dot{q}_{cond} = \frac{\dot{Q}_{cond}}{\dot{m}_{exh}} = \mu \cdot (1-y) \cdot h_{fg} \tag{A6}$$

per unit mass of GT exhaust gas, where μ is the ratio of condenser steam and GT exhaust gas flow rates. Detailed bottoming cycle calculations using a proper heat balance tool [28] have shown that the ratio μ can be determined from the following relationship:

$$\mu = \left[0.153 + 0.018 \cdot \left(\frac{T_{exh}}{100} - 11\right)\right] - 0.002 \cdot \frac{T_{stm} - 1050}{25} \tag{A7}$$

[4] The error introduced by this assumption is <1°C for all calculations of interest herein.

[5] 100% methane gaseous fuel is assumed.

Equation (A7) is valid for a SOA, 3PRH HRSG with 8 deg (°C) evaporator ΔT_{pinch} and 6 deg (°C) economizer ΔT_{subc}. It is always possible to increase the steam production in the HRSG by increasing the heat exchanger surface area via adding tube rows. It is simply a question of economic trade-off between the additional installed cost and the performance benefit. For each 2 deg (°C) decrease in the evaporator pinch, steam production from Eq. (A8) increases by 0.40%. For each 3 deg (°C) decrease in the economizer approach subcool, steam production from Eq. (A8) increases by 0.30%.

The ratio μ can easily be determined from the energy balance around the LP economizer section at the end of the HRSG. It can be shown that

$$\mu = \chi \cdot (1-\kappa) \cdot \frac{T_{\text{LP}} + \Delta T_{\text{pinch}} - T_{\text{stck}}}{T_{\text{LP}} - \Delta T_{\text{subc}} - \bar{T}_{\text{cond}}} - 0.6 \cdot \frac{f}{1+f} \tag{A8}$$

For a given GT with known T_{exh} and f, once μ is determined from Eq. (A7), Eq. (A8) can be used to calculate the HRSG stack temperature based on known design parameters with very good accuracy.

3 Steam Turbine Irreversibility. The first and second laws of thermodynamics for the steam turbine can be combined into the following form:

$$\dot{I}_{\text{ST}} = \dot{m}_s \cdot T_o \cdot (s_{\text{out}} - s_{\text{in}}) \tag{A9}$$

Note that Eq. (A9) is for a simple ST section without any extraction, admission, and leakage streams between the inlet and exit. A more generalized version can be written by combining all inlet and exit streams. This, however, does not add more insight into the discussion of the subject, so that the derivations below are based on Eq. (A9). However, even Eq. (A9) is not very amenable to a quick estimation of the ST irreversibility without resorting to detailed heat balance calculations. A more suitable formulation of Eq. (A9) can be obtained by making use of the principal exact differential (or $T \cdot ds$ equation) for the enthalpy. Integrating this exact differential between any two states and combining with the ideal gas relationship, the generic ST irreversibility can be written as

$$\dot{I}_{\text{ST}} \propto \dot{m}_s \cdot T_o \cdot (1-\eta) \cdot \frac{(PR-1)}{k \cdot (PR+1)} \tag{A10}$$

where PR is the ratio of turbine inlet and exit pressures. Equation (A10) quantifies the ST thermodynamic irreversibility with a suitable proportionality factor depending on the units used. The efficiencies considered herein are total section efficiencies including associated piping and valves. For the last ST section (the LP section) exhausting to the condenser, the efficiency is bowl to UEEP and implicitly contains the exhaust losses. For the purposes of this work, it can be modeled as a base value with a correction for the exhaust loss, i.e.

$$\eta_{\text{LP}} = \eta_{\text{base}} - \lambda \cdot l_x$$

where λ denotes the decrease in the base, bowl-to-UEEP LP efficiency per unit increase in the dry exhaust loss. A good value is $\lambda = 0.25\%$, i.e., the η_{LP} decreases by 0.25 points for each Btu/lb (2.326 kJ/kg) increase in l_x.

Note that the steam flow through each section, $\dot{m}_{s,i}$, requires detailed calculations. For the conceptual calculations herein a simpler approximation is developed by running detailed BC heat balance models for 3PRH systems and distilling the results into simple parametric formulas. Noting that the indices for the HP, IP, and the LP sections are 1, 2, and 3, respectively, steam flows for each ST section per unit GT exhaust gas can be approximated as follows:

$$\dot{m}_{s,i} = \mu_{s,i} \cdot \dot{m}_g, \quad \frac{\mu_{s,i}}{\mu} = a_i + b_i \cdot \frac{T_{\text{exh}} - 1100}{50} \tag{A11}$$

Coefficients a_i in Eq. (A11) are 0.72, 0.87, and 1.0, respectively. In Eq. (A10), coefficients b_i are 0.044, 0.013, and 0, respectively. Coefficients k_1 and k_2 for HP and IP sections are $\frac{1}{3}$, and k_3 for the LP section is 0.2. The section pressure ratios PR_i are calculated as follows:

$$PR_1 = (1 - \Delta P_{\text{rht}}) \frac{p_{\text{HP}}}{p_{\text{IP}}}, \quad PR_2 = \frac{p_{\text{IP}}}{p_{\text{LP}}}, \quad PR_3 = \frac{p_{\text{LP}}}{p_{\text{cond}}} \tag{A12}$$

References

[1] Cohen, H., Rogers, G. F. C., and Saravanamuttoo, H. I. H., 1991, *Gas Turbine Theory*, 3rd ed., Longman Scientific & Technical, Essex, England.
[2] Young, J. B., and Wilcock, R. C., 2002, "Modeling the Air-Cooled Gas Turbine: Parts 1 and 2," ASME J. Turbomach., **124**, pp. 207–222.
[3] El-Masri, M. A., 1986, "On Thermodynamics of Gas Turbine Cycles: Part 1—Second Law Analysis of Combined Cycles," ASME J. Eng. Gas Turbines Power, **108**, pp. 151–159.
[4] Chin, W. W., and El-Masri, M. A., 1987, "Exergy Analysis of Combined Cycles: Part 2—Analysis and Optimization of Two-Pressure Steam Bottoming Cycles," ASME J. Eng. Gas Turbines Power, **109**, pp. 237–243.
[5] Horlock, J. H., Young, J. B., and Manfrida, G., 2000, "Exergy Analysis of Modern Fossil-Fuel Power Plants," ASME J. Eng. Gas Turbines Power, **122**, pp. 1–7.
[6] Hofer, D. C., and Gülen, S. C., 2006, "Efficiency Entitlement for Bottoming Cycles," ASME Paper No. GT2006-91213.
[7] Moran, M. J., and Shapiro, H. N., 1988, *Fundamentals of Engineering Thermodynamics*, Wiley, New York, p. 292.
[8] Walter, J., and Searles, D. E., 1997, "Process Optimization of an Integrated Combined Cycle—The Impact & Benefit of Sequential Combustion," ASME Paper No. 97-GT-490.
[9] Kehlhofer, R. H., Warner, J., Nielsen, H., and Bachmann, R., 1999, *Combined Cycle Gas & Steam Turbine Power Plants*, 2nd ed., PennWell, Tulsa, OK.
[10] Dechamps, P. J., 1998, "Advanced Combined Cycle Alternatives With the Latest Gas Turbines," ASME J. Eng. Gas Turbines Power, **120**, pp. 350–357.
[11] Pasha, A., Ragland, A. S., and Sun, S., 2002, "Thermal and Economic Considerations for Optimizing HRSG Design," ASME Paper No. GT2002–30250.
[12] 1995, *Heat Exchange Institute Standards for Steam Surface Condensers*, 9th ed., HEI, Cleveland, OH.
[13] Hensley, J. C., 1989, "Cooling Towers," *Standard Handbook of Powerplant Engineering*, McGraw-Hill, New York, Chap. 1.9.
[14] Pritchard, J. E., 2003, "H-System™ Technology Update," ASME Paper No. GT2003-38711.
[15] Nakhamkin, M., Swensen, E. C., Wilson, J. M., Gaul, G., and Alba, J., 1995, "The Cascaded Humidified Air Turbine (CHAT)," ASME Cogen Turbo Power 1995, Vienna, Austria.
[16] El-Masri, M. A., 1988, "A Modified, High-Efficiency Recuperated Gas Turbine Cycle," ASME J. Eng. Gas Turbines Power, **110**, pp. 233–242.
[17] Jonsson, M., and Yan, J., 2002, "Exergy Analysis of Part Flow Evaporative Gas Turbine Cycles, Parts I and II," ASME Paper Nos. GT2002-30125 and GT2002-30126.
[18] Gas Turbine World, 2006, *2006 Gas Turbine World Handbook*, Pequot, Fairfield, CT.
[19] Chiesa, P., and Macchi, E., 2004, "A Thermodynamic Analysis of Different Options to Break 60% Electric Efficiency in CC Power Plants," ASME J. Eng. Gas Turbines Power, **126**, pp. 770–785.
[20] Narula, R., Zachary, J., and Olson, J., 2004, "Matching Steam Turbines With the New Generation of Gas Turbines," PowerGen Europe, Barcelona, Spain.
[21] Cotton, K. C., 1998, *Evaluating and Improving ST Performance*, 2nd ed., Cotton Fact, Rexford, NY, pp. 88–94.
[22] 2006, GT PRO Version 16.0.0, Thermoflow, Inc., Sudbury, MA.
[23] 2007, "GT24 and GT26 Gas Turbines," www.power.alstom.com.
[24] Kalina, A. I., 1984, "Combined-Cycle System With Novel Bottoming Cycle," ASME J. Eng. Gas Turbines Power, **106**, pp. 737–742.
[25] Smith, R. W., Johansen, A. D., and Ranasinghe, J., 2005, "Fuel Moisturization for Natural Gas Fired Combined Cycles," ASME Paper No. GT2005-69012.
[26] Bohn, D., 2006, "SFB 561: Aiming For 65% CC Efficiency With an Air-Cooled GT," Modern Power Systems, pp. 26–29.
[27] Boss, M. J., Gradoia, M., and Hofer, D., 2005, "Steam Turbine Technology Advancements for High Efficiency, Reliability and Cost of Electricity," POWER-GEN International, Dec. 6–8.
[28] 2004, GateCycle for Windows, Version 5.61.2.i, General Electric Company, www.gepower.com/enter.
[29] Stull, D. R., and Prophet, H., 1971, *JANAF Thermodynamic Tables*, 2nd ed., NSRDS-NBS 37, National Bureau of Standards.

Effect of Film Cooling on Turbine Capacity

T. Povey
Department of Engineering Science,
University of Oxford,
Parks Road,
Oxford, OX1 3PJ, UK

This paper describes a method that allows the effect of film cooling on the capacity of a turbine to be computed. The model is based on fundamental cooling performance parameters and is applicable to situations in which a mainstream flow is displaced by a partially mixed film cooling layer. The purpose is to quantify the error that is incurred in the engine situation when common—but simplified—assumptions are made regarding the flow, and where necessary, to provide a means of correcting the capacity for the effect of the film cooling flow. [DOI: 10.1115/1.3026564]

1 Introduction

The purpose of this paper is to describe a method that has been developed to account for the impact of film cooling on turbine capacity.

Capacity (Γ) is an important performance parameter for engine optimization. Inaccurate evaluation would lead to incorrect performance evaluation and unmatched stages. Accurate prediction and measurement is therefore the subject of considerable attention at every stage in the engine design process.

The primary influences on the capacity of a nozzle are the loading distribution [1] and the vane loss [2]. Departures from the capacity inferred on the basis of a 1-dimensional (1D) inviscid calculation can be as much as 10% and must be accounted for with the use of 3-dimensional (3D) CFD, or ideally by experimental measurement. There are a host of secondary influences, which can affect capacity by of order 2%: turbulence affects the state of the boundary layer and therefore the cascade loss [3]; 3D flow structures caused by strongly leaned, bowed, or swept vanes, and/or endwall contouring; and boundary layer separation, or separation induced by leakage flows, especially where such features are present at or near the geometric throat. Where the sonic region is formed between the wake of the adjacent vane (filled with trailing edge slot flow) and the suction surface, the geometry of the trailing edge slot (including the cut-back region if such a design is used) and the blowing rate through this slot can also influence the capacity. These effects are inherently turbine-specific in nature, and therefore not amenable to a generalized theory.

The impact of the various processes is also difficult to accurately quantify in the engine situation, and still harder to accurately predict computationally. There is also the problem of throat measurement: in cast vanes the final mean geometry can differ from the ideal and the vane-to-vane variation in this geometry can be significant. Measurement of the geometric throat is difficult in very 3D passages, and a good understanding of the 3D flow structure is required to translate this into an effect throat area. Furthermore, the mounting arrangement can have a significant influence on the effective throat area and therefore the capacity. Where capacity estimates with uncertainty of order 1% are required for performance optimization, it is very unlikely that such an accurate assessment could be made without recourse to experiment.

While all of the above issues are of importance in the context of the capacity problem, this paper is confined to a theory for modeling the impact of film cooling on turbine capacity. This subject has received little attention, but has an impact of between 0.2% and 1.7% on the capacity of a typical high pressure (HP) turbine vane with 10% film cooling (by mass ratio), depending on the assumptions made in simplified treatments. The impact of film cooling is expressed in terms of a flow correction parameter, which is derived from fundamental film cooling parameters readily available early in the design process. This allows the capacity computed on the basis of a simple model to be related to the true capacity with partially mixed out film cooling flow. The model is as applicable to the engine situation where the throat area is known, as it is to the cold/warm rig measurement, which is used indirectly to compute the engine capacity. This latter situation is the normal route by which engine capacity is computed, and is perhaps the more important application of the correction method.

Manuscript received April 10, 2008; final manuscript received July 21, 2008; published online September 30, 2009. Review conducted by Dilip R. Ballal.

2 Overview of the Model

A model is developed in which the mainstream flow is considered as displaced by the thickness of a partially mixed coolant layer, but is otherwise unaffected. The Mach number and total pressure of the partially mixed out coolant flow is computed using a method based on the control volume mixing models due to Hartsel [4] and Kollen and Koschel [5]. The boundary conditions for the control volume analysis are related to the coolant flow and hot-flow pressures and temperatures by simple but physically well-founded relationships to the metal effectiveness, ε_M, film cooling effectiveness at the throat, ε_F, cooling efficiency, η, and coolant total pressure loss coefficient, ζ_p. The angle of the film cooling holes and nominal hot-stream Mach number at the injection plane are chosen to be as representative of the nozzle as possible. Gas properties are correctly modeled in both the partially mixed film cooling layer and in the hot-stream. Solution of the equations, which is an iterative process, is discussed, as is the sensitivity of the model to inaccuracies in the estimation of the input parameters.

It is the extension of the previous loss models, and the direct link to fundamental design parameters, that allows the impact of film cooling on nozzle capacity to be computed in the engine situation.

Two examples are given in which the model is used to compute the mass flow correction (to engine capacity) for two simple methods of estimation: firstly, a crude estimate in which it is assumed that hot-stream conditions (the no film cooling case) prevail uniformly at the throat; secondly, the case in which the film cooling stream is fully mixed with the mainstream. Neither method for capacity estimation is well-founded, but both are commonly used in practical situations, the latter method being more accurate. It is shown that the second method provides an estimate of capacity that is very close to the capacity physically realized (at worst 0.1% error) at typical engine conditions. The first method is typically in error by about 1.7%. The model is also used to compute the mass flow correction required to account for film cooling between cold-rig experiments and the engine situation. It is shown that the offset is about 0.2% for typical conditions, and should be accounted for.

3 Definition of Coolant Injection Total Pressure and Temperature

In the model the following assumptions are made regarding the coolant injection total pressure and temperature.

(a) The coolant outlet total pressure p_{0c} is related to the coolant plenum total pressure p_{0cp} and the local external static pressure p_1 by the coolant total pressure loss coefficient ζ_p. The ratio p_{0cp}/p_{0h} is set to a reference value determined by the engine design.

(b) The coolant outlet total temperature T_{0c} is related to the coolant plenum total temperature T_{0cp} and the metal temperature T_w by the cooling efficiency η.

The coolant total pressure loss coefficient is defined as follows:

$$\zeta_p = \frac{p_{0cp} - p_{0c}}{p_{0cp} - p_1} \tag{1}$$

The denominator is the difference between the coolant plenum total pressure and the local external static pressure. This allows the sensitivity of the injection to the total pressure loss to be studied. Rearranging Eq. (1) we obtain the coolant outlet total pressure p_{0c}

$$\frac{p_{0c}}{p_{0h}} = \frac{p_{0cp}}{p_{0h}}(1 - \zeta_p) + \frac{p_1}{p_{0h}}\zeta_p \tag{2}$$

The cooling efficiency is defined as follows:

$$\eta = \frac{T_{0c} - T_{0cp}}{T_w - T_{0cp}} \tag{3}$$

Rearranging Eq. (3) we obtain the coolant outlet total temperature T_{0c}

$$\frac{T_{0c}}{T_{0cp}} = \eta\left(\frac{T_w}{T_{0cp}} - 1\right) + 1 \tag{4}$$

The metal effectiveness ε_M is a design parameter which is well defined for a given coolant to mainstream pressure ratio, and T_w is conveniently expressed in terms of ε_M. Where ε_M is defined by

$$\varepsilon_M = \frac{T_{0h} - T_w}{T_{0h} - T_{0cp}} \tag{5}$$

it follows that

$$\frac{T_{0c}}{T_{0cp}} = \eta\left(\frac{T_{0h}}{T_{0cp}} - 1\right)(1 - \varepsilon_M) + 1 \tag{6}$$

Thus, we obtain the coolant outlet total temperature in terms of the hot and cold feed temperatures, the cooling efficiency and the metal effectiveness $T_{0c} = f(T_{0h}, T_{0cp}, \eta, \varepsilon_M)$.

4 Evaluation of Prethroat Coolant Mass Flow Rate From the Reference Condition

The following assumptions are made in the evaluation of the (prethroat) coolant mass flow rate.

(a) The coolant enters the hot-stream at a single location (Plane 1), which is defined in terms of an area ratio with respect to the throat plane (Plane 2). The area ratio A_1/A_2 is set to be as characteristic of the vane design as possible consistent with the single injection location assumption.

(b) The Mach number of the hot-stream at Plane 1, M_{1h}, is a function of the throat Mach number, M_{2h}, the area ratio, A_1/A_2, and a specific heat ratio taken at a mean temperature (between plane 1 and plane 2), $\bar{\gamma}_h$, where the second order variations of γ_h with temperature are ignored: $M_{1h} = f(M_{2h}, A_1/A_2, \bar{\gamma}_h)$. Thus, the local static pressure at the coolant injection plane is also a function of these parameters: $p_1/p_{0h} = f(M_{2h}, A_1/A_2, \bar{\gamma}_h)$.

(c) The hot-stream conditions at Plane 1 (p_{0h}, p_1, M_{1h}, T_{0h}, T_{1h}, $c_{ph}(T_{1h})$, $\gamma_{1h}(T_{1h})$, and R_{1h}) are unaffected by the introduction of the coolant.

(d) The ratio of effective areas of the coolant injection flowpath to the vane throat, A_c/A_2, is chosen so that at the reference engine cycle-point the ratio of the prethroat-coolant to total (mixed out) throat mass flow rates $\dot{m}_c/\dot{m}_M$ is matched to the reference condition. It is noted that in the model the coolant area A_c is somewhat arbitrary, and is a means of benchmarking the model to the engine case in terms of the parameter $\dot{m}_c/\dot{m}_M$. Subsequent variations in $\dot{m}_c/\dot{m}_M$ at arbitrary (off-reference) values p_2/p_{0h} (and implicitly p_1/p_{0h} for fixed A_1/A_2) are correctly modeled. Because, as will be shown, $\dot{m}_M$ and $\dot{m}_H$ generally agree to within of order 1%, the approximation $\dot{m}_c/\dot{m}_M \approx \dot{m}_c/\dot{m}_H$ is perfectly valid at this stage of the analysis, and introduces a useful simplification. $\dot{m}_c/\dot{m}_H$ is a fundamental design parameter linked to the cooling efficiency of the vane, while A_c is somewhat arbitrary, as it depends on the pressure ratio p_{0cp}/p_{0h}, and in the model is simply a construct to allow for the realistic variation of $\dot{m}_c/\dot{m}_H$ with p_2/p_{0h}.

Consider how the area ratio A_c/A_2 is defined for the purposes of the model. The aim is that the coolant mass flow rate ratio is matched to the reference value $\dot{m}_c/\dot{m}_H$, which comes from the engine design method, at a design pressure ratio p_2/p_{0h}. A reference ratio p_{0cp}/p_{0h} is assumed, as are values of ζ_p and η. As discussed, only small second order errors are incurred at this stage in making the assumption that $\dot{m}_M = \dot{m}_H$. The (single stream) hot-stream flow is given by p_{0h}, $T_{0h}\gamma_{2h}$, R_h, and p_2. Using the normal compressible flow formulation

$$\dot{m}_c = A_c \frac{p_{0c}}{T_{0c}^{1/2}}\sqrt{\frac{\gamma_{1c}}{R_{1c}}} M_{1c}[1 + Y_{1c}M_{1c}^2]^{-Z(1c)} \tag{7}$$

and

$$\dot{m}_H = A_2 \frac{p_{0h}}{T_{0h}^{1/2}}\sqrt{\frac{\gamma_{2h}}{R_h}} M_{2h}[1 + Y_{2h}M_{2h}^2]^{-Z(2h)} \tag{8}$$

where $M_{2h} = f(p_2/p_{0h}, \gamma_{2h})$ and $M_{1c} = f(p_1/p_{0c}, \gamma_{1c})$, and where the following abbreviations have been used:

$$Y \equiv \frac{\gamma - 1}{2} \quad \text{and} \quad Z \equiv \frac{\gamma + 1}{2(\gamma - 1)} \tag{9}$$

$p_1/p_{0h} = f(M_{2h}, A_1/A_2, \bar{\gamma}_h)$ and therefore $p_1/p_{0c} = f(M_{2h}, A_1/A_2, \bar{\gamma}_h, p_{0cp}/p_{0h}, \zeta_p)$. The foregoing relationships are derived in the normal way. Rearranging Eqs. (7) and (8) in terms of A_c/A_2 gives

$$\frac{A_c}{A_2} = \left\{ \frac{\dfrac{\dot{m}_c T_{0c}^{1/2}}{M_{1c}p_{0c}}\sqrt{\dfrac{R_{1c}}{\gamma_{1c}}}[1 + Y_{1c}M_{1c}^2]^{Z(1c)}}{\dfrac{\dot{m}_H T_{0h}^{1/2}}{M_{2h}p_{0h}}\sqrt{\dfrac{R_h}{\gamma_{2h}}}[1 + Y_{2h}M_{2h}^2]^{Z(2h)}} \right\}\Bigg|_R = r_1 \tag{10}$$

Equation (10) is used to evaluate ratio A_c/A_2 at the reference condition, yielding a constant, r_1. The stated purpose was to formulate a means of evaluating $\dot{m}_c$ for an arbitrary combination of A_1/A_2 and p_2/p_{0h} (or M_{2h}). Using the result (Eq. (10)) in Eq. (7) gives

$$\dot{m}_c = r_1 A_2 \frac{p_{0c}}{T_{0c}^{1/2}}\sqrt{\frac{\gamma_{1c}}{R_{1c}}} M_{1c}[1 + Y_{1c}M_{1c}^2]^{-Z(1c)} \tag{11}$$

where r_1 has been evaluated for a fixed reference condition and fixed A_1/A_2. The sensitivity of $\dot{m}_c(p_2/p_{0h})$ to A_1/A_2 is discussed later. Consider Eq. (11); $\dot{m}_c = f(r_1, A_2, p_{0c}, T_{0c}, \gamma_{1c}, R_{1c}, M_{1c})$. As $M_{1c} = f(p_{0c}, p_1, \gamma_{1c})$ it follows that

$$\dot{m}_c = f(r_1, A_2, p_{0c}, T_{0c}, \gamma_{1c}, R_{1c}, p_1) \tag{12}$$

Accepting the approximation $p_1/p_{0h} = f(M_{2h}, A_1/A_2, \bar{\gamma}_h)$, stated previously in (b), we can replace p_1 in Eq. (12) with the variables p_{0c}/p_{0h}, M_{2h}, A_1/A_2, and γ_h. Thus Eq. (12) becomes

$$\dot{m}_c = f(r_1, A_2, p_{0c}, T_{0c}, \gamma_{1c}, R_{1c}, p_{0c}/p_{0h}, M_{2h}, A_1/A_2, \gamma_h) \tag{13}$$

The form of Eq. (13) is easy to derive, and this development allows the mass flow rate of coolant, $\dot{m}_c$, to be calculated at arbitrary conditions p_2/p_{0h} (or vane throat Mach number M_{2h}), and arbitrary coolant total conditions p_{0c}/p_{0h} and T_{0c}, while preserving the important constraint that $\dot{m}_c/\dot{m}_H$ is correct at the reference condition.

In the foregoing argument a simple but physically well-founded method has been established by which the mass flow rate of the coolant in a single injection model can be expressed in terms of fundamental vane cooling design parameters over a wide range of vane pressure ratios, while matching a design point value of the coolant to the mainstream mass flow rate.

5 Evaluation of the Total Temperature and Entrained Mass in the Mixed Layer From the Film Cooling Effectiveness

The coolant flow injected at Plane 1, $\dot{m}_c$, mixes with entrained hot gas as it traverses the passage to the throat Plane 2. The entrained mass of hot gas is defined as $\dot{m}_e$. The ratio of the coolant gas to the entrained hot gas is defined by

$$\chi \equiv \frac{\dot{m}_c}{\dot{m}_e} \tag{14}$$

The purpose of the model presented in this paper is to provide a simple method for accounting for the effect of a partially mixed coolant stream on the throat mass flow rate, for both the choked and the unchoked regimes. One application is for stage calculations in the engine design process. Although mixing models exist in which the pressure distribution, turbulence parameters, and so forth, can be used analytically to model the partial mixing of two streams, this is unnecessarily complex for the current purpose. Such a method would also require a physical benchmarking exercise. It is expedient therefore to use instead the film cooling effectiveness, ε_F, as a means of quantifying the mixing. This is a well-quantified parameter at the engine reference point, and a ready parameter at any stage in the engine design process. The physical basis for using this parameter is evident. ε_F is defined at the throat plane by

$$\varepsilon_F = \frac{T_{0h} - T_{aw}}{T_{0h} - T_{0c}} \tag{15}$$

where T_{aw} is the adiabatic wall temperature. It is advantageous for the purposes of the model that efforts are generally made in the design process to minimize spanwise variations in ε_F. Nonetheless, a spanwise average value can be taken at the throat.

In the mixing layer, a total temperature variation exists which varies smoothly from T_{aw} at the wall to T_{0h} at the edge of the mixing layer. In the model, the mixed layer is idealized so that it is represented by a layer at a single temperature T_{0m}. The relationship between T_{0m} (the temperature of the mixed out layer) and T_{aw} is determined by the temperature profile within the mixing layer. We can represent this by

$$T_{0h} - T_{aw} = \alpha(T_{0h} - T_{0m}) \tag{16}$$

Here α depends on the shape factor. For a turbulent boundary layer with a line coolant source [6] $\alpha = 1.9\ \mathrm{Pr}^{2/3}$. Thus

$$\frac{\varepsilon_F}{1.9\ \mathrm{Pr}^{2/3}} = \frac{T_{0h} - T_{0m}}{T_{0h} - T_{0c}} \tag{17}$$

Hence the equivalent temperature of the idealized single layer is given by

$$T_{0m} = T_{0h}\left(1 - \frac{\varepsilon_F}{1.9\ \mathrm{Pr}^{2/3}}\right) + T_{0c}\frac{\varepsilon_F}{1.9\ \mathrm{Pr}^{2/3}} \tag{18}$$

It is noted in passing that for a typical value of Pr=0.71, this places a lower limit on T_{0m} of $T_{0m} \approx (2/3)T_{0c} + (1/3)T_{0h}$, when $\varepsilon_F = 1$. That is, the mixed layer temperature T_{0m} is higher than the adiabatic wall temperature $T_{aw} = T_{0c}$ at $\varepsilon_F = 1$ because of the temperature profile within the thermal boundary layer. The parameter χ can now be determined from an enthalpy balance. It is clear that

$$\dot{m}_c h_{0c} + \dot{m}_e h_{0e} = \dot{m}_m h_{0m} \tag{19}$$

Manipulation yields

$$\chi = \frac{h_{0m} - h_{0h}}{h_{0c} - h_{0m}} = \frac{c_{p0m}T_{0m} - c_{p0h}T_{0h}}{c_{p0c}T_{0c} - c_{p0m}T_{0m}} \tag{20}$$

The form of Eq. (20) is $\chi = f(T_{0c}, T_{0h}, T_{0m}, c_{p0c}, c_{p0h}, c_{p0m})$, in which c_{p0m} is unknown. c_{p0m} can either be approximated or (where high gas temperatures prevail) computed by iteration with Eq. (20) using the equation for the mass weighted value of c_{p0m} evaluated at constant temperature T_{0m}

$$c_{p0m} = \frac{\dot{m}_c\, c_{pc}|_{T0m} + \dot{m}_e c_{ph}|_{T0m}}{\dot{m}_c + \dot{m}_e} = \frac{c_{ph}|_{T0m} + \chi\, c_{pc}|_{T0m}}{\chi + 1} \tag{21}$$

To solve Eqs. (20) and (21) iteratively reference must be made to tabulated gas properties. Whether Eq. (20) is solved approximately or exactly for χ, the process is to determine $\dot{m}_c$ from Eq. (13) and thus $\dot{m}_m$ from Eq. (20) if required.

The purpose of the preceding analysis is to define a simple physically well-founded method for computing the total temperature and mass flow rate of the mixed out layer. To compute the impact of this layer on the mass flow rate at the throat it remains to compute the total pressure and Mach number of the mixed out layer. This is considered immediately.

6 Properties of the Mixed Out Layer

To compute the Mach number and total pressure of the mixed out layer, it is necessary to turn to a control volume mixing model in which the continuity, momentum, and energy equations are satisfied for a control volume containing the fluid which defines the mixed layer at the throat Plane 2. Perhaps the most well known model is that by Hartsel [4], which assumes incompressible constant static pressure mixing of a single row of film cooling holes. Kollen and Koschel [5] have performed a similar analysis in which the flow is initially mixed at constant static pressure p_1. This is shown diagrammatically in Fig. 1. It is assumed that $\dot{m}_c$ and $\dot{m}_e$ mix quickly: that is, the static pressure at the coolant injection plane is the same as that at mixed out Plane 1.

Solution of the three equations yields the mixed out Mach number M_{1m} and total pressure p_{01m} at Plane 1.

$$\frac{1}{M_{1m}^2} = \frac{(1+\chi)(c_{ph}T_{0h} + \chi c_{pc}T_{0c})(1 + Y_{1h}M_{1h}^2)}{(\chi(u_{1c}/u_{1h})\cos\alpha_f + 1)^2 M_{1h}^2 c_{ph}T_{1h}} - Y_{1h} \tag{22}$$

$$\frac{p_{01m}}{p_{0h}} = \frac{(1 + Y_{1m}M_{1m}^2)^{X(1m)/2}}{(1 + Y_{1h}M_{1h}^2)^{X(1h)/2}} \tag{23}$$

$$X \equiv \gamma/(\gamma - 1) \tag{24}$$

In these expressions the velocity of injection of the coolant is u_{1c}, and the jet makes an angle α_F with respect to the hot-stream flow. The conditions of the hot-stream at Plane 1 are given by p_{0h}, p_1, M_{1h}, T_{0h}, γ_{1h}, u_{1h}, and R_h. It is noted that γ_{1h} and R_h depend on the gas composition (which in the case of an engine will contain

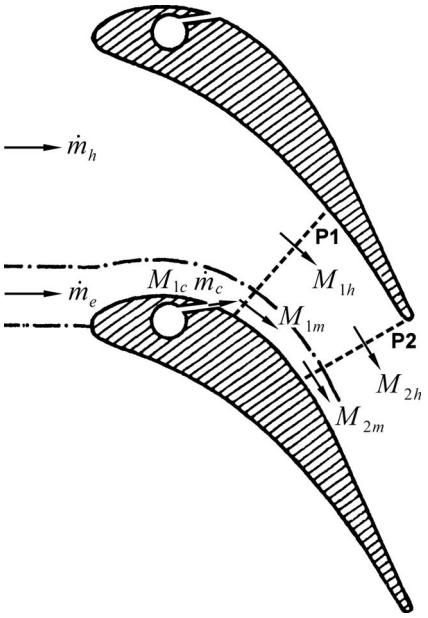

Fig. 1 Schematic of the mixing process

combustion products) and T_{0h}. The conditions of the hot-stream at Plane 2 are given by p_{0h}, p_2, M_{2h}, T_{0h}, γ_{2h}, u_{2h}, and R_{2h}. Y and X are defined in Eq. (9): subscripts indicate at which temperature and gas composition variables have been computed.

Fluid properties for the mixed out layer (R_m, γ_{1m}, and c_{p0m}) are required. Given χ, R_m follows by mass weighting

$$R_m = \frac{R_h \dot{m}_e + R_c \dot{m}_c}{\dot{m}_e + \dot{m}_c} = \frac{R_h + \chi R_c}{\chi + 1} \tag{25}$$

c_{p0m} is given by Eq. (21). Thus, γ_{0m} may be computed as

$$\gamma_{0m} = \frac{1}{1 - R_m/c_{p0m}} \tag{26}$$

The values at static conditions $c_{p1m}=f(T_{1m})$ are found with reference to tabulated gas properties $\gamma_{1m}=f(T_{1m})$. Thus X_{1m}, Y_{1m} can be calculated. The static temperature in the mixed layer T_{1m} is given by

$$T_{1m} = T_{0m}(1 + Y_{1m} M_{1m}^2)^{-1} \tag{27}$$

It is noted that Eqs. (22), (23), and (27), are solved iteratively using the value $\gamma_{1m}=f(T_{1m})$ based on the previous iteration.

The assumptions made in this analysis are as follows.

(a) One-dimensional mixing is assumed between two arbitrary pressures p_1 and p_2.
(b) The hot-stream stagnation pressure p_{0h} and throat static pressure p_2 are not influenced by the introduction of the coolant; the concept is of a very thin coolant layer in comparison to the hot-stream, which is approximately valid in most applications.
(c) Viscous and boundary layer effects are not considered. The assumption that the effects are additive is made if these are to be considered.
(d) Main and coolant fluids are assumed to be perfect gases.

The conditions of the mixed out layer at Plane 2 (the throat plane) can be computed by assuming isentropic expansion of the mixed flow between pressures p_1 and p_2. The Mach number and total pressure of the mixed out layer at Plane 1, M_{1m}, and p_{01m}, are given by Eqs. (22) and (23). The total temperature of the layer T_{0m} is given by Eq. (18). Assuming no total pressure loss between Plane 1 and Plane 2, $p_{02m}=p_{01m}=p_{0m}$, M_{2m} is given by

$$M_{2m} = \left\{ \frac{1}{Y_{2m}} \left[\left(\frac{p_{0h}(1 + Y_{1m} M_{1m}^2)^{X(1m)/2}}{p_2 (1 + Y_{1h} M_{1h}^2)^{X(1h)/2}} \right)^{1/X(2m)} - 1 \right] \right\}^{1/2} \tag{28}$$

and

$$T_{2m} = T_{0m}(1 + Y_{2m} M_{2m}^2)^{-1} \tag{29}$$

As in the analysis at Plane 1, in the solution of Eqs. (28) and (29), T_{0m}, p_{0m}, and p_2 are known, and therefore M_{2m} and T_{2m} are solved iteratively using the value $\gamma_{2m}=f(T_{2m})$ based on the previous iteration.

7 Flow Rate Correction Parameter

The flow due to the mixed layer and mainstream is related to the flow due to a hot-stream alone using the flow rate correction parameter Φ, which is now defined. The ratio of the total mass flow rate in the situation with a mixed stream to that inferred on the basis of the throat running full at the conditions of the hot-stream is given by the function Φ, thus

$$\Phi(p_2/p_{0h}) = \frac{\dot{m}_m(p_2/p_{0h}) + \dot{m}_h(p_2/p_{0h})}{\dot{m}_H(p_2/p_{0h})} \tag{30}$$

It can be shown that

$$\Phi = 1 + \frac{\dot{m}_m}{p_2 A_2} \left\{ \frac{1}{M_{2h}} \sqrt{\frac{R_{2h} T_{2h}}{\gamma_{2h}}} - \frac{1}{M_{2m}} \sqrt{\frac{R_{2m} T_{2m}}{\gamma_{2m}}} \right\} \tag{31}$$

or

$$\Phi = 1 + \left(\frac{\chi + 1}{\chi} \right) \frac{\dot{m}_c}{p_2 A_2} \left\{ \frac{1}{M_{2h}} \sqrt{\frac{R_{2h} T_{2h}}{\gamma_{2h}}} - \frac{1}{M_{2m}} \sqrt{\frac{R_{2m} T_{2m}}{\gamma_{2m}}} \right\} \tag{32}$$

The purpose of the function Φ is to allow the actual mass flow rate to be computed by correction to a simple calculation in which it is assumed that the throat conditions are uniform at the hot gas condition, H. Once Φ has been computed the following simple relation holds true:

$$\dot{m}_T(p_2/p_{0h}) = \Phi(p_2/p_{0h}) \dot{m}_H(p_2/p_{0h}) \tag{33}$$

8 Example 1: Use of Φ to Compute Engine Capacity From Measured Throat Area

An example is now given in which the flow rate correction parameter is used to compute engine mass flow rate (or capacity) for the case in which the throat area is measured. This is followed by a discussion of the sensitivity of the model to parameter variation, and finally an example is given in which the engine capacity is computed from a capacity measured experimentally in the rig situation rather than being computed from a measured area.

In this first example, the following situation is assumed.

(a) The area A_2 is directly measured, and design point values of ζ_p, η, ε_F, ε_M, p_{0cp}, T_{0cp}, p_{0h}, T_{0h}, γ_{0h}, R_h, and γ_{0c} are known, as is the reference condition value of $\dot{m}_c/\dot{m}_M$.
(b) The total engine mass flow rate (comprising two partially mixed streams) $\dot{m}_T(p_2/p_{0h})$ is required.

In this case the analysis would proceed as follows.

(i) Design point values of A_2, ζ_p, η, ε_F, ε_M, p_{0cp}, T_{0cp}, p_{0h}, T_{0h}, $\dot{m}_c/\dot{m}_M$, γ_{0h}, R_h, γ_{0c}, and R_c are identified.
(ii) Values of A_1/A_2 and α_F are chosen that are as representative as possible of the cooling system, within the constraints of the model (single injection point). The validity of this approximation is discussed in Sec. 9. Choice of A_1/A_2 then determines $M_{1h}=f(M_{2h})$, for a given working gas, and thus the nominal value of M_{1h}.
(iii) A_c/A_2 is computed so that $\dot{m}_c/\dot{m}_M$ is matched to a refer-

Table 1 Test case conditions typical of a modern HP NGV

Parameter	Nominal value	Units
ζ_p	0.7	
η	0.8	
ε_F	0.5	
ε_M	0.6	
p_{0h}	43×10^5	Pa
T_{0h}	1850	K
p_{0cp}/p_{0h}	1.025	
T_{0cp}	950	K
M_{1h}	0.3	
$\dot{m}_c/\dot{m}_H$	10	%
α_F	30	deg
M_{2h}	(0.5 to) 1.0	

ence condition at the reference value of M_{2h}; it is noted that A_c is not the geometric area of the hole but is used to match the mass flow rate at the reference condition. Realistic variation either side of the reference condition is also modeled.

(iv) The flow rate correction parameter $\Phi(p_2/p_{0h})$ is computed (Eq. (32)).

(v) The mass flow rate in the absence of cooling, $\dot{m}_H(p_2/p_{0h})$, is computed using the isentropic flow relations and measured area A_2. Thus, the corrected mass flow rate (with partially mixed film cooling) is computed using Eq. (33).

The flow rate correction parameter $\Phi(p_2/p_{0h})$ and corrected mass flow rate $\dot{m}_T(p_2/p_{0h})$ are now computed using the process outlined in (i)–(v) above, using test case conditions which are typical of a large modern civil engine at the cruise condition. The conditions are summarized in Table 1, above. The variation of specific heats with temperature for the range of conditions covered by the test case ($0.5<M_{2h}<1.0$) is shown in Fig. 2. Each value of γ is plotted against the corresponding range of temperature for $0.5<M_{2h}<1.0$. The value of R_c was taken as that for air. The value of R_h was taken as that for combustion products for a fuel-air-ratio of 0.033. The variation of γ_{1c} with temperature was taken from a correlation for air. The variations of γ_{1h}, γ_{2h}, γ_{1m}, and γ_{2m} with temperature were taken from the variations of mass weighted averages. The process is iterative and has been discussed in the context of Eq. (21).

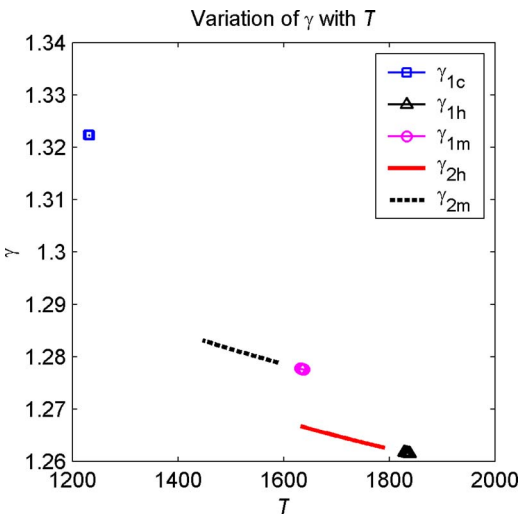

Fig. 2 Variation of γ with T

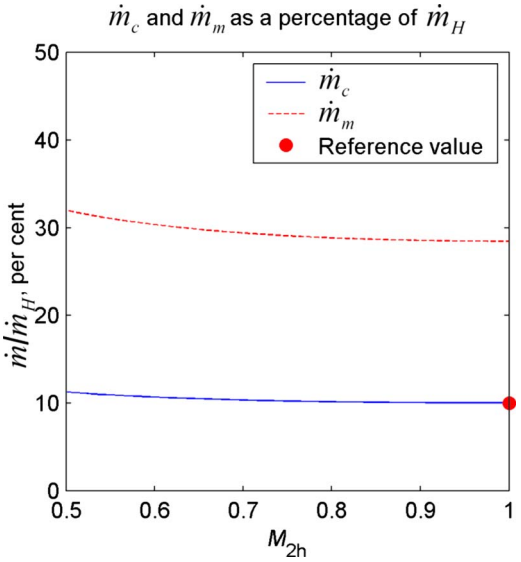

Fig. 3 Variation of $\dot{m}_c$ and $\dot{m}_m$ with M_{2h}

The variation of the mass flow rate of coolant $\dot{m}_c$ with the throat Mach number M_{2h} is shown in Fig. 3. $\dot{m}_c$ is matched to the target value $\dot{m}_c/\dot{m}_H=10\%$ at $M_{2h}=1.0$. The change in $\dot{m}_c/\dot{m}_H$ from the reference value over the range considered was 12.3%.

The variation of the flow rate correction parameter Φ with M_{2h} is shown in Fig. 4. Φ varies from 1.0160 to 1.0171 over the range considered. That is, the total mass flow rate $\dot{m}_T$ with cooling flow is larger than the mass flow rate inferred by assuming that hot gas stream conditions prevail at the throat, $\dot{m}_H$, by between 1.60% and 1.71%. At the nominal condition $M_{2h}=1.0$, the correction term is 1.67% ($\Phi=1.0167$). The variation of $\dot{m}_H$ and $\dot{m}_T$ as a function of M_{2h} is shown in Fig. 5 below. The correction is simply given by $\dot{m}_T(p_2/p_{0h})=\Phi(p_2/p_{0h})\dot{m}_H(p_2/p_{0h})$, using the value of Φ presented in Fig. 4.

9 Sensitivity to the Variation of Parameters

The sensitivity of the model to the variation around the design point of metal effectiveness, ε_M, adiabatic film effectiveness, ε_F, and internal cooling efficiency, η, is now discussed. This is rel-

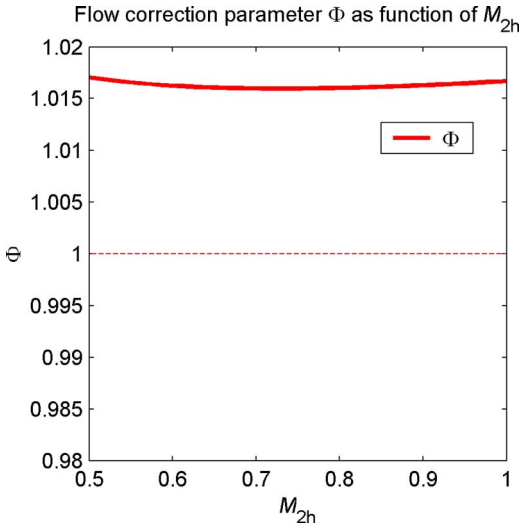

Fig. 4 Variation of the predicted value of Φ with M_{2h}

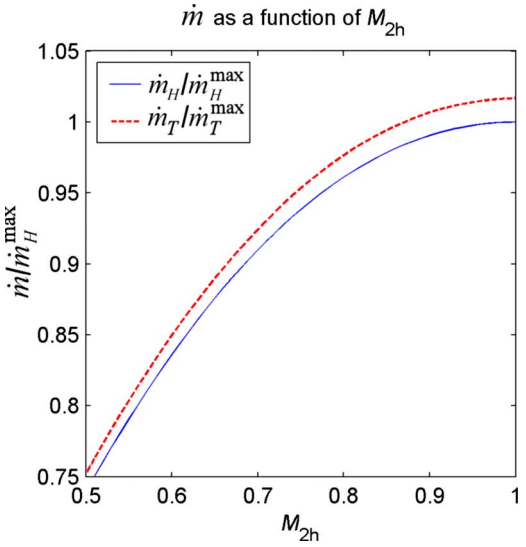

Fig. 5 Hot gas mass flow rate $\dot{m}_H$ and corrected total mass flow rate $\dot{m}_T$ as a function of M_{2h}

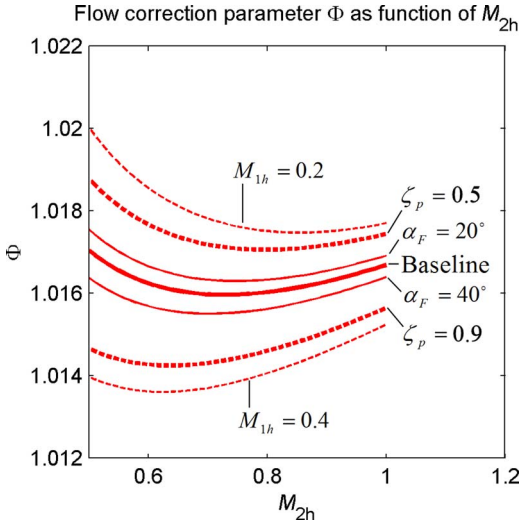

Fig. 7 Sensitivity of the flow correction parameter Φ to variation in ζ_p, M_{1h}, and α_F

evant because there is some uncertainty in each of these parameters even at a late point in the design process—the impact on the throat mass flow is of interest.

Taking the baseline conditions as those outlined in Table 1, the flow rate correction parameter Φ was computed as each of ε_M, ε_F, and η were independently varied. The following cases were considered: ε_M=0.4, ε_M=0.8, ε_F=0.3, ε_F=0.7, η=0.7, and η=0.9. It is noted that these represent much larger deviations with respect to each parameter than the typical uncertainty which would exist in the parameters at a late stage in the engine design process. The values of Φ computed in each case are presented in Fig. 6.

A decrease in internal cooling efficiency to η=0.7 causes a decrease in T_{0c}, and a corresponding increase in Φ. This is to be expected as the ratio T_{0c}/T_{0h} is the primary driver of the magnitude of the flow correction parameter. Changes in film effectiveness ε_F have a relatively modest effect on Φ in the range $0.3 < \varepsilon_F < 0.7$: an increase in film effectiveness from ε_F=0.5 to 0.7 causes an increase in Φ of approximately 0.02% over the range of M considered. Variations in the degree of mixing (in the range experienced in practice) are not significant in determining the magnitude of the correction parameter Φ. Changes in ε_M have a significant effect on Φ: a decrease in metal effectiveness from ε_M=0.6 to 0.4 (relatively hotter metal) causes a decrease in Φ of approximately −0.33%. The primary cause is that—at constant film cooling efficiency η—the coolant outlet temperature is increased, and thus the driving temperature ratio T_{0c}/T_{0h} is increased.

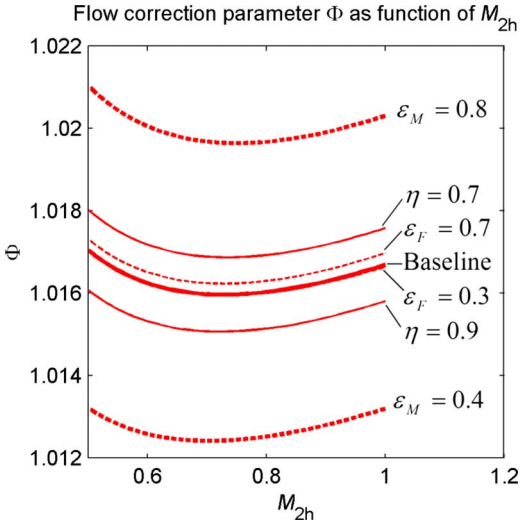

Fig. 6 Sensitivity of the flow correction parameter Φ to variation in η, ε_F, and ε_M

At M_{2h}=1.0, the baseline value of the flow correction parameter was Φ=1.0167. The range of Φ corresponding to the variations of ε_M, ε_F, and η described above was between approximately $1.0133 < \Phi < 1.0205$. This represents a change in Φ from the baseline value (Φ=1.0167) of −0.33% and +0.37%. The sensitivity of Φ to ε_M was significantly greater than to either ε_F, or η. It is noted that the magnitude of the variations in ε_M, ε_F, and η which are considered above are considerably greater than the likely uncertainty during engine design.

In conclusion, the variation in Φ over a wide range of ε_M, ε_F, and η around a baseline design point is shown to be relatively small in comparison to the absolute value of Φ, and the greatest sensitivity of Φ was to ε_M for the ranges considered.

The sensitivity of the model to the variation around the design point of coolant total pressure loss coefficient, ζ_p, the hot-stream Mach number at the injection plane, M_{1h}, and the film cooling hole angle, α_F, is now discussed. The impact on the throat mass flow of variations in these parameters is of interest.

Taking the baseline conditions as those outlined in Table 1, the flow rate correction parameter Φ was computed as each of ζ_p, M_{1h}, and α_F was independently varied. The following cases were considered: ζ_p=0.5, ζ_p=0.9, α_F=20 deg, α_F=40 deg, M_{1h}=0.2, and M_{1h}=0.4. The range of the throat Mach number was $0.5 < M_{2h} < 1.0$. The values of Φ computed in each case are presented in Fig. 7.

The variation of Φ with the cooling hole angle in the range $20 \text{ deg} < \alpha_F < 40 \text{ deg}$ was small: a decrease in α_F (measured with respect to the streamwise direction) from 30 to 20 deg gave rise to an increase in Φ of approximately 0.02% at M_{2h}=1.0. This is to be expected because of the increase in the streamwise component of momentum in the coolant jet. The variation of Φ with the coolant total pressure loss coefficient ζ_p in the range $0.5 < \zeta_p < 0.9$ was more significant: a decrease in ζ_p from 0.7 to 0.5 led to an increase in Φ of approximately 0.1% at M_{2h}=1.0. The mechanism is—as above—an increase in the streamwise component of momentum in the coolant jet. Finally, a decrease in M_{1h} is shown to give rise to an increase in Φ. This is because the mixing loss is

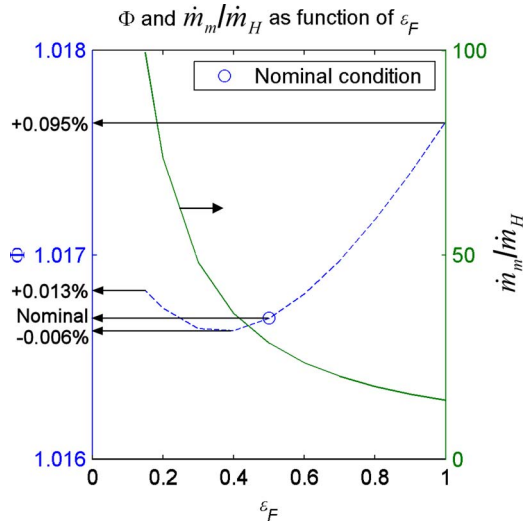

Fig. 8 Maximum variation in Φ over full range of ε_F

lower at a lower freestream Mach number. A change in M_{1h} from 0.3 to 0.2 caused an increase in Φ of approximately 0.13% at $M_{2h}=1.0$. The sensitivity of Φ to changes in ζ_p, M_{1h}, and α_F was greater for lower M_{2h}.

The variation of Φ over a wide range of ζ_p, M_{1h}, and α_F around a baseline design point is shown to be small in comparison to the absolute value of Φ, and the greatest sensitivity of Φ was to M_{1h} for the ranges considered.

The sensitivity of the flow correction parameter to the full range of film cooling effectiveness is now considered. Two cases are of particular interest; that in which the cooling flow is unmixed $\varepsilon_F=1.0$; and that in which it is fully mixed with the mainstream such that the mixed flow fills the throat $\varepsilon_F=0.15$. The numerical results show that these conditions are close to the limiting conditions, as will now be discussed.

Results at the nominal conditions presented in Table 1, for film cooling effectiveness in the range $0.15<\varepsilon_F<1.0$, are presented in Fig. 8. The condition $\varepsilon_F=0.15$ corresponds to fully mixed out flow at the throat plane. Over the full range $0.15<\varepsilon_F<1.0$, the variation of Φ is between +0.095% and −0.006% of the nominal condition $\varepsilon_F=0.5$, and +0.082% and −0.019% of the fully mixed out condition $\varepsilon_F=0.15$.

The conclusion is that at the engine design point considered, which is typical, if the total flow rate $\dot{m}_T$ were computed on the basis of fully mixed out conditions at the throat plane, the result would be correct to within 0.082% at worst, but typically to within approximately 0.02% for the range of conditions realized in practice. At the nominal condition, the error introduced by the assumption of fully mixed out conditions is approximately 0.013%.

10 Example 2: Correction of Capacity Measured in a Cold or Warm Rig to Engine Capacity

The situation discussed in Example 1 is atypical. Engine capacity is usually computed by correction of a capacity measured experimentally in a cold or warm rig to engine conditions: this is because of the practical difficulty of measuring A_2 directly. This is especially true for vanes that are either highly 3-dimensional, or for which the geometric throat is subsonic at high values (up to 1.4) of exit Mach number, as in the case of aft loaded vanes. In these cases, errors in capacity of up to 10% could result from a simple 1D inviscid analysis based on the geometric throat area at a nominal exit Mach number of unity (see Ref. [1]).

The following example considers the situation in which A_2 is not known from direct measurement, but for which capacity is measured experimentally in the cold or warm rig situation. The problem of computing the capacity at the hot engine condition from the cold-rig result is now discussed.

In this second example, the following situation is assumed.

(a) The area A_2 is unknown because direct measurement is impractical or impossible, and the total mass flow rate (with coolant streams) $\dot{m}_T(p_2/p_{0h})$ is measured experimentally at known conditions (p_{0cp}, T_{0cp}, p_{0h}, and T_{0h} directly measured) different from the engine design point. In the experiment the following would be typical: $T_{0cp}=T_{0h}$, $\gamma_{0c}=\gamma_{0h}$, and $R_c=R_h$. Furthermore p_{0cp}/p_{0h} would normally be matched to the nominal engine condition.

(b) The area A_2, and ultimately the total engine mass flow rate (comprising two partially mixed streams) $\dot{m}_T(p_2/p_{0h})$ is required. (Unlike Example 1, A_2 is unknown at this stage.)

In this case the analysis would proceed as follows.

(i) The total mass flow rate (with coolant streams) $\dot{m}_T(p_2/p_{0h})$ is measured experimentally at conditions different from the engine design point, and design point values *at the engine condition of* ζ_p, η, ε_F, ε_M, p_{0cp}, T_{0cp}, p_{0h}, T_{0h}, $\dot{m}_c/\dot{m}_M$, γ_{0h}, R_h, γ_{0c}, and R_c are identified.

(ii) Values of A_1/A_2 and α_F are chosen that are as representative as possible of the cooling system, within the constraints of the model (single injection point). Choice of A_1/A_2 then determines $M_{1h}=f(M_{2h})$, for a given working gas, and thus the nominal value of M_{1h}. It is noted that accurate knowledge of A_2 is not required at this stage.

(iii) A_c/A_2 is computed so that $\dot{m}_c/\dot{m}_M$ is matched (at engine conditions) to the engine reference condition at the reference value of M_{2h}; the same caveats as expressed in Example 1 apply regarding A_c.

(iv) The ratios A_1/A_2 and A_c/A_2, and the value of α_F computed from knowledge of the engine reference condition are used to compute $\dot{m}_c=f(M_{2h})$ at the cold-rig condition. The ratio $\dot{m}_c/\dot{m}_M$ in the cold-rig will normally be quite different from the ratio at the engine reference condition.

(v) It is assumed that the design point values at the engine condition of ζ_p, η, ε_F, and ε_M hold to good approximation in the cold-rig situation. Small errors at this stage can be shown to be insignificant in the final result.

(vi) The flow rate correction parameter $\Phi(p_2/p_{0h})$ is computed in the cold-rig situation. It is noted that in the case where $T_{0cp}=T_{0h}$, the value of $\Phi(p_2/p_{0h})$ is close to unity. Small differences from unity arise because the total pressure deficit introduced because of the mixing of the coolant stream is confined to a partially mixed layer rather than being mixed through the flow.

(vii) The mass flow rate in the absence of film cooling for the case of the cold-rig is computed using the values of $\Phi(p_2/p_{0h})$ and Eq. (33)—$\dot{m}_H(p_2/p_{0h})=\dot{m}_T(p_2/p_{0h})/\Phi(p_2/p_{0h})$—and thus the equivalent throat area A_2 is calculated from $\dot{m}_H(p_2/p_{0h})$. No exact parallel of A_2 exists for $\dot{m}_T(p_2/p_{0h})$ because in this latter case the flow is composed of two streams. This is the reason for taking the approach outlined.

Once the equivalent throat area in the absence of film cooling, A_2, is known, the flow rate in the absence of film cooling can be computed for the engine case $\dot{m}_H^{\text{engine}}$. The analysis then proceeds as with Example 1. That is, once $\dot{m}_H^{\text{engine}}$ has been computed, it remains only to compute $\Phi(p_2/p_{0h})^{\text{engine}}$ at engine conditions, and hence the value of the total mass flow rate at engine conditions with film cooling, which is given by

Table 2 Cold-rig conditions typical of a modern HP NGV

Parameter	Nominal value	Units
ζ_p	0.7	
η	0.8	
ε_F	0.5	
ε_M	0.6	
p_{0h}	2.1×10^5	Pa
T_{0h}	290	K
p_{0cp}/p_{0h}	1.025	
T_{0cp}	290	K
M_{1h}	0.3	
$\dot{m}_c/\dot{m}_H$	(7.81)	%
α_F	30	deg
M_{2h}	(0.5 to) 1.0	

$$\dot{m}_T(p_2/p_{0h})^{\text{engine}} = \Phi(p_2/p_{0h})^{\text{engine}}\dot{m}_H(p_2/p_{0h})^{\text{engine}} \quad (34)$$

The method is now illustrated with an example at typical cold-rig conditions. The conditions in the cold rig situation are summarized in Table 2 above. The mass flow rate ratio $\dot{m}_c/\dot{m}_H$ is shown in parentheses, to indicate that it is derived from a value of A_c/A_2 chosen to that $\dot{m}_c/\dot{m}_H$ is matched to the engine condition for the engine situation.

The variation of specific heats with temperature for the range of conditions covered by the test case ($0.5<M_{2h}<1.0$) is shown in Fig. 9 below. Each value of γ is plotted against the corresponding temperature range for $0.5<M_{2h}<1.0$. The values of R_c and R_h were taken as those for dry air (cold-rig experiment). The variation of γ with T is less than 0.04%, over the 50 K temperature range.

The variation of the mass flow rate of coolant $\dot{m}_c$ with the throat Mach number M_{2h} is shown in Fig. 10. At the reference condition $M_{2h}=1.0$ the mass flow rate ratio was $\dot{m}_c/\dot{m}_H=7.81\%$. It is noted that at the corresponding engine condition, which was used as the constraint for A_c/A_2, the reference value was $\dot{m}_c/\dot{m}_H=10\%$. The percentage of coolant flow is lower in the cold rig situation, as expected. Ignoring the influence of γ, and for a given pressure ratio $\dot{m}_c/\dot{m}_H \propto \sqrt{T_h/T_c}$. In the engine situation therefore, $\dot{m}_c/\dot{m}_H \propto \sqrt{1850/950}=1.40$. In the rig situation $\dot{m}_c/\dot{m}_H \propto 1.00$. The ratio of mass flow rates in the rig situation is therefore $1/1.40=0.714$ of that in the engine situation, or 7.14% versus 10%. The difference in specific heat ratios between the two situations accounts for the difference between this crude estimate and the predicted value of $\dot{m}_c/\dot{m}_H=7.81\%$. The change in $\dot{m}_c/\dot{m}_H$ over the range of M_{2h} considered was 11.7%.

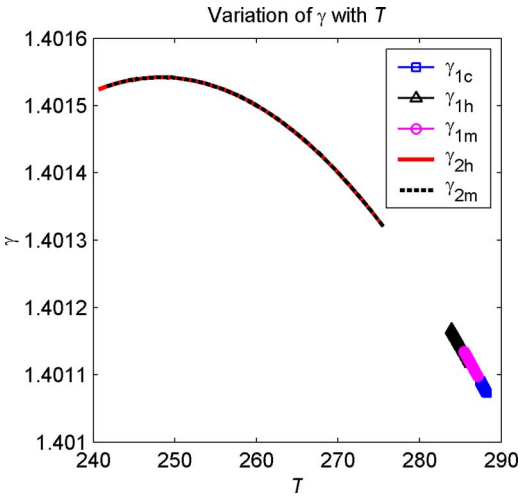

Fig. 9 Variation of γ with T for the cold-rig situation

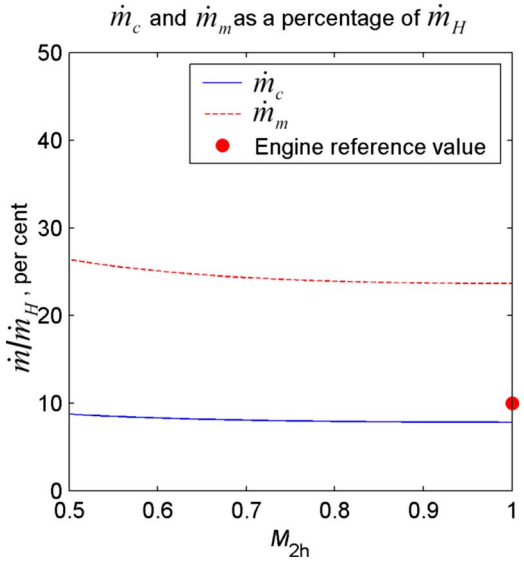

Fig. 10 Variation of $\dot{m}_c$ and $\dot{m}_m$ with M_{2h} for the cold-rig situation

The variation of the flow rate correction parameter Φ with M_{2h} is shown in Fig. 11 for the cold-rig situation. Φ varies from 0.9967 to 0.9979 over the range considered. That is, the total mass flow rate $\dot{m}_T$ with cooling flow is smaller than that inferred by taking the conditions of the hot gas stream alone (no coolant flow) $\dot{m}_H$ between 0.21% and 0.33%. The mass flow rate is lower with the coolant flow because of the total pressure loss in the mixing layer. It is noted that the total pressure loss on the mainstream flow is not modeled, but could be estimated using superposition if required: Here we are concerned with the difference in mass flow caused by the introduction of cooling flow.

For completeness, the variation of $\dot{m}_H$ and $\dot{m}_T$ as a function of M_{2h} is shown in Fig. 12 below, for the cold-rig situation. The correction is simply given by Eq. (33), using the value of Φ presented in Fig. 11.

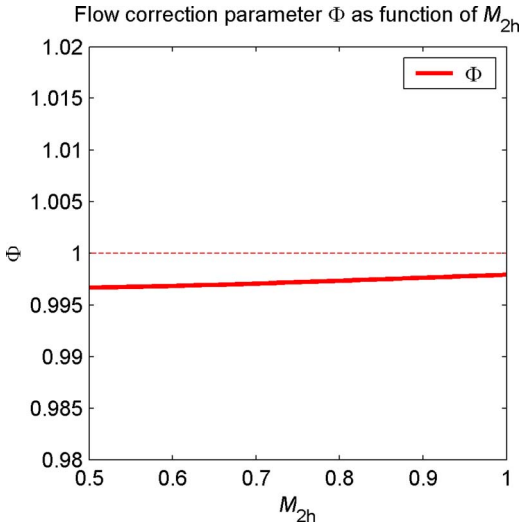

Fig. 11 Variation of the predicted value of Φ with M_{2h} for the cold-rig situation

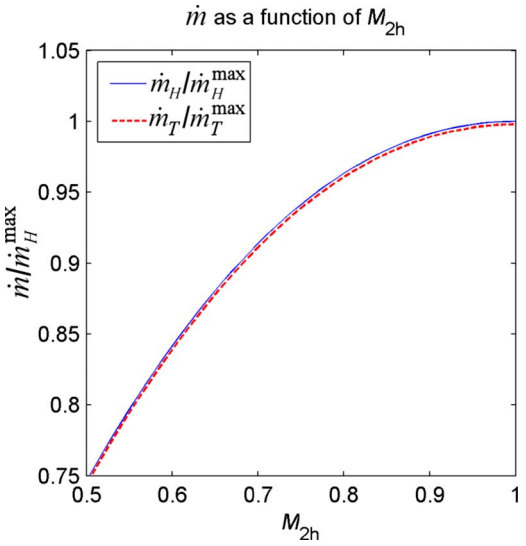

Fig. 12 Hot gas mass flow rate (flow without film cooling) $\dot{m}_H$ and corrected total mass flow rate $\dot{m}_T$ as a function of M_{2h} for the cold-rig situation

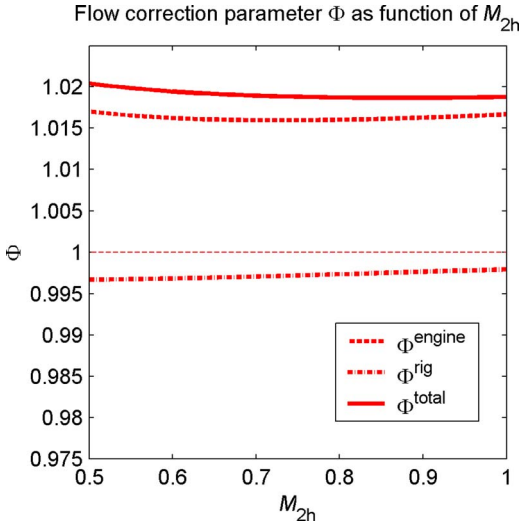

Fig. 13 Variation of Φ with M_{2h} for the cold-rig situation, the engine situation, and the combined correction

In this example, the premise was that the mass flow rate with film cooling (at the same pressure ratio as in the engine case) was measured in the rig situation. That is, the total mass flow rate $\dot{m}_T(p_2/p_{0h})$ is measured. The hot-stream mass flow rate is easily computed as follows:

$$\dot{m}_H(p_2/p_{0h})^{\text{rig}} = \dot{m}_T(p_2/p_{0h})^{\text{rig}}/\Phi(p_2/p_{0h})^{\text{rig}} \tag{35}$$

As outlined in step (vii) above, the equivalent throat area A_2 is then calculated from $\dot{m}_H(p_2/p_{0h})$. Once the equivalent throat area (that associated with a single stream) A_2 is known, the analysis proceeds as in Example 1 above. First $\dot{m}_H^{\text{engine}}$ is computed. Then $\Phi(p_2/p_{0h})^{\text{engine}}$ is computed at engine conditions. The total mass flow rate at engine conditions with film cooling is then given by Eq. (34).

It is noted that the corrections for typical cold-rig and hot engine conditions are of opposite signs, and therefore additive in terms of the magnitude of the overall correction that would result if only the hot-stream were to be taken into account in the computation of the mass flow rate in the engine situation. The corrections terms shown in Figs. 4 and 11 for the rig and engine situations, respectively, are shown on the same graph in Fig. 13. The total correction between the rig and engine is also shown. The total correction varies between $1.0187 \leqslant \Phi^{\text{total}} \leqslant 1.0204$. That is, if the mass flow rates in the engine and rig case were calculated on the basis of the mainstream (hot) streams alone, the required correction would be between 1.87% and 2.04%.

In the context of the discussion of the sensitivity of Φ to the variation of the input parameters to the model (see Fig. 8 and related argument), it was demonstrated that in the case where the throat flow is represented as a single stream, but at the fully mixed out conditions rather than at the hot stream condition, the correction term from the fully mixed condition to the engine condition varies between −0.019% (ε_F=0.4) and +0.082% (ε_F=1.0). The correction to the nominal engine condition (ε_F=0.5) from the fully mixed out condition is −0.013%. Thus, the overall correction between the rig and engine situations (at the nominal conditions) is the sum of the cold-rig correction term (to single hot-stream conditions), +0.21%, and the correction from the fully mixed throat flow to partially mixed throat flow (ε_F=0.5) in the engine situation, −0.013%. That is, an overall correction of 0.20%.

11 Summary of Correction Parameters

The flow rate correction parameters for the examples considered above (nominal conditions in Tables 1 and 2) are summarized in Table 3, below, for the nominal condition. The sign convention that is adopted is in the sense that the correction should be applied to achieve the correct engine mass flow rate from an estimate based on the method given the first column.

12 Conclusions

A simple analytic model has been developed which allows the effect of film cooling on the capacity of a turbine to be computed. The model is based on fundamental cooling performance parameters which are available at an early stage in the engine design process.

The model can be used to compute a flow correction parameter which enables the true throat flow due to a partially mixed coolant stream and unaffected mainstream to be calculated by correction to the flow calculated for a single stream. The single stream can either be at the hot-stream condition, or at the fully mixed out condition.

It has been shown that at a typical engine operating point, the correction to engine conditions of an estimate based on the single hot-stream assumption (no coolant) is approximately +1.67%. Where the mixed out flow assumption is used the correction is only −0.013%, and is therefore small enough to neglect. In the case of a cold-rig experiment with film cooling, if the flow rate that would have been inferred on the basis of a single stream calculation (without film cooling) is desired, a correction of approximately +0.21% is required from the experiment. The purpose of this corrected flow rate (single stream) in the case of a cold-rig

Table 3 Summary of flow rate correction parameters

Method of estimation	Correction to engine conditions
Engine conditions—single hot-stream	+1.67%
Engine conditions—single fully mixed stream	−0.013%
[Rig measurement—correction to single hot-stream]	[+0.21%]
Rig measurement and engine estimate at engine conditions for single hot-stream	+1.88%
Rig measurement and engine estimate at engine conditions for single fully mixed stream	+0.20

experiment is as an intermediate step in computing the mass flow rate at engine conditions. In this case the measured flow rate is lower with film cooling (than without) due to total pressure losses in the partially mixed layer.

Where a measurement of the mass flow rate in a cold-rig is to be translated to a mass flow at engine conditions, the overall correction parameter is +1.88% when the single engine stream is estimated at the hot-stream condition. When the single engine stream is estimated at the fully mixed out condition, the overall correction term is +0.20%.

The following conclusions are drawn.

(i) In most situations where an engine mass flow rate is to be estimated from a known throat area, it is sufficient to assume that the flow at the throat plane is fully mixed out. The maximum error that would be incurred in making this assumption at normal operating conditions is about 0.1%, but is typically an order of magnitude smaller, and may reasonably be neglected.

(ii) Where the flow at the engine condition is to be estimated using an area measured in a cold-rig experiment, and using fully mixed out flow (a single stream) for engine throat conditions, a correction factor of about 0.2% is applicable, and a model of the type outlined in this paper is appropriate to compute this correction.

(iii) The increase in throat mass flow rate at typical engine operating conditions (HP vane) with the introduction of 10% (as a % of total throat flow) film cooling is approximately +1.7%. Where crude estimates are required without the complexity of mass weighting, etc., a correction of this magnitude could be used. In a small region around the design point, the correction scales approximately with the percentage of coolant flow.

Nomenclature

A_1 = total flow area at injection plane
A_2 = total flow area at throat plane
A_c = equivalent coolant injection area (arbitrary)
HP = high pressure
$\dot{m}_c$ = coolant stream mass flow rate
$\dot{m}_e$ = entrained mass flow rate
$\dot{m}_h$ = hot-stream mass flow rate
$\dot{m}_m$ = mixed stream mass flow rate
$\dot{m}_H$ = mass flow rate at hot gas condition
$\dot{m}_M$ = mass flow rate of fully mixed out single stream
$\dot{m}_T$ = total mass flow rate of two streams
M_{1c} = cold stream Mach number at Plane 1
M_{1h} = hot-stream Mach number at Plane 1
M_{1m} = Mach number of mixed out layer at Plane 1
M_{2h} = hot-stream Mach number at Plane 2
M_{2m} = mach number of mixed out layer at Plane 2
p_{01m} = total pressure of mixed out layer at Plane 1
p_{0c} = cold stream injection pressure
p_{0cp} = cold stream plenum pressure
p_{0h} = hot-stream total pressure
R = specific gas constant
T_{0c} = total temperature of coolant at injection
T_{0cp} = total temperature of coolant plenum
T_{0h} = total temperature of hot-stream
T_{0m} = total temperature of mixed out layer
T_{1h} = static temperature of hot-stream at Plane 1
T_{2h} = static temperature of hot-stream at Plane 2
T_{2m} = static temperature of mixed out stream at Plane 2
T_w = wall/metal temperature
T_h = static temperature of hot-stream
u_{1c} = velocity of coolant stream at Plane 1
u_{1h} = velocity of hot-stream at Plane 1
X = $(\gamma-1)/\gamma$
Y = $(\gamma-1)/2$
Z = $(\gamma+1)/(2\gamma-2)$

Greek

α_F = angle of film cooling row with respect to surface
χ = ratio of coolant gas to entrained hot gas
ε_F = film cooling effectiveness
ε_M = metal effectiveness
Φ = flow rate correction parameter
γ = ratio of specific heats
$\overline{\gamma}_h$ = mean ratio of specific heats
η = cooling efficiency
ζ_p = coolant total pressure loss coefficient

References

[1] Afanasiev, I. V., Granovski, A. V., Karelin, A. M., and Kostege, M. K., "Effect of 3D Vane Shape on the Flow Capacity," ASME Paper No. GT2004-53095.
[2] Fielding, L., 1981, "Effect of Irreversibility on the Capacity of a Turbine Blade Row," Proc. Inst. Mech. Eng., **195**, pp. 127–37.
[3] Hoheisel, H., Kiock, R., Lichtfuss, H. J., and Fottner, L., 1987, "Influence of Free-Stream Turbulence and Blade Pressure Gradient on Boundary Layer and Loss Behaviour of Turbine Cascades," ASME J. Turbomach., **109**(2), pp. 210–219.
[4] Hartsel, J. E., 1972, "Prediction of Effects of Mass-Transfer Cooling on the Blade-Row Efficiency of Turbine Airfoils," AIAA Tenth Aerospace Sciences Meeting, CA, Jan. 17–19, AIAA Paper No. 72-11.
[5] Kollen, O., and Koschel, W., 1985, "Effect of Film Cooling on the Aerodynamic Performance of a Turbine Cascade," Paper No. AGARD CP-390.
[6] Eckert, E. R. G., and Drake, R. M., 1972, *Analysis of Heat and Mass Transfer*, McGraw-Hill, New York, pp. 453–466.

T. Coppola
S. Riscifuli
O. Tassa

Centro Sviluppo Materiali S.p.A.,
Via di Castel Romano 100,
Roma 00128, Italy

G. Pasquero
R&D,
Avio S.p.A.,
Via 1 Maggio 56,
Rivalta di Torino 10040, Italy

Thermomechanical Fatigue Behavior of Bare and Coated CMSX-4

Highly cooled turbine blades undergo very high thermal gradients during rapid engine idle-max-idle cycling. Traditional isothermal fatigue data are often insufficient for predicting service lives. A complete set of high temperature tests, in the range of 750–1050°C, was performed on single crystal alloy CMSX-4. The test program comprised tensile, creep, low cycle fatigue, and thermomechanical fatigue (TMF) tests. In particular the cycle time for TMF was 3 min, aiming to simulate the real high-power transient conditions in aircraft engines. Clockwise and counterclockwise diamond cycle types were applied on bare and coated specimens to investigate their influence on the fatigue limit. The comparison of the results obtained with the available ones from open literature is discussed. [DOI: 10.1115/1.3124666]

1 Introduction

Single crystal nickel-based alloys are widely used as turbine blade materials in gas turbine engines thanks to their excellent resistance to high temperature loadings. Coatings, such as aluminizing, formed by diffusion process are applied to provide protection against degradation due to high temperature oxidation. The major cause of failure in single crystal turbine blades are both mechanical and thermal stresses caused by strains induced by thermal gradients during rapid heating and cooling phases.

Traditionally isothermal fatigue data are used to design turbine blades, however, these do not account for the fatigue damage occurring in blades exposed to thermomechanical fatigue (TMF) tests. For example, Al coatings may crack during first engine run if exposed to high strains below the brittle to ductile transition temperature.

TMF tests are specifically designed to reproduce the temperature and strain cycles actually seen by critical locations on the blade.

In order to develop better design data and to understand what correlation exists between isothermal fatigue data and TMF ones, a test program has been undertaken to study the TMF behavior of bare and Al coated CMSX-4 single crystal material to investigate the effect of TMF cycle type and the presence of the coating on the TMF life.

2 Material

The single crystal nickel-based alloy CMSX-4 is a second generation superalloy containing 3 wt % rhenium (Re) and 70% volume fraction of the coherent γ' precipitate strengthening phase. It was developed in the 1990s by Cannon-Muskegon [1] for demanding applications on turbine blades. Due to its creep and fatigue resistance properties, CMSX-4 is a candidate material for high pressure turbine (HPT) and first stage low pressure turbine (LPT) blades.

The material used in this work has been supplied by Europea Microfusione Aerospaziale (EMA) S.p.A., Italy in the form of 16 mm diameter round bars. The material was heat treated, i.e., solution treated and precipitation hardened according to Cannon-Muskegon standard recommendation.

The cast bars were next verified for defects and orientation: only bars with less than a 10 deg difference between (100) crystal orientation and bar axis were accepted.

The chemical analysis of the cast bars is reported in Table 1.

Specimens for mechanical testing (tensile, creep, low cycle fatigue (LCF), TMF) were machined directly from the bars; one additional set of specimens for TMF testing were Al coated.

3 Test Program

All test programs, except creep tests, were performed on a servomechanical two column Mayes frame (D100 series). The testing system is composed by a real time controller based on National Instrument hardware and a LABVIEW based programmable software. The Mayes frame is equipped with MTS hydraulic grips (Model 646.10B) and a computer controlled alignment system (MTS Model 609.10). Strains are measured by means of an MTS high temperature clip gauge (Model 632.53F-14). Two different heating systems can be applied on the frame: an MTS resistance furnace (Model 653.01) for LCF and a 10 kW radio frequency (RF) induction system (Ambrell Model 8310) for TMF.

The specimens are smooth ended for locking in the hydraulic grips and have a 6 mm gauge diameter over an 18 mm central length. The gauge length is 12 mm.

Temperature control is achieved by using a thermocouple Pt/Pt/Rh (type R) welded outside the gauge length. In the setup phase, the thermal gradient was evaluated on six thermocouples welded along and around the gauge length, resulting in less than 5°C of the maximum range measured. The control thermocouple has been calibrated against a reference thermocouple in the middle gauge section both in the steady state and in the transient condition.

Both LCF and TMF tests are conducted according to the test procedure specified in Ref. [2].

All specimens were tested in the bare condition except one set for TMF testing.

The qualification program comprised the following set of tests:

- tensile from RT to 1050°C
- creep at 950°C and 1050°C
- LCF at 750°C, 850°C, and 1050°C, with a strain ratio of $R=-1$ and $R=0$
- TMF with a minimum temperature of 600°C and a maximum temperature of 1050°C, strain ratio $R=-1$

The strain rate applied in LCF tests was about 10^{-2} s^{-1}.

Contributed by the International Gas Turbine Institute of ASME for publication in the JOURNAL OF ENGINEERING FOR GAS TURBINES AND POWER. Manuscript received April 1, 2008; final manuscript received May 19, 2008; published online September 29, 2009. Review conducted by Dilip R. Ballal. Paper presented at the ASME Turbo Expo 2008: Land, Sea and Air (GT2008), Berlin, Germany, June 9–13, 2008.

Table 1 Chemical composition of CMSX-4

Cr	Co	Mo	W	Re	Ta	Al	Ti	Hf	Ni
6.5	9.5	0.6	6.4	2.9	6.5	5.5	1.0	0.1	Bal

For TMF testing, different cycle types were selected. First of all, thermomechanical finite element simulations were performed on a three-dimensional blade model of the intermediate pressure blade (IPT) of the research engine of ANTLE Framework V European Research Programme. The fast acceleration from stabilized idle power to take-off power and the return to idle was selected as the most severe engine transient. The blade is cooled by internal ribbed channels, and film cooling holes are present at the trailing edge. The internal fluid network has been included in the thermal analysis, performed with finite element (FE) code MSC/THERMAL, whereas the stress analysis has been subsequently performed with MSC/NASTRAN code. Next, the most solicited points were considered in a complete thermomechanical cycle representing the engine regime variation from idle to maximum power and returning to the idle condition.

Two zones on the blade were considered to be reproduced in TMF testing: the leading edge at airfoil midheight (testing block A) and the inner platform to airfoil fillet (testing block B). In both cases the min-max cycle temperature was 600–1050°C, while the min-max strain was calculated at 700–950°C. Both blocks were performed at a strain ratio of $R=-1$. The difference was that in block A the minimum (compressive) strain is reached in the heating step at 950°C, while in block B the minimum (compressive) strain is reached at 700°C, according to the thermal and strain history calculated from finite element.

Both blocks are performed in clockwise (CW) cycling. An additional block C was planned in counterclockwise (CCW) cycling, with the maximum tensile strain reached at 700°C, aiming to reproduce the airfoil inner web's behavior.

Two other blocks (D and E) were tested in the coated condition. The first (block D) at the same condition of block A was tested in order to quantify the oxidation effect on fatigue life. The second (block E) at the same condition of block C was tested to assess the coating cold cracking effect.

The total cycle time is 180 s, equally distributed in heating and cooling steps. The temperature history in a TMF cycle is represented in Fig. 1.

A summary of the different TMF testing cycles is reported in Fig. 2. The basic cycle is an asymmetric diamond type, with zero holding time at the extreme strains.

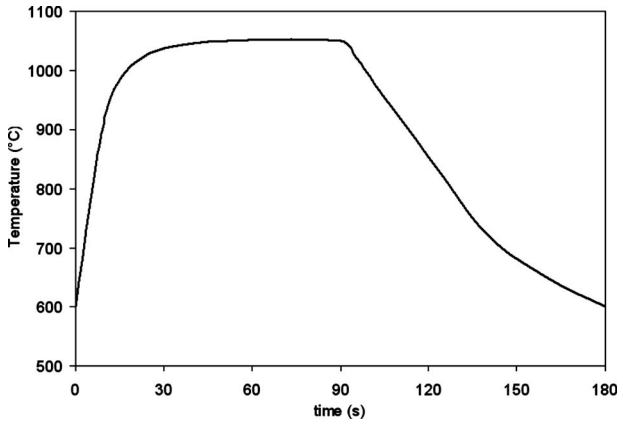

Fig. 1 Temperature versus time cycle for TMF testing

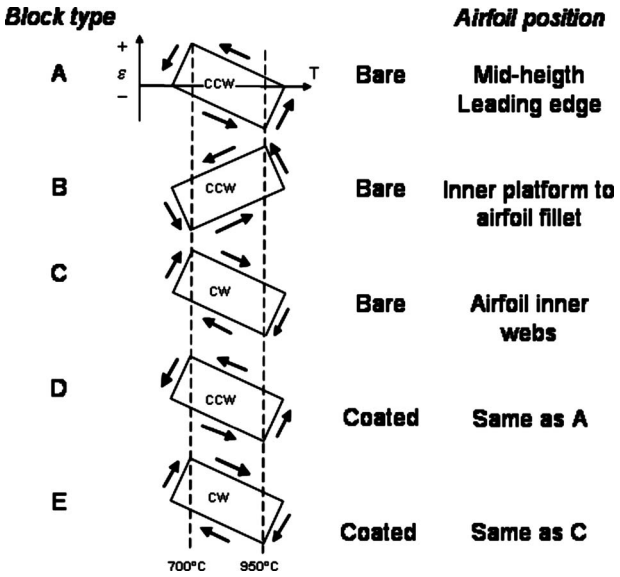

Fig. 2 TMF cycle types

4 Test Results

The results of the mechanical testing campaign are presented in the following graphs (Figs. 3–6).

In Fig. 3 the tensile test results are presented in terms of yield and maximum stress (UTS) as a function of temperature. A linear decay in the temperature range explored is found.

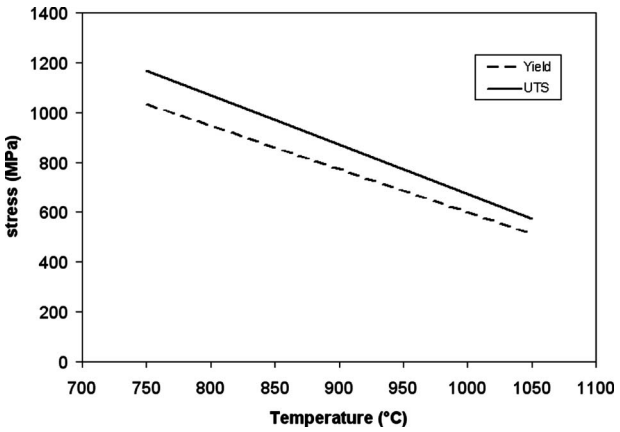

Fig. 3 Tensile test results

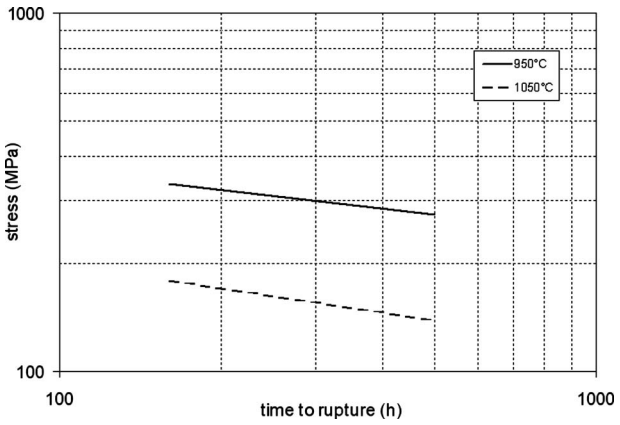

Fig. 4 Creep test results

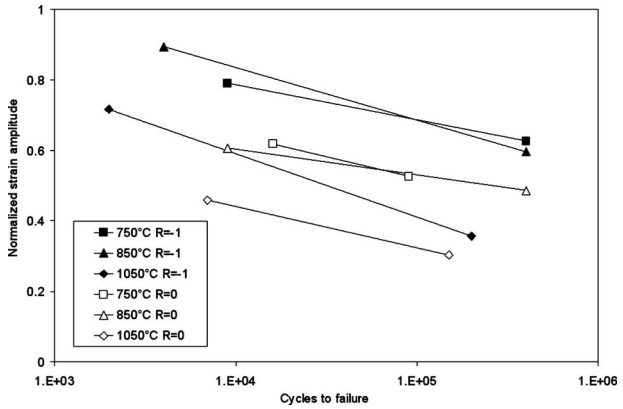

Fig. 5 LCF results

Creep test results are presented in terms of stress versus time to rupture (reported in hours) at the two testing temperatures (Fig. 4).

LCF and TMF results are reported as normalized total strain versus cycles to rupture (Figs. 5 and 6).

5 Microstructural Observation

In the fully heat treated conditions, a fine distribution of γ' particles having a size of approximately 0.5 μm is observable (Fig. 7).

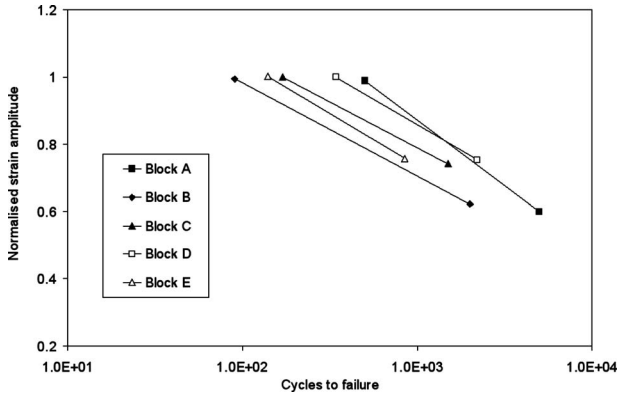

Fig. 6 TMF results

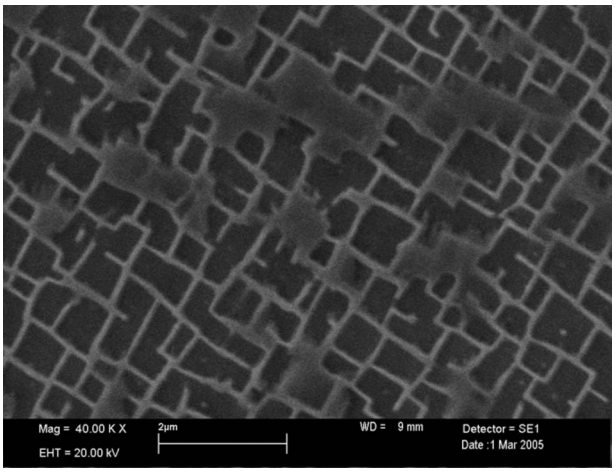

Fig. 7 SEM micrographs of fully heated treated material

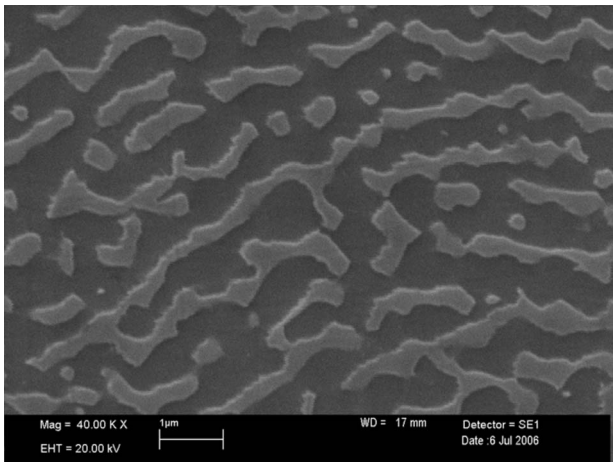

Fig. 8 SEM micrograph showing γ' morphology after creep tests at 1050°C

The temperature at which the γ' particle starts rafting under stress is around 900°C, and in Fig. 8 the microstructure of failed creep specimen tested at 1050°C is shown.

Microstructure modifications at the 0.5 μm scale are observable.

All the LCF tests show quite similar failure mechanisms that are predominantly crack initiation from a pore or oxide spike followed by planar crack propagation, and finally shear on crystallographic planes. The differences in failure mechanisms as the temperature is increased are restricted to the initiation stage; at 850°C initiation occurs generally internally at a casting pore (Fig. 9(*a*)), whereas at 1050°C initiation occurs at the surface of the specimen from an oxide spike (Fig. 9(*b*)). Scanning electron microscopy (SEM) observation of the TMF fracture surface of uncoated specimens reveals multiple crack initiation sites at the surface associated to broken oxide hillocks (Fig. 10).

Fatigue striations are found in most of tested specimens, and the crack seems to propagate simultaneously along different crystallographic planes, namely, {111} planes; slip bands are observed in the final failure surface (Fig. 11).

6 Discussion

The results are discussed first by comparison with available open literature data on similar conditions. As far as creep behavior is concerned, results are compared with data in Refs. [3,4] by considering the rupture stress as a function of the Larson–Miller parameter (LMP). In Fig. 12 the comparison is shown, indicating that the results are comparable.

The second comparison is done on LCF results, where literature data come from Refs. [1,5]. A good agreement can be observed, especially at 850°C. Longer lives are observed at 1050°C and

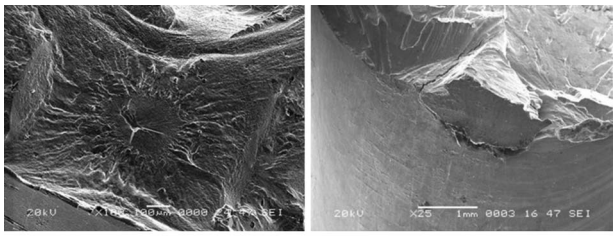

(*a*) (*b*)

Fig. 9 SEM micrographs of LCF fracture starting by (*a*) pore and (*b*) by surface

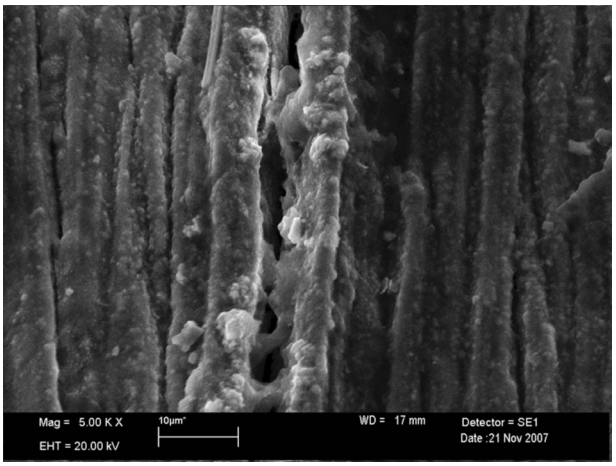

Fig. 10 SEM micrographs showing oxide hillocks on the surface of the uncoated TMF specimen

$R=-1$, while at $R=0$ the behavior is substantially similar, even if the present work data are obtained at a higher number of cycles (Figs. 13 and 14).

As far as TMF results are concerned, it can be observed that the curves for the different cycle types are substantially parallel (Fig. 6), the difference being basically only on the shifting along the number of cycles axis. To understand the difference in behavior, it is interesting to examine the hysteresis loops for the different blocks (Fig. 15). We can observe that for blocks A and C (CCW against CW at the same T), we have different loop shapes. The main difference is that for block A the loop is mainly developed in compression, while block C is in tension. This means that the plastic work is mainly dissipated in tension or compression. For tensile dissipation we can observe a higher damage effect, which lowers the measured lives.

Block B has also a loop mainly in compression as block A (they

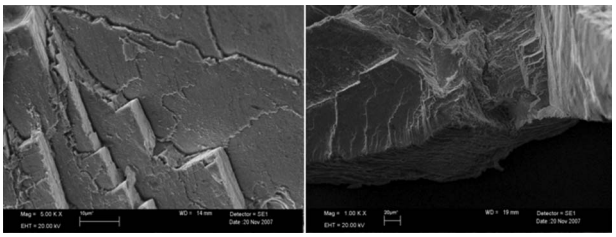

Fig. 11 SEM micrographs showing the TMF fracture of the coated specimen

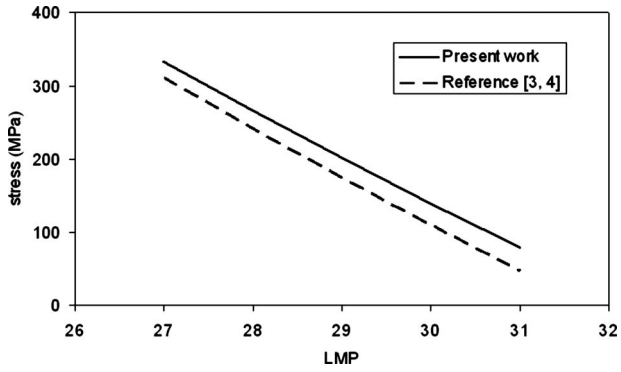

Fig. 12 Creep test results compared with literature data

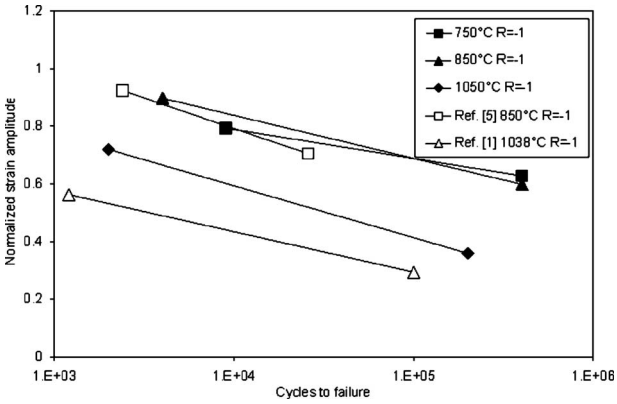

Fig. 13 LCF results at $R=-1$ compared with literature data

are both of the CCW type), but due to the different temperatures reached at the extreme strains, B the dissipated plastic work in block is higher, resulting in shorter lives.

The above observations can be quantified in terms of loop area A, calculated at the stabilized cycle (typically at mid life). In Fig. 16 the relation between the area A at maximum strain and TMF life is reported. It can be observed that a good relation exist between the loop area and TMF life.

TMF data are also compared with literature data [6]. In this case the cycling conditions are different from the present work conditions. With data in Ref. [6] obtained basically in CCW, only blocks A and B are considered for comparison. Even if the cycle

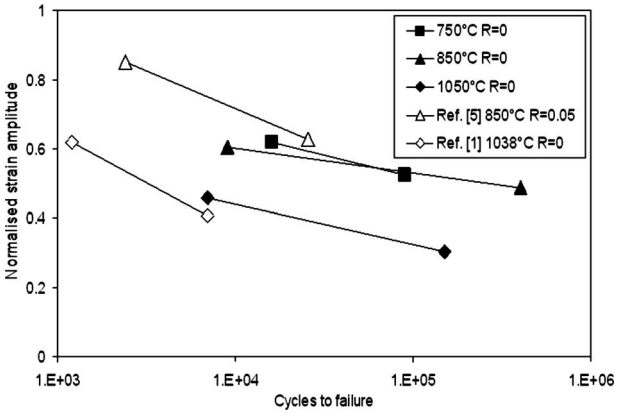

Fig. 14 LCF results at $R=0$ compared with literature data

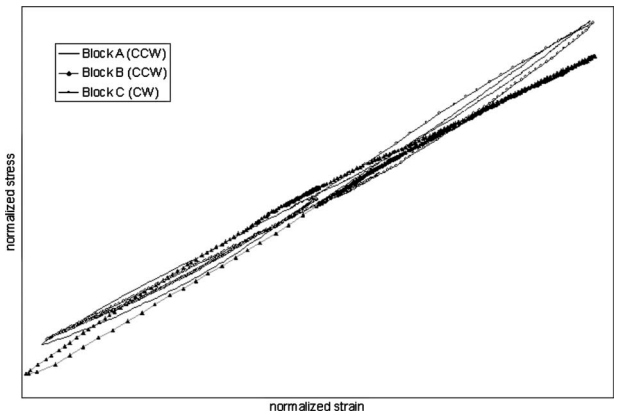

Fig. 15 Hysteresis loop at the maximum strain

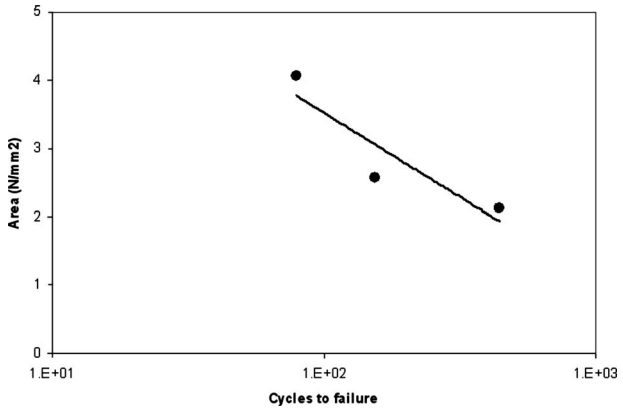

Fig. 16 Area loop at maximum strain versus TMF life

shape and the strain levels are different, the comparison presented in Fig. 17 shows that the actual data have a tendency to converge to the reference ones at low strain levels.

For coated specimens, shorter lives are observed in both block types (D and E) with respect to the corresponding bare specimens. We can explain this behavior by considering that two competitive mechanisms act during TMF: the shielding effect of coating, which should protect the material from oxidation damage, and the tendency to cracking of the coating [7]. In case of high applied strains and short lives, the second effect should be dominant, while at low strains and long lives, the first one should be expected. The results obtained seem to confirm that the coating cracking is dominant, and we can observe shorter lives for both cycle types. A further confirmation is given by the observation of the cracked coating, which shows the crack initiation in the coating (Fig. 18(*a*)) and the subsequent growth into the substrate material (Fig. 18(*b*)).

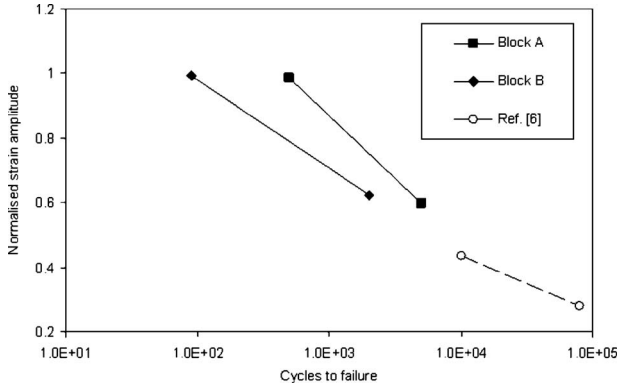

Fig. 17 TMF results compared with literature data

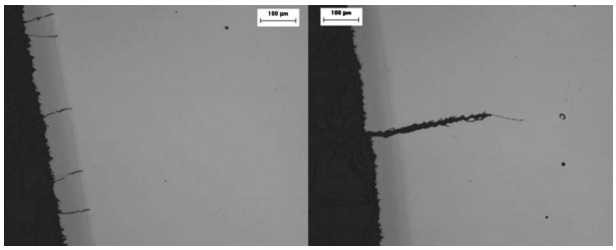

Fig. 18 Cracks in the coating (block D specimen)

The difference in duration between blocks D and E is explained not only by the cycle severity (D corresponding to A, E corresponding to C) but also by the low fracture strain of the coating at low temperatures induced by cycle type E respect to D that may induce premature brittle cracking.

7 Conclusions

The single crystal nickel-based alloy CMSX-4 was extensively investigated in tensile, creep, LCF, and TMF testing at different temperatures and loading conditions.

Creep and LCF test results were found to be in good agreement with open literature data.

Specific TMF conditions were applied, in order to evidence the cycle effect (CW and CCW), the exposure time, and the coating effect on duration.

In particular, it was observed that coated specimens exhibit lower lives due to the cracking tendency as a consequence of the elevated applied strains. A good relation between the loop area and the TMF life was also observed.

References

[1] Thomas, M. C., Helmink, R. C., Frasier, D. J., Whetstone, J. R., Harris, K., Erickson, G. L., Sikkenga, S. L., and Eridon, J. M., 1994, "Allison Manufacturing, Property and Turbine Engine Performances of CMSX-4® Single Crystal Alloy," *Materials for Advanced Power Engineering, Part II*, pp. 1075–1098.

[2] AAVV, 2004, "Validated Code of Practice for Strain-Controlled Thermo-Mechanical Fatigue Testing," TMF-Standard Project, GROWTH Programme, Project No. GRD2-2000-30014.

[3] Erickson, G. L., and Harris, K., 1994, "DS and SX Superalloys for Industrial Gas Turbines," *Proceedings of the Fifth International Conference Material for Advanced Power Engineering*, Oct. 3–6, Liege, Belgium.

[4] Fullagar, K. P. L., Broomfield, R. W., Hulands, M., Harris, K., Erickson, G. L., and Sikkenga, S. L., 1996, "Aero-Engine Tests Experience With CMSX-4® Alloy Single-Crystal Turbine Blades," ASME J. Eng. Gas Turbines Power, **118**, pp. 380–388.

[5] Schubert, F., 1994, "Cost 501, Third Round," Adv. Mater. (Weinheim, Ger.), **6**(12), pp. 901–904.

[6] Meyer-Olbersleben, F., Goldschmidt, D., and Rézai-Aria, F., 1992, "Investigation of the Thermal Fatigue Behaviour of Single Crystal Nickel Based Superalloys SRR99 and CMSX-4," *Superalloys 1992*, S. D. Antolovich, R. W. Stusrud, R. A. MacKay, D. L. Anton, T. Khan, R. D. Kissinger, and D. L. Klarstrom, eds., TMS, Warrendale, PA, pp. 785–794.

[7] Strangman, T. E., 1992, "Thermo-Mechanical Fatigue Life Model for Coated Superalloy Turbine Components," *Superalloys 1992*, S. D. Antolovich, R. W. Stusrud, R. A. MacKay, D. L. Anton, T. Khan, R. D. Kissinger, and D. L. Klarstrom, eds., TMS, Warrendale, PA, pp. 795–804.

A Study in the Process Modeling of the Startup of Fuel Cell/Gas Turbine Hybrid Systems

Michael Shelton
Jacobs Engineering Group,
Houston, TX 77072

Ismail Celik
West Virginia University,
Morgantown, WV 26505

Eric Liese

David Tucker

National Energy Technology Laboratory,
U.S. Department of Energy,
Morgantown, WV 26507-0880

As energy demands increase and the associated costs increase with that demand, newer energy alternatives are becoming more important to society. Although not new, fuel cell technology is taking a lead role in the quest for a cleaner and competitive power generation system. High efficiencies on the order of 50% are now possible with stand-alone fuel cells. When coupled with a gas turbine, efficiencies of around 70% may be expected. However, the fuel cell/gas turbine hybrid has inherent problems of stability and unpredictable response to adverse transients that first must be addressed to make this technology viable. The National Energy Technology Laboratories (NETL) in Morgantown is involved in the development of such hybrid technology. This study details a process modeling approach based on a commercial modeling package, and is associated specifically with the NETL Hybrid Performance (HYPER) research effort. Simulation versus experimental test data are presented to validate the process model during the cold flow startup phase. The results provide insight into the transients of the system built at NETL. [DOI: 10.1115/1.2830551]

Introduction

With expanding world energy needs and global environmental concerns, interest is growing in new energy sources and associated research. Most of the world's energy needs are provided by turbine-based technologies. Significant research has been directed at improving the electrical efficiencies of these smaller (under 10 MW), turbine-based systems with success currently limited to about 25–30% maximum. Fuel cell technology offers promises for significantly higher efficiencies (around 50%). The following are some of the issues limiting successful implementation of fuel cell technology:

- high temperatures normally associated with solid oxide fuel cells
- cathode poisoning
- load following and shedding

Higher technology material and engineering developments have now brought renewed interest in the commercialization of fuel cell technology and resolution of these problems.

Furthering the interest in fuel cells is the possible development of a hybrid fuel cell/turbine system that exploits the benefits of both the gas turbine and fuel cell systems. With water, CO_2, and heat being the only by-products, hybrids provide environmental incentives as well. The high efficiency and the environmentally friendly emissions make the fuel cell/turbine technology extremely attractive. The National Energy Technology Laboratories (NETL) of the Department of Energy has implemented a research program to accelerate commercialization of fuel cell/turbine technology. Foremost, this research seeks not only steady state qualification of hybrid system performance but goes one step further by seeking to develop an advanced control system for management of actual load shedding and the resultant transients. Such transients, unmanaged, are known to be detrimental to both the fuel cell and turbine.

The high cost of fuel cell damage and maintenance requires simulation in place of the physical fuel cell. The simulation is achieved through the construction of a process simulation model. PROTRAX™, a commercial dynamic process modeling system, was used to construct this initial simulation model. Concurrently, NETL has designed and built a physical test facility consisting of a turbine, compressor, combustor, and air plenum. This system (described in detail herein) represents a fuel cell with a combustor used to simulate the fuel cell. The combustor allows system simulation without the potential damaging of the fuel cell. Ongoing NETL-directed research aims to provide a modeling and testing research base. Therein, the dynamic model is to be used jointly with the test facility to

1. quantify and describe actual test data
2. identify test anomalies
3. provide for test procedures and system modifications

Overview

As stated previously, stand-alone fuel cells have been produced to operate at about a 50% efficiency. In a combined fuel cell/turbine, the turbine provides the solid oxide fuel cell (SOFC) with a preheated inlet flow. The effluent heat from the cell can then be used as heat back to the turbine. Cunnel et al. indicate that efficiencies of 70% can be expected from these hybrid systems with negligible NO_x and SO_x formation [1]. Although desulfurizer may be needed in the fuel pretreatment system, which would increase the cost, the reduction of these emissions in other industries comes at high expense and, often, at loss of thermal efficiency. Recent legislation requires that SO_x must be reduced by 60% and NO_x by 40% by 2010. According to Ormerod, carbon dioxide remains a serious concern due to the "greenhouse effect." The United Kingdom has required a reduction of CO_2 emission by 8% by 2010. Apparently, the answers lie in a low-temperature combustion (to reduce NO_x), and a very efficient power source (to reduce CO_2) operating on a low sulfur fuel (to reduce SO_x). Current technology cannot provide such a system [2].

Specifically, hybrid systems favor fuel cell/gas turbine configurations due to both the economy of scale (65% versus 25% for 300 kW systems) and the portability of these systems. Local power generation is especially attractive to remote areas and congested areas where current grid expansion may be impossible, or at best is uneconomical. Additionally, small, localized power sys-

Manuscript received October 28, 2005; final manuscript received September 21, 2007; published online September 10, 2009. Review conducted by Dilip R. Ballal.

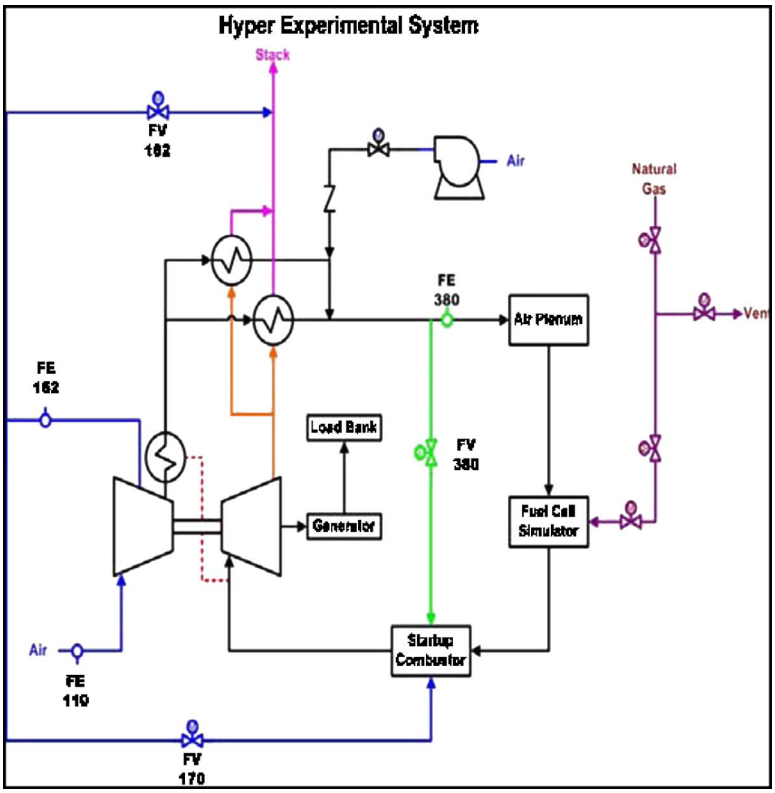

Fig. 1 HYPER process flow diagram (PFD)

tems may be less environmentally intrusive where sensitive large scale construction issues preclude needed power expansion activity.

Massardo et al. describe the problems and advantages of the smaller gas turbine-based hybrids. Loss of efficiencies is often due to smaller blade heights, Reynolds number effects, tip clearance effects, manufacturing tolerances, and surface finishes. These all combine to lower the efficiencies of the gas turbine. Such gas turbines, even when using heat recuperation, have difficulty achieving efficiencies greater than 30%. Although the President's Committee of Advisors on Science and Technology has suggested that R&D be undertaken to achieve a gas turbine efficiency of 50% by 2010, this may be overly ambitious. The achievement of higher gas turbine efficiencies may be dependent mostly on materials. Many scientists feel that hybrid fuel cell/gas turbine technology offers a much greater promise for higher efficiencies through gas turbine technology [3].

Several areas of mismatch that might be expected when a gas turbine is coupled with a SOFC are as follows:

1. the higher mass flow through the turbine increase system losses through the cell and ducts, resulting in a lower turbine inlet pressure and resultant reduced efficiency
2. the possibility of vapor-laden SOFC effluent adversely affecting the turbine performance
3. pressure and temperature transients from the turbine side associated with load shedding may also adversely impact the SOFC
4. compressor surge and stall dynamics

The NETL HYPER fuel cell/gas turbine hybrid system is designed to characterize these and other concerns.

NETL Fuel Cell/Gas Turbine System

The primary concern for starting a fuel cell/turbine system is the avoidance of compressor stall and surge. These surges can cause unfavorable pressure transients within the system and are a direct threat to the fuel cell [4,5]. Therefore, modeling of the startup condition is important to the study of a fuel cell/turbine hybrid system operability. Simulation of gas turbine startup has been shown to be useful in understanding the dynamics of turbomachinery operation [3].

Figures 1 and 2 show the process and flow diagram and the equipment/piping layout of the NETL fuel cell/turbine test facility. Black, in Fig. 1, shows the scope of modeling for this test. This testing facility is now complete and is located at the National Energy Technology Laboratories in Morgantown, WV. The test

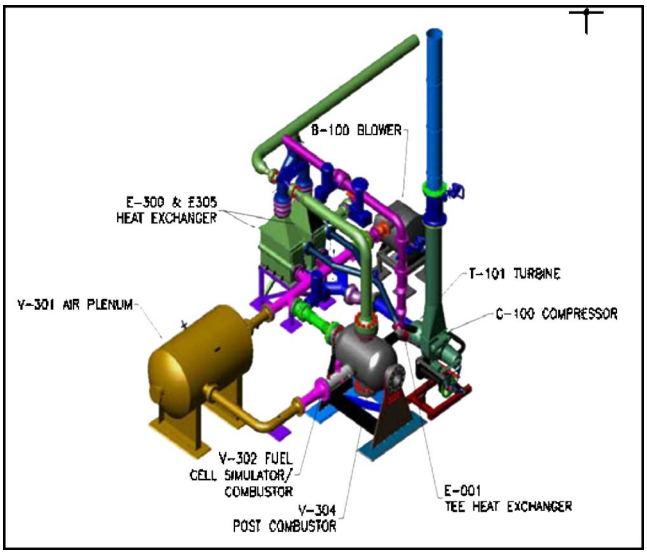

Fig. 2 The NETL HYPER model

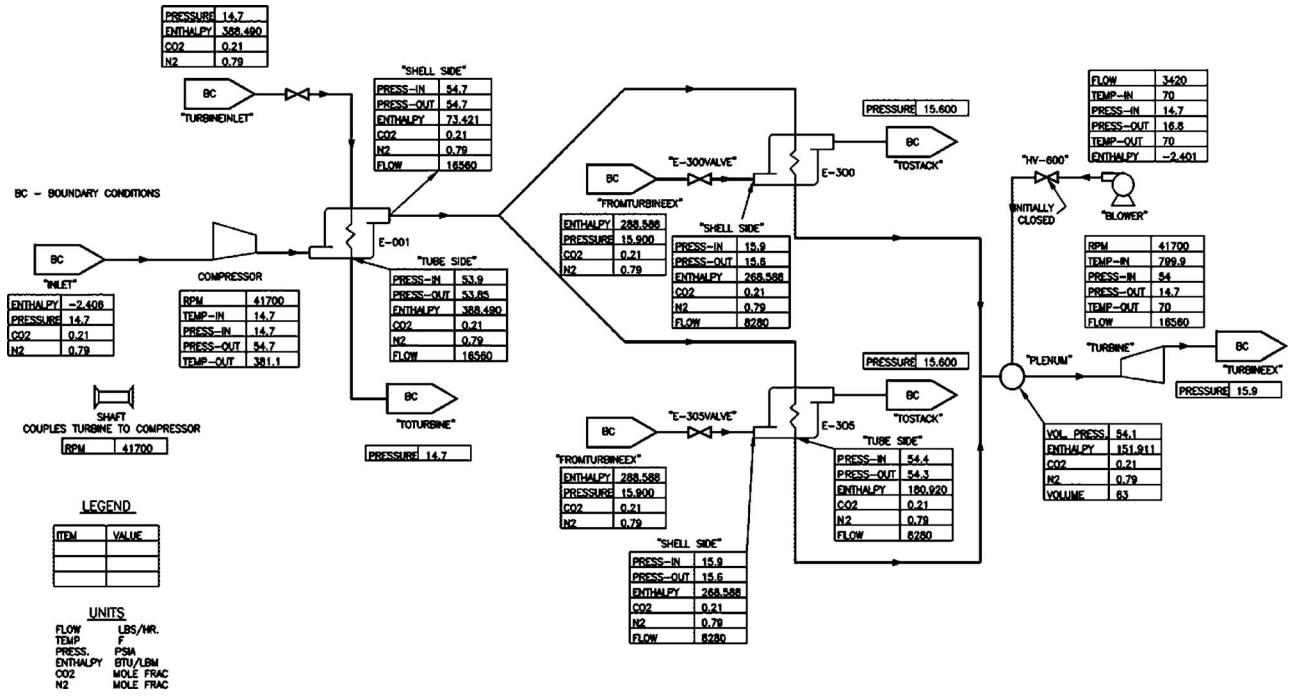

Fig. 3 PROTRAX **model process flow diagram (PFD) with initial process values**

facility is similar in size and scope to the dynamic hybrid system study conducted by Campanari [6]. Additional steady state studies of a similar fuel gas/turbine facility were completed by Rao and Samuelsen [7]. Magistri et al. discuss hybrids in general and point to the importance of the fuel cell model in the simulation [8]. However, neither of the above works specifically address startup issues.

Tucker in his HYPER test plan describes the system at the component level [9]. Due to the high cost of fuel cell repair/replacement, the NETL fuel cell/turbine hybrid system is designed to simulate an actual fuel cell without the actual fuel cell in place. This is done using a real-time model-controlled, natural gas-fired turbine/combustor. Additionally, extra system volume is added via two pressure vessels, the air plenum (V-301) and the high-temperature postcombustor (V-304). Insufficient capacity of the auxiliary power unit (APU) start motor required the use of an auxiliary blower, B-100. This blower is used only during startup. Serving direct heat recuperation are three heat exchangers, E-001, E-300, and E-305. E-001 is located in the turbine shell and consists of a one-pass, combustor (cold side) and turbine inlet (hot side) type arrangement. Two tandem, solar turbine, one-pass, primary surface heat exchangers service the compressor outlet (cold side). High-temperature (1130 F, 883 K) turbine exhaust flows to the hot side of these heat exchangers. The heat exchanger outlets service the air plenum (V-301). The air plenum serves as one of the two volumes added to the system to replicate the missing fuel cell volume and flow impedance. From the air plenum, flow enters the combustor (V-302). The combustor simulates both the fuel cell thermal and chemical behaviors. Specially designed combustor internals assure even and continued flame distribution into the postcombustor (V-304), which again serves as a postcombustion plenum volume of a fuel cell to the turbine inlet. A 120 kW Garret APU serves as the turbine/compressor. The turbine is a 400 Hz synchronous machine. A resistor bank (E-105) provides both adjustable loading and turbine isolation during periods when the turbine speed is floating without overload impacts [9].

Bleeding flow through the bleed air valve (FV-162) provides both additional loading to the turbine and turbine speed control. FV-380 allows steady flow adjustment to the fuel cell simulator during bleeding operations [9].

The cold flow bypass (FV-170) simulates sudden decreases in turbine inlet temperatures while assuring constant turbine inlet mass flow. The cold air bypass reduces turbine inlet temperatures by bypassing the heat exchangers and fuel cell simulator [9].

An advanced control system (beyond the scope of this paper) manages the process of simulating a fuel cell/turbine operation. Research based on this facility is identifying high-temperature pressure transients and forming the basis for additional/modified system control.

In July, 2003 a "cold" system test was performed where the blower provided energy for initial testing of the system. Both the bleed air and the cold flow bypass systems were not commissioned for the test. The following sequences were followed for cold commissioning of the system:

1. blower initiation
2. turbine ramp-up
3. take readings
4. system shutdown [9]

The cold flow process constitutes the basis for the model constructed for this present work and the actual data taken are compared against this model for model validation. After model validation, further model development will continue to provide process simulation for the fully operational HYPER fuel cell/turbine test facility.

Dynamic Model

PROTRAX™ has long been an industry leading process simulator software and was chosen by NETL as one of the simulation tools to be used for the HYPER project. The steps taken to develop the simulation were as follows:

1. design the overall process and issue a process flow diagram (see Fig. 3).
2. generate a more detailed process and instrumentation diagram
3. initiate final design and process simulator model development concurrently

Table 1 Major PROTRAX system variables

Process	Physical	Equipment	System
Turbine inlet temperature	Heat exchanger characterization	Turbine/compressor matching	Mass flow rate
Turbine outlet temperature	Model selection (high pressure air/gas, low pressure air/gas)	Turbine/compressor inertia determination	System initial pressure (compressor discharge)
Nodal pressures-heat exchangers	Selection of nodal types, net nodes	Absence of the postcombustor volume	Elimination of adverse pressure transients
Initial heat into the system	Mass balancing	Turbine component definition	Description of heat influx to system
Plenum characterization	Energy balancing	Blower component characterization	Valve balancing

4. utilize the test facility in two phases: (a) cold flow startup and initial testing, and (b) final "hot" operational facility fabrication
5. test process models using data from the cold flow test
6. after cold flow test validation, continue process model development for the final operational system
7. continue to utilize the process model for data definition and test criteria development.

The model, developed in association with the above requirements, is built from PROTRAX™-supplied modeling components. Table 1 shows some of the more important modeling variables. These model components are supplied with user input initial process conditions at the component level. Once components are connected to form the HYPER system, model simulation adjusts itself and any or all process component initial configurations to provide a final steady state process. This final, steady state operation process then allows for process modeling by supporting real-time process variable manipulation. In essence, the process model can be virtually operated by opening/closing valves, changing turbine speeds, and decreasing temperature, enthalpy, pressure, and a myriad of associated variables critical to the operation of the facility. The simulator balances the remainder of the process to accommodate for user-induced system changes. Similar changes to the actual test facility process variables can then be made and the system results compared to modeling results for interpretation.

The HYPER model was built initially for the cold flow test and modeling results included herein. Several small differences between the model and actual facility configurations include the following.

- All additional system volume is represented as one plenum volume instead of both the air plenum and the postcombustor as in the actual facility.
- No "cold flow bypass" or "bleed air" systems are modeled as they were not considered part of the cold flow test.
- No combustor component is included.
- The inlet to the heat exchangers E-300 and E-305 was connected to PROTRAX™ model boundary conditions and not to the turbine exhaust.

With previous modeling data and information on the turbine, the cold flow model was built with initial conditions at expected hot conditions. Since the model has no combustor, initial heat influx was achieved from the PROTRAX™ boundary condition components linked to the inlet of the heat exchangers. This configuration provided a steady heat energy source modeled after the actual turbine exhaust stream.

For model operation, valves on this steady state heat source were closed at startup and the system allowed to come to ambient conditions. At this point, during the simulation, the blower was turned on to simulate the actual cold flow test.

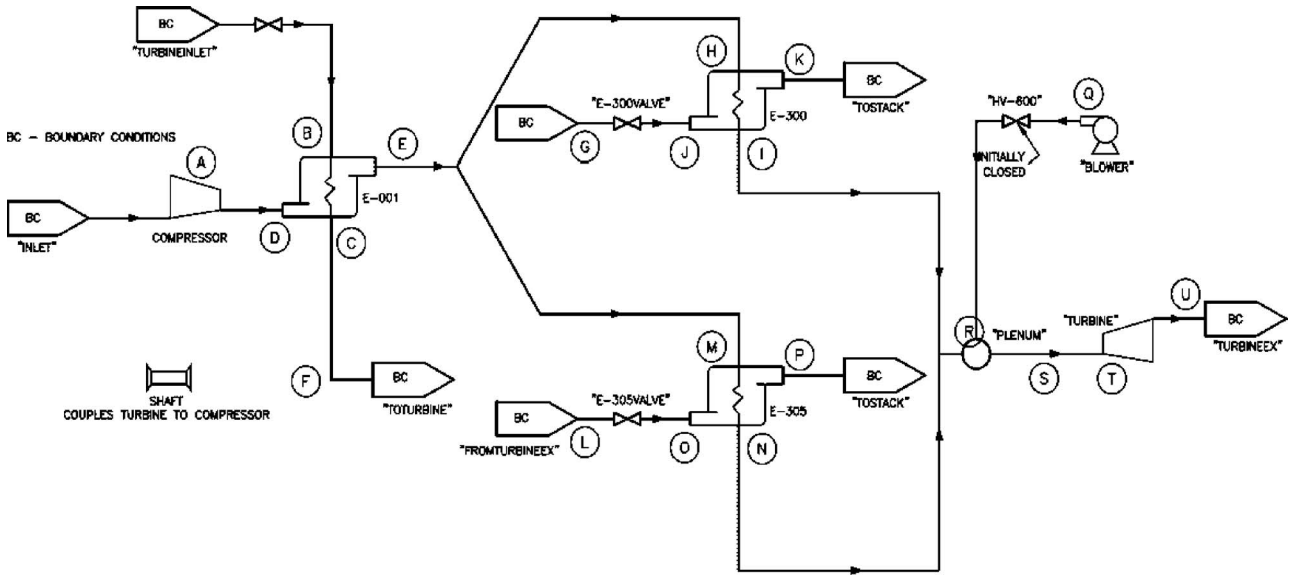

Fig. 4 PROTRAX model process flow diagram (PFD) with process node identifiers

Table 2 Node data at 150 s

Point	Mass flow	Enthalpy	Temperature
D	1707 (774)	0.69 (1.6)	82.2 (301)
E	1707 (774)	0.76 (1.77)	82.2 (301)
H	853 (387)	0.76 (1.77)	83.2 (302)
I	853 (387)	9.46 (22.0)	119.3 (322)
M	853 (387)	0.76 (1.77)	83.2 (302)
N	853 (387)	9.46 (22.0)	119.3 (322)
Q	1430 (649)	12.61 (29.3)	132.2 (329)
R	1707 (774)	9.49 (22.1)	119.8 (322)
S	3135 (1422)	11.47 (26.7)	127.6 (326)
T	3135 (1422)	11.47 (26.7)	127.6 (326)
U	3135 (1422)	9.76 (22.7)	120.6 (322)

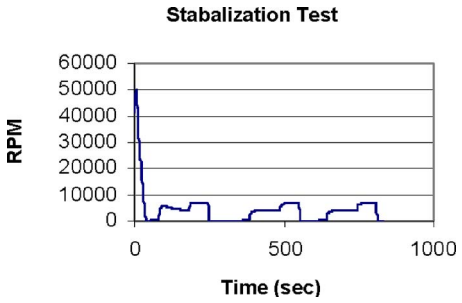

Fig. 5 Three subsequent process runs to allow system cooling

The process flow diagram for the PROTRAX™ cold flow model is shown in Fig. 3. Also included in these figures are the initial conditions for each model component. Figure 4 is the process node identifier map. This map provides alphanumeric point identification for attaching simulation results to associated nodes.

Model Mass and Energy Balance

Two stabilized data points at different locations in the model were chosen to determine the system mass and energy balance. Points at 150 s and at 250 s were chosen due to the apparent stabilized condition of the model at those times for the two blower valve discharge positions. Tables 2 and 3 provide data values at these times. The units used in the table are temperature, F (K); enthalpy, BTU/lb (kJ/kg), and mass flow, lb/h (kg/h).

Since mass enters the system only at the compressor and blower discharge, and leaves via the turbine discharge, the mass balance is simply the sum of the discharges minus the turbine discharge. Using SI units, the data at 150 s,

$$\text{Mass } D + \text{Mass } Q = \text{Mass } U \tag{1}$$

$$774 + 649 \approx 1422 \tag{2}$$

$$1423 \approx 1422 \tag{3}$$

and for data at 250 s,

$$\text{Mass } D + \text{Mass } Q = \text{Mass } U \tag{4}$$

$$1208 + 880 \approx 2092 \tag{5}$$

$$2088 \approx 2092 \tag{6}$$

However, for an energy balance, the residual heat in the heat exchangers, especially at time 150 s, becomes a source of heat as well as the discharges noted in the mass transfer calculation. Hence, the overall heat balance is given by

$$QD \times HD + QD \times (HE - HD) + QH \times (HI - HH) + QM \times (HN - HM) + QQ \times HQ + QT \times (HT - HU) = HU \times QU \tag{7}$$

In SI units, the data at 150 s give

$$774 \times 1.77 + 774 \times (1.77 - 1.6) + 387 \times (22 - 1.7) + 387 \times (22 - 1.7) + 649 \times 29.3 + 1422 \times (22.7 - 26.7) = 1422 \times 22.7 \tag{8}$$

$$31{,}240 \neq 32{,}282 \tag{9}$$

$$\Delta Q = 1042 \text{ kJ} \tag{10}$$

For data at 250 s,

$$1208 \times 7.3 + 1208 \times (7.3 - 7.3) + 602 \times (3.9 - 7.3) + 602 \times (3.9 - 7.3) + 880 \times (21.7) + 2091 \times (4 - 11.4) = 2091 \times (4.0) \tag{11}$$

$$8221 \neq 8271 \tag{12}$$

$$\Delta Q = 48.5 \text{ kJ} \tag{13}$$

The differences in the energy balance at the two time nodes (1042 kJ versus 48.5 kJ) can be explained by the initial condition of the plenum temperature. At 150 s, the plenum has not cooled down from an initial high temperature and hence, heat is being added to the system. This is obvious when one considers the 250 s time event balance. The energy balance deficit is much less at this time as the system has equilibrated and no real heat sources remain. This initial temperature condition is a result of having to start the turbine model at its 100% speed condition and ramp down to 0% speed due to numerical reasons (as seen in Fig. 5). Therefore, the system was run through two cycles of the test procedure in order to better represent actual test conditions. Figure 5 shows this repeated test process. All data presented are from the second test run.

Table 3 Node data at 250 s

Point	Mass flow	Enthalpy	Temperature
D	2663 (1208)	3.15 (7.3)	93.1 (307)
E	2663 (1208)	3.15 (7.3)	93.1 (307)
H	1328 (602)	3.15 (7.3)	93.1 (307)
I	1328 (602)	1.68 (3.9)	87.6 (304)
M	1328 (602)	3.15 (7.3)	93.1 (307)
N	1328 (602)	1.68 (3.9)	87.6 (307)
Q	1941 (880)	9.33 (21.7)	118.8 (321)
R	1328 (602)	1.68 (3.9)	87.7 (307)
S	4611 (2091)	4.91 (11.4)	100.8 (311)
T	4611 (2091)	4.91 (11.4)	100.8 (311)
U	4611 (2091)	1.70 (4.0)	87.7 (307)

Results and Discussion

Figure 5 shows the three consecutive runs. Figure 6 shows blower discharge valve positions. The runs are required to eliminate the residual heat effects from the model startup. The residual heat effects are evident in the first run, but are absent in the second run. Subsequent data presentations are from the second run. The second and third runs are virtually identical indicating that the system has cooled sufficiently.

Figures 7–18 provide both the test data and simulated data. The simulation modeled as closely as possible actual test conditions. The three test runs presented were initiated with the blower discharge valve closed. The blower discharge valve is the only

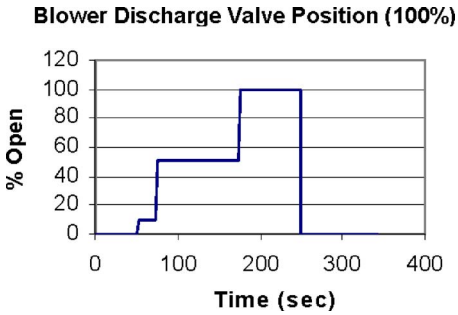

Fig. 6 Blower discharge position

method of process adjustment for both the model and the actual test run. The blower valve adjustments are apparent as spikes in the data.

The general test procedure is as follows:

(1) initiate start of test with blower on and blower discharge valve closed
(2) after about 50 s, open blower discharge valve approximately 10%
(3) run for another 25 s. Open the blower discharge valve 50% full open
(4) allow system to run and stabilize at this configuration for about 100 s
(5) open blower discharge valve to the full-opened position
(6) run for about 75 s and then shutoff
(7) repeat Steps (1)–(6)

In general, there is qualitative comparison agreement between the actual and the simulated test results. The time constants, however, vary from process model and actual data. The physical system responds slower than does the process simulation. Several

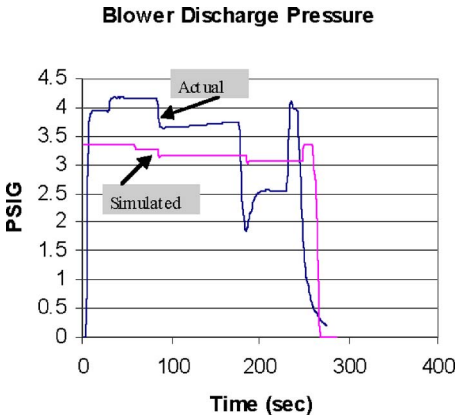

Fig. 7 Actual versus simulated blower discharge pressure

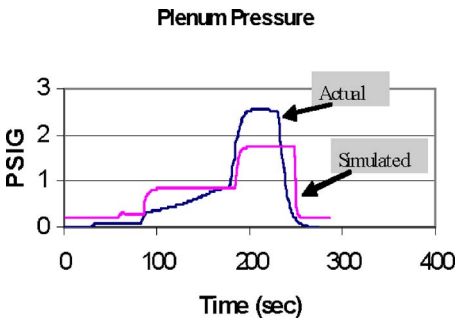

Fig. 8 Actual versus simulated plenum pressure

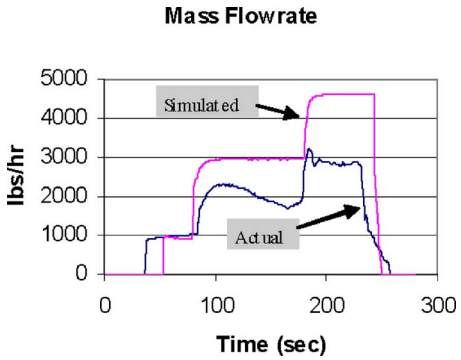

Fig. 9 Actual versus simulated mass flow rate

factors may account for this: (1) a slower blower discharge valve opening (the model is instantaneous), (2) gradual heat generation by the blower in the physical system not present in the model, and (3) heat loss in the actual heat exchangers not present in the simulated run. (The heat exchangers were blocked in on the tube side in the model.)

The blower discharge pressure, shown in Fig. 7, trended very well with parameter magnitude and direction tracking, but still shows a different time constant. One would expect a higher blower discharge pressure at lower turbine speeds, as the blower, in this configuration, would be supplying the majority of the mass flow rate to the model. As the turbine speed is increased, the blower discharge pressure drops as the compressor begins to supply the mass flow to the system.

The plenum pressure, shown in Fig. 8, shows close agreement as the actual data. The increase in plenum pressure at each increase in flow is also expected. An increased mass flow will cause an increase in turbine inlet pressure. This pressure and the plenum pressure trends are nearly identical.

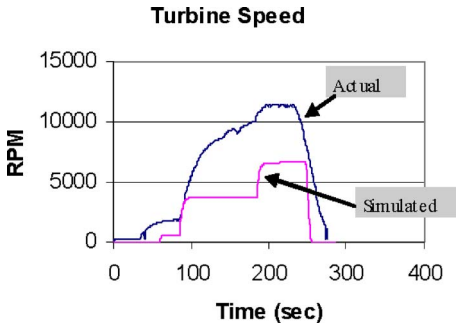

Fig. 10 Actual versus simulated turbine speed

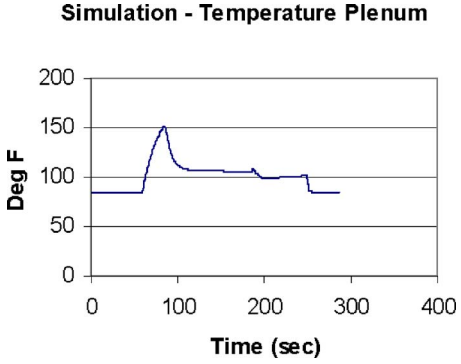

Fig. 11 Simulated plenum temperature

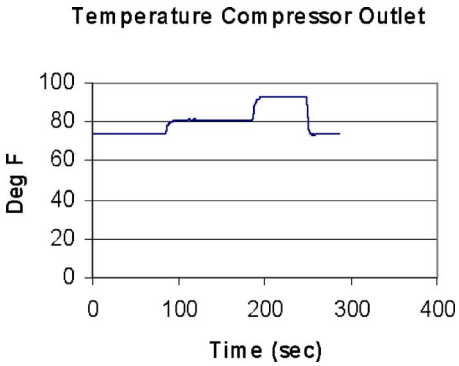

Fig. 12 Simulated compressor outlet temperature

Perhaps, the most important trend is evident in Fig. 9, depicting system mass flow rate. Although the model predicts significantly more mass flow (most probably due to the differing simulator turbine map and the actual turbine map), the trends in similarities and experiments are almost identical in magnitude and duration. Especially relevant is the simulated increase in mass flow rate at every blower discharge valve event. This transient is most likely due to the increased compressor contribution to mass flow and the subsequent reduced flow adjustment required of the blower. In each case, the blower mass flow increases and then falls, indicating a "balancing effect" between the compressor and blower. The model shows a constant process and the adjustment occurs much more quickly than the actual process.

Figure 10 provides the transients of turbine speed. Although the trend in similarities follow that in experiments, the magnitude of the model is significantly lower than the actual speed. The likely cause of this discrepancy is the PROTRAX™ "as-supplied" turbine map. Corrections to the model turbomachinery maps could bring both the turbine speed and system mass flow trends into close correlation. In particular, more consideration needs to be given to the low speed area of the maps. Additionally included are Figs. 11–13 showing temperature of the plenum, blower, and compressor outlets. Although not included in the actual test data, these figures are provided for additional information of the simulation process.

To investigate the impacts of the excessive mass, an additional run was made matching the modeled mass flow rate with that observed in the actual test run. Figures 14–18 show the results of this run. Data again point out that the difference between observed data and simulated data can best be attributed to the turbine and compressor maps used in the simulation.

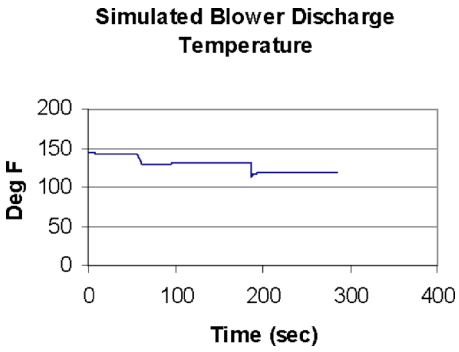

Fig. 13 Simulated temperature blower outlet

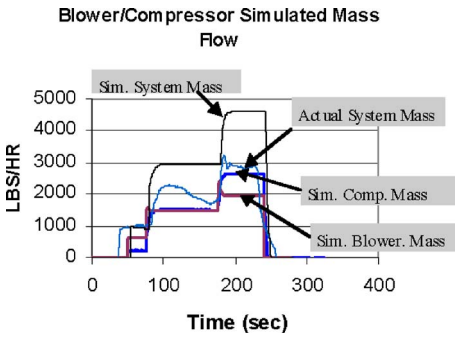

Fig. 14 Blower/compressor and system simulated mass flow

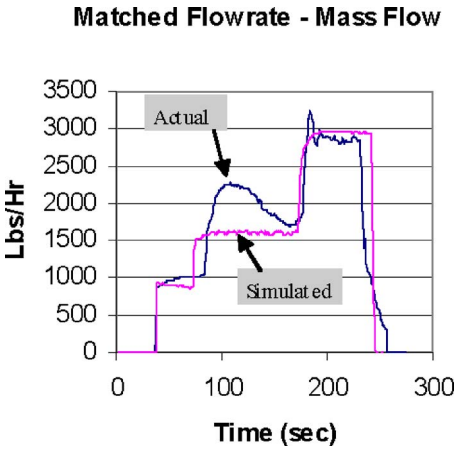

Fig. 15 Matched flow rate—mass flow

Summary and Conclusions

The union of a gas turbine and a SOFC will offer significant challenges. The NETL HYPER test facility is fabricated to inves-

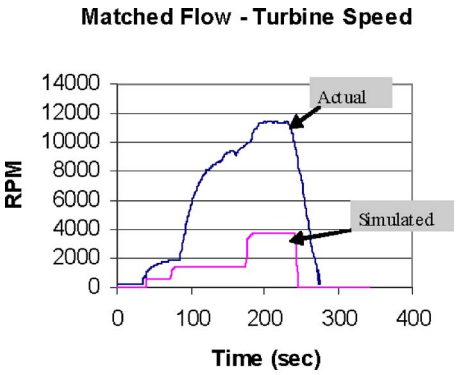

Fig. 16 Matched flow rate—turbine speed

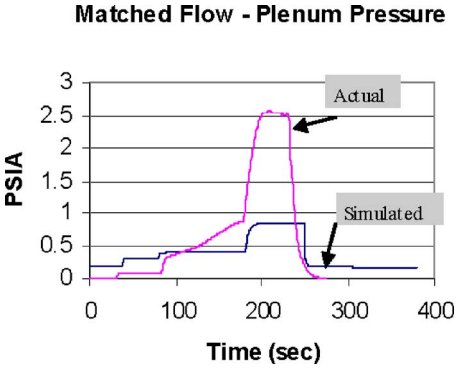

Fig. 17 Matched flow—plenum pressure

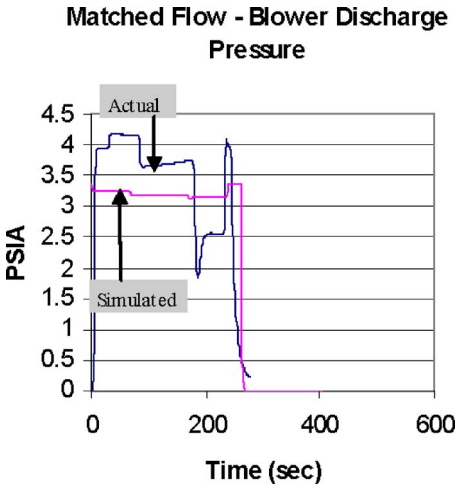

Fig. 18 Matched flow—blower discharge pressure

tigate dynamic issues. The dynamic model developed has shown significant trend correlations with initial, actual test data. Differences in actual and simulated data magnitudes are likely due to differences in the PROTRAX™ turbomachinery component maps and the actual map for the gas turbine used in the cold run. Three recommendations follow:

1. adjust the PROTRAX™ turbomachinery components map with a C++ subroutine to more closely reflect the test data, particularly the low speed area of these maps
2. connect E-300 and E-305 hot side inlets to the turbine exhaust to match the test facility and use the model for high-temperature process modeling
3. develop additional capability to start the model from ambient conditions and be able to simulate both startup and shutdown

References

[1] Cunnel, C., Pangalis, M. G., and Martinez-Botas, R. F., 2001, "Integration of Solid Oxide Fuel Cells Into Gas Turbine Power Generation Cycles, Part 2: Thermodynamic Modeling," Proc. Inst. Mech. Eng., Part A, **216**, pp. 145–154.
[2] Ormerod, M. R., 2002, "Solid Oxide Fuel Cells," Chem. Soc. Rev., **32**, pp. 17–18.
[3] Massardo, A. F., McDonald, C. F., and Korakianitis, T., 2002, "Microturbine/Fuel Cell Coupling for High-Efficiency Electrical Power Generation," ASME J. Eng. Gas Turbines Power, **124**, pp. 110–116.
[4] Edmons, H. W., Pearson, C. E., and Grant, H. P., 1955, "Compressor Surge and Stall Propagation," Trans. ASME, **77**, pp. 455–469.
[5] Shepherd, D. G., 1956, *Principles of Turbomachinery*, Macmillan, New York.
[6] Campanari, S., 2000, "Full Load and Part-Load Performance Prediction for Integrated SOFC and Microturbine Systems," ASME J. Eng. Gas Turbines Power, **122**, pp. 239–246.
[7] Rao, A. D., and Samuelsen, G. S., 2001, "A Thermodynamic Analysis of Tubular SOFC Based Hybrid Systems," *Proceedings of ASME Turbo Expo 2001*, pp. 1–12.
[8] Magistri, L., Bozzolo, M., Olivier, T., Agnew, G., and Massardo, A. F., 2003, "Design and Off-Design Analysis of a MW Hybrid System Based on Rolls-Royce Integrated Planar SOFC," *Proceedings of ASME Turbo Expo 2003*, pp. 1–8.
[9] Tucker, D., 2003, Department of Energy NETL HYPER Test Plan, Oct.

Fuel Cell/Gas Turbine Hybrid System Control for Daily Load Profile and Ambient Condition Variation

Rory A. Roberts

Jack Brouwer

G. Scott Samuelsen
e-mail: gss@uci.edu

National Fuel Cell Research Center,
University of California,
Irvine, CA 92697

Fuel Cell/Gas Turbine (FC/GT) hybrid technology is promising, but introduces challenges in system operation and control. For base-load applications, changes in ambient conditions perturb the system and it becomes difficult to maintain constant power production by the FC/GT system. If the FC/GT hybrid system is load-following, then the problem becomes even more complex. In the current study, a dynamic model of a FC/GT power plant is developed with system controls. Two cases are evaluated: (1) system controls are developed to maintain constant power and process control within acceptable constraints and (2) the FC/GT power plant is set in power following mode connected in parallel to the grid for a daily load profile scenario. Changing ambient conditions are employed in the dynamic analysis for both cases. With appropriate attention to design of the system itself and the control logic, the challenges for dynamic system operation and control can be addressed. [DOI: 10.1115/1.2833489]

Keywords: fuel cell, gas turbine, hybrid, controls, dynamic simulation, base-load

Introduction

Hybrid cycles comprised of high temperature fuel cells, such as molten carbonate fuel cells (MCFCs) or solid oxide fuel cells (SOFCs), will likely be the preferred method for generating electric power in the future, initially at the small to medium scale (250 kW to 20 MW), and later in large scale central plants (>100 MW). However, hybrid FC/GT systems are in need of significant advancement before they are introduced as commercial products. Some progress is needed to address the specific challenges that are introduced by coupling a fuel cell with a gas turbine given their disparate dynamic response characteristics.

Several entities around the world have developed steady state simulation capabilities for FC/GT systems. These include efforts of the Georgia Institute of Technology [1], the University of Genova [2–4], NFCRC [5–7], and others. Dynamic FC/GT simulation capabilities are less common, but are increasingly being developed as the demand for dynamic understanding and control development grows. Examples of previous dynamic simulation efforts include the work of University of Genova, National Energy Technology Laboratory (NETL) [7–9], FuelCell Energy [10–12], and the National Fuel Cell Research Center (NFCRC) [13–18].

Hybrid systems are sensitive to ambient conditions due the sensitivity of compressors to air density. At higher temperatures the air becomes less dense requiring a compressor to do more work to pressurize and move the air through the system. As for a hybrid system, it is challenging to maintain sufficient compressor mass flow for extreme conditions since the fuel cell is operated at a fixed temperature. If the gas turbine operates at a fixed speed, there are no options for controlling the mass flow. The total power output of the system may have to be sacrificed in order to maintain appropriate fuel cell operating temperature by lowering the load demand on the fuel cell.

Manuscript received June 16, 2006; final manuscript received September 21, 2007; published online October 1, 2009. Review conducted by Dilip R. Ballal. Paper presented at the ASME Turbo Expo 2006 Power for Land, Sea, & Air, Barcelona, Spain, May 8–11, 2006, Paper No. GT2006-90741.

Background

NFCRC has developed dynamic modeling tools for FC/GT hybrid systems. In previous work [16–18], transient performance and controls analyses of atmospheric hybrid systems with MCFCs were presented. Load perturbations were implemented to analyze the MCFC/GT hybrid response. In these investigations it was discovered that additional control loops are necessary to control the MCFC operating temperature. For example, varying fuel utilization across the MCFC provided some means for control but was limited. Variable speed operation of the gas turbine was tested and showed more promise, but still was limited in the particular system at lower power demands. For a larger turn-down in system power a bypass or auxiliary combustor is needed in parallel [14].

For part-load operation of a FC/GT hybrid, it has been shown that a variable speed gas turbine is a required feature for both pressurized [2] and atmospheric systems [15]. The variable speed gas turbine provides better control of the compressor mass flow.

In previous work, a system model was developed and compared to experimental data from the Siemens Power Corporation (SPC) SOFC/GT system [15]. A dual shaft turbine was used in SPC SOFC/GT system. The dual shaft turbine prevented the direct control of the compressor mass flow, which limited operational flexibility. The system had to be operated at the maximum power safely allowed.

In the current paper, a 1.15 MW pressurized SOFC/GT hybrid model is developed. A diagram of the system is presented in Fig. 1 and a schematic of the SOFC module is presented in Fig. 2. The system was designed around the Capstone C200 micro-turbine generator. Design parameters for the C200 [19] and the hybrid plant are presented in Table 1.

Dynamic Model. The components making up the dynamic model are the same as those presented in earlier work [14–17]. The electrochemical performance for the SOFC is based on the results presented by Kim et al. [20]. The following polarization equations are derived in terms of current density with units of current per area. This is to allow for a more straightforward comparison between fuel cells of various sizes. An anode supported planar SOFC is assumed in this study.

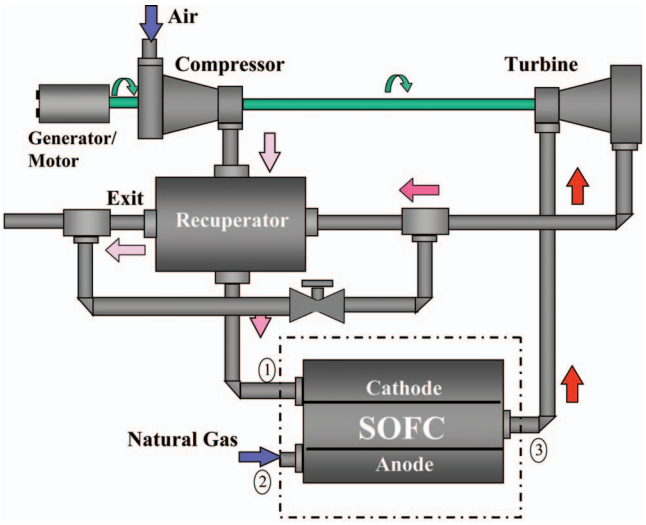

Fig. 1 Pressurized SOFC/GT hybrid cycle

In general, the most significant polarization (loss) inherent to high temperature fuel cells is cell resistance. At normal operating conditions, this is primarily due to low ionic and electronic conductivity of the high temperature materials associated with the electrolyte, anode and cathode, and interconnect conduction paths. Resistance can also be high if the cell is operating at a temperature below the optimum temperature due to the strong temperature dependence of electrolyte ionic resistivity. The loss in cell potential associated with resistance is given by Ohm's law:

$$\eta_R = iR_{\text{eff}} \tag{1}$$

Experimental data are available for measured values of resistances at various temperatures. The internal resistance is empirically fitted to the form of $\ln(R_{\text{eff}}/T)$ versus $1/T$.

Therefore,

$$\ln(R_{\text{eff}}/T) = 7509.6(1/T) - 25.855$$

$$R_{\text{eff}}(T) = T\exp(7509.6(1/T) - 25.855) \tag{2}$$

The electrochemistry provided by Kim et al. is for a single cell test. Therefore, for cell-to-stack performance, additional resistance is added to account for the resistance of interconnects, terminal blocks, and other electrical components of the stack. The amount of resistance between cells and stack connection was justified to be constant with temperature and added to achieve typical performances of SOFC stacks today [21].

Losses associated with sluggish kinetics due to low temperatures, poor availability of active electrocatalytic sites, triple-phase boundary kinetics, and/or solution and dissolution kinetics are modeled using a relationship for activation polarization. At reasonably high current densities typical of an operating cell, this polarization can be simulated by the simplified Tafel equation. The Tafel activation polarization equation can be reduced to Eq. (3). The Tafel equation is only valid for $i > i_0$. The operation range of the SOFC in this study is consistently above this limit. Therefore, applicability of the Tafel equation is an adequate assumption in this study:

$$\eta_A(i) = \frac{R_u T}{\alpha n F}\ln\left(\frac{i}{i_0}\right) \tag{3}$$

The transfer coefficient α is typically approximately 0.5 and accounts for the distribution of intermediate species at the triple-phase boundary, indicating whether these species more closely resemble reactants or products and may be quantified through experimental data. The exchange current density i_0 is dependent on temperature, pressure, and material properties. Assuming constant pressure operation Eqs. (4) and (5) provide i_0 and α, respectively, as a function of temperature [20]:

$$i_o = -0.37T^2 + 78.84T - 40{,}711 \tag{4}$$

$$\alpha = -5.73 \times 10^{-6}T^2 + 1.35 \times 10^{-2}T - 6.9 \tag{5}$$

Concentration polarization is associated with concentration gradients near the active cell surface and is dominated by the rate of diffusion of the gases through the porous electrodes as mentioned earlier. Equation (6) is the general equation used for modeling of the concentration loss in an anode supported fuel cell. The limiting current density is dependent on the partial pressures, temperatures, and the diffusivity of the electrode materials:

Table 1 Design parameters for the SOFC/GT system

Design Parameter	Value	Unit
System		
System Power	1150	kW
Combustor Efficiency	1	
Recuperator Effectiveness	1	
Heat Exchanger Effectiveness	0.4	
System Efficiency	0.73	
Gas Turbine		
Shaft Speed[a]	60,000	RPM
Turbine Inlet Temperature[a]	950	C
Turbine Efficiency	90.0%	
Mass Flow[a]	1.3	kg/sec
Compressor Inlet Temperature	15	C
Compressor Discharge Pressure[a]	435.7	kPa
Compressor Efficiency	75.0%	
Gas Turbine Power Mechanical Loss (Shaft)	$(\text{RPM}^2)8.33 \times 10^{-10}$	kW
Gas Turbine Power Electronics Efficiency	98% and 14 kW load	
Compressor Leakage	0.02	
Compressor Filter Loss	0.02	
SOFC Module		
SOFC Stack Power	960	kW
SOFC Active Area	320	m^2
Current Density	4000	A/m^2
SOFC Operating Voltage	0.75	V
SOFC Power Electronics	100.0%	
Anode Recirculation	80.0%	
SOFC Stack Fuel Utilization	85.0%	
SOFC Average Operating Temperature	900	C

[a]Willis, 2005

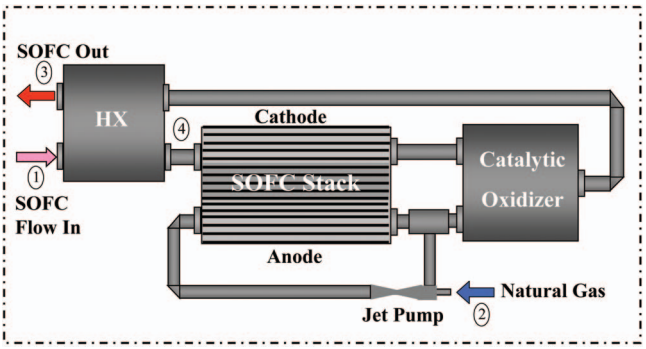

Fig. 2 SOFC module

$$\eta_C(i) = \frac{R_u T}{2F} \ln\left(1 - \frac{i}{i_{L(a)}}\right) - \frac{R_u T}{2F} \ln\left(1 + \frac{P^0_{H_2} i}{P^0_{H_2O} i_{L(a)}}\right) \quad (6)$$

i_L is the limiting current density and is the most important parameter in Eq. (6). The limiting current density is the current density at which fuel is being consumed at the same rate it is being supplied to the triple-phase boundary. This parameter is affected by the thickness and diffusivity of the electrodes. Therefore, the required partial pressure of hydrogen at the triple-phase boundary is zero when operating at the limiting current density. Using the governing binary diffusion equation in terms of partial pressures, the binary diffusion equation is simplified to Eq. (7) after setting the partial pressure of hydrogen equal to zero at the triple-phase boundary:

$$i_{L(a)} = \frac{2FP^0_{H_2} D_{\text{eff}(a)}}{R_u T d_a} \quad (7)$$

Assuming ideal gas behavior, kinetic theory with empirical data gives the following relationship for the effective diffusion coefficient $D_{\text{eff}(a)}$.

$$D_{\text{eff}(a)} = 1.37 \times 10^{-9} T^{-1.5} - 2.78 \times 10^{-5} \quad (8)$$

A similar set of equations governs cathode concentration polarization terms.

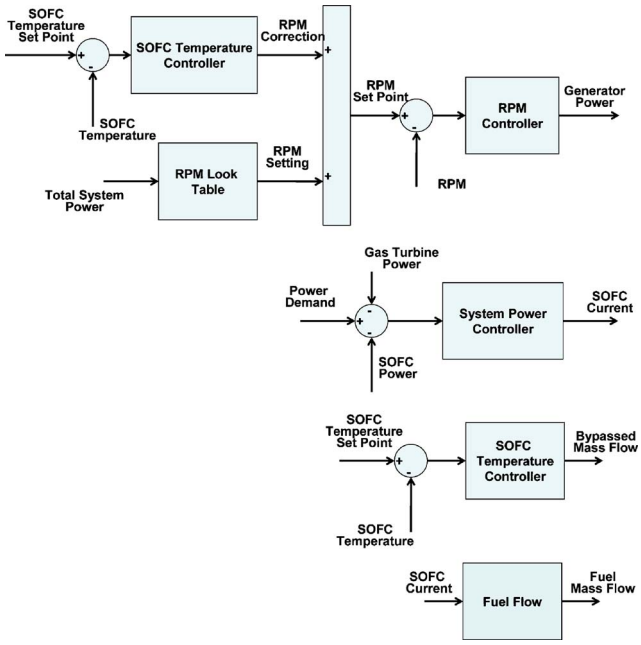

Fig. 3 Controller design

Approach

The work presented in this paper is on the controller design and dynamic analysis of a SOFC/GT hybrid system. Two different cases are presented: (1) a base-load system is exposed to changing ambient temperature and (2) a load-following system is exposed to the same ambient conditions while following a load demand curve.

The design electrical power production of the SOFC/GT hybrid system is 1.15 MW. For the base-load case, the system maintains 1.15 MW (1150 kW) of net electrical power production. The SOFC/GT hybrid system is operated in an extreme environment with a highly fluctuating ambient temperature. The ambient temperature is varied from −5°C to 30°C in a sinusoidal form to emulate the daily temperature fluctuation. This range of temperatures accounts for colder regions and hot regions where the system may be operated.

The system is tested in load-following mode with a varying load demand. The varying load is of low frequency and is essentially seen a based load operation that is slowly adjusted throughout the day. The system is subjected to the same daily ambient conditions in all cases, while meeting a sinusoidal demand of power from 1150 kW at the peak of the day to 950 kW at the minimum power production of the day.

In this study, the controllers are not tuned for optimal performance; rather, this paper focuses upon the architecture of the controller design.

Controller Design. A decentralized controller design is used to control the hybrid system. The objective of the system controllers is to maintain constant power production while maintaining the SOFC operating temperature close to its design operation temperature of 900°C. Figure 3 presents the controller design. The controller design consists of a gas turbine shaft speed controller, system power controller, SOFC average temperature and fuel flow controller. The shaft speed controller is a cascade controller with the outer loop consisting of a feed forward and a feedback controller for the RPM set point. The inner loop manipulates the gas turbine power to achieve the RPM set point provided by the outer loop. The feed forward aspect of the outer loop uses a look-up table to determine the RPM setting for a given system power. The feedback loop corrects the RPM setting for any SOFC average temperature deviations. The feedback portion is very important when the compressor is operating at an off design setting. For example, extreme ambient conditions would require RPM correction.

The system power controller manipulates the SOFC current in order to meet the power demand. The gas turbine power is treated as a disturbance for this particular controller. Therefore, the SOFC power is altered continuously by manipulating the current to meet the power demand that has not been met by the gas turbine.

There is additional control of the SOFC temperature via the bypass valve located between the turbine exhaust and the recuperator. The bypass, when used, lowers the inlet temperature to the SOFC module. The fuel flow is manipulated to achieve fuel utilization of 85%. The fuel flow controller is a feed forward controller based on the current of the SOFC. The fuel utilization after one pass through the anode section is approximately 53%.

The design electrical power production of the SOFC/GT hybrid system is 1.15 MW. For the base-load case the system maintains 1.15 MW (1150 kW) of net electrical power production. The SOFC/GT hybrid system is operated in an extreme environment with a vast fluctuating ambient temperature. The temperature changes account for colder or frigid regions and hot regions where the system may be operated.

The system is tested in load-following mode with a varying load demand. The same daily ambient conditions are applied to the system while demanding a sinusoidal power profile that varies from 1150 kW at the peak of the day to 950 kW at the minimum power production time of the day.

Results

Base-Load Case. The SOFC hybrid system is simulated in base-load mode. The system is to produce its design power while operating in varying ambient conditions. As stated before the ambient temperature is varied in the range of ±20°C. A sinusoidal temperature profile with a period of one day is used. The peak temperature is at 12 noon.

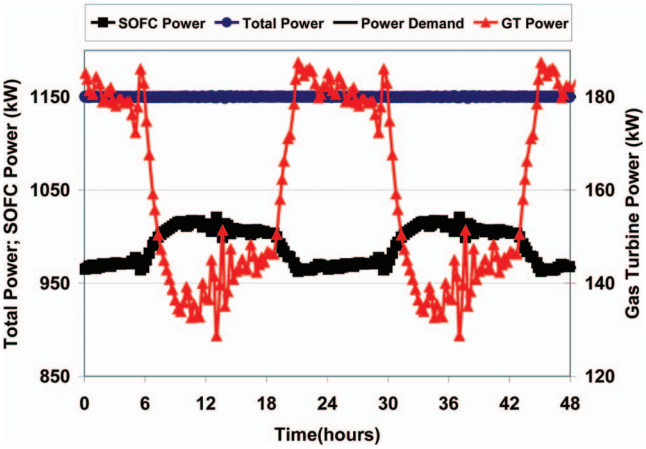

Fig. 4 Total power, SOFC power, and gas turbine power produced

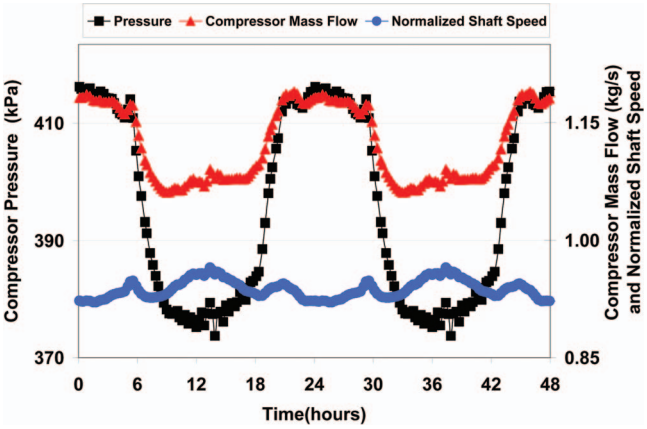

Fig. 6 Compressor mass flow, pressure, and normalized shaft speed

Figure 4 presents the total power produced by the hybrid plant along with the SOFC and the gas turbine power. The total power produced by the hybrid plant is constant with very small deviations. The gas turbine power changes dramatically to control the shaft speed. The SOFC power changes in order to compensate for the changes in the gas turbine power. Note that the simulations are computed using a much smaller time step than that presented by the symbols. Some details of the transient responses are lost so that a full two-day simulation can be presented. The simulation uses a variable time step solver with typical time step on the order of one second.

The SOFC average temperature is presented in Fig. 5 along with ambient temperature and percent bypass mass flow. The SOFC temperature is maintained within $\pm 20^{\circ}$C of the design operating temperature of 900°C. The effects of the ambient temperature are seen when plotted with the SOFC temperature. The high ambient temperature increases the compressor outlet temperature and also decreases the compressor mass flow by reducing the air density. The reduction of the compressor mass flow can be seen in Fig. 6. The dip in SOFC temperature just before 7 h is a result of the slight increase in mass flow from the compressor presented in Fig. 6 just before the mass flow sharply decreases. The mass flow from the compressor increases with the sudden increase of the shaft speed also presented in Fig. 6.

Two things promote this increase in shaft speed: (1) the ambient temperature is at the design inlet temperature of the compressor resulting in a more efficient compressor and (2) the TIT in Fig. 7 increases providing more power to the shaft. The gas turbine power increases in Fig. 1.

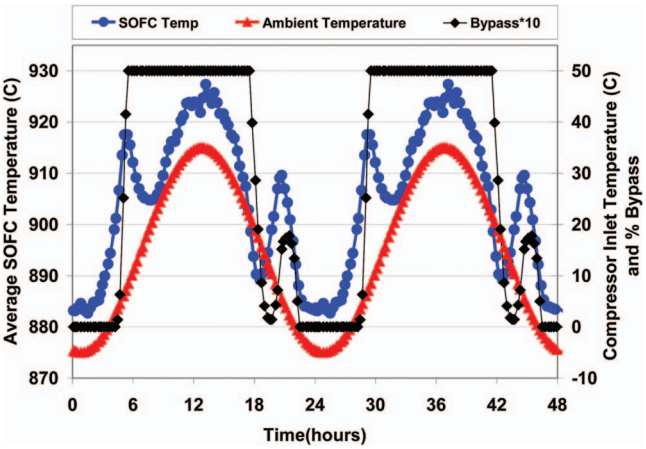

Fig. 5 SOFC average temperature, ambient temperature, and bypassed mass flow

It is shown in Fig. 4 that at 6 h it is possible to overcome this surge of net power being produced by the gas turbine. The TIT eventually lowers as the bypass valve opens and the ambient temperature continues to rise. This reduces the power produced by the turbine and thus increases the compressor work. The gas turbine power is dramatically decreased by the controllers at 7 h (Fig. 1).

According to Fig. 4, it is possible to allow the shaft speed to increase so that the SOFC can be provided sufficient air for cooling. Even though the gas turbine power is dramatically reduced, the shaft speed does not increase sufficiently. The extra work by the compressor prevents the shaft from speeding up and supplying more mass flow. The reduction of mass flow in the system reduces the operating pressure of the system in Fig. 6.

The bypass valve prevents the SOFC from overheating when the mass flow from the compressor does not fully recover. The bypass valve opens to reduce the temperature of the air entering the SOFC module. The effects of the bypass valve on the SOFC operating temperature are shown in Fig. 5. The SOFC inlet temperature (state #1 of Figs. 1 and 2) is reduced, as shown in Fig. 7. This decreases the cathode inlet temperature (see state #4 of Fig. 2), which helps prevent the SOFC stack from overheating. The cathode and turbine inlet temperature along with catalytic oxidizer temperature are presented in Fig. 7. The SOFC operating temperature rises at around 20–21 h. The bypass valve closed rapidly at this time, triggering this sudden rise in SOFC temperature. The bypass valve partially opens again when the SOFC temperature exceeds 900°C.

Figure 8 shows that the system efficiency fluctuates between 65% and 72%. At the peak ambient temperature, the gas turbine net power is reduced to sustain sufficient mass flow from the compressor. The SOFC power is increased to offset the power drop from the gas turbine. The increased power from the SOFC increases the fuel flow, which decreases the system efficiency when more fuel is required for the same net power produced by the system. The SOFC fuel utilization presented in Fig. 1.

Figure 8 also shows the fuel utilization after one pass through the anode section of the SOFC stack. After recirculation, the overall SOFC module electrochemical fuel utilization is 85%.

Load-Following Case. The same ambient temperature perturbation as presented in the previous case is applied to the hybrid system in the case presented in this section. In addition, the hybrid system must follow a load demand perturbation. The load demand

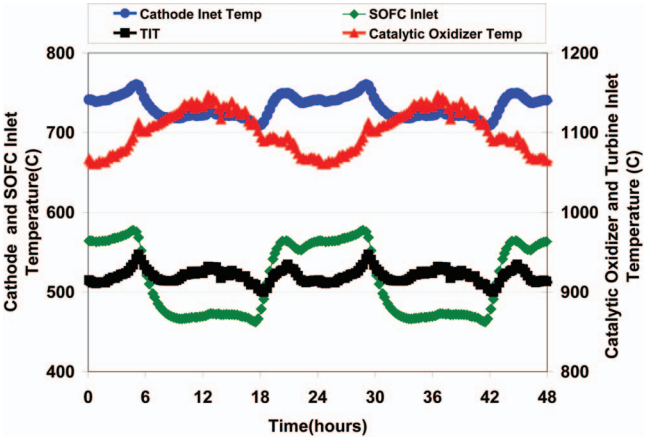

Fig. 7 SOFC, cathode, turbine inlet temperature, and the catalytic oxidizer temperature

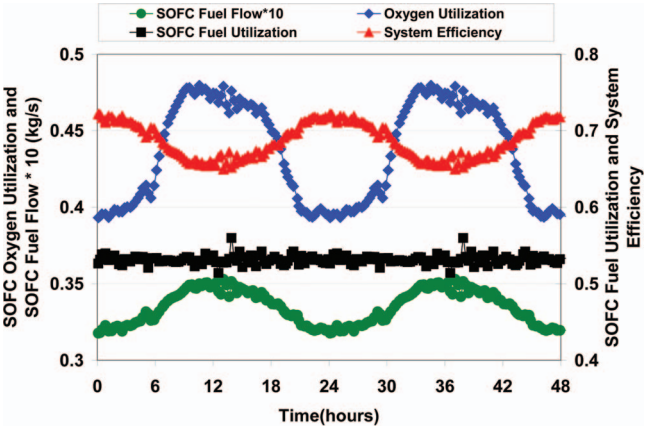

Fig. 8 System efficiency, SOFC oxygen and fuel utilization, and fuel flow

varies from 950 kW to 1150 kW. A sinusoidal power demand with a period of one day is used. The peak demand is at 12 noon.

The total power, SOFC power, and gas turbine power are presented in Fig. 9. The system was excellent in following the power demand variation. The fluctuations in gas turbine power can be

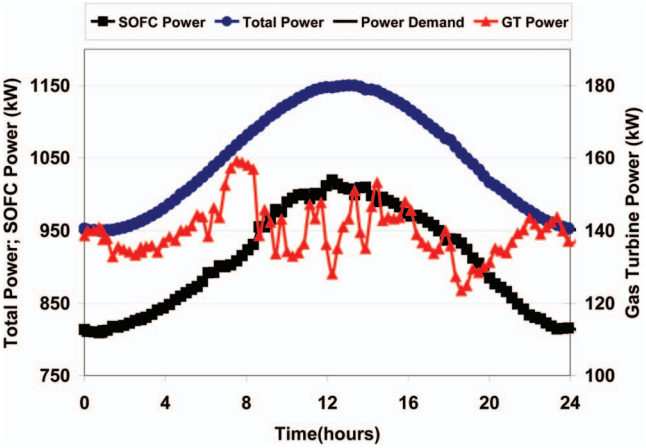

Fig. 9 Total power, SOFC power, and gas turbine power produced

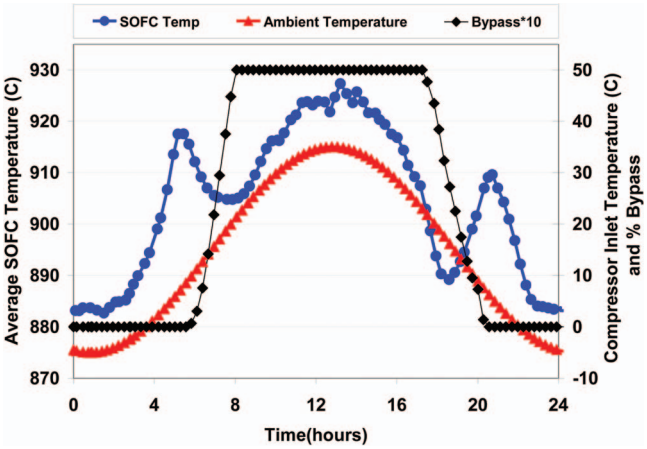

Fig. 10 SOFC average temperature, ambient temperature, and bypassed mass flow

seen in Fig. 9. The gas turbine remains around 140 kW during the entire day. Unlike the case before, the gas turbine does not reach 180 kW during the colder parts of the day since the system is operating at a lower power demand at that time of day. The SOFC power has a sinusoidal profile with fluctuations due only to the gas turbine power. If the ambient temperature had not been so extreme at 12 h, the gas turbine would have produced more net power.

The SOFC average temperature in Fig. 10 is kept within 25°C of the design temperature as in the case presented earlier. The impact of the ambient temperature on the system can be seen in Fig. 10. The same spikes and dips occur in the SOFC temperature as did in the previous case, but the logic behind them is more obvious in these results. The dip in SOFC temperature at 8 h is a result of the sudden increase in mass flow from the compressor presented in Fig. 11. The bulge in mass flow at 7 h is more apparent in this case (see Fig. 9). The mass flow from the compressor increases with the sudden increase of the shaft speed, also presented in Fig. 11. The same two causes as described in the previous section triggered this sudden change in shaft speed (1) more efficient compressor and (2) increase in TIT. The gas turbine power increases in Fig. 9 at the same time to overcome this surge of net power being produced by the gas turbine. The TIT eventually lowers as the bypass valve opens and the ambient temperature continues to rise. This reduces the power produced by the turbine and increases the compressor work as before. The gas turbine power is decreased by the controllers in Fig. 9 to allow the shaft speed to continually increase so that the SOFC can have sufficient cooling. In this case, the gas turbine power does not have to change as much since it is already at the right power range for 1150 kW system power production with 35°C ambient temperature.

Figure 12 presents the cathode and SOFC inlet temperature. The drop in both of these temperatures from the opening of the bypass valve can be seen between 7 and 17 h. There is a more dramatic change in the SOFC inlet than the cathode inlet temperature because the heat exchanger becomes more effective due to the increase in temperature differences between the SOFC inlet and catalytic oxidizer temperature. The catalytic oxidizer temperature increases from the increase in SOFC power (more anode off-gas), SOFC temperature, and the reduction of oxidant mass flow (higher oxygen utilization, Fig. 13). The TIT increases because of the catalytic oxidizer temperature increase, but less since the heat exchanger is more effective in transferring the heat from one flow than from the other.

The system efficiency in Fig. 13 has the same profile as in the earlier case, but is higher when the power production is lower due to the higher operating voltage or more efficient operation of the

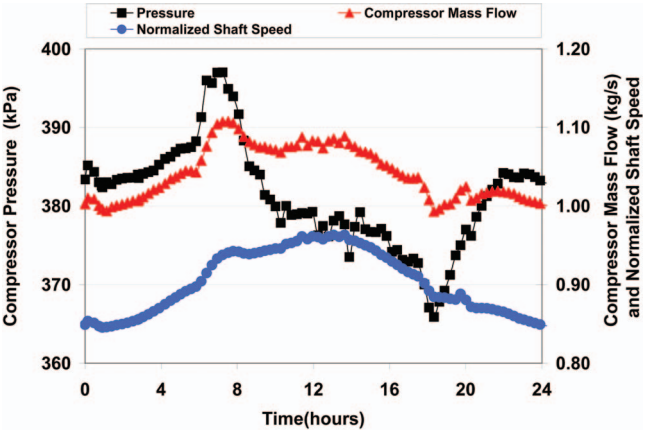

Fig. 11 Compressor mass flow, pressure, and normalized shaft speed

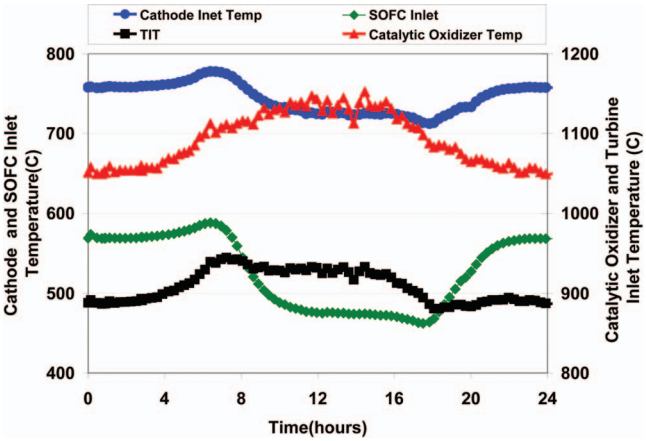

Fig. 12 SOFC, cathode, turbine inlet temperature, and the catalytic oxidizer temperature

SOFC. The oxygen utilization and the fuel utilization are similar to the case presented in the previous section. The oxygen utilization does reach higher levels of 47%, which indicates that the mass flow would be desired to be increased for better performance.

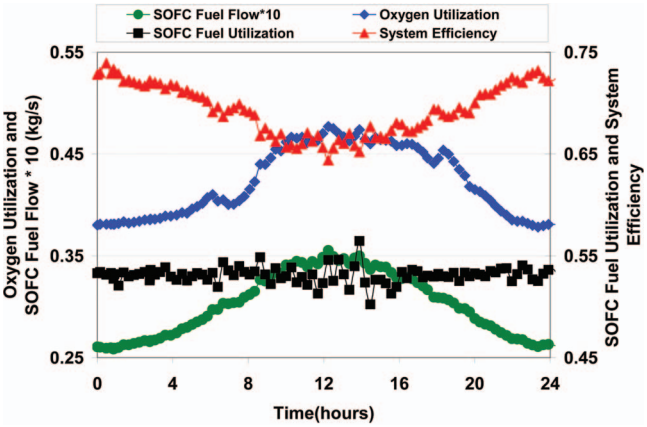

Fig. 13 System efficiency, SOFC oxygen and fuel utilization, and fuel flow

Summary and Conclusions

A SOFC/GT hybrid system was developed with controllers that allow load-following capabilities. A base-load case with varying ambient temperature for two days was simulated and presented. The system maintains constant power (100% design power) while being exposed to an ambient temperature that varies significantly from −5°C to +35°C. The system controllers responded to changes in the ambient temperature and successfully maintained the SOFC operating temperature within 20°C of the design operating temperature. The gas turbine power had to be continuously manipulated in order maintain the correct shaft speed and in turn the adequate amount of compressor mass flow.

A sinusoidal load profile was demanded of the hybrid system with peak power demand at 12 h at the same time of the peak ambient temperature. The system followed the load very well. In this case, the gas turbine remained closer to 140 kW during the entire load perturbation. The oxygen utilization increased during the load perturbation.

Ideally for a SOFC/GT hybrid system, much like a gas turbine system, the oxygen and fuel utilization would remain constant over the entire range of load demand. This fixes the air-to-fuel ratio in the SOFC module. A controller that enforces constant oxygen utilization is needed to maintain consistent SOFC average temperature and operation. Precisely controlling the compressor mass flow during large fluctuations in ambient temperature is challenging. If not carefully executed, the gas turbine can become unstable. The constant RPM approach with temperature error correction attempts to control the mass flow, but there are deviations in the SOFC temperature and oxygen utilization. These deviations are acceptable and the RPM control of the gas turbine provides a more stable means of controlling the system.

In future work, a combination of RPM control and direct mass flow control will be investigated. This type of control approach will provide stability and accurate control of the system mass flow.

Nomenclature

d = thickness of electrode, m
D_{eff} = effective diffusion coefficient, kmol/m^2
E_0 = standard theoretical potential, V
F = Faraday's constant, coulombs/mol electron
FC/GT = fuel cell/gas turbine hybrid
GT = gas turbine
i = current density of the node, A/m^2
i_0 = exchange current density, A/m^2
$i_{L(a)}$ = limiting current density for anode electrode, A/m^2
MCFC = molten carbonate fuel cell
MCFC/GT = molten carbonate fuel cell/gas turbine hybrid
n = number of contributing electrons $n=2$
NETL = National Energy Technology Laboratory
NFCRC = National Fuel Cell Research Center
P = partial pressure of species i in the bulk flow, Pa
R_{eff} = ohmic polarization loss, ohm m^2
R_u = ideal gas constant, kJ/(K* kmol)
SOFC = solid oxide fuel cell
SPC = Siemens Power Corporation
SPC-SOFC = Siemens Power Corporation solid oxide fuel cell
TIT = turbine inlet temperature
T = temperature of reaction, K
α = dimensionless transfer coefficient
η_A = activation polarization loss, V
η_C = concentration polarization loss, V
η_R = ohmic polarization loss, V

References

[1] Bessette, N. F., 1994, "Modeling and Simulation for SOFC Power Systems," *Mechanical Engineering*, Georgia Institute of Technology, Atlanta, p. 209.

[2] Costamagna, P., Magistri, L., and Massardo, A. F., 2001, "Design and Part-Load Performance of a Hybrid System Based on a Solid Oxide Fuel Cell Reactor and a Micro Gas Turbine," J. Power Sources, **96**(2), pp. 352–368.

[3] Costamagna, P., Selimovic, A., Del Borghi, M., and Agnew, G., 2004, "Electrochemical Model of the Integrated Planar Solid Oxide Fuel Cell (IP-SOFC)," Chem. Eng. J., **102**(1), pp. 61–69.

[4] Massardo, A. F., and Lubelli, F., 2000, "Internal Reforming Solid Oxide Fuel Cell-Gas Turbine Combined Cycles (IRSOFC-GT): Part A—Cell Model and Cycle Thermodynamic Analysis," ASME J. Eng. Gas Turbines Power, **122**, pp. 27–35.

[5] Rao, A. D., and Samuelsen, G. S., 2002, "Analysis Strategies for Tubular Solid Oxide Fuel Cell Based Hybrid," ASME J. Eng. Gas Turbines Power, **124**, pp. 503–509.

[6] Yi, Y., Smith, T. P., Brouwer, J., and Rao, A. D., 2003, "Simulation of a 220 kW Hybrid SOFC Gas Turbine System and Data Comparison," Proc.-Electrochem. Soc., **7**, pp. 1442–1454.

[7] Gemmen, R. S., Liese, E., Rivera, J. G., Jabbari, F., and Brouwer, J., 2000, "Development of Dynamic Modeling Tools for Solid Oxide and Molten Carbonate Hybrid Fuel Cell Gas Turbine Systems," ASME Paper No. 2000-GT-0552.

[8] Liese, E. A., Gemmen, R. S., Jabbari, F., and Brouwer, J., 1999, "Technical Development Issues and Dynamic Modeling of Gas Turbine and Fuel Cell Hybrid Systems,"ASME Paper No. 99-GT-360.

[9] Liese, E. A., and Gemmen, R. S., 2002, "Dynamic Modeling Results of a 1 MW Molten Carbonate Fuel Cell/Gas Turbine Power System," ASME Paper No. GT-2002-30110.

[10] Lukas, M. D., Lee, K. Y., and Ghezel-Ayagh, H., 1999, "Development of a Stack Simulation Model for Control Study on Direct Reforming Molten Carbonate Fuel Cell power Plant," IEEE Trans. Energy Convers., **14**, pp. 1651–1657.

[11] Lukas, M. D., Lee, K. Y., and Ghezel-Ayagh, H., 2000, "Operation and Control of Direct Reforming Fuel Cell Power Plant," IEEE Trans. Energy Convers., **14**, pp. 1651–1657.

[12] Lukas, M. D., Lee, K. Y., and Ghezel-Ayagh, H., 2002, "Modeling and cycling control of carbonate fuel cell power plants," Control Eng. Pract., **10**(2), pp. 197–206.

[13] Rivera, J. G., 2000, "Numerical Analysis of a Molten Carbonate Fuel Cell," Master's thesis, University of California, Irvine, Irvine, CA.

[14] Roberts, R. A., 2005, "A Dynamic Fuel Cell-Gas Turbine Hybrid Simulation Methodology to Establish Control Strategies and an Improved Balance of Plant," Ph.D. thesis, University of California, Irvine, Irvine, CA, p. 316.

[15] Roberts, R. A., and Brouwer, J., 2006, "Dynamic Simulation of a Pressurized 220 kW Solid Oxide Fuel Cell-Gas Turbine Hybrid System: Modeled Performance Compared to Measured Results," ASME J. Fuel Cell Sci. Technol., **3**, pp. 18–25.

[16] Roberts, R. A., Mason, J., Jabbari, F., Brouwer, J., Samuelsen, S., Liese, E., and Gemmen, R., 2003, "Inter-Laboratory Dynamic Modeling of a Carbonate Fuel Cell for Hybrid Application," ASME Paper No. GT2003-38774.

[17] Roberts, R. A., Brouwer, J., Liese, E., and Gemmen, R. S., 2004, "Dynamic Simulation of Carbonate Fuel Cell-Gas Turbine Hybrid Systems," ASME Paper No. GT2004-53653.

[18] Roberts, R. A., Brouwer, J., Liese, E., and Gemmen, R. S., 2005, "Development of Controls for Dynamic Operation of Carbonate Fuel Cell-Gas Turbine Hybrid Systems," ASME Paper No. GT2005-68774.

[19] Willis, J., 2005, "Capstone Microturbines," *ICEPAG*, Sep. 7–8, 2005, APEP, Irvine, CA.

[20] Kim, J.-W. et al., 1999, "Polarization Effects in Intermediate Temperature, Anode-Supported Solid Oxide Fuel Cells," J. Electrochem. Soc., **146**(1), pp. 69–78.

[21] Magistri, L., Traverso, A., Cerutti, F., Bozzolo, M., Costamagna, P., and Massardo, A. F., 2005, "Modeling of Pressurized Hybrid Systems Based on Integrated Planar Solid Oxide Fuel Cells (IP-SOFC) Technology," Fuel Cells, Topical Issue "Modelling of Fuel Cell Systems," **1**(5), Wiley-VCH.

On the Numerical Prediction of Finite Length Squeeze Film Dampers Performance With Free Air Entrainment

Tilmer H. Méndez
e-mail: tilmermendez@cantv.net

Jorge E. Torres
e-mail: jtorres@unet.edu.ve

Marco A. Ciaccia
e-mail: mciaccia@uc.edu.ve

Sergio E. Díaz
e-mail: sdiaz@usb.ve

Laboratorio Dinámica de Máquinas,
Universidad Simón Bolívar,
Caracas 1080-A, Venezuela

*Squeeze film dampers (SFDs) are commonly used in turbomachinery to dampen shaft vibrations in rotor-bearing systems. The main factor deterring the success of analytical models for the prediction of SFD's performance lies on the modeling of dynamic film rupture. Usually, the cavitation models developed for journal bearings are applied to SFDs. Yet, the characteristic motion of the SFD results in the entrapment of air into the oil film, producing a bubbly mixture that cannot be represented by these models. There is a need to identify and understand the parameters that affect air entrainment and subsequent formation of a bubbly air-oil mixture within the lubricant film. A previous model by and Diazand San Andrés (2001, "A Model for Squeeze Film Dampers Operating With Air Entrapment and Validation With Experiments," ASME J. Tribol., **123**, pp. 125–133) advanced estimation of the amount of film-entrapped air based on a nondimensional number that related both geometrical and operating parameters but limited to the short bearing approximation (i.e., neglecting circumferential flow). The present study extends their work to consider the effects of finite length-to-diameter ratios. This is achieved by means of a finite volume integration of the two-dimensional, Newtonian, compressible Reynolds equation combined with the effective mixture density and viscosity defined in the work of Diaz and San Andrés. A flow balance at the open end of the film is devised to estimate the amount of air entrapped within the film. The results show, in dimensionless plots, a map of the amount of entrained air as a function of the feed-squeeze flow number, defined by Diaz and San Andrés, and the length-to-diameter ratio of the damper. Entrained air is shown to decrease as the L/D ratio increases, going from the approximate solution of Diaz and San Andrés for infinitely short SFDs down to no air entrainment for an infinite length SFD. The results of this research are of immediate engineering applicability. Furthermore, they represent a firm step to advance the understanding of the effects of air entrapment on the performance of SFDs.* [DOI: 10.1115/1.2981182]

Keywords: squeeze film dampers, air entrapment, feed-squeeze flow number, dimensionless air entrainment map

1 Introduction

Squeeze film dampers are often employed in high-speed rotating machinery to provide additional external damping to rotor-bearing systems with the purpose of reducing the synchronous response of the rotor, especially while traversing critical speeds or eliminating rotor instability problems. Controlling rotordynamic instabilities and reducing large amplitude vibration in turbomachinery are key factors to gain reliability and safety [1].

The application of these dampers is widely found in aircraft gas turbine engines. In its simplest form, the SFD consists of an oil-filled annular cavity surrounding the outer race of a rolling element bearing. The outer race of the bearing, acting as the damper journal, is prevented from rotating, but it is allowed to describe whirl orbit motions around its equilibrium position, as Fig. 1 illustrates.

In open-ended SFD operation, several cavitation regimes have been found and described. In the most common of these regimes, large amplitude journal orbital motions cause air ingestion and entrapment, thus leading to the formation of a bubbly fluid and affecting the performance of the SFD [2–7]. In general, the film pressure and tangential (damping) force decrease rapidly with the air volume content in the mixture.

Diaz and San Andrés [8] advanced a model for prediction of the forced response of SFDs with air entrainment, executing circular centered orbits, and validated their results experimentally [8,9]. A modified Reynolds equation for prediction of the squeeze film pressure in a homogeneous bubbly mixture is advanced combined with correlations for effective local viscosity and density and a simple axial flow balance that allows for estimation of the amount of the freely entrained air. The compressible Reynolds equation and the effective viscosity and density correlations are applicable to any case. Yet, the axial flow balance correlation is strictly valid only for infinitely short dampers executing circular centered orbits.

This simple model is based on the fact that for infinitely short bearings the tangential flow is negligible, thus allowing for a pure axial flow balance to estimate the flow at the open end. It further assumes (a) a constant and uniform lubricant supply flow around the bearing sealed end, (b) that any flow coming in from the open end is pure air, (c) an instantaneous mixing of air and oil into the homogeneous mixture as soon as they enter the film, and (d) that all flow coming out at the open end is a homogeneous mixture. Consequently, a purely axial flow balance per unit length can be applied to yield the average air volume fraction of the mixture

Contributed by the International Gas Turbine Institute of ASME for publication in the JOURNAL OF ENGINEERING FOR GAS TURBINES AND POWER. Manuscript received March 28, 2008; final manuscript received May 6, 2008; published online September 29, 2009. Review conducted by Dilip R. Ballal. Paper presented at the ASME Turbo Expo 2008: Land, Sea and Air (GT2008), Berlin, Germany, June 9–13, 2008.

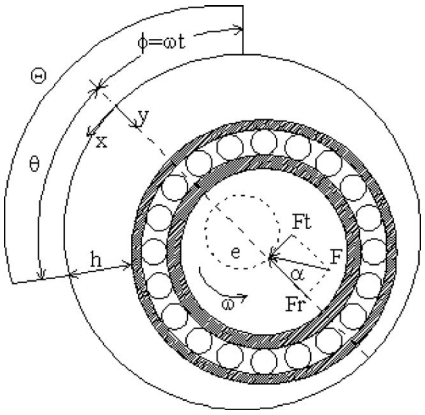

Fig. 1 Schematic outline and coordinates of the SFD

trapped in the film. Taking the discharge pressure (P_o) as the reference, the average air volume fraction can be computed as [8]

$$\beta_0 = \frac{Q_{\text{air}}}{Q_{\text{air}} + Q_{\text{oil}}} = \left[1 + \frac{2\pi\gamma}{\gamma(2\sin^{-1}(\gamma) - \pi) + 2\sqrt{1-\gamma^2}} \right]^{-1} \quad (1)$$

where γ is a dimensionless flow parameter, defined as the feed-squeeze flow number [8], that relates the lubricant feed or supply flow per unit length ($q_{\text{oil}} = Q_{\text{oil}}/\pi D$) to the squeeze flow or dynamic change in volume per unit length ($q_{\text{sqz}} = Le\omega$) within the squeeze film gap.

$$\gamma = \frac{q_{\text{oil}}}{q_{\text{sqz}}} = \frac{Q_{\text{oil}}}{\pi DLe\omega} \quad (2)$$

As Fig. 2 shows, if $\gamma > 1$ no air entrainment occurs, i.e., the through flow is sufficient to fill the volume change (or squeeze flow) caused by the journal whirl motion, and the exit flow (q_{out})

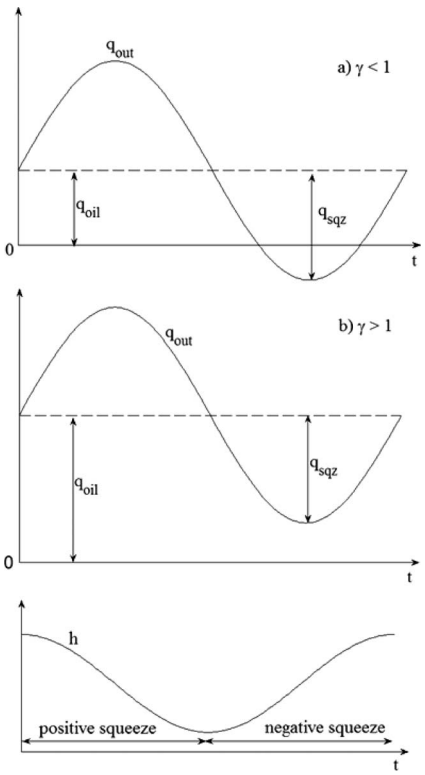

Fig. 2 Exit flow per unit length at the open end (q_{out}) versus time with uniform supply flow (q_{oil}) condition

is positive. On the other hand, air ingestion and entrapment occur if $\gamma < 1$ (the exit flow becomes negative), and the damper will operate with a bubbly lubricant mixture.

The results obtained by the research of Diaz and San Andrés [8,9] demonstrate the suitability of this approach for the prediction of the experimentally recorded behavior of SFDs with free air entrainment and the subsequent two-phase mixtures.

The objective of the present work is to advance the understanding of air ingestion and its effects on SFDs, providing a reliable tool for their design and practical implementation in high performance turbomachinery. The following extends previous studies by addressing finite length bearings, i.e., different length-to-diameter ratios.

2 Model and Boundary Conditions

The present study extends the work of Diaz and San Andrés [8] to consider the effects of length-to-diameter ratios. Thus, the compressible lubricant Reynolds equation combined with the effective mixture viscosity and density discussed by Diaz and San Andrés [8] is used:

$$\frac{4}{D^2}\frac{\partial}{\partial\theta}\left[\frac{\rho_{(\beta)}\cdot h_{(\theta)}^3}{12\cdot\mu_{(\beta)}}\frac{\partial P}{\partial\theta}\right] + \frac{1}{L^2}\frac{\partial}{\partial\hat{z}}\left[\frac{\rho_{(\beta)}\cdot h_{(\theta)}^3}{12\cdot\mu_{(\beta)}}\frac{\partial P}{\partial\hat{z}}\right] = -\omega\frac{\partial[\rho_{(\beta)}\cdot h_{(\theta)}]}{\partial\theta} \quad (3)$$

$$\mu_{(\beta)} = (1-\beta)\mu_L + \beta\mu_A \approx (1-\beta)\mu_L \quad (4)$$

$$\rho_{(\beta)} = (1-\beta)\rho_L + \beta\rho_A \approx (1-\beta)\rho_L \quad (5)$$

$$h_{(\theta)} = c + e\cos(\theta) \quad (6)$$

where β is the local air volume fraction expressed as a function of the local pressure and the reference volume fraction β_0, according to the perfect gas law for the air and assuming incompressible oil and isothermal conditions [8]:

$$\beta = \frac{1}{1 + \frac{P_{(\theta,z)} - P_v}{P_o - P_v}\left(\frac{1}{\beta_0} - 1\right)} \quad (7)$$

For the infinitely short bearing, an analytical solution is presented in Eq. (1) as a sole function of the feed-squeeze flow number (γ). For finite length applications, this analytical solution does not apply since the tangential flow cannot be neglected. Thus, the basic definition coming from the flow balance for a SFD executing circular centered orbits must be used [8]:

$$\beta_0 = \frac{Q_{\text{air}}}{Q_{\text{air}} + Q_{\text{oil}}} \quad (8)$$

where the incoming air flow must be computed numerically from the solution of the Reynolds equation, thus requiring an iterative process to obtain simultaneous convergence of β_0 and the pressure field. In this work, the compressible Reynolds equation is solved by the finite volume method (FVM), and the air incoming flow is computed as the negative fraction of the flow at the open end. For programming simplicity, a segregated iteration scheme was employed, with a global iteration on the reference volume fraction and computing a new β_0 only after convergence of the pressure field solution of the Reynolds equation is obtained.

Squeeze film dampers are fed either directly by orifices or by a circumferential feeding groove. Researchers have shown their importance on the damper behavior [10–12], and from the modeling standpoint they represent a part of the boundary conditions of the film. Recently, Rodriguez et al. [13] presented results that further reinforce the findings of Diaz and San Andres [8,14–16] and the suitability of their analytical model [8]. They also experimentally demonstrated a strong effect of the oil feeding configuration, associated with journal kinematics, on the dynamic performance of SFDs, relating both parameters to the amount of the entrained air.

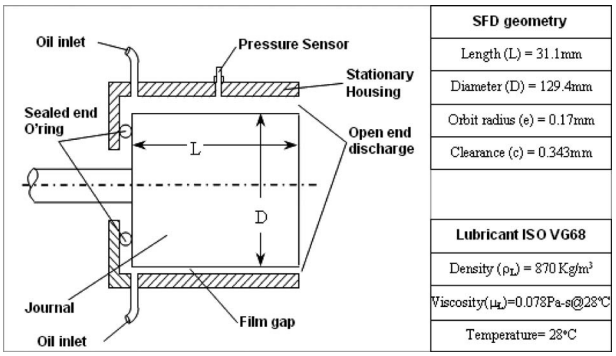

Fig. 3 SFD configuration

The usual assumption when dealing with a circumferential groove is that it represents a constant pressure reservoir. Nevertheless, the discontinuity between the circumferential groove and the thin film affects the results [17]. Diaz and San Andrés [8] considered a constant and uniform supply flow around the film lands of an infinitely short SFD, which allowed them to obtain an analytical solution for estimation of β_0. Their results agree with the experiments for the specific geometry they tested. However, in their test rig the lubricant enters the damper film through two holes 180 deg apart located at the sealed end. It is necessary to extend the analysis of boundary conditions to evaluate other configurations representative of actual SFDs. The following three sets of boundary conditions are studied.

•Uniform flow (Uf): This model considers oil supplied at a fixed flow rate, which is uniformly distributed throughout the damper perimeter.

$$q_{\text{in}(\theta)} = \frac{Q_{\text{oil}}}{\pi D} \tag{9}$$

Uniform velocity (Uv): This boundary condition simulates the feed flow at a constant velocity around the film, thus resulting in smaller flows for the smaller local film thickness.

$$v_{\text{in}(\theta)} = \frac{q_{\text{in}(\theta)}}{h_{(\theta)}} = \frac{Q_{\text{oil}}}{\pi D c} \tag{10}$$

•Uniform pressure (Up): A uniform pressure is established in the SFD's entrance. The oil lubricant enters with a flow distribution computed according to the solution of the Reynolds equation. This condition represents a large, constant pressure, supply plenum groove.

$$P_{(\theta,0)} = P_{\text{in}} \tag{11}$$

To evaluate the proposed boundary conditions, numerical studies were performed using the damper configuration used by Diaz and San Andrés [8] and depicted in Fig. 3. The test section consists of a journal mounted on a rigid shaft with an eccentric sleeve through a ball bearing. The lubricant enters the damper film through two holes 180 deg apart at the sealed end. An O-ring seals the damper journal on this side, thus forcing the flow to exit through the right end plenum. The actual feeding hole size and exact location as well as the dimensions of the gap behind the journal and around the O-ring seal are unknown but seem to work as a distribution groove for the supply flow. The oil feed flow and supply pressure are varied from 0 l/min to 4 l/min and from 0 bar to 7 bars, respectively. The hydrodynamic forces per unit length are computed by integration of the measured pressure field at the sensor location, allowing comparison to experimental results published by Diaz and San Andres [8].

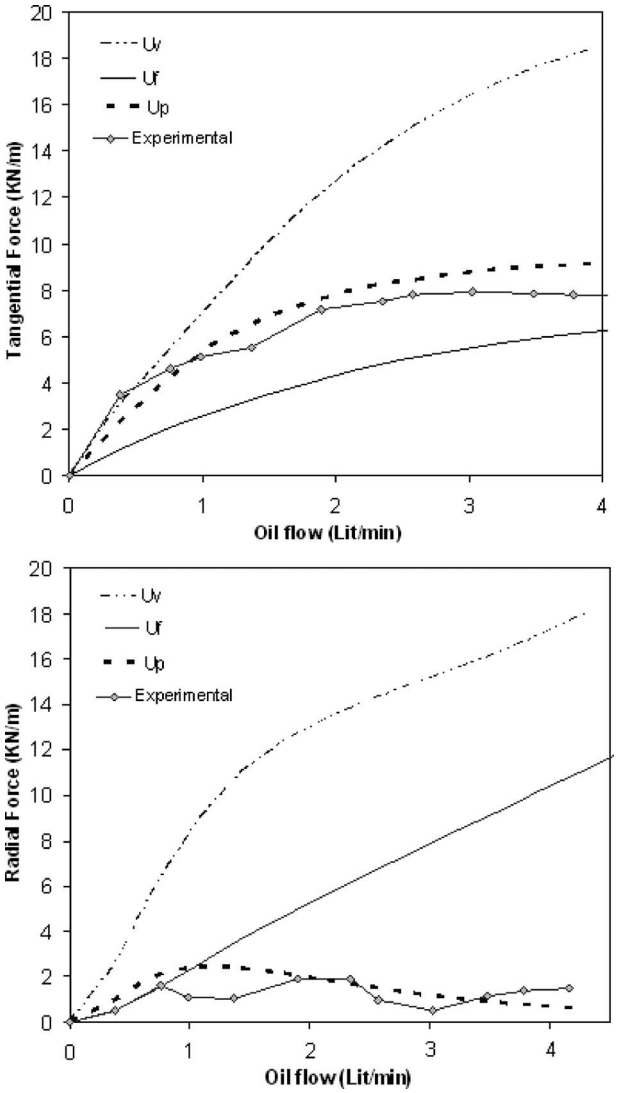

Fig. 4 Tangential and radial forces per unit length (z =16.7 mm) versus oil feed flow at a frequency of 8.33 Hz for various boundary conditions (experiments from Diaz and San Andrés [8])

3 Results

Figure 4 compares predictions of the current model (Eqs. (3)–(8)), with the three sets of boundary conditions, to the experimental measurements of Diaz and San Andrés [8]. As expected, it is clear that the Up condition resembles in a closer way the experimental results since the circumferential distribution of the axial inflow considers the variable resistance imposed by the film pressure. On the other hand, the Uv boundary condition is the one with the largest deviation. Thus, in the following, the uniform pressure boundary condition is kept for the study. In addition, the Uf boundary condition is studied for comparison purposes since it corresponds to the boundary conditions used by the previous study of Diaz and San Andrés [8] for infinitely short bearings.

Figure 5 maps trapped air volume fractions (β_0) as a function of the length-to-diameter ratio (L/D) and the feed-squeeze flow number (γ) for the uniform feed flow boundary condition (this is accomplished by varying L to achieve the desired L/D ratio and the supply flow to attain the required γ). Continuous lines denote the numerically computed volume fractions for several L/D ratios. The dotted line depicts the analytical solution of Diaz and San Andrés [8] for the infinitely short damper. L/D ratios equal to

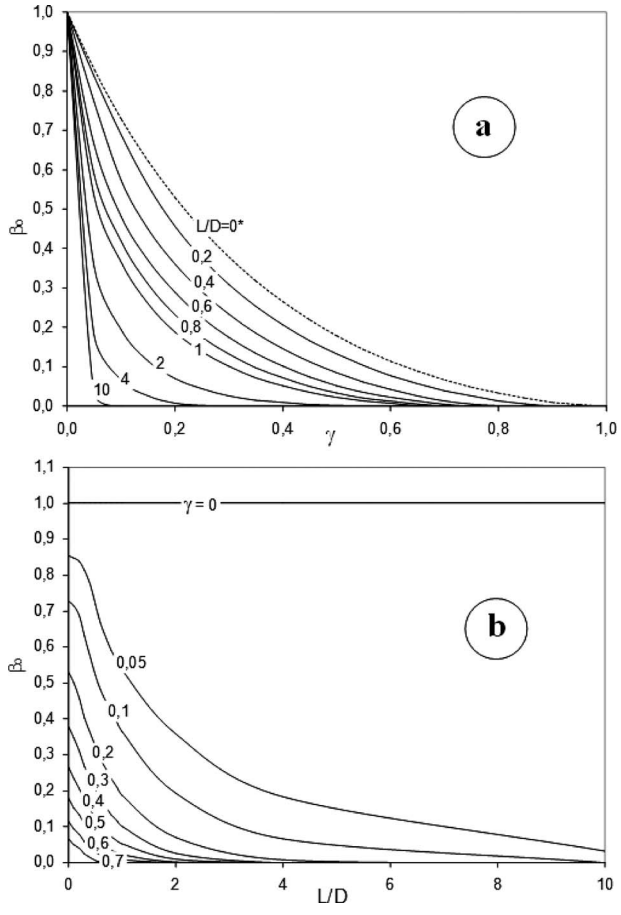

Fig. 5 Air volume fraction (β_0) versus (a) feed squeeze flow number (γ) and (b) L/D ratio for Uf boundary condition ($^*L/D=0$,... Diaz and San Andrés [8])

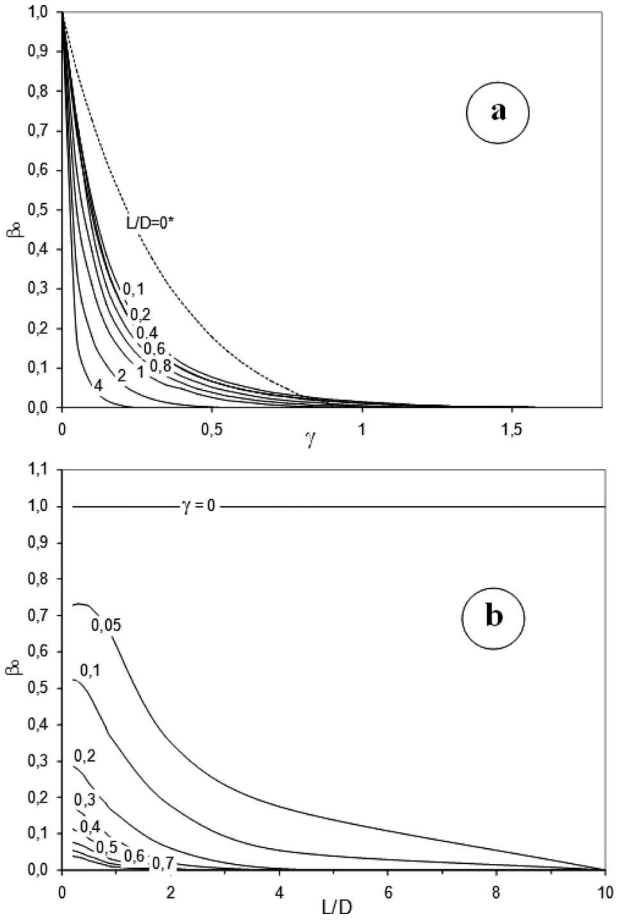

Fig. 6 Air volume fraction (β_0) versus (a) feed squeeze flow number (γ) and (b) L/D ratio for Up boundary condition ($^*L/D=0$,... Diaz and San Andrés [8])

zero result in numerical singularities and cannot be computed numerically. Yet, numerical solutions of the finite length equation with the current model show an asymptotic behavior of the solutions toward the analytical solution of Diaz and San Andrés [8] as the L/D ratio approaches zero, thus demonstrating the continuity between the analytical solution for the limit case ($L/D=0$) and the numerical model.

Figure 5(*a*) evidences that for every L/D ratio, the amount of the naturally entrained air (β_0) goes gradually from pure air ($\beta_0=1$) to pure oil ($\beta_0=0$) as the feed squeeze flow number (γ) goes from 0 to 1 and remains pure oil for $\gamma>1$. This implies that if the uniform oil feed flow boundary condition is valid, there is one value of the oil flow for every geometry and whirl motion above which no air entrainment occurs (see Eq. (2)). In an analogous way, it can also be stated that for a given geometry and oil feed flow, there is a whirl frequency or a whirl eccentricity below which no air entrainment occurs.

Completing the map, when the L/D ratio is increased, the amount of the entrained air decreases for any value of γ, except for $\gamma=0$, where there is pure air regardless of the L/D ratio, and for $\gamma\geq 1$, where there is pure oil regardless of the L/D ratio. This reduction in the amount of the entrained air for increasing L/D ratio relates directly to the increase in the tangential flow and the subsequent reduction in the squeeze flow that is displaced out of (or into) the film axially. Figure 5(*b*) makes this clear by using an alternative representation of the same map.

One particular case is the infinitely long damper, which, as the asymptotic solution for increasing L/D, accepts multiple solutions for $\gamma=0$. A feed squeeze flow number equal zero means that no oil is supplied to the damper. Infinitely long bearing implies that it has a negligible axial flow. As a result, no oil will enter or be expulsed of the film lands; thus the damper might keep any value of air volume fraction (β_0) depending on the initial condition. For any other value of γ, an infinitely long bearing will eventually fill and operate in a steady state full of oil ($\beta_0=0$).

Figure 6 depicts the trapped air volume fraction computed for the Up boundary condition (by varying L to achieve the desired L/D ratio and the supply pressure to attain the required γ). For reference purposes, the curve for $L/D=0$, from the Diaz and San Andrés [8] model, is included. It is clear that the computed results do not follow a common trend with this theory, as expected due to the difference in boundary conditions (i.e., Up versus Uf). As in the previous case, larger L/D ratios imply lower amounts of the entrained air. Also, all plots start from a pure air condition ($\beta_0=1$) for γ equal to zero and decrease rapidly as the squeeze-feed flow number grows. However, unlike the case of the uniform flow boundary condition, there is still air entrainment for values of γ greater than 1. As a result, even though the predicted amount of the entrained air is generally smaller for the uniform pressure boundary condition case (as compared with the uniform flow boundary condition), this trend is reversed for feed squeeze flow numbers near and above 1.

A qualitative explanation for the occurrence of air entrainment for feed squeeze flow numbers above 1 can be seen in Fig. 7. For the uniform pressure boundary condition, a variation of the feed flow is observed around the damper, i.e., for the same feed and discharge pressures, smaller feed flows occur at the smaller film thickness due to the increased pressure losses. Thus, as compared

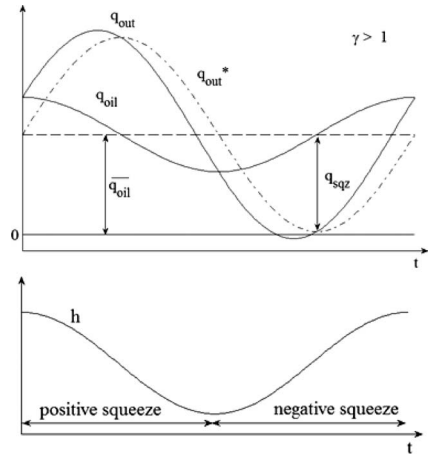

Fig. 7 Outflow (q_{out}) at the open end versus time (or angle) with uniform pressure boundary condition

with the case of the uniform flow discussed previously, represented by q^*_{out} in the figure, the actual q_{out} adds the variations due to the squeeze flow (or displaced volume, q_{sqz}) to those introduced by the variations in the feed flow. The result is that, even though the same average flow is kept, the amplitude of variation in the outflow is larger, allowing for the possibility of having reversed flow (i.e., air entrainment) even for values of γ slightly larger than 1. This poses a question on the effect of different orbit sizes since larger film thickness variations might bring larger feed flow variations, thus making it necessary to introduce additional parameters to the maps of Figs. 5 and 6. Current work is advanced to answer this question. Note that the maps presented, though dimensionless, are numerically computed for the damper configuration described above (Fig. 3) by varying the length, supply flow, or supply pressure as needed to cover the map range.

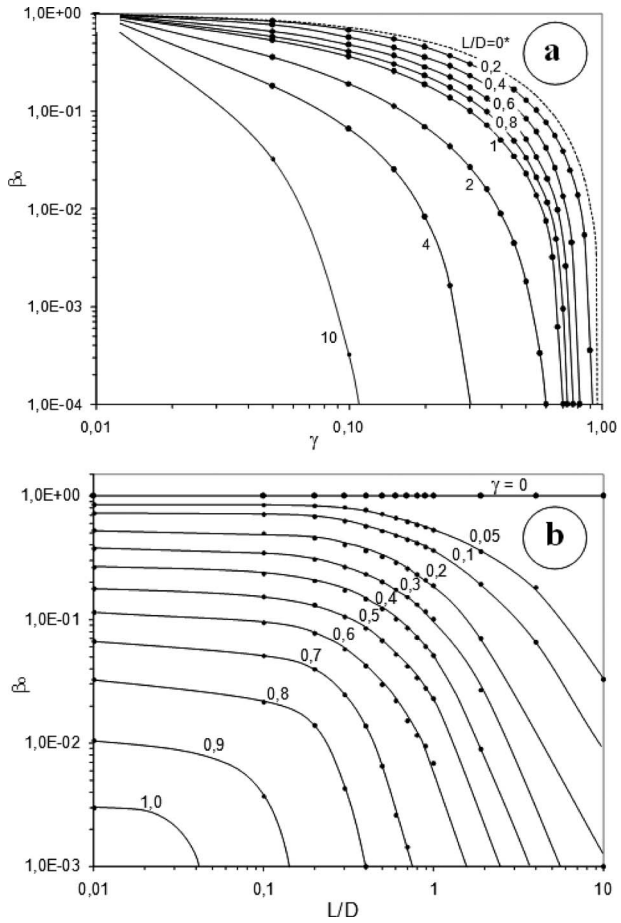

Fig. 8 Air volume fraction (β_0) versus (a) feed squeeze flow number (γ) and (b) L/D ratio for Uf boundary condition; logarithmic scale ($^*L/D=0,\ldots$ Diaz and San Andrés [8])

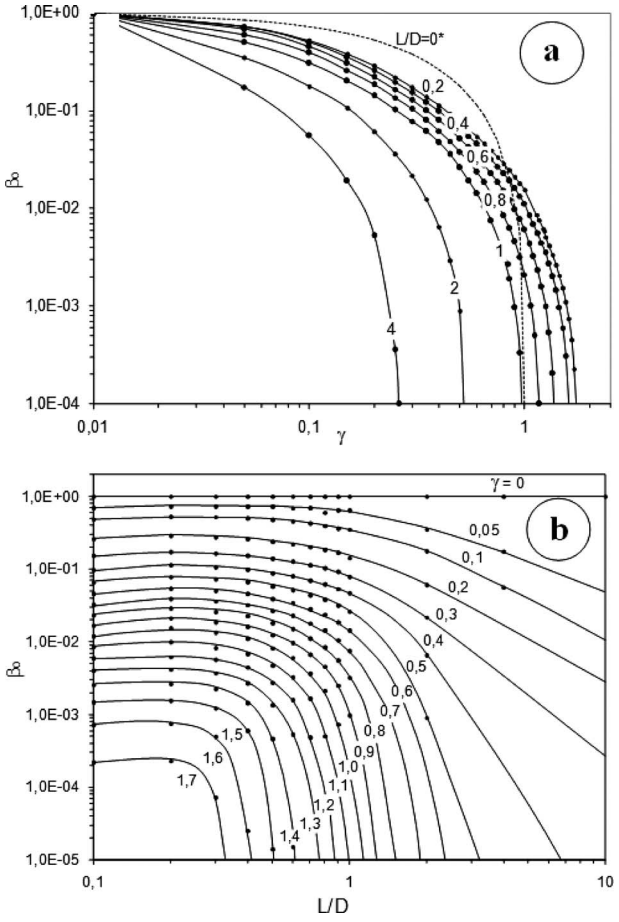

Fig. 9 Air volume fraction (β_0) versus (a) feed-squeeze flow number (γ) and (b) L/D ratio for Up boundary condition; logarithmic scale ($^*L/D=0,\ldots$ Diaz and San Andrés [8])

Figures 8 and 9 show the maps of Figs. 5 and 6 in logarithmic scale, showing trends in a clearer way. These figures indicate that, for the Up boundary condition, there is also one value of the squeeze-feed flow number (close to $\gamma=2$) above which no air entrainment occurs regardless of the L/D ratio.

Figure 10 shows the general effect of air entrainment on the performance of the SFD. Peak-to-peak dynamic pressures as well as radial and tangential forces are depicted as a function of the reference, or average, air volume fraction. The predictions of the current model correlate to experimental measurements performed on a SFD operating with controlled bubbly mixtures by Diaz and San Andrés [14,15,18]. The dynamic pressure reduces almost linearly with the air volume fraction (β_0) from the maximum value, when the damper operates with pure oil ($\beta_0=0$), to a nil value when it operates with pure air ($\beta_0=1$). A similar behavior is followed by the tangential force, thus evidencing the loss of damping capacity when air enters the SFD lands. The radial force plot evidences that the pressure profile not only reduces its magnitude but also modifies its shape, resulting in the occurrence of a radial centering force that peaks around 40% air content ($\beta_0=0.4$).

For practical purposes, however, it is necessary to present these results in terms of geometric and operating parameters when the

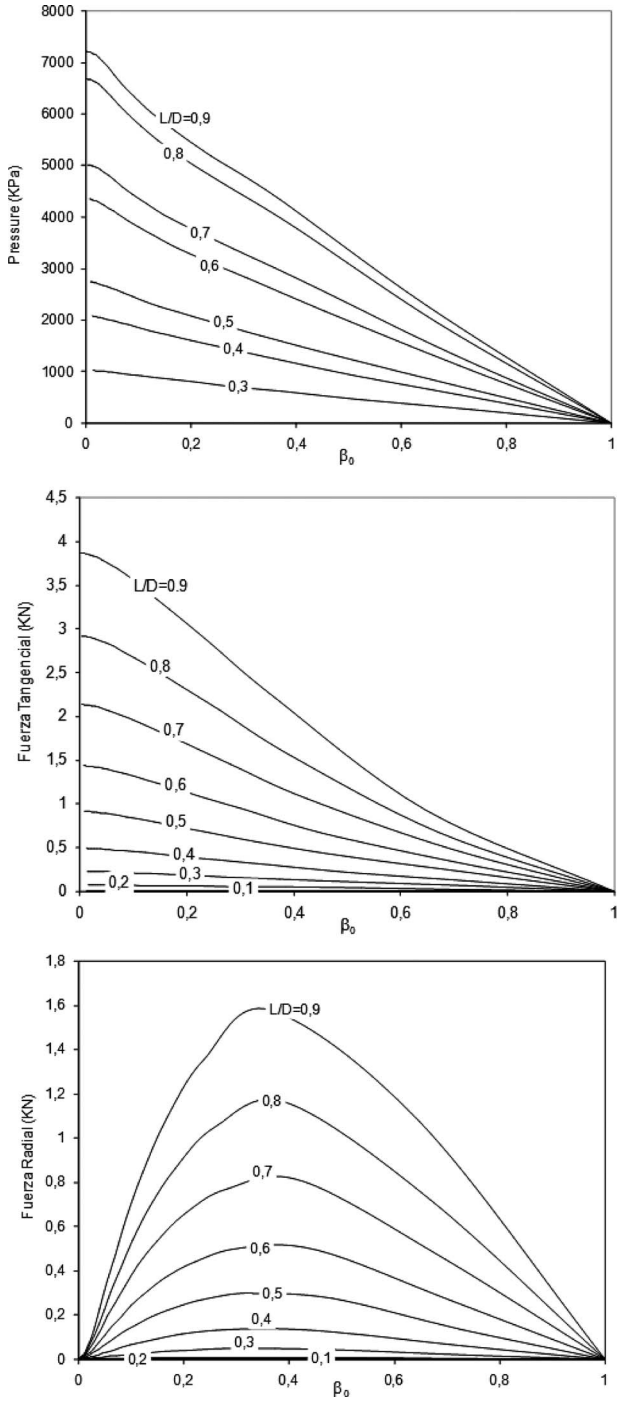

Fig. 10 Peak-to-peak pressure, tangential forces, radial forces versus air volume fraction (β_0) for the uniform pressure boundary condition at 8.33 Hz

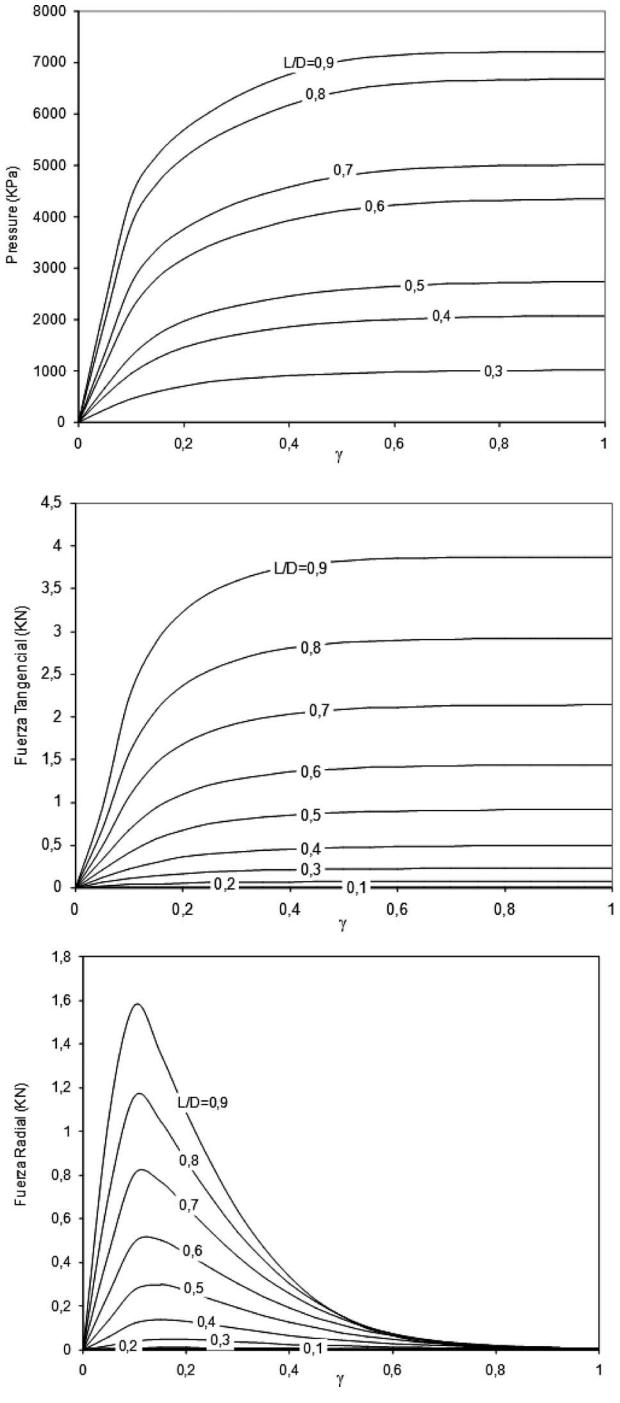

Fig. 11 Peak-to-peak pressure, tangential forces, radial forces versus feed squeeze flow number (γ) with uniform pressure boundary condition at 8.33 Hz

SFD operates with free air entrainment and β_0 is not known a priori. The maps of Figs. 5 and 6 (or Figs. 8 and 9) allow for this representation using γ and L/D as the independent parameters.

Figure 11 shows the dynamic pressures and forces predicted using the Up boundary condition versus the feed squeeze flow number for several length-to-diameter ratios (this is accomplished by varying L to achieve the desired L/D ratio and the supply pressure to attain the required γ). The tangential forces, just as the dynamic pressures, tend asymptotically to the value predicted for the incompressible lubricant (pure oil). The damping (tangential) forces reach this value relatively fast. For feed squeeze flow numbers above 0.4 the damping force is within 3% of that predicted for the pure oil condition, even though there is still air entrainment up to a value of γ close to 2. The radial (centering) force is significantly smaller than the tangential one for the whole range; however, it is below 3% of the tangential force only for γ greater than 0.6.

It is clear that by increasing the feed-squeeze flow number air entrainment could be prevented, and the incompressible Reynolds equation would properly represent the SFD. Regardless of the L/D ratio it seems that the incompressible approximation is applicable if γ is greater than 0.4 for the estimation of the damping available in the system. There will still be air present in the film as

well as a small radial centering force, but their effect should be small. However, the practicality of this approach is compromised by the cost of increasing the feed flow or reducing the speed and/or vibration amplitude. Practice has demonstrated that most SFDs operate in this regime, and the model hereby advanced addresses the most significant shortcoming of these applications, which relates to the lack of a reliable prediction of the SFD behavior in the design stages.

4 Conclusions

A new model able to estimate the performance of finite length SFDs with free air entrainment is advanced. Dimensionless maps to quantify the amount of the entrapped air as a function of the geometry and operating conditions (γ, L/D) computed with the new model are presented.

Due to the geometry and operating conditions it is difficult to establish the boundary conditions that better represent the feeding configuration. Three boundary conditions were evaluated for the simulation of the lubricant supply flow. The Up condition is proven to generate significantly better agreement with the experimental data than the previously used Uf condition.

The Uf condition is consistent with the analytically computed limit condition for infinitely short bearing of Diaz and San Andrés [8].

With the Up condition the amount of the entrained air is generally lower than with the Uf condition except for γ values near and above 1.

For the Uf condition, there is no air entrainment above $\gamma=1$; however, for the more realistic Up condition air entrainment occurs up to $\gamma=2$ approximately.

As the L/D ratio increases, the amount of the entrained air reduces.

The compressible Reynolds equation provides a reasonable approximation of the damping force for γ above 0.5. However, for most practical applications a model like the proposed one is required to estimate the amount of the entrained air and its effect on damper performance.

Although the results presented were computed and validated with a specific test rig, the assumptions made on the development of the model are general and applicable to many other configurations. The dimensionless presentation of the results readily allows for easy extrapolation of the results to different whirl frequencies, orbit radii, and damper geometries other than the ones tested. In general, these extrapolations seem reasonable. Further work is being developed to validate the model against different configurations and to test the need to consider other dimensionless parameters.

Acknowledgment

The authors acknowledge the support of USB's Dean of Research and Development, FONACIT, and USB's Machinery Dynamics Laboratory for funding this research.

Nomenclature

β = local air volume fraction
β_0 = reference air volume fraction (at discharge pressure)
c = damper radial clearance
D = damper diameter
e = orbit radius
F_t = tangential force
F_r = radial force
γ = feed-squeeze flow number
h = local film thickness
L = damper length
μ_L = oil viscosity
μ_A = air viscosity
$\mu_{(\beta)}$ = effective mixture viscosity
$P_{(\theta,z)}$ = local pressure
P_o = atmospheric (discharge) pressure
P_{in} = oil supply pressure
P_v = vapor pressure
Q_{oil} = total flow rate into the damper
q_{in} = inlet (oil) flow rate per unit length
Q_{out} = outlet (mixture) flow rate per unit length
q_{air} = air flow rate per unit length entering from ambient
v_{in} = local inlet (oil) velocity
z = axial coordinate
Θ = absolute angular coordinate
θ = relative angular coordinate
ρ_L = oil density
ρ_A = air density
$\rho_{(\beta)}$ = effective mixture density
ω = whirl frequency

References

[1] San Andrés, L., and Vance, J. M., 1986, "Experimental Measurement of the Dynamic Pressure Distributions in a Squeeze Film Damper Executing Circular-Centred Orbits," ASLE Trans. **30**(3), pp. 373–383.
[2] Childs, D., 1993, *Turbomachinery Rotodynamics*, Wiley, New York.
[3] Zeidan, F. Y., and Vance, J. M., 1989, "Experimental Investigation of Cavitation Effects on the Squeeze Film Force Coefficients," Rotating Machinery Dynamics, *Proceedings of the 12th Biennial ASME Conference on Mechanical Vibration and Noise*, Montreal , Canada; US, Sep. 17–21, pp. 237–242.
[4] Zeidan, F. Y., and Vance, J. M., 1989, "Cavitation Leading to a Two Phase Fluid in a Squeeze Film Damper," STLE Tribol. Trans., **32**(1), pp. 100–104.
[5] Zeidan, F. Y., and Vance, J. M., 1990, "Cavitation Regimes in Squeeze Film Dampers and Their Effect on the Pressure Distribution," STLE Tribol. Trans., **33**, pp. 447–453.
[6] Walton, J., Walowit, E., Zorzi, E., and Schrand, J., 1987, "Experimental Observation of Cavitating Squeeze Film Dampers," ASME J. Tribol., **109**, pp. 290–295.
[7] San Andres, L., and De Santiago, O., 2004, "Dynamic Response of Squeeze Film Dampers Operating With Bubbly Mixtures," ASME J. Eng. Gas Turbines Power, **126**, pp. 408–415.
[8] Diaz, S., and San Andrés, L., 2001, "A Model for Squeeze Film Dampers Operating With Air Entrapment and Validation With Experiments," ASME J. Tribol., **123**, pp. 125–133.
[9] Diaz, S., 1999, "The Effect of Air Entrapment on the Performance of Squeeze Film Dampers: Experiments and Analysis," Ph.D. thesis, Texas A&M University, College Station, TX.
[10] Tonnesen, J., 1976, "Experimental Parametric Study of a Squeeze Film Bearing," J. Lubr. Technol., **April**, pp. 206–213.
[11] San Andrés, L., 1992, "Analysis of Short Squeeze Film Dampers With a Central Groove," ASME J. Tribol., **114**, pp. 659–665.
[12] Chen, P. Y. P., and Hahn, E. J., 1994, "Pressure Distribution in Squeeze Film Dampers With Oil Hole Feed," Proc. Inst. Mech. Eng., Part J: J. Eng. Tribol., **208**, pp. 105–112.
[13] Rodriguez, F., Thouverez, F., and Jezequel, L., 2004, "Interaction of Squeeze Film Dampers and Hole Feed Systems and Its Influence on the Dynamics of a Jeffcott Rotor," Int. J. Rotating Mach., **10**(3), pp. 163–174.
[14] Diaz, S. E., and San Andrés, L., 1998, "Measurements of Pressure in a Squeeze Film Damper With an Air/Oil Bubbly Mixture," STLE Tribol. Trans., **41**(2), pp. 282–288.
[15] San Andrés, L., and Diaz, S., 2002, "Pressure Measurements and Flow Visualization in a Squeeze Film Damper Operating in a Bubbly mixture," Trans. ASME, J. Tribol., **124**, pp. 346–350.
[16] San Andrés, L., and Diaz, S., 2003, "Flow Visualization and Forces From a Squeeze Film Damper Operanting With Air Entrainment," ASME J. Tribol., **125**, pp. 325–333.
[17] Arghir, M., Alsayed, A., and Nicolas, D., 2002, "The Finite Volume Solution of the Reynolds Equation of Lubrication With Film Discontinuities," Int. J. Mech. Sci., **44**, pp. 2119–2132.
[18] Diaz, S. E., and San Andrés, L., 1999, "Reduction of the Dynamic Load Capacity in a Squeeze Film Damper Operating With a Bubbly Mixture," ASME J. Eng. Gas Turbines Power, **121**, pp. 703–709.

Controlling Journal Bearing Instability Using Active Magnetic Bearings

A. El-Shafei

A. S. Dimitri

Department of Mechanical Design and Production,
Faculty of Engineering,
Cairo University,
Giza 12316, Egypt

Journal bearings (JBs) are excellent bearings due to their large load carrying capacity and favorable damping characteristics. However, journal bearings are known to be prone to instabilities. The oil whirl and oil whip instabilities limit the rotor maximum rotating speed. In this paper, a novel approach is used to control the journal bearing instability. An active magnetic bearing (AMB) is used to overcome the JB instability and to increase its range of operation. The concept is quite simple: Rather than using the AMB as a load carrying element, the AMB is used as a controller only, resulting in a much smaller and more efficient AMB. The load carrying is done by the journal bearings, exploiting their excellent load carrying capabilities, and the JB instability is overcome with the AMB. This results in a combined AMB/JB that exploits the advantages of each device and eliminates the deficiencies of each bearing. Different controllers for the AMB to control the JB instability are examined and compared theoretically and numerically. The possibility of collocating the JB and the AMB is also examined. The results illustrate the effectiveness of the concept. [DOI: 10.1115/1.3078785]

1 Introduction

This paper is about a new concept [1] in load carrying and control of rotating machinery. Journal bearings (JBs) and active magnetic bearings (AMBs) are both excellent bearings for high performance rotating machinery. Actually, JBs and AMBs are two competing bearings in many markets. Both bearings' manufacturers promote their own technology. JB manufacturers promote the large load carrying capacity and high damping in JBs, while AMB manufacturers promote the controllability of the rotor system and the elimination of oil supply. However, both bearings also have their limitations. JBs are limited by the instability mechanism known as oil whirl and oil whip [2,3], while AMBs have lower load capacity and tend to be larger for the same load.

Thus it seems natural to try to combine both bearings in a single bearing concept, where the superior load carrying capacity of JBs is to be exploited along with the controllability characteristics of AMBs that can be used to control the instability of JBs. This will result in a bearing concept with high load carrying capacity with controlled instability and a smaller magnetic bearing that is not carrying any static load while providing the required control [1].

This concept of a combined JB/AMB is studied in this paper to illustrate the success of the concept. In this paper, it is assumed that the JB and the AMB are collocated, whether adjacent or integrated in a single unit. It should be noted that it is possible to integrate the JB within the AMB since the magnetic field can operate through the oil; however, choosing the appropriate clearance is a design issue since the JB requires a smaller clearance than the AMB.

It should be noted that Kasarda et al. [4] recently illustrated experimentally that it is possible to reduce subsynchronous vibration using AMBs. Earlier, Sahinkaya and Burrows [5] studied the possibility of active control of JB instability using a partial eigenstructure assignment method. In this paper, we numerically illustrate the JB instability on a Jeffcott rotor and apply three algorithms for controlling the instability using the AMB, one is based on position feedback, the second is based on acceleration feedback, while the third is designed to introduce more damping to the system. It is shown that the three AMB controllers are effective in controlling the instability of the JB.

2 Journal Bearings

Figure 1 shows a cylindrical journal bearing and the coordinate systems used [6,7]. The film thickness h at any location is given by

$$h = c - e\cos\theta \tag{1}$$

Two frames are shown: the whirling coordinate frame (r,t,z) where θ is measured from the r-axis along the minimum film thickness and the other frame is the stationary (x,y,z) frame and φ is measured from the positive x-axis, and $\theta=\varphi-\psi$, where ψ is the attitude angle. The z-axis is perpendicular to the plane of the paper.

The eccentricity e is the total eccentricity consisting of the static and dynamic eccentricities. The static eccentricity is attained when the externally applied force F is balanced by the pumping action of the journal due to its rotation, while the dynamic one results from disturbances and dynamic forces.

The forces generated in journal bearings are obtained by the solution of Reynolds equation for fluid lubrication, which takes the form

$$\frac{1}{R}\frac{\partial}{\partial\varphi}\left(\frac{h^3}{\mu R}\frac{\partial p}{\partial\varphi}\right)+\frac{\partial}{\partial z}\left(\frac{h^3}{\mu}\frac{\partial p}{\partial z}\right)=-6(e(2\dot{\psi}-\Omega)\sin\theta+2\dot{e}\cos\theta) \tag{2}$$

Using the short bearing approximation for Reynolds' equation using the boundary conditions $p=0$ at $z=\pm L/2$, we get

$$p=\frac{3\mu}{h^3}\left(\frac{L^2}{4}-z^2\right)(e(2\dot{\psi}-\Omega)\sin\theta+2\dot{e}\cos\theta) \tag{3}$$

Integrating the pressure, the forces acting on the journal in the (r,t) frame are obtained as

Contributed by the International Gas Turbine Institute of ASME for publication in the JOURNAL OF ENGINEERING FOR GAS TURBINES AND POWER. Manuscript received August 12, 2008; final manuscript received October 29, 2008; published online September 29, 2009. Review conducted by Patrick S. Keogh. Paper presented at the ASME Turbo Expo 2007: Land, Sea and Air (GT2007), Montreal, QC, Canada, May 14–17, 2007.

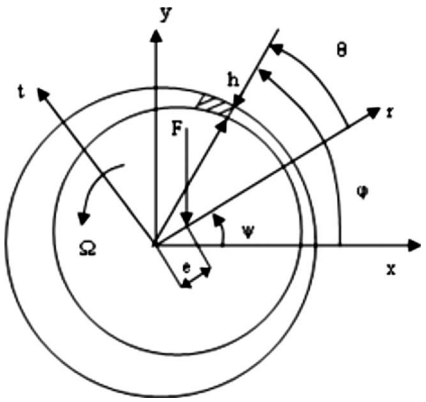

Fig. 1 Coordinate frames

$$\begin{bmatrix} F_r \\ F_t \end{bmatrix} = -\begin{bmatrix} C_{rr} & C_{rt} \\ C_{tr} & C_{tt} \end{bmatrix} \begin{Bmatrix} \dot{e} \\ e\dot{\psi} \end{Bmatrix} - \begin{bmatrix} K_r \\ K_t \end{bmatrix} e \tag{4}$$

The damping and stiffness coefficients are nonlinear functions of the position of the journal bearing and can be written as functions of the integral

$$I_{n^*}^{lm} = \int_{\theta_1}^{\theta_2} \frac{\sin^l \theta \cos^m \theta}{(1 - \varepsilon \cos \theta)^n} d\theta \tag{5}$$

The Gumbel conditions (π-film) for cavitated bearing are applied and for small perturbations about the static equilibrium position $\theta_1 = \pi$ and $\theta_2 = 2\pi$. The integral values are listed in Table 1 as function of the eccentricity ratio ε. Note that $C_{ij} = \mu RL^3/c^3 C_{ij}^*$ and $K_i = \mu\Omega RL^3/c^3 K_i^*$ where the indices i and j take the values r and t.

It can be seen that the damping and stiffness coefficients for the short journal bearing are nonlinear functions of the journal position in the bearing. Now it is more convenient for the dynamic analysis to obtain the coefficients in the x-y stationary frame. By transforming the forces from the rotating r-t frame to the x-y stationary frame the forces therefore become

Table 1 Force coefficients for short journal bearings [6]

	General	π-film
C_{rr}^*	I_3^{02}	$\frac{\pi}{2}\frac{(1+2\varepsilon^2)}{(1-\varepsilon^2)^{5/2}}$
C_{rt}^*	I_3^{11}	$\frac{-2\varepsilon}{(1-\varepsilon^2)^2}$
C_{tr}^*	I_3^{11}	$\frac{-2\varepsilon}{(1-\varepsilon^2)^2}$
C_{tt}^*	I_3^{20}	$\frac{\pi}{2}\frac{1}{(1-\varepsilon^2)^{3/2}}$
K_r^*	$-I_3^{11}/2$	$\frac{\varepsilon}{(1-\varepsilon^2)^2}$
K_t^*	$-I_3^{20}/2$	$-\frac{\pi}{4}\frac{1}{(1-\varepsilon^2)^{3/2}}$

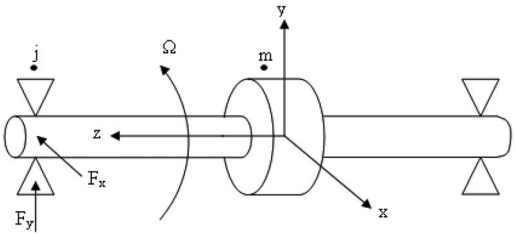

Fig. 2 Jeffcott rotor model

$$\begin{bmatrix} F_x \\ F_y \end{bmatrix} = -\begin{bmatrix} C_{xx} & C_{xy} \\ C_{yx} & C_{yy} \end{bmatrix} \begin{Bmatrix} \dot{x} \\ \dot{y} \end{Bmatrix} - \begin{bmatrix} K_{xx} & K_{xy} \\ K_{yx} & K_{yy} \end{bmatrix} \begin{Bmatrix} x \\ y \end{Bmatrix} \tag{6}$$

where

$$C_{xx} = [C_{rr}\cos^2\psi - (C_{rt} + C_{tr})\sin\psi\cos\psi + C_{tt}\sin^2\psi]$$

$$C_{xy} = [(C_{rr} - C_{tt})\sin\psi\cos\psi + C_{rt}\cos^2\psi - C_{tr}\sin^2\psi]$$

$$C_{yx} = [(C_{rr} - C_{tt})\sin\psi\cos\psi - C_{rt}\sin^2\psi + C_{tr}\cos^2\psi]$$

$$C_{xx} = [C_{rr}\sin^2\psi + (C_{rt} + C_{tr})\sin\psi\cos\psi + C_{tt}\cos^2\psi]$$

$$K_{xx} = K_{yy} = K_r$$

$$K_{xy} = -K_{yx} = -K_t$$

To determine the journal static equilibrium conditions in order to use it as initial conditions when solving numerically, the modified Sommerfeld number is used. It is defined as $S = Fc^2/\mu RL^3\Omega$, or in function of the initial eccentricity ε_o

$$S = \frac{\varepsilon_o}{4(1-\varepsilon_o^2)^2}\sqrt{16\varepsilon_o^2 + \pi^2(1-\varepsilon_o^2)} \tag{7}$$

The static and tangential forces are

$$F_{ro} = -K_r e_o \quad \text{and} \quad F_{to} = -K_t e_o$$

such that the force equilibrium is satisfied

$$F = \sqrt{F_{ro}^2 + F_{to}^2} \quad \text{and} \quad \theta_o = \tan^{-1}\frac{F_{to}}{F_{ro}}$$

Since the applied load is in the direction of negative y-axis, the resultant journal force has to be in the direction of positive y-axis to satisfy equilibrium. Thus, the initial attitude angle ψ_o must have the value of

$$\psi_o = 90 \text{ deg} - \theta_o \tag{8}$$

2.1 Model of a Jeffcott Rotor Suspended on Journal Bearing. The system shown in Fig. 2 consists of a concentrated mass centered on a massless flexible shaft with stiffness k_s rotating at speed Ω [8]. The shaft is suspended on both sides on short journal bearings. Note that the Jeffcott rotor can be considered as representing the first mode of an actual machine that operates above its first critical speed.

Due to system symmetry, the half system is modeled, considering displacements in x-y directions at both the journal j and the center disk of mass m. The journal bearing provides reaction forces F_x and F_y in the x and y directions, respectively, such that

$$k_s \begin{Bmatrix} x_j - x_m \\ y_j - y_m \end{Bmatrix} - \begin{Bmatrix} F_x \\ F_y \end{Bmatrix} = 0$$

Substituting from Eq. (6),

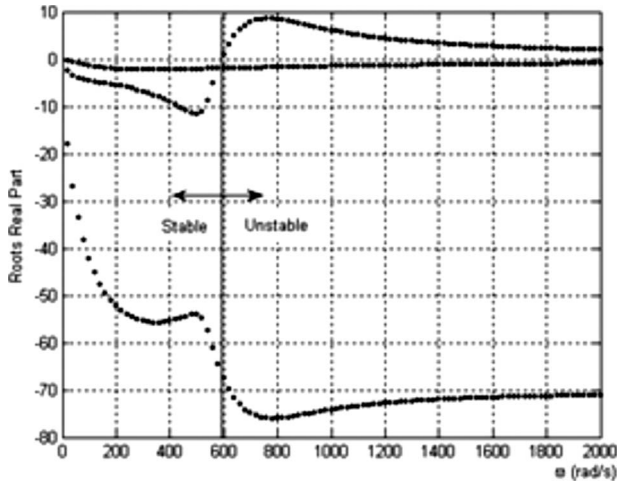

Fig. 3 Root real part

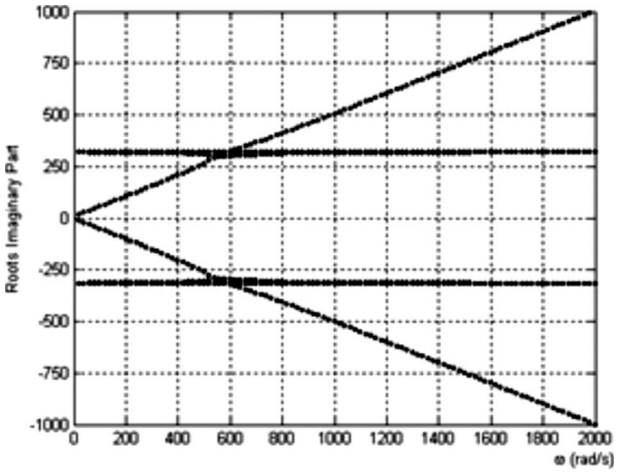

Fig. 4 Root imaginary part

$$k_s\begin{Bmatrix} x_j - x_m \\ y_j - y_m \end{Bmatrix} + \begin{bmatrix} C_{xx} & C_{xy} \\ C_{yx} & C_{yy} \end{bmatrix}\begin{Bmatrix} \dot{x}_j \\ \dot{y}_j \end{Bmatrix} + \begin{bmatrix} K_{xx} & K_{xy} \\ K_{yx} & K_{yy} \end{bmatrix}\begin{Bmatrix} x_j \\ y_j \end{Bmatrix} - k_s\begin{Bmatrix} x_m \\ y_m \end{Bmatrix} + \begin{bmatrix} C_{xx} & C_{xy} \\ C_{yx} & C_{yy} \end{bmatrix}\begin{Bmatrix} \dot{x}_j \\ \dot{y}_j \end{Bmatrix} + \begin{bmatrix} K_{xx} + k_s & K_{yy} \\ K_{yx} & K_{yy} + k_s \end{bmatrix}\begin{Bmatrix} x_j \\ y_j \end{Bmatrix} = 0$$

and re-arranging the equation in the state space form,

$$\begin{Bmatrix} \dot{x}_j \\ \dot{y}_j \end{Bmatrix} = \begin{bmatrix} C_{xx} & C_{xy} \\ C_{yx} & C_{yy} \end{bmatrix}^{-1}\left[-\begin{bmatrix} K_{xx} + k_s & K_{xy} \\ K_{yx} & K_{yy} + k_s \end{bmatrix}\begin{Bmatrix} x_j \\ y_j \end{Bmatrix} + k_s\begin{Bmatrix} x_m \\ y_m \end{Bmatrix}\right] \tag{9}$$

For the center disk, the governing equations are

$$m\ddot{x}_m + c_r\dot{x}_m + k_s(x_m - x_j) = U\cos(\Omega t)$$

$$m\ddot{y}_m + c_r\dot{y}_m + k_s(y_m - y_j) = U\sin(\Omega t) - mg \tag{10}$$

The system equations (9) and (10) can be represented in the state space form, and its dynamic behavior is governed by six simultaneous first order ordinary differential equations that can be solved numerically.

$$u_m = \dot{x}_m$$

$$v_m = \dot{y}_m \tag{11}$$

In order to study the system dynamic response and stability threshold, Eqs. (9)–(11) are solved numerically for short journal bearing having the following characteristics: coefficient of viscosity $\mu = 0.014$ N s/m^2, radial clearance $c = 25$ μm, for a shaft radius of 25.4 mm, and a bearing length $L = 0.015$ m; the bearing length to diameter ratio (L/D) is 0.3, which justifies the application of the short bearing theory.

The suspended shaft has a stiffness $k_s = 1{,}000{,}000$ N/m, mass $m = 10$ kg, and no damping. For these values, the shaft natural frequency is $\omega_n = 316.2$ rad/s (3019.7 rpm).

During simulation, a nondimensional system of equations is used, and the bearing coefficients are calculated at each step to obtain the nonlinear solution. The system eigenvalues are obtained using Taylor linearized coefficients about the static equilibrium position. The root locus map is shown in Figs. 3 and 4; the real part shows the stability limit while the imaginary part shows the system oscillation frequency.

By investigating the real part of the eigenvalues, the stability limit is found to be 594 rad/s (5672.3 rpm), which is about twice the shaft natural frequency [9]. The imaginary part is a pair and conjugate; it has a value of 316.2 rad/s, which is the shaft natural frequency that is speed independent and a speed dependent set of roots.

The stability concept can be demonstrated by plotting the nondimensional orbits for both stable and unstable cases. All displacements in the orbit plot are nondimensionalized by the clearance of the bearing. The upper orbit plots represent displacements at journal j, while the lower orbit plots represent displacements at center disk m. Orbits are represented in 2D plots to show the orbits' shapes and are plotted also with time to show stability.

The stable orbit in Fig. 5 (at $\Omega = 1000$ rpm) has a constant amplitude with time, while the unstable orbit amplitude in Fig. 6 (at $\Omega = 10{,}000$ rpm) enlarges with time until it reaches a limit cycle.

The waterfalls in Figs. 7 and 8 are plotted in order to analyze the dynamic motion dominating frequencies [10]. Figure 7 represents the x displacement at the journal j, while Fig. 8 represents the x displacement at the center disk m. Similar plots can be obtained for y-displacement and are eliminated for brevity.

Figure 8 clearly illustrates the oil whirl and oil whip phenomena. At low speeds a benign oscillation at a frequency less than half the operating speed is self-excited. This is oil whirl. As the speed increases, the oil whirl continues to exist until the rotor reaches its critical speed of about 3020 rpm. Depending on the amount of the unbalance excitation the oil whirl may disappear while the rotor crosses its critical speed, but in this case the unbalance is low enough to have the oil whirl still existing while crossing the critical speed. As the speed of the rotor increases

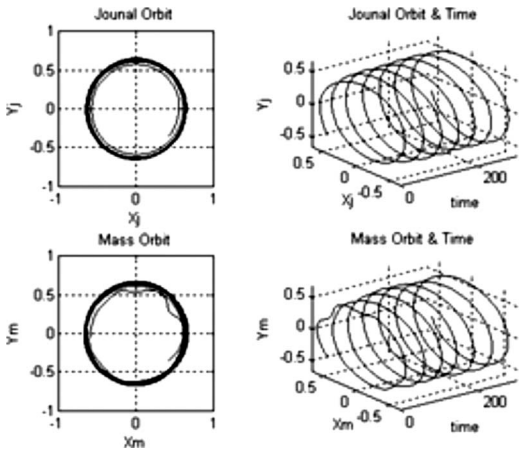

Fig. 5 Stable orbits ($\Omega = 1000$ rpm)

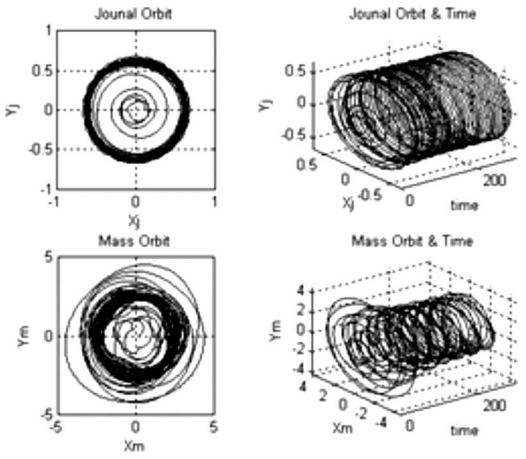

Fig. 6 Unstable orbits (Ω=10,000 rpm)

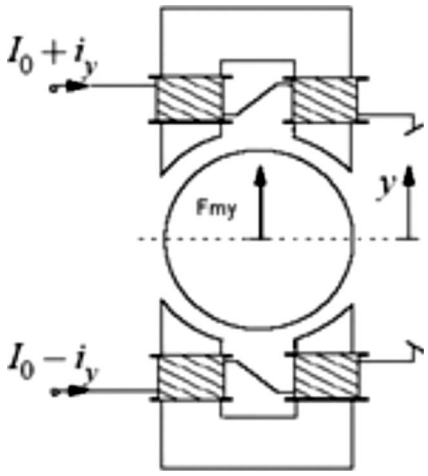

Fig. 9 Mass suspended on a radial AMB

beyond the critical speed the oil whirl at a frequency of about 40% of the running speed still exists until the frequency of the oil whirl reaches the critical speed of the rotor at 5672 rpm and the instability ensues. This is called oil whip [2,3]. The oil whip frequency locks up at the first critical speed as the rotor speed increases and causes violent vibration at the rotor.

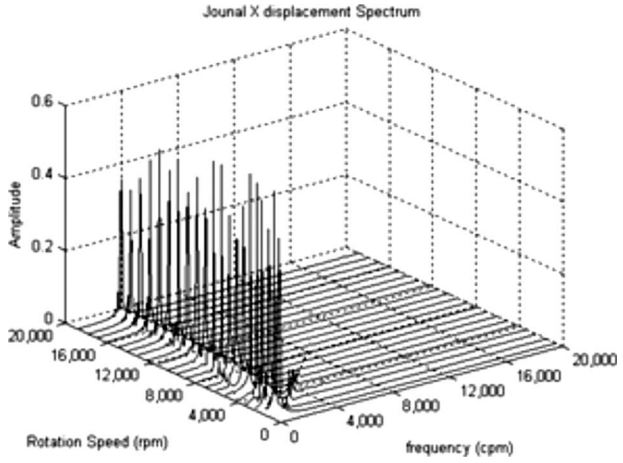

Fig. 7 Journal *X* displacement waterfall

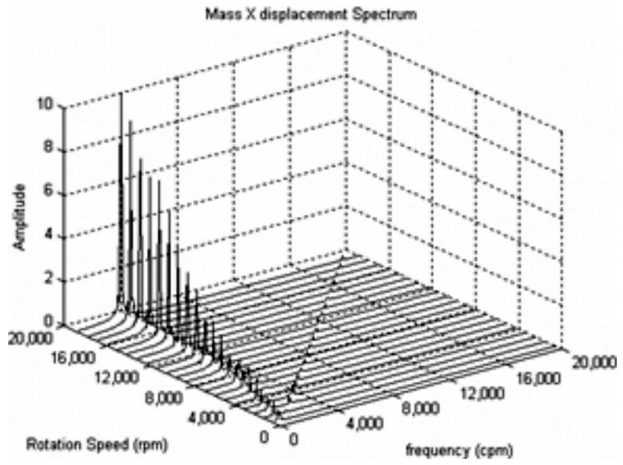

Fig. 8 Center disk *X* displacement waterfall

3 Active Magnetic Bearings

AMB technology has been available for a long period of time. It was used in the 1960s of the last century for turbomolecular pumps and in space for the magnetic suspension of momentum-wheels to control the attitude of satellites. In the late 1970s, it was first used in industrial applications in turbines. Active magnetic bearings represent a suitable solution for some applications. They also provide precise position control and vibration damping.

3.1 Modeling of Mass Suspended on AMB. The AMB is an unstable system. It tends to attract any mass. This instability is modeled by means of negative position stiffness. Different controllers are designed to overcome this instability.

The mass shown in Fig. 9 suspended on AMB can be modeled by Newton's law

$$F_{my} = m\frac{d^2y}{dt^2} \tag{12}$$

The magnetic force F_{my} is nonlinear and depends on the mass position relative to the magnetic core and the current passing through the coils. The nonlinear equation describing the magnetic force can be linearized by means of Taylor expansion in the vicinity of the operating point [11]. This linearization results in two constants: k_p is the negative position stiffness and k_c is the current stiffness; thus, the magnetic force is described by

$$F_{my} = k_p y + k_c i_y \tag{13}$$

Substituting into Eq. (12), the equation governing the mass suspended on AMB becomes

$$k_p y + k_c i_y = m\frac{d^2y}{dt^2} \tag{14}$$

The bearing constants used in this paper have the following values: $k_p = 1 \times 10^6$ N/m, and $k_c = 100$ N/A.

4 Controlling Journal Bearing Instability

JB good load carrying capacity characteristics are limited by their stability threshold condition. In order to extend these good capabilities above the stability limit, AMB is utilized to eliminate JB instabilities and to increase its range of operation [1].

JB instability is controlled by applying external forces through AMB that are equivalent to the JB undesired forces but in the opposite direction, thus removing these forces.

These external forces are proportional to the current passing in the magnetic bearing coils. The required current value is deter-

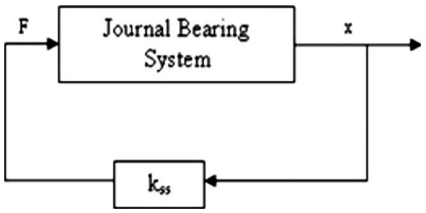

Fig. 10 Position feedback

mined depending on the controller type. In this model, both bearings are collocated, i.e., the magnetic force point of action is the same as the journal bearing one.

Three controllers are examined. In controller 1, the current is determined by measuring the journal position. On the other hand, the current in controller 2 is estimated to be proportional to the journal acceleration. The current estimation process is established for both the x and y directions. Controller 3 is a different concept, where damping is added to the system through the feedback.

This JB/AMB hybrid system equation can be derived as follows:

$$k_s \begin{Bmatrix} x_j - x_m \\ y_j - y_m \end{Bmatrix} - \begin{Bmatrix} F_x \\ F_y \end{Bmatrix} + \begin{Bmatrix} F_{mx} \\ F_{my} \end{Bmatrix} = 0$$

Recalling Eqs. (6) and (13),

$$k_s \begin{Bmatrix} x_j - x_m \\ y_j - y_m \end{Bmatrix} - \begin{bmatrix} C_{xx} & C_{xy} \\ C_{yx} & C_{yy} \end{bmatrix} \begin{Bmatrix} \dot{x}_j \\ \dot{y}_j \end{Bmatrix} - \begin{bmatrix} K_{xx} & K_{xy} \\ K_{yx} & K_{yy} \end{bmatrix} \begin{Bmatrix} x_j \\ y_j \end{Bmatrix} + k_p \begin{Bmatrix} x_j \\ y_j \end{Bmatrix} + k_c \begin{Bmatrix} i_x \\ i_y \end{Bmatrix} = 0$$

$$- k_s \begin{Bmatrix} x_m \\ y_m \end{Bmatrix} - \begin{bmatrix} C_{xx} & C_{xy} \\ C_{yx} & C_{yy} \end{bmatrix} \begin{Bmatrix} \dot{x}_j \\ \dot{y}_j \end{Bmatrix} - \begin{bmatrix} K_{xx} + k_s - k_p & K_{xy} \\ K_{yx} & K_{yy} + k_s - k_p \end{bmatrix} \begin{Bmatrix} x_j \\ y_j \end{Bmatrix} + k_c \begin{Bmatrix} i_x \\ i_y \end{Bmatrix} = 0$$

and re-arranging the equation in the state space form,

$$\begin{Bmatrix} \dot{x}_j \\ \dot{y}_j \end{Bmatrix} = \begin{bmatrix} C_{xx} & C_{xy} \\ C_{yx} & C_{yy} \end{bmatrix}^{-1} \left[- \begin{bmatrix} K_{xx} + k_s - k_p & K_{xy} \\ K_{yx} & K_{yy} + k_s - k_p \end{bmatrix} \begin{Bmatrix} x_j \\ y_j \end{Bmatrix} + k_s \begin{Bmatrix} x_m \\ y_m \end{Bmatrix} + k_c \begin{Bmatrix} i_x \\ i_y \end{Bmatrix} \right] \tag{15}$$

Equation (15) represents the JB/AMB hybrid system, while current (i_x, i_y) estimation depends on the controller type.

4.1 Controller 1: Position Feedback Controller. By investigating the journal bearing damping and stiffness matrices, the nonconservative component of the damping matrix is stabilizing the system, while the stiffness matrix can be decomposed into a symmetric k_s conservative part and a skew-symmetric k_{ss} part, which is responsible for exciting the instability [12,13]. The system can be stabilized by eliminating the skew-symmetric part of the stiffness matrix.

This is achieved by position feedback and the feedback constant is the skew-symmetric part of the stiffness matrix.

The idea is first proved on a simple system consisting of a rigid rotor suspended on a journal bearing.

The idea is illustrated in Fig. 10.

The rigid rotor suspended on the journal bearing is modeled as follows:

$$\begin{bmatrix} m & 0 \\ 0 & m \end{bmatrix} \begin{Bmatrix} \ddot{x} \\ \ddot{y} \end{Bmatrix} + \begin{bmatrix} C_{xx} & C_{xy} \\ C_{yx} & C_{yy} \end{bmatrix} \begin{Bmatrix} \dot{x} \\ \dot{y} \end{Bmatrix} + \begin{bmatrix} K_{xx} & K_{xy} \\ K_{yx} & K_{yy} \end{bmatrix} \begin{Bmatrix} x \\ y \end{Bmatrix} = 0$$

$$M\{\ddot{x}\} + C\{\dot{x}\} + K\{x\} = 0 \tag{16}$$

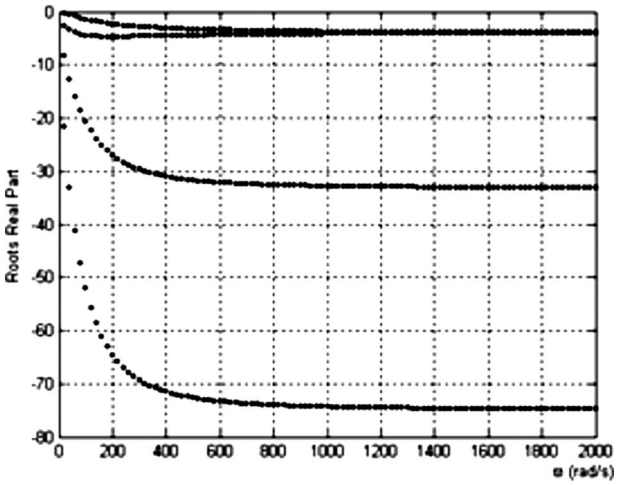

Fig. 11 Stability map

The stiffness matrix is decomposed as follows:

$$K = k_s + k_{ss}$$

where

$$k_s = (K + K')/2$$

$$k_{ss} = (K - K')/2$$

Adding the controller yields

$$M\{\ddot{x}\} + C\{\dot{x}\} + K\{x\} = k_{ss}\{x\} \tag{17}$$

The feedback k_{ss} matrix can be realized from the controller by means of the controlled currents

$$\begin{Bmatrix} i_x \\ i_y \end{Bmatrix} = \begin{bmatrix} 0 & -C_p \\ -C_p & 0 \end{bmatrix} \begin{Bmatrix} x \\ y \end{Bmatrix} \tag{18}$$

Therefore

$$k_{ss} = k_c \begin{Bmatrix} i_x \\ i_y \end{Bmatrix} = -k_c C_p \begin{Bmatrix} y \\ x \end{Bmatrix} \tag{19}$$

As obvious, the k_{ss} feedback matrix depends on both k_c that is an AMB constant and C_p, which is the controller feedback gain that can be tuned to obtain the desired feedback gain.

4.2 Jeffcott Rotor Suspended on Journal Bearing and Controlled With Position Feedback. The AMB currents are calculated by measuring the journal position

$$\begin{Bmatrix} i_x \\ i_y \end{Bmatrix} = -C_p \begin{Bmatrix} y_j \\ x_j \end{Bmatrix} \tag{20}$$

Substituting into Eq. (15), the JB/AMB hybrid system governing equation is

$$\begin{Bmatrix} \dot{x}_j \\ \dot{y}_j \end{Bmatrix} = \begin{bmatrix} C_{xx} & C_{xy} \\ C_{yx} & C_{yy} \end{bmatrix}^{-1} \left[- \begin{bmatrix} K_{xx} + k_s - k_p & K_{xy} - k_c C_p \\ K_{yx} - k_c C_p & K_{yy} + k_s - k_p \end{bmatrix} \begin{Bmatrix} x_j \\ y_j \end{Bmatrix} + k_s \begin{Bmatrix} x_m \\ y_m \end{Bmatrix} \right] \tag{21}$$

The system response is simulated by Eqs. (10), (11), and (21).

The system stability map is plotted using Taylor linearized coefficients to examine its stability [14] over the required speed range. Figure 11 shows that the system is stable. It is clear also that after a certain range ($\Omega = 500$ rad/s), the system eigenvalues tend to a constant value and become independent of the shaft rotation speed. The controller is able to remove the system instability.

Figure 12 shows the controller effect in controlling the instabil-

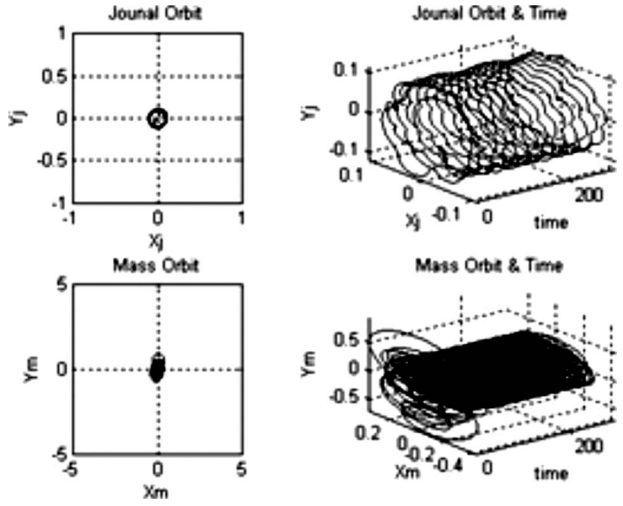

Fig. 12 Controlled orbit (Ω=10,000 rpm)

ity where the unstable orbit in Fig. 6 is replotted after using the controller, using the same scale. It can be seen that the controller succeeded in controlling the instability.

The waterfalls in Figs. 13 and 14 are plotted in order to analyze the dynamic motion frequencies of the rotor system with the controller. It can be seen that the controller was successful in control-

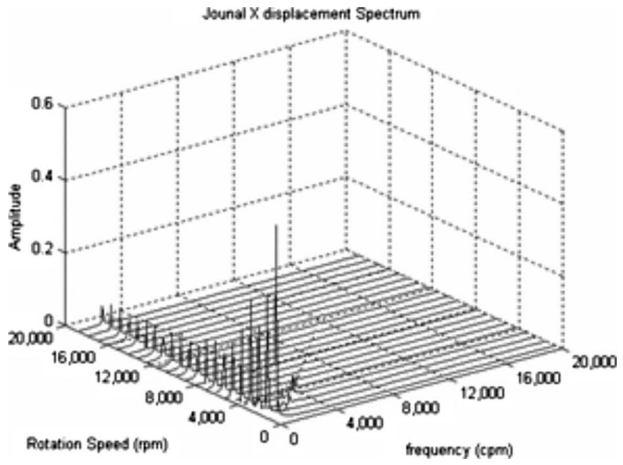

Fig. 13 Journal *X* displacement waterfall

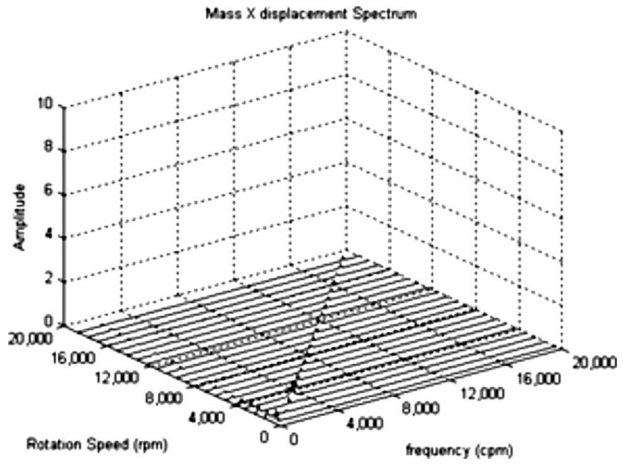

Fig. 14 Center disk *X* displacement waterfall

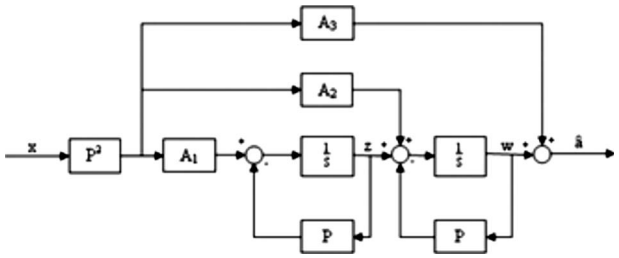

Fig. 15 Block diagram of the acceleration observer

ling the instability of both the oil whirl and oil whip. However, a low frequency component was introduced by the position feedback at the journal location. This component could not be eliminated by varying the gain of the controller.

Moreover, it should be mentioned that with this controller it was possible to control the instability with only selected values for the controller gain. Higher or lower values of the controller gain did not achieve the objective of controlling the instability.

4.3 Controller 2: Acceleration Feedback Controller. In order to generate the necessary current, JB forces are estimated by estimating the acceleration from the journal displacement using an observer structure. The current applied through AMB is proportional to the estimated acceleration; this provides the required forces proportional and opposite to those excited by the JB.

4.4 Acceleration Estimator. Acceleration is estimated by applying the force observer theory based on the journal displacement measurement [15]. The problem in obtaining acceleration from displacements that double differentiation is required, which is not preferred as noise at high frequency, is amplified.

The advantage of this estimator is that acceleration is obtained without any differentiation; rather acceleration is obtained in terms of integrator output variables, thus eliminating the noise problem.

The estimator is expressed mathematically as

$$\ddot{x} + 2\xi\omega_n\dot{x} + \omega_n^2 x = -C_a k_i \hat{a}/m \tag{22}$$

Taking the Laplace transform to obtain the acceleration observer (AO) transfer function,

$$\hat{a}(S)/x(S) = S^2 + 2\xi\omega_n S + \omega_n^2 \tag{23}$$

A low pass filter is added to remove undesired noise above a determined frequency. In this controller, the cut off frequency is suggested to be equal to the shaft rotation frequency ($P=\Omega$).

$$\hat{a}(S)/x(S) = [P^2/(S+P)^2](S^2 + 2\xi\omega_n S + \omega_n^2) \tag{24}$$

The AO can be represented by the following three equations:

$$\dot{z} = -Pz + P^2 A_1 x$$

$$w = Pw + P^2 A_2 x + z$$

$$\hat{a} = P^2 A_3 x + w \tag{25}$$

The AO can also be represented in the form of a block diagram, as shown in Fig. 15.

Comparing Eq. (25) and the AO transfer function, the AO constants are determined as

$$A_1 = \omega_n^2 + P^2 - 2P\xi\omega_n$$

$$A_2 = 2\xi\omega_n - 2P$$

$$A_3 = 1 \tag{26}$$

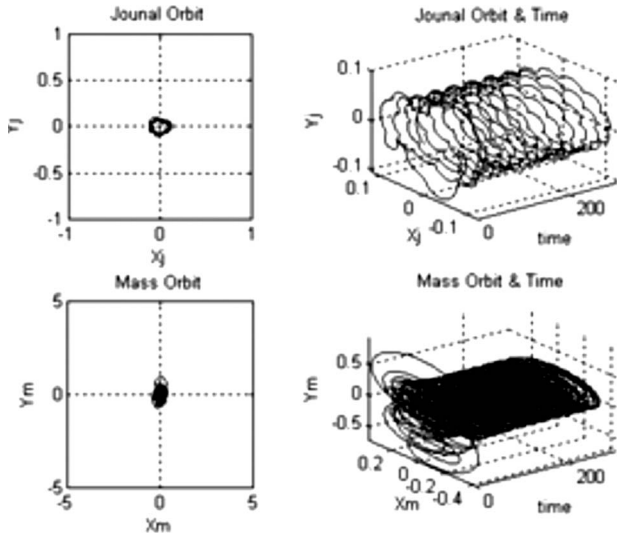

Fig. 16 Controlled orbit (Ω=10,000 rpm)

4.5 Jeffcott Rotor Suspended on Journal Bearing and Controlled With Acceleration Feedback. The AMB currents are proportional to the accelerations estimated from the displacement using the acceleration estimator described by Eq. (22).

$$\begin{Bmatrix} i_x \\ i_y \end{Bmatrix} = -C_a \begin{Bmatrix} \hat{a}_y \\ \hat{a}_x \end{Bmatrix} \tag{27}$$

Substituting into Eq. (15), the JB/AMB hybrid system governing equation is

$$\begin{Bmatrix} \dot{x}_j \\ \dot{y}_j \end{Bmatrix} = \begin{bmatrix} C_{xx} & C_{xy} \\ C_{yx} & C_{yy} \end{bmatrix}^{-1} \left[-\begin{bmatrix} K_{xx}+k_s-k_p & K_{xy} \\ K_{yx} & K_{yy}+k_s-k_p \end{bmatrix} \begin{Bmatrix} x_j \\ y_j \end{Bmatrix} + k_s \begin{Bmatrix} x_m \\ y_m \end{Bmatrix} - k_i C_a \begin{Bmatrix} \hat{a}_y \\ \hat{a}_x \end{Bmatrix} \right] \tag{28}$$

The system response is simulated by Eqs. (10), (11), (25), and (28).

Figure 16 shows the controller effect in controlling the instability where the unstable orbit in Fig. 6 is replotted after using the controller, using the same scale. It can be seen that the controller succeeded in controlling the instability.

The waterfalls in Figs. 17 and 18 are plotted in order to analyze the motion dominating frequencies.

Again it is seen that the acceleration feedback controller was quite successful in controlling both oil whirl and oil whip and nearly completely eliminating the instability. However, this controller introduced a static component at the journal that was even seen at the mass. Changing the gains, it was not possible to eliminate this static component; however, the static component magnitude depends on the gain value.

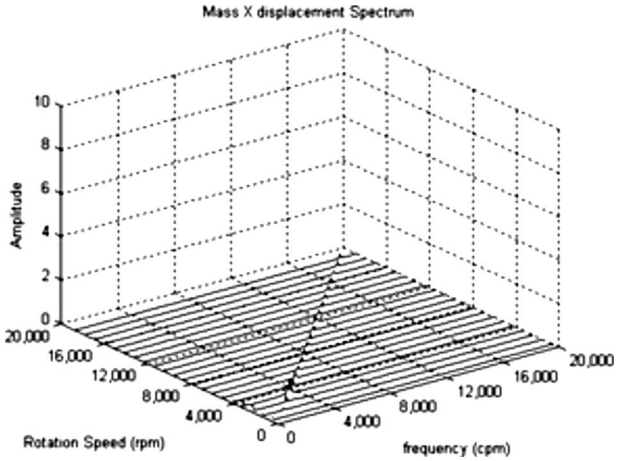

Fig. 18 Center disk *X* displacement waterfall

4.6 Controller 3: Damping Controller. Another strategy is investigated in this controller. AMB is used to add damping to the system. The AMB controlling current is obtained by the following equation:

$$\begin{Bmatrix} i_x \\ i_y \end{Bmatrix} = -C_v \begin{Bmatrix} \dot{x}_j \\ \dot{y}_j \end{Bmatrix} - C_p \begin{Bmatrix} x_j \\ y_j \end{Bmatrix} \tag{29}$$

Substituting into Eq. (15),

$$\begin{Bmatrix} \dot{x}_j \\ \dot{y}_j \end{Bmatrix} = \begin{bmatrix} C_{xx}+k_c C_v & C_{xy} \\ C_{yx} & C_{yy}+k_c C_v \end{bmatrix}^{-1} \times \left[-\begin{bmatrix} K_{xx}+k_s-k_p-k_c C_p+k_c C_p & K_{xy} \\ K_{yx} & K_{yy}+k_s-k_p+k_c C_p \end{bmatrix} \times \begin{Bmatrix} x_j \\ y_j \end{Bmatrix} + k_s \begin{Bmatrix} x_m \\ y_m \end{Bmatrix} \right] \tag{30}$$

The system response is simulated by Eqs. (10), (11), and (30). Figure 19 shows the controller effect in controlling the instability where the unstable orbit in Fig. 6 is replotted after using the

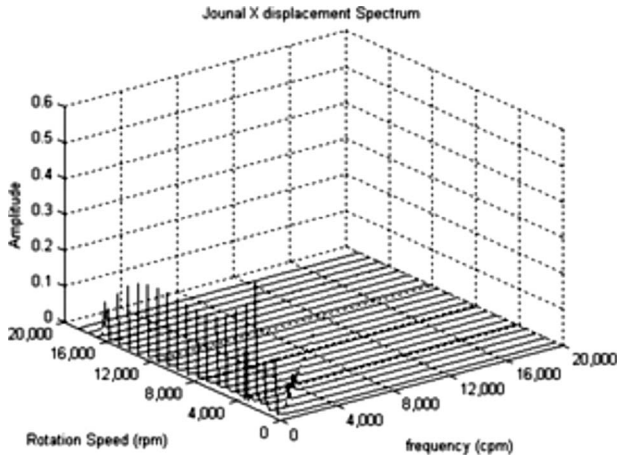

Fig. 17 Journal *X* displacement waterfall

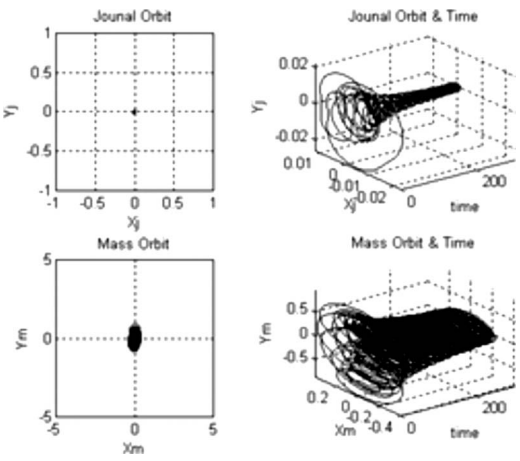

Fig. 19 Controlled orbit (Ω=10,000 rpm)

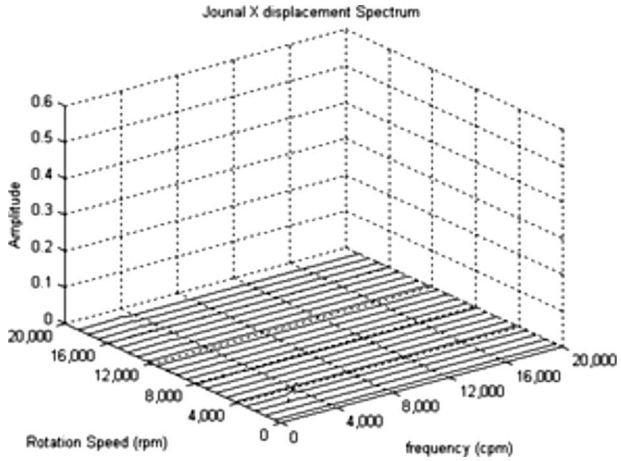

Fig. 20 Journal *X* displacement waterfall

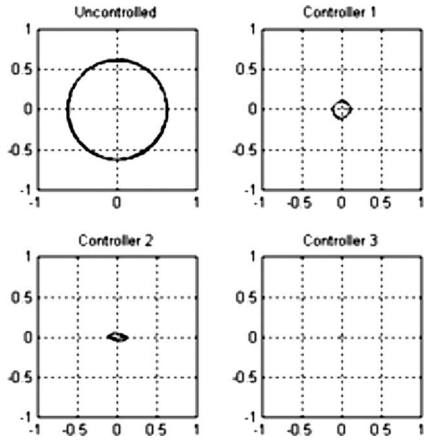

Fig. 22 Journal steady state orbit (Ω=10,000 rpm)

controller, using the same scale.

It can be seen that the controller succeeded in controlling the instability. The waterfalls in Figs. 20 and 21 are plotted in order to analyze the dynamic motion dominating frequencies. It can be seen that by far the damping controller provided the best control, and it actually should the most robust behavior in its design.

4.7 Comparison Between the Three Controllers. Figures 22 and 23 and Table 2 show the steady state orbit results for the rotor-journal bearing system without control and with the three controllers. It can be seen that the three controllers were able to control the instability.

Controller 3 with damping control is seen to achieve the best results. Moreover, the authors feel that it was the easiest to design and is actually the one with no apparent robustness issues.

5 Conclusions

This paper illustrated the concept of using the AMB to control the JB instability. The basic idea is quite simple: Rather than using the AMB as a load carrying element, the AMB is used as a controller only, resulting in a much smaller and more efficient AMB. The load carrying is done by the journal bearings, exploiting their excellent load carrying capabilities, and the JB instability is overcome with the AMB. This results in a combined AMB/JB that exploits the advantages of each device and eliminates the deficiencies of each bearing. The combined AMB/JB system can thus be used to carry larger loads and operate at higher speeds. If the well known capabilities of AMB control are also added to the system such as unbalance cancellation and integrating feedback, a much improved device would be developed.

The possibility of controlling the JB instability using AMBs has been shown in this paper to be successful. Three controllers have been applied to the combined AMB/JB system. All three controllers show efficiency in controlling the JB instability. The first controller is a position controller that controls the journal position in the bearing; the second controller is an acceleration controller where it controls the unstable dynamic forces through the estimated acceleration, while the third controller is a damping controller. The best performance was achieved with the damping controller.

Further investigations should be carried out to optimize the controllers' parameters [16] as well as considerations of combining the unbalance control and integrating feedback with the stability control in the AMB as well as study the different possibilities in locating the AMB relative to the JB position.

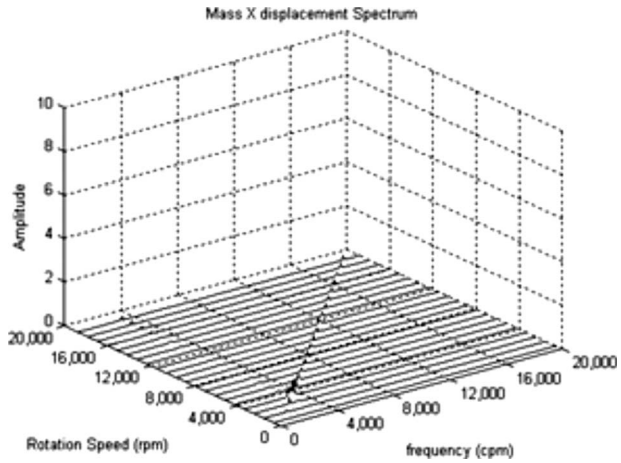

Fig. 21 Center disk *X* displacement waterfall

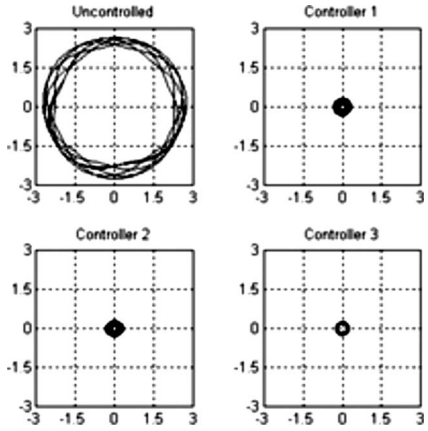

Fig. 23 Center disk steady state orbit (Ω=10,000 rpm)

Table 2 Orbit steady state amplitudes

	Journal amplitude	Reduction (%)	Center disk amplitude	Reduction (%)
Uncontrolled	0.62	- - - -	2.67	- - - -
Controller 1	0.11	82	0.33	88
Controller 2	0.05	92	0.29	89
Controller 3	0.002	99	0.26	90

Nomenclature

h = oil film thickness
c = journal bearing radial clearance
e = journal bearing eccentricity
ε = eccentricity ratio (e/c)
R = journal bearing radius
L = journal bearing length
μ = oil viscosity
p = pressure
x_m, y_m = center disk x-y displacements
x_j, y_j = journal x-y displacements
F_r, F_t = journal bearing reactions in r-t directions
F_x, F_y = journal bearing reactions in x-y directions
F_{mx}, F_{my} = magnetic bearing forces in x-y directions
m = center disk mass
k_s = shaft stiffness
c_r = damping in rotor
ω_n = shaft natural frequency
ζ = shaft damping ratio
U = shaft unbalance force
Ω = shaft rotation speed
$\ddot{x}$, $\dot{x}$, and x = acceleration, velocity, and displacement of the mass, respectively
C_p = position feedback gain
C_a = acceleration feedback gain
C_v = velocity feedback gain
i_x, i_y = magnetic bearing control currents in x-y directions
k_c = magnetic bearing current stiffness
k_p = magnetic bearing negative $(-)$ position stiffness
$\hat{a}$ = estimated acceleration
P = low pass filter cut off frequency
S = Laplace variable

References

[1] El-Shafei, A., Patent, pending.
[2] El-Shafei, A., Tawfick, S. H., Raafat, M. S., and Aziz, G., 2007, "Some Experiments on Oil Whirl and Oil Whip," ASME J. Eng. Gas Turbines Power, **129**(1), pp. 144–153.
[3] Crandall, S. H., 1995, "The Instability Mechanism Responsible for Oil Whirl and Oil Whip," *Proceedings of the Fourth Greek National Congress on Mechanics*, Democritus University of Thrace, Xanthi.
[4] Kasarda, M. E. F., Kirk, R. G., and Mendoza, H., 2005, "An Experimental Investigation of the Effect of an Active Magnetic Damper on Reducing Sub-Synchronous Vibrations in Rotating Machinery," *Proceedings of the GT, ASME Turbo Expo*, Reno-Tahoe, NV.
[5] Sahinkaya, M. N., and Burrows, C. R., 1985, "Control of Stability and the Synchronous Vibration of a Flexible Rotor Supported on Oil-Film Bearings," ASME J. Dyn. Syst., Meas., Control, **107**, pp. 139–144.
[6] El-Shafei, A., 1994, "Insights Into the Static and Dynamic Characteristics of Journal Bearings," *Proceedings of the Fourth IFToMM International Conference on Rotordynamics*, pp. 307–315.
[7] El-Shafei, A., 1995, "Modeling Fluid Inertia Forces of Short Journal Bearings for Rotordynamic Applications," ASME J. Vibr. Acoust., **117**, pp. 462–469.
[8] Crandall, S. H., 1996, "Velocity Linearization of the Dynamic Response of Journal Bearings," *Proceedings of the EUROMECH—Second European Nonlinear Oscillation Conference*, Prague, Sept. 9–13.
[9] Lee, C.-W., 1993, *Vibration Analysis of Rotors*, Kluwer, Dordrecht.
[10] Newland, D. E., 1993, *An Introduction to Vibrations, Spectral and Wavelet Analysis*, 3rd ed., Prentice Hall, New York.
[11] Polajzer, B., 2003, "Design and Analysis of an Active Magnetic Bearing Experimental System," Ph.D. thesis, Maribor University, Maribor, Slovenia.
[12] Adams, M. L., and Padovan, J., 1981, "Insights Into Linearized Rotor Dynamics," J. Sound Vib., **76**(1), pp. 129–142.
[13] Adams, M. L., 1987, "Insights Into Linearized Rotor Dynamics, Part 2," J. Sound Vib., **112**(1), pp. 97–110.
[14] Maslen, E. H., and Bielk, J. R., 1992, "A Stability Model for Flexible Rotors With Magnetic Bearings," ASME J. Dyn. Syst., Meas., Control, **114**, pp. 172–175.
[15] Chen, H. M., and Darlow, M. S., 1988, "Magnetic Bearings With Rotating Force Control," ASME J. Tribol., **110**, pp. 100–105.
[16] Allaire, P. E., and Humphris, R. R., 1986, "Effect of Control Algorithms on Magnetic Journal Bearing Properties," ASME J. Eng. Gas Turbines Power, **108**, pp. 624–632.

Loïc Salles
École Centrale de Lyon,
Laboratoire de Tribologie et Dynamique des Systèmes,
36 Avenue Guy de Collongue,
69134 Ecully Cedex, France;
Snecma—Safran Group,
77550 Moissy-Cramayel, France;
Moscow State University of Technology Named After Bauman,
Moscow 105005, Russia
e-mail: loic.salles@ec-lyon.fr

Laurent Blanc

Fabrice Thouverez

École Centrale de Lyon,
Laboratoire de Tribologie et Dynamique des Systèmes,
36 Avenue Guy de Collongue,
69134 Ecully Cedex, France

Alexander M. Gouskov
Moscow State University of Technology Named After Bauman,
Moscow 105005, Russia

Dynamic Analysis of Fretting-Wear in Friction Contact Interfaces

Fretting wear is a very important phenomenon occurring in bladed disks. It causes the blades to be replaced in turbomachines during their life-cycle. Methods exist to predict fretting-wear in quasistatic analysis. However, they do not predict all the phenomena observed in blade attachments on real turbomachines. That is why this study assumes that dynamics plays a role in fretting-wear. This paper is devoted to the realistic modeling and calculation of fretting-wear and dynamical response of structures in unilateral contact with friction. Vibration and wear phenomena present very different scales both in time and space. Therefore the difficulty is in finding methods that enable one to solve the nonlinear problem with a good compromise between the approximations made about the dynamical aspects and those linked with fretting-wear issues. Here, phenomenological examples are studied. They involve a small number of degrees of freedom with a view to understanding the complex coupling between vibration and fretting-wear. This way, they will show the relative importance of parameters. [DOI: 10.1115/1.3028229]

1 Introduction

One of the most important sources of nonlinearities in turbine is due to contact with friction at the interfaces. These nonlinearities often have a positive aspect because they introduce damping in the vibrational response. Especially, designers can put friction dampers as underplatform damper, ring damper, impact damper, etc., to reduce the amplitude of resonances. But relative displacements at the interface have a damaging aspect since fretting-wear can appear and induce cracking. Recent studies [1,2] permit us to calculate the vibrational response of bladed disks in the presence of friction in blade attachments. They can predict the dissipated energy at the interfaces. On the other hand, most fretting-wear studies in blade roots are performed in quasistatic situations. Thus, in the case of planes, they only calculate [3] or test [4] the take-off or landing situations. Nevertheless, dynamic wear can also occur when vibrations appear at a cruising rate. In quasistatic situations, displacements are more important compared with dynamic situations. But in this latter case, in spite of the fact that only microslidings are observed, they are repeated during a much longer time. Current numerical modeling does not match with the real wear observed in turbomachinery. That is why this study assumes that dynamics plays a role in fretting-wear. Because of the complexity it introduces, this hypothesis is very seldom taken into account in literature [5,6].

Wear is a very complex phenomenon because hardness, plasticity, grain structure, temperature, etc., can change wear debris creation. According to Ref. [7] around 180 laws of wear have been proposed. Recently, a new model based on dissipated energy has been proposed to quantify wear directly [8]. To quantify wear, Archard's model [9] is the most commonly used. It considers the wear volume is linked to the product of the normal force and of the sliding displacement. Classically, wear coefficient quantification is then performed through the representation of the evolution of the worn volume as a function of the normal load. The loss of matter can be known through the measurement of the loss of mass, the loss of dimensions, the evolution of Vickers microhardness imprints, or directly by surface profilometry. This model will be used in this paper. Hardness will be considered constant. The plasticity of the material will be neglected.

Different numerical approaches exist to compute wear on structures. The most common one is the finite element method (FEM) [10,11]. This tool is efficient to compute wear but it is necessary to create a very fine meshing to calculate contact normal forces. Because mesh updating is necessary to take wear into account, calculations are time consuming. A smart and more economical method is based on Winkler's foundation to predict wear [12]. Semi-analytical or boundary element methods have been also developed to predict wear [3,13]. The method of Gallego et al. [3] is an acceleration technique that efficiently improves the convergence rate. But these methods are difficult to use when the problem of contact with friction takes dynamics effects into account. In this paper we will introduce an approach based on the FEM to predict wear in dynamics. The main assumption is that a periodic steady state is reached and that wear will modify this state a little. Thus, it is possible to use methods based on multiharmonic balance and alternate frequency-time procedures [14–16].

Here, the dynamical behavior of two structures in contact with friction and wear is investigated. To start with, a simple system with two degrees of freedom is treated numerically. It will enable one to understand the phenomena coupling wear and dynamics. In case of total slip, it would be possible, to a certain extent, to uncouple the dynamics analysis and the fretting-wear calculation. In the family of cases treated here, wear provokes the relaxation of the normal pressure, inducing strong coupling. On bladed disks,

Manuscript received April 18, 2008; final manuscript received May 6, 2008; published online September 30, 2009. Review conducted by Dilip R. Ballal.

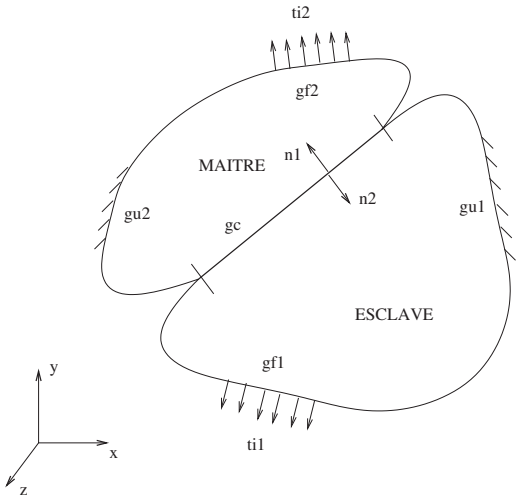

Fig. 1 Description of the problem of contact between two solids

this phenomenon occurs especially under partial slip conditions, as shown in Ref. [17]. The final purpose will be to apply the method introduced here to a more realistic bladed disk.

2 Method of Analysis

2.1 Equations of Motion and Wear: Variational Formulation. Let us consider the case of two elastic solids in contact with friction, Fig. 1. Both solids occupy two distinct domains Ω^l with smooth boundaries $\partial\Omega^l$. The boundary $\partial\Omega^l$ is divided into three disjoint parts Γ_t^l, Γ_u^l, and Γ_c. Traction forces are imposed on the first part of the boundary, displacements on the second, and contact conditions on the third part of the surface. This part of the body is unilaterally constrained in the direction normal to the surface and Coulomb's Law constrains the tangential directions. Moreover the wear phenomena occur on this part of the body. Following the formalism described by Stromberg [18], let us build the constitutive equations for an elastic body with a contact interface in situation of fretting-wear. This formalism introduces a free energy and a pseudopotential, which correspond to Signorini unilateral contact conditions, Coulomb's Law of friction, and Archard's Law of wear ((4)). The details about the way to obtain these free energy and pseudopotential can be found in Refs. [18,19]. It originates from the works of Lemaître and Chaboche [20]. In this paper we will only present the variational formulation associated with the dynamical fretting-wear problem.

For each domain Ω^l, on a time interval $[0,T]$, find $u:[0,T] \to \mathcal{V}$, $\mathcal{W}=p_N:[0,T]\to\mathcal{K}_N$, and $p_T:[0,T]\to\mathcal{F}(P_N)$ such that for each time $t\in[0,T]$,

$$\int_\Omega \rho\ddot{u}_i v_i dV + \int_\Omega E_{ijkl}\frac{\partial u_k}{\partial x_l}\frac{\partial v_i}{\partial x_j}dV + \int_{\Gamma_c} p_i v_i dA - \int_{\Gamma_t} t_i v_i dA = 0, \quad \forall \mathbf{v} \in \mathcal{V} \tag{1}$$

$$\int_{\Gamma_c} (u_N - w - g)(p'_N - p_N)dA \le 0, \quad \forall p'_N \in \mathcal{K}_N \tag{2}$$

$$\int_{\Gamma_c} \dot{u}_{T_\alpha} + (p'_{T_\alpha} - p_{T_\alpha}) + \dot{w}(\mathcal{W}' - \mathcal{W})dA \le 0, \quad \forall (p'_T, \mathcal{W}') \in \mathcal{F}(p_N) \tag{3}$$

$$\dot{w} = k_w |p_N| \|\dot{\mathbf{u}}_T\| \tag{4}$$

where

$$\mathcal{V} = \{\mathbf{v} | \mathbf{v}(\mathbf{x}) = 0, \mathbf{x} \in \Gamma_u\}$$

$$\mathcal{K}_N = \{p_N | p_N(\mathbf{x}) \ge 0, \mathbf{x} \in \Gamma_c\}$$

$$\mathcal{F}(p_N) = \{(\mathbf{p}_T, \mathcal{W}) | (\mathbf{p}_T(\mathbf{x}), \mathcal{W}(\mathbf{x})) \in F(p_N), \mathbf{x} \in \Gamma_c\}$$

These equations are, respectively, the principle of virtual work, the equivalent formulation of Signorini's unilateral contact conditions, and the inequality defining the complementary law of Coulomb's and the law of wear. $[0,T]$ represents the studied period, $\mathcal{W}$ is the dual of w, $F(p_N)$ is a closed convex set describing the friction and the wear limit criterion such that $F(p_N)=\{\|\boldsymbol{p}_T\| - \mu|p_N| + k_w p_N \mathcal{W} - k_w p_N^2 \le 0\}$, and k_w is coefficient of wear in Archard's Law. $_Kw$ must be determined experimentally. Mccoll et al. [10] determined an averaged wear coefficient from the measured wear profile for a cylinder/flat contact. He integrated this averaged coefficient in discretized Archard's Law and simulated wear evolution in a "wear box" (FEM). In our case evaluation of averaged wear coefficient can be performed for a punch plan contact. This coefficient needs to be discretized to the nodes in contact in finite element discretization.

2.2 Finite Element Discretization. The numerical discretization of Eq. (1) is based on the FEM. In the case of a dynamical study, a component mode synthesis can be coupled with the FEM. However, all the degrees of freedom where friction and wear take place must then be retained as physical coordinates. When both structures ($l=1,2$) are in contact, we can write the equations of motion for each structure as

$$\mathbf{M}\ddot{U}^{(l)} + \mathbf{C}\dot{U}^{(l)} + \mathbf{K}U^{(l)} + F_c^{(l)}(U^{(l)}, \dot{U}^{(l)}, W^{(l)}) = \boldsymbol{F}_{\text{ex}}^{(l)} \tag{5}$$

$\boldsymbol{F}_{\text{ex}}$ is the vector of external forces (periodic excitation at frequency ω) and F_c represents the nonlinear contact forces due to friction and impact. They also depend on the wear and on the materials in contact. The equation of wear (Archard's Law), which is continuous, is also discretized by FEM. Wear is calculated at the nodes (marked M) of the interface as follows:

$$\dot{\boldsymbol{w}}^M = \frac{k_w}{I^M}|P_N^M| \|\dot{\boldsymbol{U}}_T^M\| \tag{6}$$

I^M are the weighting factors for each node M, P_N is the nodal normal force, and $\dot{\boldsymbol{U}}_T^M$ is the tangential velocity of the node M. The constraints introduced by Signorini's contact conditions and Coulomb's friction are, in the FEM formalism,

$${}^t(\boldsymbol{U}_N - \boldsymbol{W} - \boldsymbol{G})(\boldsymbol{P}'_N - \boldsymbol{P}_N) \le 0, \quad \forall \boldsymbol{P}'_N \in \mathcal{K}_N^h \tag{7}$$

$${}^t\dot{\boldsymbol{U}}_T(\boldsymbol{P}'_T - \boldsymbol{P}_T) \le 0, \quad \forall \boldsymbol{P}'_T \in \mathcal{F}^h(\boldsymbol{P}_N) \tag{8}$$

where $\mathcal{K}_N^h=\{P_N^M : P_N^M \ge 0\}$ is the approximation of $\mathcal{K}_N$ and $\mathcal{F}^h(\boldsymbol{P}_N)=\{\boldsymbol{P}_T^M : \|\boldsymbol{P}_T^M\| - \mu|\boldsymbol{P}_N^M| \le 0\}$ is the approximation of $\mathcal{F}(p_N)$ with $\mathcal{W}^M=\boldsymbol{P}_N^M$.

2.3 Frequency Domain Formulation

2.3.1 Without Wear. When wear is neglected the steady-state motion is assumed to be periodic. We introduce Fourier series expansions to express displacements and forces as multiharmonic vectors.

$$\boldsymbol{U}(t) = \tilde{\boldsymbol{U}}_0 + \sum_{n=1}^{Nh} \tilde{\boldsymbol{U}}_{n,c}\cos(n\omega t) + \tilde{\boldsymbol{U}}_{n,s}\sin(n\omega t) \tag{9}$$

and the multiharmonic vector is

$$\tilde{U} = [\tilde{U}_0, \tilde{U}_{1,c}, \tilde{U}_{1,s}, \ldots, \tilde{U}_{N_h,s}]^T \quad (10)$$

A Galerkin procedure is performed to formulate Eq. (5) in the frequency domain. The size of the problem can be reduced through two exact reductions in the frequency domain on the degrees of freedom involved in the contact elements and on the relative degrees of freedom. This procedure is detailed by Nacivet et al. [2]. The equations of motion take then the following form:

$$\mathbf{Z}_r \tilde{U}_r + \tilde{\boldsymbol{\lambda}} = \tilde{F}_r \quad (11)$$

where $\tilde{U}_r$ and $\tilde{F}_r$ are the multiharmonic vectors that represent the relative contact displacements and the reduced external forces. $\mathbf{Z}_r$ is the reduced dynamic stiffness. The second reduction is possible; thanks to the assumption of little displacements. In the node-to-node formulation, the Lagrange multipliers $\tilde{\boldsymbol{\lambda}}$ are equal to the unknown contact forces. A nonlinear solver is used to find the zeros of the function

$$f(\tilde{U}_r) = \mathbf{Z}_r \tilde{U}_r + \tilde{\boldsymbol{\lambda}} - \tilde{F}_r \quad (12)$$

2.3.2 Dynamic Response With Fretting-Wear. Wear is a very slow phenomenon and the depth of wear is very small compared with the dimension of the structures in contact. We can neglect the modifications of the mass and stiffness matrices due to wear. Moreover, in this paper we will neglect the modifications of the coefficients of friction and hardness due to wear. Wear appears here as a permanent normal displacement of the interface at the scale of one period in the response of the system. Therefore, the main idea is to split time into two different scales; indeed, we consider that wear does not change the aspect of the periodic response on a little lapse of time. On this period it is still possible to describe displacements and contact forces with Fourier series. On a long duration Fourier coefficients will evolve as functions of a time variable linked with the fretting-wear phenomenon. This procedure belongs to the family of multiscale methods, described by Nayfeh and Mook [21] and by Meirovitch [22] for a single harmonic balance. Cusumano and Chatterjee [23] used a time scale separation with an averaging procedure to estimate qualitatively the dynamics of damage evolution. Here we will also use time scales splitting with an averaging procedure on each period. The Fourier series of Eq. (9) becomes

$$U(\tau, \eta) = \tilde{U}_0(\eta) + \sum_{n=1}^{Nh} \tilde{U}_{n,c}(\eta)\cos(n\tau) + \tilde{U}_{n,s}(\eta)\sin(n\tau) \quad (13)$$

where τ is the fast time scale linked with the periodic response and η is the slow time scale linked with the fretting-wear phenomena. It is possible to define η as a multiple of the period T of fretting-wear cycles. Fretting-wear does not change the pulsation of the response because it is ruled by the pulsation of the excitation, which is not affected by fretting-wear. Wear depth does not depend on τ because it does not evolve on a single period, that is why wear depends only on η.

$$W^M = W^M(\tau, \eta) = W^M(\eta) \quad (14)$$

The evolution of wear after one period is for each node in contact

$$\Delta W^M(\eta) = \int_{\text{period}} |\lambda^N(\eta, \tau)| \, . \, \|\dot{U}_T(\eta, \tau)\| d\tau \quad (15)$$

The equation of motion (11) in the frequency domain is a little changed,

$$\mathbf{Z}_r \tilde{U}_r(\eta) + \tilde{\boldsymbol{\lambda}}(\eta) = \tilde{F}_r \quad (16)$$

The term concerning wear will appear in the augmented Lagrangian used to solve this equation with the constraints of contact with friction. This procedure is described in Sec. 2.4.

2.4 Calculation of the Contact Forces. Solving Eq. (12) requires knowing the expression of the contact forces in the frequency domain. Unfortunately it is not possible to calculate a priori the multiharmonic vector $\tilde{\boldsymbol{\lambda}}$ of Lagrange multipliers in the Galerkin procedure; indeed, the function is very nonsmooth. To undertake this difficulty it is common to use the alternating frequency-time (AFT) method. Cameron and Griffin [24] pioneered the development of the AFT. Displacements and velocities are calculated in the frequency domain and transformed into the time domain using an inverse fast Fourier transform (iFFT) procedure. In the time domain a nonlinear relation gives the contact forces, which are transformed back into the frequency domain using a FFT procedure. In the time domain, contact forces may be evaluated through different methods. The easiest one is to regularize the *sign* function, depending on the velocity in the evaluation of Coulomb's forces, by another function, which is continuous. It allows a direct computation of the nonlinear friction forces [25,26]. The use of a penalty method is another popular method [14,26–29]. This penalty softens the contact between interfaces in the tangential direction (Coulomb's friction) and in the normal direction (unilateral constrained contact conditions). The additional stiffnesses may represent a damper stiffness or the contact asperity stiffness. In case of the FEM they translate the microslip, which occurs in microscale to the macroscale of finite elements. Moreover these stiffnesses may be linked to material properties, which are modified due to fretting-wear of interfaces. These contact penalty strategies require an interactive computation of the friction forces in the time domain where the separation/stick/slip transitions have to be determined at each step.

Another method has been proposed by Nacivet et al. [2] and uses augmented Lagrangians, which allow to calculate without any softening of the nonsmooth contact law concerning the friction forces. A time-marching procedure in the time domain is also required. This dynamic Lagrangian frequency-time (DLFT) method has been successfully used to predict friction damping in blade attachments [1] and to quantify the efficiency of friction ring dampers [27]. In this method, the penalty term is the same as in the augmented Lagrangian and the final (converged) result does not depend on this term, but the stability of the procedure depends on this term. Good results are generally obtained when it is taken equal to the spectral radius of the dynamic stiffness matrix.

In the next equations, the term η is omitted in the expression of Fourier coefficients. In the frequency domain, the Lagrange multiplier $\boldsymbol{\lambda}$ is formulated as a penalization of the equations of motion on the tangential and normal directions

$$\tilde{\boldsymbol{\lambda}}^T = \tilde{F}_r^T - \mathbf{Z}_r \tilde{U}_r + \epsilon_T(\tilde{U}_r^T - \tilde{X}_r^T) \quad (17a)$$

$$\tilde{\boldsymbol{\lambda}}^N = \tilde{F}_r^N - \mathbf{Z}_r \tilde{U}_r + \epsilon_N(\tilde{U}_r^N - \mathbf{W} - \tilde{X}_r^N) \quad (17b)$$

ϵ_T and ϵ_N are penalty coefficients, and $\tilde{X}_r$ is a new vector of relative displacements, which is computed in the time domain. It will be seen that it corresponds to the relative displacements, which fulfill the contact and friction laws in the time domain. The pair $(\tilde{\boldsymbol{\lambda}}, \tilde{X}_r)$ is determined through an AFT procedure. Equation (12) reduces to $f(\tilde{U}_r) = \epsilon(\tilde{U}_r - \mathbf{W} - \tilde{X}_r)$. The convergence ensures that the time domain $\tilde{X}_r$ and frequency domain $\tilde{U}_r$ match with respect to wear condition.

2.5 Prediction/Correction in the Time Domain. Now let us present the prediction/correction procedure in the time domain summarized in Fig. 2. The contact forces are calculated in the time domain where the transition criteria between the three possible states are easily formulated. Equation (17) is reformulated as

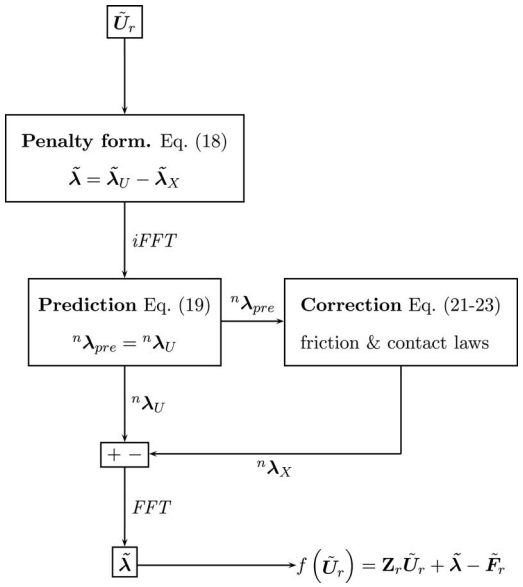

Fig. 2 Computation of the Lagrangian vector with wear

$$\tilde{\boldsymbol{\lambda}} = \begin{pmatrix} \tilde{\boldsymbol{\lambda}}^T \\ \tilde{\boldsymbol{\lambda}}^N \end{pmatrix} = \underbrace{\tilde{\boldsymbol{F}}_r - \boldsymbol{Z}_r\tilde{\boldsymbol{U}}_r + \epsilon(\tilde{\boldsymbol{U}}_r - \boldsymbol{W})}_{\tilde{\boldsymbol{\lambda}}_u} - \underbrace{\epsilon\tilde{\boldsymbol{X}}_r}_{\tilde{\boldsymbol{\lambda}}_x} \tag{18}$$

The period is split into N time steps. In this time domain each multiharmonic vector has a counterpart. $\tilde{\boldsymbol{\lambda}}$, $\tilde{\boldsymbol{\lambda}}_u$, and $\tilde{\boldsymbol{\lambda}}_x$ have, respectively, $\{\boldsymbol{\lambda}^n\}_{n=1..N}$, $\{\boldsymbol{\lambda}_u^n\}_{n=1..N}$, and $\{\boldsymbol{\lambda}_x^n\}_{n=1..N}$ as time-domain equivalents. These vectors are obtained from frequency domain variables through an iFFT procedure. A prediction/correction is used to compute the contact forces. At each time increment it assumes that the contact node is in stick situation; thus, the node does not move and $\boldsymbol{\lambda}_x^{n,T} = \boldsymbol{\lambda}_x^{n-1,T}$ and $\boldsymbol{\lambda}_x^{n,N} = 0$. The predicted contact forces are

$$\boldsymbol{\lambda}_{\text{pre}}^{n,T} = \boldsymbol{\lambda}_u^{n,T} - \boldsymbol{\lambda}_x^{n-1,T}, \quad \lambda_{\text{pre}}^{n,N} = \lambda_u^{n,N} \tag{19}$$

The corrected contact forces will be

$$\boldsymbol{\lambda}^n = \boldsymbol{\lambda}_u^n - \boldsymbol{\lambda}_x^n \tag{20}$$

$\boldsymbol{\lambda}_x^n$ will we be calculated to satisfy the contact and friction laws.

1. *Separation.* $\lambda_{\text{pre}}^{n,N} \geq 0$, the contact is lost and the forces should be zero.

$$\boldsymbol{\lambda}_x^n = \boldsymbol{\lambda}_u^n \tag{21}$$

2. *Stick.* $\lambda_{\text{pre}}^{n,N} < 0$ and $\|\boldsymbol{\lambda}_{\text{pre}}^{n,T}\| < \mu|\lambda_{\text{pre}}^{n,N}|$. In this case, the prediction verifies the contact conditions

$$\lambda_x^{n,N} = 0, \quad \boldsymbol{\lambda}_x^{n,T} = \boldsymbol{\lambda}_x^{n-1,T} \tag{22}$$

3. *Slip.* $\lambda_{\text{pre}}^{n,N} < 0$ and $\|\boldsymbol{\lambda}_{\text{pre}}^{n,T}\| \geq \mu|\lambda_{\text{pre}}^{n,N}|$. Again, there is no normal relative displacement. The correction is made assuming that the tangential contact force has the same direction as the tangential predicted force. The definition of relative velocity and the respect of Coulomb's Law give

$$\lambda_x^{n,N} = 0, \quad \boldsymbol{\lambda}_x^{n,T} = \boldsymbol{\lambda}_x^{n-1,T} + \boldsymbol{\lambda}_{\text{pre}}^{n,T}\left(1 - \mu\frac{|\lambda_{\text{pre}}^{n,N}|}{\|\boldsymbol{\lambda}_{\text{pre}}^{n,T}\|}\right) \tag{23}$$

The final step consists of transforming back the time-domain updated Lagrangian in the frequency domain using the FFT algorithm.

2.6 Calculation of the Wear Depth. As soon as the nonlinear solver has converged, we obtain the multiharmonic vectors of displacements and contact forces and also their corrected equivalents in the time domain. These values allow us to calculate the wear rate for one period using Eq. (15). The easiest strategy to compute wear evolution is to calculate wear after each period and to update vector $\boldsymbol{W}$ for the next period.

$$W^M(\eta^{k+1}) = W^M(\eta^k) + \Delta W^M(\eta^{k+1}) \tag{24}$$

Even though HBM/AFT is a fast method compared with temporal integration, the calculation of frequency responses for industrial applications can last for hours (even without fretting-wear). Therefore, calculating wear evolution with a direct time integration method will be very long. Presently, this method is used to understand the coupling phenomena between dynamics and fretting-wear. But another method is proposed to calculate the global response on τ and η. The idea is close to the principle of HBM; indeed, we use a basis of Fourier series functions to represent the time evolution in τ, which allows to transform the nonlinear equations in an algebraic problem. The same idea is applied with η but it gives a basis of monomial series. Thus, all the Fourier coefficients and wear are defined as

$$W(\eta) = W_0 + W_1\eta + W_2\eta^2 + \cdots \tag{25}$$

$$\tilde{\lambda}(\eta) = \tilde{\lambda}_0 + \tilde{\lambda}_1\eta + \tilde{\lambda}_2\eta^2 + \cdots \tag{26}$$

$$\tilde{U}(\eta) = \tilde{U}_0 + \tilde{U}_1\eta + \tilde{U}_2\eta^2 + \cdots \tag{27}$$

Let us introduce operator $\boldsymbol{P}$ and its inverse $\boldsymbol{P}^{-1}$, such that $\boldsymbol{P}\tilde{\boldsymbol{U}}_r$ is the vector of the multiharmonic polynomial coefficients. Its size is $(2*N_h+1)\cdot(m+1)$, where m designates the degree of the polynomial.

$$\boldsymbol{P}\tilde{\boldsymbol{U}}_r = [\tilde{\boldsymbol{U}}_{\mathbf{0},\mathbf{0}}, \ldots, \tilde{\boldsymbol{U}}_{\mathbf{0},\boldsymbol{m}}, \tilde{\boldsymbol{U}}_{1,0,c}, \tilde{\boldsymbol{U}}_{1,0,s}, \ldots, \tilde{\boldsymbol{U}}_{N_h,m,s}]^T \tag{28}$$

The first subscript is the harmonic order and the second subscript corresponds to the degree of the monomial in the polynomial. Equation (16) is transformed as

$$\boldsymbol{Z}_r^p\boldsymbol{P}\tilde{\boldsymbol{U}}_r + \boldsymbol{P}\tilde{\boldsymbol{\lambda}} = \boldsymbol{P}\tilde{\boldsymbol{F}}_r \tag{29}$$

The procedure of prediction/correction to calculate contact force and wear is conserved, but there are new steps. Indeed, now two time scales are considered. The procedure is illustrated in Fig. 3. Thus, the predicted forces are predicted from Eq. (29) the same way as in the precedent part, but now we have a double discretization in the time domain: one for each period and one for long times; both are linked with η. Each time step is defined by a pair (t^n, η^k). To transform the variable of Eq. (29) a calculation of the multiharmonic coefficient function must first be performed at each η^k and, then, an iFFT procedure must be used. At each time step (t^n, η^k) contact forces are corrected to satisfy the contact and friction conditions. At the end of period k wear is updated for the next period. At the end of the loop on $(n,k) = (N, N_{\text{final}})$, we have obtained the dynamical evolution on each period (time scale: τ), the evolution of contact forces due to wear (time scale: η) and wear at each contact node. These vectors are transformed in the frequency domain using FFT and the coefficients of polynomial from the value of multiharmonic coefficient at each η^k using $\boldsymbol{P}$. The new values are introduced in Eq. (29) to verify the convergence.

3 Numerical Example

The method developed above is applied to a simple model with two degrees of freedom, which allows one to understand the coupling between wear and dynamics.

3.1 2DOF With Wear. To start with, let us study a system made of two masses in contact with friction. The movements are only in the tangential direction. On the normal direction is applied

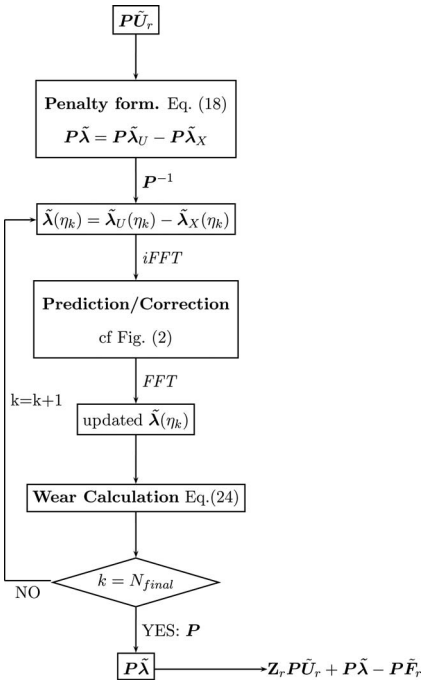

Fig. 3 Computation of the Lagrangian vector

a displacement that constrains a spring. The system is represented in Fig. 4. The nonlinear dynamics equations are only on the tangential direction. On the normal direction, only the first mass will wear and the wear depth leads to the relaxation of the spring and the normal contact force decreases. The equations of this system are

$$m_1\ddot{x}_1 + c_1\dot{x}_1 + k_1x_1 + F_{nl} = F_{\text{ex}} \tag{30a}$$

$$m_2\ddot{x}_2 + c_2\dot{x}_2 + k_2x_2 - F_{nl} = 0 \tag{30b}$$

$$\Delta w(nT) = K_w \int_{nT}^{(n+1)T} F_N \|\dot{x}_2 - \dot{x}_1\| dt \tag{30c}$$

$$F_N = k_n \cdot (u_0 - w) \tag{30d}$$

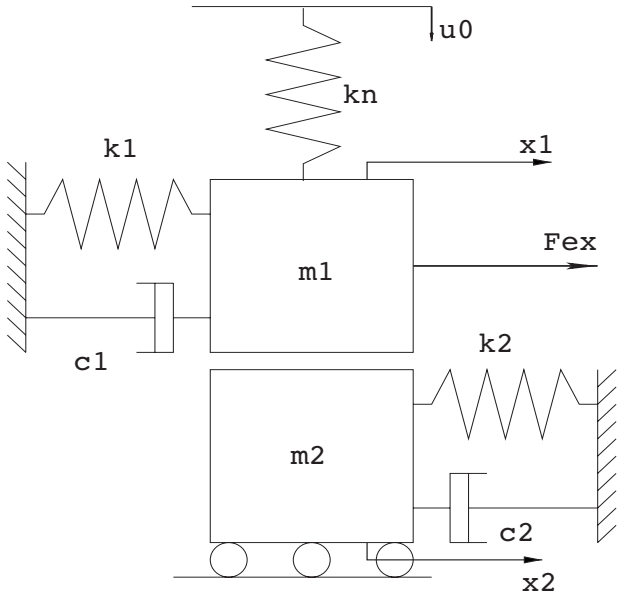

Fig. 4 2DOF model

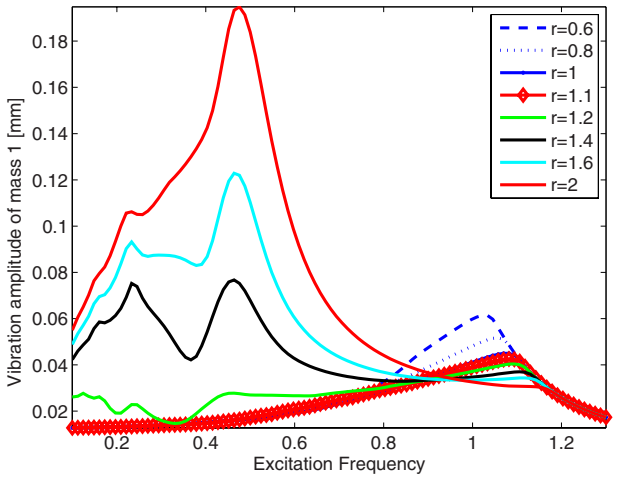

Fig. 5 Frequency response of mass m_1 for several levels of excitation force

F_{nl} designates the tangential friction forces, which must respect Coulomb's Law. To solve the nonlinear problem, the DLFT is used with different numbers of harmonics to test the influence of this parameter. The choice of relaxing the normal force when wear increases is due to the fact that in a real 3D problem the whole contact area is not in the situation of stick-slip, that is why areas will remain without wear (total sticking zone). The result is the decrease in normal pressure in the area of wear. In this system, unit masses have been chosen, $k_1 = \pi^2$ and $k_2 = 7\pi^2$, and the viscous damping ratio is 0.1%. Thus, the two modes (stick situation and mass m_1 free) are, respectively, at 1 Hz and 0.5 Hz. An initial normal force of 10 N ($k_n = 1 \times 10^7$ N m^{-1} and $u_0 = 1 \times 10^{-3}$ mm) and a friction coefficient $\mu = 1$ are imposed. The coefficient of wear rate K_w is arbitrarily chosen equal to 1.0×10^{-6}. We impose an excitation force in cosine and we will study three cases for the amplitude of excitation: 6 N, 10 N, and 14 N. Indeed there are three possible situations depending on the ratio $r = (F_{\text{ex}}/\mu F_N)$: If the excitation is too small the masses m_1 and m_2 are all the time in sticking situation, if the ratio is bigger than a certain value (not calculated but depending on the dynamical properties of the system) the mass m_1 is during one period often in sliding situation, and the third case occurs if the sliding situation appears but the sticking duration is longer in one period. These three cases modify

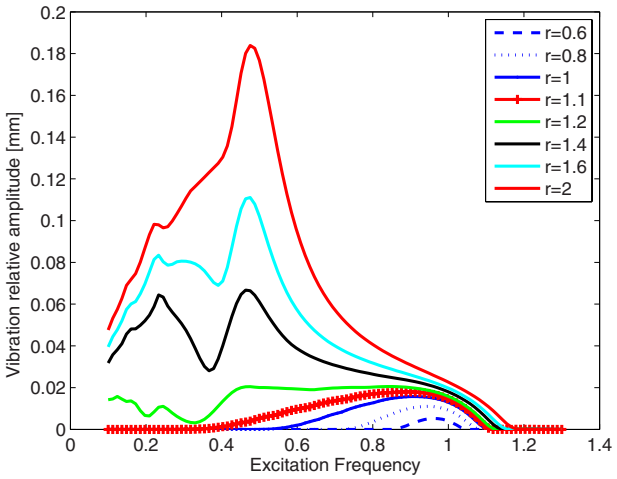

Fig. 6 Frequency response of relative displacement for several levels of excitation force

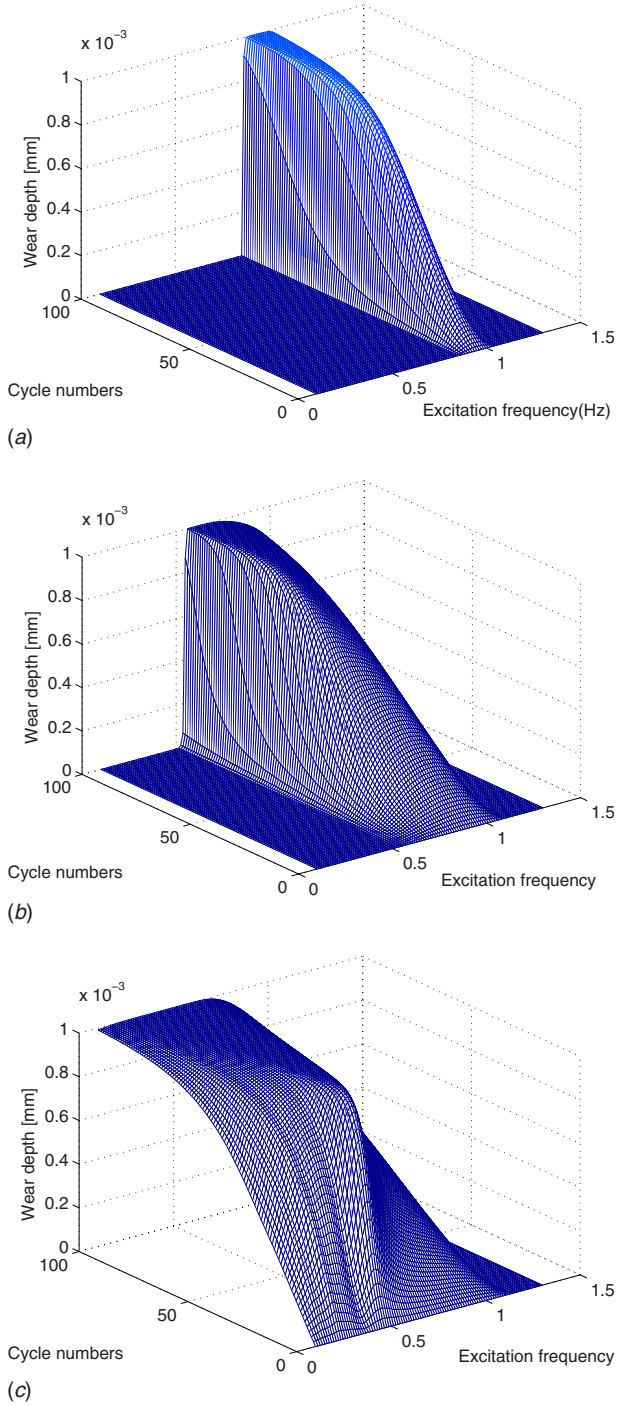

Fig. 7 Wear depth evolution on a frequency range for F_{ex} =6 N (*a*), F_{ex}=10 N (*b*), and F_{ex}=14 N (*c*)

the dynamic response and the wear evolution. The first case is not studied because wear does not occur.

With this model let us consider the evolution of wear as a function of the number of fretting cycle and for different frequencies. We plot the frequency response function of mass m_1 as a function of the number of fretting cycles. A test has been performed to determine the influence of the number of harmonics on the precision of the results; The reference is given by a direct time integration. Twenty-one harmonics are finally used. The results in Figs. 5 and 6 give the calculated frequency response functions (FRFs) for different ratios of excitation force.

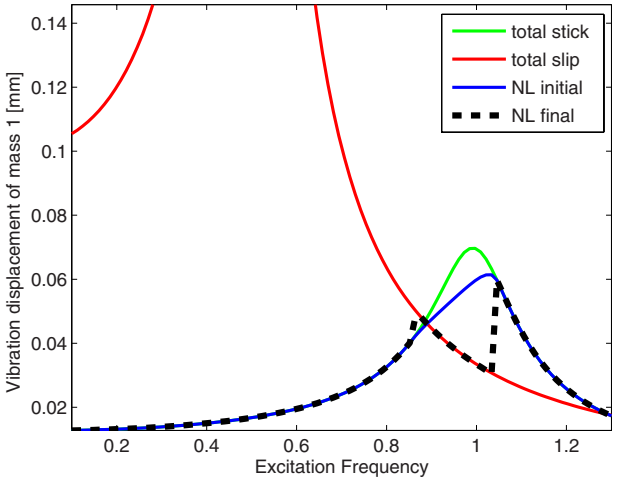

Fig. 8 Pseudofrequency response of vibration amplitude of mass m_1 for four cases

Figure 5 shows that for certain ratios subharmonic resonances exist. Let us consider the behavior of the modal response of the system in the presence of wear.

3.1.1 DLFT Method and Direct Time Integration on the Slow Time Scale. First we impose a level of excitation force of 6 N. The evolution of the wear depth is calculated as a function of the frequency and of the number of fretting cycles. The results are reported in Fig. 7(*a*).

We can see what happens in Fig. 8 where are reported FRFs of mass m_1 free, mass m_1 and m_2 in stick situation, and pseudo-FRF for nonlinear (NL) system at the initial cycle and after 100 normalized fretting-wear cycles.

They show that for this ratio of excitation wear does not appear in all the ranges of frequency. The plateau after a certain number of cycles exists. The functions giving the evolution of wear have points of maximal slope. We can separate evolution in three steps. First wear evolution is low because the relative speed is low. After that there is an area where the wear evolution accelerates because of the increase in relative displacement due to the decrease in the normal force and at the end of the evolution the displacement is important but the normal force is nearly zero and wear stops. The point of maximal slope corresponds to the maximum of wear rate. This figure shows the influence of dynamics on wear evolution. Figure 9(*a*) illustrates the influence of wear on the dynamic response. In this figure two resonances appear with the increase in wear. Due to wear, the behavior changes. With wear augmentation, mass m_1 is more and more in slip situation and the system tends to a system where mass m_1 is free.

The second imposed excitation force is 14 N. Figures 9(*c*) and 7(*c*) show, respectively, the pseudo-FRF of mass m_1 and wear evolution. For this ratio of excitation force, the frequency slot where wear appears is more important and there is a frequency where wear evolution functions do not have a point of maximal slope. In this case for initial fretting cycle, sliding period lengthens more than sticking period in one vibration period and wear rate is maximum in this cycle and decreases with fretting-wear cycle. For this excitation force the system is closer to the sliding mode than to the sticking mode—that is why wear is faster at about 0.5 Hz where there is maximum relative displacement. Figures 9(*b*) and 7(*b*) represent vibration response and wear evolution for $F_{ex}=10\cos(\omega t)$. It is an intermediate situation where the resonance without wear is at 1 Hz and when wear increases resonance appears at 0.5 Hz. These three examples show how coupling between wear and vibration can be illustrated for a 2DOF oscillator.

Now let us consider the importance of the number of harmonics on the results. We have calculated for different harmonics num-

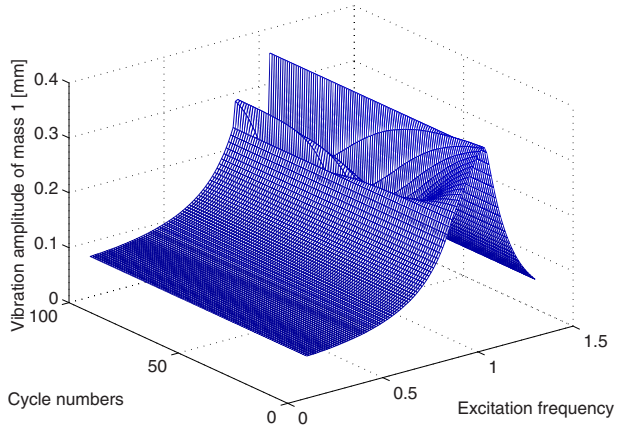

(*a*)

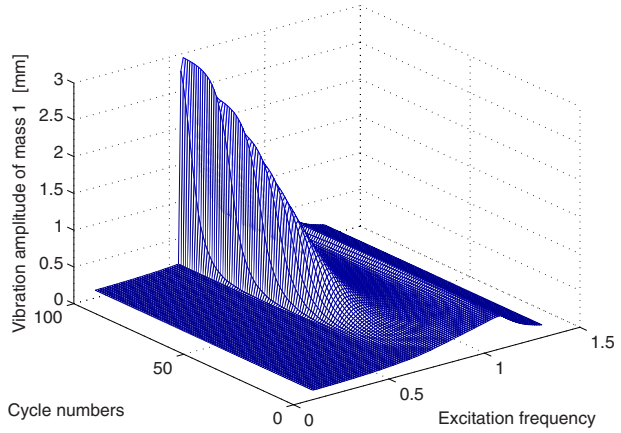

(*b*)

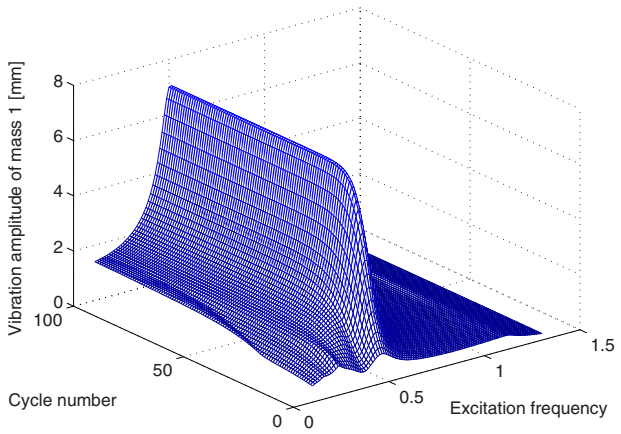

(*c*)

Fig. 9 Pseudofrequency response of vibration amplitude of mass m_1 for F_{ex}=6 N (*a*),F_{ex}=10 N (*b*), and F_{ex}=14 N (*c*)

bers and drawn the wear evolution in Fig. 10 with F_{ex}=10 N and f=0.7 Hz. This figure shows that the convergence increases with the harmonics number. A large number of harmonics are not necessary to have an acceptable result. Indeed, for more complex structures with a lot of degrees of freedom it is interesting not to increase harmonics number but to decrease the calculation time.

3.1.2 Polynomial Approximation of Wear Evolution. Now let us present the results obtained with the method where the evolution in η is assumed to be polynomial. We have selected N_h=3 and a degree of polynomial equal to 4. The level of excitation force is 10 N. The wear evolution is illustrated in Fig. 11 for direct

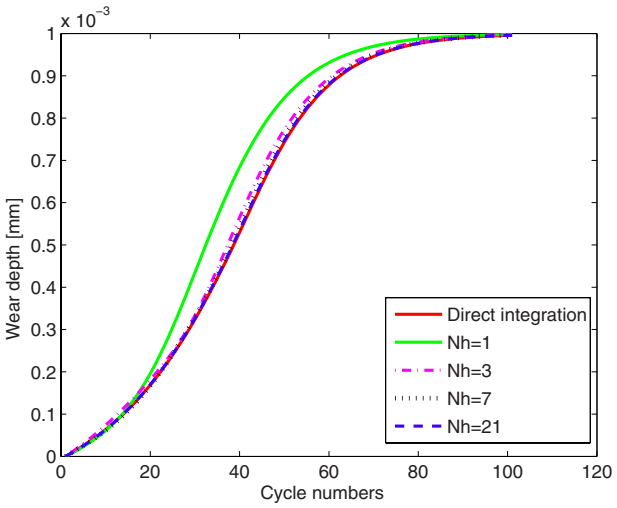

Fig. 10 Wear depth evolution with different harmonics orders

time integration, for the DLFT with integration in η, and for polynomial DLFT. Figure 12 shows wear evolution; the results looks like the results found with DLFT and for direct time integration in

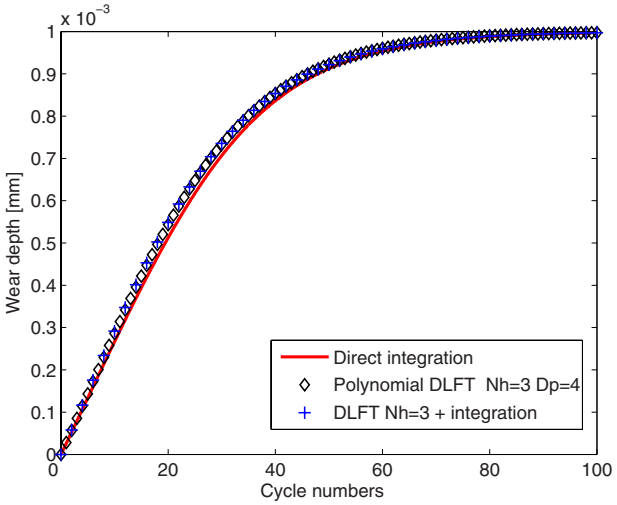

Fig. 11 Wear depth evolution with three methods

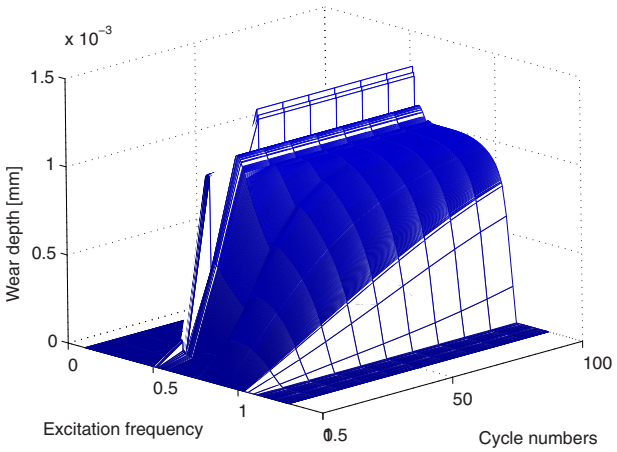

Fig. 12 Wear depth evolution with polynomial approach for F_{ex}=10 N

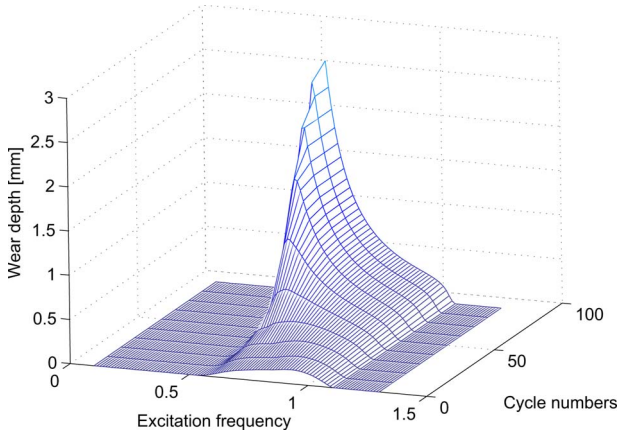

Fig. 13 Relative displacements with DLFT and integration

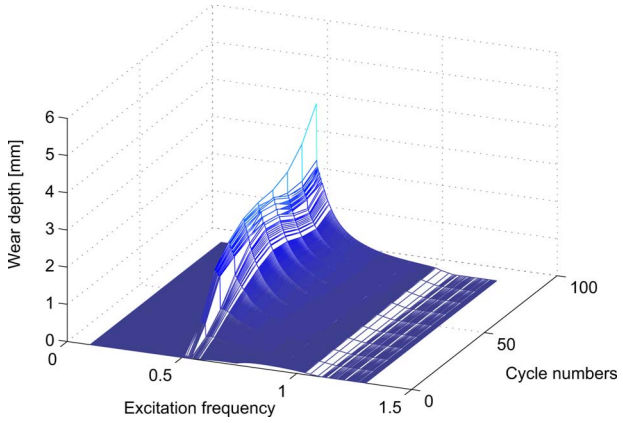

Fig. 14 Relative displacements with polynomial DLFT

η in Fig. 7(*b*). To compare both, the evolutions of relative displacement in frequency and η are drawn. The DLFT results are in Fig. 13 and the results from the polynomial approach are in Fig. 14. Our new method allow us to approximate results found with multiple DLFT with one nonlinear calculation for each frequency. Nevertheless polynomial approximation is not the most adapted function to fit wear evolution, and future work will try to use other functions such as Weibull function or similar functions used in maintenance engineering.

4 Conclusions

Two methods to predict wear and vibration response have been proposed. The efficiency of the first numerical method—DLFT and time integration—is proved for simple examples. It would be slow for industrial structures but has allowed us to understand the coupling between wear and dynamics. The second method—with polynomial projection—needs more developments to be adapted for industrial structures. The future works will focus on developing new functions to formulate wear on the slow time scale, especially above the point of maximal slope. Special attention will be paid to convergence issues.

Acknowledgment

Thanks go to Snecma for technical and financial support. This work took place in the framework of the MAIA mechanical research and technology program sponsored by CNRS, ONERA, and SAFRAN Group.

Nomenclature

F_c = nodal force of contact
K_w = wear coefficient in Archard's Law
$\mathbf{M}, \mathbf{C}, \mathbf{K}$ = mass, viscous damping, and stiffness matrices
$\boldsymbol{U}$ = time-domain displacement vector
$\boldsymbol{W}$ = wear depth
Z_r = reduced dynamic stiffness
$\underset{\sim}{\ }$ = multiharmonic vectors
$\underset{\_}{\ }^{r}$ = relative value
$\underset{\_}{\ }^{T}, \underset{\_}{\ }^{N}$ = tangential and normal directions
η = slow scale of time
$\boldsymbol{\lambda}, \tilde{\boldsymbol{\lambda}}$ = Lagrangian multipliers in time and frequency domains

References

[1] Charleux, D., Gibert, C., Thouverez, F., and Dupeux, J., 2006, "Numerical and Experimental Study of Friction Damping in Blade Attachments of Rotating Bladed Disks," Int. J. Rotating Mach., **2006**, p. 71302.
[2] Nacivet, S., Pierre, C., Thouverez, F., and Jezequel, L., 2003, "A Dynamic Lagrangian Frequency—Time Method for the Vibration of Dry-Friction-Damped Systems," J. Sound Vib., **265**, pp. 201–219.
[3] Gallego, L., Nélias, D., and Jacq, C., 2006, "A Comprehensive Method to Predict Wear and to Define the Optimum Geometry of Fretting Surfaces," ASME J. Tribol., **128**, pp. 476–486.
[4] Paulin, C., Fouvry, S., and Deyber, S., 2005, "Wear Kinetics of Ti–6Al–4V Under Constant and Variable Fretting Sliding Conditions," Wear, **259**, pp. 292–299.
[5] Levy, G., 1980, "Modeling of Coulomb Damping and Wear of Vibrating Systems," Wear, **64**(1), pp. 57–82.
[6] Sextro, W., 2002, *Dynamical Contact Problems with Friction: Models, Methods, Experiments and Applications*, Springer, New York.
[7] Meng, H., and Ludema, K., 1995, "Wear Models and Predictive Equations: Their Form and Content," Wear, **181–183**, pp. 443–457.
[8] Fouvry, S., Liskiewicz, T., Kapsa, P., Hannel, S., and Sauger, E., 2003, "An Energy Description of Wear Mechanisms and Its Applications to Oscillating Sliding Contacts," Wear, **255**, pp. 287–298.
[9] Archard, J., 1953, "Contact and Rubbing of Flat Surface," J. Appl. Phys., **24**, pp. 981–988.
[10] McColl, I., Ding, J., and Leen, S., 2004, "Finite Element Simulation and Experimental Validation of Fretting Wear," Wear, **256**, pp. 1114–1127.
[11] Öqvist, M., 2001, "Numerical Simulations of Mild Wear Using Updated Geometry With Different Step Size Approaches," Wear, **249**, pp. 6–11.
[12] Põdra, P., and Andersson, S., 1997, "Wear Simulation With the Winkler Surface Model," Wear, **207**, pp. 79–85.
[13] Sfantos, G., and Aliabadi, M., 2006, "Application of BEM and Optimization Technique to Wear Problems," Int. J. Solids Struct., **43**, pp. 3626–3642.
[14] Guillen, J., and Pierre, C., 1999, "An Efficient, Hybrid, Frequency-Time Domain Method for the Dynamics of Large-Scale Dry Friction Damped Structural Systems," Iutam Symposium on Unilateral Multibody Contacts.
[15] Csaba, G., 1998, "Forced Response Analysis in Time and Frequency Domains of a Tuned Bladed Disk With Friction Dampers," J. Sound Vib., **214**, pp. 395–412.
[16] Petrov, E., and Ewins, D., 2003, "Analytical Formulation of Friction Interface Elements for Analysis of Nonlinear Multi-Harmonic Vibrations of Bladed Disks," ASME J. Turbomach., **125**, pp. 364–371.
[17] D. Laxalde, L. Salles, L. Blanc, and Thouverez, F., 2008, "Non-Linear Modal Analysis for Bladed Disks With Friction Contact Interfaces," ASME Paper No. GT2008-50860.
[18] Stromberg, N., 1997, "An Augmented Lagrangian Method for Fretting Problems," Eur. J. Mech. A/Solids, **16**, pp. 573–593.
[19] Klarbring, A., 1990, "Derivation and Analysis of Rate Boundary-Value Problems of Frictional Contact," Eur. J. Mech. A/Solids, **9**, pp. 53–85.
[20] Lemaître, J., and Chaboche, J., 1990, *Mechanics of Solid Materials Mécanique des Matériaux Solides English*, Cambridge University Press, Cambridge.
[21] Nayfeh, A., and Mook, D., 1979, *Nonlinear Oscillations*, Wiley-Interscience, New York.
[22] Meirovitch, L., 2004, *Methods of Analytical Dynamics*, Dover, New York.
[23] Cusumano, J., and Chatterjee, A., 2000, "Steps Towards a Qualitative Dynamics of Damage Evolution," Int. J. Solids Struct., **37**, pp. 6397–6417.
[24] Cameron, T., and Griffin, J., 1989, "An Alternating Frequency/Time Domain Method for Calculating the Steady-State Response of Nonlinear Dynamic Systems," ASME Trans. J. Appl. Mech., **56**, pp. 149–154.
[25] Sanliturk, K., Ewins, D., Elliott, R., and Green, J., 2001, "Friction Damper Optimization: Simulation of Rainbow Tests," ASME J. Eng. Gas Turbines Power, **123**, pp. 930–939.
[26] Petrov, E., and Ewins, D., 2001, "Models of Friction Damping With Variable Normal Load for Time-Domain Analysis of Vibrations," *Proceedings of the International Conference on Noise and Vibration Engineering (ISMA)*, ISMA, Leuven, Belgium.
[27] D. Laxalde, F. Thouverez, J. Sinou, and J. Lombard, 2007, "Qualitative Analysis of Forced Response of Blisks With Friction Ring Dampers," Eur. J. Mech.

A/Solids, **26**, pp. 676–687.
[28] Poudou, O., and Pierre, C., 2003, "Hybrid Frequency-Time Domain Methods for the Analysis of Complex Structural Systems With Dry Friction Damping," *Proceedings of the AIAA/ASME/ASCE/AHS/ASC Structures, Structural Dynamics and Materials Conference*, AIAA, New York, Vol. 1, p. 111.
[29] Ciğeroğlu, E., and Özgüven, H., 2006, "Nonlinear Vibration Analysis of Bladed Disks With Dry Friction Dampers," J. Sound Vib., **295**, pp. 1028–1043.

Numerical Analysis of the Shaft Motion in the Journal Bearing of a Gear Pump

R. Castilla
Department of Fluid Mechanics,
LABSON,
U.P.C.: Colom 11,
Terrassa E-08222, Spain

M. Gutes
ArvinMeritor,
Albert Einstein Str., 14-20,
Dietzenbach D-63128 , Germany

P. J. Gamez-Montero

E. Codina

Department of Fluid Mechanics,
LABSON,
U.P.C.: Colom 11,
Terrassa E-08222, Spain

This paper describes a numerical analysis of the dynamics of the shaft in the journal bearing of a gear pump. The modulus and direction of the load is a function of the relative position of the gears, causing a precession motion around an equilibrium position. The mean load is the function of the working pressure of the gear pump. The numerical analysis presented in this paper combines the equation of motion of the journal-gear set, based on the linearization of the fluid film load, with calculation of the load due to the pressure distribution on the gears. The damping and stiffness coefficients for the motion equation are calculated with the distributions around the shaft of the pressure and its derivatives. These distributions are calculated from the Reynolds equations using an in-house 2D finite element code with quadrangular elements; the equation of motion is solved with a fifth-order Runge–Kutta scheme. The results provide the stabilized position of the shaft for certain conditions, and allow limitation of the working pressure and the angular velocity of the pump in order to minimize, or to avoid, metal-metal contact and consequent wear of material. The results are compared with experiments and previously reported numerical results. [DOI: 10.1115/1.3126771]

1 Introduction

The dynamic behavior of a gear pump shaft with journal bearings is numerically analyzed. A gear pump is a type of positive displacement pump that uses two gears for fluid transport (in the present case, the fluid is mineral oil) from the suction zone to the discharge zone. Typically, this discharge zone is under high pressure, between 100 bars and 300 bars. Experimentally, it has been found that these types of pumps can present material wear due to failure of the journal bearing. The aim of this work is to numerically determine how the pump journal bearings move under these conditions. It is particularly interesting to establish the limits for rotational velocity and working pressure at which the fluid film is broken.

The first publications on journal bearings were mainly related to crankshafts [1,2], turbines [3], and solution of the Reynolds equation [4,5]; usually, the finite element method for a finite journal length has been used for this purpose [2,6,7]. The method of mobilities is normally applied for linearizing the equations, although it has been reported to underestimate cycle average eccentricity and overestimates minimum film thickness of up to 25% in comparison with a more rigorous method [8]. Some authors [9,10] have proposed linearizing the pressure distribution as well as the load in order to calculate the motion of the shaft, since that should allow a more precise study of the stability. Regarding the motion of the shaft, some investigation has been carried out on the orbits described by it [11,12]. Kirk and Gunter [13,14] used a short bearing approximation for the study of the nonlinear journal response. Rao et al. [15] developed an analytical method for the calculation of the dynamical coefficients. Additionally, studies of numerical analysis of plain journal bearings [16,17] and herringbone-grooved journal bearings [18–20], principally used in miniature rotors, have been reported.

Analytical approaches are usually based on the Ocvirk theory (short bearings) or the Sommerfeld theory (long bearings). In the present work, Lund's method [21–23] is used to linearize the load on the journal. A 2D finite element method code is used for calculation of the coefficients of the motion equation, which are a function of the pressure distribution and its derivatives in position and velocity. The pressure distribution is calculated with the Reynolds boundary condition, since the half-Sommerfeld boundary condition generates a discontinuity of the derivative of the pressure distribution around the cavitation area [18]. The pressure is atmospheric at both ends of the bearing. This condition is accomplished at the gear side of the journal with depressurization slots that allow the bearing to communicate with the inlet section of the pump. This also avoids leakage due to high pressure gradients.

The load on the shaft is calculated by integrating the pressure distribution over the gears, considering the phase of the gearing cycle. Thus, the load is dynamic and is related to a realistic work situation in a gear pump.

2 Theoretical Model

The load on the journal is caused by the pressure distribution around the gears and the contact force between them. The two gear wheels, one driving and the other driven, are held between two compensation plates, and this set is mounted inside the case. This type of construction implies that only the internal forces and the gap between pieces will determine the behavior of the pump.

The pressure distribution can be divided into three sections, as indicated in Fig. 1. Two of them, in the upper central zone and in the lower central zone, are the pressure at the inlet and the outlet, respectively, and can be considered uniform. The third section is modeled as a linear interpolation between the two values of the pressures in the inlet and the outlet. The outlet pressure, which is determined by the impedance of the circuit, is not only acting on the discharge chamber, but also in a rather large region around the gears due to a decompression slot placed on the compensation plates. The green region in the center of the gearing zone represents the oil trapped between two subsequent contact points. Its pressure is considered equal to the outlet pressure until the teeth are open to the inlet region.

The pressure distribution is then modeled as

$$P = \begin{cases} P_s & \text{if } 0 \le \theta \le \theta_s \\ A\theta + B & \text{if } \theta_s \le \theta \le \theta_d \\ P_d & \text{if } \theta_d \le \theta \le \theta_c \end{cases} \quad (1)$$

Manuscript received November 10, 2008; final manuscript received March 13, 2009; published online October 2, 2009. Review conducted by Patrick S. Keogh.

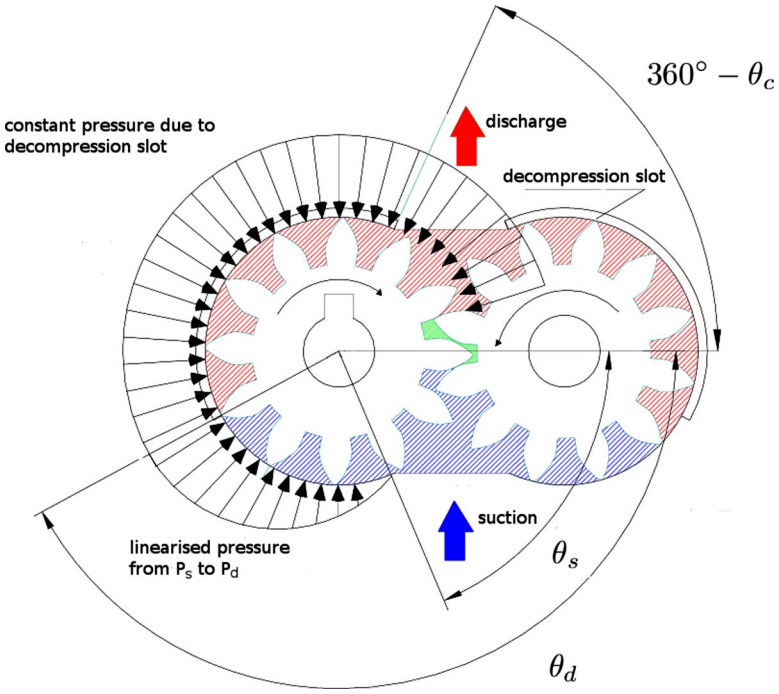

Fig. 1 Distribution of pressure in the gearwheels

where P_d and P_s are the pressures at the discharge and the suction zone, respectively, which are limited by the angles θ_d and θ_s; $A = (P_d - P_s/\theta_d - \theta_s)$; and $B = P_d - (P_d - P_s/\theta_d - \theta_s)\theta_d$. This distribution can be varied according to the design of the compensating plates in order to balance the load over the journal.

The load is calculated as two contributions: $\boldsymbol{W}_1$ is the load due to the inlet pressure and the linear distribution $(0 < \theta < \theta_d)$, and $\boldsymbol{W}_2$ is the load due to the outlet pressure. Thus, the horizontal and vertical components of W_1 are

$$W_{1x} = \int_0^{\theta_s} HRP_s \cos\theta d\theta + \int_{\theta_s}^{\theta_d} HR(A\theta + B)\cos\theta d\theta + \int_{\theta_d}^{\theta_c} HRP_d \cos\theta d\theta \tag{2}$$

$$W_{1z} = \int_0^{\theta_s} HRP_s \sin\theta d\theta + \int_{\theta_s}^{\theta_d} HR(A\theta + B)\sin\theta d\theta + \int_{\theta_d}^{\theta_c} HRP_d \sin\theta d\theta \tag{3}$$

where H and R are the width and the radius, respectively, of the gears. This yields

$$W_{1x} = HR[(P_s - A\theta_s - B)\sin\theta_s - (P_d - A\theta_d - B)\sin\theta_d + A(\cos\theta_d - \cos\theta_s) + B\sin\theta_d + P_d \sin\theta_c] \tag{4}$$

$$W_{1z} = HR[-(P_s - A\theta_s - B)\cos\theta_s + (P_d - A\theta_d - B)\cos\theta_d + A(\sin\theta_d - \sin\theta_s) - B\cos\theta_d - P_d\cos\theta_c] \tag{5}$$

and the polar coordinates are calculated with

$$|\boldsymbol{W}_1| = \sqrt{(W_{1x})^2 + (W_{1z})^2}$$

$$\theta_{W_1} = \text{arctg}\left(\frac{W_{1z}}{W_{1x}}\right) \tag{6}$$

For the outlet pressure the load is

$$W_{2x} = -P_d H|\boldsymbol{AN}| \tag{7}$$

$$W_{2z} = -P_d H|\boldsymbol{ND}| \tag{8}$$

where P_d is the outlet pressure, H is the height of the gear wheels, D is the contact point, A is the vertex between the outlet chamber and the gears case, and N is the intersection between vertical line in A and horizontal line in D (see Fig. 2).

The total load on the shaft is the sum of both contributions $\boldsymbol{W} = \boldsymbol{W}_1 + \boldsymbol{W}_2$, plus the contact force between both gears. This load is calculated with a computer program, which, with the essential data (number of teeth, modulus of gear, rotational speed, working pressures, and so on), simulates the gearing and calculates the contact point and the total vector load over both gears for each phase of the gearing cycle. The results of this load for the angle

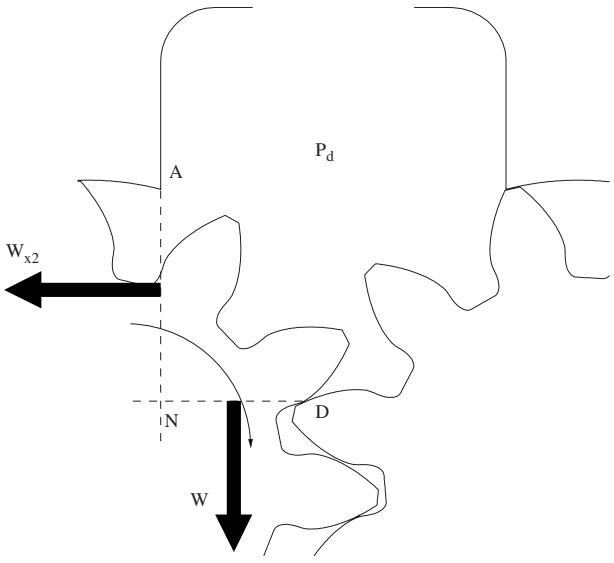

Fig. 2 Calculation of the load on the driving gear due to the pressure in the discharge

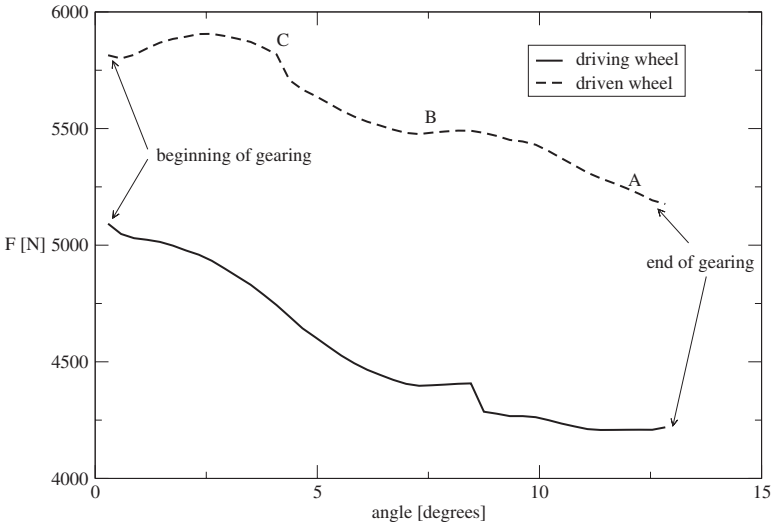

Fig. 3 Load on the gear wheels for a working pressure of 150 bars

interval with teeth contact are shown in Fig. 3 for the modulus, and Fig. 4 for the load angle. The pump in this simulation rotates at 2000 rpm and the outlet pressure is 150 bars.

In these figures, it is observed that, although the angle of the load on both gears is almost symmetrical, the load on the driven gear is larger than that on the driving one, with a difference of approximately 10%. This occurs because, for the driving gear, the contact force subtracts from the resulting force due to the pressure distribution and, for the driven gear, it adds to the resulting force. This point agrees with careful examination of the case in a real gear pump, which shows a slightly higher wear in the side of the driven gear [21]. The total load used for the simulation of the journal dynamics is the one over the more loaded driven gear.

The steps observed in Figs. 3 and 4, for 4 deg for the driven gear and 8 deg for the driving gear, are a consequence of the sudden opening and closing of the chamber with the oil trapped between teeth in the gearing region, combined with the effect of the decompression slots (see Fig. 1).

The equation of motion of the journal is as follows:

$$\begin{bmatrix} m_a & 0 \\ 0 & m_a \end{bmatrix} \begin{bmatrix} \Delta\ddot{x} \\ \Delta\ddot{z} \end{bmatrix} = \begin{bmatrix} W\cos\phi \\ W\sin\phi \end{bmatrix} - \begin{bmatrix} w_x \\ w_z \end{bmatrix} \tag{9}$$

where m_a is the journal-gear mass and is the total load due to the pressure distribution on the gear and the teeth contact, and w is the reaction of the fluid film on the journal. The x and z directions and the total load angle ϕ are referred to the journal coordinate system, as displayed in Fig. 5. In this figure, the height of the fluid film h and the coordinate θ are also shown, as well as the equilibrium angle Ψ.

The force w on the journal due to the fluid film is linearized with Lund's method [21,22].

$$\begin{bmatrix} w_x \\ w_z \end{bmatrix} = \begin{bmatrix} (w_x)_0 \\ (w_z)_0 \end{bmatrix} + \begin{bmatrix} k_{xx} & k_{xz} \\ k_{zx} & k_{zz} \end{bmatrix} \begin{bmatrix} \Delta x \\ \Delta z \end{bmatrix} + \begin{bmatrix} b_{xx} & b_{xz} \\ b_{zx} & b_{zz} \end{bmatrix} \begin{bmatrix} \Delta\dot{x} \\ \Delta\dot{z} \end{bmatrix} \tag{10}$$

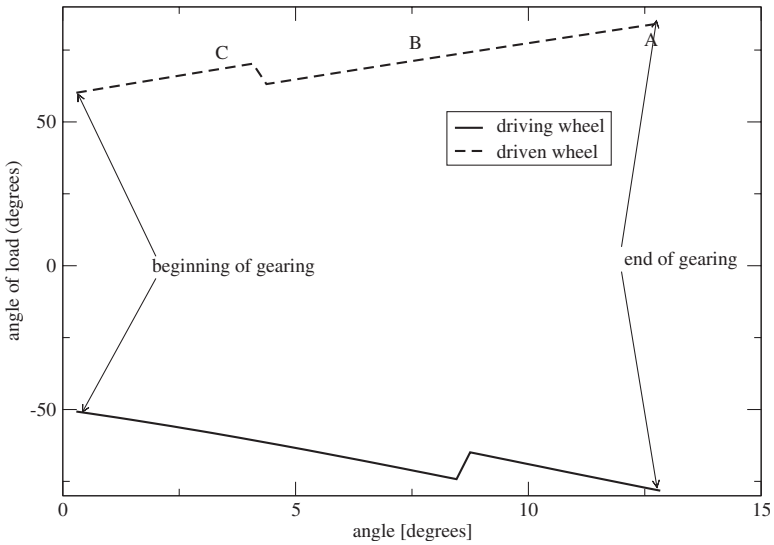

Fig. 4 Angle of load on the gear wheels for a working pressure of 150 bars

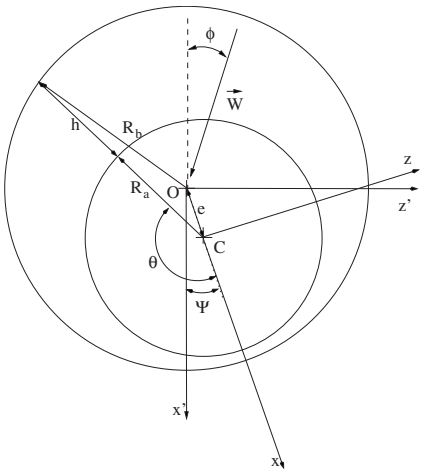

Fig. 5 Coordinate systems of the journal bearing

where $(w_x)_0$ and $(w_z)_0$ are the forces in the initial position, k_{ij} are the stiffness coefficients, and b_{ij} are the damping coefficients.

The values of these coefficients are calculated with

$$\begin{bmatrix} (w_x)_0 \\ (w_z)_0 \end{bmatrix} = \begin{bmatrix} \int_y \int_\theta p_0 \cos\theta R_a d\theta dy \\ \int_y \int_\theta p_0 \sin\theta R_a d\theta dy \end{bmatrix} \tag{11}$$

$$\begin{bmatrix} k_{xx} & k_{xz} \\ k_{zx} & k_{zz} \end{bmatrix} = \begin{bmatrix} \int_y \int_\theta p_x \cos\theta R_a d\theta dy & \int_y \int_\theta p_z \cos\theta R_a d\theta dy \\ \int_y \int_\theta p_x \sin\theta R_a d\theta dy & \int_y \int_\theta p_z \sin\theta R_a d\theta dy \end{bmatrix} \tag{12}$$

$$\begin{bmatrix} b_{xx} & b_{xz} \\ b_{zx} & b_{zz} \end{bmatrix} = \begin{bmatrix} \int_y \int_\theta p_{\dot{x}} \cos\theta R_a d\theta dy & \int_y \int_\theta p_{\dot{z}} \cos\theta R_a d\theta dy \\ \int_y \int_\theta p_{\dot{x}} \sin\theta R_a d\theta dy & \int_y \int_\theta p_{\dot{z}} \sin\theta R_a d\theta dy \end{bmatrix} \tag{13}$$

where

$$p_0 = (p)_0 \quad p_x = \left(\frac{\partial p}{\partial x}\right)_0 \quad p_z = \left(\frac{\partial p}{\partial z}\right)_0 \quad p_{\dot{x}} = \left(\frac{\partial p}{\partial \dot{x}}\right)_0 \quad p_{\dot{z}} = \left(\frac{\partial p}{\partial \dot{z}}\right)_0 \tag{14}$$

are the solutions of the Reynolds equations,

$$\left[\frac{1}{R_a^2}\frac{\partial}{\partial\theta}\left(\frac{h^3}{12\eta}\frac{\partial}{\partial\theta}\right) + h^3\frac{\partial}{\partial y}\left(\frac{1}{12\eta}\frac{\partial}{\partial y}\right)\right]\begin{pmatrix} p_0 \\ p_x \\ p_z \\ p_{\dot{x}} \\ p_{\dot{z}} \end{pmatrix} = \begin{pmatrix} \frac{\Omega}{2}\frac{\partial h}{\partial\theta} \\ -\frac{\Omega}{2}\left(\sin\theta\frac{3\cos\theta}{h}\frac{\partial h}{\partial\theta}\right) - \frac{h^3}{4\eta R_a^2}\frac{\partial p_0}{\partial\theta}\frac{\partial}{\partial\theta}\left(\frac{\cos\theta}{h}\right) \\ \frac{\Omega}{2}\left(\cos\theta\frac{3\sin\theta}{h}\frac{\partial h}{\partial\theta}\right) - \frac{h^3}{4\eta R_a^2}\frac{\partial p_0}{\partial\theta}\frac{\partial}{\partial\theta}\left(\frac{\sin\theta}{h}\right) \\ \cos\theta \\ \sin\theta \end{pmatrix} \tag{15}$$

where Ω is the angular velocity, η is the viscosity of the fluid, and h is the fluid film height, as shown in Fig. 5. A complete deduction of these equations can be found in Ref. [22].

In each instant, given e and ψ, the equations in Eq. (15) are solved by using an in-house developed finite element code. The dynamical coefficients are then calculated by integrating the pressure and its derivatives (Eqs. (11)–(13)), and the new values of e and ψ are computed with a fifth-order Runge–Kutta method [24] on the equation of motion (9). The time step for this equation is calculated as

$$\Delta t = \frac{\min(t_x, t_z)}{50} \tag{16}$$

where

$$t_i = 2\pi\sqrt{\frac{m_a}{k_{ii}}}, \quad i = x,z \tag{17}$$

so that it is guaranteed that the shorter period of the oscillatory motion will be computed with, at least, 50 timesteps. Nevertheless, if the solution of Eq. (9) yields an eccentricity larger than 1, then the timestep is divided by two. That process is repeated so many times as needed to obtain $e<1$. That can result in a very slow simulation when the journal is close to the bearing wall, but it ensures the stability of the solution. Nevertheless, a minimum distance to the wall is defined so that it is assumed contact metal-metal, and the program stops.

The solution of Eq. (15) has been obtained with the usual finite element code in a two-dimensional four-node quadrilateral mesh. The dimensions of the computational domain were $L\times 2\pi$, where L is the length of the journal. The size of the mesh was of 2500 elements, 25 in the direction of the journal axis and 100 in the direction of the angle θ. The boundary conditions are periodical in the θ direction and zero pressure on both ends in the axis direction.

3 Numerical Results

The main characteristics of the simulations are summarized in Table 1.

As a preliminary numerical experiment sinusoidal variable load, with constant x-direction, has been applied to the journal bearing. The amplitude of the variation of the load modulus is 10% of the mean load. The results of this preliminary experiment will be compared with the results with the actual gear pump load at the end of the section

For the actual gear pump load, Fig. 6 displays the trajectory of the center of the journal with a constant rotational velocity of 1000 rpm. In this and subsequent figures, until Fig. 9, the position of the shaft center C, in relation with the bearing center O, is

Table 1 Main characteristics of the journal of the simulations

Parameter	Value	Units
c	5×10^{-5}	m
R_a	0.0091	m
L	0.0197	m
η	0.02	Pa s
ρ	885	kg/m^3
z	12	-
R	0.0188	m
H	0.025	m
Pressures	10, 100, 150, 200	bar
Velocities	1000, 1500, 2000	rpm

plotted. The maximum value of the radial distance is the clearance of the journal bearing (see Fig. 5). The working pressure has been modified from 10 bars to 200 bars. It is observed that there is solid contact for 200 bars of outlet pressure and that, for 150 bars, the eccentricity is so large that it cannot be considered in the existence of fluid film. It can be concluded that, at this velocity, the pressure has a limit value of 150 bars if the fluid film in the journal bearing is to be conserved.

If the velocity is increased to 1500 rpm, as shown in Fig. 7, the eccentricity diminishes and contact is avoided even for 200 bars of working pressure. Nevertheless, in this case, the existence of a fluid film is still uncertain. Only for 2000 rpm (Fig. 8) the eccentricity is so small that the fluid film can be considered preserved.

In all cases, the initial position of the center of the journal is 3×10^{-5} m in the x-direction, since it has been observed that the computation time for reaching equilibrium can be rather large otherwise.

Generally, the journal orbits have a triangular shape with an approximate size of 10×5 μm, and they become smaller when the pressure increases.

On the other hand, there is a great difference in the shape of the orbit for low pressure (represented in this case with 10 bars) and high pressure. At low pressure, it has an ill-defined shape and a small eccentricity. At higher pressure, the eccentricity increases very quickly and the shape has a better defined triangular shape.

Figure 9 displays the orbits of the journal when the working pressure is maintained at a constant 150 bars, and the velocities are 1000 rpm, 1500 rpm, and 2000 rpm. It is observed that the eccentricity lessens and the angle increases when the velocity increases, as described by the hydrodynamic classical theory [22].

Although it cannot be seen in Figs. 6–9, the rotation of the shaft is counterclockwise, as is the precession movement around the center of the orbit. The results show 12 precession cycles per revolution, which is the number of teeth of a gear. In each of these precession orbits, three phases can be observed depending on the force acting on the gear (Fig. 10), as follows:

- sudden change in the z direction of the load (point A).
- the shaft reacts to this change, and moves quickly from A to B.
- the shaft is in hydrodynamic equilibrium with these new conditions (point B).
- the x and z components of the load change smoothly with the rotation of the gear. The shaft tends to center by reducing the eccentricity and by increasing the equilibrium angle (from B to C).
- sudden change in the x component of the load (point C).
- the shaft reacts to this change, and moves quickly from C to A.
- turning again, with a new pair of teeth (point A).

Compared with the journal motion with a sinusoidal load with constant direction, it seems that the variability of the load angle plays a major role in the orbit size. The load angle is, in average, located in 60 deg, but is has a variability of ±10 deg, as shown in Fig. 4. The variation in the position angle of the journal is not so large in its equilibrium orbit trajectory, but it is much larger than when there is no angular variation of the load.

As in Ref. [25], following Ref. [26], a Reynolds number can be defined as

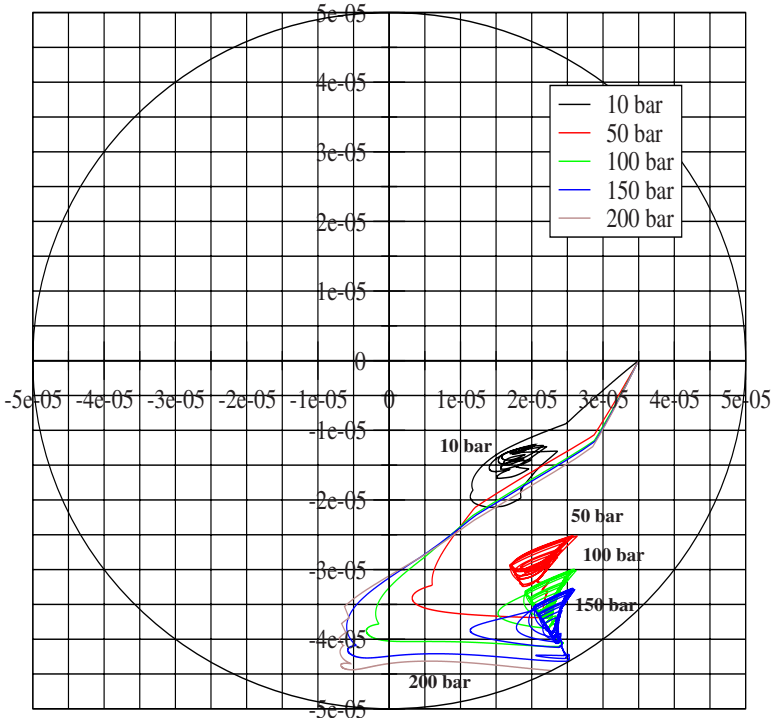

Fig. 6 Orbits of the center of the shaft for 1000 rpm

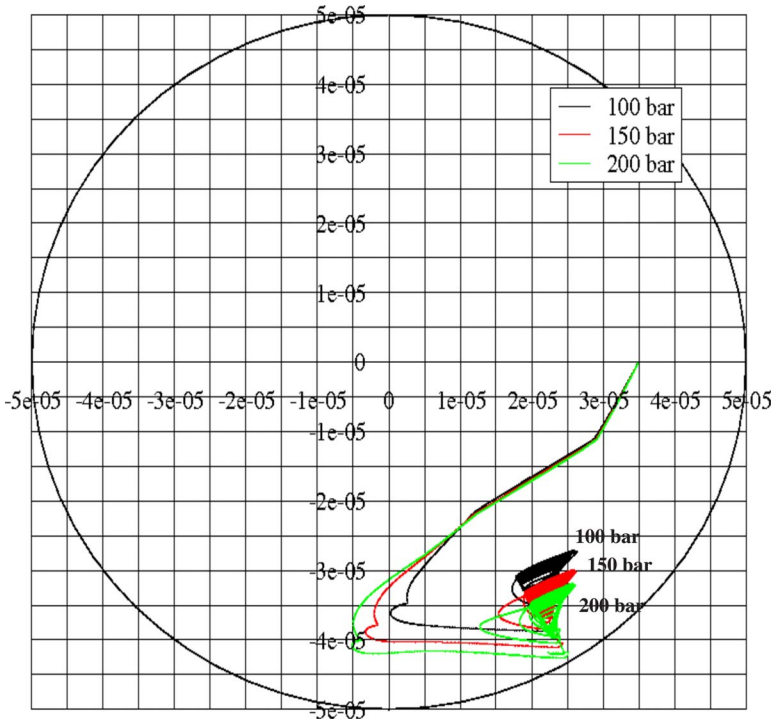

Fig. 7 Orbits of the center of the shaft for 1500 rpm

$$\mathrm{Re} = \frac{\rho \omega c^2}{\eta} \tag{18}$$

and a nondimensional working pressure, in a similar way than the Sommerfeld nondimensional load, as

$$P^* = \frac{P}{\omega \eta}\left(\frac{c}{R_a}\right)^2 \tag{19}$$

In Ref. [25] a critical value of 100 is obtained for P^* in order to keep the shaft in the 95% of maximum relative eccentricity, which can be considered as a security zone for avoiding metal-metal contact. If this limitation is applied to the journal bearing simulated in the present work, it obtains a critical pressure of 70 bars for 1000 rpm, 105 bars for 1500 rpm, and 140 bars for 2000 rpm,

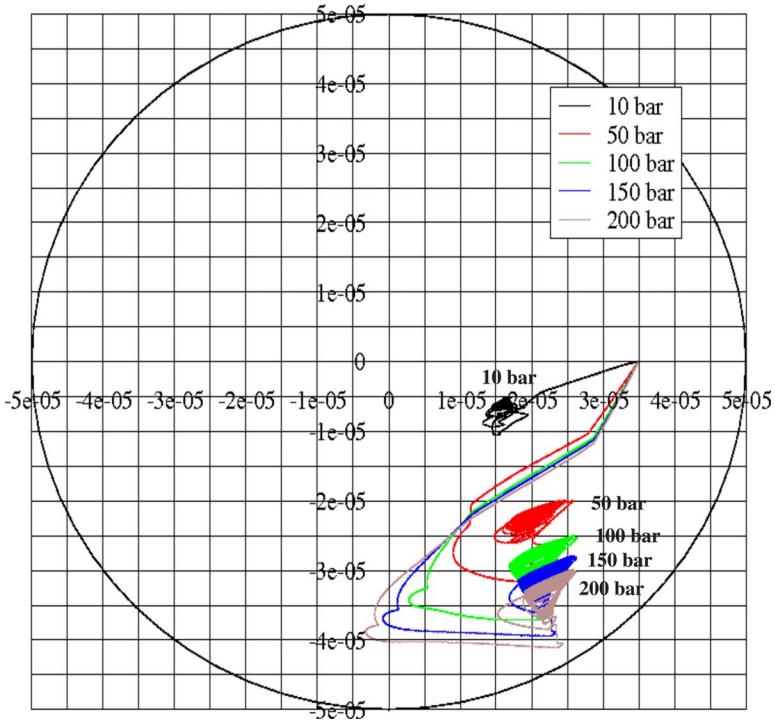

Fig. 8 Orbits of the center of the shaft for 2000 rpm

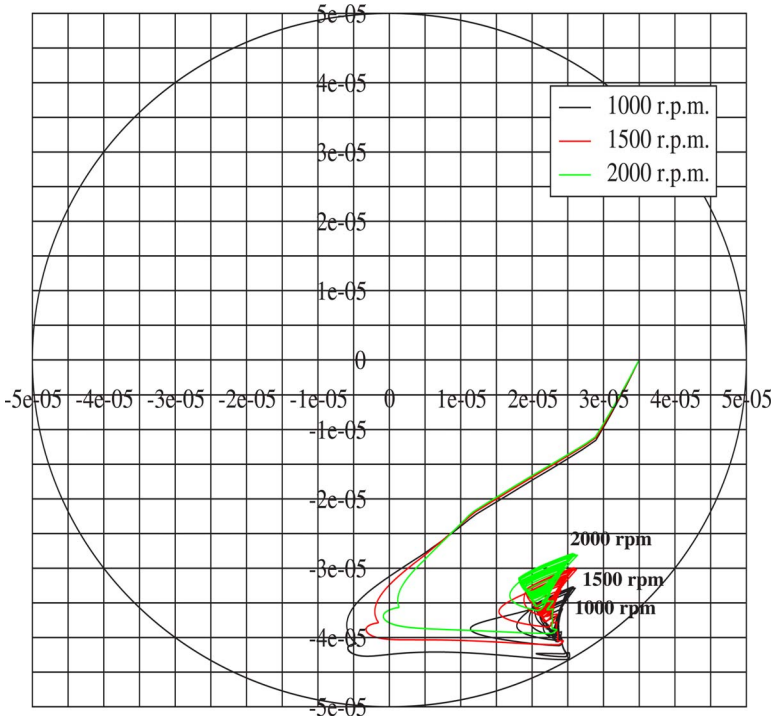

Fig. 9 Orbits of the center of the shaft for 150 bars

which are in good agreement with the results presented in this work (100 bars, 150 bars, and 200 bars) provided that the definition of P^*_{cr} as three times the characteristic nondimensional pressure, P^*_{ch} (obtained from an exponential regression), is rather conservative. Another way to establish this limitation is defining a minimum rotational velocity for a given working pressure as

$$\omega_{min} \approx \frac{P}{100\eta}\left(\frac{c}{R_a}\right)^2 \tag{20}$$

which, for the particular case of the simulated pump, yields $\omega_{min} \approx 14.4P$, with P in bar and ω_{min} in rpm. This condition is plotted in Fig. 11.

The comparison of numerical results and experimental ones, reported in Ref. [25], are also reproduced in Fig. 12, where the exponential regression is also plotted with a solid line. The agreement for the range of P^* simulated is rather good, especially for high values of P^*. For lower values, the simulation tends to underestimate the relative eccentricity compared with experimental results. The relative sizes of the orbits are, on the contrary, overestimated.

The results can be also compared with the numerical work in Ref. [26]. Although the Reynolds numbers in Ref. [26] are bigger than in the numerical and experimental results reported here, the agreement with El-Shafei's experiment for Re=0 is excellent. Figure 13 shows the polar plot of results for the numerical simulation of the present paper and those from Ref. [26]. It also includes the results for the sinusoidal load. The agreement is even better with the latter, which suggests that the variation in load direction plays a major role, especially in the equilibrium angle. The comparison in eccentricity can be done by definition, as in El-Shafei's work, of a modified Sommerfeld load as

$$S = \frac{Lc^2}{\mu RL^3\Omega} \tag{21}$$

The plot of S versus ε is shown in Fig. 14. The agreement with Ref. [26] is very good for the sinusoidal load. The actual gear pump load slightly underestimates the relative eccentricity, but, as noted above, the change in the equilibrium angle is more important.

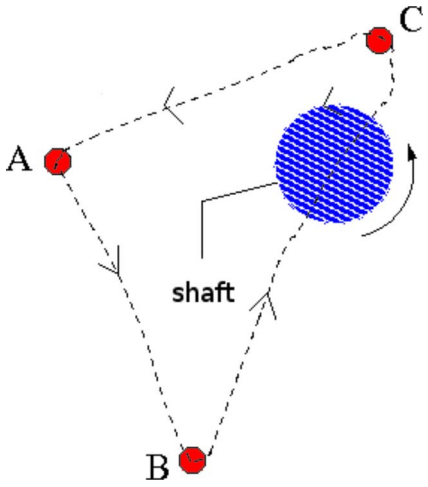

Fig. 10 Descriptive scheme of the precession movement of the shaft

4 Final Discussion and Conclusions

A tool for the numerical analysis of the motion of the shaft in the journal bearing of a gear pump is presented. It combines resolution of the equation of motion derived from the linearization of the fluid film load with a fifth-order Runge–Kutta scheme, calculation of the pressure distribution and its derivatives around the journal, and the load on the gears due to pressure distribution in the pump case. As far as the authors are aware, there is no such tool available for the study on the gear pump performance, although its usefulness would be undeniable in minimizing bearing wear.

The wear in the case of a real pump has been checked, and it confirms the predominant direction of the load calculated for the

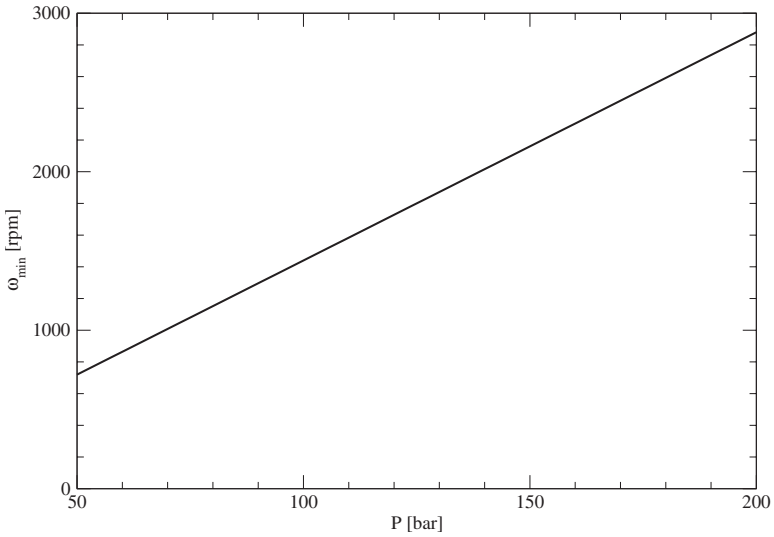

Fig. 11 Minimum rotational velocity as a function of the working pressure for the simulated gear pump

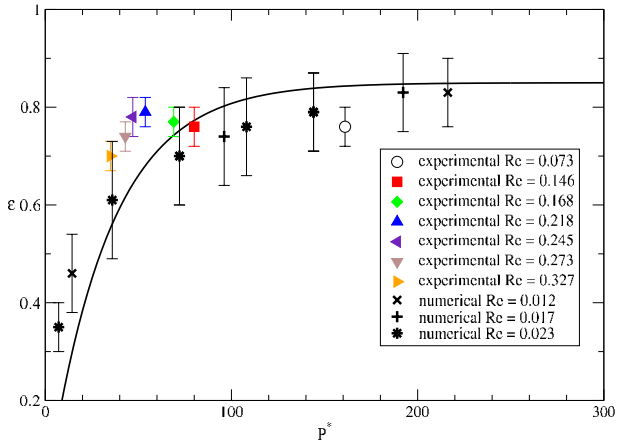

Fig. 12 Comparison of relative eccentricity with experimental results in Ref. [25]

gears. Moreover, it is also been stated that the wear related to the driven gear is larger than that for the driving one, which agrees with measurements [21].

The simulations have been carried out with different working pressures and rotational velocities, with the geometry of a real pump, and with the main characteristics summarized in Table 1. The results show that there is a risk of metal-metal contact for a working pressure of 150 bars if the rotational velocity is below 1000 rpm, and it can go up to 200 bars for a rotational velocity of up to 1500 rpm. 200 bar was the maximum working pressure tested. These results suggest that, for normal working pressure of this pump (around 100–150 bar), with a rotational velocity below 1000 rpm, the fluid film will probably be broken. That is in quite good agreement with experimental results, provided that the given limitation $P^*_{cr}=100$ is rather conservative.

Concerning the shape of the precession orbits, except for at very low pressure (simulated as 10 bars) where there is no defined shape, the orbits are triangles with the frequency of the gearing. It is worth noting that the size of these orbits decreases when the

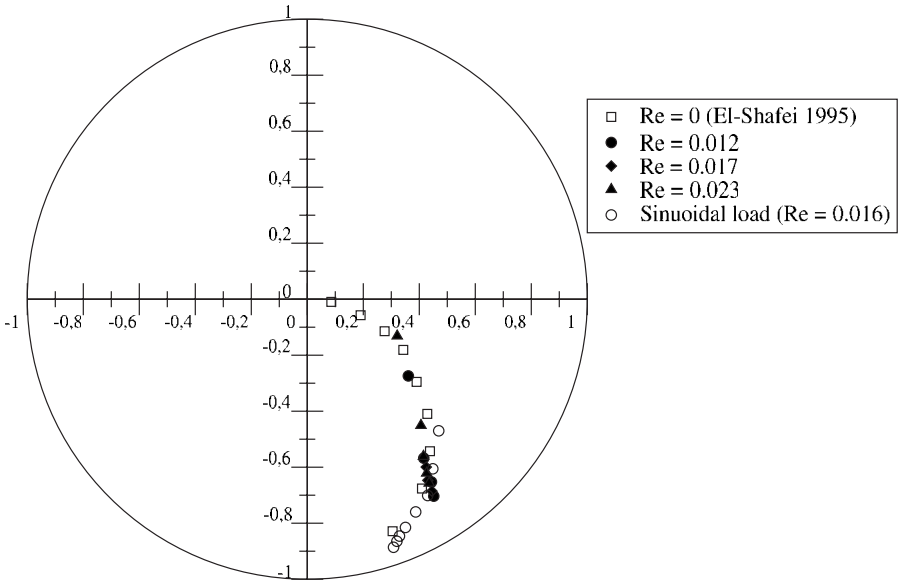

Fig. 13 Comparison with results in Ref. [26]

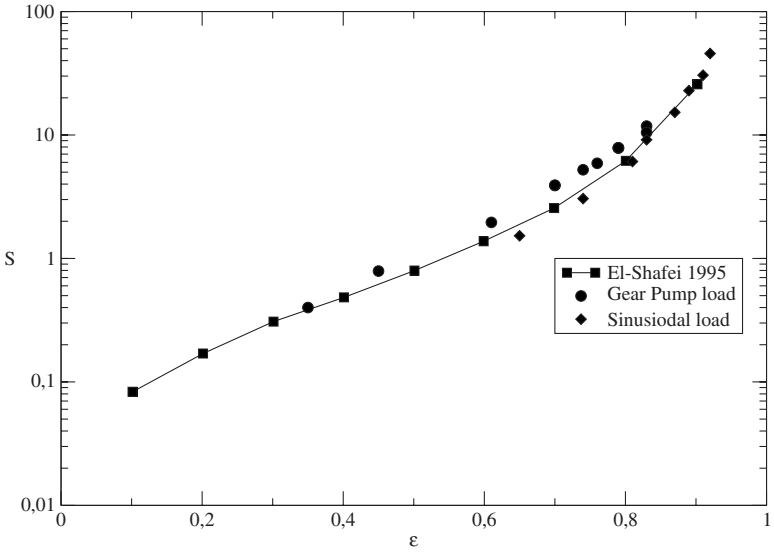

Fig. 14 Modified Sommerfeld load versus relative eccentricity for the results in Ref. [26], the sinusoidal load and the gear pump load

working pressure increases. However, this size diminishes when the rotational velocity decreases. In general, the orbits are smaller when the eccentricity grows larger. It seems that the simulation overestimates the relative size of the orbits. However, the clearance in experiments is four times such in the numerical simulations (due precisely to wear at high P^*), and, hence, the absolute size of the orbit is more similar for both cases, at least for $P^* < 100$.

The eccentricity is in excellent agreement with the results presented in Ref. [26] for Re=0, principally for the sinusoidal load, without change in load direction. When the load direction changes, as in the actual gear pump load, the equilibrium angle does not agree, not only with El-Shafei results, but also, with the sinusoidal load, which has been calculated with the same code. It seems that the change in load direction tends to lower the equilibrium angle for low eccentricity ($\varepsilon \lesssim 0.7$) and to raise it for higher relative eccentricity.

Nomenclature

H = width of the gears (m)
L = length of the journal (m)
P = pressure at the pump case (Pa)
P^* = nondimensional pressure
R = radius of the gears (m)
R_a = radius of the journal (m)
Re = Reynolds number
S = nondimensional modified Sommerfeld load
W = load on the gears (N)
b = damping coefficient (N s m^{-1})
c = clearance of the bearing (m)
h = height of the fluid film on the journal (m)
k = stiffness coefficient (N m^{-1})
m_a = mass of the shaft-gear set (kg)
p = pressure distribution on the journal (Pa)
t = characteristic time for shaft motion (s)
w = load on the journal (N)
z = number of teeth
(x,z) = coordinate system of journal (m)
(x',z') = coordinate system of bearing (m)

Greek Symbols

ϕ = angle of the total load
Ψ = equilibrium angle of the load
θ = angle in gears and in journal
η = viscosity of the fluid Pa s
ρ = density of the fluid kg m^{-3}
Ω = angular velocity s^{-1}

Subindex

ch = characteristic
cr = critic
d = discharge
s = suction

References

[1] Booker, J., 1969, "Dynamically Loaded Journal Bearings: Maximum Film Pressure," ASME J. Lubr. Technol., **91**(3), pp. 534–543.
[2] Goenka, P. K., 1984, "Dynamically Loaded Journal Bearings: Finite Element Method Analysis," Trans. ASME, J. Tribol., **106**(4), pp. 429–439.
[3] Aitken, M. B., and McCallion, H., 1992, "Parametric Minimum Film Thickness Performance of an Elastic Big-End Bearing Under Inertial Load," Proc. Inst. Mech. Eng., Part C: Mech. Eng. Sci., **206**(1), pp. 3–12.
[4] Sharma, D., Athre, K., Biswas, S., and Iyenger, S. R. K., 1991, "Solution of Reynolds' Equation for a Non-Newtonian Lubricant in a Journal Bearing Implementing the Moving Boundary Conditions," Tribol. Int., **24**(2), pp. 85–89.
[5] Zhang, Y., 1990, "Starting Pressure Boundary Conditions for Perturbed Reynolds Equation," ASME J. Tribol., **112**(3), pp. 551–555.
[6] McIvor, J., and Fenner, D., 1989, "Finite Element Analysis of Dynamically Loaded Flexible Journal Bearings: A Fast Newton-Raphson Method," Trans. ASME, J. Tribol., **111**(4), pp. 597–603.
[7] Zhang, J. X., and Roberts, J. B., 1996, "Solutions for the Combined Motion of Finite Length Squeeze Film Dampers Around the Bearing Center," ASME J. Tribol., **118**(3), pp. 617–622.
[8] Yu, B., and Sawicki, J. T., 2002, "Comparison of Mobility Method and Mass Conservation Method in a Study of Dynamically Loaded Journal Bearings," Int. J. Rotating Mach., **8**(1), pp. 71–79.
[9] Christensen, E., Tonnesen, J., and Lund, J. W., 1976, "Dynamic Film Pressure Measurements in Journal Bearings for Use in Rotor Balancing," ASME J. Eng. Ind., **98**(1), pp. 92–100.
[10] Klit, P., and Lund, J., 1986, "Calculation of the Dynamic Coefficients of a Journal Bearing, Using a Variational Approach," Trans. ASME, J. Tribol., **108**, pp. 421–425.
[11] Mitchell, J., Holmes, R., and Byrne, J., 1965, "Oil Whirl of a Rigid Rotor in 360 Journal Bearings: Further Characteristics," Proc. Inst. Mech. Eng., **180**, pp. 593–609.
[12] Myrick, S. T. J., and Rylander, H. G., 1976, "Analysis of Flexible Rotor Whirl and Whip Using a Realistic Hydrodynamic Journal Bearing Model," ASME J. Eng. Ind., **98**(4), 1135–1144,.
[13] Kirk, R. G., and Gunter, E. J., 1975, "Short Bearing Analysis Applied to Rotor Dynamics. Part 1. Theory," ASME J. Lubr. Technol., **98**(1), pp. 47–56.
[14] Kirk, R. G., and Gunter, E. J., 1976, "Short Bearing Analysis Applied to Rotor Dynamics Part 2. Results of Journal Bearing Response," ASME J. Lubr. Technol., **98**(2), pp. 319–329.

[15] Rao, T., Biswas, S., Hirani, H., and Athre, K., 2000, "Analytical Approach to Evaluate Dynamic Coefficients and Nonlinear Transient Analysis of a Hydrodynamic Journal Bearing," Tribol. Trans., **43**(1), pp. 109–115.
[16] Kakoty, S. K., and Majumdar, B. C., 2000, "Effect of Fluid Inertia on Stability of oil Journal Bearings," ASME J. Tribol., **122**(4), pp. 741–745.
[17] Pai, R., and Majumdar, B. C., 1991, "Stability of Submerged Oil Journal Bearings Under Dynamic Load," Wear, **146**, pp. 125–135.
[18] Jang, G. H., Lee, S. H., and Kim, H. W., 2006, "Finite Element Analysis of the Coupled Journal and Thrust Bearing in a Computer Hard Disk Drive," ASME J. Tribol., **128**(2), pp. 335–340.
[19] Jang, G. H., and Yoon, J. W., 2002, "Nonlinear Dynamic Analysis of a Hydrodynamic Journal Bearing Considering the Effect of a Rotating or Stationary Herringbone Groove," ASME J. Tribol., **124**(2), pp. 297–304.
[20] Jang, G. H., and Yoon, J. W., 2003, "Stability Analysis of a Hydrodynamic Journal Bearing With Rotating Herringbone Grooves," ASME J. Tribol., **125**(2), pp. 291–300.
[21] Gutes, M., 2008, "Estudio de un cojinete hidrodinámico y movimiento del eje conducido en una bomba de engranajes externos," Ph.D. thesis, Technical University of Catalonia, Terrassa, Barcelona.
[22] Hamrock, B. J., 1994, *Fundamentals of Fluid Film Lubrication*, McGraw-Hill, New York.
[23] Lund, J. W., and Thomsen, K. K., 1978, "A Calculation Method and Data for the Dynamic Coefficients of oil Lubricated Journal Bearings," *Topics in Fluid Film Bearing and Rotor Bearing System*, ASME, New York, pp. 1–28.
[24] Press, W. H., Teukolsky, S. A., Vetterling, W. T., and Flannery, B. P., 1992, *Numerical Recipes in Fortran 77*, Cambridge University Press, Cambridge, England.
[25] Castilla, R., Gutes, M., Gamez-Montero, P. J., and Codina, E., 2009, "Experimental Study of the Shaft Motion in the Journal Bearing of a Gear Pump," ASME J. Eng. Gas Turbines Power, **131**, p. 052502.
[26] El-Shafei, A., 1995, "Modeling Fluid Inertia Forces of Short Journal Bearings for Rotordynamic Applications," ASME J. Vibr. Acoust., **117**, pp. 462–469.

Effect of Experimental Conditions on Gas Core Length and Downward Velocity of Free Surface Vortex in Cylindrical Vessel

Hideaki Monji
e-mail: monji@kz.tsukuba.ac.jp

Tatsuya Shinozaki

University of Tsukuba,
1-1-1 Ten-nodai,
Tsukuba 305-8573, Japan

Hideki Kamide

Takaaki Sakai

Japan Atomic Energy Agency,
4002 Narita, O-arai,
Ibaraki 311-1393, Japan

This paper deals with characteristics of surface vortex in a cylindrical vessel. One of the characteristics is a gas core length, which is important to estimate the onset condition of the gas entrainment but influenced easily by the experimental condition. In the experiment using water, the effects of the water temperature, water level, and the surface tension on the gas core length were investigated. The onset condition of the gas entrainment is sometimes estimated by using the Burgers vortex model but the real flow in the vessel is different from the model. The velocity fields were measured by particle image velocimetry (PIV) and the velocity gradient of the downward flow was discussed. The proper flow conditions for the Burgers vortex model are a high water level and a high flow rate. [DOI: 10.1115/1.3078704]

1 Introduction

Gas entrainment by vortices on a free surface in sodium-cooled fast reactor plants is an important phenomenon to design them. Therefore, this phenomenon was investigated by many researchers [1–4]. In the experiments for a steady vortex on a free surface, the vortex and gas entrainment were observed in a cylindrical vessel using water instead of sodium [2]. Water was injected along the vessel wall and flowed out from the outlet on the bottom. Because circulation and downward flow were induced, the gas entrainment was occurred by the vortex.

Because the fluid properties are different between water and sodium, the experimental results cannot be applied to the sodium-cooled fast reactor directly. However, there are some studies on the effects of fluid properties on the gas entrainment induced by a vortex, using alcohol, glycerin, surfactant-water solution, or sodium, and the experimental results using water can be applied through the relation found in these studies on the effects of fluid properties [5,6].

On the other hand, unsteady feature of the free surface vortex was also investigated. By the observation in experiments simulating flow in an upper plenum, the vortices on a free surface suddenly appeared and grew in a short time; finally the gas entrainment occurred. Therefore, the gas entrainment is an unsteady phenomenon. In order to consider the unsteadiness of the phenomenon, the free surface vortex in a cylindrical vessel was investigated with a periodically fluctuating water flow rate [7,8].

Our experiments on the free surface vortex under the steady and unsteady conditions in a cylindrical vessel have been done by using water as a working fluid under the room condition [7,8]. The room condition means that the pressure is the atmospheric pressure and the temperature is the room temperature. The results sometimes showed differences between the experiments. For example, the measured gas core length, which is one of the most important indices characterizing the free surface vortex, changed between experiments done in spring and summer. The experimental equipment and the experimental condition were the same. As a result of verification of the experiments, we estimated that a little difference of water temperature influenced the gas core length.

In this study, the effect of the experimental condition on the free surface vortex is investigated. The water temperature, water level, and surface tension were systematically changed and the gas core length was measured by image processing. Based on the experimental results, the effect of such parameters on the behavior of the free surface vortex was discussed.

In the discussion, we focused on the water level in the vessel. In our experimental equipment, the circulating water velocity or a circumference velocity was changed with the water level. However, the change in the gas core length could not be explained only by the water velocity. It was needed to consider the change in the flow structure. The velocity field on the longitudinal cross section of the cylindrical vessel was measured by PIV and also the downward velocity in the vessel was measured by dye tracing. The experimental results showed that the downward velocity gradient changed with the water level and the gas core length also changed. The downward velocity gradient is one of the important factors for the flow field in the Burgers vortex model, which is used to theoretically obtain the onset condition of the gas entrainment. Furthermore, the downward velocity gradient was assumed to be constant in the theory but it was not in the experiment. The experimental results showed that the constant area of the velocity gradient changed with the water level and the flow rate.

2 Experimental Apparatus and Measurement System

2.1 Experimental Apparatus. Figure 1 shows a schematic of the experimental apparatus, which was a simple loop consisting of a cylindrical vessel or a test section, a rectifier of water flow, a pump, and an electromagnetic flowmeter. The test section was the cylindrical vessel of 20 cm inner diameter. The water was fed to the loop until the set depth of the water at the test section. After that, the water was driven by the pump and flowed to the test section through the rectifier. The inlet part was a rectangle channel of 20 mm width. The water flowed into the test section along the tangential direction of the wall through the rectangle channel. Therefore, the water flowed circularly in the vessel. The outlet pipe was connected to the center on the bottom of the cylindrical

Manuscript received August 20, 2008; final manuscript received September 11, 2008; published online September 29, 2009. Review conducted by Dilip R. Ballal. Paper presented at the 16th International Conference on Nuclear Engineering (ICONE16), Orlando, FL, May 12–15, 2008.

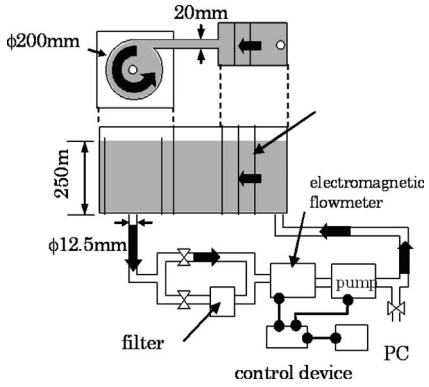

Fig. 1 Experimental apparatus

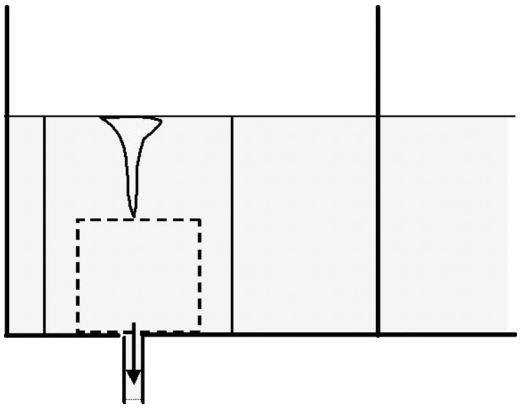

Fig. 2 Measurement area for longitudinal cross section by PIV

vessel and the water flowed out from the outlet pipe. The diameter of the outlet pipe was 12.5 mm. In the test section, circulation and downward flow of the water were simultaneously observed.

The water flowed through the electromagnetic flowmeter connecting to the outlet pipe and returned to the pump. The test section, rectifier, and bottom pipe were made of a transparent acrylic resin to observe the flow. Furthermore, a water jacket was attached to the cylindrical vessel to reduce the distortion of the image through the vessel wall.

In order to control the water flow rate, the pump and the flowmeter were connected through a control device and a personal computer.

2.2 Measurement System. In the experiment, the gas core length, and the vertical and horizontal flow fields were mainly measured. The gas core length was measured by the image processing. The flow fields were measured by the dye tracing and the PIV.

The gas core shape of the vortex formed in the cylindrical vessel was observed and taken by charge coupled device (CCD) cameras. A telecentric lens was attached at the CCD camera [9]. By using the telecentric lens, the object size can be kept constant even if the object is near or far from the lens. Therefore, it is very convenient to measure the gas core length because the position of the gas core fluctuates a little under the constant water flow rate.

The gas core shape was obtained by image processing where the original image was changed to a binary image and the outline of the vortex shape was extracted from the binary image [6]. Based on the outline, the location, length, and shape of the gas core can be known.

The velocity field on the cross section of the cylindrical vessel was measured by using PIV. The flow images on the horizontal cross section and the longitudinal cross section of the vessel were taken by the CCD camera. Thus, the flow image was taken through the transparent plate of the vessel. Fluorescent particles were used as tracers for PIV. By using an optical filter, the reflection of the laser light on the vessel wall can be cut and a clear tracer image can be taken.

As mentioned below, the longest gas core length in the experiment was less than 10 cm. The cross section for PIV was set below the gas core and the velocity field obtained did not contain the gas core region.

The velocity field on the longitudinal or vertical cross section was also set as not containing the gas core. The measured area was 160×160 mm^2 rectangular shape on the bottom plate and its horizontal center is at the center of the cylindrical vessel, as shown in Fig. 2. Because the measurement area was set at below the gas core, i.e., water single phase flow area, the laser sheet and the images were not influenced by the gas core, such as reflection and refraction. The image size is 1024 pixel $\times$ 1024 pixel and the minimum resolution is 0.164 mm/pixel.

In the flow structure around the free surface vortex, a velocity gradient of the downward flow is one of the important factors as shown in the Burgers vortex model. In order to measure the velocity gradient on the path line, the dye tracing was done. A droplet of dye (about 0.2 ml) was put on the surface at the circumference of the vortex, and the tip of the dye was taken by a high-speed camera with the telecentric lens after moving with the water flow. The dye was made of blue ink diluted by the same amount of water. Before the experiment, the dye was put into the stagnant water and it was confirmed that the dye moved neither up nor down. The frequency of the high-speed camera was less than 300 Hz and depended on the flow velocity.

Figure 3 shows the flow of the dye. These images cover the whole area of the cylindrical vessel to understand the flow pattern of the dye. In that case, the gas core was very small and a dimple. At $t=0$ s, the droplet of the dye was put on the surface. The dye moved spirally with the flow ((b) $t=0.5$ s). At $t=4$ s, the tip of the dye reached the outlet and the core of the vortex was observed by the dye. For image processing at the downward velocity measurement, closed-up images of 160×160 mm^2 were used.

3 Experimental Results

3.1 Effect of Water Temperature. The length of a free surface vortex and the onset condition of the gas entrainment can be experimentally obtained but they are influenced by the experimental condition. Therefore, the effects of several experimental conditions are examined.

Figure 4 shows the relation of the gas core length and the water temperature and also the critical flow rate of the gas entrainment for two cases. Beyond the critical value of the water flow rate, the bubble detachment was observed from the tip of the gas core and it was at the beginning of the gas entrainment. Under the same water flow rate, the gas core length was longer with the higher water temperature. The average change in the gas core length with the water temperature was about 8.5%/°C for the water flow rates 4.5 l/min and 6.0 l/min. The critical water flow rate of the gas entrainment tended to be also small with the water temperature. Note that the water temperature was changed from 20°C to 40°C. When we use "the room temperature," the temperature includes this region. It can easily happen at 40°C as the water temperature under the use of a pump in summer. Figure 4 shows that the temperature effect cannot be neglected even if the temperature is in room temperature.

The density, the viscosity, and the surface tension change with the water temperature. Figure 5 shows the relation of the radial Reynolds number N and the gas core length. The definition of the radial Reynolds number is

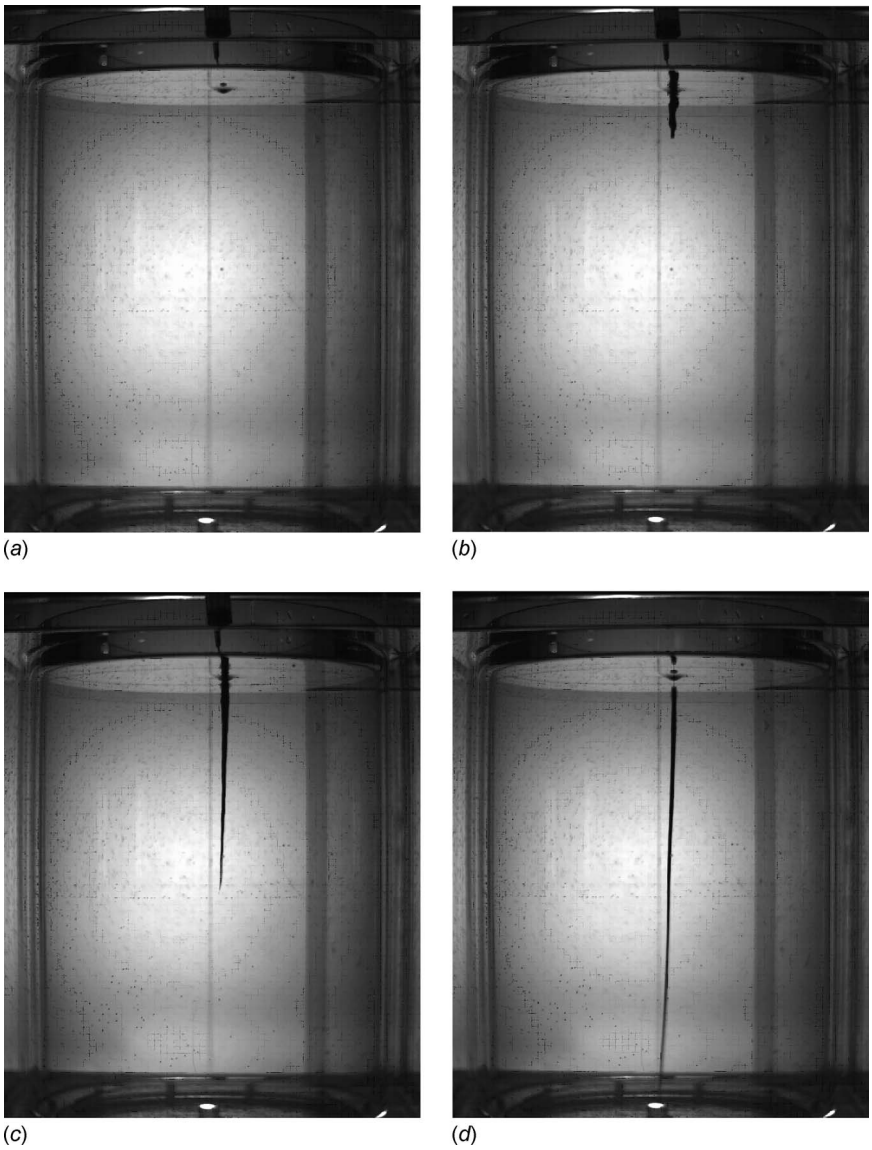

Fig. 3 Dye moving with the flow

$$N = \frac{Q}{h\nu} \tag{1}$$

Here, Q denotes the water flow rate, h is the water level, and ν is the kinematic viscosity of the water. The experimental results may be on a line except for the case of 40°C. The reason why the case of 40°C showed the difference from the other cases is not clear but the surface tension might influence the gas core length. On the other hand, the results could not be put on a line with the Weber number. Therefore, the viscosity effect is the most part of the temperature effect in this temperature region.

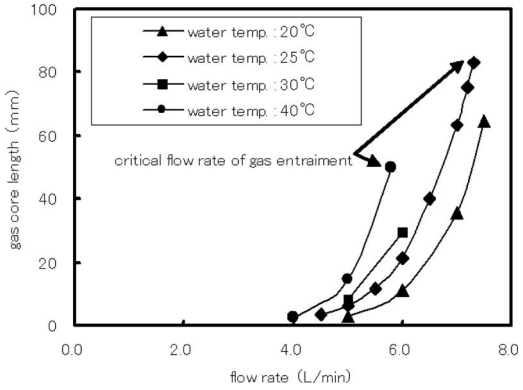

Fig. 4 Effect of water temperature on gas core length

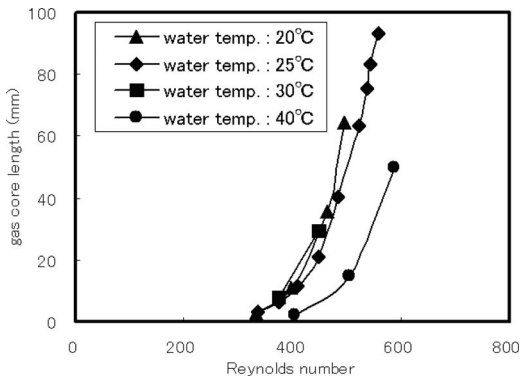

Fig. 5 Gas core length of various Reynolds numbers

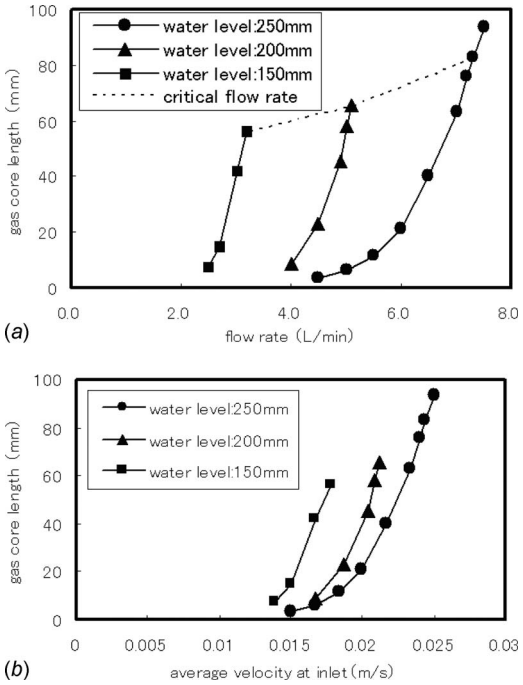

Fig. 6 Effect of water level on gas core length: (*a*) flow rate dependence and (*b*) inlet velocity dependence

3.2 Effect of Water Level. Next, the effect of the water level was examined. Figure 6(*a*) shows the gas core length under three kinds of water level. The dashed line shows the critical water flow rate of the gas entrainment. As structural characteristics of the experimental apparatus, the water velocity into the vessel increases with the lower water level even if the water flow rate is the same. In order to eliminate the water velocity effect at the inlet, the gas core length was arranged with the inlet velocity. The experimental data, however, showed the dependence of the water level. This result shows that the flow structure such as the downward water flow velocity and its region is changed with the water level. Therefore the water level effect on the gas core length was nonlinear and it was difficult to show the change in the gas core length with the water level quantitatively by an average rate. The change in the gas core length was more than five times of the gas core length for 5 cm difference of the water level in the case of the water level at 15 cm, and about two times in the case of the water level at 20 cm.

3.3 Effect of Surface Tension. The effect of the surface tension was also examined by the use of a surfactant. Figure 7 shows the gas core length in the cases of different surfactant concentrations. The surface tensions measured by Wilhelmy method were

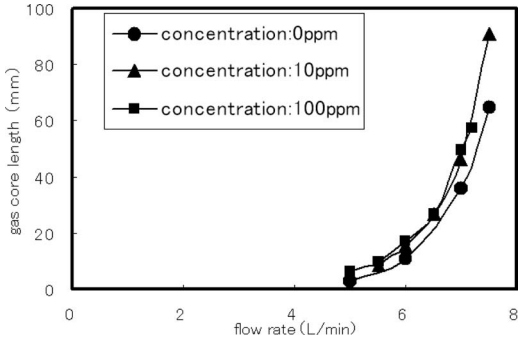

Fig. 7 Effect of surfactant on gas core length

69.8 dyn/cm, 52.5 dyn/cm, and 42.1 dyn/cm for 0 ppm, 10 ppm, and 100 ppm of surfactant concentrations, respectively. The viscosity changed within 2% by addition of the surfactant. Qualitatively, the gas core length at the same flow rate increased with the surfactant and small surface tension but the effect of the surface tension is very nonlinear. The change in the gas core length increased to 120% in the case of water with 100 ppm of surfactant, compared with the case of water without the surfactant. Because of the nonlinear effect, it was difficult to arrange the experimental result only using the Weber number.

The form of the entrained bubble was also influenced by the surface tension. The entrained bubble was a spherical bubble as shown in Fig. 8(*a*), in the water without the surfactant. In the case of using a surfactant, the entrained bubble was a small spherical bubble as shown in Fig. 8(*b*)(1) but sometimes, a very long bubble shown as Fig. 8(*b*)(2). The frequency of the long bubble was very small but the volume ratio of the long bubble in the total entrained gas volume was not small. The long bubble may come from the separation at the column of the gas core, while the spherical bubble is separated at the tip of the gas core.

3.4 Velocity Distribution Measured by PIV. The flow characteristics of the free surface vortex are sometimes discussed with the Burgers vortex model, where the radial, circumferential, and vertical velocities are

$$u(r) = -\frac{1}{2}\alpha r \tag{2}$$

$$v(r) = \frac{\Gamma_\infty}{r}\left[1 - \exp\left\{-\left(\frac{r}{r_1}\right)^2\right\}\right] \tag{3}$$

$$w(r) = \alpha z \tag{4}$$

respectively, in an infinite region. In the model, the constant vertical velocity gradient α characterizes the flow field. Because the experiment is done in a finite cylindrical vessel, the real flow structure is different from the Burgers vortex model and it is important to clarify the difference.

Figure 9 shows the velocity field measured by PIV, where Fig. 9(*a*) shows the magnitude of the velocity and Fig. 9(*b*) shows the velocity vectors. Only in the experiment measuring flow fields by PIV the diameter of the outlet pipe was 15 mm. The water level was 250 mm and the water temperature was $(20 \pm 1)\,^\circ$C. The water flow rate was 4.5 l/min. The velocity field was the longitudinal cross section including the center of the outlet. The laser sheet for PIV was not influenced by the gas core because the velocity field under the gas core was measured. The gray level in Fig. 9(*a*) corresponds to the speed of the water at that point. The black level corresponds to 0 mm/s and the white level corresponds to 150 mm/s, as shown in the legend under the figure. The flow field was not axisymmetric because the structure of the test section was not axisymmetric. The inlet of the water of the vessel is located on one side of the wall and the outlet of the water of the vessel is located on the center of the bottom plate. Therefore, the vortex shape was three dimensional. There are two white areas and a black area between them near the center. The black area is the center of the vortex and the circumferential velocity is small in the area. Inversely, the white area shows the high circumferential velocity region as shown in Fig. 9(*b*).

Figure 10(*a*) shows the circumferential velocity distribution along the radial direction at the water depth $z = 125$ mm for three kinds of water flow rate, which is measured by PIV on the cross section of the cylindrical vessel. Figure 10(*b*) shows the circulation Γ based on the circumferential velocity distribution. The vortex seems to be a compound vortex but the circulation increases with the radial location r in the vessel.

Figure 11 shows the distribution of the downward velocity along the horizontal axis y of the velocity field shown in Fig. 9. The origin of y is located on the center of the outlet. The ordinate denotes the downward velocity and its negative value corresponds

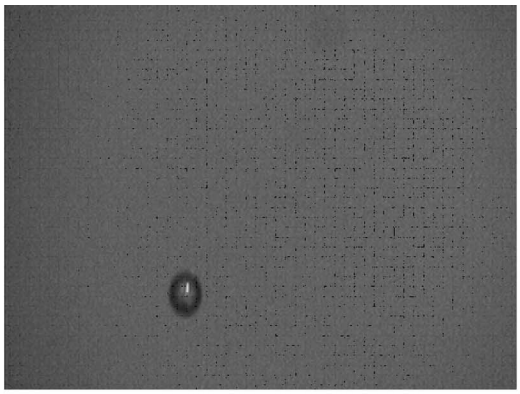

(*a*)

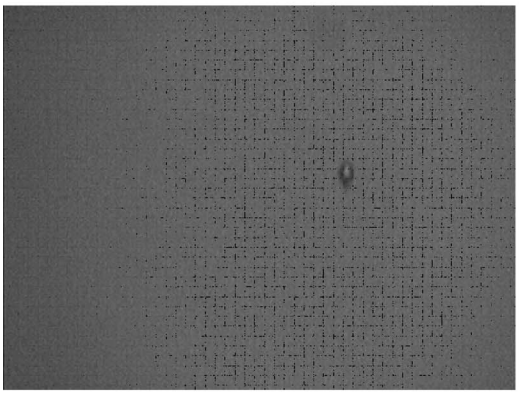

(*b-1*)

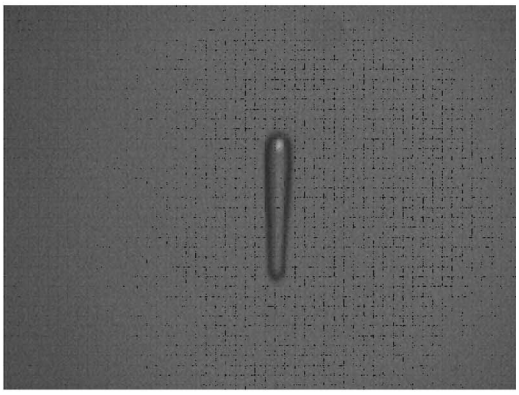

(*b-2*)

Fig. 8 Detached bubble from the gas core: (*a*) water, (*b*)(1) water with surfactant (100 ppm), and (*b*)(2) water with surfactant (100 ppm)

to the upward flow. The downward velocity was almost zero except the center region and the downward flow were observed near the center. At the center or further inside of the flow, the upward flow was inversely observed. The water mainly flowed out through the downward flow area. The intensity of the upward and downward flow decreases with the distance from the outlet but the upward flow was observed even at 150 mm as the water depth. Figure 12 also shows the downward velocity distribution along the horizontal axis in the case of the water flow rate of 6 l/min. The distribution profile also shows the downward velocity and the upward velocity at the core region.

Figure 13 show the downward velocity at the constant radial position y along the vertical axis z or the water depth. The axis y denotes the position from the center of the outlet. The negative value corresponds to the left side position from the center and vise versa. The downward velocity distribution is very different from each other between the left and right sides. The reason why they are not the same is that the cylindrical vessel and the flow structure are not axisymmetric as shown in Fig. 9. The vortex shape was the three dimensional. The core center on the surface was not on the center of the vessel while the core center on the bottom was the center of the vessel.

As shown in Eqs. (2)–(4), the downward velocity gradient is one of the important factors for the Burgers vortex model but it could not be obtained based on the distribution along the water depth at constant radial position in the experiment because the vortex shape was three dimensional. Instead of taking the value at the constant radius position, Fig. 14 shows the distribution of the maximum downward velocity on the same water depth, which increases with the water depth z monotonically. Because the maximum downward velocity is expected near the free surface vortex, the gradient of the maximum downward velocity at the cross section can be used as the downward velocity gradient in the Burgers vortex model. But the gradient based on Fig. 14 is not enough because the velocity in Fig. 14 is not the maximum velocity on the cross section. It is the maximum velocity at the water depth in the two-dimensional velocity field measured by PIV. Because the velocity gradient along the vortex is needed to compare the Burgers vortex model, the dye tracing measurement was done as discussed in Sec. 3.4.

3.5 Dye Tracing. Figure 15 shows the traveling velocity of dye. A little dye was put on the surface near the center of the free surface vortex. The dye moved downward with the flow and the tip of the dye was traced by using a high-speed video camera. The traveling velocity was calculated based on the tip of the dye. Because the dye moves with the downward flow, the velocity along the vortex is expected to be obtained from the measurement of the dye traveling. The dye could be clearly traced by image processing in the area under the gas core. The experiment was done twice under the same condition.

The experimental condition is as follows: The water level was 250 mm and the water temperature was $(20 \pm 1)\,^{\circ}\mathrm{C}$. The diameter of the outlet pipe was 12.5 mm. In Fig. 15, the dashed line denotes the velocity of the flow having the constant velocity gradient (called as the constant gradient velocity), which is calculated assuming that the velocity is zero on the surface and the area average velocity corresponding to the flow rate at the outlet. In the Burgers vortex model, the constant velocity gradient mentioned above is used for the velocity gradient α. However, the general feature of the velocity profile obtained in the experiment was as follows: The traveling velocity was small near the surface and

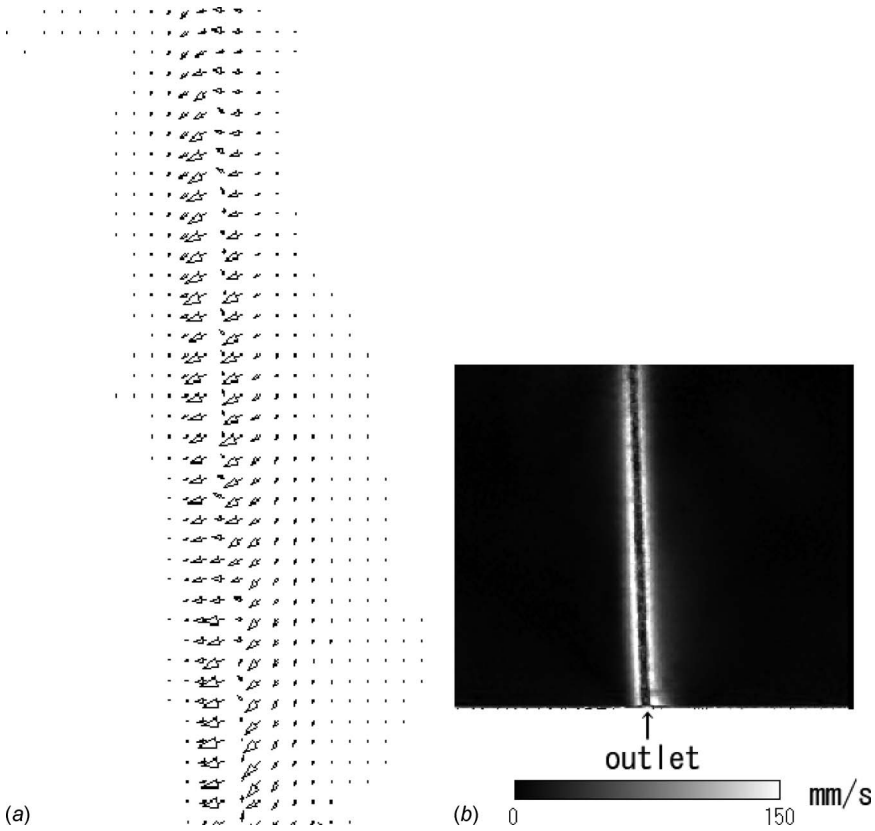

Fig. 9 Velocity field on the longitudinal cross section (flow rate of 4.5 l/min): (*a*) magnitude of velocity and (*b*) velocity vectors (close-up of vortex)

increased nonlinearly. The velocity gradient was almost constant after reaching the middle depth in the vessel. Near the outlet or the bottom plate the traveling velocity increased suddenly again. Comparing with the constant gradient velocity, the velocity of the dye could be classified into three flow regions as follows:

(a) *Region 1*. Near the surface, the velocity gradient is smaller than that of the constant gradient velocity or dashed line.
(b) *Region 2*. In the middle of the vessel, the velocity gradient is close to that of the constant gradient velocity.
(c) *Region 3*. Near the outlet or the bottom plate, the velocity gradient is larger than that of the constant gradient velocity.

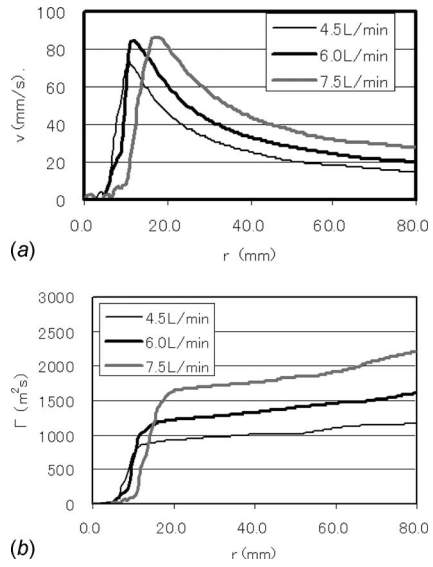

Fig. 10 Velocity and circulation distribution along the radial direction: (*a*) circumferential velocity and (*b*) circulation

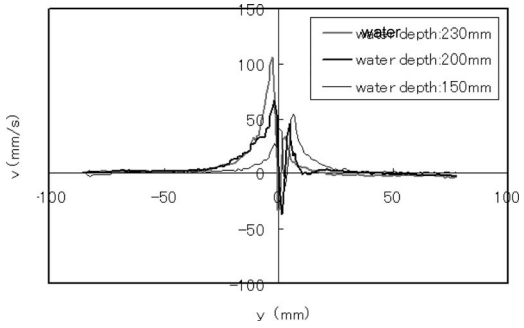

Fig. 11 Downward velocity distribution along the horizontal axis (flow rate of 4.5 l/min)

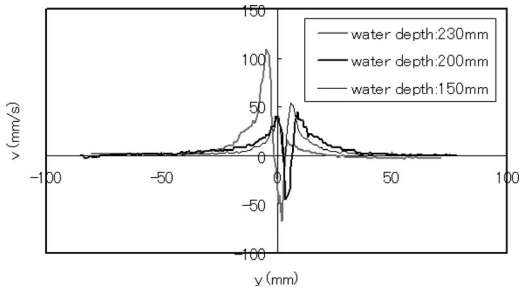

Fig. 12 Downward velocity distribution along the horizontal axis (flow rate of 6.0 l/min)

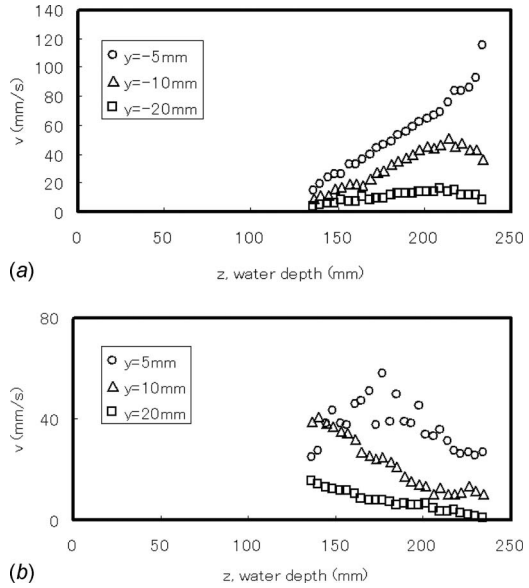

Fig. 13 Downward velocity distribution along the water depth, *z*: (*a*) left hand side and (*b*) right hand side

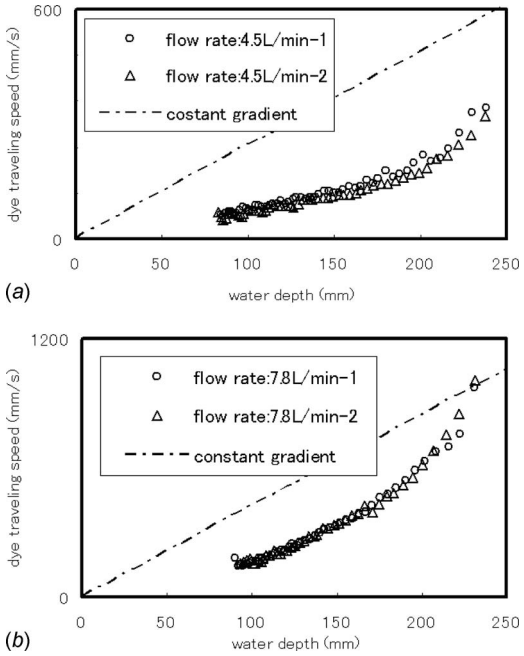

Fig. 15 Traveling speed of dye: (*a*) flow rate of 4.5 l/min and (*b*) flow rate of 7.8 l/min

Table 1 shows the range of each region in the experiment. The range is expressed by using the water depth. In Region 2, the velocity gradient in the experiment is close to that of the constant gradient velocity, which is the velocity gradient used in the Burgers vortex model. Therefore, the experimental condition where Region 2 covers widely in the vessel is suitable for the Burgers vortex model. For the case of a small flow rate, the range of Region 2 was wide for a low water level. For the case of the high water level, the range was wide for the high flow rate. Considering all cases, the range of Region 2 was wide for a high flow rate and a high water level.

4 Conclusions

In order to investigate the effect of the experimental condition on the free surface vortex in the cylindrical vessel, the experiment measuring the gas core length was done. The results showed that the gas core length changed with the water temperature even if it was the room temperature. The water temperature influenced the gas core length through its viscosity. The average change in the gas core length with the water temperature was about 8.5%/°C in the temperature range of 20–40°C in the experiment.

Furthermore, the water level also influenced the gas core length. It changed to two times of the length for 25% increase in the water level. The effect was nonlinear because the change in the water level did not only influence the circulating water velocity but also the downward velocity. The downward velocity was measured by PIV and the dye tracing. The downward velocity measured by the dye tracing was proper to be used as the velocity along the vortex in the Burgers vortex model. In the case of a high water level and a high water flow rate, the gradient of the downward velocity was constant and close to that used in the Burgers vortex model.

The surface tension effect to the gas core length was also investigated. It was nonlinear effect and the gas core length increased to 120% in the remarkable case.

Table 1 Region of each flow pattern

Flowrate (l/min)	Region 1	Region 2	Region 3
	Water level: 250 mm		
2.4	90–220	-	220–250
3.0	90–220	-	220–250
4.5	90–210	-	210–250
6.0	90–180	180–210	210–250
7.5	-	90–180	180–250
7.8	-	90–180	180–250
	Water level: 200 mm		
2.4	40–170	-	170–200
3.0	40–180	-	180–200
3.6	40–140	140–170	170–200
4.5	40–120	120–160	160–200
4.8	40–90	90–150	150–200
5.4	-	70–120	120–200
	Water level: 150 mm		
1.8	20–90	90–130	130–150
2.4	-	30–100	100–150
2.7	-	30–90	90–150
3.0	-	30–80	80–150
3.3	-	70–90	90–150

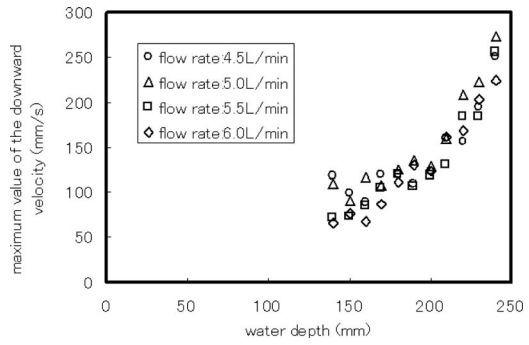

Fig. 14 Maximum downward velocity at the water depth based on the velocity fields measured by PIV

Nomenclature

N = radial Reynolds number
Q = water flow rate (m^3/s)
h = water level (m)
r = radial position (m)
r_1 = characteristic radius (m)
t = time (s)
u = radial velocity (m/s)
v = circumferential velocity (m/s)
w = vertical velocity (m/s)
z = vertical position or water depth (m)
y = radial position on velocity fields obtained by PIV (m)

Greeks

Γ = circulation (m^2/s)
α = vertical velocity gradient (1/s)
ν = kinematic viscosity of the water (m^2/s)

References

[1] Eguchi, Y., Yamamoto, K., Funada, T., Tanaka, N., Moriya, S., Tanimoto, K., Ogura, K., Suzuki, T., and Maekawa, I., 1994, "Gas Entrainment in the IHX Vessel of Top Entry Loop-Type LMFBR," Nucl. Eng. Des., **146**, pp. 373–381.

[2] Moriya, S., 1998, "Experimental Study of Scale Effects on Onset Conditions of Gas Entrainment by Free Surface Vortices," Abiko Research Laboratory, Central Research Institute of Electric Power Industry, Report No. U97073.

[3] Takahashi, M., Inoue, A., Aritomi, M., Takenaka, Y., and Suzuki, K., 1988, "Gas Entrainment at Free Surface of Liquid, (I)," J. Nucl. Sci. Technol., **25**(2), pp. 131–142.

[4] Takahashi, M., Inoue, A., Aritomi, M., Takenaka, Y., and Suzuki, K., 1988, "Gas Entrainment at Free Surface of Liquid, (II)," J. Nucl. Sci. Technol., **25**(3), pp. 245–253.

[5] Hiranuma, T., Yamamoto, K., Iwashige, K., Takakuwa, M., and Tokoi, H., 1997, "Experimental Study on Liquid Properties' Effect on Gas Entrainment Phenomena Induced by Vortices," *Proceedings of NURETH-8*, p. 1735.

[6] Hiranuma, T., Iwashige, K., Tokoi, H., and Takakuwa, M., 1998, "Study of Gas Entrainment Inception Induced by Vortex in Sodium," *Proceedings of AESJ Fall Meeting in 1998*, pp. 414–415.

[7] Monji, H., Akimoto, T., Miwa, D., and Kamide, H., 2004, "Unsteady Behavior of Gas Entraining Vortex on Free Surface in Cylindrical Vessel," *Proceedings of the Fourth Japan-Korea Symposium on Nuclear Thermal Hydraulics and Safety*, pp. 190–194.

[8] Monji, H., Akimoto, T., Miwa, D., and Kamide, H., 2005, "Behavior of Free Surface Vortices in Cylindrical Vessel Under Fluctuating Flow Rate," The 11th International Topical Meeting on Nuclear Reactor Thermal-Hydraulics (NURETH-11), Paper No. 429.

[9] Fournel, T., Coudert, S., Fournier, C., and Ducottet, C., 2003, "Stereoscopic Particle Image Velocimetry Using Telecentric Lenses," Meas. Sci. Technol., **14**(4), pp. 494–499.

Advanced High Temperature Gas-Cooled Reactor Systems

Yasuyoshi Kato[1]
Research Laboratory for Nuclear Reactors,
Tokyo Institute of Technology,
2-12-1-N1-2, O-okayama,
Meguro-ku, Tokyo 152-8550, Japan

Three systems have been proposed for advanced high-temperature gas-cooled reactors: a supercritical carbon dioxide (S-CO_2) gas turbine power conversion system, a new microchannel heat exchanger (MCHE), and a once-through-then-out (OTTO) refueling scheme with burnable poison (BP) loading. A S-CO_2 gas turbine cycle attains higher cycle efficiency than a He gas turbine cycle because of reduced compression work around the critical point of CO_2. Considering temperature reduction at the turbine inlet by 30°C through intermediate heat exchange, the S-CO_2 indirect cycle achieves an efficiency of 53.8% at a turbine inlet temperature of 820°C and a turbine inlet pressure of 20 MPa. This cycle efficiency value is higher by 4.5% than that (49.3%) of a He direct cycle at a turbine inlet temperature of 850°C and 7 MPa. A new MCHE has been proposed as an intermediate heat exchanger between the primary cooling He loop and the secondary S-CO_2 gas turbine power conversion system and as recuperators of the S-CO_2 gas turbine power conversion system. This MCHE has discontinuous "S-shaped" fins providing flow channels resembling sine curves. Its pressure drop is one-sixth that of a conventional MCHE with a zigzag flow channel configuration, but it has the same high heat transfer performance. The pressure drop reduction is ascribed to suppression of recirculation flows and eddies that appear around bend corners of the zigzag flow channels in the conventional MCHE. An optimal BP loading in an OTTO refueling scheme eliminates the shortcoming of its excessively high axial power peaking factor, reducing the power peaking factor from 4.44 to about 1.7, and inheriting advantages over the multipass scheme because it obviates reloading in addition to fuel handling and integrity checking systems. Because of the power peaking factor reduction, the maximum fuel temperatures are lower than the maximum permissible values of 1250°C for normal operation and 1600°C during a depressurization accident. [DOI: 10.1115/1.3098416]

1 Introduction

Current high-temperature gas-cooled reactors (HTGRs) use helium (He) as the core cooling medium; the He heated in the core is introduced directly into a gas turbine for generating electricity. The turbine inlet pressure is usually around 7 MPa, taking account of pressure resistance of reactor pressure vessels (RPVs). The core outlet temperature is around 850°C. The cycle efficiency is almost independent of the turbine inlet pressure, when He is used as the working fluid of the gas turbine, which is about 45% at 850°C.

In contrast to the direct cycle, an indirect cycle is also possible. In the indirect cycle, heat generated in the core is transferred to a secondary cooling system, which has a gas turbine for electricity generation. This indirect cycle has the advantage such that it completely prevents deposition of fission product (FP) contamination to turbomachinery, whereas leakage of small amounts of FPs is unavoidable for the coated-particle fuels that are usually used for HTGR cores. The indirect cycle therefore reduces the radiation dosage incurred through maintenance of the turbomachinery. Another advantage of the indirect cycle is that the turbine inlet pressure is not limited by the pressure resistance of the RPV because the secondary cooling system is independent of the primary He cooling system. In contrast to the pressure independence of a He cycle, the efficiency of a supercritical carbon dioxide (S-CO_2) cycle considerably increases concomitantly with the turbine inlet pressure. When the gas turbine inlet pressure is raised from 7 MPa to 20 MPa, the S-CO_2 cycle provides about 3–11% higher cycle efficiency than the He Brayton cycle, depending on the turbine inlet temperature [1]. Its higher efficiency is ascribed to reduced compression work around the critical point of CO_2 and consideration of variation in CO_2 specific heat with pressure and temperature into the cycle configuration.

Modern fossil-fuel steam turbine power plants operate at supercritical pressures ($P > 22.09$ MPa). Recently designed ultrasupercritical pressure plants operate at 31.0 MPa and have a thermal efficiency of about 46%. Therefore, to raise the gas turbine inlet pressure to 31 MPa is acceptable from the perspective of the pressure resistance of their components. According to the preliminary design of the S-CO_2 gas turbine, its power density is higher by a factor of about 3 than those of the steam turbines. Therefore, the turbine inlet pressure is compromised to 20 MPa in this study, considering unforeseen technological problems that might result from differences in the power density between the steam and the S-CO_2 gas turbines.

The turbomachinery size of the S-CO_2 reference is about one-fifth that of the He cycle [2]. This is an additional advantage of the S-CO_2 cycle.

Recuperators with high-pressure operation, high-temperature resistance, and high heat transfer performance are the most crucial component for a gas turbine cycle. A promising candidate for use as a high-efficiency recuperator is a printed circuit heat exchanger (PCHE), which is an application of microchannel heat exchanger (MCHE) technology. Typically, PCHEs are manufactured using chemical etching and diffusion bonding. Flow channels are etched chemically into metal plates; subsequently, the etched plates are stacked and produced as one block by diffusion bonding. In contrast to typical plate fin heat exchangers, a very small flow channel or microchannel pattern is readily producible. Equation (1) shows that reduction in the hydraulic diameter engenders a decreased active length L or heat exchanger size at the same Colburn j factor, Pr, and NTU conditions [3]

[1]Present address: MCX Institute, 2-5-10-105, O-okayama, Meguro-ku, Tokyo 152-0033, Japan.

Manuscript received November 6, 2008; final manuscript received November 6, 2008; published online October 1, 2009. Review conducted by Dilip R. Ballal. Paper presented at the Fourth International Topical Meeting on High Temperature Reactor Technology (HTR2008), Washington, DC, September 28, 2008–October 1, 2008.

$$j = \frac{D_h}{4L}\mathrm{Pr}^{2/3}\, NTU \tag{1}$$

Therein, NTU is the number of thermal units, and

$$NTU = (T_{\mathrm{out}} - T_{\mathrm{in}})/\Delta T_{LMTD} \tag{2}$$

The diffusion bonding technology maintains the parent material strength because of the lack of flux, braze, or filler in the heat exchanger core, which provides high corrosion and temperature resistance.

A new MCHE with S-shaped fins was developed for recuperators of S-CO_2 gas turbine nuclear reactors [4] using the three-dimensional (3D) computational fluid dynamics (CFD) FLUENT code [5]. This MCHE provided 6–7 times lower pressure drop, while maintaining almost equivalent heat transfer performance compared with that of a conventional MCHE with zigzag fins. This promising performance was confirmed experimentally using a S-CO_2 heat transfer test loop. Dimensionless empirical correlation equations were obtained for the Nusselt number and the pressure drop factor [6].

Fuels of two types have been used in HTGR cores: pebble bed and block fuels. A pebble fuel core can provide advantages of low excess reactivity and a high load factor through continuous refueling. Continuous refueling is usually done using a multipass refueling scheme, in which a mixture of fresh and irradiated fuel pebbles is loaded from the top of the core. The fuel pebbles discharged from the bottom of the core are checked for their integrity and burnup. The irradiated fuel pebbles are then reloaded into the core for an additional burning cycle if their burnup is lower than the target, which is usually about 100 GW d/t. Each pebble passes through the core about 6–10 times before being transferred from the core to the spent fuel tanks. The drawback of this scheme is that the radioactive spent fuel pebbles must be checked and reloaded repeatedly. Another refueling scheme is a once-through-then-out (OTTO) refueling scheme, by which the pebbles pass through the core only once [7]. This refueling scheme presents the advantage of simplifying the plant system because it obviates the pebble fuel checking system and the transfer mechanism for reloading. However, an important shortcoming of this scheme is that fresh pebbles with large k_∞ in the upper part of the reactor core cause an excessively high axial power peaking factor.

A burnable poison (BP) loading principle has been proposed for the OTTO refueling HTGR pebble fuel core to alleviate the problem described above: axial power peaking can be minimized when k_∞ of the fuel pebble is kept constant by adding BP during its axial movement [8]. The OTTO refueling scheme with BP loading based on the principle explained above has advantages over a multipass scheme because of the lack of systems and operations for fuel checking and reloading. The drawback of the excessive high peaking factor diminishes over time.

2 Results and Discussion

2.1 S-CO_2 Gas Turbine Cycle. Cycle efficiencies of He and CO_2 cycles were calculated using PROPATH as a database for thermophysical properties of fluids [9]. Evaluation conditions are presented in Table 1.

Specific heat at constant pressure C_p of CO_2 is dependent on pressure and temperature, whereas C_p of He is constant and C_p of CO_2 in the recuperator is considerably lower in the low-pressure high-temperature side (connected to the turbine outlet) than in the high-pressure low temperature side (connected to the compressor outlet). Consequently, CO_2 cannot be preheated to such a temperature at the core inlet because it provides maximum cycle efficiency. This temperature mismatch problem is avoided if the flow is optimally bypassed to the compressor before precooling. Hereinafter, a cycle with a bypass flow cycle, as presented schematically in Fig. 1, is called a "partial precooling" cycle [1].

Figure 2 shows that the cycle efficiency of the CO_2 partial precooling cycle is about 3–11% higher at a turbine inlet pressure of 20 MPa than that of the conventional He Brayton cycle, depending on the turbine inlet temperature. Considering a turbine inlet temperature lowered by 30°C through intermediate heat exchange, the S-CO_2 indirect cycle achieves a cycle efficiency of 53.8% at a core outlet temperature of 850°C and a turbine inlet pressure of 20 MPa. This cycle efficiency value is higher by 4.5% than that (49.3%) of a He direct cycle at a turbine inlet temperature of 850°C and 7 MPa. Its higher efficiency is ascribed to reduced compression work around the critical point of CO_2 and consideration of variation in CO_2 specific heat with pressure and temperature into the cycle configuration. The cycle efficiency is enhanced to 55.4% in the S-CO_2 cycle when the turbine inlet pressure is raised to 30 MPa.

Table 1 Cycle efficiency evaluation conditions

Parameters			Values
Efficiency		Turbine efficiency (%)	90
		Compressor efficiency (%)	90
		Recuperator efficiency (%)	95
Pressure Drop (%)[a]	Usual Brayton cycle	Reactor	1.5
		Precooler	1.02
		Intercooler	0.58
		Recuperator (H/L)[b]	1.99/0.66
	Partial precooling cycle	Reactor, precooler, and intercooler	Same as above
		Recuperator (H/L)[b]	2.65/0.88

[a]Percent pressure drop in each component relative to the reactor outlet pressure.
[b]High/low temperature side of a recuperator.

2.2 Microchannel Heat Exchangers. A conventional zigzag flow channel model for PCHE is portrayed in Figs. 3 and 4.

The conventional PCHE flow path comprises a set of continuous zigzag flow channels. Each flow channel is regarded as a small pipe with many bends. In a bent pipe, swirl flows, eddies, and recirculation flows occur around a bend corner, as depicted in Fig. 5, thereby increasing the pressure drop. The pressure drop depends on the bend angle, the number of bends, and their curvature; in fact, the pressure drop decreases concomitantly with the angle and the curvature enlargement. If those swirl flows, recirculation flows, and eddies are suppressed, the pressure drop will be reduced.

Simulations were done in two flow path models with zigzag and S-shaped fins. Velocity distributions are compared in Fig. 6, showing that the zigzag fin model forms fast fluid flow bands, as depicted in Fig. 6(*a*). The fast fluid flow bands enhance the formation of eddies and recirculating fluid flows. In contrast, the S-shaped fin model does not form fast fluid flow bands, but forms a uniform fluid flow velocity profile over the flow channels, as given in Fig. 6(*b*), having suppressed the eddies and recirculating fluid flows. The simulation results also indicate that the pressure

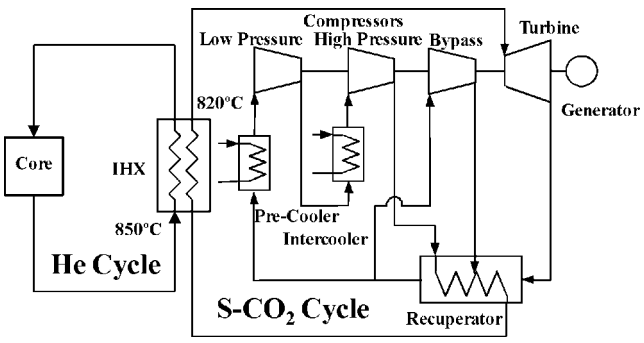

Fig. 1 Partial precooling cycle configuration

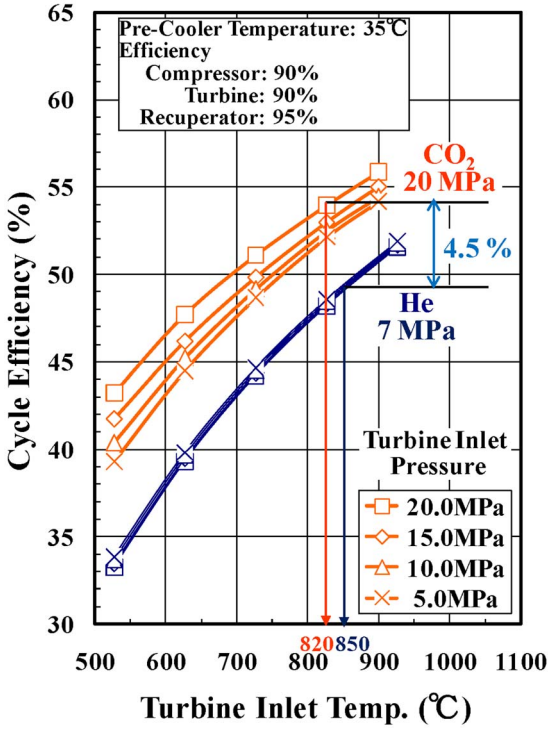

Fig. 2 Cycle efficiencies of S-CO_2 cycle and He cycle in the one-intercooler system

drop is mainly ascribed to energy consumption because of the flow direction change, eddy formation, and recirculating flows. Therefore, the pressure drop is expected to be lower in the S-shaped fin model than in the zigzag fin model.

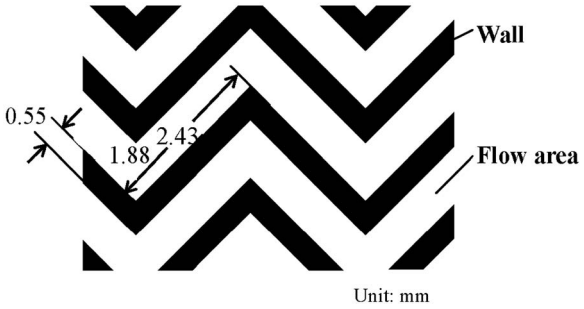

Fig. 3 Conventional zigzag model

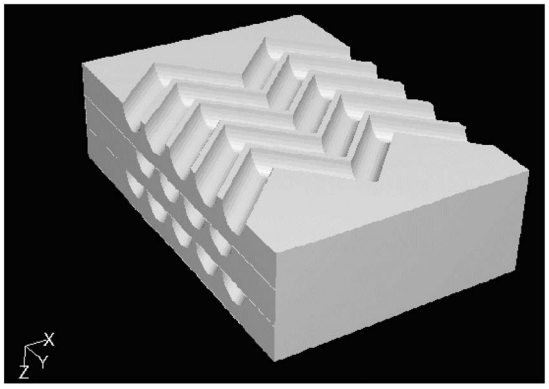

Fig. 4 Zigzag model in three dimensions

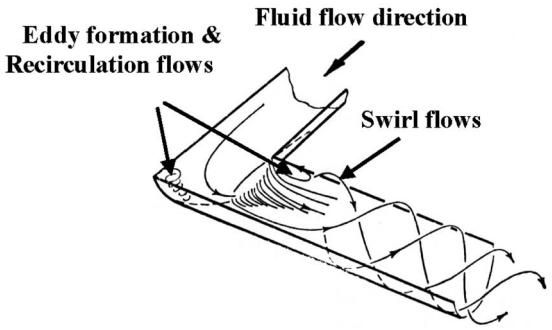

Fig. 5 Swirl flows, eddies, and recirculation flows in a bent pipe. (From Japan Society of Mechanical Engineers, "JSME Data Book, Hydraulic Losses in Pipes and Ducts," Maruzen Co. Ltd., Tokyo, Japan, Fig. 4.74, p. 80.)

Pressure drop and heat transfer performance were calculated for various fin models. The result in Fig. 7 shows that the S-shaped fin model attains six times lower pressure drop relative to the zigzag flow path model, while maintaining almost identical heat transfer performance; the sinuous model provides almost equal low-pressure drop at the expense of 20% lower heat transfer performance; the louver fin model results in a pressure drop that is three times higher, with 10% less heat transfer performance than that given by the S-shaped fin model.

2.3 OTTO Refueling With Burnable Poison. Based on the BP loading principle [8], the optimal BP particle radius and number per pebble were determined to provide the minimum change of k_∞ with fuel depletion through burnup calculations in the unit cell lattice using the Monte Carlo neutron transport MVP code [10] and the JENDL-3.3 library [11].

The unit cell lattice consists of one central fuel pebble surrounded by a coolant layer, as illustrated in Fig. 8.

A reflective boundary condition was applied. Design parameters of the pebble are presented in Table 2. Spherical BP particles are distributed randomly together with TRISO-coated fuel particles [12] in a free fuel zone in a fuel pebble using the statistical geometry model of the MVP code. To determine the optimal radius and number of BP particles, the k_∞ and burnup reactivity swing were used as optimization parameters. The reactivity swing is defined as the maximum difference of k_∞ values from the initial to the target burnup of 100 GW d/t. The target k_∞ is set at 1.05 ± 0.02 at any burnup time to ensure the core criticality when a neutron leakage effect is considered for unit cell calculations.

Unit cell calculations were done parametrically, changing the B_4C particle radius and the volume ratio of one fuel pebble to total B_4C particles. Contour lines of the initial k_∞ and burnup reactivity swing were drawn from the results of the unit cell calculations in coordinate planes of the B_4C particle radius and (one fuel pebble/total B_4C particle) volume ratio in Figs. 9(*a*) and 9(*b*), respectively. In Fig. 9(*b*), the constraint of initial $k_\infty = 1.05$ given in Fig. 9(*a*) is superimposed onto the contour lines of the burnup reactivity swing. The optimal B_4C loading was determined from Fig. 9(*b*) as a combination of the radius and volume ratio to minimize the burnup reactivity swing and to ensure the criticality constraint of the target $k_\infty = 1.05$. Therefore, the optimal radius and volume ratio are selected, respectively, as 90 μm and 22.4. The pebble-to-BP-particle volume ratio of 22.4 is converted to 1650 B_4C particles per pebble from a simple calculation.

Figure 10 shows that k_∞ of the fuel pebble is kept almost constant during burnup at the optimal radii and quantities of B_4C. At this optimal combination, the reactivity swing is reduced from 38% to about 2%. The total burning fraction of ^{10}B is more than 0.97 at the target burnup of 100 GW d/t. The optimal Gd_2O_3 loading was determined similarly as 16 particles per fuel pebble

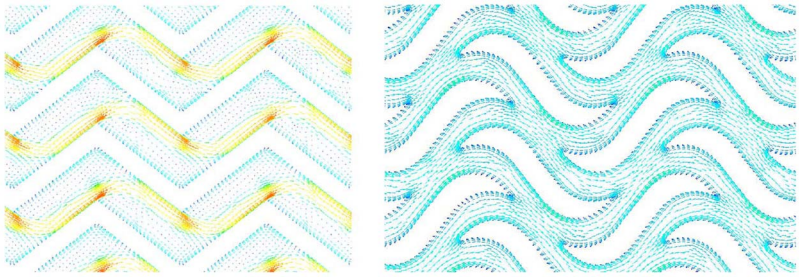

Fig. 6 Velocity distributions

and radius of 950 μm, which reduces the reactivity swing from 38% to 1.5%, as presented in Fig. 10. The ^{155}Gd and ^{157}Gd burning fraction at the target burnup is about 0.99 [8].

In addition to B_4C and Gd_2O_3, the optimal BP loading was determined for Er_2O_3 and CdO; the neutronic performance in lattice calculations was evaluated, as presented in Table 3. Regarding CdO, two different sizes of CdO particles are necessary. The larger ones are intended to control long-term reactivity; the smaller ones are intended to control short-term reactivity.

The neutronic performance was evaluated in a whole-core model for a pebble fuel HTGR core with thermal power of 600 MWt. The annular core has a cylindrical reflector with a 1.7 m radius at the center. The outer radius of the pebble region is 2.6 m. The effective core height is 9.4 m. A 0.25-m thick void region is located between the top of the fuel zone and the bottom of the top reflector. Table 4 presents detailed design parameters of the core.

To simulate OTTO refueling, the pebble region is divided radially into three pebble flow channels with equal radial distance of 0.3 m, as presented in Fig. 11. Figure 12 shows that the core height is divided axially into ten equal volume zones, which are numbered from top to bottom. The fuel pebbles are discharged from the core, and fresh fuel pebbles are loaded into the first zone, when the fuel attains an average burnup of 10 GW d/t, at the tenth zone. Fuel pebbles in the other zones move progressively to the next lower zone. In this simulation, all fuel pebbles in the three pebble flow channels move through the core with equal speed. Neutronic calculations for the core were performed using the MVP code [10] and the JENDL-3.3 library [11]. The equilibrium state was attained after 15–20 refueling cycles. Each fuel pebble remains inside the core for about 30 months before being discharged to a spent fuel tank.

Table 5 presents the neutronic performance of the core at the equilibrium state. Figure 13 portrays the relative axial power distribution at the pebble flow channel, where maximum power peaking occurs. The maximum power density reaches 23.3 MW/m^3 around the core top; the power density is approximately zero at the core bottom when no BP is added to the fuel pebble. The power peaking factor is 4.44; HTGR cores with pebble fuel normally operate at fuel core power densities of 4–10 MW/m^3.

Using the axial power distribution, the axial fuel temperature distributions were calculated at the normal operation condition. As depicted in Fig. 14, the maximum fuel temperature is about 1204°C at the top of the core. When BP is added to the fuel

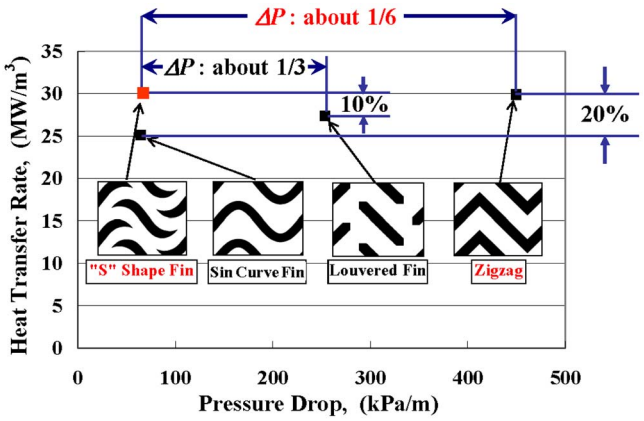

Fig. 7 Heat transfer rate versus pressure drop. Pressure drop per unit length, ΔP, heat transfer rate per unit volume, Q/V, are calculated as $\Delta P=(P_{in}-P_{out})/L_x$, $Q/V=Q/(L_x\times L_y\times L_z)$.

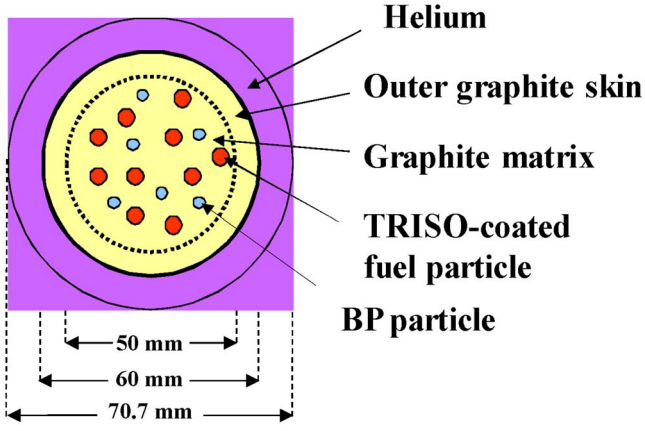

Fig. 8 Unit cell lattice model in the MVP code

Table 2 Fuel design parameters

Fuel pebble	
Fuel	UO_2
^{235}U enrichment (wt %)	16.0
Uranium mass (g/pebble)	9
UO_2 density (g cm^{-3})	10.4
Graphite matrix density (g cm^{-3})	1.75
Pebble diameter (mm)	60
Free fuel zone diameter (mm)	50
Power rating (W/pebble)	973
Fuel temperature (K)	1200
Target burnup (GW d/t)	100
Coated fuel particle	
Type	TRISO
Fuel kernel diameter (μm)	500
Coating material	PyC/PyC/SiC/PyC
Thickness (μm)	95/40/35/40
Density (g cm^{-3})	1.05/1.90/3.18/1.90

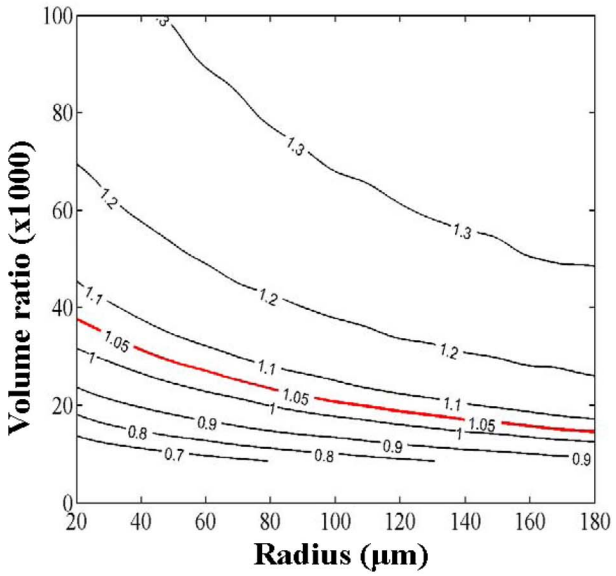

a) Initial k_∞

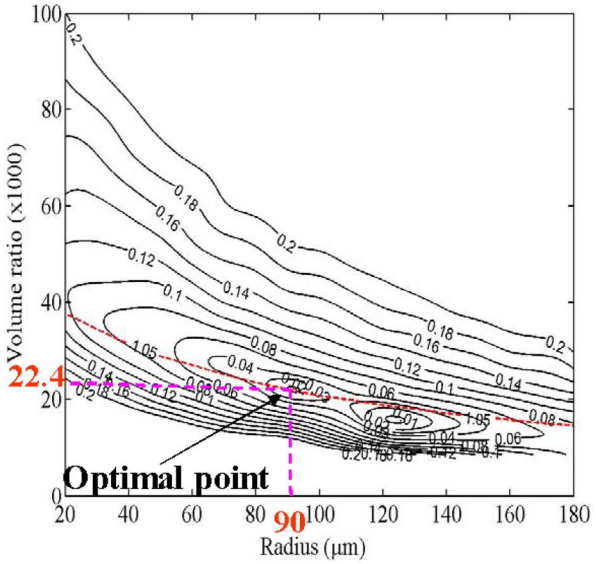

b) Reactivity swing

Fig. 9 Contour lines of initial k_∞ and reactivity swing

pebbles, the power density decreases around the top of the core, taking the highest value around the middle of the core, as depicted in Fig. 13. Consequently, the power peaking factor is reduced from 4.4 to 1.61 in the B_4C added core and to 1.64 in the Gd_2O_3 added core. In the Er_2O_3 added core, the maximum power density is reduced to 8.67 MW/m^3 and the power peaking factor is reduced to 1.67. For CdO, particles of two types with different radii were added to fuel pebbles. The maximum power density is reduced to 8.93 MW/m^3; the power peaking factor is 1.70.

Although the power densities at the core top are excessively high when no BP is added, the maximum fuel temperature is lower than the maximum permissible temperature of 1250°C, as presented in Fig. 14. Because the power profile becomes flatter in the BP-added core, the maximum fuel temperatures appear around the axial position, at two-thirds of the position from the core top. The maximum temperatures are within the range of 1000–1020°C when BP is added. The safety margin, which is

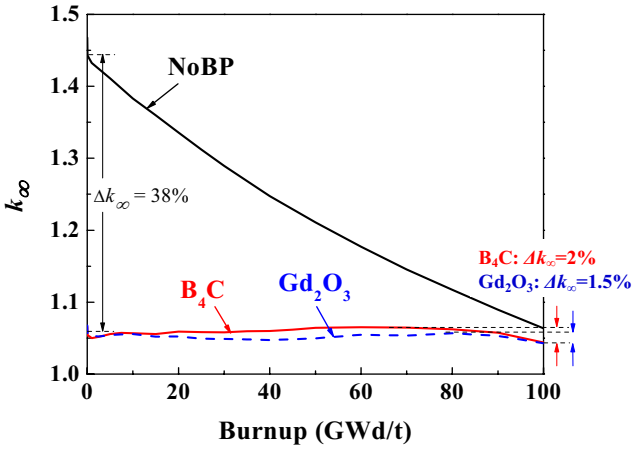

Fig. 10 k_∞ change with burnup at the optimal radius and number BP particles

Table 3 Optimal BP loading and neutronic performance

	BP particle			Neutronic performance		
Material	No./ pebble	Radius (μm)	Weight (10^{-3} g/ pebble)	Initial k_∞	Δk (%)	BP burning fraction (%)
No BP	-	-	-	1.445	38	-
B_4C	1650	90	12.7	1.055	2	97
Gd_2O_3	16	950	425.2	1.057	1.5	>99
Er_2O_3	110	550	662.3	1.028	3.5	94
CdO	2+7	1900+1000	707.3	1.058	4	>99

Table 4 Core design parameters

	Core
Thermal power (MWt)	600
Height (m)	9.4
Inner/outer radius (m)	1.7/2.6
Pebble packing fraction	0.61
Average power (MW/m^3)	5.25
Materials	
Fuel	UO_2
Coolant	He
Reflector	Graphite
Coolant	
Inlet/outlet temperature (°C)	500/85
Inlet pressure (MPa)	7.0
Flow rate (kg/s)	330.2
Reflector	
Thickness of top reflector (m)	1.0
Thickness of bottom reflector (m)	2.0
Thickness of outer reflector (m)	1.0
Thickness of carbon side reflector (m)	0.5

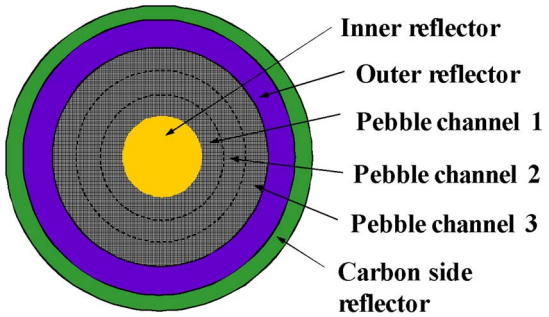

Fig. 11 Radial *x*-section of the pebble bed HTGR core

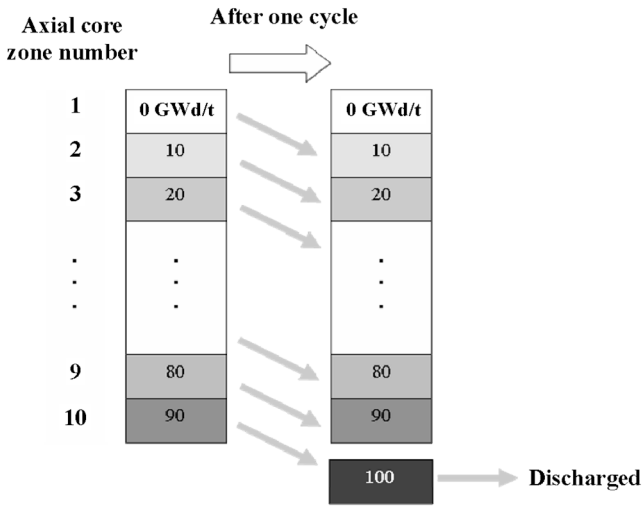

Fig. 12 OTTO refueling model

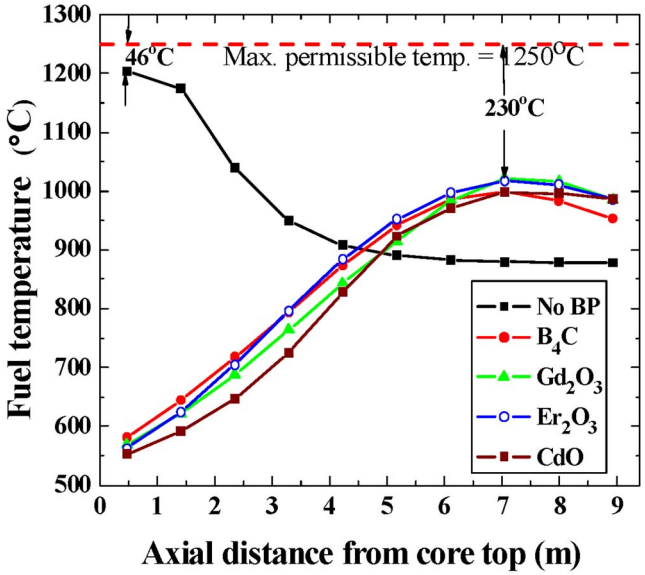

Fig. 14 Maximum fuel temperature in normal operation

defined as the difference of maximum fuel temperature and the maximum permissible value, increases in the OTTO refueling core from about 46°C to 230–250°C, when BP is added.

The safety of HTGRs is ascribed to their low power density, large thermal capacity, and high-temperature resistance of the fuel. The maximum power rating of each module and the high surface-to-volume ratio of the core were chosen such that, in the event of a depressurization accident, adequate cooling would be provided without the need for forced convection. Past experiments have shown that the SiC layer of TRISO fuel limits the release of highly hazardous fission products such as ^{137}Cs to less than 0.01% of inventory up to 1600°C [12,13], but the retention capability decreases rapidly as the temperature increases to beyond 1600°C. At 1800°C, releases of 10% of the ^{137}Cs inventory have been described [13]. Therefore, in a depressurization accident, the maximum fuel temperature must not exceed the maximum permissible temperature of 1600°C to ensure fission product retention in TRISO-coated fuel particles.

Figure 15 shows the fuel temperature change after a depressurization accident occurs and after the reactor is shut down. When no BPs are added to fuel pebbles, the fuel temperature increases to 2825°C, which far exceeds the maximum permissible value of 1600°C. The maximum fuel temperatures are, respectively, about 1528°C and 1547°C when B_4C and Gd_2O_3 are added. When Er_2O_3 and CdO are added, the peak temperatures are about 1577°C and 1595°C, respectively, each of which is lower than the maximum permissible temperature of 1600°C. Safety requirements are fulfilled for decay heat removal from the core in a depressurization accident.

Table 5 Neutronic properties in whole-core calculations

Items	No BP	B_4C	Gd_2O_3	Er_2O_3	CdO
k_{eff}	1.163	1.022	1.024	1.025	1.039
Maximum power density (MW/m^3)	23.3	8.47	8.63	8.77	8.93
Power peaking factor	4.44	1.61	1.64	1.67	1.70

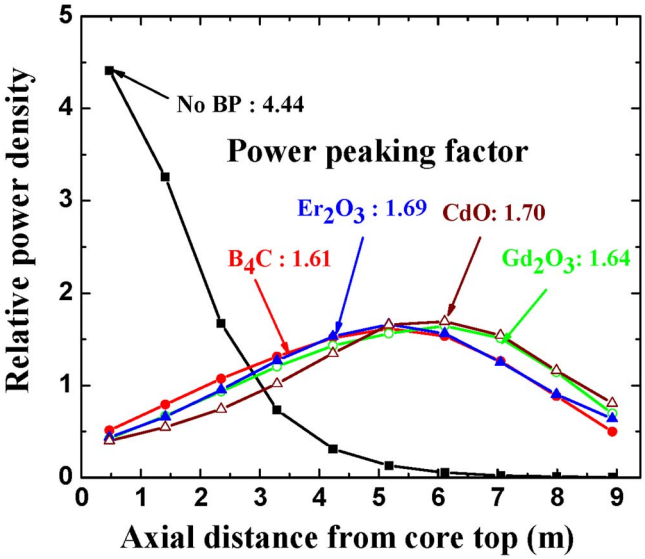

Fig. 13 Axial power distribution in the channel where power peaking appears

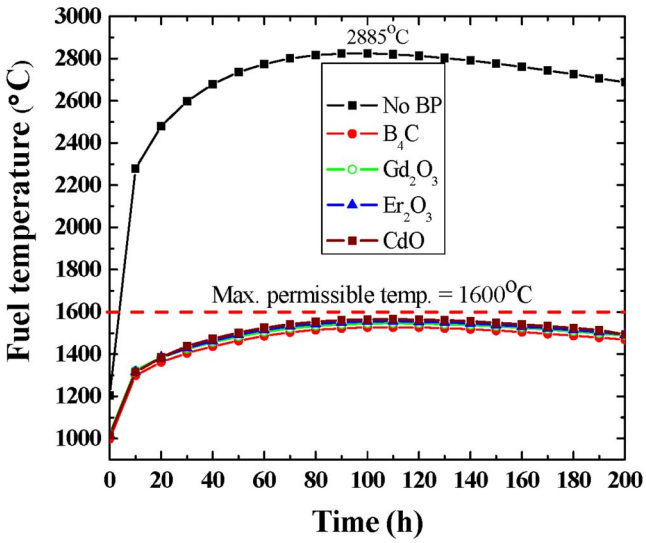

Fig. 15 Maximum fuel temperature at depressurization accident

3 Conclusions

The S-CO_2 gas turbine power conversion system, new MCHE with S-shaped fins, and OTTO refueling scheme with optimal BP loading are promising for advanced HTGR systems judging from the following.

(1) The S-CO_2 indirect cycle achieves 4.5% higher cycle efficiency of 53.8% at a turbine inlet temperature of 820°C and a turbine inlet pressure of 20 MPa than that (49.3%) of a He direct cycle at 850°C and 7 MPa. It completely prevents deposition of fission product contamination to turbomachinery, resulting in the reduction in radiation dosage in maintenance of the turbomachinery. Its turbomachinery is one-fifth the size of the He cycle turbomachinery.
(2) The S-shaped fin MCHE attains six times lower pressure drop relative to the conventional zigzag flow path model, while maintaining equal heat transfer performance.
(3) An optimal BP loading in an OTTO refueling scheme eliminates the shortcoming of its excessively high axial power peaking factor, reducing the power peaking factor from 4.44 to about 1.7. It also inherits advantages over the multipass scheme because it requires neither fuel handling and integrity checking systems nor reloading. Because of the power peaking factor reduction, the maximum fuel temperatures are lower than the maximum permissible values of 1250°C during normal operation and 1600°C in a depressurization accident.

Nomenclature

J = Colburn j factor
D_h = hydraulic diameter (mm)
L = active flow length (mm)
Pr = Prandtl number
NTU = number of thermal units
T = temperature (°C)

Subscripts

in, out = inlet, outlet
$LMTD$ = logarithmic mean temperature difference

References

[1] Kato, Y., Nitawaki, T., and Muto, Y., 2004, "Medium Temperature Carbon Dioxide Gas Turbine Reactor," Nucl. Eng. Des., **230**, pp. 195–207.
[2] Muto, Y., and Kato, Y., 2006, "Turbomachinery Design of Supercritical CO_2 Gas Turbine Fast Reactor," *Proceedings of the 2006 International Congress on Advances in Nuclear Power Plants (ICAPP'06)*, Reno, NV, Jun. 4–8, Paper No. 6094.
[3] Hesselgreaves, J. E., 2001, "Compact Heat Exchangers, Selection, Design and Operation," Pergamon, New York, pp. 126–128 and pp. 35–38.
[4] Tsuzuki, T., Kato, Y., and Ishizuka, T., 2007, "High Performance Printed Circuit Heat Exchangers," Appl. Therm. Eng., **27**, pp. 1702–1707.
[5] Fluent, Inc., 2003, *Fluent 6.1 User's Guide*, Fluent Inc., Lebanon, NH.
[6] Ngo, T. L., Kato, Y., Nikitin, K., and Tsuzuki, N., 2007, "Heat Transfer and Pressure Drop Correlations of Microchannel Heat Exchangers With S-Shaped and Zigzag Fins for Carbon Dioxide Cycles," Exp. Therm. Fluid Sci., **32**, pp. 560–570.
[7] Hansen, U., Schulten, R., and Teuchert, E., 1972, "Physical Properties of the "Once Through Then Out" Pebble-Bed Reactor," Nucl. Sci. Eng., **47**, pp. 132–139.
[8] Tran, H. N., and Kato, Y., 2008, "Optimization of Burnable Poison Loading for HTGR Cores With OTTO Refueling," Nucl. Sci. Eng., **158**, pp. 264–271.
[9] Ito, T. (representative), and PROPATH Group, 1990, *PROPATH: A Program Package for Thermo-Physical Properties of Fluids, Version 10.2*, Corona, Tokyo, Japan.
[10] Nagaya, Y., Okumura, K., Mori, T., and Nakagawa, M., 2005, "MVP/GMVP II: General Purpose Monte Carlo Codes for Neutron and Photon Transport Calculations Based on Continuous Energy and Multigroup Methods," Report No. JAERI-1348.
[11] Shibata, K., Kawano, T., Nakagawa, T., Iwamoto, O., Katakura, J., Fukahori, T., Chiba, S., Hasegawa, A., Murata, T., Matsunobu, H., Ohsawa, T., Nakajima, Y., Yoshida, T., Zukeran, A., Kawai, M., Baba, M., Ishikawa, M., Asami, T., Watanabe, T., Watanabe, Y., Igashira, M., Yamamuro, N., Kitazawa, H., Yamano, N., and Takano, H., 2002, "Japanese Evaluated Nuclear Data Library Version 3 Revision-3: JENDL-3.3," J. Nucl. Sci. Technol., **39**, pp. 1125–1136.
[12] Nabielek, H., Kuhnlein, W., and Schenk, W., 1990, "Development of Advanced HTR Fuel Elements," Nucl. Eng. Des., **121**, pp. 199–210.
[13] Minato, K., Sawa, K., Koya, T., Tomita, T., Ishikawa, A., Baldwin, C. A., Gabbard, W. A., and Malone, C. M., 2000, "Fission Product Release Behavior of Individual Coated Fuel Particles for High-Temperature Gas-Cooled Reactors," Nucl. Technol., **131**, pp. 36–47.

High Temperature Interaction Between UO_2 and Carbon: Application to TRISO Particles for Very High Temperature Reactors

Stéphane Gossé
Christine Guéneau
Thierry Alpettaz
Sylvie Chatain

DEN/DANS/DPC/SCP/LM2T,
CEA Saclay,
91191 Gif-sur-Yvette Cedex, France

Christian Chatillon
SIMAP,
CNRS,
ENSEEG BP75 Grenoble,
38402 Saint-Martin d'Hères Cedex, France

*For very high temperature reactors, the high level operating temperature of the fuel materials in normal and accidental conditions requires studying the possible chemical interaction between the UO_2 fuel kernel and the surrounding structural materials (C, SiC) that could damage the tristructural isotropic particle. The partial pressures of the gaseous carbon oxides formed at the fuel (UO_2)-buffer (C) interface leading to the build up of the internal pressure in the particle have to be predicted. A good knowledge of the phase diagram and thermodynamic properties of the uranium-carbon-oxygen (UCO) system is also required to optimize the fabrication process of "UCO" kernels made of a mixture of UO_2 and UC_2. Thermodynamic calculations using the FUELBASE database dedicated to Generation IV fuels (Guéneau, Chatain, Gossé, Rado, Rapaud, Lechelle, Dumas, and Chatillon, 2005, "A Thermodynamic Approach for Advanced Fuels of Gas Cooled Reactors," J. Nucl. Mater., **344**, pp. 191–197) allow predicting the phase equilibria involving carbide and/or oxycarbide phases at high temperature. Very high levels of $CO_{(g)}$ and $CO_{2(g)}$ equilibrium pressures are obtained above the $UO_{2\pm x}$ fuel in equilibrium with carbon that could lead to the failure of the particle in case of high oxygen stoichiometry of the uranium dioxide. To determine the deviation from thermodynamic equilibrium, measurements of the partial pressures of $CO_{(g)}$ and $CO_{2(g)}$ resulting from the UO_2/C interaction have been performed by high temperature mass spectrometry on two types of samples: (i) pellets made of a mixture of UO_2 and C powders or (ii) UO_2 kernels embedded in carbon powder. Kinetics of the $CO_{(g)}$ and $CO_{2(g)}$ as a function of time and temperature was determined. The measured pressures are significantly lower than the equilibrium ones predicted by thermodynamic calculations. The major gaseous product is always $CO_{(g)}$, which starts to be released at 1473 K. From the analysis of the partial pressure profiles as a function of time and temperature, rates of $CO_{(g)}$ formation have been assessed. The influence of the different geometries of the samples is shown. The factors that limit the gas release can be related to interface or diffusion processes as a function of the type of sample. The present results show the utmost importance of kinetic factors that govern the UO_2/C interaction.* [DOI: 10.1115/1.3098430]

1 Introduction

In very high temperature reactors (VHTRs), the high operating temperature requires predicting the interaction between the materials in the tristructural isotropic (TRISO) particle. Among the factors controlling the thermomechanical properties of the TRISO particle, the internal pressure resulting from the release of some fission products and $CO_{(g)}$, and $CO_{2(g)}$ species inside the particle are important to assess. In fact, high levels of pressure could lead to particle failure. Release of $CO_{(g)}$ and $CO_{2(g)}$ results in the chemical interaction between the UO_2 fissile kernel and its surrounding carbon layer (buffer). The study of the UO_2/C interaction requires a good thermodynamic description of the uranium-carbon-oxygen ternary system at high temperature. It is generally known that UO_{2+x} oxide interacts with carbon from 1000 °C to form gaseous carbon oxides $CO_{(g)}$ and $CO_{2(g)}$ [1].

Manuscript received November 30, 2008; final manuscript received December 12, 2008; published online October 1, 2009. Review conducted by Dilip R. Ballal. Paper presented at the Fourth International Topical Meeting on High Temperature Reactor Technology (HTR2008), Washington, DC, September 28–October 1, 2008.

Thermodynamic calculations show that the equilibrium $CO_{(g)}$ and $CO_{2(g)}$ pressures in the two phase domain $[UO_{2\pm x}/C]$ strongly depend on the oxygen potential μ_{O_2} in the system, and thus on the stoichiometry of $UO_{2\pm x}$ (Fig. 1).

The calculated equilibrium pressures of $CO_{(g)}$ are higher than those of $CO_{2(g)}$. The contribution of $CO_{2(g)}$ is low, when the O/U ratio is lower than 2 and $CO_{(g)}$ pressure can be considered as the total pressure above the system. The contribution of $CO_{2(g)}$ to the total pressure starts to be significant for O/U ratio higher than 2.

Previous studies on the kinetic of the reaction between UO_2 and C [2,3] showed that a significant decrease in the reaction rate occurs as a function of the degree of conversion of the reaction leading to different kinetic models reviewed in [4]. The small amounts of gases formed in comparison with those expected at thermodynamic equilibrium are due to the mechanisms involved in the reaction routes (diffusion or interface).

These statements were confirmed by high temperature mass spectrometry (HTMS) experiments carried out on several kinds of samples: (i) UO_2+C green pellets and (ii) UO_2 kernels embedded in carbon black. In both cases, formation of a gaseous phase

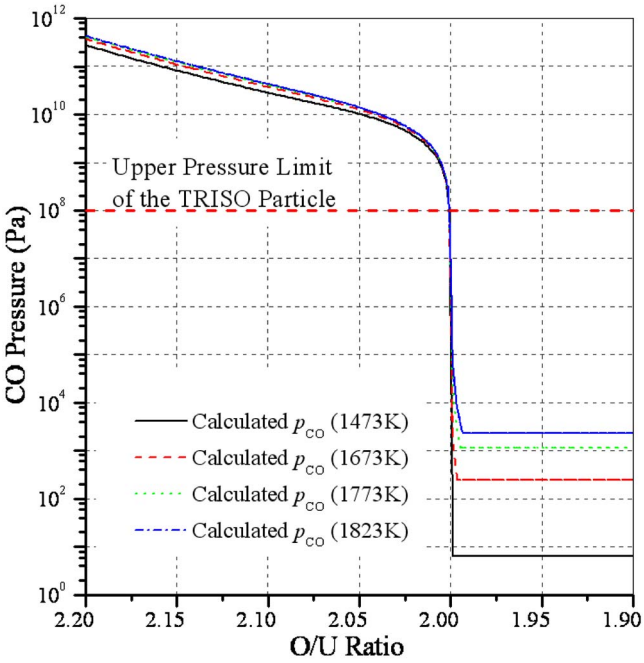

Fig. 1 Variation in CO pressure as a function of the O/U ratio near the stoichiometry of UO_2

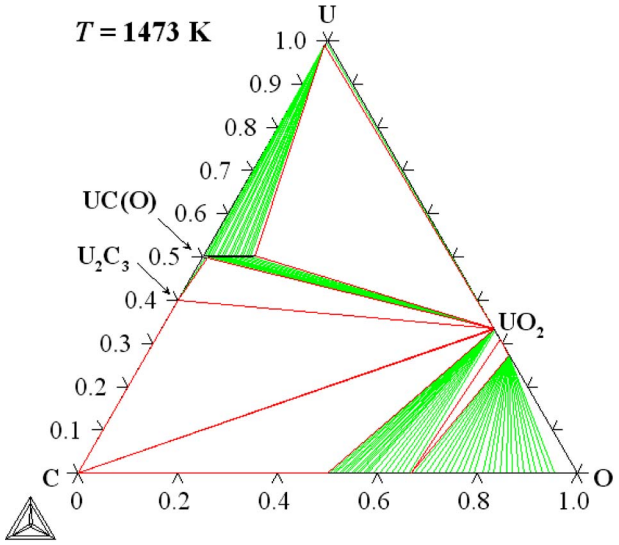

Fig. 2 Calculated UCO isothermal section at 1473 K

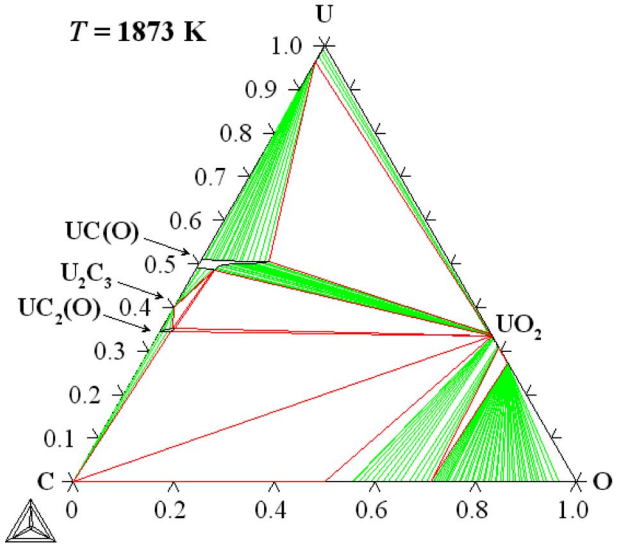

Fig. 3 Calculated UCO isothermal section at 1873 K

mainly constituted of $CO_{(g)}$ was observed coming from the UO_2-C interaction for temperatures higher than 1200 K [5].

$CO_{(g)}$ and $CO_{2(g)}$ ionic intensities were measured versus time during heat treatments at fixed temperature in (UO_2+C) mixtures using high temperature mass spectrometry. The partial pressures were determined by taking into account the total weight loss of the samples. The evolution of the overall composition of the sample versus time could also be calculated. For the pellets, the correlation of the measured gaseous partial pressures to the variation in the sample composition versus time shows a first step of reduction in UO_{2+x} by carbon into nearly stoichiometric UO_2 ($T < 1200$ K) that occurs during sample heating. This phenomenon is associated with a sharp release of $CO_{(g)}$ and $CO_{2(g)}$. Then, at higher temperature ($T > 1200$ K), $CO_{(g)}$ becomes the major gaseous species. Once uranium dioxide reaches its oxygen composition limit (O/U=1.998), uranium carbide starts to form. During all the experiments, a stationary pressure state is never obtained after several hours. However, in a three phase region of the phase diagram, containing UO_2, uranium carbide, and carbon, the partial pressure may be fixed at a given temperature.

In the case of the UO_2 kernels in carbon powder, the results differ. First, the first step of sharp gas release does not occur. Second, the kinetic regime seems to be different. The interface regime is difficult to establish at the beginning of the reaction between UO_2 and carbon.

The first part of this study deals with thermodynamic calculations of $CO_{(g)}$ and $CO_{2(g)}$ equilibrium pressures using the FUELBASE database for Generation IV fuel materials. Then, the experimental results obtained by HTMS on the interaction between UO_{2+x} and carbon are reported. Different kinetic models were used to analyze the experimental data on the uranium carbide formation as a function of the sample geometry [2,3,6–12]. The kinetics is controlled either by diffusion or interface mechanisms.

2 Thermodynamic Study of the UCO Ternary System

In the framework of the ACTINET European network for actinide science[1] the thermodynamic database FUELBASE is developed in order to calculate phase diagrams and associated thermodynamic properties on advanced nuclear fuels. It is built using the calculation of phase diagrams method [13].

In the uranium-oxygen-carbon system, the $CO_{(g)}$ and $CO_{2(g)}$ partial pressures control the phase equilibria through the oxygen potential of the system. The ternary database was developed from the descriptions of UO [13] and uranium carbide (UC) [14] binary systems (Figs. 2 and 3). Some ternary interaction parameters have been added to describe the uranium oxycarbide phases. For $T < 1873$ K, the two stable carbides are U_2C_3 and $UC_{1\pm x}O_y$. For higher temperatures, the $UC_{2\pm x}O_y$ carbide phase forms.

The oxycarbide $UC_{1\pm x}O_y$ (fcc_b1 structure) extends from $UC_{1\pm x}$ binary carbide that dissolves oxygen (Fig. 3). The oxygen solubility limit in this phase is about 15–17 at. %. The other phase is $UC_{2\pm x}O_y$ (body-centered-tetragonal (bct) structure) that corre-

[1]http://www.actinet-network.org.

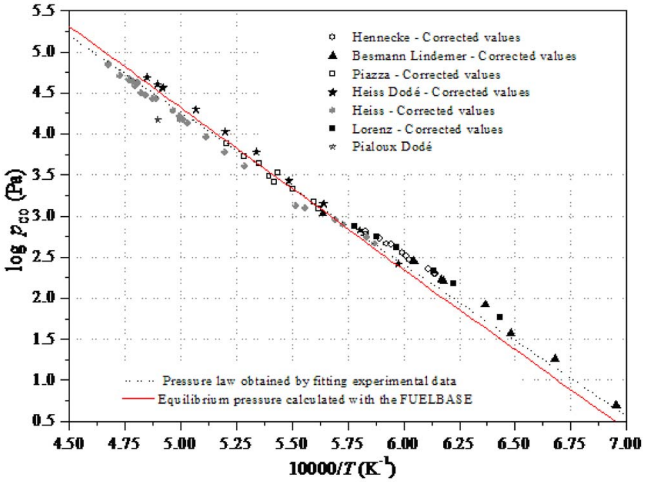

Fig. 4 Critical review of $CO_{(g)}$ pressure from in the UO_2-UC_2-C three phase domain

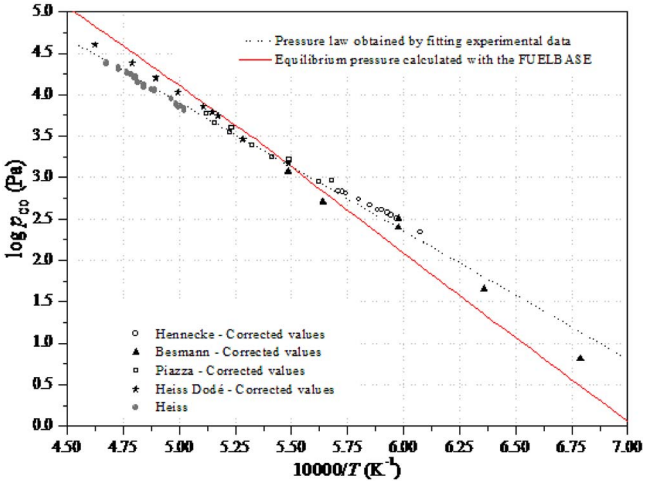

Fig. 5 Critical review of $CO_{(g)}$ pressure in the UO_2-UC_2-UC three phase domain

sponds to the binary $UC_{2\pm x}$ phase, in which several atomic percent of oxygen dissolve. The oxygen solubility limit in this phase is not well known [13].

In the UC binary system [14], $UC_{2\pm x}$ is described as a high temperature phase. Some authors reported that this phase is stabilized by oxygen leading to the formation of the dioxycarbide at a lower temperature in the ternary than in the binary system. However, this statement is still object of controversy.

3 UO_2 Versus UCO Fuel Kernels for VHTR

The studies on the interaction between UO_2 and carbon were carried out in the frame of the fabrication of UCO VHTR fuels formed via the carbothermic reaction

$$UO_2 + 3C = UC + 2CO_{(g)}$$

With larger relative carbon amounts $(C/UO_2 > 4)$

$$UO_2 + 4C = UC_2 + 2CO_{(g)}$$

Because of its low oxygen potential, which tends to increase with irradiation, a mixture of UO_2 and UC_2 maintains a lower value of the $CO_{(g)}$ pressure inside the particle, in comparison with a single UO_2 fuel kernel [15]. In fact, in case of the equilibrium between a UO_2+UC_2 mixture and its carbon coating, the variance of the system is monovariant. Then, the $CO_{(g)}$ pressure only depends on the temperature and is not a function of composition, as is the case for a single UO_2 phase in equilibrium with carbon (Figs. 4 and 5). For example, the $CO_{(g)}$ pressure inside the UO_2-UC_2-C three phase domain of the UCO system is defined as (Eq. (1))

$$\log p_{CO} = 13.528 - \frac{18{,}525}{T} \tag{1}$$

The UCO kernels also have the advantage of increasing the thermal conductivity in the presence of uranium carbides. Under irradiation, these reactions of UO_2 reduction by carbon also occur in the oxycarbide fuel. But the low oxygen potential level allows maintaining lower $CO_{(g)}$ release that tends to increase the pressure inside the particle. Then, coating failures are reduced and the use of oxycarbide kernels allows operating under higher burnups.

4 High Temperature Interaction Between UO_2 and Carbon

According to the experimental results of Ainsley et al. [16], reduction in hyperstoichiometric oxide ($UO_{2.10}$) occurs into two successive steps. First, hyperstoichiometric oxide is reduced. The UO_2 composition reaches an O/U ratio close to 1.99. This initial reaction occurs in the temperature range 800–1000°C. Then, the uranium monocarbide UC starts to form. This second step becomes significant at 1150–1200°C.

The main models to describe the kinetics of formation of uranium carbide during the UO_2/carbon interaction are listed in Refs. [2,3,9].

The kinetic model applied by Lindemer et al. [9] was developed by Ginstling and Brounshtein [6] for the diffusion process occurring in spherical particles. From this model, the carbide layer growth can be determined using the temporal decrease in the initial radius (r_0) of the UO_2 spherical particle

$$\frac{1}{3} - \left(\frac{r(t)}{r_0}\right)^2 \times \left(1 - \frac{2r(t)}{3r_0}\right) = \frac{k_D t}{r_0^2} \tag{2}$$

Depending on the experimental conditions, Mukerjee et al. [2,3] proposed several kinetic models: (i) under vacuum, the UO_2 reduction is controlled by reagent-product interface reactions, whereas (ii) under argon flow, the controlling step is $CO_{(g)}$ diffusion through the layer of uranium carbide. The reaction mechanism proposed by Mukerjee is based on the work of Stinton et al. [17], in which UC_2 was substituted by UC. Stinton et al. [17] postulated that during the carbothermic reduction in UO_2 microspheres, the carbide nucleation at the surface of UO_2 particle is extremely fast. The particle is instantaneously covered by a thin carbide layer. The carbothermic controlling steps can be due to interface or diffusion reactions.

When the diffusion through the product layer is so fast that the reagents cannot sufficiently quickly combine with the interface reaction to reach equilibrium, the reaction rate is controlled by interface phenomena. This assumption leads to a relation [2,10] that highlights the dependence of the degree of conversion (ξ) on the initial radius of the particle (r_0)

$$1 - (1 - \xi)^{1/3} = \frac{k \cdot t}{r_0} \tag{3}$$

The reference used to define the degree of conversion (ξ) is related to the minor solid reactant. This reactant is the less abundant from the points of view of the stoichiometric coefficients and the initial conditions of the reaction. Then, it is the first depleted in the case of a total reaction. In the case of our samples made of a mixture of UO_2 (60 mol %) and carbon (40 mol %), the degree of conversion (ξ) is defined as a function of the carbon molar amount in the mixture, which is calculated by subtracting the $CO_{(g)}$ and $CO_{2(g)}$ releases

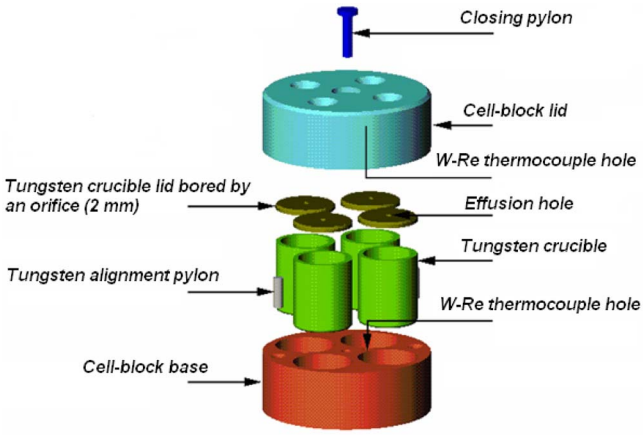

Fig. 6 Cell block with multiple effusion Knudsen cells

$$\xi = \frac{n_C^0 - n_C^t}{n_C^0} \tag{4}$$

Jander [11] developed a model for planar diffusion. It is also suitable for packed to the packed powders in the case of a low thickness circular diffusion. In this model, the penetration of a reagent through the product separating two reactive phases is the determining step. Then the temporal dependence of the product layer formation is inversely proportional to its thickness.

From this model, Jander deduced the following parabolic law, which can be written according to the ξ parameter. This equation is a function of the constant K and the diffusion coefficient D [3]

$$[1 - (1 - \xi)^{1/3}]^2 = \frac{2KDt}{r_0^2} \tag{5}$$

Jander's equation was modified by Zhuravlev et al. [12]. In this model (Eq. (6)), the authors assume that the activity of the reagent is proportional to the fraction that did not react

$$\left[\frac{1}{(1 - \xi)^{1/3}} - 1\right]^2 = \frac{2KDt}{r_0^2} \tag{6}$$

Valensi and Carter's model consider that the diffusion proceeds through a layer of constant composition. This model also takes into account the difference between the product and the reactant densities. After a valid first order approximation, the model appears as a simplified relation (Eq. (7))

$$\ln(1 - \xi) = \frac{kt}{r_0^2} \tag{7}$$

In order to determine the formation rate of the uranium carbide, these kinetic models were used to analyze the $CO_{(g)}$ and $CO_{2(g)}$ pressure measurements using HTMS.

5 Experiment

High temperature mass spectrometry, coupled with Knudsen effusion cells, is an accurate experimental technique suitable for gas partial pressure measurements [18–20]. The Knudsen cell is a closed crucible with a lid, which has a hole, whose dimensions are small with respect to the surface of the sample (Fig. 6).

With such geometry, no collision occurs in the rarefied evaporating gas flow. The molecular beam goes through a diaphragm directly in the ionization chamber of a mass spectrometer maintained under high vacuum. Inside the mass spectrometer, the gas ionization will generate positive charged ions that are extracted from the ionization chamber, and accelerated by an electric field. Then, the molecules are separated according to their mass/charge ratio by a high frequency electric field.

$CO_{(g)}$ and $CO_{2(g)}$ ionic intensities are monitored as a function of time and temperature. Using the Knudsen–Hertz relation (Eq. (8)) and from the total mass loss of the sample, the vapor flows of $CO_{(g)}$ and $CO_{2(g)}$ are determined versus time during the carbothermic reaction. The variation in the overall composition of the sample in the UCO system is also determined. The total amount of gas corresponds to the total mass loss of the sample at the end of the experiment

$$\frac{dn_i}{dt} = \frac{sCp_i}{\sqrt{2\pi M_i RT}} \tag{8}$$

In addition, $CO_{(g)}$ and $CO_{2(g)}$ partial pressures are determined, coupling the previous equation with the spectrometric relation (Eq. (9)). The global method used to determine the vapor flows and pressures (e.g., $CO_{(g)}$ and $CO_{2(g)}$) using HTMS is detailed in Ref. [5].

$$p_i S_i = I_i T \tag{9}$$

6 Samples

In both types of samples, the relative mole fractions of the reactants are the same: 40% of C (~0.075 *g*) and 60% of UO_2 (~2.5 *g*). Carbon black powder used for the two types of samples was the same. Crucibles made of graphite were used.

In the case of the pellets, the samples were made by mixing black carbon and UO_2 powders. Two batches were manufactured with different initial uranium dioxide stoichiometries: 2.06 and 2.15. To obtain compact pellets, these powders were packed and compacted using a press under inert atmosphere. The oxygen composition of the uranium dioxide was controlled by an oxidation protocol of UO_2 into U_3O_8 using thermogravimetry.

To study the influence of the sample geometry on kinetics, UO_2 kernels with a diameter of 500 μm were placed in a graphite crucible and embedded in black carbon. After the tests, the samples were characterized using X-ray diffraction (XRD), scanning electron microscopy (SEM), and energy dispersive spectroscopy (EDS).

7 Results for the Pellets

The measurements were performed in the temperature range 1473–1623 K. Formation of $CO_{(g)}$ and $CO_{2(g)}$ was not significant enough at 1273 K to study the reaction at the fuel operating temperature of the VHTR. The $CO_{(g)}$ and $CO_{2(g)}$ pressure profiles versus time and temperature have been previously described in Ref. [5]. $CO_{2(g)}$ is formed jointly with $CO_{(g)}$, mainly at the beginning of the reaction. This $CO_{(g)}$ formation occurs during the heating of the pellet. This phenomenon is reproducible and explains the overlap of the curves from one run to another. Then, the contribution of $CO_{(g)}$ becomes the major one when the UO_2 is less oxidized. Likewise, the $CO_{2(g)}$ signal becomes nearly constant, close to the spectrometric background level (Fig. 7).

After the first peak due to the fast reduction in UO_{2+x} into $UO_{1.99}$, the $CO_{(g)}$ pressure decreases with time. Then a sharp increase in the $CO_{(g)}$ pressure occurs with a maximum at 70–120 min depending on temperature. Then the $CO_{(g)}$ pressure decreases with time. This change can be interpreted as a transition between two kinetic regimes (Fig. 8).

As previously reported in Ref. [5], the mechanisms associated with the $CO_{(g)}$ and $CO_{2(g)}$ releases are too complex to be represented by a single model. Several coupled kinetic models have to be used to correctly describe this interaction. Finally, the reactional mechanism seems to be governed by successive interface and diffusion phenomena.

7.1 Interface Mechanism. After the first $CO_{(g)}$ and $CO_{2(g)}$ release and before the interface reaction (corresponding to the

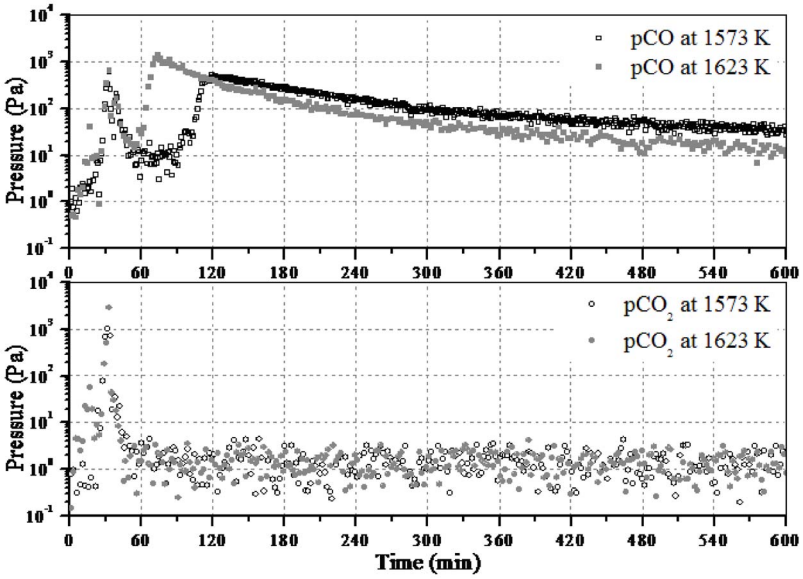

Fig. 7 Measurement of $CO_{(g)}$ and $CO_{2(g)}$ pressures versus time for the UO_2 +C pellets at 1573 K and 1623 K

second increase in the pressure), a latent period occurs, during which no gas is formed, and whose duration depends on temperature (Fig. 7).

The interface phenomena are interpreted using the degree of conversion (ξ) as variable and using the model developed by Spencer and Topley [10] and also used by Mukerjee et al. [3]. The model is considered as valid if a linear transform as a function of time is obtained (see the left part of Eq. (3)).

The interface mechanism starts between 60 min and 150 min for the three runs made at higher temperatures (1573 K, 1606 K, and 1623 K). At lower temperature (1473 K) the kinetic is slower and the interface phenomenon occurs later. This is due to a longer latency time, during which the degree of conversion remains stationary (Fig. 9).

The activation energy associated with the interface mechanism is calculated according to an Arrhenius law (Eq. (10))

$$k = A \cdot \exp\left(\frac{-E_a}{RT}\right) \tag{10}$$

The activation energy of the interface controlling step is 326 kJ/mol.

This experimental value is close to that reported in the literature, except for the value of Danger and Besson [7]. It is in very good agreement with the data of Mukerjee obtained in case of interface phenomena (Table 1).

7.2 Diffusion Mechanism. The second step of the reaction is described by a diffusion model toward the uranium carbide layer. This second mechanism is consistent with the sample observations that show regions constituted of uranium carbide. This phase is located along the porosities that are formed due to $CO_{(g)}$ release during the carbothermic reaction.

At the first stage of the reaction, uranium carbide is formed in a scattered way. The contact between UO_2 and carbon is maintained. When the degree of conversion (ξ) increases, a uranium carbide layer forms and prevents any physical contact between carbon and UO_2. The interface mechanisms of initially involved reactants are stopped by the uranium carbide barrier. Progres-

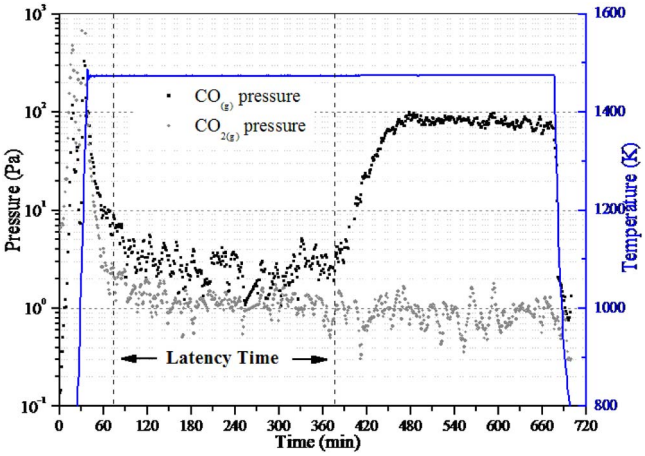

Fig. 8 $CO_{(g)}$ and $CO_{2(g)}$ pressure measurements versus time. Illustration of the latency time before the pressure increase due to the interfacial reaction (T=1473 K).

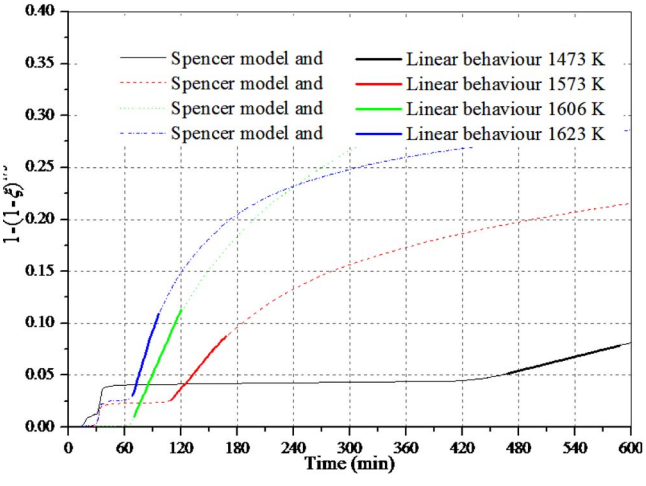

Fig. 9 Application of Spencer's model (Eq. (3)) to the experimental degree of conversion (ξ) of the UO_2+C reaction at 1473 K, 1573 K, 1606 K, and 1623 K. The bold straight lines represent the domain of validity of the interface model.

Table 1 Activation energies of the reaction between UO_2 and carbon

Authors	Reactional mechanism	Kinetic model	E_a (kJ/mol)
Ainsley	First order mechanism	Valensi–Carter	385
Danger	Diffusion in UC_2	Valensi–Carter	280
Lindemer	O diffusion in UC_2	Ginstling	377
Mukerjee (vacuum)	Reaction at the UO_2/UC_2 interface	Spencer	334
Mukerjee (gas flow)	Diffusion reactions	Valensi–Carter	368

sively, they are replaced by diffusion mechanisms occurring through the thick product layer. Once the diffusion mechanism is established, $CO_{(g)}$ and $CO_{2(g)}$ form with a slower rate than in the case of interface reaction. For the experiments performed at 1573 K, 1606 K, and 1623 K, this transition is characterized by a slow change in slope from $t=180$ min for both of the diffusion models of Jander [11] and Zhuravlev et al. [12]. This progressive change in slope represents the transition from interface to diffusion process.

Three HTMS runs performed in the 1573–1623 K range were analyzed using the model of Zhuravlev et al. (Eq. (6)). Except for the experiment at 1606 K, which is shorter than both others, no differences clearly appear between the slopes. These close reaction rates let us assume that the activation energy of the diffusion process is lower than in the case of interface phenomena (Fig. 10). This assumption has to be confirmed by further experiments in a larger temperature range.

8 Results for the Kernels

Concerning the kernels ($\varnothing=500$ μm), the $CO_{(g)}$ and $CO_{2(g)}$ profiles are slightly different. First, the first sharp release observed in the pellets does not occur during heating (Fig. 11). $CO_{2(g)}$ contribution is always negligible with regard to $CO_{(g)}$.

This change can be due to the difference in specific area of the two kinds of samples. The amount of available oxygen on the surface of the uranium dioxide is much higher in the case of the micrometric UO_2 powders ($\varnothing \approx 100$ μm) than in the case of the kernels.

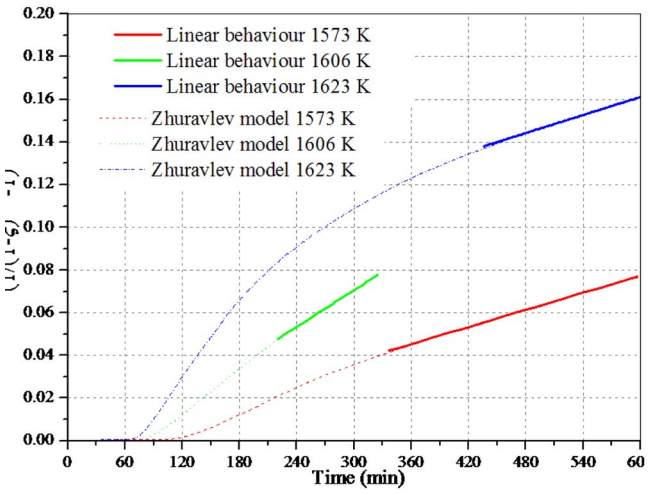

Fig. 10 Application of Zhuravlev's model (Eq. (6)) to the experimental degree of conversion (ξ) of the UO_2+C reaction at 1573 K, 1606 K, and 1623 K. The bold straight lines represent the domain of validity of the diffusion model.

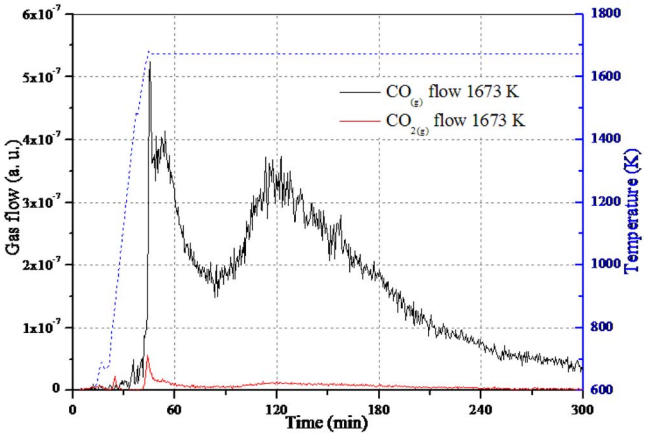

Fig. 11 $CO_{(g)}$ and $CO_{2(g)}$ releases from ionic intensities measurements by high temperature mass spectrometry at 1673 K

Second, the $CO_{(g)}$ release is lower in the kernels than in the pellets. For example, there is a two order of magnitude gap between the measured pressures at 1573 K. This release is characterized by a long duration peak with a nearly linear decrease in pressure with time. The $CO_{(g)}$ release is also characterized by a shoulder. This profile seems to be the sum of two successive peaks. Moreover, the expected plateau of pressure due to the monovariant conditions in the UCO system in this three phase domain seems to be almost reached at 1523 K for slow kinetic rates and also at 1673 K for faster rates (Figs. 12 and 13).

The analysis of the measurements was performed using all previously reported kinetic models.

At 1573 K, no model is valid despite the almost linear behavior of Valensi's model (Fig. 14). This is confirmed by the analysis of the data measured at 1673 K that clearly shows that Valensi's model is no longer valid for the whole duration of the run (Fig. 15).

At 1623 K, Zhuravlev's model seems to be the more suitable to fit the experimental data from $t=180$ min (Fig. 16). But the decrease in the reaction rate seems to result once more from the contribution of successive phenomena. Nevertheless, Spencer's model is not an appropriate fit at the beginning of the reaction as an interface process, as in the case of the pellets.

To determine kinetics of the UO_2 carbothermic reduction, the data were analyzed in the same way as in the case of the pellets by

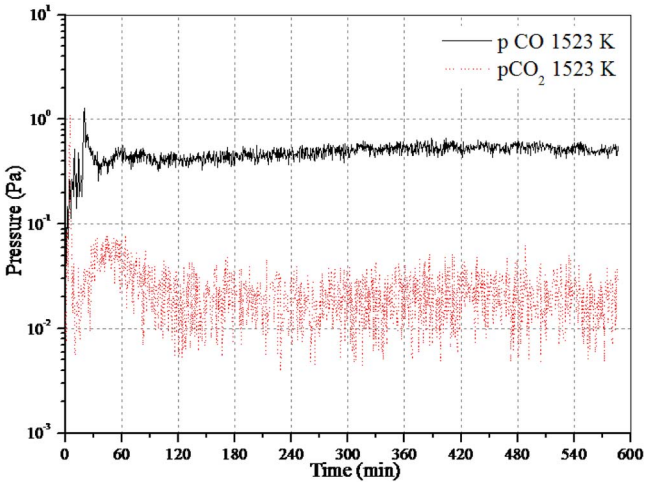

Fig. 12 Measurement of $CO_{(g)}$ and $CO_{2(g)}$ pressures versus time for the UO_2 kernels in a carbon black bed at 1523 K

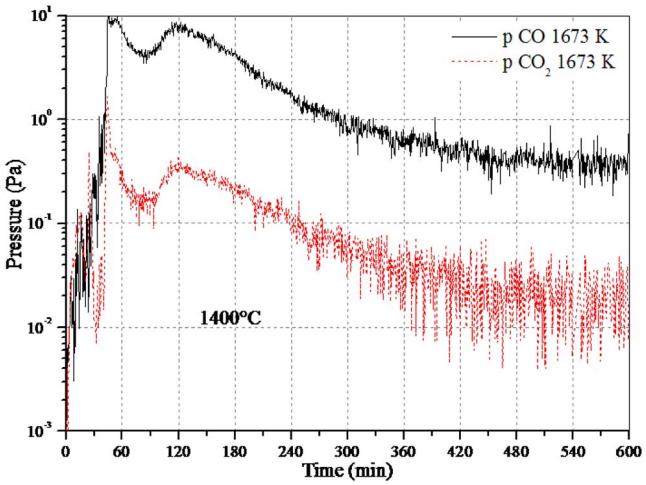

Fig. 13 Measurement of $CO_{(g)}$ and $CO_{2(g)}$ pressures versus time for the UO_2 kernels in a carbon bed 1673 K

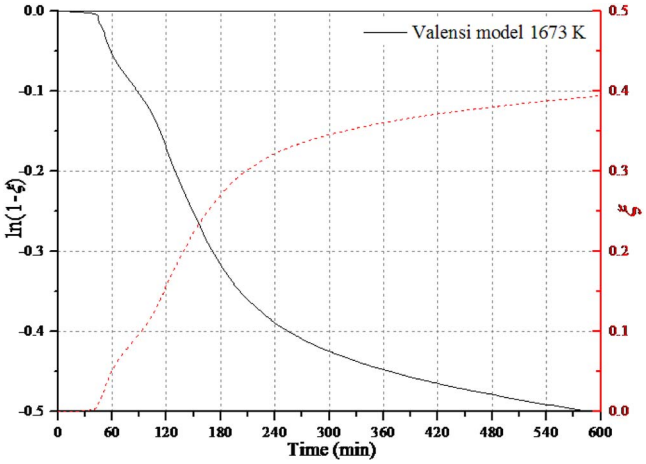

Fig. 15 Application of Valensi's model (Eq. (7)) to the experimental degree of conversion (ξ) of the reaction between UO_2 kernels and carbon black at 1673 K

using two successive mechanisms. The best fits are obtained using a diffusion model for the second part of the reaction. However, the use of an interface model for the first part of the reaction does not allow fitting the measurements, as in the case of the pellets. Further experiments will have to be performed to confirm that an interface model can be used for the kernels.

9 Analyses

The analyses of the samples made of UO_2 kernels embedded in black carbon are presented. Analyses performed on the pellets were presented in Ref. [5]. The analyses on the kernels are detailed in Ref. [14].

After being embedded in resin, sections of the samples were observed. In most of the cases, the nearly spherical shape of the kernels is maintained. Thin layers are observed at the outer part of the kernels that are slightly separated from the inner part of the sphere (Fig. 17).

The UO_2 and UC phases have been identified by X-ray diffraction. The peaks related to the presence of carbon are mainly due to the graphite from the crucible, but also to residual carbon that has not reacted with UO_2 kernel (Fig. 18).

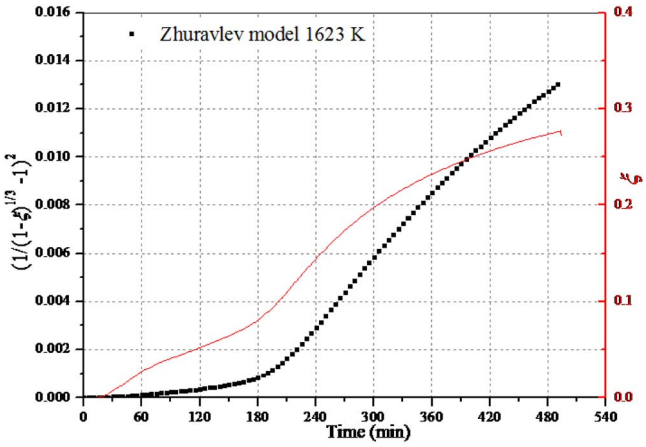

Fig. 16 Application of Zhuravlev's model (Eq. (6)) to the experimental degree of conversion (ξ) of the reaction between UO_2 kernels and carbon black at 1623 K. The right scale represents the degree of conversion (ξ).

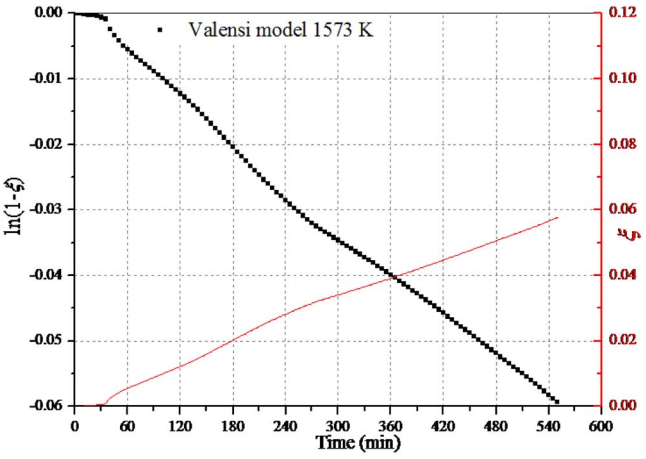

Fig. 14 Application of Valensi's model (Eq. (7)) to the experimental degree of conversion (ξ) of the reaction between UO_2 kernels and carbon black at 1573 K. The right scale represents the degree of conversion (ξ).

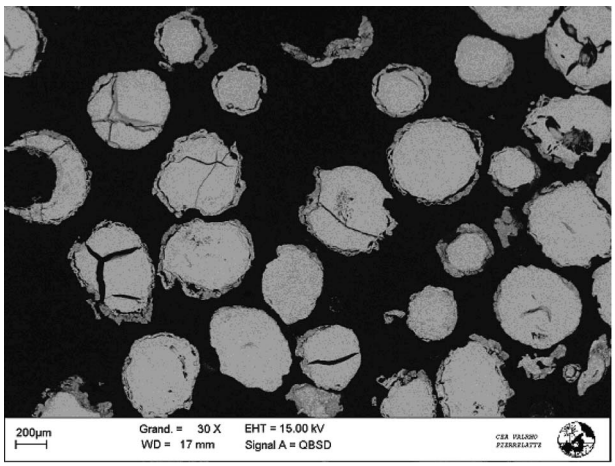

Fig. 17 View of the UO_2 kernels by scanning electron microscopy after heat treatments at 1623 K

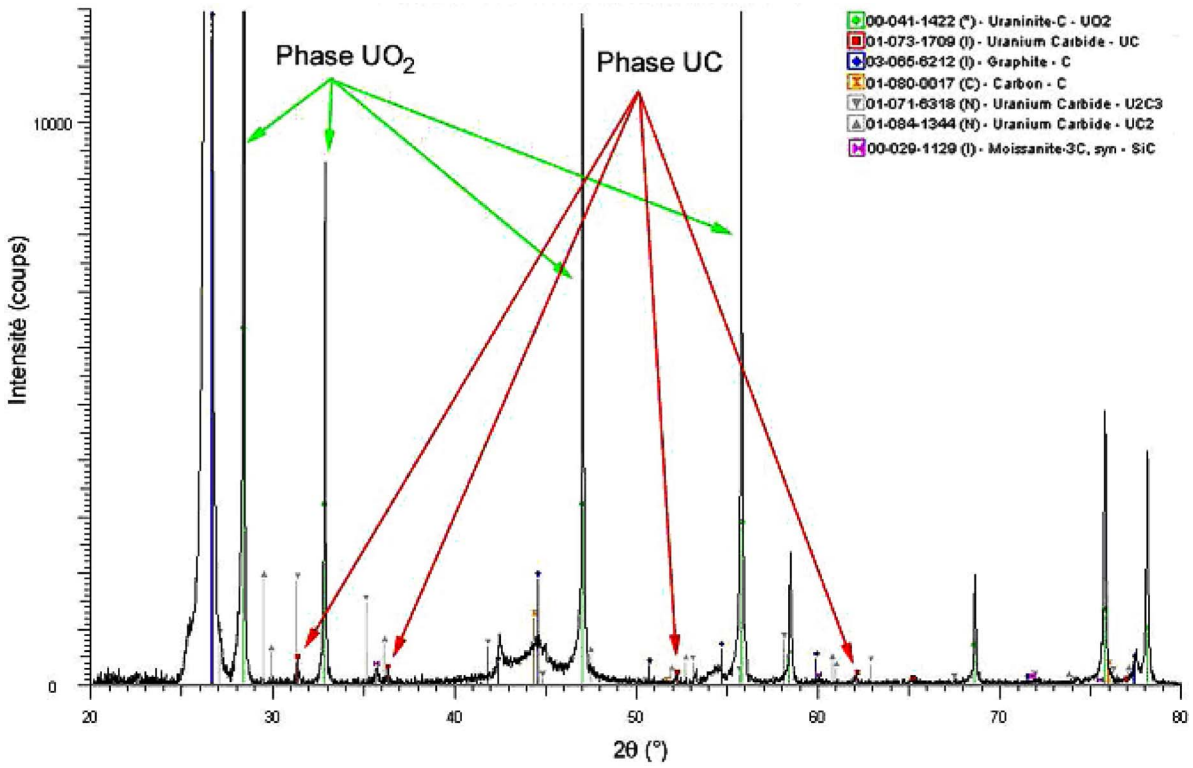

Fig. 18 X-ray diffractogram of UO_2 kernels in a carbon bed after the 1623 K experiment (the UC phase and the UO_2 phase are shown)

XRD did not show the existence of U_2C_3 and UC_2 carbides. It only means that these carbides can be present, but in proportions lower than the limit of detection of the method (about 4 vol %).

The UO_2 and UC phase distribution inside the TRISO kernels is presented in Ref. [14]. In most of the case, the interaction between UO_2 and carbon led to the formation of a UC layer at the outer part of the kernel [14]. But, in some specific cases, microstructures resulting from "nonuniform" reaction mechanisms are observed, as described by Lindemer et al. [9]. In the experiments of Lindemer et al., such specific microstructure is obtained when high heating rates were applied (50°C/min and 100°C/min). These high rates induce strong thermal gradients inside a particle, in spite of its low diameter ($\varnothing$=500 μm) [21]. The sections of the kernel have the same nonuniform microstructure, as shown in Fig. 19. The UO_2 phase is in the inner part of the sphere, where a throat is observed. On one side of the particle, UO_2 reaches the outer part of the particle (Fig. 19).

This observation points out the amoeba effect that leads to the migration of the UO_2 kernel toward the hot side of the TRISO particle. This phenomenon is governed by the transport of carbon via the gas phase due to significant thermal gradients. However, such gradients should not exist in the HTMS furnace. According to Lindemer et al. [9], the reaction rate of the nonuniform type of conversion is between two and five times faster than for the uniform centripetal one.

10 Summary

The thermodynamic modeling of the UCO system is an essential tool to understand the high temperature behavior of the high temperature reactor (HTR) fuel materials. The FUELBASE database was used to calculate $CO_{(g)}$ pressures in equilibrium with the condensed phases as a function of O/U ratio and temperature.

HTMS experiments were performed on UO_2+C pellets and on UO_2 kernels in black carbon. The results confirm the strong interaction between UO_2 and carbon in the 1473–1673 K range. This interaction is characterized by releases of $CO_{(g)}$ and $CO_{2(g)}$, whose profiles are related to a first step of reduction in UO_{2+x} by C into nearly stoichiometric UO_2, and then by a second step of formation of the UC carbide during the reduction in UO_2 by C. With both pellets and kernels, the measured pressures of $CO_{(g)}$ are low in comparison with thermodynamic predictions due to kinetic limitations. The following observations are made.

1. For the pellets, $CO_{2(g)}$ is formed at the beginning of the reaction when the oxide is hyperstoichiometric. Then, $CO_{(g)}$ appears later and becomes the main gas species, when the UO_2 is less oxidized. The $CO_{(g)}$ release profile suggested

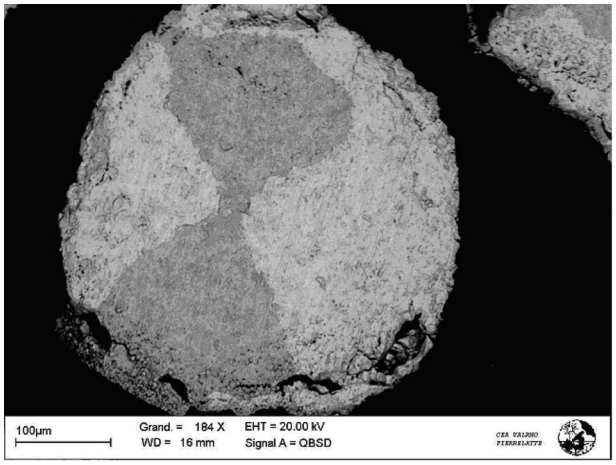

Fig. 19 View of a nonuniform profile of a UO_2 kernels by SEM after heat treatments at 1673 K (UO_2 is the dark phase and UC is the light phase)

applies to different kinetic models from the literature. The reaction seems to be governed by successive interface and diffusion phenomena. Before the interface reaction, a latency time occurs, during which the pressures are almost stationary. Then, the transition from the first mechanism (interface) toward the second (diffusion) appears. From the experiments, the activation energy of the interface controlling step has been assessed. The measured activation energy of 326 kJ/mol is in good agreement with the values from the literature.

2. Concerning the kernels, the profiles are different. The $CO_{(g)}$ and $CO_{2(g)}$ peaks do not appear during heating of the sample and the $CO_{2(g)}$ contribution is negligible. Furthermore, the kinetics is much slower in comparison with the pellets. The pressure plateau is nearly reached in the three phase domain. Nevertheless, the pressures are more than one order of magnitude lower than the expected equilibrium $CO_{(g)}$ pressures. As in the case of the pellets, a single kinetic model cannot fit the whole experiment. The reaction between UO_2 and carbon seems to result from the contribution of successive phenomena to the pellets. Zhuravlev's model seems to be the more suitable to fit the experimental data in the end of the experiments. But Spencer's interface model does not seem to be the appropriate fit for the beginning of the reaction. Some additional experiments will have to be performed to determine if the first part of the kinetics is due to interface phenomena. The analyses performed on the samples made of UO_2 kernels embedded in carbon black are presented.
3. Generally, the UO_2 kernels remain nearly spherical, and they are surrounded by a thin layer of UC. The X-ray pattern reveals the presence of UO_2 and UC phases. Some specific particles were observed, resulting from a nonuniform reactional mechanism, as described by Lindemer. Nevertheless, a high thermal gradient should not be obtained in our HTMS furnace. Another origin will have to be found to explain such behavior of the particles.

Acknowledgment

The authors thank EDF and AREVA-NP for financial support of this study. The authors also acknowledge A. Duhart Baronne and F. Charollais from CEA Cadarache (DEN/DEC/SPUA) for the supply of the UO_2 kernels.

Nomenclature

$\varnothing$ = diameter
C = clausing coefficient
ξ = degree of conversion
I_i = measured ionic intensity of the i species
K,k = reaction rate constant
k_D = diffusion rate constant (cm^2/s)
m = sample mass
M_i = molar mass of the i species
n_C = moles of carbon at t
n_C^0 = moles of carbon at t_0
p_i = partial pressure of the i species
R = perfect gas constant
s = section of the effusion hole
S_i = sensitivity of spectrometer for the i species
t = time (0=initial, f=final)
T = temperature (K)
μ = chemical potential

References

[1] Guéneau, C., Chatain, S., Gossé, S., Rado, C., Rapaud, O., Lechelle, J., Dumas, J. C., and Chatillon, C., 2005, "A Thermodynamic Approach for Advanced Fuels of Gas Cooled Reactors," J. Nucl. Mater., **344**, pp. 191–197.
[2] Mukerjee, S. K., Dehadraya, J. V., Vaidya, V. N., and Sood, D. D., 1990, "Kinetic Study of the Carbothermic Synthesis of Uranium Monocarbide Microspheres," J. Nucl. Mater., **172**, pp. 37–46.
[3] Mukerjee, S. K., Dehadraya, J. V., Vaidya, V. N., and Sood, D. D., 1994, "Kinetics and Mechanism of UO_2+C Reaction for UC/UC_2 Preparation ," J. Nucl. Mater., **210**, pp. 107–114.
[4] Gossé, S., Guéneau, C., Chatain, S., and Chatillon, C., 2006, "Critical Review of Carbon Monoxide Pressure Measurements in the Uranium-Carbon-Oxygen Ternary System," J. Nucl. Mater., **352**(1–3), pp. 13–21.
[5] Gossé, S., Guéneau, C., Chatain, S., and Chatillon, C., 2008, "Kinetic Study of the UO_2/C Interaction by High-Temperature Mass Spectrometry," Nucl. Eng. Des., **238**(11), pp. 2866–2876.
[6] Ginstling, A. M., and Brounshtein, B. I., 1950, "Diffusion Kinetics of Reactions in Spherical Particles," J. Appl. Chem. USSR, **23**(12), pp. 1327–1338.
[7] Danger, G., and Besson, J., 1974, "Etude Cinétique de la Carboréduction du Dioxyde d'Uranium," J. Nucl. Mater., **54**, pp. 190–198.
[8] Carter, R. E., 1961, "Kinetic Model for Solid-State Reactions," J. Chem. Phys., **34**(6), pp. 2010–2015.
[9] Lindemer, T. B., Allen, M. D., and Leitnaker, J. M., 1969, "Kinetics of the Graphite-Uranium Dioxide Reaction From 1400°C to 1756°C ," J. Am. Ceram. Soc., **52**, pp. 233–237.
[10] Spencer, W. D., and Topley, B., 1929, "Chemical Kinetics of the System Ag_2CO_3=Ag_2O+CO_2," J. Chem. Soc., **1**, pp. 2633–2650.
[11] Jander, W., 1927, "Solid State Reactions at High Temperature," Z. Anorg. Allg. Chem., **163**(1), pp. 1–30, in German.
[12] Zhuravlev, V. F., Lesokhin, I. G., and Tempelman, R. G., 1948, "Kinetics of Reactions in the Formation of Aluminates and the Contribution of Mineralizers to the Process," J. Appl. Chem. USSR, **21**(09), pp. 887–890.
[13] Guéneau, C., Baïchi, M., Labroche, D., Chatillon, C., and Sundmann, B., 2002, "Thermodynamic Assessment of the Uranium-Oxygen System," J. Nucl. Mater., **304**(2–3), pp. 161–175.
[14] Chevalier, P. Y., and Fischer, E., 2001, "Thermodynamic Modelling of the C-U and B-U Binary Systems," J. Nucl. Mater., **288**, pp. 100–129.
[15] Petti, D. A., Dolan, T. J., Miller, G. K., Moore, R. L., Ougouag, A. M., Oh, C. H., and Gougar, H. D., 2002, "Modular Pebble-Bed Reactor Project Laboratory-Directed Research and Development Program FY 2002 Annual Report," Report No. EXT-02-01545.
[16] Ainsley, R., Harder, B. R., Hodge, N., Sowden, R. G., White, D. B., and Wood, D. C., 1963, "Carbides as Reactor Fuels: Preparation from Oxides and Sintering Characteristics," *Proceedings of the New Nuclear Materials Including Non-Metallic Fuels Conference*, Prague, 1, pp. 349–376.
[17] Stinton, D. P., Tiegs, S. M., Lackey, W. J., and Lindemer, T. B., 1979, "Rate-Controlling Factors in the Carbothermic Preparation of UO_2-UC_2-C Microspheres," J. Am. Ceram. Soc., **62**(11-12), pp. 596–599.
[18] Heyrman, M., 2004, "Etude par Spectrométrie de Masse à Haute Température du Système Al_2O_3-C: Application aux Fours d'Elaboration sous Vide," Ph. D. thesis, INPG, Grenoble, France.
[19] Baïchi, M., Chatillon, C., Guéneau, C., and Chatain, S., 2001, "Mass Spectrometric Study of UO_2–ZrO_2 Pseudo-Binary System," J. Nucl. Mater., **294**(1–2), pp. 84–87.
[20] Carlson, K. D., 1967, *The Characterization of High Temperature Vapors Chapter 5: The Knudsen Effusion Method*, J. L. Margrave, ed., Wiley, New York, Chap. 5, pp. 115–129.
[21] Boinski, F., Gossé, S., Dugne, O., and Guéneau, C., 2008, "XRD and SEM/EDS Study of the Phases Distribution in the UO_2+C Reactional System at High Temperature," *Proceedings of the Fourth Conference on HTR Technology*, Washington, DC, Sept. 28–Oct. 1.

Creep Effects on Design Below the Temperature Limits of ASME Section III Subsection NB

T.-L. Sham
Fellow ASME
Oak Ridge National Laboratory,
1 Bethel Valley Road,
P.O. Box 2008, MS-6155,
Oak Ridge, TN 37831-6155
e-mail: shamt@ornl.gov

Robert I. Jetter
Consultant
Fellow ASME
Pebble Beach, CA 93953

Daniel R. Eno
Consultant
Guilderland, NY 12084

Some recent studies of material response have identified an issue that crosses over and blurs the boundary between ASME Boiler and Pressure Vessel Code Section III Subsection NB and Subsection NH. For very long design lives, the effects of creep show up at lower and lower temperature as the design life increases. Although true for the temperature at which the allowable stress is governed by creep properties, the effect is more apparent, e.g., creep effects show up sooner, at local structural discontinuities and peak thermal stress locations. This is because creep is a function of time, temperature, and stress, and the higher the localized stress, the lower in temperature creep begins to cause damage. If the threshold is below the Subsection NB to NH temperature boundary, 700°F for ferritic steels and 800°F for austenitic materials, then this potential failure mode will not be considered. Unfortunately, there is no experience base with very long lives at temperatures close to but under the Subsection NB to NH boundary to draw on. This issue is of particular interest in the application of Subsection NB rules of construction to some high temperature gas-cooled reactor concepts. The purpose of this paper is, thus, twofold: one part is about statistical treatment and extrapolation of sparse data for a specific material of interest, SA-533 Grade B Class 1; the other part is about how these results could impact current design procedures in Subsection NB.
[DOI: 10.1115/1.3126263]

1 Introduction

The ASME Boiler and Pressure Vessel (B&PV) Code, Section III, Subsection NB provides construct rules for Class 1 nuclear components. The Subsection NB code materials and their corresponding primary stress limits are tabulated in Section II, Part D, Tables 2 (ferrous materials) and 2B (nonferrous materials). Table 4 of Part D gives the stress limits for bolting materials. The Subsection NB rules shall not be used for materials at design temperatures that exceed the maximum temperature limits listed in the applicability columns of these tables. They are 700°F for ferritic steels and 800°F for austenitic steels. For temperatures above these limits the rules of construction for Class 1 nuclear components are provided in Section III, Subsection NH, but the number of approved Subsection NH code materials is much more limited.

Current view among many concerning Code boundary of Subsections NB and NH is that creep effects do not need to be considered for temperatures below 700°F for ferritic steels in reactor pressure vessel (RPV) applications. While this is undoubtedly true for typical light water reactor operating temperatures, it may not be true for higher normal operating metal temperatures that are pushing against the 700°F boundary, e.g., at 660°F, and for a long design life, e.g., 60 years. This is particularly poignant with the consideration of localized high stress areas. The reason is that creep deformation depends on stress, time, and temperature and does not have a strict temperature cut-off that separates creep from noncreep regimes. This could potentially affect the primary stress limits and impact RPV sizing. The potential impact could also likely show up at structural or metallurgical discontinuities. If there is a real problem in the RPV due to creep effects at 660°F, it is not likely to show up until the component is well into its operating life.

Creep data at these low temperatures are very difficult to develop as it is not practical to perform creep tests for such long durations. Accelerated tests would in general be relied on to generate data for extrapolation. The only currently available data that could provide limited information in framing the issue of whether or not the consideration of creep is needed for the RPV in the upper temperature limit of Subsection NB for very long design lives are those that supported the development of Code Case N-499, which provides rules of construction for two specific low-alloy steels: SA-533 Grade B Class 1 (SA-533B UNS K12539) plates and SA-508 Grade 3 Class 1 forgings (UNS K12042) and their weldments for short-term temperature excursions above the temperature limit of 700°F.

2 A533B Database

The creep database submitted by McCoy [1] to the ASME Code committee that supported the development of Code Case N-499 was a subset of the data reported by McCoy [2]. It consisted of 50 creep rupture test results from four SA-533B plate heats. The applied stresses ranged from 1 ksi to 75 ksi, and the test temperatures ranged from 700°F to 1100°F. Of the 50 test results, 15 tests were reported to have terminated in creep rupture, and 35 tests were reported to have terminated prior to the occurrence of creep rupture. All four heats were represented in each group of results. Test data included time to 1% strain ($t_{1\%}$), time to start of tertiary creep (t_{tertiary}), and time to creep rupture (t_r), where applicable. The longest creep rupture time was 3378 h and the shortest was 23.5 h. The longest test time where the test was terminated before creep rupture took place was 25,921 h and the shortest was 285 h.

As the objective of Code Case N-499 was to develop time dependent primary stress limits for limited numbers of short-term elevated temperature excursions, only the tests that resulted in creep rupture were analyzed during the development of the code case. However, the results from those tests that were terminated before creep rupture occurred do provide valuable information on the creep rupture behavior at longer exposure times. This can be accomplished by treating these results as censored data and to

Manuscript received October 20, 2008; final manuscript received November 24, 2008; published online October 2, 2009. Review conducted by Dilip R. Ballal. Paper presented at the 4th International Topical Meeting on High Temperature Reactor Technology (HTR2008), Washington, DC, September 28–October 1, 2008.

Table 1 Negative two-log-likelihood values

Model	-2LL for $t_{1\%}$	-2LL for t_{tertiary}	-2LL for t_r
MRM	126.45	115.64	71.50
Orr–Sherby–Dorn	167.94	133.12	88.30
Larson–Miller	164.87	130.91	86.52
Manson–Haferd	132.29	116.96	71.73
Manson–Succop	164.76	129.38	86.08
Mean only	181.09	146.29	96.07

Table 2 Parameter estimates for the MRM model

	$t_{1\%}$	t_{tertiary}	t_r
β_0	$-1.394\,312\times10^{2}$	$-1.379\,852\times10^{2}$	$-1.366\,732\times10^{2}$
β_1	$2.350\,708\times10^{5}$	$2.350\,708\times10^{5}$	$2.350\,708\times10^{5}$
β_2	$2.598\,133\times10^{1}$	$2.598\,133\times10^{1}$	$2.598\,133\times10^{1}$
β_3	$-4.578\,777\times10^{4}$	$-4.578\,777\times10^{4}$	$-4.578\,777\times10^{4}$
γ	$9.926\,518\times10^{-1}$	$1.222\,379\times10$	$1.435\,087\times10$

estimate the model parameters using maximum likelihood estimation. The strategy is then to use the results from the entire SA-533B database to develop a statistical model, and to extrapolate the resulting statistical model to conditions that are of interest to addressing the effects of creep at lower temperatures and longer exposure times. However, it should be recognized that extrapolation far away from the test conditions of a database might not always be reliable; hence, one should be mindful of this in assessing the extrapolated results. Nevertheless, in the absence of data that are more representative of the conditions of interest, the results presented herein provide the first opportunity to explore this difficult subject.

3 Statistical Methods

Following Eno et al. [3], each of the three time responses was analyzed via regression modeling as a function of applied stress (σ, ksi) and temperature (T, °F), using the following linear model forms:

$$\ell n(t) = \beta_0 + \frac{\beta_1}{T_R} + \beta_2 \ell n(\sigma) + \frac{\beta_3}{T_R}\ell n(\sigma) \tag{1}$$

$$\ell n(t) = \beta_0 + \beta_1 T_R + \beta_2 \ell n(\sigma) + \beta_3 T_R \ell n(\sigma) \tag{2}$$

where $T_R = T + 460$ is the absolute temperature in Rankine. The parameters β_0, β_1, β_2, and β_3 were estimated using several common creep parametrizations, all of which are special (in some cases constrained) cases of Eqs. (1) and (2)

- Mendelson–Roberts–Manson (MRM) uses Eq. (1) (no parameters fixed at zero)
- Orr–Sherby–Dorn uses Eq. (1), with the parameter β_3 fixed at zero
- Larson–Miller uses Eq. (1), with the parameter β_2 fixed at zero
- Manson–Haferd uses Eq. (2) (no parameters fixed at zero)
- Manson–Succop uses Eq. (2), with the parameter β_3 fixed at zero

4 Statistical Results

The five regression model formulations described above were fit to each of the three responses ($t_{1\%}$, t_{tertiary}, and t_r) via the method of maximum likelihood estimation. A log-normal distribution was assumed for each response variable's random error distribution. Table 1 summarizes the optimized value of negative two log-likelihood (-2LL) for each model and each response. For two nested models (that is, two models for which one represents a restriction of the other), a statistical test for the adequacy of the simpler (restricted) model can be performed based on the difference in -2LL between the two fitted models. This difference will have an asymptotic chi-squared distribution, with degrees of freedom equal to the difference in number of parameters between the two nested models.

From Table 1, it can be observed that the restricted version of Eqs. (1) and (2) (namely, Orr–Sherby–Dorn, Larson–Miller, and Manson–Succop) provides significantly inferior fits than the unrestricted versions (MRM and Manson–Haferd). There is a slight preference for the MRM model over the Manson–Haferd model for each of the three responses, on the basis of the optimized -2LL values. Therefore, subsequent calculations will be based on the MRM model.

Also included in the last row of Table 1 are the -2LL values for simple "mean only" models for the three responses; these models assume no dependence of the response on applied stress or temperature. Based on a comparison of these -2LL values with the values for the MRM model, it can be seen that the overall dependence of each response on the predictors (stress and temperature) is statistically significant.

For a ruptured specimen, the time to the start of tertiary creep is necessarily shorter than the rupture time. However, when the regression results are extrapolated far away from the database, it is possible that the extrapolated value of t_{tertiary} could be larger than that of t_r when the regressions for the response times are performed independently. In order to prevent such an undesirable feature and yet to be able to explore the effects of creep at low temperatures and longer exposure times, the results to be reported in Secs. 5 and 6 were obtained by assuming that each of the regression variables, β_1, β_2, and β_3, has the same value for all three response times, while the variable β_0 has different value for each response time. Table 2 displays the estimated parameters for the MRM models, for the three response variables. The parameter γ is the estimated residual standard deviation, quantifying "data scatter" in the natural logarithm time space.

Equation (1) for the MRM model can be recast in the form

$$t = A \times \exp\left(\frac{Q}{RT_R}\right) \times \sigma^{m(T_R)} \tag{3}$$

where $A \equiv \exp(\beta_0)$, $Q \equiv R\beta_1$, $m \equiv \beta_2 + \beta_3/T_R$, and R is the universal gas constant. Note that $Q > 0$ and $m < 0$.

Figures 1–3 display the measured times from the database versus the predicted times from the MRM model. The solid symbols represent exact (uncensored) times; the crosses represent right censored times. In interpreting these plots, a tight fit to the database should have the exact times falling near the identity (one-to-one) line, and the crosses should tend to fall below the identity line. Of course, data scatter will also be exhibited by the data, so

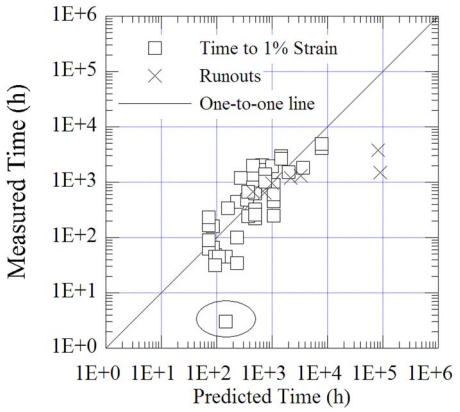

Fig. 1 Measured versus predicted time to 1% strain for SA-533B

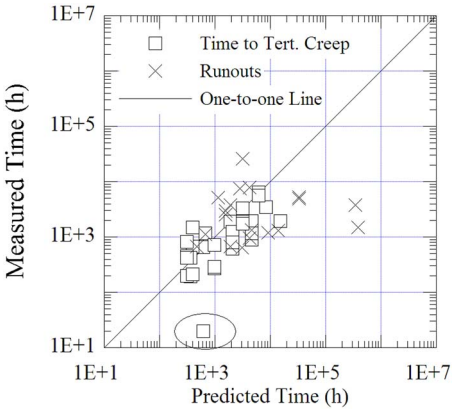

Fig. 2 Measured versus predicted time to start of tertiary creep for SA-533B

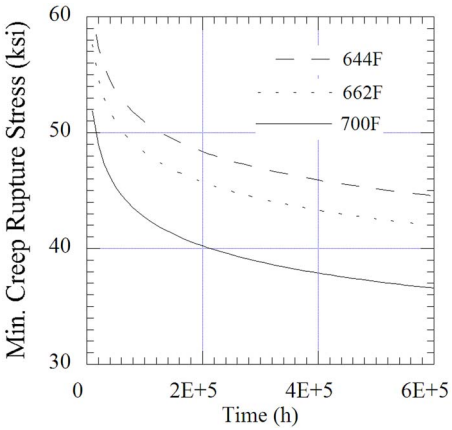

Fig. 3 Measured versus predicted creep rupture time for SA-533B

these tendencies will not be perfect, even for a good fit. Also, a large fraction of right censored data points (e.g., for the rupture time fit) will tend to push the prediction line higher; this is appropriate, since the right censored points tend to exhibit resistance to reaching the response criterion (e.g., rupture).

The results shown in Fig. 3 can also be viewed from a different perspective. The region below the one-to-one line is where the actual time is shorter than the predicted time. If the tests of all the 50 specimens were carried out till rupture, it would be expected that somewhere around 25 data points are below the line, and 25 above the line. However, there are only 10 rupture data below the line in the figure, with many of the "survivors" below the one-to-one line, and had the tests been continued to rupture, some of them would have ruptured below and some above the one-to-one line. From Figs. 1–3, a single low outlier (the low measured time) is evident in all three plots. The outlier (circled) in all three plots corresponds to the same specimen.

Confidence and prediction bounds (PBs) for times to 1% strain, start of tertiary creep, and rupture can be made from the MRM fits, based on Eq. (1) and the coefficient estimates in Table 2. The q quantile confidence bound (CB) of $\ell n(t)$ can be estimated as

$$CB[\ell n(t)]_q = \{x\}^t \cdot \{\beta\} + z_q \cdot (se)_q \tag{4}$$

where

$$\{x\}^t = \lfloor 1, T_R^{-1}, \ell n(\sigma), T_R^{-1}\ell n(\sigma) \rfloor \tag{5}$$

$$\{\beta\}^t = \lfloor \beta_0, \beta_1, \beta_2, \beta_3 \rfloor \tag{6}$$

with z_q represents the q quantile of the standard normal distribution, and $(se)_q$ is the standard error of a predicted quantile of $\ell n(t)$ at specified absolute temperature T_R, stress σ, and q quantile. For example, the 0.05 and the 0.95 quantiles are computed with using $z_{0.05}=-1.645$ and $z_{0.95}=+1.645$ in Eq. (4), respectively.

The standard error, $(se)_q$, can be computed as

$$(se)_q = \sqrt{\{y_q\}^t \cdot [V] \cdot \{y_q\}} \tag{7}$$

where

Table 3 Covariance matrix [*V*] for different response times

	Time to 1% strain, $t_{1\%}$				
	β_0	β_1	β_2	β_3	γ
β_0	$2.492387\times10^{+02}$	$-3.965339\times10^{+05}$	$-4.801997\times10^{+01}$	$8.110106\times10^{+04}$	0.0
β_1	$-3.965339\times10^{+05}$	$6.315536\times10^{+08}$	$7.604371\times10^{+04}$	$-1.287563\times10^{+08}$	0.0
β_2	$-4.801997\times10^{+01}$	$7.604371\times10^{+04}$	$9.581778\times10^{+00}$	$-1.594818\times10^{+04}$	0.0
β_3	$8.110106\times10^{+04}$	$-1.287563\times10^{+08}$	$-1.594818\times10^{+04}$	$2.672820\times10^{+07}$	0.0
γ	0.0	0.0	0.0	0.0	1.137413×10^{-02}
	Time to onset of tertiary creep, t_{tertiary}				
	β_0	β_1	β_2	β_3	γ
β_0	$2.487363\times10^{+02}$	$-3.961219\times10^{+05}$	$-4.797869\times10^{+01}$	$8.102603\times10^{+04}$	0.0
β_1	$-3.961219\times10^{+05}$	$6.315536\times10^{+08}$	$7.604371\times10^{+04}$	$-1.287563\times10^{+08}$	0.0
β_2	$-4.797869\times10^{+01}$	$7.604371\times10^{+04}$	$9.581778\times10^{+00}$	$-1.594818\times10^{+04}$	0.0
β_3	$8.102603\times10^{+04}$	$-1.287563\times10^{+08}$	$-1.594818\times10^{+04}$	$2.672820\times10^{+07}$	0.0
γ	0.0	0.0	0.0	0.0	2.494689×10^{-02}
	Time to rupture, t_r				
	β_0	β_1	β_2	β_3	γ
β_0	$2.477154\times10^{+02}$	$-3.952839\times10^{+05}$	$-4.787905\times10^{+01}$	$8.085488\times10^{+04}$	0.0
β_1	$-3.952839\times10^{+05}$	$6.315536\times10^{+08}$	$7.604371\times10^{+04}$	$-1.287563\times10^{+08}$	0.0
β_2	$-4.787905\times10^{+01}$	$7.604371\times10^{+04}$	$9.581778\times10^{+00}$	$-1.594818\times10^{+04}$	0.0
β_3	$8.085488\times10^{+04}$	$-1.287563\times10^{+08}$	$-1.594818\times10^{+04}$	$2.672820\times10^{+07}$	0.0
γ	0.0	0.0	0.0	0.0	6.490728×10^{-02}

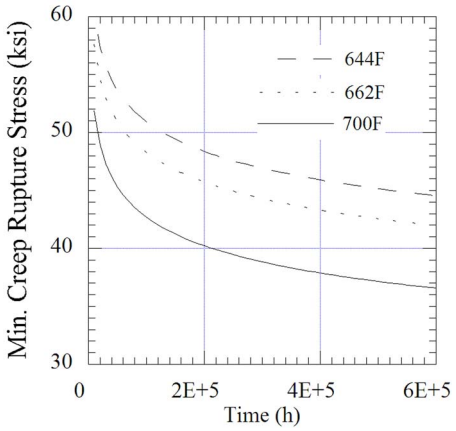

Fig. 4 Extrapolated minimum creep rupture stress for SA-533B

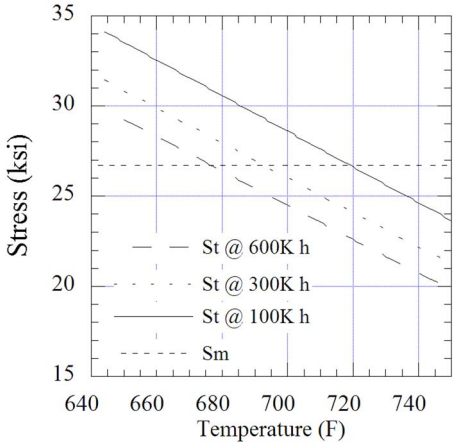

Fig. 5 Extrapolated time-dependent primary stress limits around the NB/NH temperature boundary for SA-533B

$$\{y_q\}^t = \lfloor 1, T_R^{-1}, \ell n(\sigma), T_R^{-1}\ell n(\sigma), z_q \rfloor \quad (8)$$

and $[V]$ is the covariance matrix of the parameter estimate vector $\{\mu\}$, with

$$\{\mu\}^t = \lfloor \beta_0, \beta_1, \beta_2, \beta_3, \gamma \rfloor \quad (9)$$

Covariance matrices estimated from the fitted models for the three fitted models are given in Table 3. The percentile prediction bound of $\ell n(t)$ can be estimated as

$$PB[\ell n(t)]_q = \{y_q\}^t \cdot \{\mu\} + z_q \cdot (se)_q \quad (10)$$

Since the response variable in a creep experiment is *time*, the predicted quantiles are appropriately expressed in terms of time for fixed stress and temperature (cf., Eqs. (4) and (10)). If a bound on stress is desired for fixed temperature and time, this can be obtained by algebraic rearrangement of the prediction equation for $\ell n(t)$. However, since the prediction standard error is a function of stress, this algebraic equation will in practice require numerical solution. For example, for a fixed temperature T_R, a given time t_0, and a prescribed q quantile, the corresponding stress σ can be computed from Eq. (10) numerically. Figure 4 shows the examples of extrapolated creep rupture stress curves from the regression results as a function of time at 644°F, 662°F, and 700°F.

5 Time-Dependent Primary Stress Limit

Based on extrapolations in time up to 600,000 h and in the temperature range of 644–750°F, the values of the time-dependent primary stress limit, S_t, were established, following the Subsection NH procedure, as the smaller of

- 100% of average stress required to obtain a total strain of 1%
- 80% of the minimum stress to cause initiation of tertiary creep
- 67% of the minimum stress to cause rupture

A quantile value of $q=0.05$ was used in the prediction bounds to determine the minimum stresses in the above criteria. The values of S_t as a function of temperature at 100,000 h, 300,000 h, and 600,000 h are shown in Fig. 5. Figure 6 shows the S_t values as a function of time at 644°F, 662°F, and 700°F. The criterion that controls the S_t values for the conditions considered in these figures is two-thirds of minimum rupture stress. The time-independent primary stress limit, S_m, is also shown in these two figures for comparison.

It should be noted that sizing methods in Subsections NB and NH are somewhat different. In Subsection NB, the wall thickness is sized based on the design condition while both design condition (based on 100,000 h allowables as in Section VIII) and operating conditions are used in Subsection NH. Further, the limit in Subsection NB on P_m is S_m and on P_L+P_b is $1.5S_m$, while in Subsection NH the limit on P_m is S_{mt}, on P_L+P_b is $1.5S_m$, and in addition, the limit on $P_L+(P_b/1.25)$ is S_t. Since the Subsection NH limit of S_{mt} is the lesser of S_m and S_t, the limits on the general membrane stress intensity P_m from Subsections NB and NH can be compared by considering the relative magnitudes of S_m and S_t.

The extrapolated results in Figs. 5 and 6 show that the time-independent primary stress limit S_m is lower, and, hence, conservative than the time-dependent primary stress limit S_t for times up to 600,000 h at 644°F and 662°F. At the Subsection NB cut-off temperature of 700°F, S_m is nonconservative for lifetimes beyond approximately 220,000 h.

The preceding discussion relates to effect of creep on the primary stress limit; however, the effects of creep will show up at a lower temperature at local structural discontinuities and peak thermal stress locations, where the local stress is higher than the primary membrane stresses. In Subsection NH, these peak stress locations are considered in establishing negligible creep criteria above which time and temperature the effects of creep must be considered with explicit evaluation procedures. These criteria are based on the idea that the localized peak stress will be limited by the flow strength of the material.

One of the negligible creep criteria in Subsection NH, article T-1324 is

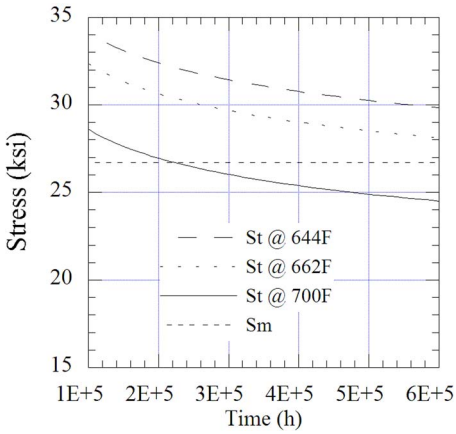

Fig. 6 Extrapolated time-dependent primary stress limits as a function of time for SA-533B

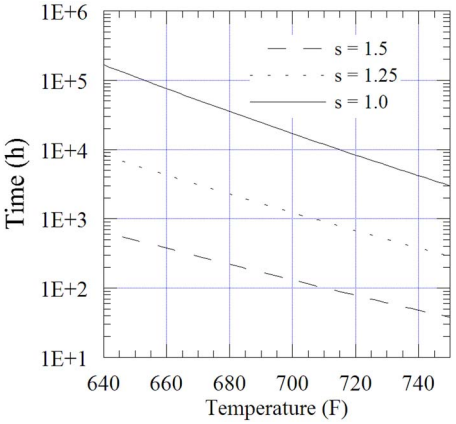

Fig. 7 Negligible creep curves for SA-533B

$$\sum_i \frac{t_i}{t_{id}} \leq 0.1 \tag{11}$$

where t_i is total duration of time during the service lifetime that the metal is at temperature T_i, and t_{id} is the rupture time given by the minimum rupture stress that is equal to $S_y|_{T_i}$, the minimum monotonic yield strength at temperature T_i, times a factor s which is equal to 1.5. The factor s is based on a factor of 1.25 to bring the minimum monotonic yield strength at temperature to the average value, and a factor of 1.2 to account for cyclic hardening of austenitic stainless steel in order to approximate the achievable stress state at geometric discontinuities. The appropriate value of s for ferritic steels such as SA-533B is not known.

The negligible creep time-temperature curves for selected values of the factor s can be obtained by using the yield strength at temperature from Table Y-1 of Section II Part D, the rupture time from Eq. (10) with $q=0.05$, and the negligible creep criterion of Eq. (11) using the equality sign. These curves are shown in Fig. 7. As can be seen from the plots in Fig. 7, the use of $s=1.5$ per article T-1324 of Subsection NH is very limiting and Code efforts to reassess the appropriate value to be used as the minimum creep rupture stress in determining the rupture time in Eq. (11) are needed. It is also noted that the factor 0.1 on the right hand side of Eq. (11) is applicable to all materials, per article T-1324 of Subsection NH. However, the negligible creep criteria are developed based on the assessment of the impact of creep damage on the fatigue performance. Since the creep-fatigue interaction as captured by the creep-fatigue interaction diagram of Subsection NH Appendix T is material specific, the factor on the right hand side of Eq. (11) should account for the differences in creep-fatigue behavior of different materials, e.g., the difference in the "knee" of the creep-fatigue interaction diagram.

6 Discussion

To put the results that were presented in Figs. 4–6 into perspective, it is good to recognize that the extrapolations are based on a small database with relatively short-term creep data as compared with the extrapolated times of 500,000–600,000 h. Thus, definitive conclusions could not be drawn based on these results. However, the results shown in these figures do underscore the need to develop longer term confirmatory creep rupture data, and to follow-up on the creep-fatigue issue to ensure that creep effects are properly accounted for in design for very long operating lives.

Creep-rupture and fatigue damage are the areas that need particular attention for SA-508 Grade 3 Class 1 and SA-533B steels and their associated weldments to assess the current temperature boundary between Subsections NB and NH. These areas requiring attention are closely related to the definition of when creep effects become significant. Simplified bounds for creep ratcheting, strain and deformation limits, and use of simplified rules to bound stress concentrations are related issues that also need to be considered. To address these issues, it is important to understand how ratcheting, strain limits, and creep-fatigue affect the integrity of a structure differently.

Creep-fatigue is a localized issue, whereas ratcheting is based, conceptually, on the interaction of the core stress and linearized through-wall stress (in the Bree model). Also, creep-fatigue is a direct failure mode whereas ratcheting is not. Cyclic life can, conceptually, be influenced directly by creep rupture damage at lower temperature whereas ratcheting would most likely be influenced by degraded tensile properties due to aging, or, potentially, cyclic softening, either from long term exposure at normal operation and/or short-term higher temperatures. Within the negligible creep regime, Subsection NH relies on $3\bar{S}_m$ where the limit is based on the relaxation strength to ensure shakedown.

Test data are needed to address creep rupture and creep-fatigue, and the issues of whether or not the material properties at normal operating temperatures are compromised by short-term higher temperature off normal conditions. Data on the relaxation strength under these conditions will also be helpful in addressing the issue. Due to a lack of operational experience in using SA-508 Grade 3 Class 1 and SA-533B pressure vessel steels at these high temperatures for very long times, confirmatory data on thermal aging, environmental effect, and neutron irradiation embrittlement are needed to also assess their impact on the Code transition temperature.

7 Summary

The SA-533B creep data that supported Code Case N-499 were analyzed using statistical models. The regression results were extrapolated to very long times, up to 600,000 h, in order to explore the effects of creep on long design lives and at metal temperatures that are below the Subsection NB limit of 700°F.

Based on the extrapolated results, it was found that RPV sizing based on Subsection NB rules might not be conservative, and one of the negligible creep criteria of Subsection NH could not be satisfied, for designs with long design lifetimes and at metal temperatures that are within the limit of Subsection NB. This suggests that design for creep-fatigue interaction might be necessary toward the later part of the operating life of the RPV. Code efforts to reassess the negligible creep criteria are recommended.

These concerns notwithstanding, it is good to recognize that these observations were based on the extrapolation of a very small database, with relatively short creep times, to conditions that are very far away from those employed in the tests. Thus, definitive conclusions could not be drawn based on these results. However, the results presented in this paper do underscore the potential problems of an artificial temperature boundary between Subsections NB and NH, particularly with future high temperature gas-cooled reactor (HTGR) components that have very long lifetimes and metal temperatures that push against this boundary. Hence Code development efforts are sorely needed in order to push the HTGR technology forward.

Acknowledgment

T.-L. Sham is grateful to Bill Corwin of the Oak Ridge National Laboratory and Richard Wright of the Idaho National Laboratory for the support of this work. This work was sponsored by a contractor of the United States Government under Contract No. DE-AC05-00OR22725 with the United States Department of Energy.

Nomenclature

A = pre-exponential factor
ℓn = natural logarithm
m = temperature-dependent stress exponent
NB = ASME Boiler and Pressure Vessel Code, Section III, Subsection NB

NH = ASME Boiler and Pressure Vessel Code, Section III, Subsection NH
P_b = primary bending stress
P_L = local membrane stress
P_m = primary membrane stress
q = quantile
Q = apparent activation energy
R = universal gas constant
s = fraction of yield strength at temperature, used in the negligible creep criterion
$(se)_q$ = standard error of a predicted quantile q
S_m = time-independent allowable primary stress
$3\bar{S}_m$ = within the negligible creep regime, Subsection NH relies on this limit, which is based on the relaxation strength to ensure shakedown
S_{mt} = operating condition allowable primary stress
S_t = time-dependent allowable primary stress
$S_y|_{T_i}$ = yield strength at temperature T_i
T = temperature (°F)
T_i = temperature for the ith sustained load period
T_R = absolute temperature (R)
t = time
t_0 = given time
$t_{1\%}$ = time to 1% total strain
t_i = service time for the ith sustained load period
t_{id} = calculated rupture time for the ith sustained load period
t_r = time to rupture
t_{tertiary} = time to onset of tertiary creep
z_q = q quantile of the standard normal distribution
-2LL = negative two log-likelihood
β_0 = regression parameter
β_1 = regression parameter
β_2 = regression parameter
β_3 = regression parameter
γ = residual standard deviation estimate
σ = stress (ksi)
$[V]$ = covariance matrix of the parameter estimate vector
$\{x\}$ = vector of independent variables
$\{x\}^t$ = transpose of vector $\{x\}$
$\{y_q\}$ = vector containing the independent variables and z_q
$\{y_q\}^t$ = transpose of vector $\{y_q\}$
$\{\beta\}$ = regression parameter vector
$\{\beta\}^t$ = transpose of vector $\{\beta\}$
$\{\mu\}$ = parameter estimate vector
$\{\mu\}^t$ = transpose of vector $\{\mu\}$

References

[1] McCoy, H.E., 1990, data ackage submittal to ASME B&PVC SG-ETC, SC II SG-SFA, and SG-ETD, Apr. 17.
[2] McCoy, H. E., 1989, "Tensile and Creep Properties of SA533 Grade B Class 1 Steel," ORNL, Oak Ridge, TN, Dec., Report No. ORNL/TM-11338.
[3] Eno, D.R., Young, G.A., and Sham, T.-L., 2008, "A Unified View of Engineering Creep Parameters," Paper No. ASME PVP2008-61129.

Mining Process and Product Information From Pressure Fluctuations Within a Fuel Particle Coater

Douglas W. Marshall
e-mail: douglas.marshall@inl.gov

Charles M. Barnes
e-mail: charles.barnes@inl.gov

Department of Fuel Fabrication,
Battelle Energy Alliance, LLC,
Idaho National Laboratory,
U. S. Department of Energy,
P.O. Box 1625,
Idaho Falls, ID 83415-3855

The next generation nuclear power/advanced gas reactor (NGNP/AGR) fuel development and qualification program included the design, installation, and testing of a 6-in. diameter nuclear fuel particle coater to demonstrate quality tri-structural isotropic (TRISO) fuel production on a small industrial scale. Scale-up from the laboratory-scale coater faced challenges associated with an increase in the kernel charge mass, kernel diameter, and a redesign of the gas distributor to achieve adequate fluidization throughout the deposition of the four TRISO coating layers. TRISO coatings are applied at very high temperatures in atmospheres of dense particulate clouds, corrosive gases, and hydrogen concentrations over 45% by volume. The severe environment, stringent product and process requirements, and the fragility of partially-formed coatings limit the insertion of probes or instruments into the coater vessel during operation. Pressure instrumentation were installed on the gas inlet line and exhaust line of the 6-in. coater to monitor the bed differential pressure and internal pressure fluctuations emanating from the fuel bed as a result of bed and gas "bubble" movements. These instruments are external to the particle bed and provide a glimpse into the dynamics of fuel particle bed during the coating process and data that could be used to help ascertain the adequacy of fluidization and, potentially, the dominant fluidization regimes. Pressure fluctuation and differential pressure data are not presently useful as process control instruments, but data suggest a link between the pressure signal structure and some measurable product attributes that could be exploited to get an early estimate of the attribute values. [DOI: 10.1115/1.3126772]

Keywords: pressure fluctuations, Hurst exponent, spouted bed, particle properties

1 Introduction

The second phase of the NGNP/AGR fuel development and qualification program included the design, installation, and testing of a 6-in. diameter nuclear fuel particle coater at a Babcock & Wilcox Nuclear Operations Group facility in Lynchburg, VA, to demonstrate TRISO fuel production on an industrial scale. Scale-up faced the challenges associated with a 20-fold increase in the kernel charge to the coater (relative to the 2-in. laboratory-scale coater used in process development), a 21% increase in the kernel diameter (350–425 μm kernel), and the redesign of a gas distributor to achieve adequate fluidization throughout the deposition of the four TRISO coating layers shown in Fig. 1.

TRISO coatings are applied in a graphite vessel at temperatures well in excess of service temperatures for many materials and instruments (1300–1500°C) and with gas environments that include dense particulate clouds, corrosive gases, and hydrogen concentrations over 45% by volume (Table 1). The severe coating temperatures exceed the service temperature of many metals and materials commonly used for probes. Stringent chemical purity requirements for the coated particles further limit the choice materials because contamination from probe abrasion can compromise in-pile particle performance by leading to an increased probability of coating failures [1].

Additionally, the need to assure isolation of the hydrogen atmosphere from oxygen sources and control of radioactive and fissile materials preclude the insertion of many kinds of probes and instruments into the coater vessel during operation. Furthermore, the presence of probes in the bed could result in damage to delicate TRISO coating layers as they are forming on the particles, resulting in an increased product reject fraction and increased probability of coating failures during fuel irradiation.

The coatings are applied by thermally decomposing reactant gases to form either a carbon or silicon carbide layer on the particles. The gases must be kept relatively cool as they pass through the distributor nozzle to prevent premature decomposition and excessive distributor fouling. This is achieved by using unheated coating gases and diverting some of the diluent gas (argon or hydrogen) around the nozzle exterior to affect some cooling of the nozzle flange in contact with the coating vessel.

The gases heat up rapidly as they pass through the distributor nozzle and enter the bed, resulting in nearly explosive expansion of the gases. The thermal expansion is augmented by an increase in the total moles of gas, due to decomposition of the coating gases, for all coatings but the buffer deposition.

Correlations developed and used in industry to calculate minimum gas velocities to fluidize or spout a particle bed do not necessarily apply to the high temperature coating process with the rapid gas expansion at the inlet. The uncertainty regarding the adequacy of the gas flows to properly spout the fuel particles in the coater vessel led to an effort to monitor the pressure fluctuations that have been observed at the gas inlet.

2 Method

A compact Kobold high-precision pressure transducer (0–10 psig range) was installed on the gas inlet line to the 6-in. coater to monitor pressure fluctuations emanating from the fuel bed as a

Manuscript received November 14, 2008; final manuscript received November 25, 2008; published online October 2, 2009. Review conducted by Dilip R. Ballal. Paper presented at the Fourth International Topical Meeting on High Temperature Reactor Technology (HTR2008), Washington, DC, September 28–October 1, 2008.

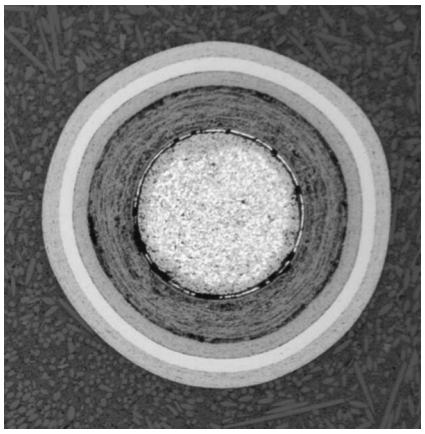

Fig. 1 Cross section of a TRISO-coated nuclear fuel particle showing coating layers

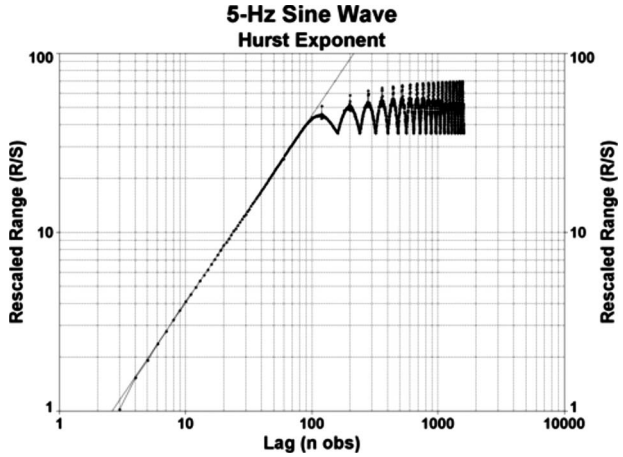

Fig. 2 Pox diagram of a 5-Hz sine wave sampled at 400 Hz

result of bed and gas bubble movements. The length of the pressure line was kept as short as reasonably possible to keep signal attenuation and smoothing minimal. The instrument tubing was purged with a slow flow of argon ($\sim$100 cc/min) to keep the line clear and free of hydrogen and coating gases. A differential pressure transmitter was also installed between the gas inlet and the coater exhaust to monitor changes in the differential pressure across the gas distributor and bed. The high-pressure line is in common with the high-precision transducer while the low-pressure line is dedicated to the transmitter.

These instruments were added to provide a glimpse into the dynamics of coater bed during the coating process, to provide data that could be used to help ascertain the adequacy of fluidization, and to help identify the dominant fluidization regimes.

Pressure data were manually collected, using LABVIEW 8.2 software, at prescribed intervals during the deposition of each coating layer; specifically, 1 min into the deposition, at the midpoint, and 1 min prior to ending each coating layer deposition. Changes in the pressure signal structure can be observed as a result of changes in the particle properties (average density, diameter, aspect ratio, etc.). Data were collected for 6–8 s intervals at 400 Hz and subsequently filtered. The high-precision pressure fluctuation signal was band-pass filtered between 0.25 Hz and 150 Hz to preclude aliasing and to center the data at an average of zero to facilitate comparisons of one signal to another. Differential pressure data were low-pass filtered at 3 Hz to smooth fluctuations and to provide the mean differential pressure across the gas distributor and the particle bed. Raw (unfiltered) pressure data were used to determine total system back pressure, as measured from the gas inlet.

Filtered pressure data were analyzed using power spectral densities (PSDs), short-term Fourier transforms (STFTs), and calculating Hurst exponents (rescaled range analysis). Peak amplitude and frequency data were extracted from the PSDs, and the regressed slopes (Hurst exponents) and standard deviations were extracted from ranges on the Pox plots [2].

The Hurst exponents are estimated by the slopes of the line on a rescaled range plot (Pox diagram), as shown in Fig. 2, computed for given ranges along the abscissa (Table 2). Slopes having values near 1.0 indicate a persistent trend in the sample data (i.e., successive data points predict the trend of subsequent points), slopes near 0.5 indicate a randomness to the data, and slopes near 0.0 indicate an antipersistent trend. The periodic nature of the pressure fluctuations is manifested, in this case, by the undulating segment of the rescaled range plot beyond a lag of 70 observations.

The selected ranges in Table 2 were chosen from natural breaks in the average slope observed over several Pox diagrams obtained during the particle coating tests. The break points fit well with most of the layers, which exhibit changes in slope, but are less than ideal for the buffer layer that would be better described by a narrower range for the H_{1b} exponent. For this study, the ranges on the Pox diagram for the Hurst exponent estimates were not customized for each respective layer.

The Hurst exponents for a 5-Hz sine wave, estimated from the slopes of the curve on the Pox diagram in Fig. 2, are given below and clearly show persistency for low lag values and antipersistency for higher lag values.

$$H_{1a}: \quad 1.0536 \pm 0.0058 (3 \leq n \ \text{obs} \leq 20)$$

$$H_{1b}: \quad 1.0539 \pm 0.0027 (20 \leq n \ \text{obs} \leq 70)$$

$$H_{2}: \quad 0.1174 \pm 0.0143 (120 \leq n \ \text{obs} \leq 600)$$

$$H_{3}: \quad 0.0689 \pm 0.0209 (600 \leq n \ \text{obs} \leq 1600)$$

3 Discussion and Results

Many methods commonly used to estimate the minimum fluidizing velocity for a bed of particles incorporate the Archimedes number (Eq. (1)) into the calculation of the particle Reynolds

Table 1 Approximate coating process conditions

Coating	Inlet gases	Exhaust gases	T_{coating} (°C)
Buffer	60% C_2H_2	60% H_2	1430
	40% Ar	40% Ar	
Pyrocarbon	70% Ar	55% Ar	1285
	16.2% C_2H_2	45% H_2	
	13.8% C_3H_6		
Silicon Carbide	98.5% H_2	95.6% H_2	1475
	1.5% CH_3SiCl_3	4.4% HCl	

Table 2 Ranges from which Hurst exponents were estimated

Hurst exponent	Lag range along abscissa
$H_{1a} \pm \sigma_{1a}$	$3 \leq n$ obs ≤ 20
$H_{1b} \pm \sigma_{1b}$	$20 \leq n$ obs ≤ 70
$H_2 \pm \sigma_2$	$120 \leq n$ obs ≤ 600
$H_3 \pm \sigma_3$	$600 \leq n$ obs ≤ 1600

Table 3 Particle and layer properties

	Layer thickness Θ_L (μm)	Layer density ρ_L (g/cc)	Particle diameter d_p (μm)	Particle density ρ_p (g/cc)	Volume ratio V/V_K
Kernel	—	—	429	10.71	1.00
Buffer	100	1.05	629	4.11	3.15
IPyC	40	1.89	709	3.44	4.51
SiC	35	3.20	779	3.38	5.99
OPyC	40	1.89	859	3.00	8.03

number at incipient fluidization [3–5]. Similarly, correlations for estimating the minimum spouting velocity of a spouted particle bed are proportional to the particle diameter and particle density as shown in Eq. (2) [6].

$$\mathrm{Ar} = \frac{d_p^3 \rho_g (\rho_p - \rho_g) g}{\mu^2} \tag{1}$$

$$U_{\mathrm{ms}} = f(d_p, \rho_p, \rho_g, D_c, D_{\mathrm{or}}, H_{\mathrm{bed}}) \tag{2}$$

The first two attributes listed in Eq. (2) are the mean particle diameter and absolute particle density. The other attributes are the mean gas density, column diameter, gas inlet orifice diameter, and bed height. It is clear that particle attributes have significant impacts on particle fluidization. Other parameters that have been identified as contributors when scaling a spouted bed include the particle sphericity and material properties such as the angle of internal friction [7] and the coefficient of restitution [8]. It is reasonable to assume that pressure fluctuations emanating from the bed as a result of bed and bubble movement would be influenced by particle properties. If so, then one could hypothesize that the structure of the pressure fluctuation signal may reveal information about the collective particle attributes.

Table 3 gives the coating layer and particle properties, assuming a spherical particle, along with target coating layer thicknesses and representative layer densities. The table also shows the volume expansion relative to the initial charge of kernels. Actual layer and average particle properties will vary depending on particle sphericity and mean coating layer thickness and density.

3.1 Buffer Layer. Deposition of the 100 μm carbon buffer layer on the fuel kernels results in a 60% decrease in particle density and more than a 300% increase in particle/bed volume. The initial static bed depth of the bare kernels in the coater is estimated to be 3.9 cm, which is too shallow to form a well-developed spout or particle bed circulation pattern until most of the buffer has been applied. Evidence of a shift in bed fluidization during buffer deposition is seen in the PSD and short-term Fourier transform (STFT) plots, shown in Figs. 3 and 4(*a*)–4(*c*).

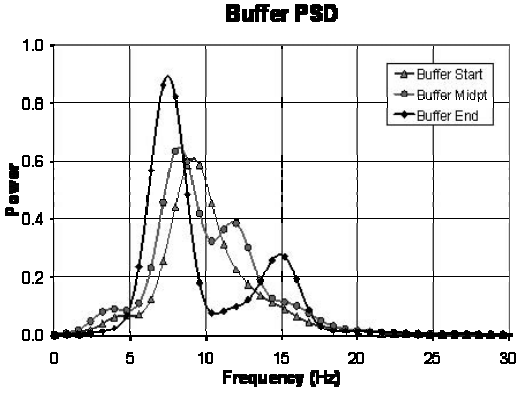

Fig. 3 Representative PSD of the buffer deposition

The starting PSD plot shows a relatively broad, monomodal power distribution, and the STFT for the same sample period shows a weak structure over time. The midpoint sample exhibits a bimodal PSD and a disordered STFT structure. It is interesting to note that the buffer sample taken at the end of the deposition period exhibits a bimodal distribution for the PSD and a strongly structured STFT, as evidenced by the columnar contour plot. The presence of a bimodal distribution on the PSD and strong structure on the STFT plot is considered to be indicative of a desirable fluidization regime for the coater used to generate this data.

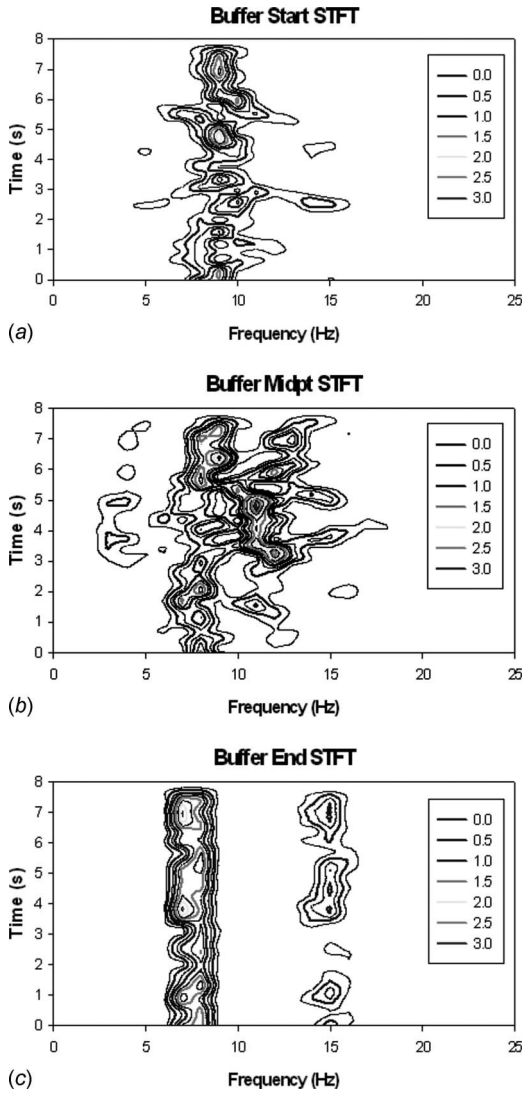

Fig. 4 Representative STFT plot (*a*) at the start of buffer deposition, (*b*) at the midpoint of buffer deposition, and (*c*) at the end of buffer deposition

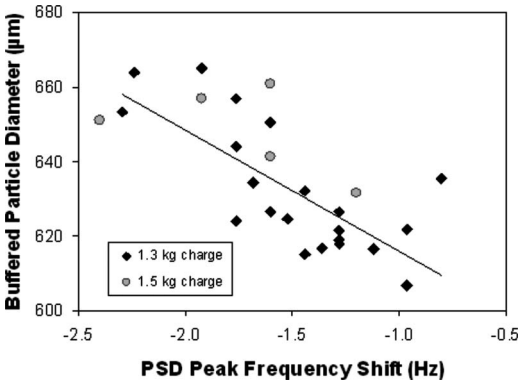

Fig. 5 Plot of the buffered particle diameter versus a shift in the PSD peak-power frequencies ($\omega_{1,end}$-$\omega_{1,start}$)

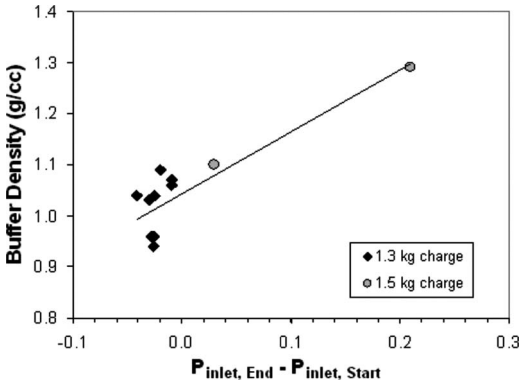

Fig. 7 Plot of buffer density correlated with the change in coater gas inlet backpressure

The change in the average particle properties and bed mass produces a progressive shift in the PSD peak power to lower frequencies. Plots of the buffered particle diameter versus the change in peak-power frequency and the ratio of the ending and starting frequencies are given in Figs. 5 and 6. The buffered particle diameters were calculated based on automated optical measurements of mounted and sectioned particles. These figures confirm that the shift in peak-power frequencies is influenced by the particle properties. The use of the frequency difference or the frequency ratio is insensitive to the initial kernel charge masses of 1.3 kg or 1.5 kg.

However, the poorly structured fluidization at the start of the buffer deposition and variability in the timing of manual pressure fluctuation data collection have introduced sufficient uncertainty in the peak-power frequency determinations to preclude a precise estimation of the buffered particle diameter or the thickness of the buffer layer.

Buffer density determinations require that particle samples be drawn from the coater vessel after the buffer deposition and prior to subsequent coatings. Consequently, only limited data are available. When samples are available for buffer density determinations, the procedure uses pressured mercury to obtain the "envelope" density of the coated kernel and the buffer density is calculated by extracting the kernel contributions to the mass and diameter. Variability in the kernel diameter and the delicate nature of the buffer (easily crushed) result in substantial uncertainty and scatter in the buffer density determinations.

Figure 7 shows a possible relationship between the density of the buffer coating and the change in the average backpressure detected at the gas inlet (including the sum of the gas distributor, bed, and soot filter differential pressures). Buffer density data are sparse because of limited capacity to obtain "hot" buffer samples. The density analysis is imprecise because buffer density is inferred from analysis of the buffer-coated particles via a mercury pycnometry technique. Taken collectively, the data seem to show a trend correlating pressure buildup in the coater with density of the buffer coating, but taken separately by charge mass, the data appear to be less convincing.

Figure 8 shows a possible relationship between the calculated buffer-coated particle density and the ratio of the dominant peak frequencies from the PSD plots ($\omega_{end}/\omega_{start}$). As previously observed with the buffered particle diameters, the particle densities appear to correlate well with the ratios of ending to starting characteristic frequencies and to be independent of the charge mass within the range of charge masses tested in this study.

The apparent precision in the buffer density estimations shown in Figs. 7 and 8 may be artifacts of limited data. As more data become available, more extensive data scatter will likely be manifested in the plots.

3.2 Inner Pyrocarbon Layer. Early coating process development efforts focused on the use of spherical zirconia beads as a surrogate kernel to avoid the expense of forming natural uranium oxide–uranium carbide spheres (a.k.a. natural uranium oxycarbide (NUCO)).

The density of yttria-stabilized zirconia is approximately 6.0 g/cc and the density of NUCO kernels is near 10.9 g/cc. However, a buffer-coated NUCO particle has a density near 4.2 g/cc, which makes it possible to select a zirconia kernel with a mean diameter and density similar to that of a NUCO kernel with about half of the buffer layer applied. All of the recognized scaling relations were closely matched [7,8], which are thought to provide hydrodynamic similitude.

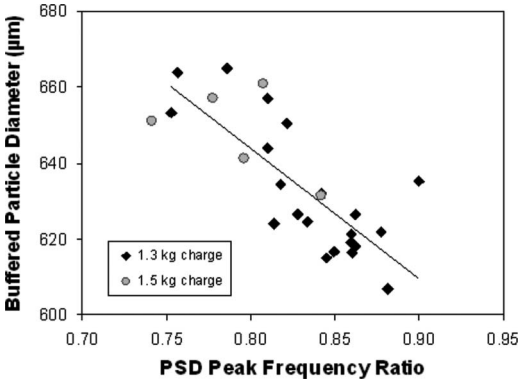

Fig. 6 Plot of the buffered particle diameter versus the ratio of PSD peak-power frequencies ($\omega_{1,end}/\omega_{1,start}$)

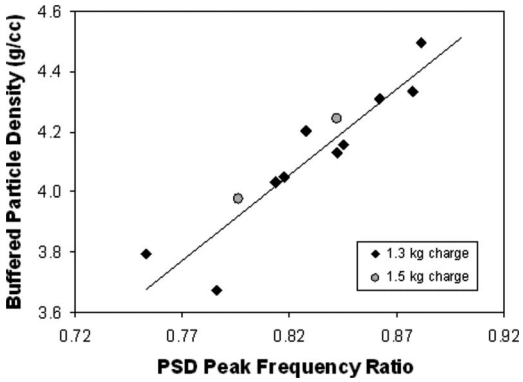

Fig. 8 Plot of buffer density versus the ratio of PSD peak-power frequencies ($\omega_{1,end}/\omega_{1,start}$)

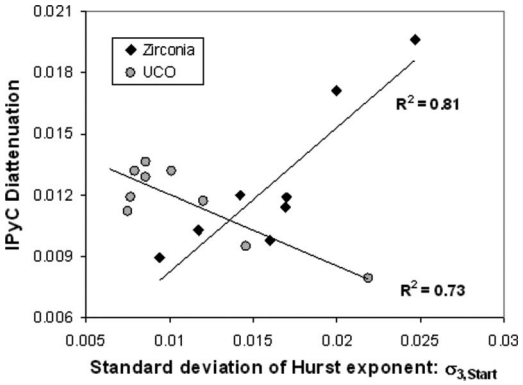

Fig. 9 Example of apparent disagreement in relationships

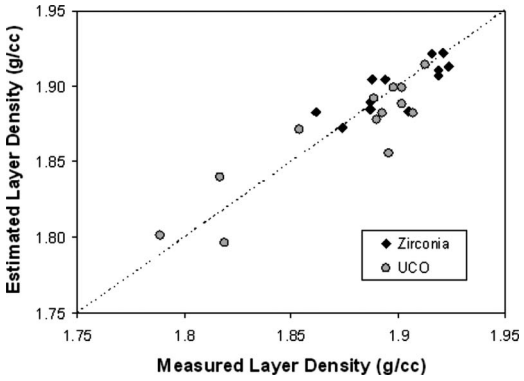

Fig. 11 Estimated versus measured IPyC density

In spite of this effort to achieve similitude with the coated particles, differences in the thermal diffusivities and/or rotational inertia of the partially-coated particles may have led to differences in the apparent relationships between the structure of the pressure fluctuations and particle properties. An example of this phenomenon is the linear regression of the inner pyrocarbon (IPyC) diattenuation and the standard deviation of the Hurst exponent estimated with a lag of $600 \leq n$ obs ≤ 1600 (Fig. 9). The regression fit factor (R^2) is similar for the coated surrogate and NUCO-coated particles, but the slopes of the regressions have opposite signs.

An effort has been made to use relationships that are consistent in the slope magnitude and sign throughout the study. Many promising relationships have been discounted because of inconsistencies between correlations for the surrogate and the NUCO particles. It is not known whether the differences arise because the thermal properties of the kernels influencing the rate of heat exchange with the incoming coating gases, whether the differences in particle rotational inertia and particle angular velocities influence particle-particle interactions, or if the apparent relationships are falsely indicated.

Contrary to expectations, no consistent relationships were discovered for estimating the diameter and density for the IPyC-coated particles or the IPyC thickness.

There are apparent correlations with coating attributes that are less intuitive, but may be impacted by the same gas and particle properties that affect the fluidization. One of these is the anisotropy (diattenuation) of the pyrocarbon layers (Fig. 10).

Anisotropy is a measure of the degree of persistent structure or order in the pyrolytic carbon crystallites and is used as a predictor of coating layer performance during irradiation. A proven correlation between the pyrocarbon anisotropy and pressure signals could be used to screen product, thereby reducing the sampling frequency and possibly signaling unexpected process changes in the pyrocarbon deposition; thereby avoiding subsequent production runs yielding product that does not meet specifications.

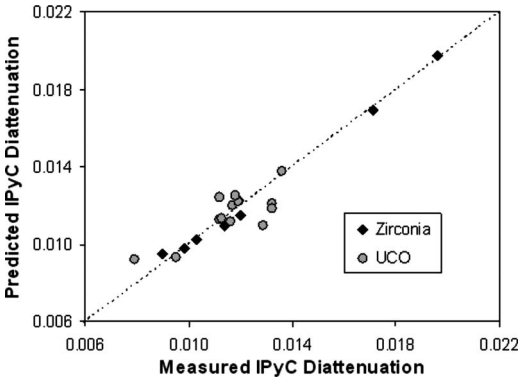

Fig. 10 Estimated versus measured IPyC diattenuation

The IPyC anisotropy in Fig. 10 was estimated via a quadravariate linear regression of the Hurst exponents and the change in coater inlet backpressure (Eq. (3)). The particles with a zirconia kernel were regressed independently from those with a NUCO kernel. Although the coefficients may differ in value, their signs are consistent for each of the terms.

$$N_{\mathrm{IPyC}} = N_o + a \cdot H_{1a,\mathrm{Mid}} + b \cdot \sigma_{3,\mathrm{Mid}} + c \cdot H_{2,\mathrm{End}} + d \cdot (P_{\mathrm{inlet,End}} - P_{\mathrm{inlet,Start}}) \quad (3)$$

It is expected that the amount of data scatter in Fig. 10 will increase as more data become available and are included in the regression.

The IPyC layer density (Fig. 11) was fitted to a parabolic equation of a Hurst exponent midway through the coating deposition ($H_{1a,\mathrm{Mid}}$) and the extreme spread of pressures sampled at the end of the IPyC deposition (Eq. (4)). Some uncertainty is introduced by run-to-run variability in the average particle diameters and densities of the underlying buffer-coated particle and the final IPyC-coated particle, which diminishes the precision of the pyrocarbon density estimate.

$$\rho_{\mathrm{IPyC}} = \rho_o + a \cdot P_{\mathrm{ES,End}} + b \cdot P^2_{\mathrm{ES,End}} + c \cdot H_{1a,\mathrm{Mid}} + d \cdot H_{1a,\mathrm{Mid}} \quad (4)$$

The mass of the bed following IPyC deposition can be calculated from measured and assumed densities, diameters, and thicknesses for the kernel, buffer, and IPyC layers. The uncertainties in the measured and calculated properties reduce the precision of the bed mass estimation. The estimated bed mass seems to correlate with the extreme spread of the pressure fluctuations at the coating midpoint, the standard deviation of the midpoint pressure fluctuations, the amplitude of the minor peak in the power spectral density, and the frequency of the major peak on the PSD at the end of the coating (Eq. (5)). The segregation of data by the initial charge mass is evident in Fig. 12 as evidenced by the clustering of the data around different estimated bed masses. No other physical properties of the IPyC-coated particle seem to correlate well and consistently, between the kernel types, with the pressure fluctuation signals.

$$M_{\mathrm{bed}} = a \cdot P_{\mathrm{ES,Mid}} + b \cdot \sigma_{\mathrm{fluct,Mid}} + c \cdot A_{2,\mathrm{Mid}} + d \cdot \omega_{1,\mathrm{End}} \quad (5)$$

3.3 Silicon Carbide Layer. An important attribute that is measured on the silicon carbide (SiC) coating layer is the aspect ratio, which is an indicator of particle sphericity. This ratio is computed from the radial maxima and minima of a particle cross section measured from the geometric center of the particle. A high aspect ratio (>1.06) leads to excessive stress accumulation in the SiC layer and could lead to in-pile SiC failures and fission product

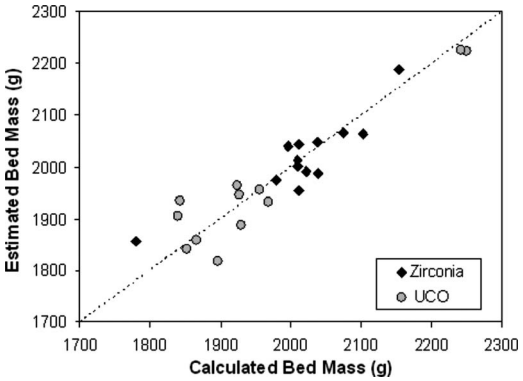

Fig. 12 Estimated versus calculated bed mass after IPyC deposition

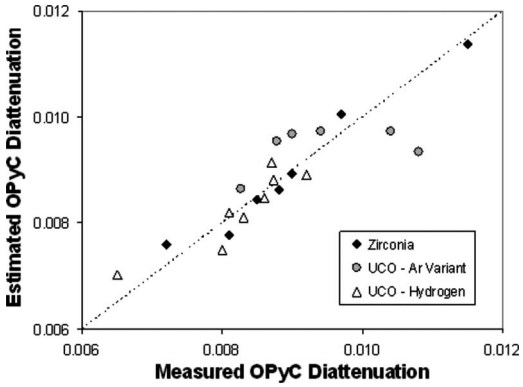

Fig. 14 Estimated versus measured OPyC diattenuation

releases from the particle. No data are available for the SiC aspect ratio of the coated zirconia surrogate particles, so the pressure data correlated with the aspect ratio for coated NUCO particles cannot be refereed for consistency. Nonetheless, the data presented in Fig. 13 hold promises for future estimation of the SiC aspect ratio when correlated with the standard deviations and extreme spread of the pressure fluctuations and the frequency of the dominant peak on the PSD (Eq. (6)). The estimation of SiC aspect ratio is not independent of whether the fluidizing gas is hydrogen or a hydrogen-argon blend in spite of deliberate efforts to achieve similar fluidization by adjusting the total gas flow to the coating reactor. It is thought that the presence of argon in the fluidizing gas, the somewhat lower deposition temperatures, and the lower superficial gas velocities may influence the nature of SiC fouling on the coater wall and therefore change the particle-wall interaction. Furthermore, the accretions that collect on the gas injection nozzle restrict the gas ports during the argon variant runs than otherwise. This influences the orifice gas velocity and the total backpressure, which is reflected in changes to some regressed coefficients. Consequently, the coefficients for the equation were regressed separately for the two cases.

$$\mathrm{AR}_{\mathrm{SiC}} = 1 + a \cdot \sigma_{\mathrm{fluct,Mid}} + b \cdot P_{\mathrm{ES,End}} + c \cdot \sigma_{\mathrm{fluct,End}} + d \cdot \omega_{1,\mathrm{Mid}} \tag{6}$$

Although correlations were found for additional particle properties (e.g., particle density, particle diameter, bed mass, etc.), none were consistent between the coated zirconia surrogate and NUCO kernels; differing in the signs of the regressed coefficients and statistical fit.

3.4 Outer Pyrocarbon Layer. Many of the outer pyrocarbon (OPyC) particle properties are calculated based on measured values for the previous layer thicknesses and densities. Errors propagated from one layer to subsequent layers make it difficult to reliably quantify relationships between pressure signals and particle properties. The anisotropy, or rather the diattenuation of the OPyC layer is not dependent on measured substrate values. The variables that correlate well with the OPyC diattenuation are the final coater inlet differential pressure and the standard deviation of fourth Hurst exponent at the start of the OPyC deposition, and change in gas inlet back pressure over the course of the deposition (Eq. (7) and Fig. 14).

$$N_{\mathrm{OPyC}} = N_0 + a \cdot DP_{\mathrm{inlet,Start}} + b \cdot \sigma_{3,\mathrm{Start}} + c \cdot (P_{\mathrm{inlet,End}} - P_{\mathrm{inlet,Start}}) \tag{7}$$

The regression for the OPyC diattenuation of coated NUCO particles appears to have a very good fit. This is partially due to the limited data. As additional data become available, the scatter in the plot in Fig. 14 is expected to increase.

Considerable data do exist for the OPyC layer density, which have been correlated with the standard deviations of three Hurst exponents; two at the start of the coating and one at the end (Eq. (8) and Fig. 15). The OPyC layer density can be measured by the sink-float method after the layer is broken off of several coated particles. With the accessibility of the OPyC layer for analysis, the need to estimate the density has less impact on the program than would the ability to estimate IPyC properties. Because the density can be measured directly, the estimation of the density is not dependent on the substrate or subject to a propagation of errors.

$$\rho_{\mathrm{OPyC}} = \rho_o + a \cdot \sigma_{2,\mathrm{Start}} + b \cdot \sigma_{3,\mathrm{Start}} + c \cdot \sigma_{3,\mathrm{End}} \tag{8}$$

Finally, the aspect ratio of the fully-coated TRISO fuel particle can be estimated based on the standard deviations of Hurst exponents quantified for each of the three sample sets taken during the deposition of the OPyC (Eq. (9) and Fig. 16). The data show that the amplitude of the pressure fluctuations during OPyC deposi-

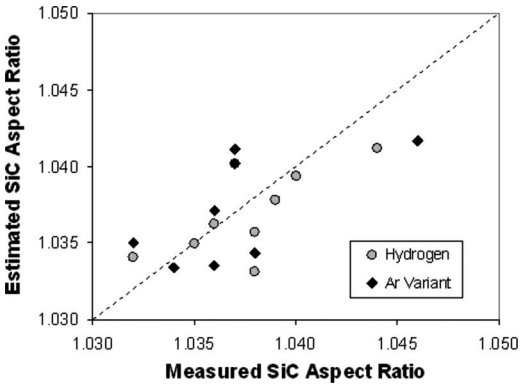

Fig. 13 Estimated versus measured SiC aspect ratio

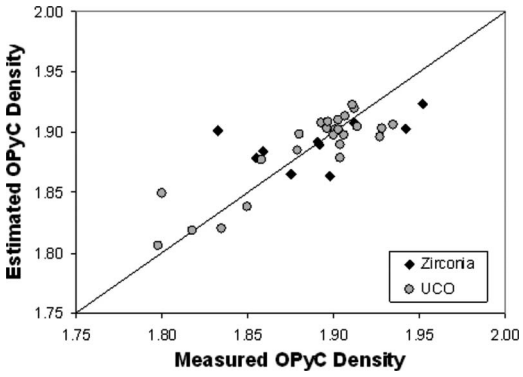

Fig. 15 Estimated versus measured OPyC layer density

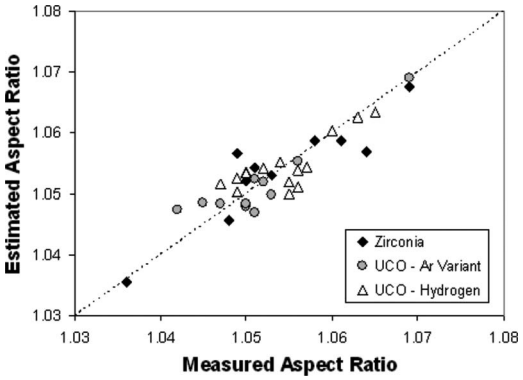

Fig. 16 Estimated versus measured OPyC aspect ratio

tion, following the deposition of SiC in an argon-hydrogen atmosphere, is less than the amplitude following the deposition of SiC in hydrogen alone. Consequently, the correlations for the aspect ratio were computed for each case. The coating runs using the zirconia surrogate did not include any SiC depositions in an argon-hydrogen atmosphere, but the data were regressed independently from the data from the NUCO runs because plots of the data for the coated zirconia surrogates and the NUCO appear to be in different populations. The signs of some coefficients differ between the zirconia and NUCO runs in this case.

$$AR_{\mathrm{OPyC}} = AR_o + a \cdot \sigma_{3,\mathrm{Start}} + b \cdot \sigma_{1a,\mathrm{End}} + c \cdot \sigma_{1b,\mathrm{End}} + d \cdot \sigma_{3,\mathrm{End}} \tag{9}$$

One would anticipate that the correlations between similar properties of the IPyC and OPyC coatings would be similar, if not identical sets. For instance, the PSD frequencies, amplitudes, and the Hurst exponents used to estimate the IPyC anisotropy ought to be the same set used for the OPyC anisotropies. The same expectation holds for other particle properties. This is not yet the case. It is expected that some insight will be obtained as this analysis is broadened to include Lyapunov exponents, Kologorov entropies, etc., and insights from work being conducted around the world to exploit pressure fluctuation signals in the study of particle bed behavior in fluidized beds.

4 Conclusions

Pressure fluctuations resulting from the movement of gas through a fluidized particle bed contain some information regarding the particle properties. A variety of techniques have been used to reduce the data to sets that can be correlated with specific properties of either the particle or the coating layers. The prospect of using pressure fluctuation signals to estimate properties is attractive because estimated values could be available several days before analytical measurements can be completed and reliable correlations could reduce the quantity of samples that would need to be analyzed and reduction of off-specification runs resulting from instrument/controller drift or failures.

Caution is warranted in exploiting this method because of the following.

1. Hurst exponents and their standard deviations have not been mapped to specific physical movements in the bed and the selected ranges were somewhat arbitrary.
2. The connection between pulse frequencies, PSD peaks, and Hurst exponents are described only empirically. A theoretical basis needs to be developed.
3. Due to the highly empirical nature of this study, the results may not be readily exported to systems having different particle or gas properties or a different vessel configuration.

Acknowledgment

Pressure fluctuation data were collected by Babcock & Wilcox Nuclear Operations Division in Lynchburg, VA, during the course of coating tests. This manuscript has been authored by Battelle Energy Alliance, LLC, under Contract No. DE-AC07-05ID14517 with the U.S. Department of Energy.

Nomenclature

A_1, A_2 = amplitudes of the first and second peaks on the power spectral density plots
Ar = Archimedes number
AR_X = radial aspect ratio (max:min) of the particle after coating x
D_c = diameter of the coater cylinder
D_{or} = gas orifice diameter
DP_X = differential pressure from gas inlet to exhaust during coating x
d_p = mean particle diameter
g = gravitational constant
H_n = Hurst exponent n
H_{bed} = height of the particle bed
M_{bed} = estimated/calculated bed mass
N_{IPyC}, N_{OPyC} = diattenuation of the pyrocarbon layer
P = gas inlet backpressure
P_{ES} = extreme spread of the pressure fluctuations during the 6–8 s sampling
U_{ms} = minimum gas velocity required to spout a particle bed
V, V_K = particle bed volume (K=bare kernels)
μ = fluidizing gas viscosity
Θ_L = layer thickness
ρ_g, ρ_L, ρ_p = density of the fluidizing gas, layer, or particle
σ_{fluct}, σ_n = standard deviation of the pressure fluctuations or the Hurst exponent (H_n)
ω_1, ω_2 = frequencies of the first and second peaks on the power spectral density plot

References

[1] Lessing, P. A., and Heaps, R. J., 1994, "Strength of Silicon Carbide Layers of Fuel Particles for High-Temperature Gas-Cooled Reactors," Nucl. Technol., **108**, pp. 207–234.
[2] Xu, J., Bao, X., Wei, W., Shen, S., Bi, H. T., Grace, J. R., and Lim, C. J., 2004, "Characterization of Gas Spouted Beds Using the Rescaled Range Analysis," Can. J. Chem. Eng., **82**, pp. 37–47.
[3] Geldart, D., 1986, *Gas Fluidization Technology*, John Wiley and Sons, New York.
[4] Davidson, J. F., Clift, R., and Harrison, D., 1985, *Fluidization*, 2nd ed., Academic, London.
[5] Kunii, D., and Levenspiel, O., 1991, *Fluidization Engineering*, 2nd ed., Butterworth-Heinemann, Newton, MA.
[6] Mathur, K. B., and Epstein, N., 1974, *Spouted Beds*, Academic, New York.
[7] He, Y.-L., C. J. Lim, and J. R. Grace, 1997, "Scale-Up Studies of Spouted Beds," Chem. Eng. Sci., **52**(2), pp. 329–339.
[8] Xu, J., Ji, Y., Wei, W., Bao, X., and Du, W., 2007, "Scaling Relationships of Gas-Solid Spouted Beds," ECI Conference, 12th International Conference on Fluidization, Paper No. 65.

Development of Local Heat Transfer Models for Safety Assessment of High Temperature Gas-Cooled Reactor Cores—Part I: Pebble Bed Reactors

Richard Stainsby
Matthew Worsley
Andrew Grief
Frances Dawson
Mike Davies
Paul Coddington
Jo Baker

AMEC Nuclear,
Knutsford, Cheshire WA16 8QZ, UK

Ana Dennier
AMEC NSS,
Toronto, ON, M591X6 Canada

This and the subsequent paper present models developed for determining fuel particle and fuel element temperatures in normal operation and transient conditions in high temperature reactor cores. Multiscale modeling concepts are used to develop the models for both pebble bed and prismatic core types. This paper, Part I, presents the development of the model for pebble bed reactors. Comparison is made with finite element simulations of an idealized "two-dimensional" pebble in transient conditions, and with a steady-state analytical solution in a spherical pebble geometry. A method is presented for determining the fuel temperatures in the individual batches of a multibatch recycle refuelling regime. Implementation of the multiscale and multibatch fuel models in a whole-core computational fluid dynamics model is discussed together with the future intentions of the research program. [DOI: 10.1115/1.3126775]

1 Introduction

The United States Nuclear Regulatory Commission (NRC) identified several research tasks under the thermal fluids and accident analysis technical areas for advanced reactors, to gain an understanding of advanced models that may be used in the United States licensing review of these designs. The first of these tasks was to perform a phenomena identification and ranking (PIRT) exercise for generic high-temperature gas-cooled reactor (HTGR) designs, such as those proposed to be candidates for the next generation nuclear plant (NGNP). This PIRT exercise identified the phenomena, quantified their importance, and reviewed the current state of knowledge associated with the heat transfer mechanisms associated with transferring heat from the fuel and transferring it to the coolant in normal operation, or transmitting it to the pressure vessel wall in fault conditions.

The successful design for NGNP will possibly be based on one of two technologies; either a pebble bed reactor (PBR) or a prismatic core modular reactor (PMR). PBR technology is based on that of previous German plants and is embodied in the current design proposed by PBMR in South Africa.

In late 2007, a research program was devised to address the high priority issues arising from the PIRT analysis, specifically, addressing those phenomena ranked as being highly important having, simultaneously, a low level understanding. This paper presents theoretical models that have been developed, or are planned, to enable the behavior of PBR systems to be predicted based on the PIRT findings with respect to PBRs. Such predictions will be used to gain an understanding of the response of typical systems when subjected to a range of normal operation and fault condition transients, both with respect to the behavior of the core and the fuel, and ultimately, to include the wider plant, specifically a coupled power conversion system.

This paper presents a model developed for determining fuel particle and fuel pebble temperatures in normal operation and anticipated transient without scram (ATWS) conditions based on multiscale modeling techniques. This model is qualified by comparison with finite element simulations of an idealized "two-dimensional" pebble in transient conditions, and with analytical solutions in steady state. A method is presented for determining the fuel temperatures in the individual batches of a multibatch recycle refueling regime.

Implementation of the multiscale and multibatch fuel models in a whole-core computational fluid dynamics (CFD) model is discussed together with the future intentions of the research program.

2 Theoretical Model Development

Determination of the fuel temperatures in a pebble bed high HTGR core requires the temperature field to be modeled over a wide range of length scales. For convenience, these have been classified into three groups and are referred to here as the macroscopic scale, mesoscale, and microscale, in order of descending length scales.

The largest length scale, the macroscopic scale, resolves the temperature distribution on a scale of the whole reactor down to the size of a cell that contains a few hundred down to a few tens of pebbles—or a few meters down to a few centimeters. A thermal hydraulic solution on this length scale requires the pebble bed to be subdivided into a number of such computational cells, and is able to calculate the mean coolant velocity, pressure, and temperature in each cell together with the average surface temperature of the pebbles. Commercial CFD codes, or bespoke codes based on standard CFD solution methods, are suitable for solving for the flow and temperature fields on the macroscopic scale. However, the details of the temperature distribution within individual pebbles and in and around the individual tristructural isotropic (TRISO) particles within the pebbles are on scales that are too small to be resolved by the CFD code. As such, subgrid scale models are constructed and applied to recreate these fine-scale temperature fields from the cell-averaged values predicted by the CFD code.

The mesoscale is taken to represent the length scales that range from a collection of a few pebbles down to the size of a collection of a few TRISO particles—or a few centimeters down to a few

Manuscript received November 28, 2008; final manuscript received February 12, 2009; published online October 7, 2009. Review conducted by Dilip R. Ballal. Paper presented at the Fourth International Topical Meeting on High Temperature Reactor Technology (HTR2008), Washington, DC, September 28–October 1, 2008.

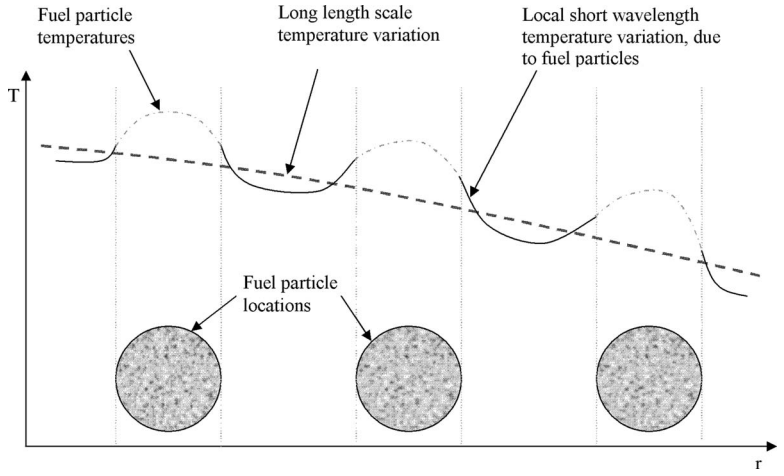

Fig. 1 Sketch of part of the radial temperature distribution through a pebble

millimeters. If the heat generation from the particles is smeared over the volume of the heated zone within a pebble, the mesoscale temperature distribution within a pebble can be determined by solving a one-dimensional conduction equation in the spherical coordinate system of the pebble. Also on the mesoscale, the pebble exchanges heat with the coolant flowing through the computational cell and with other pebbles in the cell. These heat exchanges are complicated further by the fact the cell contains randomly mixed pebbles with widely different irradiations, possibly different enrichments, and therefore different power outputs.

The microscale resolves the temperature field on the scale of an individual TRISO particle, ranging from a few millimeters down to a few tens of micrometers. The microscale temperature field within and around a TRISO particle can be calculated by solving a one-dimensional conduction equation in the spherical coordinate system of the particle.

Resolving the temperature field simultaneously on three different length scales is an established technique known as multiscale modeling. In essence the technique involves successively averaging the behavior of the smaller scale, when progressing upwards through each of the larger length scales. The overall behavior of the system is solved for on the largest scale, and then each solution on the smaller scales is used as a magnifying glass to progressively zoom in on the behavior at the finer scales.

This section concentrates on the development and of the micro and meso subgrid scale models that enable the fuel kernel and moderator temperatures to be calculated. Finally, the development of a multiscale model in spherical geometry is presented and applied to a realistic pebble geometry that contains coated particles.

2.1 Multiscale Modeling. The objective of the work is to develop one-dimensional transient models that are able to represent the thermal behavior of the fuel kernels and the surrounding graphite of the pebble that can be embedded within CFD and system-code models of the whole core. The models, therefore, have to be simple and fast running, but also must accurately represent the physics. The technique used to achieve this is known as multiscale analysis, in which separate differential equations are solved for each of the length scales. In general, detail is progressively smeared out as the length scales become larger, and the spatial extent of the domains is decreased as the length scales become smaller. The overall solution is obtained from the addition of all of the solutions on all of the different length scales. In this paper, only two length scales are considered in detail, the micro- and mesoscales as defined above. In a CFD analysis of the whole core, a third scale is introduced, the macroscale, whose length scale is that of the reactor core itself and in which the individuala pebbles are smeared out to form a heat generating and heat transmitting porous medium.

The solution of a conduction equation in spherical geometry with the heat source smeared out over the particle-containing region of a pebble allows the graphite temperature within a fuel pebble to be computed. However within the pebble, there are localized short wavelength temperature perturbations caused by the presence of discrete TRISO fuel particles.

The resulting temperature profile is sketched in Fig. 1. Within a multiscale model of a pebble, the whole pebble is treated as the mesoscale domain and a fuel particle surrounded by a representative sphere of graphite is taken to be the microscale domain. The radius of the microscale domain is determined from the volume of a sphere (a microsphere) that contains the particle's share of the pebble core graphite as shown in Fig. 2.

2.2 One-Dimensional Example. A good way to explain the multiscale method is by way of a one-dimensional example. Consider the one-dimensional bar in which there are three embedded discrete heat sources as shown in Fig. 3.

The bar is $2L$ long and has a fixed temperature of T_D at either end. The distribution of power density along the bar is as shown in Fig. 4(a).

This power distribution can be decomposed into two further distributions which represent the averaged, or smeared, distribution and a perturbation about the mean respectively, as shown in Fig. 4(b), and represented in Eq. (1) as follows:

$$\dot{q}'''(x) = \bar{q}''' + \hat{q}'''(x) \tag{1}$$

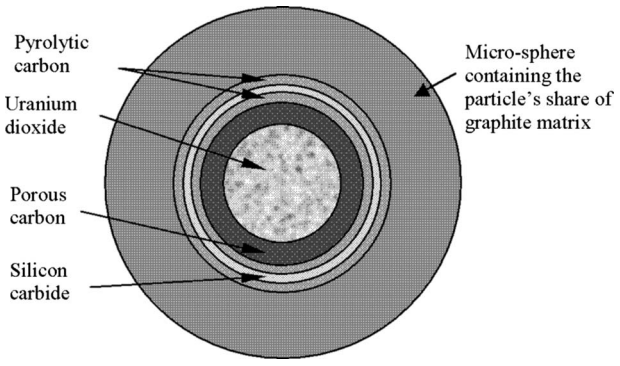

Fig. 2 A "microsphere" containing a single TRISO particle and its share of the surrounding graphite

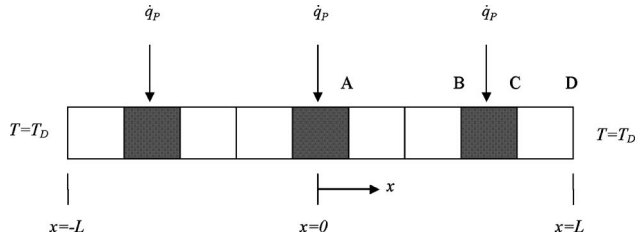

Fig. 3 One-dimensional heated bar problem with three discrete heat sources

It can be seen, therefore, that over the interval of a heated segment plus its share of the unheated neighboring segments, the perturbation represents a matched pair of a heat source and a heat sink. This decomposition introduces the sources and sinks directly into the differential equation; therefore, the corresponding source and sink behavior will be apparent in the microscale solution without having to be imposed as an additional constraint.

The temperature field can be similarly decomposed into

$$T(x) = T_M(x) + T_\mu(\hat{x}) \tag{2}$$

where T_M is the mesoscale temperature variation and T_μ is the microscale temperature variation. The microscale length coordinate is $\hat{x}$, and this has the same units as x but has an origin at the center of each heated segment.

The transient one-dimensional conduction equation is

$$\rho c_P \frac{\partial T}{\partial t} = \frac{\partial}{\partial x}\left(k(x)\frac{\partial T}{\partial x}\right) + \dot{q}'''(x,t) \tag{3}$$

This is decomposed into an equation corresponding to each part of the source term:

$$(\rho c_P)(x)\frac{\partial T_M}{\partial t} = \frac{\partial}{\partial x}\left(k(x)\frac{\partial T_M}{\partial x}\right) + \bar{q}'''(t) \tag{4a}$$

for the mesoscale and

$$(\rho c_P)(\hat{x})\frac{\partial T_\mu}{\partial t} = \frac{\partial}{\partial \hat{x}}\left(k(\hat{x})\frac{\partial T_\mu}{\partial \hat{x}}\right) + \hat{q}'''(\hat{x},t) \tag{4b}$$

for the microscale.

The decomposition itself is not an approximation, however, the use of "smeared" or effective properties for the conductivity, density, and specific heat capacity in the mesoscale equation is an approximation.

The mesoscale equation is solved over the whole domain shown in Fig. 3, with the heat source uniformly distributed over

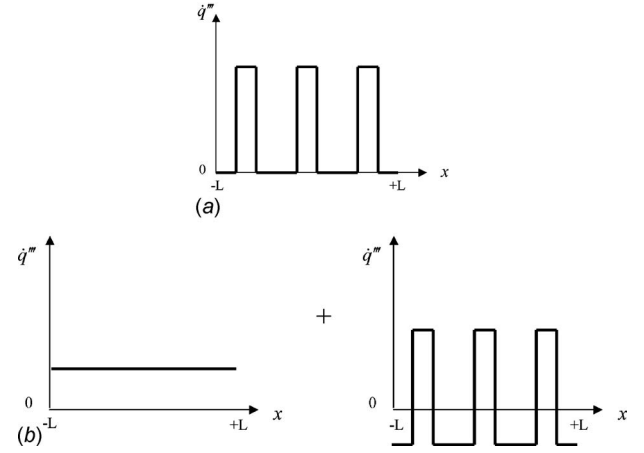

Fig. 4 (*a*) Power distribution and (*b*) decomposed power distribution

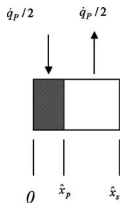

Fig. 5 Microscale domain

the domain. The microscale solution is solved over a subdomain consisting of a heated segment, plus its share of the surrounding unheated material. The distribution of power on the microscale is symmetric about the center of a heated segment; therefore, advantage is taken to half the size of the microscale domain, as shown in Fig. 5.

The boundary conditions on the microscale domain are a zero temperature gradient at the center of the heated segment and the same at the outer edge of the unheated segment.

As the microscale temperature field is a perturbation, it has a zero mean, so the only constraint on microscale temperatures is that it should have a zero mean, resulting in the condition

$$\int_0^{\hat{x}_p} T_\mu d\hat{x} = -\int_{\hat{x}_p}^{\hat{x}_s} T_\mu d\hat{x} \tag{5}$$

Strictly, for compatibility with transient behavior, the microscale solution should have zero-mean internal energy, but it is assumed that the specific heat capacities of the heated and unheated segments are the same in this example, so the zero-mean temperature condition is equivalent.

2.3 Application to a Cylindrical Pebble. While the one-dimensional linear domain serves as a good demonstration of the method, a more realistic scenario is presented by the concept of a fictitious cylindrical pebble. This has the same features as a spherical pebble in that heat can flow around the heated particles (or pins in this case) as well as through them. However, the problem is still considered to be one dimensional, with the presence of the particles smeared in both the radial and circumferential directions in the mesoscale domain. Provision is also made to smear the thermal conductivity and heat capacity variations in both directions, so these quantities are represented by effective or average values.

The mesoscale transient conduction equation in cylindrical polar coordinates is

$$\overline{(\rho c_P)}\frac{\partial T_M}{\partial t} = \frac{1}{r}\frac{\partial}{\partial r}\left(r k_{\text{eff}}\frac{\partial T_M}{\partial r}\right) + \bar{q}'''(t) \tag{6}$$

Similarly, the microscale equation is

$$(\rho c_P)(\hat{r})\frac{\partial T_\mu}{\partial t} = \frac{1}{\hat{r}}\frac{\partial}{\partial \hat{r}}\left(\hat{r}k(\hat{r})\frac{\partial T_\mu}{\partial \hat{r}}\right) + \hat{q}'''(\hat{r},t) \tag{7}$$

The cylindrical pebble is assumed to consist of a circular cylinder of matrix material in which there is a cylindrical heated zone that contained 36 cylindrical heated particles, which were equally spaced on a triangular lattice. As in a real pebble, a margin of unheated graphite surrounds the heated, particle containing, zone. Figure 6 shows the assumed geometry of the test case (including the radial lines along which results are subsequently plotted).

The particles are 1 mm in diameter with a 1.972 mm (0.0776 in.) radial pitch, giving a 2.065 mm (0.0813 in.) circumferential pitch. The radius of the pebble is 8.874 mm (0.3494 in.), and in the mesoscale model, the heat generating zone is assumed to be 3.5 radial pitches in radius, 6.902 mm (0.2717 in.). The volume fraction of particles within the heated zone is 0.1942. The material properties chosen were not representative of a real pebble, but these gave reasonable temperature variations and a sensible tran-

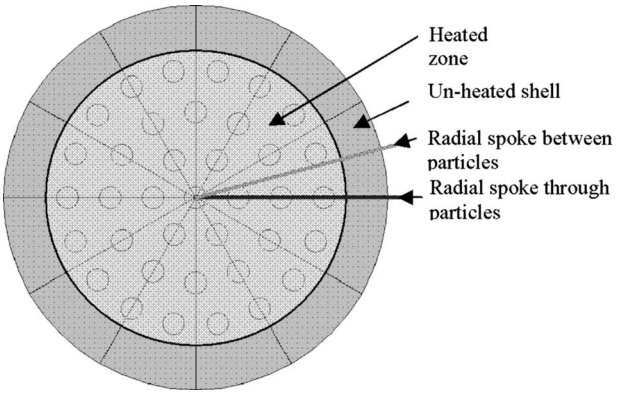

Fig. 6 Schematic representation of the cylindrical pebble

sient response in a model that was on the scale of a few millimeters. The matrix conductivity was set to 5000 W/m K (2889 $Btu^{-1}\,h^{-1}\,ft^{-1}\,°F^{-1}$) and the particle conductivity set to 2000 W/m K 1156 $Btu^{-1}\,h^{-1}\,ft^{-1}\,°F^{-1}$)—giving an effective conductivity of the matrix and particles of 4305.6 W/m K (2488 $Btu^{-1}\,h^{-1}\,ft^{-1}\,°F^{-1}$) obtained using Maxwell's method [1]. The power density in the particles was stepped up from zero to 50 GW/m^3 (4.831×10^9 $Btu^{-1}\,h^{-1}\,ft^{-1}\,°F^{-1}$) at the start of the transient. The density-specific heat capacity product was set to be 1 GJ/m^3 K (14.8×10^3 $Btu^{-1}\,h^{-1}\,ft^{-1}\,°F^{-1}$) everywhere. Based on the volume fraction of 0.1942, the radius of the microcylinder was 1.135 mm (0.4465 in.). Different time steps were used on the two length scales, with 5×10^{-4} s being used on the microscale and 1.5×10^{-2} s being used on the mesoscale. The initial conditions were a temperature of 20°C (68°F) with a microscale perturbation of 0°C (0°F) everywhere in the pebble. The outer surface temperature of the pebble was held constant at 20°C (68°F).

The multiscale differential equations were solved by finite differences, with different time scales used for the two length scales. To test the scheme, the finite difference schemes were explicit which allowed them to be implemented easily in a spreadsheet. The spreadsheet solved both differential equations, added the solutions to recover the temperature field, and plotted the results.

The reference solution in this case was obtained from a finite element solution of the original, or undecomposed and two-dimensional, heat conduction equation. The geometry shown in Fig. 6 was represented by an ABAQUS finite element model, which was run to obtain both steady state and transient solutions. An example of the predicted steady state temperature distribution is shown in Fig. 7.

A comparison of the steady-state temperatures predicted by the finite element model with those obtained from the new multiscale model is shown in Fig. 8. The finite element results plotted along the two radial spokes, shown in Fig. 11, are shown together with the underlying mesoscale part of the solution. It can be seen that the particle temperatures are resolved well and that the mesoscale temperature distribution on its own is reasonably representative of the matrix temperatures between the particles.

Comparisons of temperature profiles between the finite element method and the multiscale model have been made at different time steps and agreement is good throughout the transient, with differences in the predicted particle temperatures being generally less than 0.5°C (0.9°F). Figures 9 and 10 show two such comparisons at 0.165 s and 0.66 s, respectively. Figure 9 shows that the particles respond on a much shorter timescale, that the bulk of the pebble and that the initial temperature rise in each particle is independent of its position in the pebble. Figure 10 shows that 0.5 s later, the particle temperature fields tend to interact with each other and with the pebble external boundary condition and raise the temperature of the pebble preferentially toward the center.

2.4 Spherical Pebble. It is a small step to progress from the fictitious cylindrical pebble to a real spherical pebble. The mesoscale transient conduction equation in spherical polar coordinates, assuming spherical symmetry, is

$$(\rho c_P)(r)\frac{\partial T_M}{\partial t} = \frac{1}{r^2}\frac{\partial}{\partial r}\left(r^2 k(r)\frac{\partial T_M}{\partial r}\right) + \bar{q}'''(t) \tag{8}$$

Similarly, the microscale equation is

$$(\rho c_P)(\hat{r})\frac{\partial T_\mu}{\partial t} = \frac{1}{\hat{r}^2}\frac{\partial}{\partial \hat{r}}\left(\hat{r}^2 k(\hat{r})\frac{\partial T_\mu}{\partial \hat{r}}\right) + \hat{q}'''(\hat{r},t) \tag{9}$$

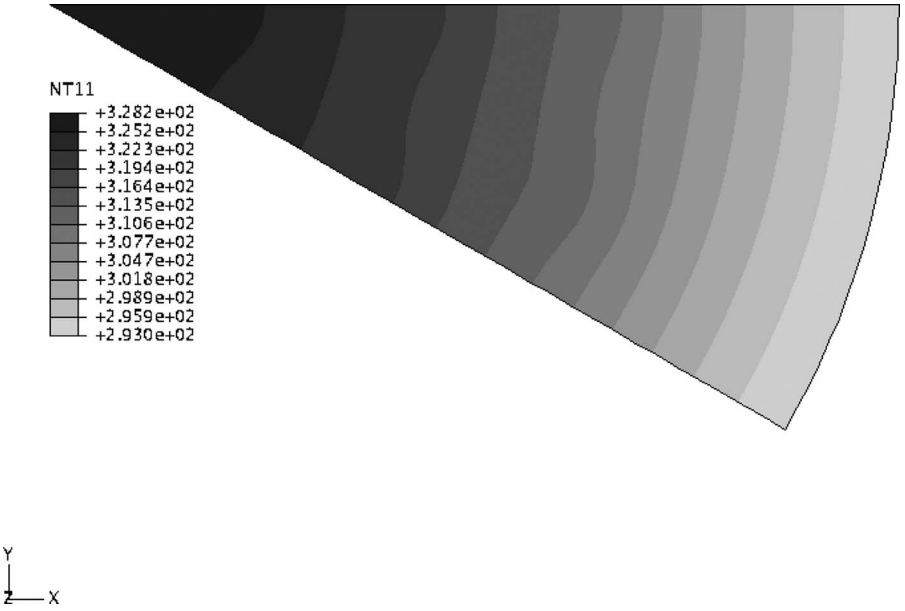

Fig. 7 Finite element prediction of the steady-state temperature distribution within the cylindrical pebble

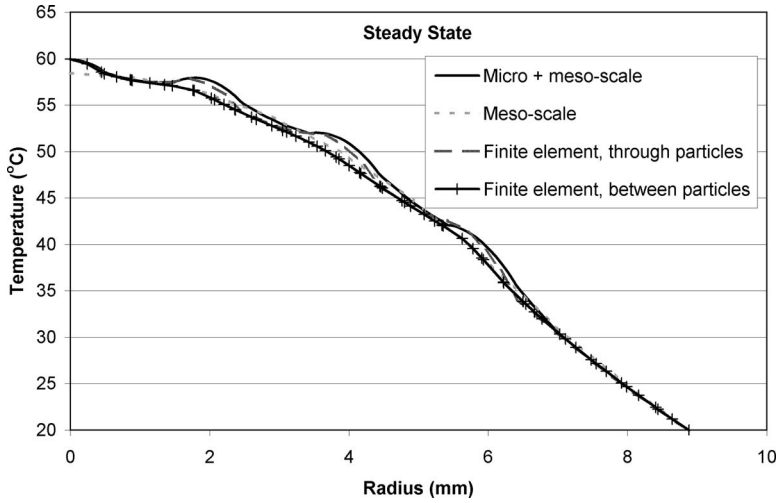

Fig. 8 Comparison of steady-state radial temperature profiles predicted by finite element analysis and the multiscale model

The finite difference equations for the micro- and mesoscales were coded into an Excel spreadsheet. The spreadsheet was set up to solve for pebble and particle temperatures in a spherical domain that represented a PBMR pebble. The pebble contains 15,000 spherical particles of 0.92 mm (0.0362 in.) diameter, these particles are modeled as TRISO particles with the four layers of coating represented by elements of appropriate thicknesses and conductivities. The model was set with a particle-free layer of

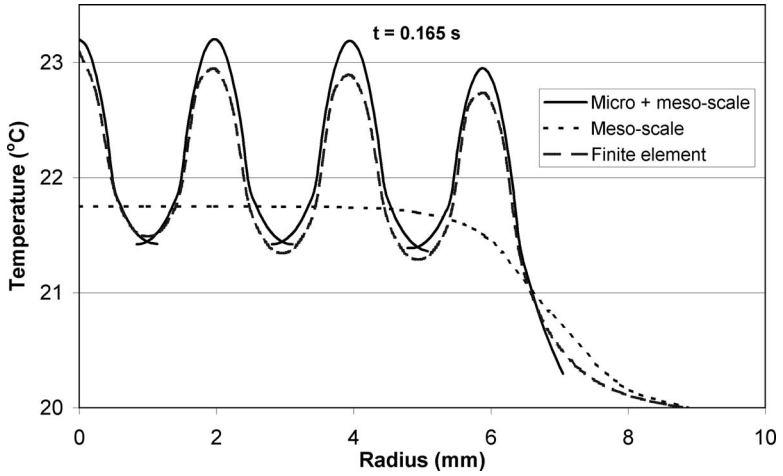

Fig. 9 Comparison of transient temperature profiles at 0.165 s

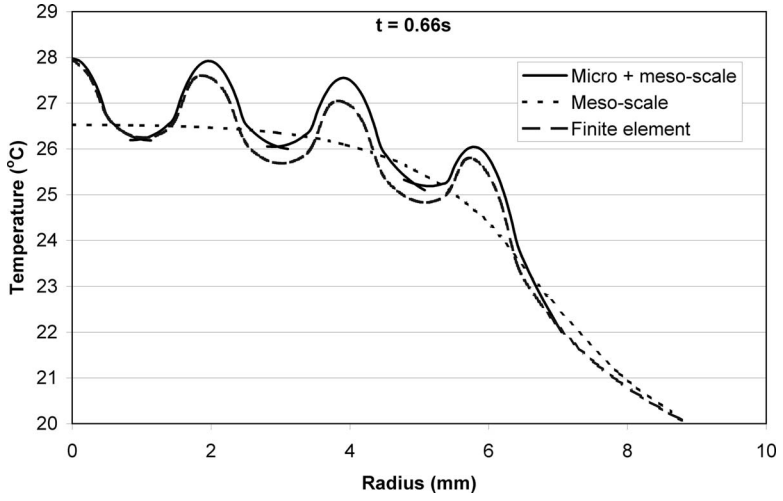

Fig. 10 Comparison of transient temperature profiles at 0.66 s

Table 1 TRISO fuel particle coating geometry and material properties

Region	Material	Outer diameter	Thermal conductivity
Kernel	Uranium dioxide	500×10^{-6} m (0.01969 in.)	3.7 W/m K (2.139 $Btu^{-1}\ h^{-1}\ ft^{-1}\ °F^{-1}$)
Coating 1	Porous carbon	690×10^{-6} m (0.02717 in.)	0.5 W/m K (0.289 $Btu^{-1}\ h^{-1}\ ft^{-1}\ °F^{-1}$)
Coating 2	Pyrolytic carbon	770×10^{-6} m (0.03031 in.)	4.0 W/m K (2.311 $Btu^{-1}\ h^{-1}\ ft^{-1}\ °F^{-1}$)
Coating 3	Silicon carbide	840×10^{-6} m (0.03307 in.)	16.0 W/m K (9.245 Btu h ft °F)
Coating 4	Pyrolytic carbon	920×10^{-6} m (0.03622 in.)	4.0 W/m K (2.311 $Btu^{-1}\ h^{-1}\ ft^{-1}\ °F^{-1}$)

graphite around its periphery. The radius of the pebble is 30 mm (1.181 in.), and the heat generating zone has a radius of 25 mm (0.984 in.). The volume fraction of particles within the heated zone is 0.09344. The material properties were set to values representative of those of a PBMR pebble [2]. The graphite matrix conductivity was set to 15 W/m K (8.667 $Btu^{-1}\ h^{-1}\ ft^{-1}\ °F^{-1}$), this represents an irradiated value and is taken from [3] and the particle coating and kernel dimensions and conductivities were set according to those shown in Table 1.

Maxwell's method [1] was used to determine the effective conductivity of the graphite-TRISO particle mixture and this gave a value of 13.7 W/m K (7.916 $Btu^{-1}\ h^{-1}\ ft^{-1}\ °F^{-1}$). The pure graphite value was applied to the pebble shell outside of the heated zone.

The power density in the particle kernel was stepped up from zero to 902.3 MW/m^3 (87.2×10^6 $Btu^{-1}\ h^{-1}\ ft^{-3}$) at the start of the transient, this value was chosen because it is the average kernel power in PBMR. The density-specific heat capacity product (volumetric heat capacity) was set to be 1690 $kJ/m^3\ K$ (25 $Btu^{-1}\ ft^{-3}\ °F^{-1}$) everywhere in this test problem. In a real pebble, the different material layers will have different, and temperature dependent, volumetric heat capacities. These are included in the model by assigning appropriate values to the corresponding radial increments in the microscale finite difference solution, while using the volume-weighted smeared values in the mesoscale model.

Based on the PBMR particle volume fraction of 0.09344, the radius of the microsphere (a particle's share of the graphite) was 1.012 mm (0.03984 in.). Different time steps were used on the two length scales, with 1×10^{-4} s being used on the microscale and 0.1 s being used on the mesoscale. The initial conditions were a temperature of 20°C (68°F) with a microscale perturbation of 0°C (0°F) everywhere in the pebble. The outer surface temperature of the pebble was held constant at 20°C (68°F).

Figure 11 shows the final steady-state temperature distribution through the pebble and through four particles centered at distances of 0 mm (0 in.), 6.667 mm (0.2625 in.), 13.333 mm (0.5249 in.), and 20 mm (0.7874 in.) from the center of the pebble. Also shown is the mesoscale temperature profile obtained from an analytical solution of the steady-state mesoscale conduction equation. The agreement between the finite difference and analytical mesoscale solutions was good indicating that the finite difference solution was implemented correctly.

A further test on the model was to look at the initial rates of temperature increase in the particles and in the bulk of the pebble. Early in the transient, external heat loss from a particle or from a pebble are both negligible and all of the heat input goes into raising the temperature of the material. For the pebble this simplification gives

$$\left.\frac{\partial T_M}{\partial t}\right|_{t=0} = \frac{\bar{q}'''}{(\rho c_P)}$$

and similarly for a particle

$$\left.\frac{\partial T_\mu}{\partial t}\right|_{t=0} = \frac{\hat{q}'''}{\rho c_P}$$

Figure 12 shows the development of the microscale temperature at the particle center with time. The initial expected rate of change of temperature is also shown. It can be seen that the particle center microscale temperature reaches a steady state after about 2000 time steps (0.2 s) and the initial rate of temperature rise agrees with the expected gradient as shown by the straight line.

Figure 13 shows the development of the mesoscale temperature at the pebble center with time. The initial expected rate of change of temperature is also shown. It can be seen that the pebble center mesoscale temperature reaches a steady state after about 2000 mesoscale time steps (200 s) and the initial rate of temperature rise agrees with the expected gradient as shown by the straight line.

The development of mesoscale radial temperature profiles with time is shown in Fig. 14. Development of the radial temperature

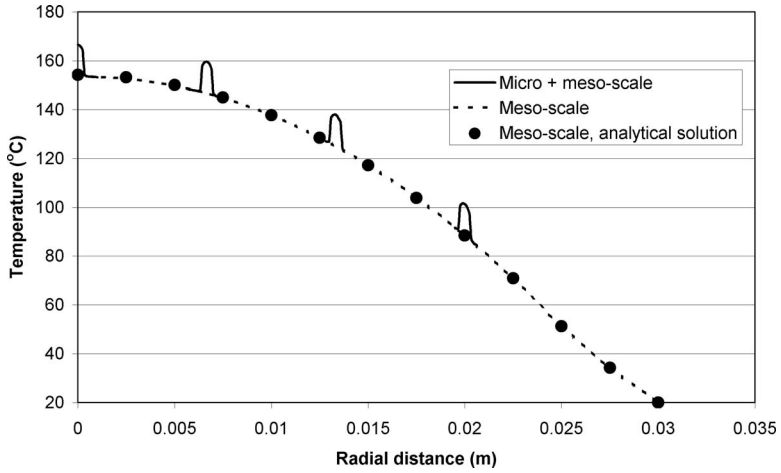

Fig. 11 Radial temperature profile within a pebble passing through four specimen particles

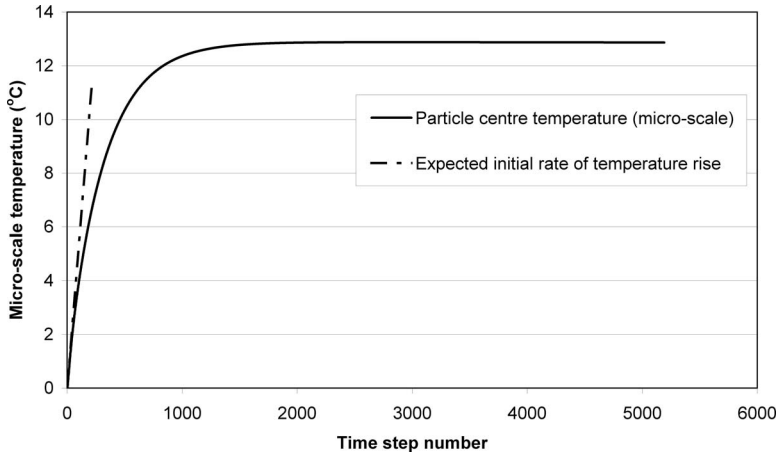

Fig. 12 Development of the microscale temperature at the center of a particle

profiles with time through a microsphere is shown in Fig. 15. The sharp temperature drop over the inner coating, the porous carbon layer, can be seen clearly. The negative microscale temperature over the surrounding graphite outside of the particle is small compared with the particle center temperature.

3 Implementation in a Macroscale Model

The multiscale model presented here is suitable for implementation in a macroscale CFD model of a complete pebble bed reactor. In such a model, the pebble would be modeled as a heat generating, and heat conducting, porous medium. The coupling with the model of this paper would be through the surface temperatures of the pebbles and these would be resolved in the CFD calculation as the solid-phase temperatures within the porous medium. The fluid and solid-phase temperatures within the porous medium would be coupled by heat transfer coefficients derived from correlations, such as those presented in the German KTA rules [4].

The main limitation of the model presented here is that it will only determine the temperature of an average pebble at a given location in the core. In reality, the core will contain fuel from a number of different batches, with different burnups which are randomly mixed. A further step is required, therefore, to determine the actual fuel temperatures in a multibatch core. This step involves considering the heat flows between all of the batches in a given computational cell, between each of the batches and the coolant, and between each of the batches and the neighboring computational cells. Based on these considerations, an equation has been derived, which relates the pebble surface temperatures of the individual batches to the average surface temperature of all batches at a give location in the core as follows:

$$T^i_{\text{surf}} = \bar{T}_{\text{surf}} + \frac{\dfrac{m}{m_i}\dot{q}^i_{\text{gen}} - \dot{q}_{\text{gen}}}{\lambda A + C + \sum_{k}^{\text{neighbors}} B_k}$$

where m_i/m is the fraction of batch i pebbles in a given computational cell, $\dot{q}_{\text{gen}}$ and $\dot{q}^i_{\text{gen}}$ are the total heat generation and fraction generated in batch i in the cell, λ is the coolant convective heat transfer coefficient, C is the pebble-to-pebble effective conductance, and B_k is the effective conductance to the neighboring computational cells in the macroscopic model of the pebble bed. Obtaining a value for the effective heat transfer coefficient is straightforward [4], and the B_k can be obtained from a correlation for effective conductivity in a pebble bed, such as the Zehner–Schlunder correlation [5]. The conductance between neighboring

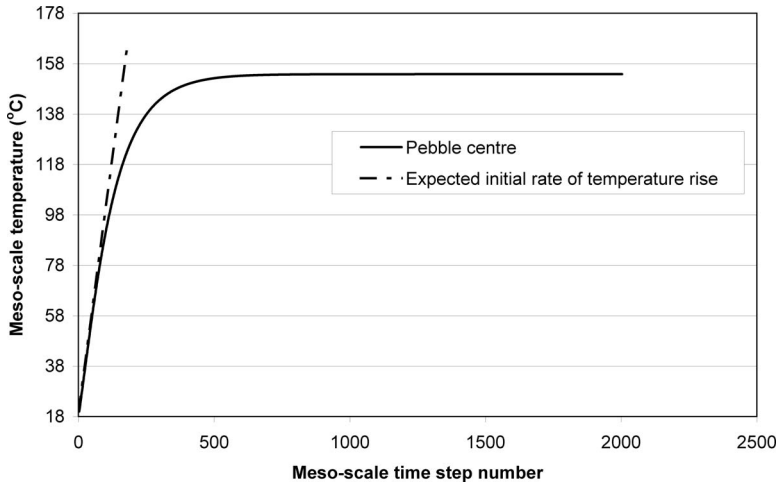

Fig. 13 Development of the mesoscale temperature at the center of the pebble

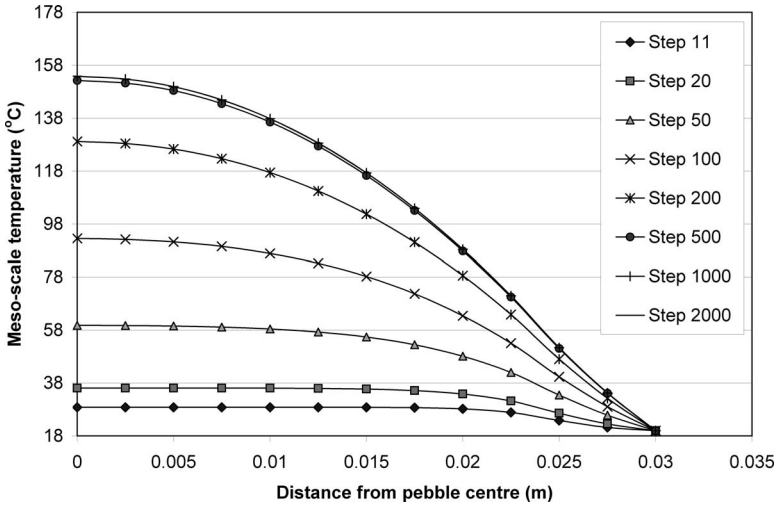

Fig. 14 Development of mesoscale temperature profiles with time

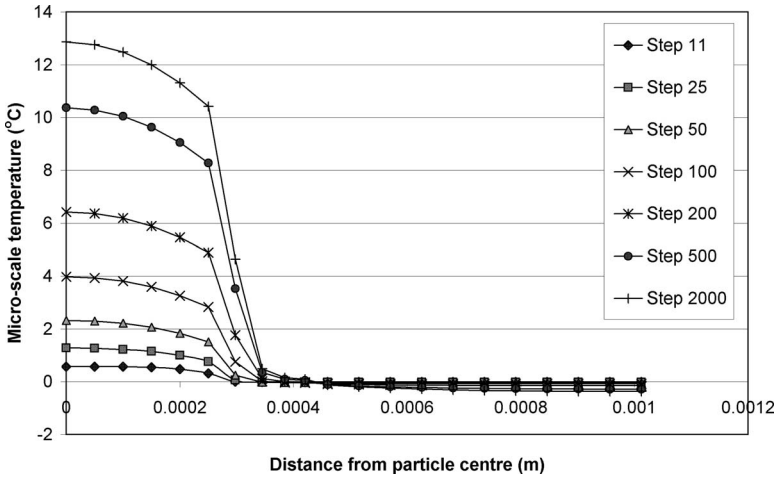

Fig. 15 Development of microscale temperature profiles within a coated particle with time

pebbles should be obtainable from some of the component terms within the Zehner–Schlunder correlation. Investigation of the evaluation these heat exchange coefficients is the subject of a subsequent phase of the current research program

4 Conclusion

This paper presents a multiscale model that allows the fine-scale detail of the temperature distributions both in the pebbles and in the particles that are within the pebbles to be resolved. The model is based on the solution of a pair of one-dimensional finite difference equations, both of which are uncoupled and computationally efficient to solve.

Comparison of the modeling approach in linear and cylindrical geometries with exact and finite element solutions respectively shows that the multiscale model gives good results in both steady-state and transient simulations.

The model has been applied to a spherical PBMR pebble geometry and compared with a steady-state analytical model on the mesoscale. Comparison of the predicted initial rates of temperature rise, both for the particles and the whole pebbles, in a transient shows good agreement with the values expected from the magnitude of the power density and volumetric heat capacities.

Implementation of the pebble and particle temperature models in a macroscopic model of the whole core has been considered. An adaptation to allow the fuel temperatures in a multibatch core to be determined has been presented.

Acknowledgment

This work was supported by the USNRC Office of Nuclear Regulatory Research.

Nomenclature

A = surface area of pebbles in a macroscale computational cell
B_k = intercell (macroscale) conduction coefficients
C = interbatch conduction coefficient
c_p = specific heat capacity
k = thermal conductivity
k_{eff} = effective thermal conductivity of a composite
L = length
$\dot{q}_P$ = particle power

$\dot{q}_{gen}$ = heat generated in a macroscale computational cell
$\dot{q}'''$ = power density
$\bar{q}'''$ = average or mesoscale power density
$\hat{q}'''$ = microscale power density perturbation
r = radial distance from pebble center
$\hat{r}$ = radial distance from particle center
t = time
T = temperature
T_M = mesoscale temperature field
T_μ = microscale temperature field
T_{surf} = pebble surface temperature
x = mesoscale linear distance
$\hat{x}$ = microscale linear distance
λ = convective heat transfer coefficient
ρ = density

References

[1] Carslaw, H. S., and Jaeger, J. C., 1959, *Conduction of Heat in Solids*, 2nd ed., Oxford University Press, New York, p. 428.
[2] IAEA CRP 5, "Evaluation of High Temperature Gas Cooled Reactor Performance," Draft TECDOC II.
[3] OECD, 2005, "PBMR Coupled Neutronics/Thermal Hydraulics Transient Benchmark The PBMR-400 Core Design," NEA/NSC/Document No. V-03, Sept.
[4] 1983, "Reactor Core Design of High-Temperature Gas-Cooled Reactors. Part 2: Heat Transfer in Spherical Fuel Elements," KTA 3102.2, Nuclear Safety Standards Commission (KTA), Germany, Jun.
[5] 1984, *VDI-Wärmeatlas: Berechnungsblätter für den Wärmeübergang*, 4th ed., Verein der Deutsche Ingenieure, Düsseldorf.

Development of Local Heat Transfer Models for the Safety Assessment of High Temperature Gas-Cooled Reactor Cores—Part II: Prismatic Modular Reactors

Richard Stainsby
Matthew Worsley
Frances Dawson
Joakim Baker
Andrew Grief
Paul Coddington

AMEC Nuclear,
Knutsford,
Cheshire WA16 8QZ, UK

Ana Dennier
AMEC NSS,
Toronto, ON, M5G 1X6, Canada

This paper extends the work of Part I to be applicable to prismatic block fuel elements and presents a model developed for determining fuel compact and fuel block temperatures of a prismatic core modular reactor. The model is applicable both in normal operation and under fault conditions and is an extension of the multiscale modeling techniques presented in Part I. The new model has been qualified by comparison with finite element simulations for both steady-state and transient conditions. Furthermore, a model for determining the effective conductivity of the block fuel elements—important for heat removal in loss of flow conditions—is presented and, again, qualified by comparison with finite element simulations. A numerical model for predicting conduction heat transfer both within and between block fuel elements has been developed, which, when coupled with the above multiscale model, allows simulations of whole cores to be carried out, while retaining the ability to predict the temperatures of individual coolant channels and individual coated particles in the fuel if required. [DOI: 10.1115/1.3126770]

1 Introduction

This paper presents a model developed for determining fuel compact, fuel block, and coolant temperatures in normal operation and fault conditions based on multiscale modeling techniques. Fuel particle temperatures can be obtained using a modification of the approach presented in Part I, in which spherical pebbles are replaced by cylindrical fuel compacts.

A method for determining the effective conductivity of the fuel elements has been developed and is qualified against finite element simulations.

An initial attempt at predicting conduction heat transfer both within and between block fuel elements is presented, and the results of the models have been compared with detailed finite element simulations.

The ability to resolve heat transfer on length scales ranging from a few meters down to a few microns within the same model is very powerful and allows a complete assessment of the fuel and structural temperatures within a core to be made. More significantly, this level of resolution facilitates interactive coupling with neutronics models to enable the strong temperature/reactivity feedbacks, inherent in such cores, to be resolved correctly.

2 Multiscale Modeling

A model, which is able to predict the thermal hydraulic behavior of a prismatic high temperature gas-cooled reactor (HTGR) core, needs to be able to resolve the temperature distribution on three distinct length scales. These are referred to here as the macro, meso, and micro length scales. The largest length scale, the macroscopic scale, resolves the coolant, temperature, and power distributions from the scale of the whole core down to a fraction of the size of a fuel element. In such a model a complete hexagonal fuel element could be the smallest scale resolved, with all of the coolant channels therein being represented by a single effective channel, and similarly, all of the channels containing fuel compacts represented by two identical effective fuel channels (on average, there are two fuel channels for every coolant channel in a Fort St. Vrain fuel block). A better macroscopic resolution would be obtained if each hexagonal block was subdivided into six triangular sectors, with each sector being represented by a single coolant channel and two fuel channels.

The mesoscale resolves the temperature distribution on all length scales that is of the order of the pitch of the channels within a block. Therefore, the mesoscale model resolves the local temperature distribution around the single effective coolant channel and the pair of effective fuel channels. In practice, it was found that the modeling on these length scales was best carried out using two separate models. The first, the supermesoscale model, resolves temperatures on the scale of the pitch between coolant and fuel channels. The second, henceforth known as the mesoscale model, resolves detail on the slightly finer scale within and close to a fuel compact.

Coupling between the macro- and supermeso-/mesoscale models allows for the local temperature distributions to be combined with the macroscopic temperature fields so that global heat flows due to the power distribution and external heat losses influence the temperature of individual coolant and fuel channels. Modeling the microscopic scale behavior of individual tristructural isotropic (TRISO) particles within a fuel compact is dealt with in detail, in the context of pebble bed HTGRs in Ref. [1].

Resolving the temperature field simultaneously on different length scales is an established mathematical technique known as multiscale modeling. In essence, the technique involves successively averaging the behavior of the smaller scales when progressing upwards through the larger scales. The overall behavior of the system is solved for on the largest scale and then each smaller-scale solution is used as a magnifying glass to progressively zoom-in on the behavior at the finer scales.

Manuscript received November 28, 2008; final manuscript received October 17, 2008; published online October 7, 2009. Review conducted by Dilip R. Ballal. Paper presented at the Fourth International Topical Meeting on High Temperature Reactor Technology (HTR2008), September 28–October 1, 2008, Washington, DC.

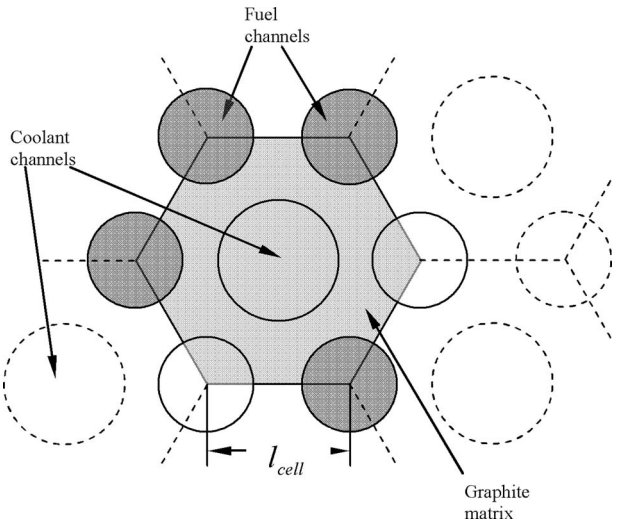

Fig. 1 Unit cell of one coolant and six fuel channels

3 Supermeso- and Mesoscale Models

This section concentrates on the development and qualification of models that resolve temperatures on the supermeso- and mesoscales, by which the fuel compact and graphite temperatures can be calculated together with the heat transferred to the coolant. The assumption in the development of these models is that the coolant flow distribution and local coolant temperature are known, having been supplied by a macroscopic model of the reactor, and that the power distribution is known, either having been prescribed as input to the model or obtained from a coupled neutronics calculation.

3.1 Theoretical Approach. Neglecting heat conduction in the axial direction, for the moment, reduces the problem to a 2D transient conduction problem with heat generation. Expressing this in polar coordinates with the origin of the coordinate system at the center of the coolant channel gives

$$(\rho c_P)(r,\theta)\frac{\partial T}{\partial t} = \frac{1}{r}\frac{\partial}{\partial r}\left(rk(r,\theta)\frac{\partial T}{\partial r}\right) + \frac{1}{r^2}\frac{\partial}{\partial \theta}\left(k(r,\theta)\frac{\partial T}{\partial \theta}\right) + \dot{q}'''(r,\theta,t)$$

If heat generation in the graphite of the block is neglected, the heat generation has a simple distribution that has a finite value inside the fuel compacts and zero elsewhere. The above partial differential equation can be solved in two dimensions using, for example, the finite element (FE) method. However, the simple form of the heat generation distribution combined with the simple circular shapes of the coolant channel and fuel compact allows a reasonably accurate multiscale simplification of the domain to be constructed. Such a multiscale decomposition allows the important features of the temperature field, such as the heat fluxes through the coolant channel and fuel compact surface, mean graphite and compact temperatures, and coolant channel wall and fuel compact center temperatures, to be calculated from the solution of a pair of 1D equations with acceptable accuracy, without the computational burden of solving many transient 2D FE models.

The hexagonal unit cell, as shown in Fig. 1, has an across-corners dimension of twice the pitch of the channels and is itself made up of the equivalent of three smaller hexagons; one that surrounds the coolant channel, with the other two comprising the sum of the six 1/3 hexagons that surround the neighboring fuel channels. These smaller hexagons are all of the same size and have an across-flats dimension that is the channel pitch.

The supermesoscale model is defined within an annular domain (see Fig. 2). The domain is centered on the coolant channel in the original hexagonal unit cell, with the outer diameter chosen to be the same as the across-corners dimension of the original hexagon and the inner diameter being that of the coolant channel. The choice of outer radius, r_B, was made so that the distance from the centers of a fuel compact to the center of the coolant channel is preserved at the expense of not obtaining an equivalent area. The inner radius, r_{chn}, is simply the radius of the coolant channel. The inner radius of the heated zone, r_A, was chosen to give the same area as the hexagonal cell that contains the coolant channel.

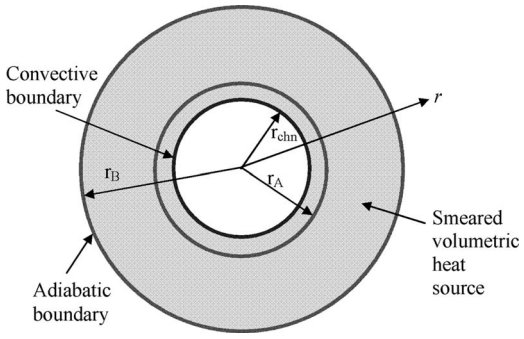

Fig. 2 The supermesoscale domain

The hexagon of graphite surrounding a fuel compact is represented by the mesoscale model. This is a circular domain (Fig. 3), which preserves the same cross-sectional area. The inner and outer radii of this annulus are chosen to be the fuel compact radius, r_{fuel}, and the radius that gives the same area as the hexagonal cell that surrounds a fuel compact, r_D, respectively. The distance from the center of the coolant channel to the center of a compact is the same as the distance between the centers of two neighboring compacts, and so the hexagonal cell surrounding a fuel compact is the same size as the hexagon surrounding the coolant channel, i.e., $r_D = r_A$.

Figure 4 shows the original unit cell with the supermeso- and mesoscale domains overlaid. The area over which the supermeso- and mesoscale domains overlap is identified by the large shaded

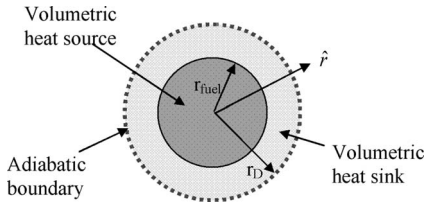

Fig. 3 The mesoscale domain

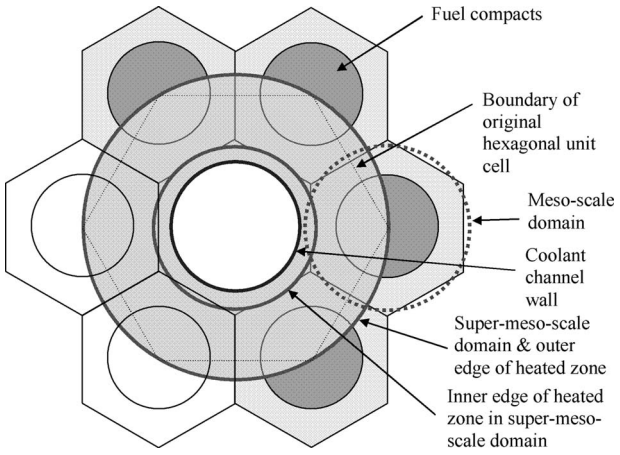

Fig. 4 Original hexagonal unit cell with supermeso- and mesoscale domains overlaid

annulus and this becomes the smeared heat generating zone in the supermesoscale model. The area of the shaded zone is larger than the area of the six 1/3 hexagons of the fuel compacts. This increased area has to be respected when assigning the volumetric heat source and heat capacity to ensure that the total heat generation and thermal inertia within the supermesoscale model are correct.

With heat generation in the graphite of the block neglected, and assuming that all of the compacts generate the same power and that heat generation within a compact is uniformly distributed, the heat generation has a distribution that is described by a mean value plus a perturbation within the heated zone (the region shown between r_A and r_B in Fig. 2) and zero outside of it

$$\dot{q}'''(r,\theta,t) = \bar{q}'''(t) + \hat{q}'''(\hat{r},t) \quad \text{for} \quad r > r_A$$

$$\dot{q}'''(r,\theta,t) = 0 \quad \text{for} \quad r < r_A$$

where the radial coordinate with respect to the center of the fuel compact is not an independent variable in this context, but a function of r and θ.

The mean power density is the power generated averaged over the area of the heated zone in the original hexagonal geometry, where A_{hex} is the area of the hexagonal unit cell including the sectors of fuel compacts and the coolant channel that lie within, which in this case is three times the area of a hexagon that surrounds a fuel compact (or the small hexagon that surrounds the coolant channel, therefore $A_{\text{hex}}=3\pi r_A^2$).

The heat generated by two fuel compacts ($6\times 1/3$) is the heat input into the hexagonal unit cell

$$\bar{q}'''(t) = \frac{2\dot{q}_f''' r_{\text{fuel}}^2}{A_{\text{hex}}/\pi - r_A^2} = \frac{\dot{q}_f''' r_{\text{fuel}}^2}{r_A^2}$$

However, in the approximation of the geometry, shown in Fig. 3, the heated zone is circular and has a greater area than the original hexagonal unit cell. Therefore, the average power density is reduced so that the total heat input is preserved

$$\bar{q}_{\text{eff}}'''(t) = \frac{A_{\text{hex}}/\pi - r_A^2}{r_B^2 - r_A^2}\bar{q}'''(t) = \frac{2r_A^2}{r_B^2 - r_A^2}\bar{q}'''(t)$$

The perturbation is described, with respect to the distance from the center of a compact, as

$$\hat{q}'''(\hat{r},t) = \dot{q}_f'''(t) - \bar{q}'''(t) \quad \text{for} \quad 0 < \hat{r} < r_{\text{fuel}}$$

$$\hat{q}'''(\hat{r},t) = -\bar{q}'''(t) \quad \text{for} \quad r_{\text{fuel}} < \hat{r} < r_D$$

i.e., a heat source within the compact and heat sink in the surrounding graphite. The temperature field is decomposed into supermesoscale (T_{SM}) and mesoscale (T_M) contributions

$$T(r,\theta,t) = T_{\text{SM}}(r,t) + T_M(\hat{r},t)$$

where again, in this context, $\hat{r}$ is not an independent variable, but is a function of r and θ.

The 2D transient conduction equation with heat generation in cylindrical coordinates is decomposed into a pair of 1D equations representing heat transfer on the supermeso- and mesoscales with the effective mean power density and the power density perturbation assigned to these equations respectively. Azimuthal conductivity variations are smeared and the heat capacity is corrected for the nonpreservation of domain area (as mentioned above) to give effective values, which gives the supermesoscale differential equation as

$$\overline{(\rho c_P)}(r)\frac{\partial T_{\text{SM}}}{\partial t} = \frac{1}{r}\frac{\partial}{\partial r}\left(r k_{\text{eff}}(r)\frac{\partial T_{\text{SM}}}{\partial r}\right) \quad \text{for} \quad r_{\text{chn}} < r < r_A$$

$$\overline{(\rho c_P)}(r)\frac{\partial T_{\text{SM}}}{\partial t} = \frac{1}{r}\frac{\partial}{\partial r}\left(r k_{\text{eff}}(r)\frac{\partial T_{\text{SM}}}{\partial r}\right) + \bar{q}_{\text{eff}}'''(t) \quad \text{for} \quad r_A < r < r_B$$

where ρc_p is an appropriate average heat capacity and k_{eff} is an appropriate thermal conductivity.

For the mesoscale,

$$(\rho c_P)(\hat{r})\frac{\partial T_M}{\partial t} = \frac{1}{\hat{r}}\frac{\partial}{\partial \hat{r}}\left(\hat{r} k_{\text{eff}}(\hat{r})\frac{\partial T_M}{\partial \hat{r}}\right) + \hat{q}'''(\hat{r},t)$$

Using a forward difference for the time derivative gives an explicit finite difference equation for the supermesoscale temperature distribution for $r_{\text{chn}} < r < r_A$ as

$$T_{\text{SM}i}^{t+\Delta t} = T_{\text{SM}i}^{t} + \frac{\Delta t}{\overline{(\rho c_P)}_i}\frac{1}{r_i(r_{ei}-r_{wi})}\left(r_{ei}k_{\text{eff},ei}\frac{T_{\text{SM}i+1}^{t} - T_{\text{SM}i}^{t}}{r_{i+1}-r_i} - r_{wi}k_{\text{eff},wi}\frac{T_{\text{SM}i}^{t} - T_{\text{SM}i-1}^{t}}{r_i - r_{i-1}}\right)$$

where the radii and conductivities of the "east" (or high r) and "west" (or low r) faces of the control volume that surrounds node i are, respectively

$$r_{ei} = \frac{(r_{i+1}+r_i)}{2}, \quad r_{wi} = \frac{(r_i + r_{i-1})}{2}, \quad k_{\text{eff},ei} = k_{\text{eff}}(r_{ei}), \quad k_{\text{ef}f,wi} = k_{\text{eff}}(r_{wi})$$

Similarly for $r_A < r < r_B$

$$T_{\text{SM}i}^{t+\Delta t} = T_{\text{SM}i}^{t} + \frac{\Delta t}{\overline{(\rho c_P)}_i}\frac{1}{r_i(r_{ei}-r_{wi})}\left(r_{ei}k_{\text{eff},ei}\frac{T_{\text{SM}i+1}^{t} - T_{\text{SM}i}^{t}}{r_{i+1}-r_i} - r_{wi}k_{\text{eff},wi}\frac{T_{\text{SM}i}^{t} - T_{\text{SM}i-1}^{t}}{r_i - r_{i-1}}\right) + \frac{\Delta t}{\overline{(\rho c_P)}_i}\bar{q}_{\text{eff},i}'''(t)$$

For the mesoscale,

$$T_{Mi}^{t+\Delta t} = T_{Mi}^{t} + \frac{\Delta t}{(\rho c_P)_i}\frac{1}{\hat{r}_i(\hat{r}_{ei}-\hat{r}_{wi})}\left(\hat{r}_{ei}k_{ei}\frac{T_{Mi+1}^{t} - T_{Mi}^{t}}{\hat{r}_{i+1}-\hat{r}_i} - \hat{r}_{wi}k_{wi}\frac{T_{Mi}^{t} - T_{Mi-1}^{t}}{\hat{r}_i - \hat{r}_{i-1}}\right) + \frac{\Delta t}{(\rho c_P)_i}\hat{q}_i'''(t)$$

The boundary conditions applied to the supermesoscale equation are a convective boundary condition at the coolant channel surface and adiabatic boundary at the outer edge of the domain. However, at the inner edge of the heated zone, the contribution from the mesoscale solution has to be included because the convective boundary condition applies to undecomposed temperature field and the contribution from the mesoscale solution is significant because the length scales of both domains are similar. For simplicity, the contribution from the mesoscale solution is added at the surface of the coolant channel, while this is an approximation, it is believed to be not significant as the inner edge of the heated zone is only a small radial distance from the coolant channel wall. The channel wall boundary temperature is

$$T_{\text{chn}}^{t+\Delta t} = T_{\text{SM0}}^{t+\Delta t} + T_{Mn}^{t+\Delta t}$$

and the surface heat flux crossing the coolant channel wall is

$$\dot{q}_{\text{chn}}''' = h(T_{\text{chn}}^{t+\Delta t} - T_{He}) = h(T_{\text{SM0}}^{t+\Delta t} - T_{He} + T_{Mn}^{t+\Delta t})$$

In an explicit scheme, this is approximated by using "old" temperatures

$$\dot{q}_{\text{chn}}'' = h(T_{\text{chn}}^{t} - T_{He}) = h(T_{\text{SM0}}^{t} - T_{\text{He}} + T_{Mn}^{t})$$

This heat flux is used in the above supermesoscale finite difference equation to replace the conductive heat flux term at the channel wall. The adiabatic boundary at the outer edge of the supermesodomain is applied by setting the temperature gradient at the boundary to zero. The boundary conditions on the mesoscale

Table 1 Parameters and their values used in the multiscale model

Coolant channel radius	r_{chn}	8 mm (0.3150 in.)
Supermesoscale heated zone inner radius	r_A	9.9757 mm (0.3927 in.)
Supermesoscale domain outer radius	r_B	19 mm (0.7480 in.)
Fuel compact radius	r_{fuel}	6.25 mm (0.2461 in.)
Mesoscale domain outer radius	r_D	9.9757 mm (0.3927 in.)
Area of hexagonal unit cell	A_{hex}	937.9055 mm^2 (1.4538 in^2)
Graphite conductivity	k_g	30 W/m/K (17.3337 Btu/h/ft/°F)
Fuel compact conductivity	k_f	20 W/m/K (11.5558 Btu/h/ft/°F)
Supermeso-effective conductivity for $r<(r_B-r_{\text{fuel}})$	$k_{\text{eff}}(r)$	30 W/m/K (17.3337 Btu/h/ft/°F)
Supermeso-effective conductivity for $r>(r_B-r_{\text{fuel}})$	$k_{\text{eff}}(r)$	24.0945 W/m/K (13.9215 Btu/h/ft/°F)
Graphite heat capacity	(ρc_P)	2.9068 $\text{MJ/m}^3\text{/K}$ (43.342 Btu/ft^3/°F)
Fuel compact heat capacity	(ρc_P)	2.9068 $\text{MJ/m}^3\text{/K}$ (43.342 Btu/ft^3/°F)
Supermeso-effective heat capacity for $r<r_A$	(ρc_P)	2.9068 $\text{MJ/m}^3\text{/K}$ (43.342 Btu/ft^3/°F)
Supermeso-effective heat capacity for $r>r_A$	(ρc_P)	2.2125 $\text{MJ/m}^3\text{/K}$ (32.990 Btu/ft^3/°F)
Actual power density in compact	$\dot{q}'''_f$	33.41 MW/m^3 (3.228×10^6 Btu/h/ft^3)
Supermesomean power density	$\bar{q}'''$	13.1144 MW/m^3 (1.267×10^6 Btu/h/ft^3)
Supermeso-effective mean power density	$\bar{q}'''_{\text{eff}}$	9.9820 MW/m^3 (0.9645×10^6 Btu/h/ft^3)
Mesoscale power density inside compact	$\hat{q}'''$	20.2956 MW/m^3 (1.961×10^6 Btu/h/ft^3)
Mesoscale power density outside compact	$\hat{q}'''$	−13.1144 MW/m^3 (-1.267×10^6 Btu/h/ft^3)
Convective heat transfer coefficient	h	2615 $\text{W/m}^2\text{/K}$ (460.5 Btu/h/ft^2/°F)
Coolant bulk temperature	T_{He}	20°C (68°F)

domain are symmetrical at the compact center and adiabatic at the outer edge of the domain.

The finite difference equations for the supermeso- and mesoscales were coded into a Microsoft Excel spreadsheet and solved by a simple explicit time-marching procedure. The spreadsheet was set up to solve for a transient in which the power is stepped-up from zero to its nominal value in the compacts at $t=0$. Table 1 contains all of the parameters that were used in the model, based on the gas turbine modular helium reactor (GT-MHR) specifications. The initial condition was for the supermesoscale temperature field to be set to 20°C (68°F) everywhere and for the mesoscale temperature field to be set to 0°C (32°F) everywhere.

Figure 5 shows the temperature profiles plotted along a line that connects the centers of the coolant channel and a fuel compact at times of 1.29 s and 5.6 s (effectively steady state). Also plotted in these figures are the corresponding FE solutions for the same times.

3.2 Finite Element Calculations. In order to qualify the supermeso- and mesoscale models, reference solutions were generated using the FE method to solve the fundamental steady-state and transient heat conduction equations in two dimensions without simplification.

The steady-state and transient FE models of a small section fuel block consisting of 1/12 of the periphery of a coolant channel and 1/6 of an adjacent fuel channel with a proportionate region of graphite in between. The FE program code for this work was ABAQUS/CAE version 6.7-1.

A 2D FE model was produced of a small region of a Fort St. Vrain GT-MHR fuel block. The 2D model represents a horizontal slice through a fuel block passing through six fuel channels surrounding a single coolant channel. The cross section is shown in Fig. 6 and the reduced subregion chosen to be modeled, by making use of symmetry, has been highlighted. The modeled region consists of 1/6 of a fuel channel (and compact within) surrounded by the graphite of the fuel block bounded by a coolant channel wall on one edge and symmetry planes on all of the others. All of the straight edges are symmetry planes and are assumed to be adiabatic. The curved edge representing the coolant channel wall has a forced convection boundary condition, on which a convective heat transfer coefficient and mean coolant temperature are specified.

A FE mesh was constructed within the solution domain made-up from eight-node quadratic quadrilateral elements. In total, the mesh contained 725 elements and 2288 nodes. A contour plot of temperature obtained from the steady-state model is shown in Fig. 7. Figure 5 shows the steady-state temperature distribution along the lower edge of the FE model, from the wall of the coolant channel to the center of the fuel compact (plotted against the analytical solution model).

The transient model was run using the same material properties and boundary conditions as for the steady-state model. In this case, however, the model was assigned a uniform initial temperature of 670°C (1238°F) everywhere (the coolant temperature) with initially zero heat generation in the fuel compact. The power density in the fuel compact was then ramped-up to its nominal steady-state value of 33.41 MW/m^3 (3.228×10^6 Btu/h/ft^3) over 0.001 s to approximate a step change in heat input.

It can be seen in Fig. 5 that the temperatures at the channel wall predicted by the supermesoscale model are higher than the FE solution. This difference is explained by the fact that the convective boundary condition at the wall is applied to the actual temperature field, i.e., to the sum of the supermeso- and mesoscale contributions, via

$$\dot{q}''_{\text{chn}} = h(T'_{\text{chn}} - T_{He}) = h(T'_{\text{SM0}} + T'_{Mn} - T_{He})$$

At all times, the agreement of the supermesoscale+mesoscale solutions with the FE solutions is very close, with the difference in the predicted fuel compact center temperature always remaining less than 1°C (1.8°F). The largest differences are in the predicted channel wall temperatures early in the transient (1.32°C [2.38°F] at 1.29 s). This discrepancy is believed to be due to the small errors introduced by the heated zones in the two circular domains not overlaying each other exactly and the approximation of combing the two solutions at the boundary of the domain rather than at the inner edge of the heated zone. The error is not large, but it can drive the coolant channel wall to be slightly colder than the coolant in the first second of the transient.

In practice, this slight undercooling of the channel wall is not believed to be an issue as it can be trapped in the whole reactor code allowing the wall temperature to be fixed to the coolant temperature value until later in the transient. Some care will be needed to ensure that situations in which the coolant will be hotter than the channel wall in reality are handled correctly—hot gas

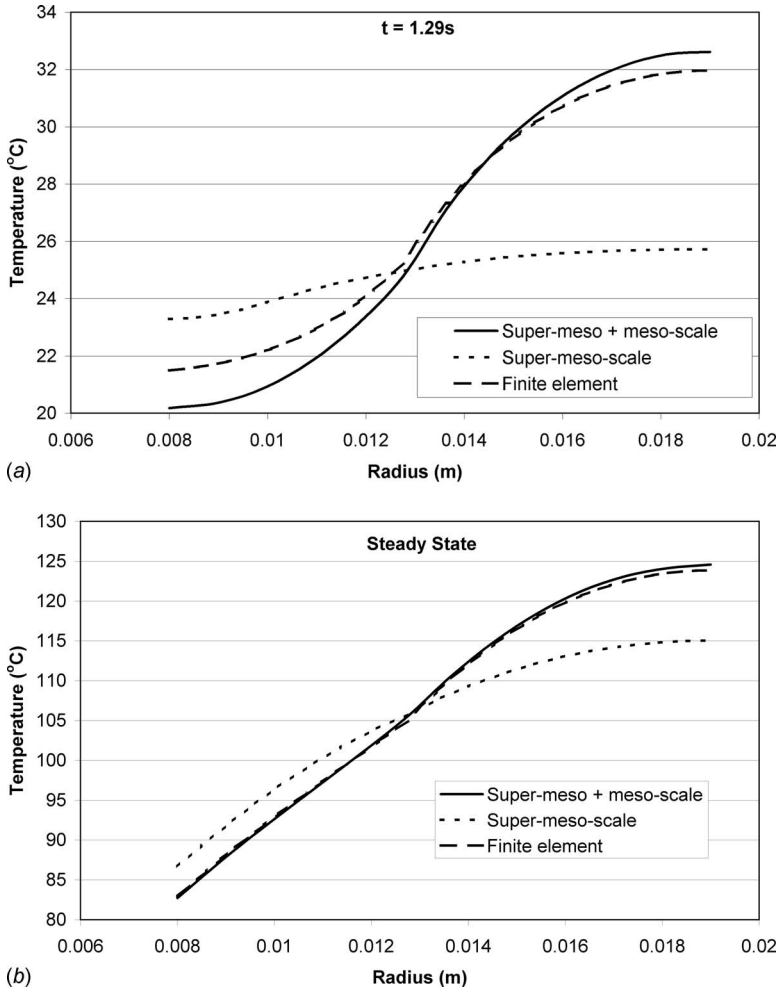

Fig. 5 Multiscale temperatures along a line between the coolant channel and fuel compact at (*a*) 1.29 s and (*b*) steady state

returning to the reactor inlet following a load rejection would be one such situation.

4 Effective Conductivities Using Maxwell's Method

In Sec. 2, models to predict heat transfer on length scales typical of the distance between an individual coolant channel and its surrounding fuel channels, or as defined previously, the mesoscale, were discussed. On the mesoscale, the geometry and material properties of the individual structures can be resolved directly. However, modeling of heat transfer on a larger length scale, the macroscopic scale, which governs the flow of heat both within and between fuel elements, requires the fine-scale thermal conductivity variations to be smeared. This smearing of the individual conductivities must be performed on the scale of individual fuel elements, or more precisely, on the scale of the computational cells used in such a macroscopic model, typically 1/6 or 1/24 of the cross-sectional area of an individual fuel element. On these scales, the conductivity will be anisotropic, with the conductivity in the axial direction being different to the values in the transverse directions. Each fuel element contains three materials (on the mesoscale): graphite, helium, and the fuel compact composite—consisting of a mixture of graphite and TRISO coated particles. Owing to the prismatic structure of a fuel element, the axial conductivity can be calculated using a simple volume weighted average. However, the transverse conductivities are more difficult to determine because of the complex shape of the heat conduction paths in these directions.

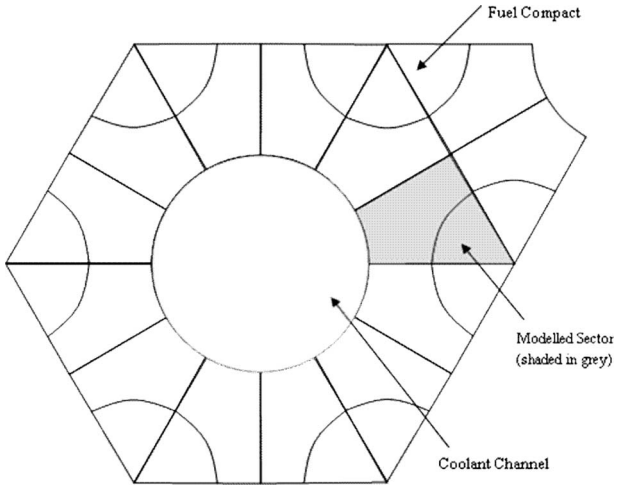

Fig. 6 Region of fuel block and sector chosen for the FE model

This section presents an analytical method by which the effective thermal conductivities in the transverse directions can be calculated. This method is based on Maxwell's method [2], extended to handle three materials and cylindrical inclusions. Maxwell's method is strictly only applicable to dilute mixtures and does not take account of any structure in the geometrical configuration of the inclusions.

Table 2 Analytical and FE results for effective conductivity, values in parenthesis are in Btu/h/ft/°F

Material conductivity (W/m/K)			Effective conductivity (W/m/K)		
Graphite k_m	Fuel k_f	k_m/k_f	From FE	Analytical	% diff.
30 (17.33)	20 (11.56)	1.5	17.45 (10.08)	17.55 (10.14)	0.59
40 (23.11)	20 (11.56)	2	21.41 (12.37)	21.64 (12.50)	1.07
50 (28.89)	20 (11.56)	2.5	25.2 (14.56)	25.55 (14.76)	1.41
60 (34.67)	20 (11.56)	3	28.9 (16.70)	29.37 (16.97)	1.63
20 (11.56)	20 (11.56)	1	13.17 (7.61)	13.14 (7.59)	−0.23
15 (8.67)	20 (11.56)	0.75	10.81 (6.25)	10.7 (6.18)	−1.00
40 (23.11)	10 (5.78)	4	18.15 (10.49)	18.5 (10.69)	1.89

There was a need to qualify the analytical model, particularly with regard to application of the method when the composite must be assumed to be isotropic and when such a composite cannot be considered to be a dilute mixture. As such, a set of FE models were produced to provide effective conductivity values for comparison. Within these FE models, two perpendicular orientations of the hexagonally arranged fuel channels, relative to the principal direction of heat flow, have been studied to see if the effective conductivities are anisotropic in the transverse directions.

4.1 Analytical Model. In Maxwell's original theory, the temperature field around a single spherical particle within a background temperature gradient is computed analytically. A relationship is then obtained between the perturbation to the far-field temperature distribution caused by the particle and the thermal conductivity of the particles itself. This relationship is then used as a basis for calculating the effective conductivity of a suspension of a large number of such particles.

Maxwell's analysis has been rederived to model the effective thermal conductivity, in a direction normal to the cylinders' axis, of a composite material consisting of matrix material and a number of cylindrical inclusions of two different materials.

The effective thermal conductivity, k_{eff}, can be obtained in terms of the known thermal conductivities of the matrix material and cylinders, denoted by k_1, k_2, and k_m, plus the volume fractions, α_1 and α_2, of the cylinder materials:

$$k_{\text{eff}} = k_m \left[1 - \frac{A + B}{(k_m + k_1)(k_m + k_2) + A + B} \right]$$

where

$$A = \alpha_1 (k_m - k_1)(k_m + k_2)$$

$$B = \alpha_2 (k_m - k_2)(k_m + k_1)$$

The thermal conductivity parallel to the cylinders should be evaluated using a simple area-weighted averaging process.

4.2 Finite Element Validation. Two FE models were established to investigate the isotropy of the thermal conductivity with respect to the transverse directions of the fuel block. As such, the first model was oriented assuming that the principal temperature gradient, and consequently the heat flow, was aligned with an across-flats direction, while the second model assumed that the heat flow was in the across-corners direction.

Table 2 shows the results of a comparison between effective conductivity, as predicted by the Maxwell method and as derived from FE simulations.

Comparison of the analytical and FE methods shows that the former produces effective conductivities that agree well with those of the latter over a range of matrix to fuel compact conductivity ratios that is wider than will be encountered in practice. For fuel compact conductivities that are as low as 25% of the matrix conductivity, the analytical method produces effective conductivities that are within 2% of those obtained by the FE analysis.

5 Macroscale Model

The macroscale conduction model accounts for intrablock conduction through a single fuel block and for interblock conduction across the gap between two separate fuel blocks. The supermesoscale+mesoscale solution for a typical fuel compact and coolant channel is assumed to apply at the center of a macroscale solution cell, which in the cases described here, corresponds to a triangular sector describing 1/6 of a fuel block.

The intrablock model is used to relate the sector centroid to boundary heat flow and the boundary temperature. The interblock model accounts for both conduction and radiation across an interblock gap, given the boundary temperatures of the sectors on either side of the gap.

5.1 Macroscale Conduction Model. On the macroscale, heat transfer from one sector to another takes place from the center of one sector to the center of its neighbor. The temperature on the boundary of the sector, T_b, is derived from the centroid temperature, T_g, using semi-analytical 1D models of the temperature distribution across a sector. The simplest of these models relies on the assumption of no heat input and no convective cooling, resulting in a linear temperature profile. The more complex models take explicit account of the effect of the fuel channels and the heat sinks provided by the coolant channels, and are valid for use under normal power conditions.

The heat flow transferred over the gap between fuel blocks is calculated as the sum of the heat radiated across the gap plus the heat conducted through the stagnant helium (the conductivity of which is calculated using the German Nuclear Safety Standards Commission (KTA) correlation for helium [3]).

5.2 Macroscale Modeling of Two Sectors and an Interblock Gap. A complete model of a pair of sectors with an interblock gap (Fig. 8) was created in a Microsoft Excel spreadsheet. Each sector has its own centroid temperature T_g and coolant temperature T_{He}. Each sector also has a temperature, T_b, defined on its boundary with the adjacent sector. An initial guess is entered for the block-to-block heat flow (this is entered as the centroid to boundary heat flow for the first sector, $\dot{q}'_{b12}$, and the negative of this is automatically used for the centroid to boundary flow in the second sector). The temperatures and heat flows within each block are calculated by the spreadsheet using the steady-state analytical supermeso- and mesoscale solutions described above, with the macroscale heat removal term, $\dot{q}'''_{\text{macro}}$, defined by the block-to-block heat flow.

The sector boundary temperatures are calculated from the block-to-block heat flow and the sector centroid temperatures. The boundary temperatures and interblock heat transfer model can

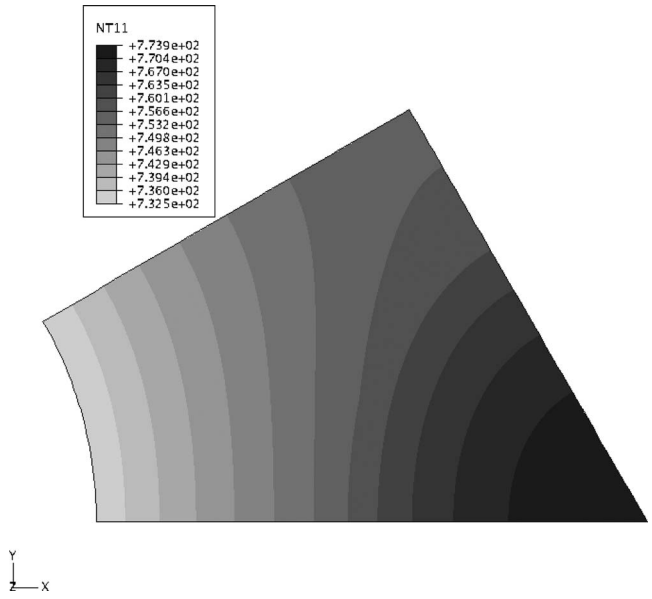

Fig. 7 Steady-state temperature distribution as calculated by the FE model

then be used to recalculate the block-to-block heat flux, which in an unconverged solution will not be the same as the block-to-block flux used as the initial guess.

A self-consistent solution is found using a very simple iterative scheme, which is coded into a Visual Basic macro. Given the current value of the heat transfer from block 1, $\dot{q}'_{b12,j}$, and the value calculated from the interblock heat transfer model, $\dot{q}'_{i12,j}$, a revised guess for the next iteration is given by $\dot{q}'_{b12,j+1}=\mu\dot{q}'_{i12,j}$, where $0<\mu<1$ is an under-relaxation parameter.

The model was used to calculate analytic solutions for two slightly different variants. Variant 1 had step change in power between the two blocks: 1.5 times the nominal power density in the first (48.549 MW/m^3 [4.6909×10^6 Btu/h/ft^3]) and 0.5 times the nominal value in the second (16.183 MW/m^3[1.5636×10^6 Btu/h/ft^3]). The coolant temperature and pressures were 670°C (1238°F) and 70 bar (1015 psi), respectively. Variant 2 used a nominal power density (32.366 MW/m^3[3.1272×10^6 Btu/h/ft^3]) in both triangular sectors but with coolant temperatures of 670°C (1238°F) in the first and 570°C (1058°F) in the second.

Steady-state FE calculations were also made, and the maximum fuel temperature, maximum coolant channel wall temperature, average boundary temperature, and block-to-block heat fluxes compared against the analytical models. Figure 9 shows the

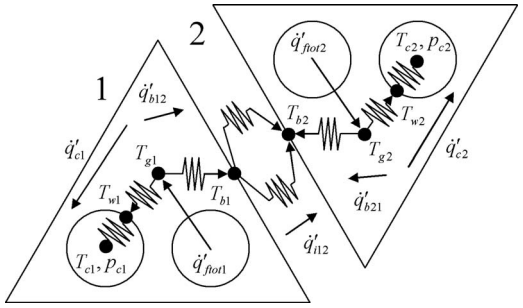

Fig. 8 Two-sector and interblock gap model

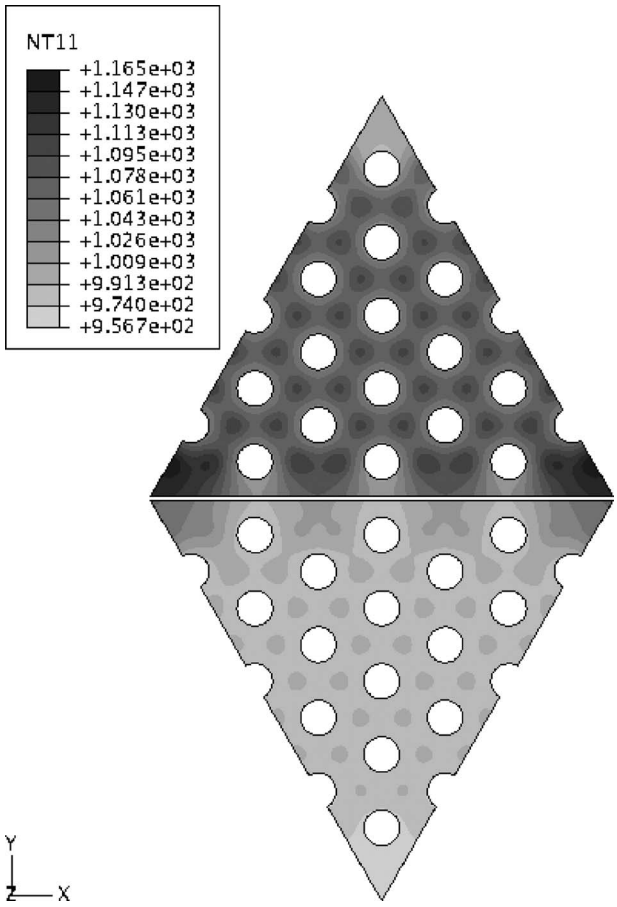

Fig. 9 Two-sector and interblock gap temperatures (Variant 1) as predicted by FE calculations

temperature solution in the FE model of Variant 1. The "hot spots" in the corners of the sectors are clearly visible.

In both variants the FE calculations predict maximum fuel compact and coolant channel wall temperatures that compare well with the analytical results, agreeing within ~3°C (~5°F; ~0.3%). The temperature difference across the gap agree within 2 K and the sector 1 to sector 2 heat flows agree to within ~0.2 kW/m (~0.2×10^3 Btu/h/ft; ~6%). The absolute boundary temperatures are, however, warmer in the FE model, which finds average values that are ~12–14°C (~22–25°F) higher than the analytical values. This discrepancy is likely to be due to the effect of the hot spots in the corners of the sector, which arises due to the slight undercooling of the fuel in these locations. In general, the agreement in temperatures and heat fluxes is excellent. For Variant 1, the analytical model predicts an interblock heat flow of 3.83 kW/m (3.98×10^3 Btu/h/ft), while the FE model predicts 4.07 kW/m (4.23×10^3 Btu/h/ft). For Variant 2, the analytical and FE-predicted heat flows are 4.17 kW/m and 4.02 kW/m (4.34×10^3 Btu/h/ft and 4.18×10^3 Btu/h/ft) respectively. The error in the interblock heat fluxes, ~0.2 kW/m (~0.2×10^3 Btu/h/ft) in both cases, is only a small fraction (~5%) of the total interblock flux of ~4 kW/m (~4.2×10^3 Btu/h/ft), which itself is only a small fraction (~3%) of the power supplied by the fuel (147.6 kW/m [153.5×10^3 Btu/h/ft] in a nominal power block) since most of the heat is transferred straight from a fuel compact into its neighboring coolant channels.

6 Conclusions

A multiscale model of a prismatic HTGR core has been successfully constructed using a series of models stepping down from the macroscopic to the microscopic length scales, progressively resolving the detail in the solution.

The supermesoscale+mesoscale models are capable of closely matching the temperatures and heat flows predicted by FE calculations. The macroscale model relies on the use of effective conductivities derived using Maxwell's method. Multiple FE calculations have been used to qualify this approach.

In general, the FE results show that, in normal operation with forced cooling, the temperature distribution within a block follows the power distribution. If the power density varies linearly across the block, then the macroscopic temperature also varies linearly. Similarly if the power distribution is flat, then the macroscopic temperature distribution is also flat. Heat loss from (or heat gain through) the edges of the block only perturbs the temperatures in the edge rows of coolant and fuel channels and does not propagate into the center of the block.

These findings have important consequences for the way in which macroscopic heat transfer is modeled in a coarse-grid whole core model or system code. First, the assumption of linear temperature variations within the sectors of the blocks is a poor approximation. Second, the assumption that the real variation in power density can be approximated by determining the power density at the centroid of each sector, which is then applied in a piecewise-constant manner over the sectors, is also a poor approximation.

The first of the above consequences demands either a much finer subdivision of the sectors, or for the linear temperature profile to be substituted by a better approximation. In this work, the latter approach was adopted in which the analytical solution to an equivalent 1D problem, with a distributed heat source and distributed temperature-dependent heat sink, was derived and imposed as the assumed temperature variation. The second consequence demands that the power gradient within each sector be included in the analytical solution, this has not been addressed in the current work and, consequently, only comparisons with the FE models in which piecewise constant power distributions were applied have been made.

It is believed, therefore, that the macroscopic model presented here is suitable for reactor static calculations, but requires some development to handle realistic and continuous spatial variations in power density and coolant temperature. Similarly, a further development is necessary to handle correctly the transition to no flow conditions.

Acknowledgment

This work was supported by the USNRC office of Nuclear Regulatory Research.

Nomenclature

A_{hex} = area of hexagonal unit cell
c_p = specific heat capacity
h = convective heat transfer coefficient
k_g = graphite conductivity
k_f = fuel compact conductivity
$k_{\text{eff}}(r)$ = supermeso-effective conductivity
$\dot{q}_f'''$ = actual power density in compact
$\bar{q}'''$ = supermesomean power density
$\bar{q}'''_{\text{eff}}$ = supermeso-effective mean power density
$\hat{q}'''$ = mesoscale power density perturbation
r_A = supermesoscale heated zone inner radius
r_B = supermesoscale domain outer radius
r_{chn} = coolant channel radius
r_D = mesoscale domain outer radius
r_{fuel} = fuel compact radius
ρ = density
t = time
T_{He} = coolant bulk temperature

References

[1] Stainsby, R., Worsley, M., Grief, A., Dennier, A., Dawson, F., Davies, M., Coddington, P., and Baker, J., 2008, "Development of Local Heat Transfer Models for Safety Assessment of Pebble Bed High Temperature Gas-Reactor Cores," *Proceedings of the 14th International Topical Meeting on High Temperature Reactor Technology*, Sept.

[2] Carslaw, H. S., and Jaeger, J. C., 1959, *Conduction of Heat in Solids*, 2nd ed., Oxford University Press, Oxford, UK, p. 428.

[3] 1978, "KTA Rule 3102.1 Reactor Core Design for High-Temperature Gas-Cooled Reactor. Part 1: Calculation of the Material Properties of Helium," Nuclear Safety Standards Commission (KTA), Germany.

Condenser Tube Examination Using Acoustic Pulse Reflectometry

N. Amir

O. Barzelay

A. Yefet

T. Pechter

AcousticEye Ltd.,
4 Harechev,
Tel Aviv, 67771, Israel

Acoustic pulse reflectometry (APR) has been applied extensively to tubular systems in research laboratories for purposes of measuring input impedance, bore reconstruction, and fault detection. Industrial applications have been mentioned in the literature, though they have not been widely implemented. Academic APR systems are extremely bulky, often employing source tubes of 6 m in length, which limits their industrial use severely. Furthermore, leak detection methods described in the literature are based on indirect methods, by carrying out bore reconstruction and finding discrepancies between the expected and reconstructed bore. In this paper we describe an APR system designed specifically for detecting faults commonly found in industrial tube systems: leaks, increases in internal diameter caused by wall thinning, and constrictions. The system employs extremely short source tubes, in the order of 20 cm, making it extremely portable, but creating a large degree of overlap between forward and backward propagating waves in the system. A series of algorithmic innovations enable the system to perform the wave separation mathematically, and then identify the above faults automatically with a measurement time on the order of 10 s per tube. We present several case studies of condenser tube inspection, showing how different faults are identified and reported. [DOI: 10.1115/1.3125302]

1 Introduction

During the last several decades, acoustic pulse reflectometry has been studied in several research laboratories for probing tubular systems. The principles of APR are simple to explain, though the theoretical and practical difficulties involved in implementation of this technology are numerous.

1.1 APR Basics. An acoustic pulse injected into a semi-infinite straight walled tube will propagate down the tube without generating any reflections. This pulse can be measured by mounting a small microphone with its front surface flush with the internal tube wall, through a hole in this wall. The microphone will measure the pulse once only, as it passes over the microphone diaphragm.

If however, the pulse encounters a discontinuity in cross section, a reflection is created. The amplitude and form of the reflection is determined by the characteristics of the discontinuity; a constriction will create a positive reflection, whereas a dilation (increase in cross section) will create a negative reflection. Neither of these discontinuities will change the shape of the pulse in their vicinity, but the reflection measured by the microphone will be an attenuated and smeared replica of the impinging pulse, due to propagation losses [1]. A hole in the tube wall, on the other hand, will create a reflection having a more complicated shape, affected by the size of the hole and the radiation of acoustic energy to the space outside the tube [2]. Schematic examples of these cases are presented in Fig. 1.

Though some of the acoustic energy present in the original pulse is reflected at discontinuities, some of this energy continues to propagate down the tube. Any further discontinuities will once again create reflections. Therefore, diagnosing the internal condition of the tube is a matter of correctly interpreting the reflections as they arrive back to the microphone. One aspect of the interpretation is straightforward; the time of arrival of a reflection can be used to calculate the precise location of the discontinuity, since such reflections propagate at the speed of sound. The second aspect of interpretation is more complicated, as it involves inferring the exact nature of the discontinuity from the detailed shape of the reflection. In a practical system the pulse shape is constrained by the capabilities of the transducer, therefore it is more complicated than in the schematic example in Fig. 1.

The conceptual system described above needs to be translated to an actual system that can be implemented in the laboratory before it can become a usable tool. This is described in Sec. 1.2.

1.2 Components of a Practical APR System. A practical APR system requires a transducer to create the pulse, and a microphone that measures this pulse and the ensuing reflections. Several practical difficulties present themselves immediately when constructing such a system.

1. *Pulse shape.* Ideally, the pulse to be used would be a true impulse of zero width and infinite amplitude, which is clearly not feasible. In practice, the pulse should be made as narrow as possible in the time domain, with as little "ringing" as possible, which translates to a shape which is wide and flat as possible in the frequency domain.
2. *False reflections from the transducer.* As reflections from faults propagate back down the system, they impinge on the transducer after passing over the microphone. These could be mistakenly interpreted as reflections from further faults.
3. *Signal overlap*. A major problem that occurs in an APR system is an overlap between right- and left-propagating signals. The false reflections returning from the transducer can overlap over the microphone with reflections arriving from the pipe system, once again creating difficulties in interpreting them.
4. *Signal interpretation.* Collecting all the above signals and interpreting them correctly is a complex problem in itself.

Various solutions to the above problems exist, some of them appearing in the scientific literature. One of the main obstacles toward using APR systems in the field has been the most widespread solution to problem Nos. 2 and 3 (transducer reflections and ensuing signal overlap). Examining Fig. 2, tubes S1 and S2, called "source tubes," located on either side of the microphone, are made as long as practically possible. This enables reflections from faults in the tube to propagate fully over the microphone before reflections from the transducer are created. Such tubes are often several meters in length, depending on the length of the object being examined. This causes the overall system to be extremely bulky and inconvenient for field tests.

Signal interpretation methods found in the literature depend mainly on a procedure termed "bore reconstruction" [2–5]. In this procedure, the reflections from the examined system are processed to obtain a full reconstruction of the internal bore of the measured tube. This might seem ideal, but unfortunately this method is associated with numerical instabilities which become more pronounced as the examined tube becomes longer.

Though APR has been used in various research labs [2,4,5] for several applications, the problems stated above have prevented this technology from being used widely as a diagnostic tool in the

Manuscript received August 13, 2008; final manuscript received August 24, 2008; published online October 1, 2009. Review conducted by Dilip R. Ballal. Paper presented at the ASME Power 2008 (Power2008), Orlando, FL, July 22–24, 2008.

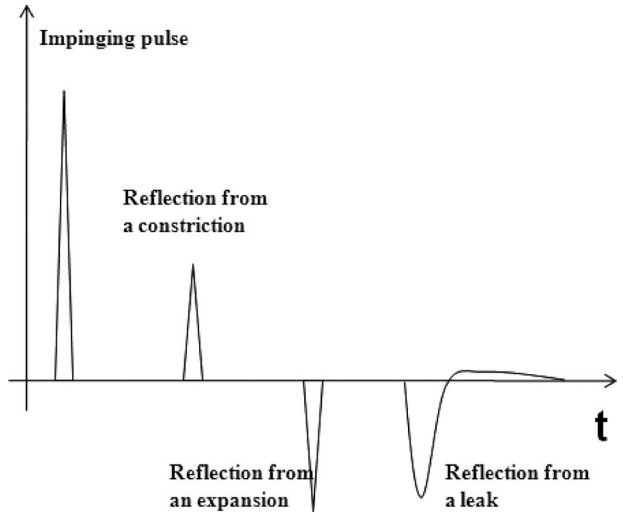

Fig. 1 Schematic examples of reflections from discontinuities

field. This is despite the fact that APR has several potential advantages over more established technologies such as eddy-current, among them: no need to traverse a probe along the pipe, no dependence on tube wall material, rapid test time, and the ability to test bent and coiled tubes.

The rest of this paper presents some of the steps taken in development of a portable test system based on APR, incorporating novel solutions to the problems presented above. We describe some characteristics of the system itself, and present numerous results from using this equipment in the lab and in the field.

2 Taking the Technology From the Laboratory to the Field

The first challenge toward creating a mobile APR was to reduce its size. This consisted mainly of reducing the source tubes to 20 cm each. Thus the entire assemble of transducer, microphone, and source tubes could be fitted into a handheld probe. All of the electronics related to synthesizing the pulse, amplifying, capturing, and analyzing the results were fitted into a separate unit.

Shortening of the source tubes creates overlap between right and left-propagating waves, which are then separated using advanced signal processing methods, as detailed in a recently submitted patent application [6,7]. Some further attenuation of reflections from the transducer was achieved by inserting several layers of acoustically absorbent material at the connection between the transducer and source tube S1.

Once the signal containing the reflections actually due to faults in the tube is isolated from the repeated reflections due to the source, this signal must be scanned in order to determine if any faults actually exist, and if so—what kind of discontinuity caused them (constriction, dilation, or hole). This must be carried out while taking into account that background noise is always present, potentially causing false identifications.

Since the focus of the present paper is on demonstrating test results rather than technology, we will not go into detailed descriptions of underlying the signal processing algorithms. Sections. 3.1 and 3.2 will describe the performance of the industrial APR in laboratory, as well as field conditions.

3 Applying APR

Several factors determine whether the APR system identifies faults correctly: the level of background noise, the distance of the fault down the tube (since the pulses decay over distance, due to friction with the tube walls), and the accuracy of the detection algorithms. In order to isolate these factors as far as possible, extensive testing was carried out in the laboratory before venturing out into the field.

We first present results of several experiments conducted in laboratory conditions, where we could create known faults and then determine whether the APR system could identify them correctly.

3.1 Generic Examples From Laboratory Measurements. Initial tests were conducted on aluminum tubing, with an internal diameter of 25.4 mm, and wall thickness of 1.04 mm. Though aluminum is not used for condenser tubes, APR is insensitive to the material the tubes are made of; therefore aluminum was used

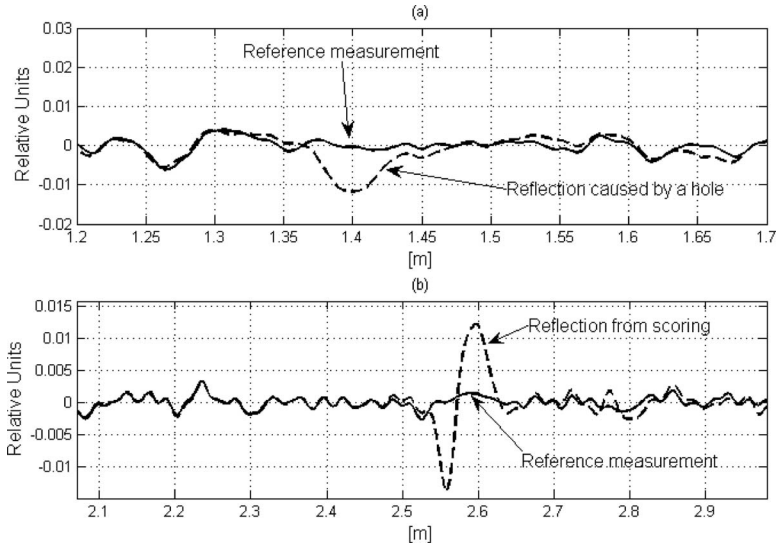

Fig. 2 (*a*) A segment of a measurement showing a reflection from a hole in the tube wall, versus a reference measurement of tube without a hole. (*b*) A segment of a measurement showing a reflection from scoring of the tube wall, versus a reference measurement. Scoring creates a local enlargement of cross section, therefore the reflection is a negative pulse followed by a positive one.

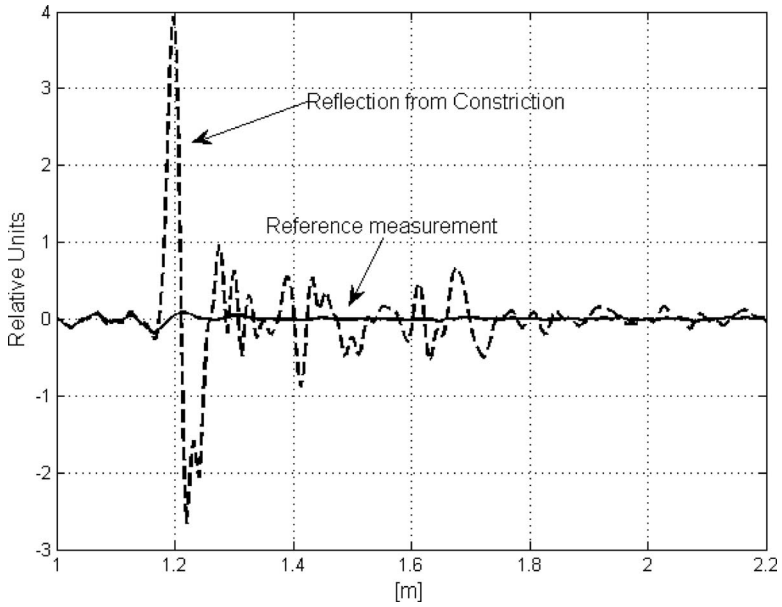

Fig. 3 A segment of a measurement showing a reflection from a constriction created by a washer in the tube, versus a reference measurement. The constriction is a local decrease in cross section, therefore the reflection is a positive pulse followed by a negative one.

as matter of convenience. The same results would be obtained whether they were made of brass, steel, titanium, or any other rigid material. Several generic faults were created; a hole of 0.7 mm diameter was drilled in one tube. Another tube was scored on the inside with a lathe, to simulate local erosion, and a washer was inserted in a third tube to create a local constriction. Figures 2 and 3 show the resultant measurements registered by the APR system. All three types of faults show up clearly as compared with a reference measurement taken from a different tube. These tubes were of 3 m in length, which is shorter than most condenser tubes, but the results were found extremely encouraging. Algorithms for automatic detection and classification of faults were also developed, though these will not be discussed here in detail.

3.2 Field Tests. Field tests of the APR system described here were next conducted on several condensers found in power plants in the USA, Europe, and Israel. Such tests proved beneficial in refining the APR system's operation and of course to the operators of the power plants themselves. Results of two such tests are described below as typical test cases: one case of emergency maintenance and one case of routine maintenance.

3.2.1 Test Case I Emergency Maintenance. In February 2008, water chemistry sensors in one of the turbines in the Reading power plant in Tel Aviv, Israel, indicated that cooling saltwater used in the condenser was leaking into the steam. Since this took place during a season of peak load, the turbine could not be stopped completely. Instead, emergency measures were taken by the maintenance staff. The condenser has four separate quadrants, which can be emptied independently. Temporary plugs were inserted in a large number of pipes in a quadrant that was under suspicion. The following night this quadrant was emptied once more, several columns of plugged pipes were re-opened, and then examined using APR. It is noteworthy that the turbine was opera-

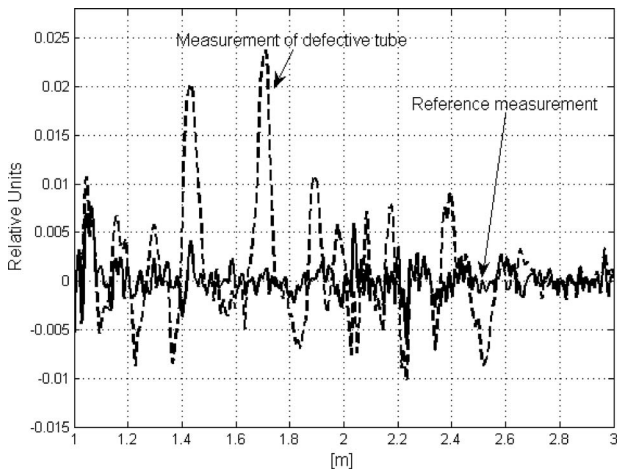

Fig. 4 A segment of a measurement taken from the reading condenser

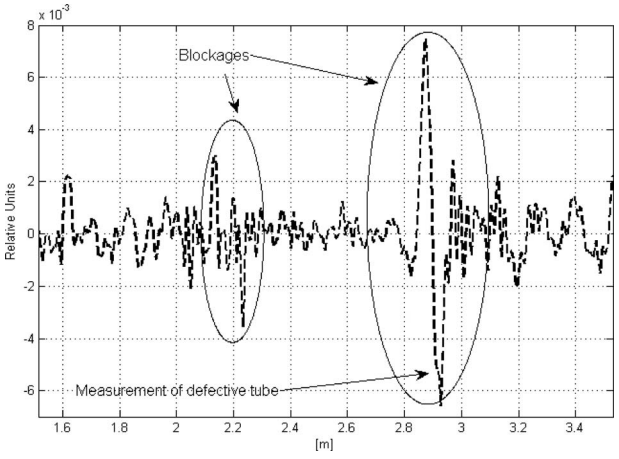

Fig. 5 A segment of a measurement showing two local blockages, indicated by a constriction (positive spike) followed by a dilation indicating return to nominal cross section (negative spike)

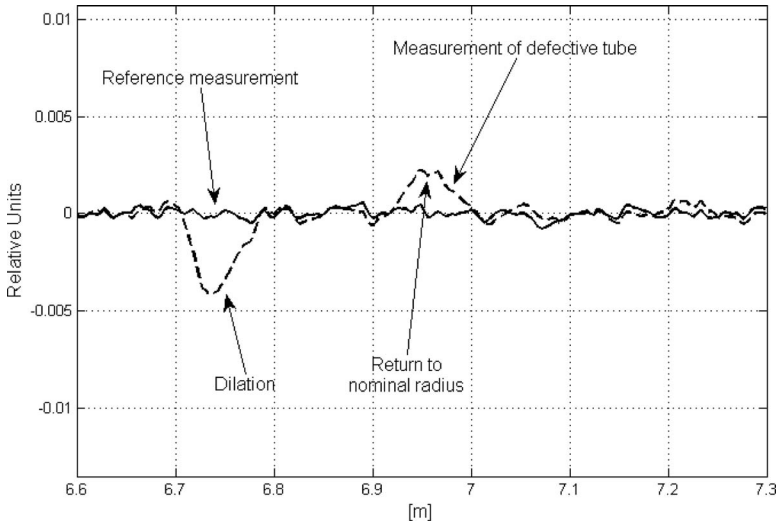

Fig. 6 A measurement showing local increase in cross section—a dilation—followed by return to nominal cross section

tive at the time, so that the levels of background noise were extremely high. As the results will show, this had no significant impact on the measurements.

Due to an extremely tight schedule, measurements were performed and then analyzed on the spot. The tubes were only partially cleaned prior to analysis. Six tubes out of the 200 that were examined were found to have both large accumulations of deposits and suspected leaks. The measurement from one of these is presented in Fig. 4.

These six tubes were plugged. Subsequently, the power plant maintenance team informed us that that the power plant output increased by 15% the following day.

3.2.2 Test Case II Routine Maintenance. In this case, APR was used to examine a condenser opened for routine maintenance, at the Miami Dade Resource Recovery Facility. The face plates covering one side of the condenser were removed, exposing the tubes to inspection. One quadrant of the condenser, composed of 1140 pipes, was fully inspected in 190 min, giving an inspection time of 10 s per tube. Inspecting this condenser using APR revealed interesting information regarding the internal state of the tubes.

APR, similarly to other methods, requires that tubes be cleaned prior to inspection. This is necessary so that deposits do not cover any possible instances of holes or pitting. Since APR does not use a traversing probe, there is no danger that measuring uncleaned tubes will damage the equipment, but it can affect the integrity of the measurement. One of the interesting facts that came to light when inspecting this condenser was that the cleaning had not been carried out thoroughly. APR measurements give a clear indication in such cases, showing the presence of many slight constrictions due to deposit buildups which had not been cleaned off. One typical measurement of such a case is shown in Fig. 5. In this condenser it was found, for instance, that the lower two to three tubes in each column had not been cleaned.

The Miami condenser, using fresh water in a closed loop as a coolant, exhibited less deposits than the Tel Aviv condenser. The latter uses filtered seawater, which can sometimes cause shellfish to grow in the condensers, blocking some of the tubes. Nevertheless, several full or nearly full blockages were found in the Miami condenser, which could easily have damaged other types of test equipment.

Finally, an interesting pattern of wall tube degradation appeared in one area of the condenser. A majority of the 80 pipes found in columns 35 to 43 exhibited one of two indications: either a local increase in cross section, indicating pitting, or an increase of cross section throughout approximately the last half meter of the tube, on average. Figures 6 and 7 show one measurement each, typifying the above faults.

The fact that these faults were concentrated in one region of the condenser is probably due to some flow pattern in the condenser. In any case, these tubes were flagged for periodic surveillance or replacement.

4 Summary

The examples shown above, taken from both laboratory and field tests, demonstrate the abilities of APR very well. The results presented here demonstrate a single aspect of the APR system, showing in detail how faults in the examined tube are manifested in the registered signals. Additional aspects of our instrument, crucial in making it a useful tool have been only touched upon. The usability of the graphic user interface (GUI), the ability of the incorporated software to scan an entire set of measurements and produce a report automatically, indicating all the faults found in a condenser along with detailed descriptions of each—these are important features in themselves, which aid in turning a promising technology into a productive tool.

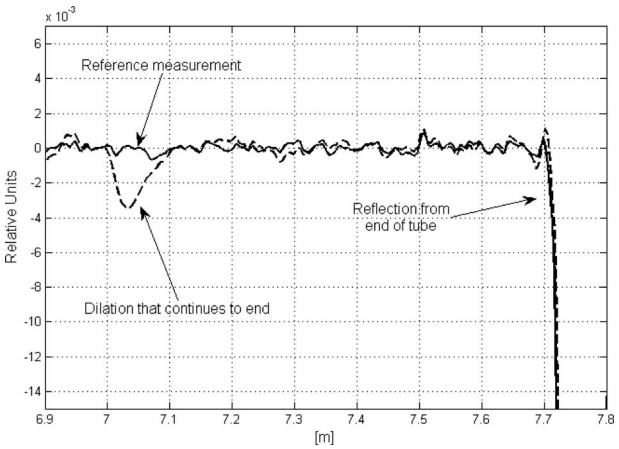

Fig. 7 A measurement showing increase in cross section down to the end of the pipe—a dilation not followed by a return to nominal cross section

References

[1] Amir, N., Shimony, U., and Rosenhouse, G., 1996, "Losses in Tubular Acoustic Systems—Theory and Experiment in the Samples Time and Frequency Domains," Acustica, **82**(1), pp. 1–8.

[2] Chilekwa, V., Sharp, D. B., and Hill, T. J. W., 2003, "Leak Detection in Musical Wind Instruments Using Acoustic Pulse Reflectometry," *Proceedings of the Stockholm Music Acoustic Conference, (SMAC 03)*, Stockholm, Sweden, Aug. 6–9.

[3] Amir, N., Shimony, U., and Rosenhouse, G., 1995, "A Discrete Model for Tubular Acoustic Systems With Varying Cross Section—The Direct and Inverse Problems. Part 1: Theory," Acustica, **81**, pp. 450–462.

[4] Amir, N., Shimony, U., and Rosenhouse, G., 1995, "A Discrete Model for Tubular Acoustic Systems With Varying Cross Section—The Direct and Inverse Problems. Part 2: Experiments," Acustica, **81**, pp. 463–474.

[5] Chilekwa, V., and Sharp, D., 2005, "Detection, Location and Sizing of Multiple Leaks in Ducts," Forum Acusticum.

[6] Application and Methods for Non-Destructive Testing of Tubular Systems, PCT Application No. IL05/000860, pending.

[7] Application and Methods for Non-Destructive Testing of Tubular Systems, USPTO Application No. 60/703,450, pending.

Low Temperature Combustion Using Nitrogen Enrichment to Mitigate NO_x From Large Bore Natural Gas Fueled Engines

Munidhar S. Biruduganti

Sreenath B. Gupta

Raj Sekar

Argonne National Laboratory,
Argonne, IL 60439

Low temperature combustion is identified as one of the pathways to meet the mandatory ultra low NO_x emissions levels set by the regulatory agencies. Exhaust gas recirculation (EGR) is a well known technique to realize low NO_x emissions. However, EGR has many built-in adverse ramifications that negate its advantages in the long term. This paper discusses nitrogen enrichment of intake air using air separation membranes as a better alternative to the mature EGR technique. This investigation was undertaken to determine the maximum acceptable level of nitrogen enrichment of air for a single-cylinder spark-ignited natural gas engine. NO_x reduction as high as 70% was realized with a modest 2% nitrogen enrichment while maintaining power density and simultaneously improving fuel conversion efficiency (FCE). Any enrichment beyond this level degraded engine performance in terms of power density, FCE, and unburned hydrocarbon emissions. The effect of ignition timing was also studied with and without N_2 enrichment. Finally, lean burn versus stoichiometric operation utilizing nitrogen enrichment was compared. Analysis showed that lean burn operation along with nitrogen enrichment is one of the effective pathways for realizing better FCE and lower NO_x emissions.
[DOI: 10.1115/1.3125301]

1 Introduction

The demand for large bore stationary engine efficiencies greater than 50% (by 2010) and extremely low pollutant emissions, particularly NO_x, has become the imperative need of the hour. NO_x emissions pose severe health threats, and therefore its reduction is deemed necessary. Natural gas is one of the most widely used clean burning fuels in large bore stationary engines [1,2]. Research for fuel conversion efficiency (FCE) improvement and emissions reduction in these engines led to the development of innovative concepts, such as homogeneous charge compression ignition (HCCI), micropilot ignition, exhaust gas recirculation (EGR), etc. While, each concept has its advantages and limitations [3–7], EGR has proved to be a very effective tool to reduce in-cylinder temperature and hence NO_x. However, EGR has many built-in adverse ramifications that negate its advantages in the long term. Some of them include combustion contamination, greater control system complexity, application variability, materials and durability, decreased fuel economy, lubricant contamination, and increased particulate matter emissions.

Nitrogen enriched air (NEA) is an effective alternative to EGR without the undesired consequences. This could be achieved using a mature technology which involves selective permeation of gases using an air separation membrane (ASM) [8]. Oxygen-rich and nitrogen-rich streams are produced by pumping air through a nonporous polymeric membrane [9,10].

2 Experimental Setup

A single-cylinder EngineTech (RSi130Q) spark-ignited natural gas research engine was used to investigate nitrogen-enriched combustion on its performance and emissions characteristics. The engine details are given in Table 1 and Fig. 1 shows the schematic of the experiment. Simulated turbocharging (turbocharger efficiency of 60%) was achieved by controlling intake and exhaust tank pressures. An Altronic CD200 ignition module allowed ignition timing (IT) sweep between 10 deg and 40 deg before top dead center (BTDC).

Natural gas was injected into the intake manifold by two electronically-controlled gas injectors. The fuel flow rate was controlled by changing the pulse width to the gas injectors to a maximum time limit based on exhaust and inlet valve closing events. This prevented natural gas from being "short-circuited" to the exhaust during the valve overlap period resulting in better FCE.

High speed in-cylinder pressure was measured using a Kistler 6013B pressure transducer for combustion analysis. The pressure signal was phased with respect to crank angle using an optical shaft encoder, coupled to the engine crankshaft. Combustion analysis was performed by a Win600e system receiving pressure signal via Kistler charge amplifier which converts the charge signal to a voltage signal.

Engine-out emissions were measured using an integrated assembly of analyzers (HORIBA MEXA 7100) comprising of a heated flame ionization detector (HFID) for hydrocarbons measurement, a chemiluminescence detector for NO_x measurement, a paramagnetic analyzer for oxygen measurement, and infrared analyzers for CO and CO_2 measurements.

3 Results and Discussion

The objectives of this effort are as follows:

1. Identify the maximum nitrogen enrichment level without compromising the engine performance.
2. Quantify the NO_x reduction benefit through NEA.
3. Evaluate the effect of spark or ignition timing with NEA.
4. Evaluate the best mode of engine operation vis-à-vis lean burn or stoichiometric.

NEA was obtained by mixing nitrogen and air in the intake manifold. All NEA related data presented in this paper were acquired with bottled N_2. The boosted intake air temperature was not increased to typical compressor outlet conditions. O_2 based equivalence ratio (ψ), Eq. (1), defined as the ratio of actual (measured) fuel flow to O_2 flow ratio to the stoichiometric fuel flow to O_2 flow ratio is introduced as a replacement for the conventionally used equivalence ratio. The test matrix established for the experiment is given in Table 2

$$\psi = \frac{[\text{fuel/oxygen}]_{\text{actual}}}{[\text{fuel/oxygen}]_{\text{stoic}}} \tag{1}$$

4 Nitrogen Enrichment

NEA is the air containing N_2 in excess of 79.05% (by volume). It was observed from previous research [11] that NO_x reduction using NEA is proportional to engine load. This is primarily due to the prevalent higher flame temperatures for higher engine loads. However, excessive engine control (turbo charging, fuel injection, etc.) and variation in equivalence ratio were beyond the scope of that effort. All experiments in this study were performed at full load, i.e., 12 bar brake mean effective pressure (BMEP) and 1800 rpm. Figure 2 shows NO_x as a function of NEA at ignition timing of 20 deg BTDC. NEA was varied from 0% to 3.5%. There is

Manuscript received September 22, 2008; final manuscript received September 30, 2008; published online October 2, 2009. Review conducted by Dilip R. Ballal. Paper presented at the 2008 Spring Conference of the ASME Internal Combustion Engine Division (ICES2008), Chicago, IL, April 27–30, 2008.

Table 1 Engine details

Engine	Single cylinder, four stroke, spark ignited
Bore (mm)	130
Stroke (mm)	140
Comp. ratio	11:1
Displacement (L)	1.857
Power (kW)	33
Speed (rpm)	1800
Ignition system	Capacitance discharge ignition

Table 2 Test matrix (full load: 12 bar BMEP, speed: 1800 rpm)

Parameter	NEA (%)	ITBTDC	ψ
NEA	0–3.5	20	0.9–1.1
IT	0	25–40	0.7
	2	25–40	0.78
ψ	0	MBT	0.58–0.97
	2	MBT	0.65–1.05

significant drop in NO_x emissions as NEA is increased. NO_x reduces primarily due to the "diluent effect" of N_2 yielding lower combustion temperatures. Bulk gas temperature is an exponential component in the NO_x formation mechanism. Therefore, even a slight change in bulk gas temperature can significantly alter NO_x formation. Acceptable engine operation was limited to below 3% NEA due to excessive misfires resulting in a power loss. All NEA levels yielded excellent NO_x reduction reaching as high as 90% at 3.5% NEA. However, FCE decreased simultaneously as shown in Fig. 3. FCE is defined as the ratio of the engine brake power to the fuel energy feed rate based on the lower heating values of the fuel. The drop in FCE for the 2% NEA condition was rather modest amounting to less than 1.5 percentage points (<4% fuel penalty) compared to higher enrichment levels which rose to an unacceptable 5 percentage points (13% fuel penalty). The coefficient of variation of indicated mean effective pressure (COV_{IMEP}), a parameter used to measure engine stability exceeded the accepted value of 5%. Therefore, N_2 enrichment in this study was limited to 2%. Relatively low level of NEA required means that an ASM could be used with minimal parasitic losses and is more economical to implement than otherwise. The O_2 based equivalence ratio (ψ), as shown in Fig. 3, varied from 0.91 (air) to 1.03 (3.5% NEA). It was observed that when N_2 was introduced into the inlet manifold, ψ increases proportionately because it displaces a portion of air that would otherwise be utilized during combustion. The lack of sufficient O_2 alters the chemical reaction rates and engine performance.

Figure 4 displays the cylinder pressure, heat release rates, and the mass fraction burn (MFB) trends for different NEA conditions. Cylinder pressure was averaged over 100 consecutive engine cycles for combustion analysis. The peak pressures decrease with NEA resulting in lower bulk gas in-cylinder temperatures. N_2 enrichment increases the phasing of the peak pressure relative to TDC. Both the heat release rates and the mass fraction burn rates decrease with NEA. Mass fraction burn is defined as the instantaneous burned mass normalized by the total mass of charge in the cylinder. The phasing of the heat release curves shifts more into the expansion stroke of the engine cycle which leads to a loss in power and FCE. NEA delays the 10% burn rate considerably which is often referred to ignition delay. The crank angle duration between 0% and 3% NEA for 10% and 50% MFB levels increases progressively from 3 deg to 8 deg. This behavior implies that NEA lowers burning rates and prolongs combustion duration due to slower flame development and propagation speeds. The lower heat release rates, longer combustion duration, and retarded phasing of heat release rates all contribute to NO_x reduction.

5 Ignition Timing

This section investigates the effect of ignition timing on engine performance between the misfire and knock limits. Figure 5 shows FCE and NO_x emissions as a function of ignition timing for full load condition with 0% NEA (air) and 2% NEA. The timing sweep ranged from 25 deg to 40 deg BTDC. The O_2 based equivalence ratio ψ was 0.7 for 0% NEA and 0.78 for 2% NEA respectively. Stable engine operation was compromised with NEA with retarded ignition timing beyond 25 deg BTDC. At $\psi=1$, the maximum advance in ignition timing was 25 deg BTDC. NO_x emissions increased consistently with advanced ignition timings both with and without NEA. Advancing the ignition timing to enhance combustion characteristics increases the peak cylinder pressure as more fuel is burned earlier in the combustion cycle, i.e., closer to TDC. The exponential increase in peak cylinder pressure causes elevated bulk gas temperatures thus yielding higher NO_x emissions. However, NO_x was always lower with NEA due to the lower combustion temperatures. Retarding the ignition timing decreases the peak cylinder pressure and shifts it into the expansion stroke thereby lowering NO_x. However, combustion quality is compromised as the ignition timing is retarded especially with NEA. FCE peaked at 30 deg BTDC and remained constant even at 25 deg BTDC. However, when ignition timing was advanced beyond 30 deg BTDC, the combustion process advanced simultaneously shifting the heat release rates before TDC. Energy released before TDC reduces the net work output because it opposes the momentum of the piston. At the most advanced ignition timing, i.e., 40 deg BTDC, an occasional engine knock was observed with 0% NEA. However, since NEA slows down the chemical reaction rates, engine knock was not observed at this condition.

6 Effect of O_2 Based Equivalence Ratio, Ψ

Lean burn combustion offers the benefit of higher FCE compared to stoichiometric mode. However, introduction of diluents at lean conditions could potentially lead to misfire and combustion

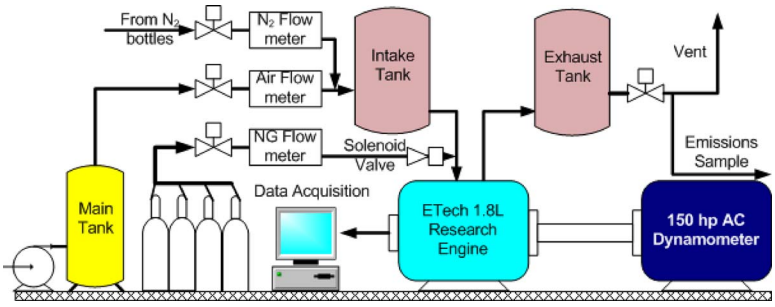

Fig. 1 Schematic of experimental setup

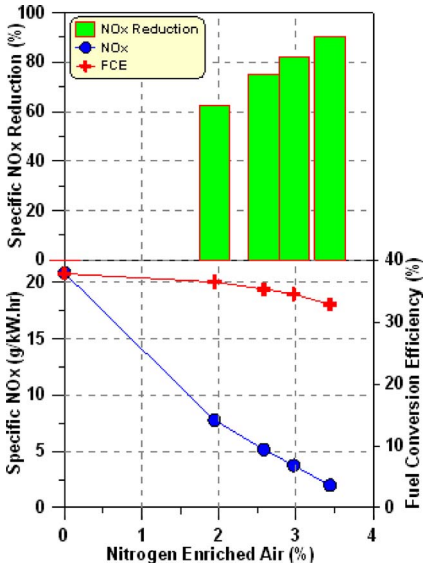

Fig. 2 Spec. NO_x as function of NEA (12 bar BMEP, 1800 rpm, and IT: 20 deg BTDC)

quality degradation. Tests were performed to quantify stable engine operating limits under lean and stoichiometric conditions and the amount of NO_x reduction benefit that could be achieved while maintaining acceptable FCE. Figure 6 shows the NO_x and FCE trends for both 0% NEA and 2% NEA conditions with respect to O_2 based equivalence ratio, ψ at maximum brake torque (MBT).

NO_x emissions, with 0% NEA, peaked for ψ of 0.7 and decreased rapidly for leaner mixtures due to lower combustion temperatures. Also, since less fuel is consumed to produce the same power output, FCE improved as high as 39% under these conditions. However, after the lean combustion limit was reached frequent engine misfire lowered FCE (ψ=0.58). NO_x decreased when the mixture was made fuel rich (ψ>0.7). Similar trend was observed for 2% NEA condition. NO_x reduces with N_2 enrichment for all ψ. Also, the extent of NO_x reduction is dependent on ψ. The highest percentage reduction of NO_x (84%) was achieved at ψ of 1.02 followed by the lean burn condition (50%) which was ψ of 0.65. NEA reduces the engine operating range because of incomplete combustion beyond these lean limits. The intermediate range of ψ (0.7–0.9) produced significant NO_x. Therefore, lean burn operation with NEA is considered favorable.

7 Conclusions

A single-cylinder spark-ignited natural gas engine was used to study the effect of NEA, IT, and ψ. The results obtained lead to the following conclusions.

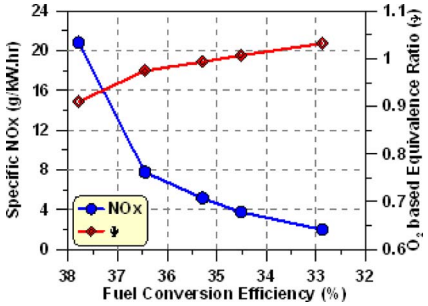

Fig. 3 Spec. NO_x and ψ as a function of FCE (12 bar BMEP, 1800 rpm, and IT: 20 deg BTDC)

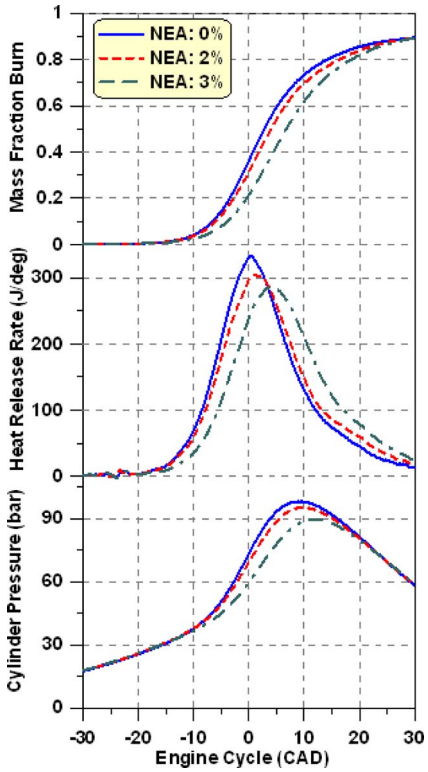

Fig. 4 Combustion pressure analysis as a function of NEA (12 bar BMEP, 1800 rpm, and IT: 20 deg BTDC)

1. N_2 enrichment using ASM could be an effective alternative to EGR.
2. N_2 enrichment lowers NO_x primarily due to low temperature combustion (LTC).
3. NO_x reductions were between 20–85% based on operating regime.
4. Stoichiometric engines in conjunction with ASM could re-

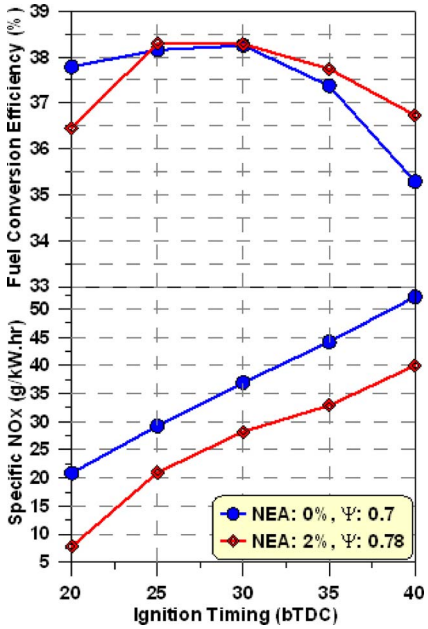

Fig. 5 Spec. NO_x and FCE as function of ignition timing (12 bar BMEP and 1800 rpm)

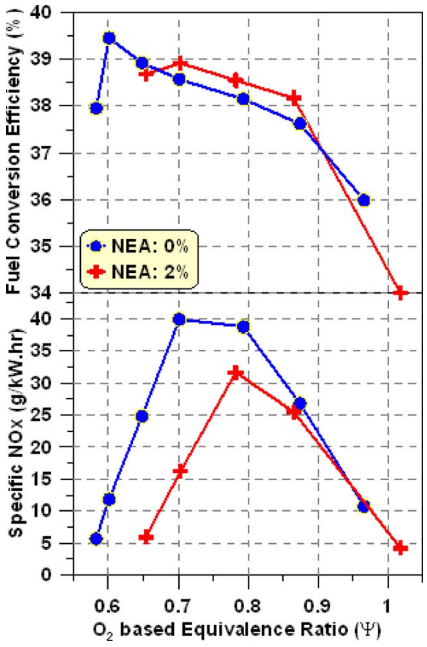

Fig. 6 Spec. NO_x and FCE as a function of ψ at MBT ignition timing

duce NO_x emissions by an order of magnitude to meet regulations with minimal hardware modifications.

5. FCE as high as 39% (ASM power requirements unaccounted) and low NO_x can be realized with N_2 enrichment at lean mixtures (ψ=0.65).
6. NEA extends the benefits of lean combustion even further.
7. Advanced ignition systems along with N_2 enrichment could offer tremendous engine performance improvements.
8. Future experiments will be conducted with ASM to quantify its power requirements and effectiveness.
9. A 70% reduction in NO_x emissions was obtained for full load (12 bars) with 2% NEA operated at MBT ignition timing.

The concept of using N_2 enrichment to reduce NO_x emissions will be investigated further using an ASM on a commercial large bore multicylinder engine. It is anticipated that the membrane parasitic penalties could be about 1.5% due to the lower N_2 flow requirement for natural gas operation compared to earlier diesel engine tests (lean burn).

Acknowledgment

The authors wish to acknowledge the financial support of the U.S. Department of Energy Contract No. DE-AC02-06CH11357.

References

[1] Liss, W. E., and Thrasher, W. H., 1991, "Natural Gas as a Stationary Engine and Vehicular Fuel," SAE Paper No. 912364.
[2] Unich, A., Bata, R. M., and Lyons, D. W., 1993, "Natural Gas: A Promising Fuel for I.C. Engines," SAE Paper No. 930929.
[3] Stanglmaier, R. H., and Roberts, C. E., 1999, "Homogeneous Charge Compression Ignition (HCCI): Benefits, Compromises, and Future Engine Applications," SAE Paper No. 1999-01-3682.
[4] Karim, G. A., 1983, "The Dual Fuel Engine of the Compression Ignition Type-Prospects, Problems and Solutions—A Review," SAE Paper No. 831073.
[5] Krishnan, S. R., Biruduganti, M., Mo, Y., Bell, S. R., and Midkiff, K. C., 2002, "Performance and Heat Release Analysis of a Pilot-Ignited Natural Gas Engine," Int. J. Engine Res., **3**(3), pp. 171–184.
[6] Biruduganti, M., 2002, "Effect of Injection Timing and Pilot Quantity on the Performance of a Dual Fuel Engine," MS thesis, University of Alabama, Tuscaloosa.
[7] Krishnan, S. R., Srinivasan, K. K., Singh, S., Bell, S. R., Midkiff, K. C., Gong, W., and Will, M., 2004, "Strategies for Reduced NO_x Emissions in Pilot-Ignited Natural Gas Engines," ASME J. Eng. Gas Turbines Power, **126**, pp. 665–671.
[8] Winston Ho, W. S., and Sirkar, K. K., 1992, *Membrane Handbook*, Chapman & Hall, New York.
[9] Poola, R. B., Stork, K. C., Sekar, R. R., Callaghan, K., and Nemser, S., 1998, "Variable Air Composition With Air Separation Membrane: A New Low Emissions Tool for Combustion Engines," SAE Trans., **106**, pp. 332–346.
[10] Poola, R., and Sekar, R., 2001, "Simultaneous Reduction of NO_x and Particulate Emissions by Using Oxygen-Enriched Combustion Air," ASME ICE, Vol. 37-1.
[11] M. Biruduganti, S. B. Gupta, S. McConnell, and R. Sekar, 2004, "Nitrogen Enriched Combustion of a Natural Gas Engine to Reduce NO_x Emissions," ASME Paper No. ICEF2004-843.

The Plant Feature and Performance of Double MS (Modular Simplified and Medium Small Reactor)

Tomohiko Ikegawa
Energy and Environmental Systems Laboratory,
Hitachi, Ltd.,
7-2-1 Omika-cho,
Hitachi-shi, Ibaraki 319-1221, Japan
e-mail: tomohiko.ikegawa.jm@hitachi.com

Yukiko Kawabata
Hitachi-GE Nuclear Energy, Ltd.,
1-1 Saiwai-cho 3-chome,
Hitachi-shi, Ibaraki 317-0073, Japan

Yoshihiko Ishii
Energy and Environmental Systems Laboratory,
Hitachi, Ltd.,
7-2-1 Omika-cho,
Hitachi-shi, Ibaraki 319-1221, Japan

Masayoshi Matsuura

Shizuka Hirako

Hitachi-GE Nuclear Energy, Ltd.,
1-1 Saiwai-cho 3-chome,
Hitachi-shi, Ibaraki 317-0073, Japan

Takashi Hoshi
Japan Atomic Power Company,
1-1 Kanda-Mitoshiro-cho,
Chiyoda-ku, Tokyo 101-0053, Japan

A new concept of a small and medium sized light water reactor, named the double MS: modular simplified and medium small reactor (DMS) was developed. The main features of the DMS relative to overcoming the scale demerit are the miniaturization and simplification of systems and equipment, integrated modulation of construction, standardization of equipment layouts, and effective use of proven technology. The decrease in the primary containment vessel (PCV) height is achieved by reducing the active fuel length of the DMS core, which is about 2 m compared with 3.7 m in the conventional boiling water reactor (BWR). The short active fuel length reduces the drop in core pressure and overcomes the natural circulation system. By using the lower steam velocity in the upper plenum in the reactor pressure vessel (RPV), we can adopt a free surface separation (FSS) system. The FSS eliminates the need for a separator and thus helps minimize the RPV and PCV sizes. In order to confirm transient performance, the DMS plant performance under transient conditions was evaluated using the TRACG code. TRACG code, which can treat multidimensional hydrodynamic calculations in a RPV, is well suited for evaluating the DMS reactor transient performance because it can evaluate the void fraction in the chimney and therefore evaluate the natural circulation flow. As a result, the maximum change in the minimum critical power ratio of the DMS was 0.14, almost the same as for the current advanced boiling water reactor (ABWRs). In order to improve safety efficiency, developing an emergency core cooling system (ECCS) for the DMS was considered. The ECCS configuration in the DMS was examined to achieve core coverage and economic efficiency from the following: (1) eliminating high-pressure injection systems, (2) adopting passive safety-related systems, and (3) optimizing distribution for the systems and power source for the ECCS. In this way, the configuration of the ECCS for the DMS was established, providing the same level of safety as the ABWR and the passive systems. Based on the results of the loss of coolant accident analysis, we confirmed that the core can be covered by this configuration. Therefore, the plant concept was found to offer both economic efficiency and safety.
[DOI: 10.1115/1.3125305]

1 Introduction

The importance of nuclear power as an energy source must increase in importance, based on the need for energy security and reduction in greenhouse gas emissions. Development of nuclear power plants was mainly aimed at large-capacity power generation to increase cost efficiency (construction cost per unit power output). On the other hand, the need for medium and small sized distributed power sources was expected to increase, especially in developing countries, where initial investments for plant construction are limited, and electricity transmission networks have not been fully constructed, although energy demands have continued to rise. Thus, the double MS: modular simplified and medium small reactor (DMS) concept, which has cost efficiencies comparable to those of current large-capacity nuclear plants, was developed as a 400 MWe class light water reactor (LWR) [1–7]. This paper describes the summary of the DMS concept, plant transient performances, and the establishment of an emergency core cooling system (ECCS) composition with high economy and safety.

2 Development Targets and Plant Concept

2.1 Development Targets. The development targets set for developing small and medium-sized reactors are as follows:

(1) plant output of the 400 MWe class
(2) construction cost competitive with that of existing ABWRs
(3) level of safety equivalent to that of existing ABWRs

2.2 Plant Concept. Figure 1 shows the DMS plant concept with particular attention paid to overcoming the scale disadvantage and achieving the development targets above.

The main features of the DMS are as follows.

(1) Simplified reactor core structures. Application of a small-sized natural circulation reactor, elimination of steam separators, and application of a small-sized reactor pressure vessel (RPV).
(2) Simplified systems. Adoption of two main steam lines and passive systems, common use of systems, and a simplified ECCS structure.
(3) Rationalized layouts. Adoption of a compact primary containment vessel (PCV) and a building layout in which simplified systems and facilities are applied.

3 Plant System Design

3.1 Core System and Characteristics. The DMS adopts a design that not only eliminates reactor internal pumps (RIPs), but also maximizes the advantage of a natural circulation system by utilizing the good compatibility between short length fuel assemblies and the natural circulation system as shown in Fig. 2. The short length fuel assemblies help the core flow rate increase, resulting in low drops in core pressure and a higher design margin

Manuscript received August 29, 2008; final manuscript received September 10, 2008; published online October 1, 2009. Review conducted by Dilip R. Ballal. Paper presented at the 16th International Conference on Nuclear Engineering (ICONE16), Orlando, FL, May 12–15, 2008.

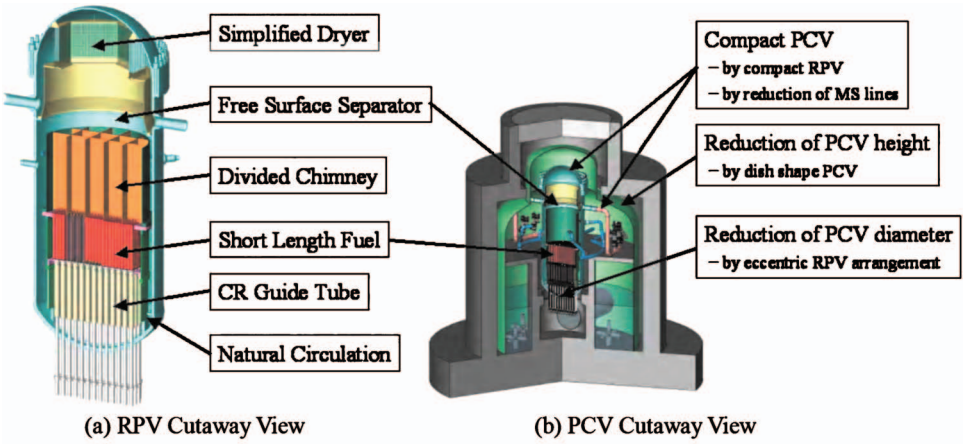

Fig. 1 DMS plant concept

for core stability. The use of short length fuel assemblies also leads to a reduction in the RPV's height because the lower drop in core pressure reduces the required chimney height.

The short length fuel assembly (ΔL: fuel assembly length) yields in a particular height reduction effect of $6 \times \Delta L$ in reactor building height, $4 \times \Delta L$ in PCV height, and $2 \times \Delta L$ in RPV height. The short length fuel assembly also reduces the number of floors necessary in the reactor building, resulting in a shorter construction period.

We have evaluated the feasibility of the natural circulation system, the core stability, and the thermal margin of the core.

Regarding the natural circulation system, we have considered all pressure drops along the natural circulation loop. The current design method for the BWR core includes an evaluation of the drop in core pressure and the void fraction in the chimney. As a result, we have confirmed that the natural circulation reactor system of the DMS provides a sufficient core flow rate.

Based on the evaluated core flow rate, we have evaluated the stability characteristics by using an analysis code. As a result, we confirmed that the core design of the DMS is feasible with respect to core stability. The use of short length fuel assemblies affords a sufficient design margin for channel stability of the DMS core. As for core stability that includes the feedback between the thermal hydraulics and core nuclear features, important factors include the reactivity feedback by the void coefficient, time constants, and flow gain of the natural circulation loop. In this study, we checked these sensitivities for core stability and confirmed the feasibility of the DMS core.

It is important in core design to evaluate the core thermal margins, the minimum critical power ratio (MCPR), and the maximum linear heat generation ratio (MLHGR). For the DMS core with 10×10 fuel assemblies, the core power density is lower than that of the conventional BWR, so that the DMS core has a sufficiently large thermal margin.

3.2 FSS. By adopting a natural circulation system, it is expected that steam and liquid water can be separated by gravitational force, given the low rate of steam evaporation at the reactor core outlet. According to an experimental work [8], steam separators are unnecessary at a steam evaporation speed of 0.7 m/s or less, and according to a semitheoretical study [9], it is possible to eliminate steam separators altogether. For these reasons, a gravity

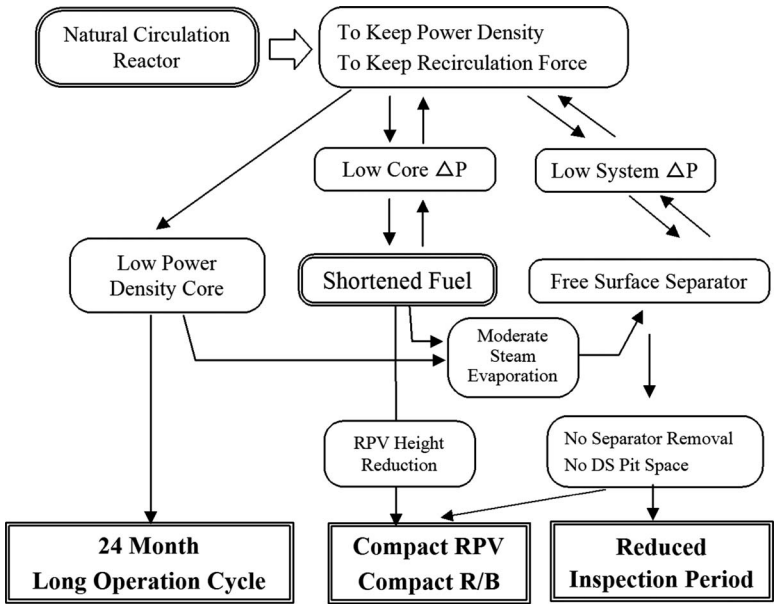

Fig. 2 Compatibility of natural circulation reactor and short length fuel assembly

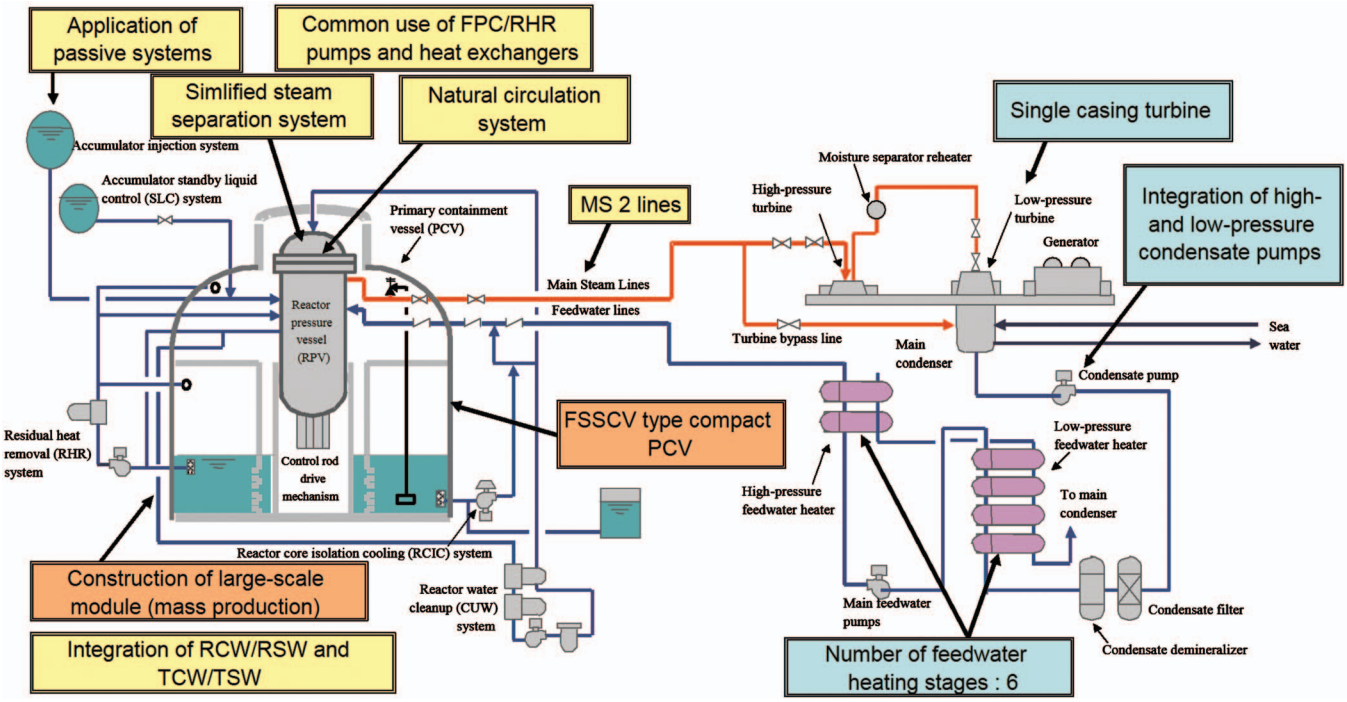

Fig. 3 System configuration

steam separation type of free surface separation (FSS) (without steam separators) is proposed for the DMS. Adopting FSS affords many advantages for the DMS, such as an increased natural circulation flow rate due to the elimination of steam separators, simplified core internal components, a more compact RPV, and a shorter annual inspection period. Moreover, eliminating the steam separators can reduce RPV height (by about 2.5 m). The size of the RPV is determined so as to meet certain design conditions, and it is expected that the only major reactor internal components would be the reactor core, shroud, and chimney.

3.3 System Design of NSSS and BOP. Figure 3 shows the system configuration of the nuclear steam supply system (NSSS) and balance of plant (BOP). The DMS was rationalized by a reduction of systems, use of large-capacity equipment, systems having integrated functions, passive systems, and non-specific devices. For example, the DMS adopts a system of two main steam lines, a single casing turbine, and a single train for the cooling water (CW) system by utilizing large-capacity components.

The reactor building cooling water (RCW) system and turbine building cooling water (TCW) system were integrated into a single system, so are the fuel pool cooling and filtering (FPC) system and the suppression pool clean up (SPCU) system. Gas turbine type emergency generators were also adopted. As for passive systems, an accumulator injection system was employed for the ECCS with a view to reduce cost. Looking at the BOP specifications for the 400 MWe class, a TCDF-52 reheat cycle turbine system and six feedwater heaters were adopted. In addition, a low-pressure condensation pump and a high-pressure condensation pump were integrated into a single common pump, and feedwater heaters were designed as a single train. Table 1 lists the other system specifications.

3.4 Plant Layout Planning and Construction Planning. The PCV and reactor building of the DMS were designed as compact as possible from an economical standpoint. A compact PCV (17 m$\phi\times$24.4 mH) can be achieved by utilizing a dish-shaped drywell and eccentric RPV arrangement, that is, installing the RPV not at the actual center but at an eccentric center of the PCV. A suppression chamber type of PCV was adopted for the DMS based on the abundant designs and operation experience acquired from existing BWR plants. In the DMS plant, the coolant blown down from the RPV fills the lower drywell. In contrast, existing ABWRs were designed to retain drawn-down water from filling the lower drywell in the pressure suppression pool beforehand. In this way, putting the water-filled volume of the lower drywell into the accumulator injection system can optimize the suppression pool of the DMS. Moreover, the concept of a building layout that contributes to reducing construction cost was established by applying a steel-plate-reinforced concrete structure to simplify the building shape and building structure. The size of the reactor building can be minimized by both PCV compactness and system simplification. In particular, a lower reactor building height allows

Table 1 DMS design specifications

Item	DMS 400 MWe class
Plant output	428 MWe/1200 MWt
Core	
Fuel	2.0$m\times$568
Ave. discharge exposure	45 GW d/t
^{235}U enrichment	4.2 wt %
Batch size	3.0
Power density	44 kW/l
CR/CRD	137
MS	500$A\times$2
FDW	300$A\times$2
ECCS	3 active systems+1 passive system
Turbine	TCDF-52
Main component and buildings	
RPV	5.8 m$\phi\times$15.5 mH
PCV	17 m$\phi\times$24.4 mH
R/B	41 m$\times$36 m$\times$42 mH

Table 2 DMS modeling specifications

Item	Value
Modeling of RPV	
Nodalization	R-Z two-dimensional
Separators and dryer	Not included
Divided chimney	About 3 m above core
FSS region	About 3 m above divided chimney
Control systems	
Feedwater flow	Same as for ABWR
Pressure	
Main steam lines	
Diameter	500*A*
Length	
SRV pressure setpoint	Same as for ABWR

Table 3 Analysis conditions

Item	Value
Thermal power	105% of rated power
RPV dome pressure	about 7.2 MPa
FDW temperature	about 489 K
Reactor kinetics model	Point-reactor kinetics model
Reactivity coefficients	
Void	Same as for ABWR
Doppler	
Scram	

a reduction in the number of floor levels from six in existing ABWRs to four, thereby contributing significantly to the shortening of the construction period.

4 Transient Performance Evaluation

4.1 Modeling and Analysis Conditions. The DMS plant performance under transient conditions was evaluated using the TRACG code [10]. This code, which can treat multidimensional hydrodynamic calculations in the RPV, is well suited for evaluating the transient performance of the DMS reactor because it can evaluate the void fraction in the chimney and therefore evaluate the natural circulation flow.

Table 2 shows the specifications used for modeling the DMS. The RPV of the DMS was modeled with R-Z two-dimensional geometry.

Since the DMS adopted the FSS system, steam separators were not included in this model. The height of the divided chimney region to obtain the sufficient natural circulation flow was about 3 m, and the height of the FSS region located above the divided chimney to obtain adequate separation of steam from water was about 3 m. Since only proven equipment was used, the feedwater flow control system, the pressure control system, and the pressure setpoint of the safety relief valve (SRV) opening of the DMS were assumed to be the same as for a current ABWR. The specifications of the main steam lines are highly site dependent, so they could not be set precisely. However, we found that the main steam line specifications barely affected the results of the transient analyses since the DMS has a large steam volume in the divided chimney region. Therefore, we made use of the previous input of current BWRs to set these specifications. For example, we tentatively assumed that a main steam line length of the DMS was the same as for current ABWRs.

Table 3 shows the analysis conditions for the transient performance evaluation. Referring to the licensing safety evaluation, thermal power, RPV dome pressure, and feedwater temperature were conservatively set to 105% of rated power, about 7.2 MPa, and about 489 K, respectively, which is the same as for current BWRs. Since the control rods were inserted uniformly in load rejection with total turbine bypass failure (LRNBP) and loss of feedwater heating (LFWH) events, the point-reactor kinetics model was used to evaluate the plant transient performance of the DMS. Three reactivity coefficients (void, Doppler, and scram) were assumed to be the same with a current ABWR. In addition, it was conservatively assumed that the time for inserting control rods into the core was the same with a current ABWRs, although the fuel rod length of the DMS is about half as long as current ABWRs.

4.2 Selection of Events to be Evaluated. Referring to current BWRs, generator LRNBP and LFWH were selected as critical transient events. They are the most severely recognized events as a pressure increase and a thermal power increase event, respectively.

4.3 Evaluation of LRNBP Case. Fast closure of the turbine control valves (TCVs) was initiated whenever there was an electrical grid disturbance occurring, which results in significant loss of electrical load on the generator. The TCVs were required to close as rapidly as possible to prevent excessive overspeeding of the turbine generator rotor, and at the same time, the turbine bypass valves were signaled to open in the fast opening mode. In this study, although the possibility of all of turbine bypass failure, which results in the maximum pressure increase, is realistically low, the failure of these valves was assumed conservatively. Since turbine bypass valves do not open, closure of the TCVs causes an increase in system pressure and reactor shutdown.

Figure 4 shows the analytical result. The turbine control valves were rapidly closed after the load rejection event occurred. Turbine control valves closure with the total failure of opening of turbine bypass valves generates a scram signal, then the reactor scram is initiated. Heat flux increased to about 110% of rated power at about 1.0 s, and the natural circulation flow barely changed, resulted in a maximum ΔMCPR of 0.08 at about 1.5 s, which is lower than that of LFWH case shown in the next section. The reason that the heat flux only increased to 110% was that the DMS had a large steam region volume in the divided chimney and the FSS region. As a result, the change rate of the void fraction in accordance with the pressure increase rate in the core is small.

The maximum pressure in the RPV was 7.9 MPa at about 2.8 s, since the SRVs were opened rapidly at about 2.8 s to reduce the RPV pressure.

4.4 Evaluation of LFWH Case. It was assumed that one of the six feedwater heaters was lost, and that the feedwater temperature gradually decreased from 488 K to 433 K. A decrease of feedwater temperature causes an increase of the core inlet subcooling, which can collapse the core void, and then the core power increases.

As shown in Fig. 5, the maximum heat flux, calculated using the neutron flux, increased to 121% of rated power when a scram occurred at 121 s. The maximum ΔMCPR of the DMS was 0.14. Taking into consideration the fact that the same reactor kinetics model and the analysis condition for current ABWRs were used to evaluate transient performance of the DMS, we supposed that the ΔMCPR of the DMS was almost the same as that for current ABWRs.

5 ECCS Composition and Safety Evaluation

5.1 Simple and Enhanced Safety System. The ECCS was simplified without sacrificing the performance of existing systems by adopting a hybrid system of active components and static equipment. The main features were described as follows: Adopt-

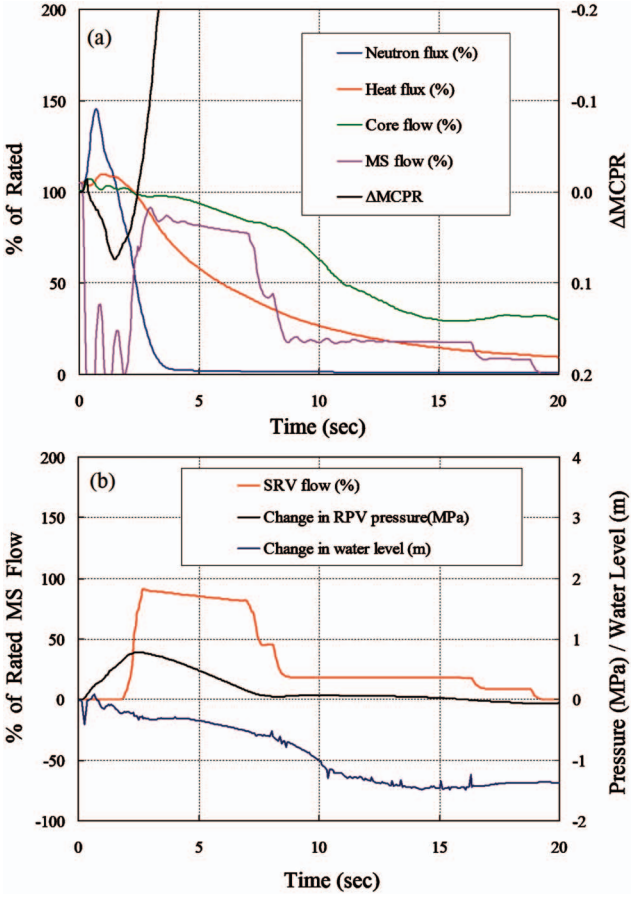

Fig. 4 Result of load rejection with total turbine bypass failure event

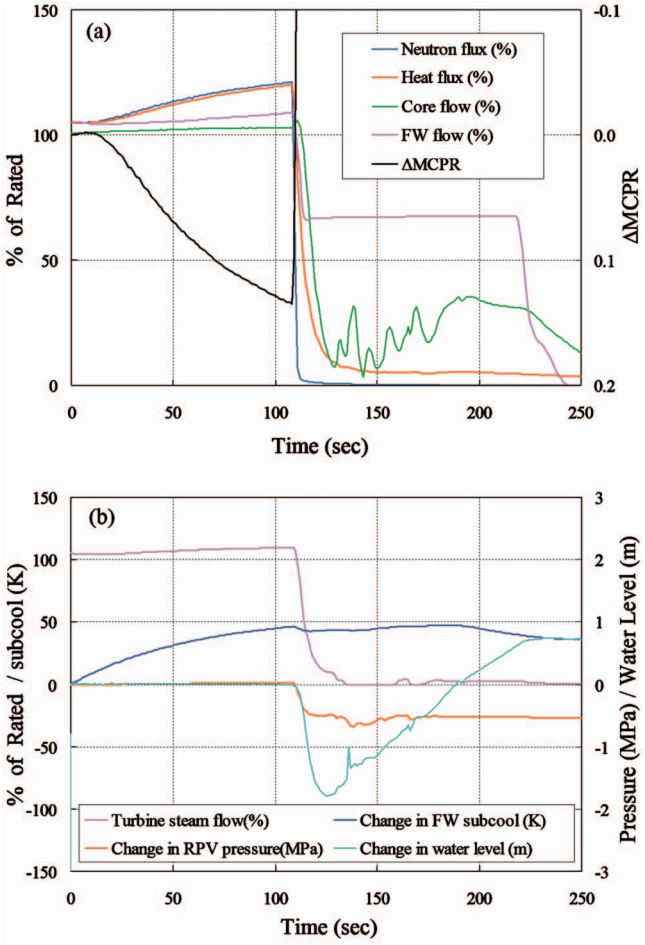

Fig. 5 Result of loss of feedwater heating event

ing passive equipment for the safety system leads to improved reliability and a reduced amount of maintenance. There is also the possibility of reducing the system scale and equipment needed through a combination of active components. The accumulator injection system that injects make-up water from the accumulator tank to the nuclear reactor for loss of coolant accident (LOCA) was adopted as passive equipment in the DMS. The accumulator injection system can inject water into the RPV at 0.5 MPa in conjunction with the automatic depressurization system (ADS), and is an effective system for short-term injection in case of LOCA. The required capacity of the high-pressure injection system could be reduced under a depressurized condition of 0.5 MPa by using the ADS; moreover, the high pressure core flooder (HPCF) system was eliminated and the necessary capacity of the reactor core isolation cooling (RCIC) system reduced by about 60%.

Since the capability for injection into the RPV and PCV from outside the PCV was improved by installing the accumulator injection system, the DMS was expected to be more robust in countering a severe accident. In other words, water from the accumulator injection system was shifted to a suppression pool or a lower drywell via the nuclear reactor. The free volume of water in the accumulator tank was equivalent in capacity to the lower drywell of the PCV being filled, for which use of the in-vessel retention (IVR) function was expected.

The number of divisions of safety functions, on the other hand, influences the divisions of separation in the power supply system, the cooling water system, and building layouts, largely affecting the amount of equipment needed. From the standpoint of improved economy, the DMS assumed a composition of three divisions like ABWR as a base, with the equipment capacity of ECCS being optimized for the DMS. Figure 6 shows the ECCS configuration chart for ABWR. Each of the three divisions within the ECCS network has one HPCF system and one low pressure flooder system (LPFL). Moreover, there is a diesel generator in each division as an emergency power source.

We initially focused on the HPCF system that affected the capacity of the emergency power source. The required flow rate of the high-pressure injection system in a small reactor becomes smaller in line with less output. However, because a pump head equal to that of a large-scale reactor is necessary, the emergency power source capacity increases, requiring pumps for both the small-flow and high-flow pump heads.

Due to the adoption of the natural circulation reactor system

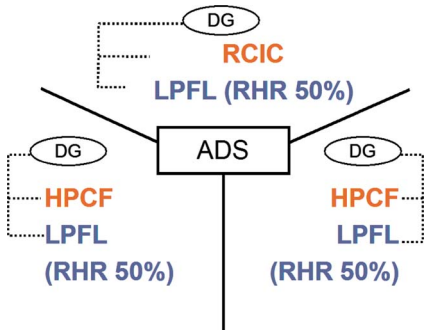

Fig. 6 ECCS configuration chart for ABWR

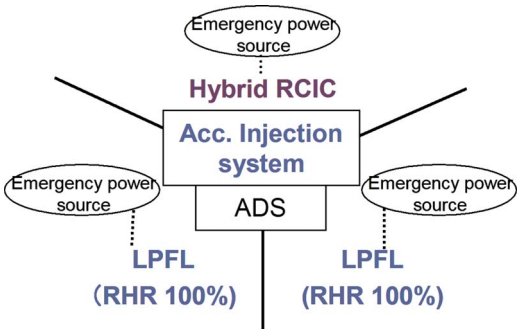

Fig. 7 ECCS configuration chart for DMS

employed in the DMS, the coolant inventory in the reactor is greater than that in a forced circulation reactor system. Moreover, adopting the accumulator injection system previously mentioned and optimizing the number of ADS valves achieved the proper injection capability, and thus the high-pressure injection system was considered unnecessary. Consequently, the capacity of the emergency power supply was reduced by about 30%.

We then focused on the LPFL system. This system has a residual heat removal (RHR) function using a heat exchanger. Given the larger heat exchangers used in existing ABWRs due to increased output, the capability was set at 50% with three divisions. However, because of its small-to-medium-sized output, no such restriction was placed on the DMS. Therefore, from the standpoint of economy, a 100%×2 division composition for the LPFL system was assumed for the DMS. In addition, a hybrid reactor core isolation cooling (RCIC) system was incorporated as a passive system, assuming the adoption of the above mentioned accumulator injection system, and the composition with the hybrid RCIC system. Past RCIC injects the coolant into the nuclear reactor by driving the RCIC turbine, which uses the high pressure steam of the nuclear reactor. By using the hybrid RCIC system, when the nuclear reactor pressure falls below pressure which is necessary to drive the RCIC turbine, hybrid RCIC pump switches its driving source to an electric motor automatically. Therefore, because the reactor core injection water becomes available at low pressure, long-term reactor core cooling can be expected. As a result, the ECCS is divided into three sections, thereby achieving high social acceptance and reliability. In addition, because a supplementary system was not needed except for a small-capacity power source for the electric motor, the amount of equipment required was reduced.

5.2 Performance Evaluation of DMS Safety Function. The ECCS composition for the DMS was determined upon examining the abovementioned considerations. Figure 7 shows the ECCS configuration chart for the DMS. The system that operated at LOCA was examined, with LOCA analysis being conducted. It was clear that reactor core flooding was maintained even when the reactor water level decreased, assuming a broken LPFL pipe as a result of analyzing the most severe case. Figure 8 shows the change in reactor water level at this time.

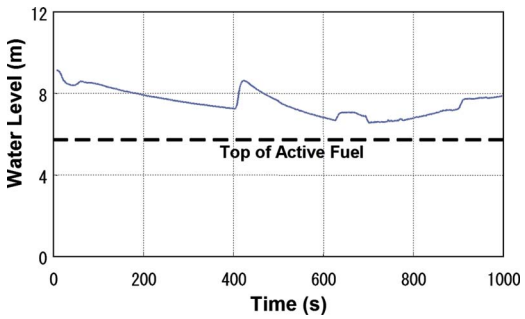

Fig. 8 Safety analysis results (LPFL breaking LOCA)

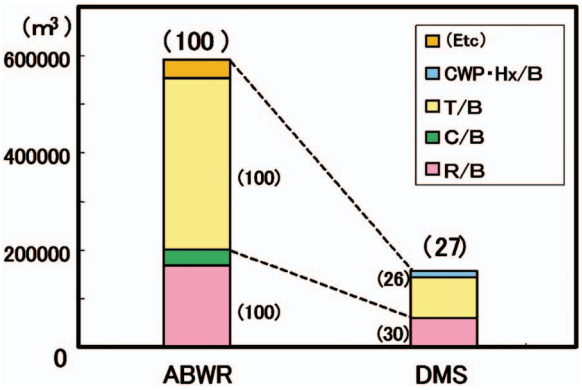

Fig. 9 Comparison of building capacity

6 Economic Evaluation

The DMS was adopted as the plant concept, targeting practical use at an early stage and with high economy. The economy of the DMS was evaluated based on building capacity as described in Sec. 4.4 and a variety of equipment, and then compared with a previous ABWR. Figure 9 compares building capacity between the ABWR and DMS. As a result, the amounts of main equipment and building capacity were both reduced, and higher economy was achieved as compared with the existing plant.

7 Conclusions

The DMS concept was developed for highly economical small and medium-sized reactors. It is based on the simplified reactor core structure, many simplified systems, and rationalized layouts. The natural circulation system and the FSS system are the main features of the simplified reactor core structure.

In this study, transient performance of the DMS was evaluated using TRACG code, which can treat multidimensional hydrodynamic calculations in the RPV. Transient performance analysis for LRNBP event and LFWH event showed that the maximum change in the ΔMCPR of LRNBP and LFWH were 0.08 and 0.14, respectively. Therefore, we confirmed that the transient performance using TRACG in the DMS concept were basically feasible.

In addition, we have confirmed the design feasibility of the DMS core. The use of large-capacity equipment, systems with integrated functions, passive systems, and nonspecific devices makes it possible to simplify many systems. It was also possible to significantly reduce building capacity for the DMS as compared with ABWR through the simplification and rationalization of systems and equipments. Moreover, by optimizing the ECCS divisions (i.e., eliminating the high-pressure injection system and adopting passive equipment in the ECCS configuration), an ECCS offering high economy and safety can be configured. Thus, a plant concept offering high economy and which alleviates the scale disadvantage was achieved through such rationalization.

Acknowledgment

The Japan Atomic Power Co. took the initiative in developing the DMS plant concept.

Nomenclature

ACC = accumulator
C/B = control building
CR = control rod
CRD = control rod drive

CUW = reactor water clean-up system
CWP = circulating water pump
DG = diesel generator
DS = dryer and separator
FDW = feedwater system
FSSCV = free standing steel containment vessel
Hx/B = heat exchanger building
MS = main steam
R/B = reactor building
RSW = reactor service water system
T/B = turbine building
TSW = turbine service water system

References

[1] Miki, M., Horiuchi, T., Yoshimoto, Y., Sumida, I., Murase, M., Akita, M., and Niino, T., 1988, "Development of Natural Circulation Small and Medium Sized Boiling Water Reactor: HSBWR-600," *The Thermal and Nuclear Power*, 39, pp. 839–853, in Japanese.

[2] Hida, T., and Ito, G., 2003, "Status of Innovative Small-Sized LWR Development in Japan," *Proceedings of the Second Asian Specialist Meeting on Future Small-Sized LWR Development*, pp. 1-1–1-4.

[3] Moriya, K., Tominaga, K., Matsuura, M., Ando, K., Yokouchi, S., Iimura, Y., and Yasuda, Y., 2003, "Basic Concept of the DMS (Modular Simplified Medium Small Reactor) as Small Sized LWR," *Proceedings of the Second Asian Specialist Meeting on Future Small-Sized LWR Development*, pp. 13-1–13-7.

[4] Ando, K., Yokouchi, S., Hirako, S., Tominaga, K., Moriya, K., and Hida, T., 2005, "Development of the DMS (1)—Plant Concept and System Design for the DMS," *Proceedings of 13th International Conference on Nuclear Engineering, ICONE13–50682*, Beijing, China.

[5] Chaki, M., Tominaga, K., Matsuura, M., Moriya, K., and Hida, T., 2005, "Development of a Small Medium Reactor (DMS) and Its Core System Characteristics," *Proceedings of 11th International Congress on Advances in Nuclear Power Plants*, Seoul, Korea, Paper No. ICAPP'05-5257.

[6] Yokouchi, S., Shimizu, Y., Inoue, S., Tominaga, K., and Hida, T., 2005, "Development of Medium Small BWR "DMS"," *Proceedings of 11th International Conference on Nuclear Energy System for Future Generation and Global Sustainability*, Tsukuba, Japan, Paper No. GLOBAL2005-454.

[7] Hino, T., Chaki, M., Tominaga, K., Matsuura, M., and Hida, T., 2006, "Development of Medium Small BWR "DMS" (Double MS: Modular Simplified & Medium Small Reactor)," *Proceedings of the International Congress on Advances in Nuclear Power Plant*, Reno, NV, Paper No. ICAPP'06-6280.

[8] Joint US EURATOM R&D Program, 1965, "Steam Separation Technology Under the Euratom Program, Part 1," Report No. ACNP-65002.

[9] Kataoka, I., and Ishii, M., 1984, "Mechanistic Modeling of Pool Entrainment Phenomenon," Int. J. Heat Mass Transfer, **27**(11), pp. 1999–2014.

[10] Hara, T., Anegawa, T., Kawamura, S., Andersen, J. G. M., Kozaki, T., and Takii, T., 1999, "TRACG Application to Licensing Analysis," *Proceedings of the Seventh International Conference on Nuclear Engineering*, Tokyo, Japan, Paper No. ICONE7-7311.